# Shielding Strategies for Human Space Exploration

Edited by
J. W. Wilson, J. Miller, A. Konradi, and F. A. Cucinotta
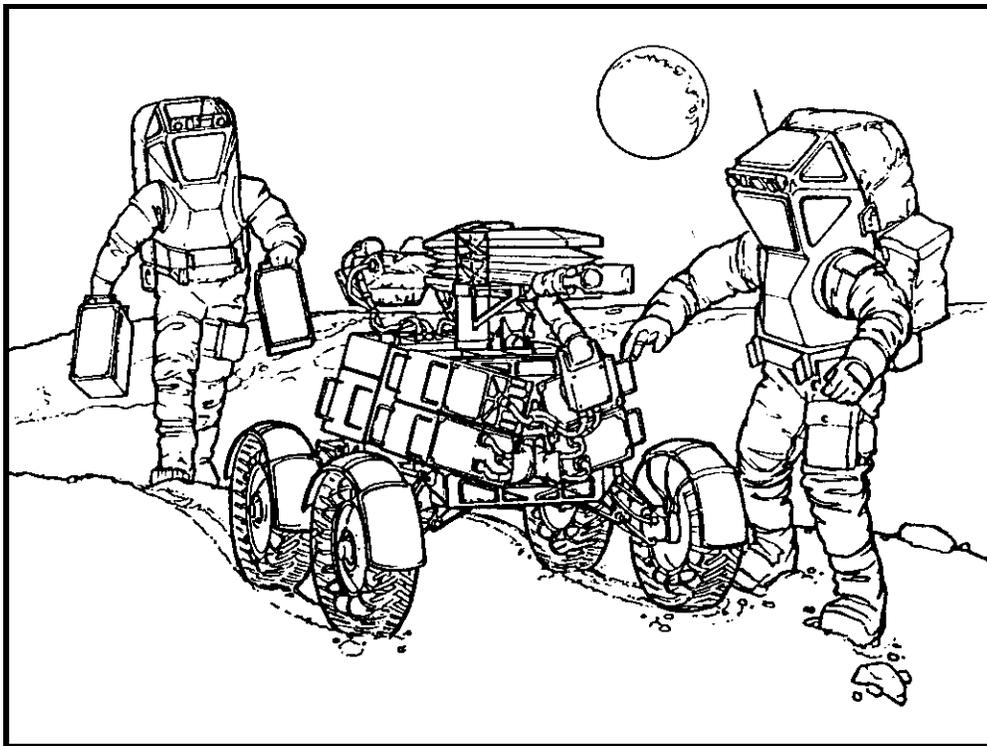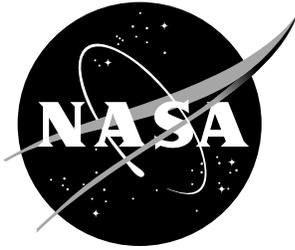
Shielding Strategies for Human Space Exploration

Edited by
J. W. Wilson
Langley Research Center • Hampton, Virginia

J. Miller
Lawrence Berkeley National Laboratory • Berkeley, California

A. Konradi
Lyndon B. Johnson Space Center • Houston, Texas

F. A. Cucinotta
Langley Research Center • Hampton, Virginia

December 1997

Cover art:

"500 kilometers from the lunar base, astronauts make quick work of a rare service call on one of the exploration-class teleoperated rovers. Drawing by Paul Hudson. Vehicle and suit design by Brand Griffin. Copyright 1993."

PREFACE

On December 6–8, 1995, a group of twenty-nine scientists and engineers representing four NASA centers and Headquarters, DOE Lawrence Berkeley Laboratory, NOAA Space Environment Laboratory, the National Academy of Science Space Science Board, aerospace industries, and several universities convened a "Workshop on Shielding Strategies for Human Space Exploration" at the Johnson Space Center in Houston, Texas. The provision of shielding for a Mars mission or a Lunar base from the hazards of space radiations is a critical technology since astronaut radiation safety depends on it and shielding safety factors to control risk uncertainty appear large. The purpose of the workshop was to define requirements for the development and evaluation of high performance shield materials and designs and to develop ideas regarding approaches to radiation shielding. The workshop was organized to review the recent experience on shielding strategies gained in studies of the "Space Exploration Initiative (SEI)," to review the current knowledge base for making shield assessment, to examine a basis for new shielding strategies, and to recommend a strategy for developing the required technologies for a return to the Moon or for Mars exploration.

The uniqueness of the current workshop arises from the expected long duration of the missions without the protective cover of the geomagnetic field in which the usually small and even neglected effects of the Galactic Cosmic Rays (GCR) can no longer be ignored. It is the peculiarity of these radiations for which the interaction physics is yet to be fully understood and for which the biological action is not yet quantified. In this light the shield characteristics in terms of their protective qualities are uncertain (or even unknown) at this time and the challenge is to provide a basis for guidance to the materials engineer in determining or developing shield materials. Other unique aspects of the workshop come from the fuller realization that the high launch cost and the resultant complexity associated with parasitic shielding require efficient use of the main architectural structure as shielding and that the factors defining that structure and the associated materials are essential knowledge elements in protecting the astronaut. Clearly, the shield design process is a multidisciplinary venture, and this diverse nature is noteworthy in the workshop attendance and content.

The backdrop for the workshop was provided by the seven papers of the first session, including an introduction to the special considerations of deep space missions, the current status of environmental knowledge, review of design studies for the SEI, review of the current uncertainties in astronaut health risks from the GCR exposures and the resultant biological response to GCR radiation components, and a review of the impact of current uncertainties on the specification of shield protective characteristics. The available GCR environmental models have greatly improved with estimated uncertainties on the order of 10 to 15 percent for the most important components, but lesser components need better definition, and the time dependence is only characterized as the intensities at successive

solar minima and maxima. Furthermore, the anomalous component is not yet included in the most recent model but will have minimal impact on shield design. Solar particle events remain problematic in the sense that the appropriate event intensity to which design should be made and the corresponding probability of occurrence are uncertain. The SEI studies have shown that shield requirements for protection against GCR in a Mars or long duration lunar mission are sufficient to protect against the historical solar events of cycles 19 through 22. Although sufficient shielding can be provided, there is still the possibility of an accidentally high exposure to a solar event during surface operations or Extra Vehicular Activity (EVA) which is more in the domain of medical practice than shielding per se. Further analysis of the GCR shield requirements demonstrate that uncertainty in the shield properties and biological response to GCR are sufficiently large that the introduction of safety factors results in unacceptably high mission costs. A focus of the workshop was the problem of making useful specific recommendations in the light of these uncertainties.

The second session of eleven papers covered the multidisciplinary database and computational procedures for shield design and the methods used in integration of the diverse databases into a workable design methodology. The required physical databases and the methods of development were covered in the first four papers of that session. The related factors which impact shielding in the domain of human operations and requirements were covered in three papers including the construction and materials in habitats, hardsuits, and rovers. Specific habitat construction technologies for a lunar base and the equipment requirements for use of *in situ* materials were covered in two papers. The methods of handling the complex geometries, including the human geometric factors and the final integration into design software for specific missions, are covered by the final two papers of the session.

The final session of four papers covered materials development, including testing issues and the validation of the design process. The use of laboratory ion beams for validation of shield material concepts and space flight validation of the design process are discussed. An assessment of the current state of knowledge and current shield issues are discussed in the final paper.

The working sessions were divided into two groups. Group A makes recommendations concerning the development of shield materials and concepts. Group B recommends a program for evaluation of shield performance and testing.

Contents

EXECUTIVE SUMMARY

The Human Exploration and Development of Space Enterprise calls for the development of space operations at costs comparable to the cost of corresponding terrestrial technologies to allow the effective exploitation of space. A critical issue is the mitigation of space related environmental hazards by means that have limited impact on developmental and operational costs. Among those environmental hazards is the exposure to space radiation which is a primary limiting factor to the duration of time allowable to any individual in the space environment. The radiation exposure health risks to the astronaut must be maintained at acceptable levels currently taken as

- Not more than 3 percent lifetime excess fatal cancer risks
- Prevention of radiation sickness which may impact mission safety (lethality, vomiting, nausea,..)

Other radiation related health risk limitations may be added as they become known. For example, functional impairment of the central nervous system may be a limiting health factor. Exposure limitation requirements to maintain acceptable levels of risk are most uncertain because there is little experience in human exposure or even animal exposure for these types of radiations on which to base such exposure limits. Current estimates on limits for whole body exposure in the LEO environment (assumed to be mainly proton exposure) are 25 cSv in any 30 day period, 50 cSv within any year, and 100 - 400 cSv within a career depending on age at exposure and gender. The 30 day exposure limit is to control early responses which may impact mission safety, while the annual and career limits are to control the cancer risks later in life and depends on the latency period for tumor development and differences in male and female sensitivity. These limits are assumed adequate for the LEO environment when protons are the main source of exposure but are not applicable when significant contributions come from the galactic cosmic rays (GCR).

Exposure limits have not been established for GCR exposures since the biological risks to the ions of high charge and energy (HZE) are not known. Using LEO exposure limits as a 'guide' to controlling health risks in deep space operations, the National Council on Radiation Protection (NCRP) estimated in their report 98 (1989) on 'Guidance on Radiation Exposures in Space' that 2.5 g/cm^2 of aluminum would be required to meet the 50 mSv annual exposure limit (used for LEO operations) based on the calculations of the Naval Research Laboratory (NRL) cosmic ray shielding code. Furthermore, the particles of high charge and energy (HZE) dominate the exposures for which the LEO exposure limitations are not applicable, resulting in large uncertainty in shield requirements since cancer induction rates from HZE particles are unknown. Aside from the uncertainty in cancer induction rates, uncertainty in shield transmission properties also limit shield design. For example, the NASA Langley Research Center HZETRN code with the first nuclear fragmentation database NUCFRG1 required 17.5 g/cm^2 of aluminum (seven times that estimated by NRL) to achieve the same annual exposure limitation. Since the Fe ions of the deep space environment contributed up to 30 percent of the estimated health risk, aluminum shield transmission

measurements were made for Fe ions at the LBL Bevalac and BNL AGS facilities resulting in the improved nuclear fragmentation database NUCFRG2. The most current estimates of shielding required to achieve the LEO exposure limits is in excess of 50 g/cm^2 of aluminum resulting in an enormously negative impact on mission developmental cost. This recent history in shield code development emphasizes the uncertainty in shield transmission factors according to current technology and the need for further study of material transmission properties at HZE accelerator facilities for not only Fe ions but the many other HZE ions found in the deep space environment.

UNCERTAINTY IN RADIATION PROTECTION

A guiding principle in radiation protection (as well as in other safety matters) is that if errors in estimating safety related factors are made they must be made in favor of the health of the astronaut. For this reason it is important to understand the sources of uncertainty and their relative magnitude. These uncertainties have a large negative impact on mission design costs and current estimates of excess design cost is over $10B for a Mars mission. An incentive in reducing shield design uncertainty is to reduce mission costs. The uncertainty in estimating the astronaut risk on a given mission within a given structure is given by lack of knowledge in three factors:

- Knowledge of the external environment
- Understanding the modifications of the external environment in reaching the spacecraft interior
- The added risk to the astronaut by exposure to the interior environment

External Environment. The uncertainty in the GCR environment near Earth (1 AU) is about 15 percent for 3 to 9 month projections and about 25 percent in long-term projections based on a solar modulation model assuming an isotropic diffusion coefficient within the solar system. The GCR intensities will increase with increasing distance from the sun as the diffusion coefficient increases approximately with the square root of the radial distance, and these effects are not defined by current models. The greatest environmental uncertainty for deep space missions is the solar event exposure. Unlike the GCR which are ever present and vary slowly over the solar cycle, the solar particle events (SPE) appear randomly within the cycle with intensities and spectral content which differ greatly from event to event. Statistical models have been developed for the low energy (10 and 30 MeV) event fluence levels near Earth and the radial gradient in approaching Mars orbit are uncertain but appear to decline as radial distance to the third power (1/r3). Statistical models in the range of 50 to 100 MeV are required but unavailable for manned mission design. A design criteria based on improved environmental models needs to be defined.

Internal Environment. Understanding the modification of the external environment by the spacecraft structure requires transport codes and adequate nuclear databases. The predicted integral LET spectra of the environment within the shuttle (a largely aluminum structure) differ from measurement by as much as 1.5-2.7 over the spectral range of 7 to 40 keV/micron with an rms error over the whole spectral range of 43 percent. Measured secondary light ion spectra differ by 30 percent for hydrogen isotopes and about a factor of 2 for helium isotopes. Measurements for materials other than aluminum (the shuttle primary material) are not available. There are no

reliable measurements of the neutron component. A primary limitation on the estimation of the interior environment within a spacecraft is the adequacy of the nuclear database defining the cross sections for the fragmentation of the incident HZE ions and the production of secondary light ions and neutrons. Systematic errors in current experimental fragmentation data will not allow the unambiguous testing of nuclear fragmentation models, and light ion production measured in shuttle measurements demonstrate the need for introducing cluster wave functions into particle knockout processes. Furthermore, the excitation energies for few nucleon removal in heavy ion fragmentation events are expected to be controlled by the nuclear core states and clustering in the outer shells of the nucleus and will strongly affect the final fragment distribution for small mass removal. The development of a nuclear structure database as input to the fragmentation models is a high priority, and experimental guidance on nuclear structure parameters is required in model validation. These structure parameters would be best evaluated in proton beam experiments where cluster knockout is observed directly, from which state parentage ratios are extracted. The final test of the fragmentation database will require systematic testing with the major components of the GCR environment with appropriate shield materials in precision laboratory measurements. As fragmentation models improve, other physical processes need to be included in the transport codes such as meson production and transport of their secondary products. Additional testing of the transport procedures and environmental models will require further experiments in space exposures with appropriate instrumentation.

Astronaut Risks. The specification of astronaut health risks requires the evaluation of the radiation fields at the specific tissues and the resulting response of those tissues to the physical insult. Use of NIH computerized anatomical data sets could improve the geometry definition of the human body and resulting estimates of the interior radiation fields at specific tissue sites. Given the radiation fields present at specific tissues, adequate tissue response models are required to estimate the health risks. It is generally regarded that space proton exposure risks are adequately represented by conventional dosimetric relationships with a linear energy transfer (LET) dependent quality factor. The uncertainty in resulting health risks are associated with a factor of 2 to 3 uncertainty in the low LET risk coefficient and a factor of 2 to 5 in the high LET risk coefficients (quality factor). Risk coefficients for HZE components are yet undefined for human risks, although data on mammalian cell mutations and neoplastic transformations and animal experiments on harderian gland tumor formation show a more complicated dependence on radiation quality than that given by a simple LET dependence. Clear evidence on biological response indicates that the energy deposited in biological tissues per unit particle path is insufficient data to define biological risks but must include the lateral spread of the energy deposit into the surrounding tissues. Such human risk models are as yet undefined and risk model development is hampered by the paucity of biological data.

Shield effectiveness. The particles transmitted through a shield material depend on the appropriate atomic and nuclear cross sections, but the effectiveness of the shield for reducing the risk to the astronaut depends on the relative contribution of those transmitted particles to the health risk. The effectiveness of a shield material is known to depend on the assumptions within the biological risk model. Even the biological endpoints within the same biological system show differing shield effectiveness for different materials. Although as a general rule, low

atomic number materials with high hydrogen content are most effective, the shield design cannot be specified until the biological response to specific ion types is fully understood.

Other factors will affect material choices, among them are structural requirements and design costs. Polymers and polymeric composites are attractive and have good structural properties. Their developmental use in the aircraft industry will provide the needed construction techniques at competitive costs. Development of specific polymeric systems for maximum shield effectiveness would be one direction of investigation for future exploration missions. Other onboard materials such as food and bio-waste can provide a protection advantage by integration into the shield design. Local materials on the lunar and Mars surfaces may likewise allow cost advantage in developing surface habitation module shielding using local materials. An adequate understanding of these materials' protective properties is a necessary prerequisite.

RECOMMENDATIONS OF THE WORKSHOP

The recommendations of the workshop were of two types: the first recommendations concerned engineering design related issues, and the second concerned the physics of the interactions. Five categories of shielding materials/concepts were recommended for further study including (1) new materials currently under development for space applications need evaluation as to their radiation transmission properties, (2) high performance shield materials need to be identified and new materials developed, (3) utilization of in-situ materials requires knowledge of their properties requiring reconnaissance and testing to design equipment for processing, (4) combinations of materials to selectively filter specific components such as boron to absorb low energy neutrons, and (5) dynamic shielding concepts including movable and active shielding components as magnetic shields and plasmas. Shield properties should be tested in laboratory experiments and in space flight. Mission impact evaluation requires a baseline mission definition and trade studies to evaluate the advantage of specific materials. It was concluded by the workshop that additional laboratory testing of transport methods and databases is required to assure accurate evaluation of shield properties. It was also agreed that sufficient accelerator time is not currently available for the task and that a means to expand the beam time available needs to be found. Environmental models for SPE events need expansion to include He ions, HZE ions, and high energy components. Uncertainties in shield effectiveness due to uncertainties in risk models need evaluation and knowledge of how those uncertainties affect shield design is needed. The track structure about specific ion tracks has not been measured, and spectral distributions about the tracks of 0.1 GeV protons and 0.6 GeV/nucleon iron ions would be a critical test of current models. Finally, the overall design codes for shields should be tested in spaceflight experiments with adequate diagnostic instrumentation before commitment to a final Mars design.

CHAPTER 1

PRELIMINARY CONSIDERATIONS

by

John W. Wilson[1]

Francis A. Cucinotta[1]

Judy L. Shinn[1]

Myung-Hee Kim[2]

Francis F. Badavi[3]

[1]NASA Langley Research Center, Hampton, Virginia 23681
[2]National Research Council—NASA LaRC Research Associate
[3]Christopher Newport University, Newport News, Virginia 23601

Chapter 1

PRELIMINARY CONSIDERATIONS

INTRODUCTION

The radiations in space are of three sources consisting of every known particle including energetic ions formed from stripping the electrons from all of the natural elements. The radiations are described by field functions for each particle type over some spatial domain as a function of time. The three sources of radiations are associated with different origins identified as those of galactic origin (Galactic Cosmic Rays, GCR), particles produced by the acceleration of the solar plasma by strong electromotive forces in the solar surface and acceleration across the transition shock in a propagating coronal mass ejection (Solar Energetic Particles, SEP), and particles trapped within the confines of the geomagnetic field. The GCR constitutes a low level background which is constant outside the solar system but is modulated over the solar cycle according to changes in the interplanetary plasma which excludes the lower energy galactic ions from the region within several AU of the sun [1]. The SEP are associated with some solar flares which produce intense burst of high energy plasma propagating into the solar system along the confines of the sectored interplanetary magnetic field [2] producing a transition region in which the SEP are accelerated. The trapped radiations consist mainly of protons and electrons within two bands centered on the geomagnetic equator reaching a maximum at 3,600 km followed by a minimum at 7,000 km and a second very broad maximum at 10,000 km [3]. The trapped radiations are experienced in passage of a spacecraft from Low Earth Orbit (LEO) to interplanetary space and can be of some importance if the passage time is more than several minutes. The main focus of the workshop is on the long time spent outside the earth's magnetic field where exposures of concern are the SEP and the GCR.

In prior manned space missions, the GCR have been considered negligible since the mission times were relatively short and the main radiation concern was the very intense SEP events which can rise unexpectedly to high levels, delivering a potentially lethal dose in a few to several hours which could cause death or serious radiation illness over the following few days to few weeks if precautions are not taken [4]. The most intense such event known occurred on August 4–5, 1972 between the Apollo 16 and Apollo 17 missions [5]. The potential effects of this event on a lunar landing has been a source of popular speculation [6]. Such events continue to be a concern to space operations.

Deep space missions introduce a new challenge to astronaut protection as the accumulation of exposures to GCR ions can significantly increase the risks of cancer to the astronaut [7]. It is interesting to note that limitation of GCR cancer induction in long-term deep space missions provides sufficient protection against the early effects of SEP events unless the astronaut is away from his ordinary protective quarters as he would be on EVA or surface exploration in an unshielded or lightly shielded rover [8]. A large contribution of the exposure to astronauts is contributed by the ions of high charge and energy (HZE) for which there is little experience on the examination of shield properties [8] or biological response [9]. Studies have been made on the physical processes by which HZE ions interact with other nuclei in the search for unique states of nuclear matter [10], but little work has been done for high accuracy cross sections and particle yields necessary as a database for shield evaluation [11, 12]. In order to develop shielding technology, we have had to rely on nuclear model calculations which are evaluated by comparison with the limited available experimental data [13, 14]. Of the cross section and yield measurements that have been made, the experimental systematic errors are sufficiently large to limit model evaluation [15, 16].

The unusual character of the HZE ions [17] is illustrated in figure 1. In the figure are tracks of cosmic ions as seen in nuclear emulsion. The energy deposited in the emulsion is mediated by secondary electrons produced by the interaction of the passing ion with the atomic electrons of the emulsion. The proton on the left is losing energy at the rate (Linear Energy Transfer, LET) of 2–3 keV/micron compared to the Fe ion of 1,200–1,900 keV/micron. The electrons recoil from the ion impact at up to twice the speed of the passing ion and propagate the energy tens of microns from the ion path, giving width to the track as shown in the figure [18]. A mammalian cell is on the order of several tens of microns with a nucleus on the order of 10 microns containing most of the encoded DNA required for cell function and replication. A single Fe ion will deposit a significant amount of its energy in passing through the cell. An equal amount of energy (same dose) would require several hundred protons, which would be randomly distributed over the cell interior in distinction to the Fe ion, which if passing through the nucleus, is a devastating event. Vast differences in biological response are expected and are in fact observed, as will be discussed by Drs. Stan Curtis and Tracy Yang. It will become apparent that the lateral extent of the track will be an important parameter in predicting biological action in addition to the usual parameter of LET [19]. As yet a clear understanding of the risks to the astronaut from such ions is lacking [7].

In view of the lack of understanding the biological effects and the corresponding dosimetry of such ions, the astronauts exposure risk might best be placed on a risk basis as opposed to limiting dose equivalent as is done in terrestrial exposures [20]. It has been recommended that a three percent risk of excess fatal cancer for a career exposure of the astronaut would be acceptable [7]. This is about the same as the risk currently recommended for a terrestrial radiation worker earning a living at an industrial, medical, or research facility—estimated as about three to four percent [21]. A second risk limit is imposed on the astronaut due to the potential exposure to SEP, for which any effects of early radiation illness (lethality, vomiting, nausea, ...) is to be prevented [7]. Of course the means of predicting astronaut risks are limited by the lack of understanding of the biological action of the HZE ions, which is a topic of intense interest to the NASA Radiation Health Program [22].

Shield design

The shield design problem consists of three parts. The first step is to predict the astronaut risk for a given mission scenario and corresponding design architecture to accomplish the mission. If the astronaut's risk is higher than acceptable limits, then a redesign phase must be attempted until an acceptable risk is achieved [23, 24]. One must evaluate construction methods for the design in terms of mission objectives and costs before the mission design is approved. These steps are shown in figure 2. One must then demonstrate that the resulting risk is in accordance with the protection principle [7] of keeping the risk As Low As Reasonably Achievable (ALARA).

Since the shield encompasses the full spacecraft structure, the architectural design and material choices are important [23, 24]. The architecture is set by not only the mission objectives but by human related factors such as efficient human performance [23, 24], living quarters, work areas, other protection and support systems (meteoroid bumper, hardsuit design, heat shield composition, food and water storage, biowaste management, ...). Even such factors as to where the astronaut spends his leisure time and work activity are important. The methods of construction also impact the overall exposure (onsite EVA, local material composition, ...). Mission objectives such as surface exploration and the need to provide local protection (perhaps using a rover vehicle) and the relation of the mission to the solar cycle are all important mission related factors. The iterative design process shown in figure 2 is a multidisciplinary activity and requires efficient computational procedures for evaluation of the associated astronaut risk to allow appropriate trade studies in the design process. This multidisciplinary nature of the design process became most apparent in the Space Exploration Initiative studies of the recent past, and those studies will be reviewed by John Nealy and Lisa Simonsen.

Human performance factors and their implications for shielding choices are reviewed by Dr. Barbara Woolford. Construction technologies for a lunar base in which the issue of using local materials as opposed to prefabricated structures to be transported to the moon is given by Lisa Simonsen. The equipment needs for excavation of local materials to be formed into shielding structures, including operational requirements, is reviewed by Dr. Leslie Gertsch. The development of hardsuits and their inherent shielding materials for lunar construction or exploration is reviewed by Dr. Bruce Webbon. The rover required for surface operations is reviewed by John Connolly.

Another complicating factor in the shield design process is the possible use of active shield elements such as magnetic fields [25]. Preliminary analysis on the use of super conducting magnetic technology indicates some usefulness in reducing the health risk from SEP but little value in protection from GCR. Equivalent protection is derived for GCR by turning the magnetic field off and allowing the apparatus to act as a passive shield with an improved mass distribution. Better yet is to replace the apparatus with an equal mass of polyethylene, which provides more protection at greatly reduced cost and results in a system exhibiting no single point failure mode as does the cryogenic system of the superconductor magnetic shield system. Although the development of high temperature superconductors may improve the reliability, the problem of the massive structural elements to support the field remains problematic.

Risk estimation

The central element in shield evaluation is the estimation of risk to the astronaut and the control of that risk through choice of material arrangement and composition. We may ask the question as to the knowledge requirements to allow such an estimation. The essential features of risk evaluation are shown schematically in figure 3. First the external environment as the associated particle fields present at the spacecraft location as a function of time must be given. The most recent environmental models and their associated uncertainty will be discussed by Dr. Badhwar. The exterior environment interacts with the shield structure, consisting of the full architecture including equipment and supplies for the mission. The transmission properties of each architectural element must be known as well as the geometric arrangement in order to evaluate the radiation fields within the structure to which the astronaut is exposed. Due to the irregular geometric structure the interior environment is highly anisotropic with large spatial gradients [23, 24]. The interior environment is further modified in arriving at the local tissues within the astronauts body and depends on the transmission properties of the astronaut tissues and the geometric arrangement of those tissues relative to the anistropies and gradients of the interior fields [26]. These factors place demands on the evaluation of the fields at the local tissue sites within the astronaut's body under the conditions of a dynamic geometry and temporally fluctuating boundary condition.

To evaluate risk to the astronaut we must further evaluate the energy absorption events within the local tissues [20, 27]. Such events depend on the particle environment at the local tissue site as discussed but also an evaluation of the secondary electron fields about the ion paths [28]. Within the highly correlated electron fields is the information on track structure and LET which forms the basis for evaluation of biological response [7, 29, 30]. Dr. Cucinotta will review the computational models for evaluation of the transmission properties including the associated nuclear models which affect the particle fields and the associated atomic interaction models used in handing off the energy to the highly correlated secondary electron fields in local tissues near the ion path. Our current state of knowledge on electron production in ion-atom collisions is reviewed by Dr. Eugene Rudd.

The coupling to biological response models requires a knowledge of the internal structure of the cell and the sensitivity of those structures to the spatially dependent electron fields [30]. The NCRP recommended that the dose equivalent with the associated low LET cancer risk coefficients could be used as a guideline for preliminary studies of space exploration [7]. Indeed the studies during the Space Exploration Initiative (SEI) of a few years ago were all commissioned on the basis of dose equivalent as the means of estimating astronaut risk. These past studies will be reviewed by John Nealy and Lisa Simonsen. The use of dose equivalent with its associated LET dependent quality factors assumes that the biological risk is independent of the width of the ion track. The uncertainty associated with this system of dosimetry will be discussed by Dr. Curtis. Dr. Yang will then review the biological evidence for track width dependent effects observed in biological systems tested at HZE ion accelerator facilities. In that the purpose of shielding is to reduce biological effects of the exposure, the impact of track structure dependent effects on evaluation of shield worth is also reviewed by J. W. Wilson.

The elements required in the evaluation of astronaut risk for a specific mission is indicated in figure 4. Each block is associated with a particular computation procedure or database. The dashed boxes indicate the experimental hardware used to characterize the environment in validation experiments either in the laboratory or in flight. The risk evaluation is implemented in a larger system analysis context in which the associated databases and computational procedures are integrated for mission analysis as reviewed by John Nealy and Garry Qualls. In practice, shielding is never an isolated issue and modern computational procedures allow shielding to be integrated into the full mission design process.

Shield technology requirements

In the implementation of the system indicated in figure 4, there are requirements which must be addressed to allow the operation within the design methodologies for shielding in deep space exploratory missions. Fast computational codes are required to evaluate risks in design trade studies. The codes need to be evaluated in laboratory experiments [31] to ensure that the material transmission characteristics are accurately represented by the computational model and the associated atomic and nuclear database [32]. Dr. Miller will review the current status on code and database validation. The final connection to biological models is through the highly correlated electron fields within the astronaut tissues and relies on the accurate representation of the atomic collision processes which is reviewed by Dr. Rudd. The development of adequate astronaut risk models remains an important issue to be resolved [22].

In the design process one develops the shield design concept which must be validated by laboratory testing. The development of required materials testing and processing techniques is reviewed by Dr. Thibeault. The accuracy of the astronaut risk estimates rely on the validity of the design methods used and the current lack of adequate testing leaves uncertainty in the design. It is currently mandatory that the specific testing of the final design in controlled laboratory experiments be performed to ensure that the design will perform as predicted [32]. The shield laboratory validation effort is reviewed by Dr. Miller. Although laboratory testing will allow evaluation of the predicted transmission properties of specific ion types the final astronaut risk depends on other quantities such as the specific environment and the spacecraft and body geometry. Adequate testing of the integrated design process including environmental models can only be accomplished under flight conditions and especially with human phantoms. The validity of such test requires definitive onboard instrumentation to allow evaluation of the environmental components important to biological injury [33]. The flight validation of shielding concepts will be discussed by Dr. Badhwar.

An added demand on shield technology is the requirement to support space biology experiment design and analysis within the NASA Space Radiation Health Program's efforts to provide a scientific basis for evaluation of astronaut risk on future NASA missions [22]. The primary thrust of the program is to relate ground based biology data to exposure conditions in the space environment. The relation of biology data obtained in ground studies in which restrictions on particle types and energies in the earth's 1-g field must be modified by computational models

to estimate the biological response in the complex space radiation environment, and microgravity places demands on the ability of computational shield models to accurately specify the transmitted particles through the shield materials. Otherwise the effects of microgravity in the space experimental results will be obscured by computational inaccuracy unless highly reliable methods of evaluation of the transmitted particle environment, within the spacecraft structure is provided to the space biology experimentalist. This places great demands on the physical description and the corresponding computational models used which must be carefully validated prior to the final analysis of the space biology data.

Risk uncertainty and mission costs

There are several current issues alluded to in the foregoing which need to be resolved. The transmission properties of shield materials and astronaut tissues are uncertain as is our knowledge of the energy absorption events at local tissue sites, and the resulting biological response is also poorly understood [34]. Such issues require additional testing in both laboratory and flight experiments. The net result of current uncertainties is overly conservative designs and excessive mission construction and launch costs [35]. A study of the effects of risk uncertainty on mission cost were made with the following assumptions. The uncertainty in the astronaut risk consists of the biological risk uncertainty from HZE exposure components (δ_b on the order of a factor of 5 to 10) and the uncertainty in the transmission factors [36, 37] for the HZE components (δ_t on the order of a factor of 2 to 3). The design of the shield must incorporate a safety factor to ensure the risks incurred by the astronaut on the mission are within accepted limits. The safety factor required by the uncertainties are used as a basis for estimating the excess shield cost as a function of level of uncertainty. The mission cost of the Apollo program is used as the cost model with an added factor for the Mars mission. The result is shown in figure 5. If the biological uncertainty is reduced to a factor of 3 as a result of a vigorous radiobiology program, then the excess mission cost could be as large as $40B. If in addition to reducing the biological uncertainty to a factor of 3, the uncertainty in the transmission factors are reduced to the 10 percent level, then an added $30B reduction in excess mission cost would be achieved. It is clear from these results that the research costs associated with reducing the uncertainty in the biological response and the shield transmission properties would be small compared to the impact on the mission cost.

Current obstacles in shield technology development

Space experiments alone cannot support the high resolution studies required to improve our knowledge of shield transmission properties for several reasons. The space radiations are mixed field components. The particle types, the direction of incidence, as well as the energy is poorly known for specific events within the shield material. Furthermore the count rate is low and the resulting poor statistics will not allow unambiguous testing of models. The instrumentation for space experiments are of low resolution compared to typical laboratory equipment so that the data obtained is of limited quality. Perhaps the largest obstacle is the large cost of space experimentation compared to that in the laboratory.

It follows that the primary obstacle to the development of HZE shielding technology is the lack of a dedicated HZE accelerator. Experiments now progress only with the availability of 1–2 weeks per year at the Brookhaven National Laboratory AGS for space shielding and biology experiments. Although such a program is helpful it will not likely resolve the many uncertainties now present in astronaut risk estimation. Still, such laboratory experiments are required to develop high precision models of the material transmission properties.

Although the laboratory validation experiments are indispensable, the space flight experiment's role is likewise indispensable and totally complementary. Only by space experimentation can we ensure that the space environmental models, the material transmission models, and the spacecraft geometry models work together properly to evaluate the interior environment to the required degree of accuracy. Only through a combined effort of laboratory and space flight validation can we be assured that the exposure fields to which the astronaut is subjected are adequately defined.

Workshop objectives

The objectives of the workshop are three-fold. First is a review of the status of shield design technology. What do we know about the environment, the material transmission properties, and the relation to astronaut risks. The knowledge utilized in the SEI studies and how was it integrated into the shield design process is reviewed. The knowledge limitations on the SEI studies and the impact on mission objectives and costs are examined.

Second, we will seek to define clearly the knowledge requirements for shield design in deep space missions. We will seek a logical basis for controlling astronaut radiation risks. We will seek answers to the questions: How can we ensure we can build what we design? How can we be sure the design has in fact achieved the desired risk limitation? Is it possible to quantify these requirements into a handbook? What is the best approach to achieving our goals?

Third, what is required to further shield design technology? Must we have accurate knowledge of the biological response? How can we improve our understanding of the HZE transmission properties? Can we progress without HZE laboratory studies? Are there inexpensive space flight experiments to accomplish our goals and can we demonstrate this is true?

REFERENCES

1. G. D. Badhwar, F. A. Cucinotta, P. M. O'Neill: Depth-dose relationships for cosmic rays at various solar minima. *Radiat. Res.*, **134**: 9–15, 1993.

2. D. F. Smart, M. A. Shea: Solar proton events during the past three solar cydes. *J. Spacecraft and Rockets*, **26**: 403–415, 1989.

3. E. G. Stassenopolous: Charged particle radiation exposure of geostationary satellites. *High-Energy Radiation Background in Space*, A. C. Rester, Jr., J. I. Trombka, eds. AIP Conference Proceedings 186, New York, pp. 3–63, 1986.

4. J. W. Wilson, F. M. Denn: Preliminary analysis of the implications of natural radiations on geostationary operations. NASA TN D-8290, 1976.

5. J. E. Nealy, L. C. Simonsen, S. A. Striepe: Natural radiation environment fluence and dose predictions for missions to the moon and Mars. Proceedings of the New Horizons in Radiation Protection and Shielding, April 26–May 1, American Nuclear Society, La Grange Park, Illinois, pp. 181–187, 1992.

6. J. A. Michener: Space, Random House, New York, 1982.

7. National Council on Radiation Protection and Measurements: Guidance on radiations received in space activities. NCRP Rep. No. 98, 1989.

8. J. W. Wilson, L. W. Townsend, W. Schimmerling, G. S. Khandelwal, F. Khan, J. E. Nealy, F. A. Cucinotta, L. C. Simonsen, J. L. Shinn, J. W. Norbury: Transport methods and interactions for space radiations. NASA RP 1257, 1991.

9. W. Schimmerling: Radiobiological problems in space—an overview. *Radiat. & Environ. Biophys.,* **31**: 197–199, 1992.

10. D. Strottman: Status of Fluid Dynamic Models for Relativistic Heavy Ion Reactions. *Nuclear Physics,* **A566**: 245c–256c, 1994.

11. J. W. Wilson, L. W. Townsend, F. F. Badavi: A semiempirical nuclear fragmentation model. *Nuclear Instrum. & Methods*, **B18**: 225–231, 1987.

12. J. Miller: Ground-based simulations of galactic cosmic ray fragmentation and transport. *Adv. Space Res.,* **14(10)**: 831–840, 1994.

13. F. A. Cucinotta: Forward production of protons in relativistic 12-C-nucleus collisions. *J. Phys. G: Nucl. Parl. Phys.*, **20**: 1803–1815, 1994.

14. L. W. Townsend, J. W. Wilson, R. K. Tripathi, J. W. Norbury, F. F. Badavi, F. Khan: HZEFRG1: An energy dependent semiempirical nuclear fragmentation model. NASA TP 3310, 1993.

15. J. W. Wilson, J. L. Shinn, L. W. Townsend, R. K. Tripathi, F. F. Badavi, S. Y. Chun: NUCFRG2: A Semiempirical Nuclear Fragmentation Model. *Nucl. Instr. Meth.*, **B94**: 95–102, 1994.

16. J. W. Wilson, R. K. Tripathi, F. A. Cucinotta, J. L. Shinn, F. F. Badavi, S. Y. Chun, J. W. Norbury, C. J. Zeitlin, L. L. Heilbronn, and J. Miller: NUCFRG2: An Evaluation of the Semiempirical Nuclear Fragmentation Database. NASA TP 3533, 1995.

17. F. B. McDonald: Review of galactic and solar cosmic rays. Second Symposium on Protection Against Radiations in Space, NASA SP-71, 1965.

18. R. Katz, E. J. Kobetich: Particle tracks in emulsion. *Phys. Rev.*, **186**: 344–351, 1969.

19. R. Katz, B. Ackerson, M. Homayoonfar, S. C. Sharma: Inactivation of cells by heavy ion beams. *Radiat. Res.*, **47**: 402–405, 1971.

20. S. B. Curtis, J. E. Nealy, J. W. Wilson: Risk cross sections and their application to risk estimation in the galactic cosmic ray environment. *Radiat. Res.*, **141**: 57–65, 1995.

21. National Council on Radiation Protection and Measurements: Limitation of exposure to ionizing radiation. NCRP Report No. 116, 1993.

22. W. Schimmerling: Space and radiation protection: Scientific requirements for space research. *Radiat. Environ. Biophys.*, **34**: 133–137, 1995.

23. L. C. Simonsen, J. E. Nealy, L. W. Townsend: Concepts and strategies for lunar base radiation protection: Prefabricated versus *in situ* materials. SAE Technical Paper Series No. 931370, 1992.

24. J. E. Nealy, J. W. Wilson, and L. W. Townsend: Solar flare shielding with regolith at a lunar base site. NASA TP-2869, 1988.

25. L. W. Townsend, J. W. Wilson, J. L. Shinn, J. E. Nealy, L. C. Simonsen: Radiation Protection Effectiveness of a Proposed Magnetic Shielding Concept for Manned Mars Missions. SAE Technical Paper Series No. 901343, 20th Intersociety Conference on Environmental Systems, Williamsburg, VA, July 9–2, 1990.

26. J. W. Wilson, J. E. Nealy, J. S. Wood, G. D. Qualls, W. Atwell, J. L. Shinn, L. C. Simonsen: Variations in astronaut radiation exposure due to anisotropic shield distribution. *Health Phys.*, **69**: 34–45, 1995.

27. J. W. Wilson, M. Kim, W. Schimmerling, F. F. Badavi, S. A. Thibeault, F. A. Cucinotta, J. L. Shinn, R. Kiefer: Issues in space radiation protection: Galactic cosmic rays. *Health Phys.*, **68**: 1–9, 1995.

28. F. A. Cucinotta, R. Katz, J. W. Wilson, R. R. Dubey: Radial dose distributions in the delta-ray theory of track structure. AIP Proceedings, **362**: 245–265, 1996.

29. F. A. Cucinotta, J. W. Wilson: Initiation-promotion model of tumor prevalence in mice from space radiation exposures. *Radiat. Environ. Biophys.*, **34**:145–149, 1995.

30. R. Katz, R. Zachariah, F. A. Cucinotta, C. Zhang: Survey of cellular radiosensivity parameters. *Radiat. Res.*, **140**: 356–365, 1994.

31. C. J. Zeitlin, K. A. Frankel, W. Gong, L. Heilbronn, E. J. Lampo, R. Leres, J. Miller, W. Schimmerling: A modular solid state detector for measuring high energy heavy ion fragmentation near the beam axis. *Radiat. Meas.*, **23**: 65–84, 1994.

32. W. Schimmerling, J. Miller, M. Wong, M. Rapkin, J. Howard, H. G. Speiler, B. V. Jarrert: The fragmentation of 670 AMeV neon-20 as a function of depth in water. I. Experiment. *Radiat. Res.*, **120**: 36, 1989.

33. G. D. Badhwar, F. A. Cucinotta, L. A. Braby, A. Konradi: Measurements on the shuttle of the LET spectra of galactic cosmic radiation and comparison with the radiation transport model. *Radiat. Res.*, **139**: 344–351, 1994.

34. F. A. Cucinotta, L. W. Townsend, J. W. Wilson, J. L. Shinn, G. D. Badhwar, R. R. Dubey: Light ion components of the galactic cosmic rays: Nuclear interactions and transport theory. *Adv. Space Res.*, **17(2)**: 77–86, 1996.

35. J. W. Wilson, J. W. Nealy, W. Schimmerling, F. A. Cucinotta, J. S. Wood: Effects of radiobiological uncertainty on vehicle and habitat shield design for missions to the moon and mars. NASA TP-3312, 1993.

36. L. W. Townsend, F. A. Cucinotta, J. W. Wilson: HZE reactions and database development. In *Biological effects and physics of solar and galactic cosmic radiation,* eds. C. E. Swenberg et al., Plenum Press, New York, pp. 787–811, 1993.

37. J. L. Shinn, S. John, R. K. Tripathi, J. W. Wilson, L. W. Townsend, J. W. Norbury: Fully energy dependent HZETRN (A galactic cosmic ray transport code). NASA TP 3243, 1992.

| H | He | Li | Be | B | C | N | O |
| Z = 1 | Z = 2 | Z = 3 | Z = 4 | Z = 5 | Z = 6 | Z = 7 | Z = 8 |

50 μm

| Ne | Na | Mg | Si | Ca | Ti | Fe |
| Z = 10 | Z = 11 | Z = 12 | Z = 14 | Z = 20 | Z = 22 | Z = 26 |

50 μm
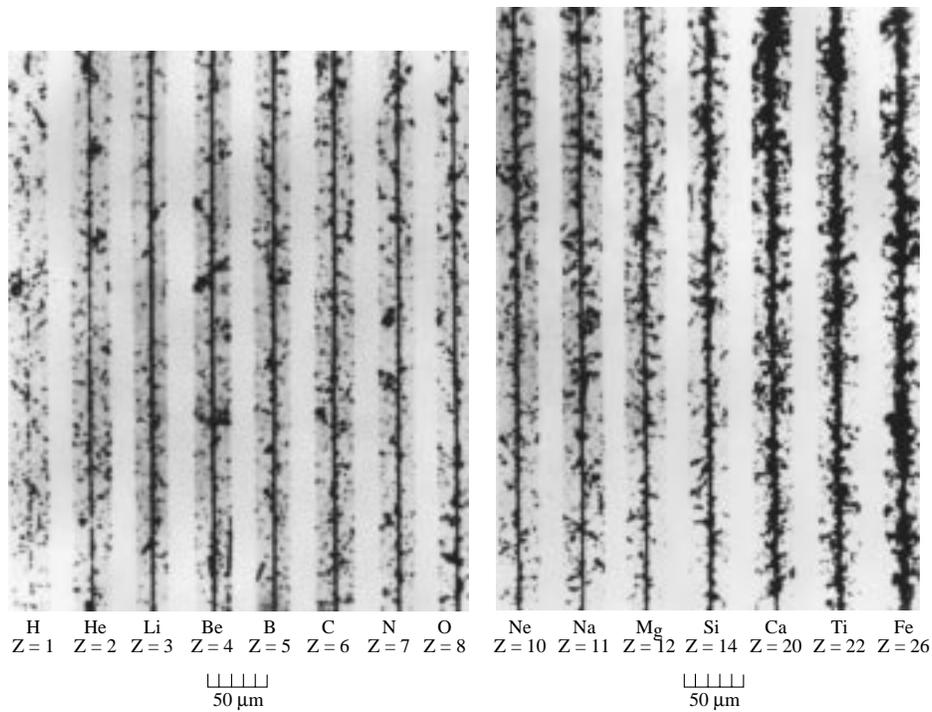
Figure 1. Cosmic-ray ion tracks in nuclear emulsion. (Taken from McDonald, 1965.)
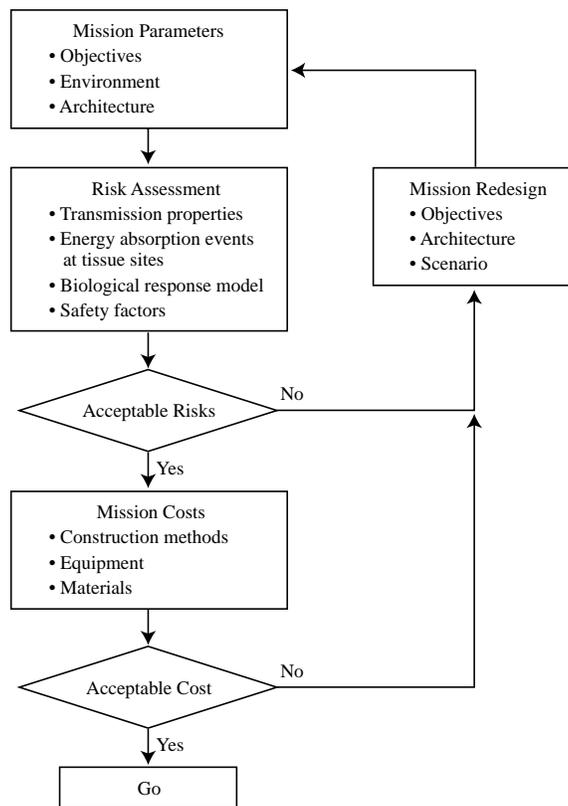
Figure 2. Integrated radiation shield design process.

1. External environment
    a. Trapped radiations
    b. Solar flare particles
    c. Galactic cosmic rays

2. Interior environment
    a. Transport properties
    b. Shield geometry
    c. Computational procedures

3. Energy absorption events at
    specific tissue sites
    a. Tissue transport properties
    b. Human geometry
    c. Computational procedures

4. Astronaut risk model
    a. Track structure and high LET effects
    b. Protracted and frationated components
    c. Extrapolate the low LET, single exposure
   database

Figure 3. Astronaut risk assessment knowledge requirements.
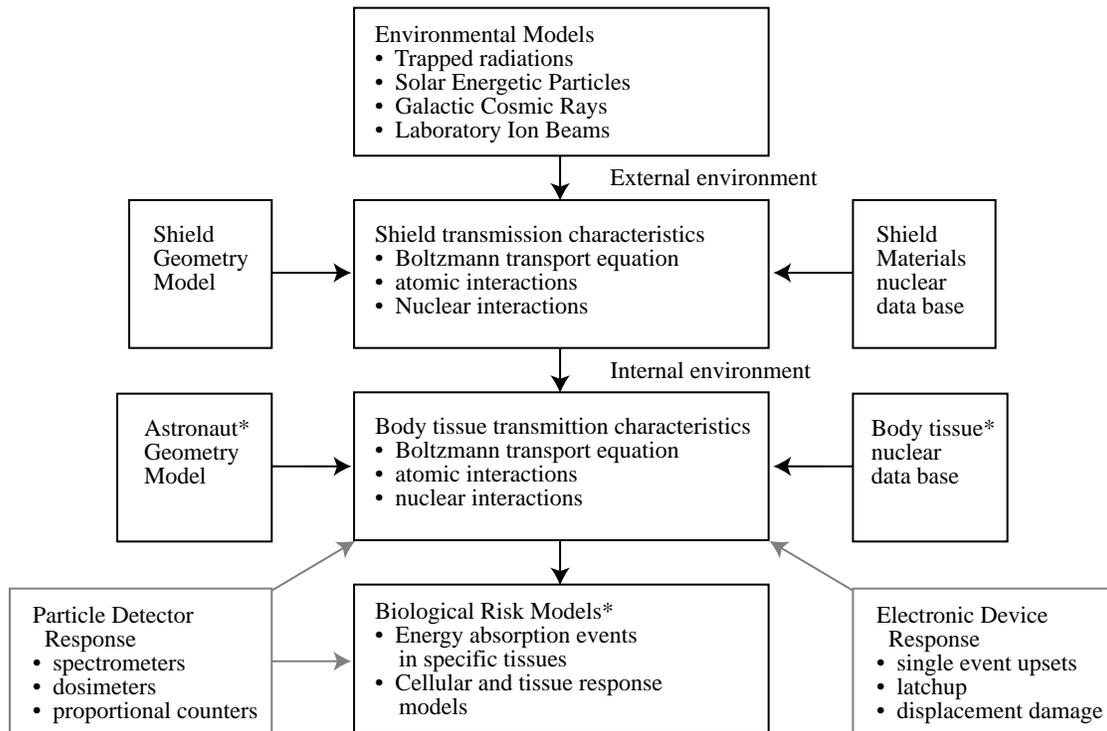

Figure 4. Components of space shield design technologies.
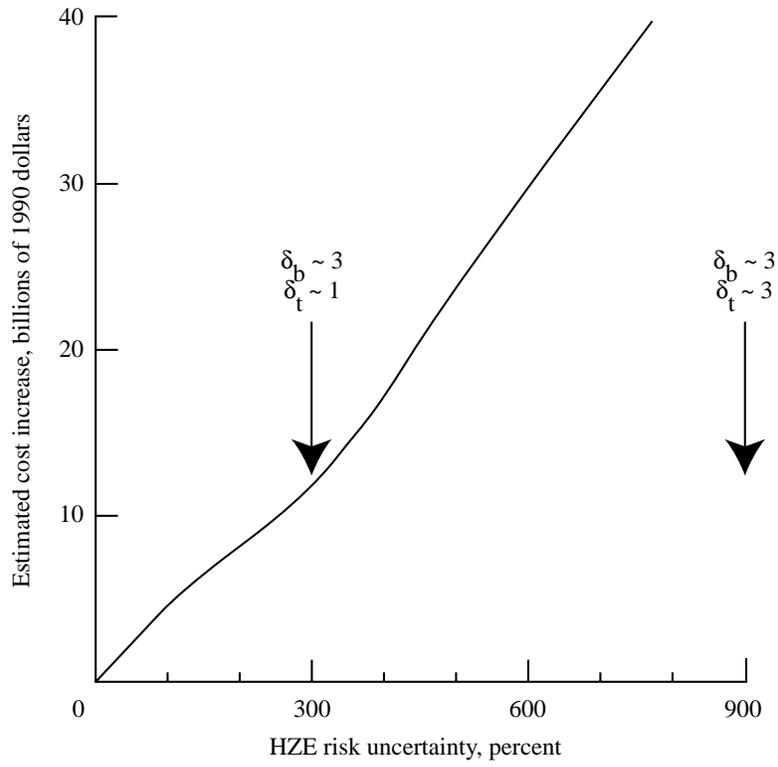
Figure 5. Mars mission costs increase dramatically with risk uncertainty.

CHAPTER 2

DEEP SPACE RADIATION SOURCES, MODELS, AND ENVIRONMENTAL UNCERTAINTY

by

Gautam D. Badhwar[1]

[1]NASA Johnson Space Center, Houston, Texas 77058-3696

Chapter 2

DEEP SPACE RADIATION SOURCES, MODELS, AND ENVIRONMENTAL UNCERTAINTY

SUMMARY

There are three major sources of charged particle radiation in free space: (1) Galactic Cosmic Radiation (GCR), (2) Solar Energetic Particles (SEPs), and (3) Anomalous Cosmic Radiation (ACR). Reaccelerated SEPs (RESPs) are also present but play a relatively minor role. We briefly review each of the major components and describe their current descriptive model.

GALACTIC COSMIC MODEL

GCR come from outside our solar system (a region extending nearly 100 AU from the sun). The GCR contains particles of all charges from protons to uranium nuclei with energies from a few MeV/n to nearly 10^{15} MeV/n. Figure 1 shows the "quiet-time" energy spectra for H, He, C, N, and O measured at 1 AU (IMP-7 and IMP-8). The basic characteristics of these spectra are the peaks near a few hundred MeV/n with flux falling away at both lower and higher energies. The upturn of flux around 30–40 MeV/n is due to the ACR component.

The basic requirements for any phenomenological cosmic radiation model are (1) correctly reproduce the elemental abundances as a function of energy/nucleon, (2) correctly reproduces the energy spectra of all the major elements (H, He, C, O, Si, and Fe nuclei), (3) correctly reproduces the energy spectra of secondary particles (Li, Be, B nuclei), (4) correctly models the observed solar cycle dependence of flux at 1 AU, (5) has capability to predict, with reasonable accuracy, GCR spectra in the future, (6) can take the isotopic composition into account (mean mass), and (7) has the capability to extrapolate the current observation towards the outer heliosphere. Following these basic requirements, Mewaldt *et al.* [1] suggested that the differential energy spectrum, $j\left(Z,E,t,r,q,f\right)$, be expressed in terms of separable terms:

$$j = j_o(Z,E) \times F_t(Z,E,t) \times F_r(Z,E,t) \times F_q(Z,E,t) \times F_f(Z,E,t) \qquad (1)$$

where $j_o(Z,E)$ is the local interstellar spectrum of particle with charge Z, and the four terms $F(Z,E,t)$ are the time, radial, heliolatitude, and heliolongitude dependent functions respectively. The angular terms are important for relatively low energy particles and are not considered further. The radial gradient can be taken into account in

models to be described below fairly easily, although this is not a particularly large effect for Mars-type manned missions. We thus focus on the time-dependent function for solar modulation.

The first significant descriptive model of the cosmic ray environment was made by Adams *et al*. [2, 3] in their model called the CREME model. This model provided a reasonably accurate characterization of the cosmic ray composition and energy spectra. There were two drawbacks of this model: (1) the solar modulation effects were predicted in terms the solar F10.7 flux, and (2) He was used as a reference spectrum for $3 \leq Z \leq 16$. The F10.7 does not track solar modulation. ^{3}He has contributions up to 25% of the total He component, depending on the energy/nucleon, and because of its different charge to mass ratio than ^{4}He and "secondary" GCR nuclei, leads to significant errors in their spectra. It however remains a very useful model.

There are four new models, all pretty much based on the standard diffusion-convection theory of solar modulation by Badhwar and O'Neill [4], Nymmik *et al*. [5], Adams and Lee [6] and Chennete *et al.* [7]. All of these represent a significant improvement over the CREME model. They incorporated the most recent data on composition and spectra. We refer the reader to the reference paper by Badhwar and O'Neill [4] for details and the relative accuracy.

Figure 2 shows the 1973 data on H, He, O, and Fe and prediction of the Badhwar and O'Neill model. The fits are fairly good. Figures 3 and 4 give the predicted worst case solar minimum and solar maximum, differential and integral energy spectra for these four nuclei. By correlating the deceleration parameter, $\phi(t)$, with both the neutron monitor rate and the sunspot number, this model has the capability to predict GCR spectra roughly 3 and 9 months ahead with reasonable accuracy. Tables 1 and 2 give the relative accuracy of various models. These results show that we now have the ability to predict the spectra within rms error of nearly 15% in the short term and about 25% in the long term.

ANOMALOUS COSMIC RAYS

As already described, the anomalous cosmic rays (ACRs) are singly-charged interplanetary particles. Elements H, He, C, N, O, Ne, and Ar have been observed. They originate from neutral interstellar particles that are swept into the heliosphere and photoionized by solar UV or charge exchange with the solar wind. These singly ionized

Table 1. Error Analysis of Iron Data

YEAR	TIME	ϕ (JSC)	ε (%) JSC	ϕ (Fitted)	ε (%) Fitted	ε (%) MSU
1968	1968.704	926	9.12	869	7.66	25.9
1973	{1972.704, 1973.33 – 1973.92}	602	9.17	832	8.17	19.6
1974	1974.603	590	7.35	577	7.01	17.9
1979	{1979.416 – 1982.0}	1177	13.33	1132	13.66	15.1
1980	1979.79 – 1980.45	1000	16.15	1260	6.21	13.0
Average ε			11.02		8.54	18.3

Table 2. Error Analysis of Oxygen Data

YEAR	TIME	ϕ (JSC)	ϵ (%) JSC	ϕ (Fitted)	ϵ (%) Fitted	ϵ (%) MSU
1969	1969.416	1171	20.97	1253	16.05	27.2
1973	1973.35, 1973.94	604	4.49	606	4.40	19.1
1974–1978	1974.66 – 1978.66	544	9.95	583	8.23	12.9
1980	1979.79 – 1980.45	1000	5.49	1013	5.20	7.8
1990	1990.66 – 1991.25	1512	7.05	1545	3.96	29.9
Average ϵ			9.59		7.57	19.4

particles are then convected into the outer heliosphere, and accelerated to kinetic energy of ten's of MeV/n. About 100 MeV/n oxygen ions were observed on low earth orbiting satellite SAMPEX.   Because of rather low kinetic energy, these particles have not played a significant role in shielding design considerations so far. However, these particles can cause single event upsets in electronic devices that are under low shielding mass. The particle fluxes are strongly modulated by solar activity and they show a strong radial gradient. Figure 5, taken from Cummings and Stone [8], shows the energy spectra of all of ACR particles measured near the time of solar minima of 1987 and 1994 from Voyager 1 and 2 spacecrafts. Their results show that if the energy is scaled appropriately, all of these ions have the same spectral form. These results can be used to more clearly model the ACR component.

SOLAR PARTICLE RADIATION

The particle emission from the active sun can result in copious flux of highly energetic particles. For crew health purposes, only events with fluence of >10 MeV protons greater than $3 \times 10^7/cm^2$ are important. These events are fortunately very rare. The number of such events and their integrated fluence varies greatly from one solar cycle to the next. There is an emerging consensus that the source of these particles is due to the acceleration of some fraction of solar wind ions due to interplanetary shocks generated by fast coronal mass ejections. The intensity-time profiles of many of these events clearly show that interplanetary shocks do accelerate ions to high energies.

The particle flux seen by an observer inside the solar system depends greatly on the topology and characteristics of the Interplanetary Magnetic Field (IMF) encountered by these particles. There is both a longitudinal and radial gradient. The longitudinal gradient depends on how the field lines are connected to the observer. The radial gradient, for a well connected event, follows the classical geometry, and falls off as a power law in distance, *R,* roughly as $R^{-3.3}$.

There are three important issues in planning manned exploratory missions that are related to these events: (1) fluence frequency distribution, (2) the expected flux and energy spectra, and (3) the largest likely event to be encountered during the mission. There is no accepted solar proton classification scheme. Terminology of *ordinary* and *anomalously large* events has frequently, but mistakenly, been employed. Frequency distribution follows a log-normal approximation [9]. Smart and Shea [10] separated events in decades of >10 MeV peak flux, a system

recently adopted by Stassinopoulos *et al.* [11] also. Nymmik *et al.* [12] followed a classification system separated by one standard deviation in fluence. Recent work by Smart and Shea [13], however, shows that there is steeping of the slope of frequency-peak flux by one around a peak flux of $10^3/cm^2$ s sr. Thus, high peak flux events have a reduced number than would be expected from an extrapolation of more *normal* events. This was originally noted by Lingenfelter and Hudson [14] and is consistent with very recent analysis of ^{14}C and other data by Reddy [15]. These observations do not violate the log-normal behavior because of the rather poor statistics. Thus its quite plausible that the source of these large events is different than more normal events.

Nymmik *et al.* [16], following an extension of the Feynman *et al.* [9] model, provided a means to calculate the expected energy spectrum. The most commonly used form, a power law in rigidity, describes the spectra for each 1σ separation in flux. The average spectra of peak flux is given by

$$F(R)dR = C'\left(R/R_{30}\right)^{-\gamma}$$ (2)

where the power law index is

$$\gamma = 16.9\left[F(\geq 30)\right]^{-0.068}$$ (3)

and $C' = 10^{-8}F(\geq 30)$. R_{30} is the rigidity of a 30 MeV proton (297 MV). Nymmik *et al.* [12] make the *explicit assumption* that this same power law index applies for the average event and not just the peak flux. They show that if C´ is replaced by 0.077 $[F(\geq 30)]^{0.92}$, the integral energy spectra of averaged event fluences does not contradict experimental data from any of the observed events, including the large events of February 1956, November 1960, August 1972, and October 1989 (Figure 6). This analysis suggests that there is a systematic steeping of the energy spectra as the peak flux increases.

Nymmik [16] modified this model suggesting that γ is energy dependent and given by

$$\gamma = \gamma_o\left(E/30\right)^\alpha$$

where γ_o is the spectral index at $E > 30$ MeV. Table 1 in Nymmik's paper provides the new relevant coefficients. An interesting observation from his analysis suggests that for best connected events (west limb) the spectral index is nearly independent of fluence and falls off sharply for east limb events. For events with integrated fluence greater than about 10^8 protons/cm^2 the index is 4.5, irrespective of the position.

In developing any shielding strategy, the assumed form of the *worst case* energy spectrum is very important. Townsend *et al.* [17] assumed an *ad hoc* form that combined the flux from one event with slope from another. This is clearly in violation of Nymmik *et al.* model and adds significantly to radiation burden or risk. Wilson *et al.* [18] have used an envelope event in which the maximum fluence observed at each energy is used. Shielding from this spectrum is dominated by the August 1972 event for shields less than 10 g cm^{-2} and by the February 1956 event beyond 15 g cm^{-2} [19]. Recently, Miroshnichenko [20] has tried to place an upper intensity-energy limit based on

both data and physical grounds. However, he multiplied his intensities by ten at each energy to generate this "utmost" spectra. The shape of his spectra is more reasonable. It is suggested that either the energy spectrum of *very large* (VL) events in Nymmik's classification be used for this analysis and account be taken of the confidence limits provided in the model or the September–October 1989 event spectrum multiplied by 10 in flux be used for shielding calculations [Smart, March 1996, Private Communication]. This is likely to lead to a lower shielding requirement than has been the case. Any shielding strategy has to balance the risk with cost. The problem is rather similar to a number of other problems faced by designers. For example, how high should the North sea dikes be to prevent flooding of productive land in Holland? Large scale flooding, large magnitude earthquakes, severe hurricanes, etc. are rare events. However, the cost of the damage, as well as the cost of prevention of this damage, rises very steeply with the magnitude of such events. In such cases, careful considerations of the probability distributions of such events must be taken seriously into consideration. For example, should one develop a shielding strategy to guard against, say an event twice as large as one ever observed? Clearly, such a plan would be prohibitively expensive in the example cited. It then becomes important to know whether the frequency distribution follows a long tail distribution of Pareto type (power law) or is log-normal. Further careful statistical analysis is needed.

Particle flux from SPEs can also be reaccelerated by the same processes as the ACR. These reaccelerated SPE (RSPE) events have energies comparable to the anomalous component.

We conclude that models of large fluence solar particle events of interest for radiation risk mitigation require additional work. It is difficult to quantify the true uncertainties of such models. The Nymmik [16] model provides a quantitative way to estimate these uncertainties.

REFERENCES

1. R. A. Mewaldt, A. C. Cummings, J. H. Adams Jr., P. Evanson, W. Fillius, J. R. Jokipii, R. B. McKibben, and P. A. Robinson Jr.: Toward A Descriptive Model of Galactic Cosmic Rays in the Heliosphere, in *Proceedings of Interplanetary Particle Environment*, JPL Publication 88-28, April 15, 1988 (Eds. J. Feynman, and S. Gabriel).

2. J. H. Adams Jr.: Cosmic ray effects on microelectronics, Part IV, NRL Memorandum Report 5901, 1986.

3. J. H. Adams Jr., R. Silberberg, and C. H. Tsao: Cosmic ray effects on microelectronics, Part I: Near-earth particle environment, NRL Memorandum Report 4506, 1981.

4. G. D. Badhwar and P. M. O'Neill: Galactic cosmic radiation model and its applications, *Adv. Space Res.,* **17**, 7–17 (1996).

5. R. A. Nymmik, M. I. Panasyuk, T. I. Pervaya, and A. A. Suslov: A model of galactic cosmic ray fluxes, *Nucl. Tracks & Radiat. Meas.,* **20**, 427–429 (1992).

6. J. Lee and J. H. Adams Jr., Long-Term modulation effects on the primary cosmic rays, *Proc. 23rd International Cosmic Ray Conference (Calgary),* **3**, 621–625 (1993).

7.   D. L. Chenette, T. G. Guzik, and J. P. Wefel, The LET spectrum and its uncertainty during the CRRES mission, *Adv. Space Sci.,* **14**, 809–813 (1994).

8.   A. C. Cummings, E. Stone: *Proceedings of the 24th International Cosmic Ray Conference (Rome, Italy),* **4**, (1995).

9.   J. Feynman, T. P. Armstrong, L. Dao-Gibner, and S. Silverman: *J. Spacecraft and Rockets,* **2 7** , **4,** 403–410 (1990); J. Feynman, G. Spitale, J. Wang, and S. Gaberial: *J. Geophys. Res.,* **98**, 281–294 (1993).

10. D. F. Smart and M. A. Shea: *Solar Physics,* **16**, 484–487 (1971).

11. E. G. Stassinopoulous, G. J. Brucker, D. W. Nakamura, C. A. Stauffer, G. B. Gee, and J. L. Barth: IEEE Transactions on Nuclear Science (April 1996).

12. R. A. Nymmik: *Proc. 23rd International Cosmic Ray Conference,* **3**, 29–32, University of Calgary, Calgary, Alberta (Canada).

13. D. F. Smart and M. A. Shea: Solar Radiation, Encylopedia Britannica (1996).

14. R. E. Lingenfelter and H. S. Hudson: *Proceedings Conf. on Ancient Sun* (Eds. R. O. Pepin and J. A. Eddy, R. B. Merrill), Pergamon Press, pp. 69–79 (1980).

15. R. Reddy: Los Almos National Laboratory (1996).

16. R. A. Nymmik: Behavioural Features of Energy Spectra of Particles Fluences and Peak Fluxes in Solar Cosmic Rays, *Proc. 24th International Cosmic Ray Conference (Rome, Italy) ,* **4**, 65–68 (1995).

17. L. W. Townsend, J. W. Wilson, J. L. Shinn, and S. B. Curtis: Human exposure to large solar particle events in space, *Adv. Space Res.,* **12**(2), 339–348 (1992).

18. J. W. Wilson, J. E. Nealy, W. Schimmerling, F. A. Cucinotta, and J. S. Wood: Effects of radiobiological uncertainty on vehicle and habitat shield design. NASA TP-3312 (1994).

19. J. W. Wilson and F. M. Denn: Preliminary analysis of the implications of natural radiations on geostationary operations. NASA TN D-8290 (1976).

20. L. I. Miroshnichenko: Upper Intensity-Energy Limit and Utmost Spectrum for Solar Cosmic Rays, *Proceedings of 24th International Cosmic Ray Conference (Rome, Italy)*, **4**, 62–65 (1995).
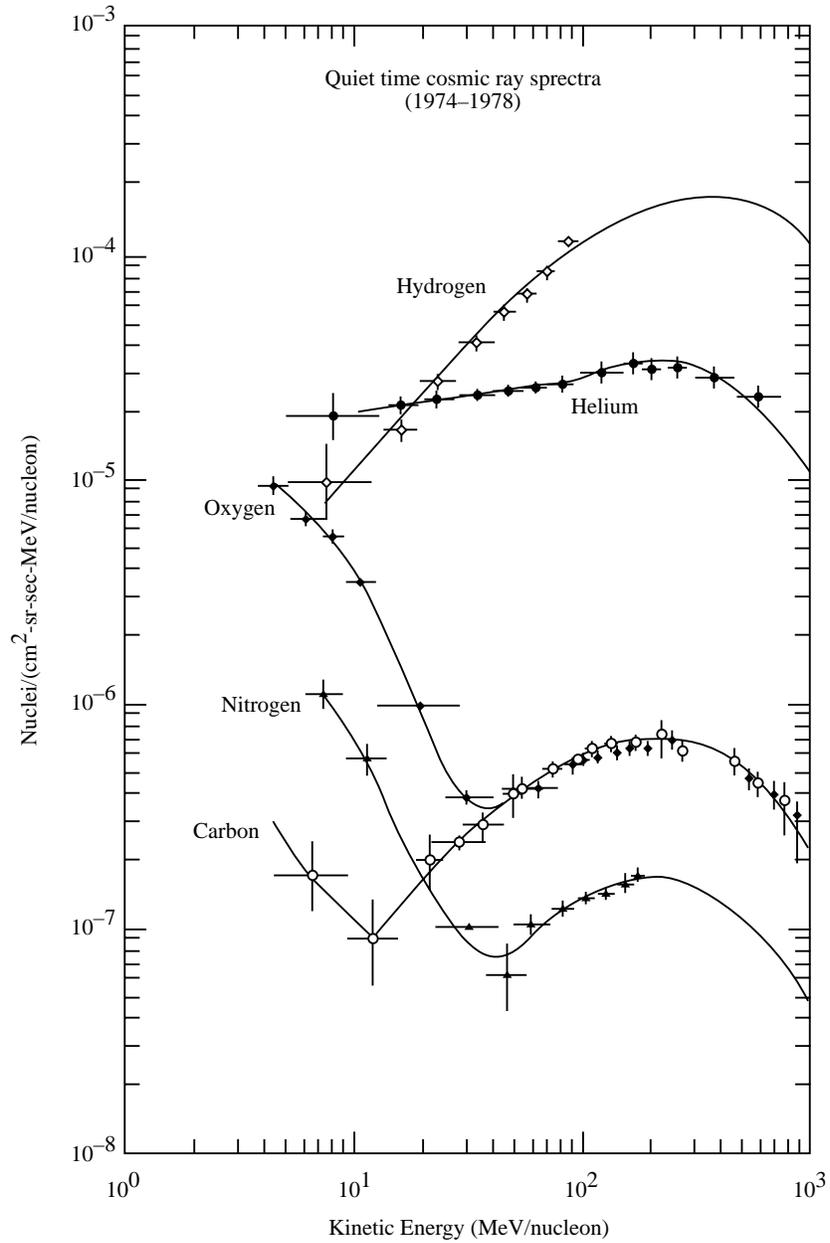
Figure 1. Quiet-time energy spectra from IMP-1/2.
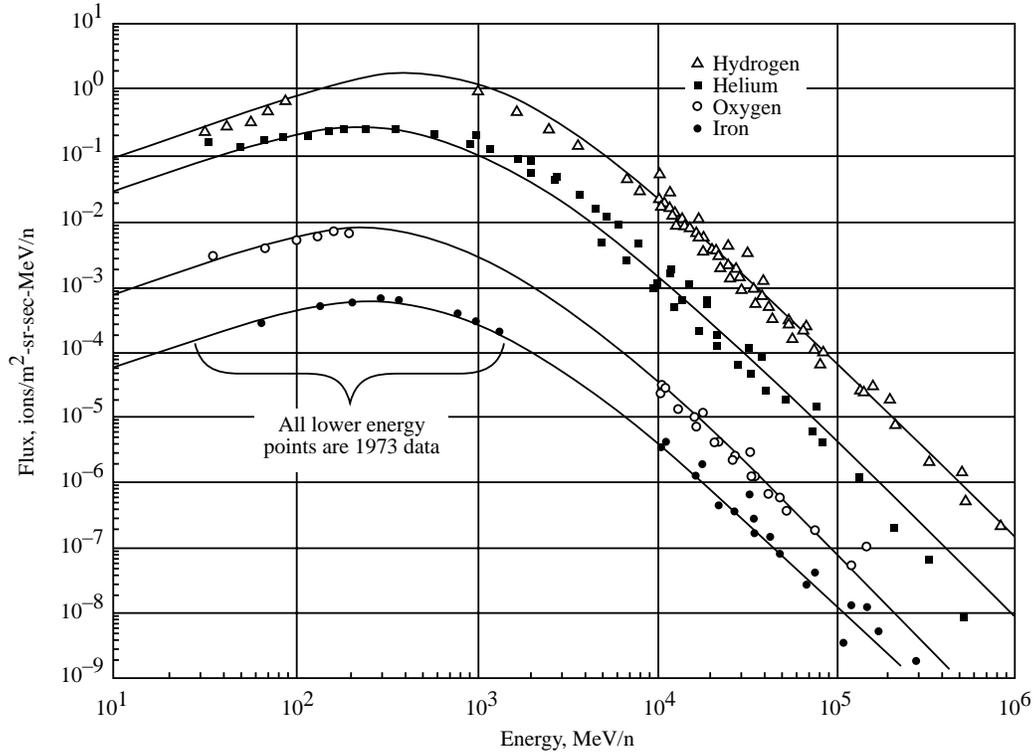
Figure 2. Fit of the Fokker-Planck diffusion equation to 1973 differential energy spectra.
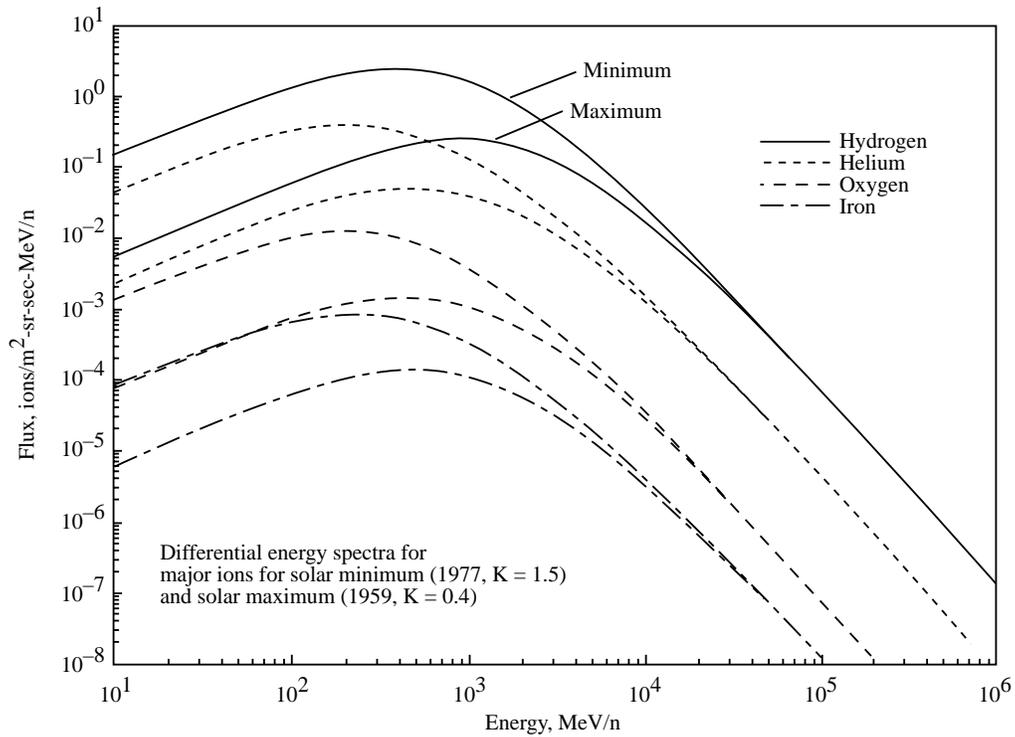

Figure 3. "Worst-case" differential energy spectra (solar minimum and solar maximum).
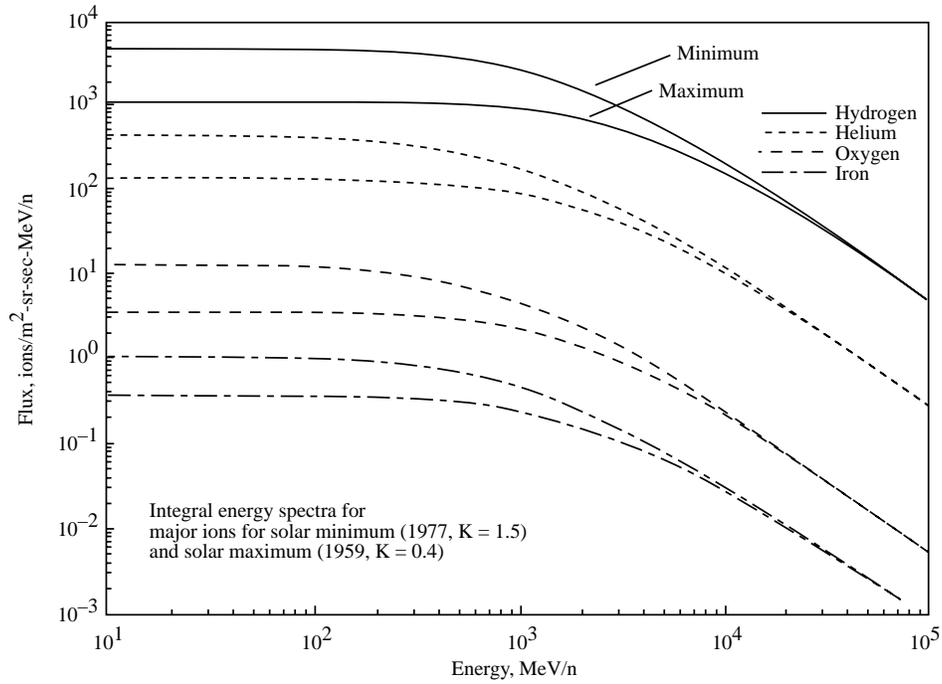
Figure 4. "Worst-case" integral energy spectra (solar minimum and solar maximum).
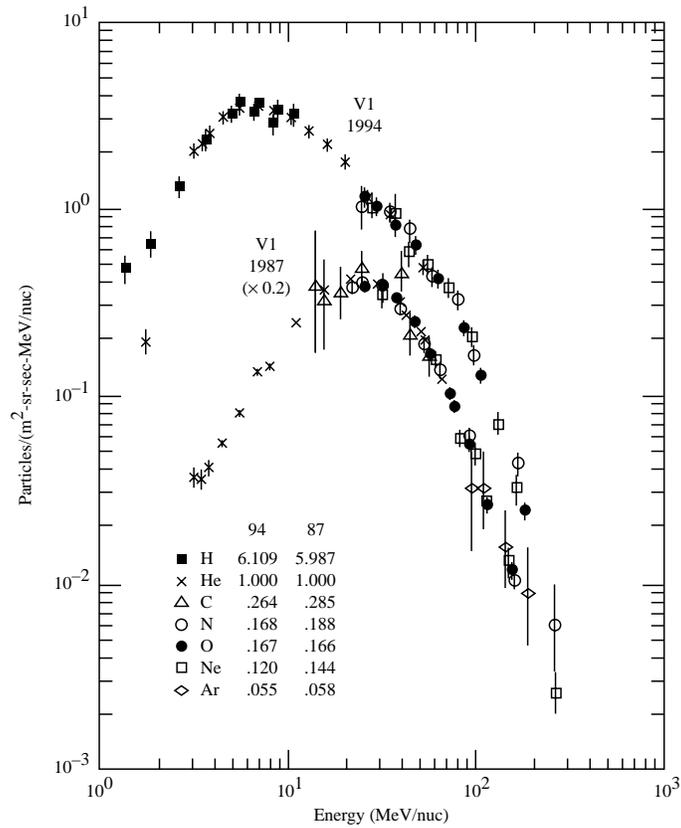

Figure 5. Energy spectra of anomalous cosmic rays.
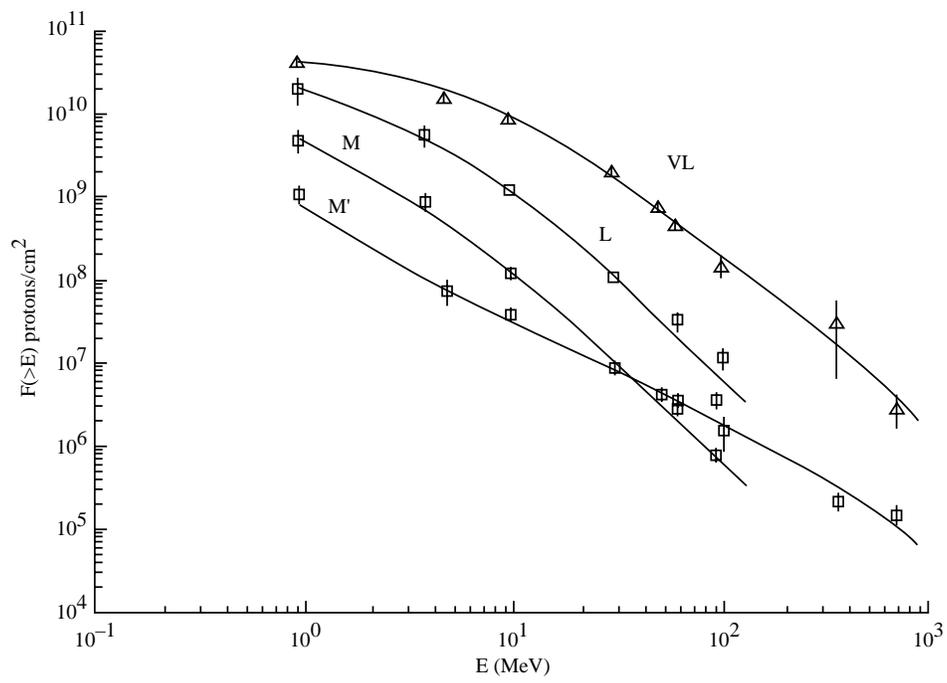
Figure 6. SPE energy spectra from Nymmik [16].

CHAPTER 3

SEI ANALYSIS OF DEEP SPACE VEHICLE SHIELDING

by

John E. Nealy[1] (Ret.)

Lisa C. Simonsen[1]

Garry D. Qualls[2]

[1]NASA Langley Research Center, Hampton, Virginia 23681
[2]AS&M, Inc., Hampton, VA 23665

Chapter 3

SEI ANALYSIS OF DEEP SPACE VEHICLE SHIELDING

SUMMARY

The purposes of this entry are twofold: (1) to present a computational scheme for estimation of high energy space radiation particle fluences and exposures for anticipated interplanetary missions, and (2) to illustrate by specific example of a representative Mars Transfer Vehicle an analysis that would pertain to a visit to that near planet. Although earlier (1985–92) space environment scenarios and conventional dosimetric exposure analyses are implemented, it is concluded that relatively long-duration interplanetary missions are possible with regard to the radiation exposures expected to be encountered during such missions.

INTRODUCTION

Well over two decades have elapsed since the Apollo flights in which humans ventured beyond the earth's protective magnetic shield and entered interplanetary space. While these excursions were recognized to be subject to space radiation hazards, their short duration tended to minimize the risks involved. The next stepping-stones in space exploration are envisioned to be of much longer duration stays on the moon, and possibly semi-permanent habitation on Mars. Such scenarios have forced much more detailed and concerted investigations of the potential effects of prolonged exposure to the high energy space radiation environment. Radiations in deep space of most concern are energetic protons emitted by the sun during flare activity and the Galactic Cosmic Rays (GCR) composed of stripped nuclei of the atomic elements. The exposure to this environment, as interpreted from recent satellite measurements, will be thousands of times greater than that which exists on Earth. In addition, free-space charged particle fluxes may vary both temporally and spatially by several orders of magnitude. Thus, considerable attention must be given to exposures and corresponding health risks due to this environment.

Enormous advances in the knowledge of the deep space environment, principally provided by measurements from instrumented satellite platforms, have taken place since the era of the Apollo lunar flights. In addition, significant improvements have been [1, 2] and continue to be made in predicting the phenomena associated with high energy charged particle transport through various materials. This work utilizes recent environment information and transport methods to establish a data base and computer algorithm to obtain reasonable estimates of exposures, possible shield requirements, and subsequent incurred dose for a variety of interplanetary missions. Some of the

contents of the current data base, structure of the algorithm, representative implementation for candidate Mars mission scenarios, and recommendations for upgrading are described in the following sections.

ENVIRONMENT DATABASE

For purposes of the present SEI mission analyses, the modeled environment is broken into three categories: (1) the galactic cosmic rays, (2) the extremely large (giant) solar proton flares, which occur about 2 or 3 times per solar cycle, and (3) the more frequently occurring "ordinary" solar proton flares, of which observations indicate some 50 to 75 take place during the 7 to 8 year period of increased solar activity.

Galactic Cosmic Rays

Particle fluxes for GCR were taken from the Naval Research Laboratory CREME (Cosmic Ray Effects in Micro-Electronics) model for solar minimum and maximum conditions [3]. The flux spectra at solar minimum are shown in figure 1a; the fluxes are greatest at this time in the solar cycle. At solar maximum, the GCR fluxes are reduced according to the energy-dependent ratios shown in figure 1b. The particle fluxes have been placed into five groupings for convenience of illustration. Modulation of the GCR fluxes between solar minimum and maximum within the solar cycle has been incorporated by means of a weighting function derived from the intensity of 10.7-cm radiance (F10.7 index) of solar activity as observed during solar cycle XXI (1975–1986).

Large Solar Proton Flares

On singular occasions during the course of the 7–8 years of high solar activity during the solar cycle, gigantic proton flares (sometimes referred to as "anomalously large events") occur which may produce more energetic protons than are released by the totality of the more numerous smaller flares occurring in the cycle period. Fluence spectra for six such events observed during the last four solar cycles are shown in figure 2 for a distance of one astronomical unit (AU) from the sun. For other locations in the solar system a $1/R^2$ dependence for the fluence is assumed, where R is the distance of the target (spacecraft) from the sun in AU.

Ordinary Solar Proton Flares

Events in this category are defined as those having an integral fluence of at least 10^7 particles/cm^2 for protons with energies greater than 10 MeV, but which remain distinctly smaller in magnitude than the much more infrequent giant flares. During Solar Cycle XXI (1975–1986), 55 such flare spectra were recorded on instrumented satellite platforms [4], and are used as the basis for modeling this space radiation constituent. Figure 3a depicts the fluence spectra for these smaller flares and the calculated total cycle fluence. Again, a $1/R^2$ dependence for the flares is assumed. The wide ranges of flare sizes and spectral characteristics are apparent. (Note that no proton flares in the "very large" category occurred in this cycle.) Similarities in the number of "ordinary" flares occurring and their frequency of occurrence are seen in data from the past three solar cycles [5]. The Solar Cycle XXI data have been used to construct an exposure model for these normally occurring flares during the course of a solar cycle, in which a cumulative occurrence distribution function has been derived and used in conjunction with total cycle fluence and

corresponding dose functions to determine an average value of exposure due to such flares. The cumulative distribution function is shown in figure 3b.

ALGORITHM STRUCTURE

The computational procedure, which utilizes the environment and dose-vs.-depth data base, also requires mission definition and trajectory specification inputs, along with a selection of user-defined options. This program has been previously described [6], and a computational flow chart is given in figure 4. The mission definition information includes time of commencement, mission duration, and heliocentric distance as a function of time. When proximity to planets or moons produces shadowing of the radiation field, the program can take this into account. Additional input parameters required also include the following:

— Number of large flares included (0 to 6);

— Large flare spectrum selection (2/56, 11/60, 8/72, 8/89, 9/89, 10/89);

— Times of occurrence of large flares;

— Operational shield amount (equivalent g/cm^2 H$_2$O);

— Storm shelter shield amount ("   );

— Percent crew time in storm shelter.

Calculations are made over each time interval as defined by the input trajectory, and cumulative fluences and/or doses are recorded on a data file for post-processing analysis. The code has proven to be very efficient with regard to execution time, and versions have been created for either stand-alone implementation or inclusion in trajectory codes as a subroutine.

RESULTS FOR SAMPLE CALCULATIONS

500-day Mars Mission

A conceptual manned Mars mission, taking place during a time of high solar activity, is chosen to illustrate the use of the code. The proposed scenario is representative of a 500-day class mission [7] for a piloted spacecraft powered by a nuclear thermal rocket. The spacecraft leaves the vicinity of Earth in February 2014, proceeds directly to Mars, spends a month in low circular orbit about Mars, and returns to Earth on a trajectory which swings by Venus. A relatively harsh flare environment is selected in which two large flares (spectra for 11/60 and 8/89) are specified to occur when the heliocentric distance of the spacecraft is less than 1 AU. Trajectory details are shown in figure 5. The shield amount for normal crew operations is specified as 2 g/cm^2, with a storm shelter shielding of 20 g/cm^2. During both large and ordinary events, the crew is assumed to have full storm shelter protection, and an additional 33 percent of crew time (eight hours per day) is specified as being routinely spent in the storm shelter. The cumulative dose equivalents for the complete mission are given in Table 1, where both slab (or equivalent sphere) doses are presented along with those evaluated according to the Computerized Anatomical Man (CAM)

Table 1. 500-Day Mission Cumulative Dose Equivalents, cSv (rem).

	Slab Doses		CAM Doses		
	0 cm	5 cm	Skin	Eye	BFO
Ordinary Flares	0.43	0.22	0.26	0.26	0.12
Large Flares	37.46	25.91	29.93	27.38	17.95
GCR	48.79	37.65	39.02	38.32	30.85
Total	86.98	63.78	66.21	66.95	48.92

Model [8]. A noteworthy result is that the 5-cm depth slab dose, often used to approximate the BFO dose, is substantially larger than the more detailed CAM model result. It is emphasized that mission total particle fluence spectra generated may be used in more detailed transport calculations in which vehicle configuration effects may be addressed more accurately.

Mars Transfer Vehicle Analysis[1]

The reference mission used in this analysis is an opposition class mission which has a total mission time of 555 days. The mission begins on January 17, 2014 with an outbound transfer time of 280 days. The inbound leg includes a Venus swingby. Using this mission timeline, sample radiation environments were selected as test cases. Each of these sample environments includes GCR and one or more solar proton flares. The flare spectra used in these test cases are the solar flares which occurred in August, September, and October of 1989. The computational procedure described above was used to estimate the doses in each of the test cases behind various water shield thicknesses. Dose-versus-water shield depth curves were then generated for each of the assumed environments.

A computerized solid model of the Mars transfer vehicle was created which includes a detailed representation of the habitat module. The model was generated using the Solid Modeling Aerospace Research Tool (SMART) software developed within the Space Systems Division at Langley. The model was then converted to Wavefront format for application in the ray-tracing program RadICal (Radial Intersection Calculation). This program considers the volume, density, and relative location of objects in the spacecraft and determines an equivalent water shield thickness distribution for the entire vehicle (including all fuel tanks in their respective states of depletion during the course of the mission) as a function of solid angle for 4π steradians surrounding a specified target point using 1922 rays at equal solid angles. Cutaway views of the modeled habitat configuration are shown in figure 6a and 6b, and the corresponding thickness distribution is given in figure 7. A target point was chosen inside the crew quarters as the location of interest and 1922 directional doses were calculated by interpolation/extrapolation along the previously calculated dose vs. depth curves using the thickness distribution. These directional doses were then

---

[1]This unpublished analysis was performed by Ms. Andrea L. Schmidt of Kansas State University while engaged with the Langley Aerospace Research Summer Scholars (LARSS) program, whose activities were directed by Lisa C. Simonsen.

integrated over the 4π solid angle to obtain the crew total incurred dose at the target point. Both outbound and inbound configuration thickness distributions were used to evaluate mission exposures. The differences in shielding amounts are representative of the quantity of fuel and tank structure carried by the entire vehicle during the various mission phases.

Through this process, dose estimates were calculated for GCR during both transfer legs and the surface stay along with eight possible flare scenarios. The worst case flare scenario studied was that in which the three 1989 flares occurred near the Venus swingby. For this case the combined GCR and flare doses were determined to result in a skin dose of 41 cSv and a BFO dose of 26 cSv. These total doses are incurred over a period of approximately 1.5 years. The largest doses incurred during any 30-day period were estimated as 23 and 8 cSv for the skin and BFO doses, respectively. These results indicate that a Mars transfer vehicle similar to this configuration is capable of providing a significant amount of shielding for the crew.

CONCLUDING REMARKS

The database described above provides a rather detailed representation of the interplanetary heavy-charged particle environment with regard to the species, their energy distributions, and their spatial and temporal behavior. In addition, the data include dosimetric results from calculations utilizing comprehensive transport codes which have incorporated a realistic treatment of particle-shield interaction processes. Clearly, many assumptions have been made in the formulation of the procedure, several of which are reiterated below:

— All solar flares deliver entire fluence and dose instantaneously
— Shield attenuation data are strictly applicable to water only, and are approximately valid for other high-hydrogen content materials
— Isotropic radiation fields are inherently assumed
— Slab or sphere shield geometries are implied in the dosimetric data
— Trapped radiation contributions for near-Earth operations are neglected

Furthermore, it is recognized that the current database is subject to periodic modification as new environmental measurements are made and as high energy charged particle dosimetric risk assessments evolve. After all of the qualifying factors and assumptions are taken into account, it is felt that such a computational procedure as described herein should be of considerable value in mission analysis and trade studies related to those future endeavors for which space radiation exposures are deemed to be an important consideration.

REFERENCES

1. J. W. Wilson, et al.: BRYNTRN: A Baryon transport model, NASA TP-2887, 1989.
2. L. W. Townsend, J. E. Nealy, J. W. Wilson, and L. C. Simonsen: Estimates of Galactic Cosmic Ray Shielding Requirements During Solar Minimum, NASA TM-4167, 1990.

3. J. H. Adams, Jr., R. Silberberg, and C. H. Tsao: Cosmic Ray Effects on Microelectronics: Part I: The Near Earth Particle Environment, NRL Memo. Rept. 4506 Pt.-1, U.S. Navy, Aug. 1981. (Available from DTIC as AD A103 897).

4. J. N. Goswami, R. E. McGuire, R. C. Reedy, D. Lal, and R. Jha: Solar Flare Protons and Alpha Particles During the Last Three Solar Cycles, *J. Geophys. Res.*, **93(A7)**, 1988.

5. D. F. Smart and M. A. Shea, Solar Proton Events During the Past Three Solar Cycles, *J. Spacecraft*, **26**, **6**; 1989.

6. J. E. Nealy, S. A. Striepe, and L. C. Simonsen: MIRACAL: A Mission Radiation Calculation Program for Analysis of Lunar and Interplanetary Missions, NASA TP-3211, 1992.

7. R. D. Braun, R. W. Powell, and L. C. Hartung: Effect of Interplanetary Trajectory Options on a Manned Mars Aerobrake Configuration. NASA TP-3019, 1990.

8. M. P. Billings and W. R. Yucker: The Computerized Anatomical Man (CAM) Model, NASA CR-134043, 1973.
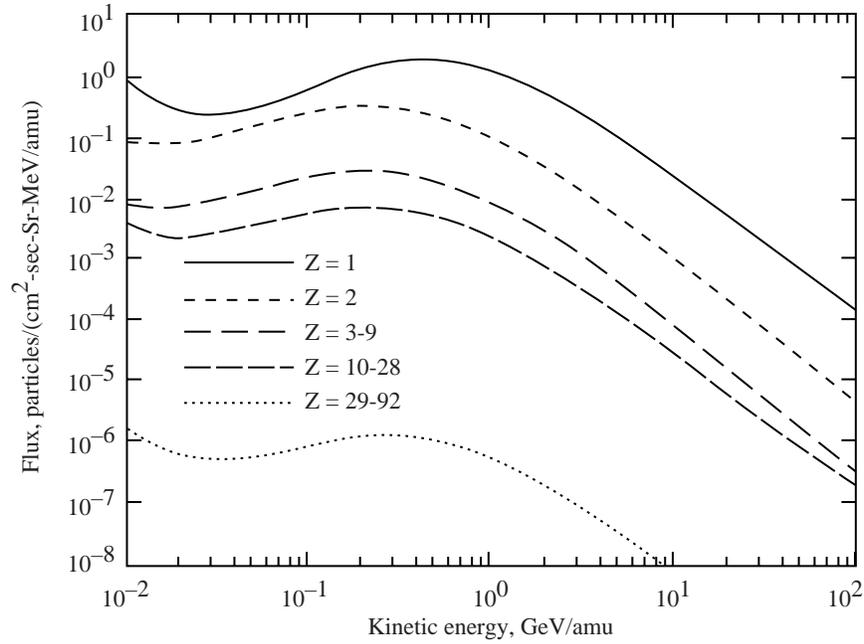
(a) Solar Minimum Flux Spectra (maximum flux).
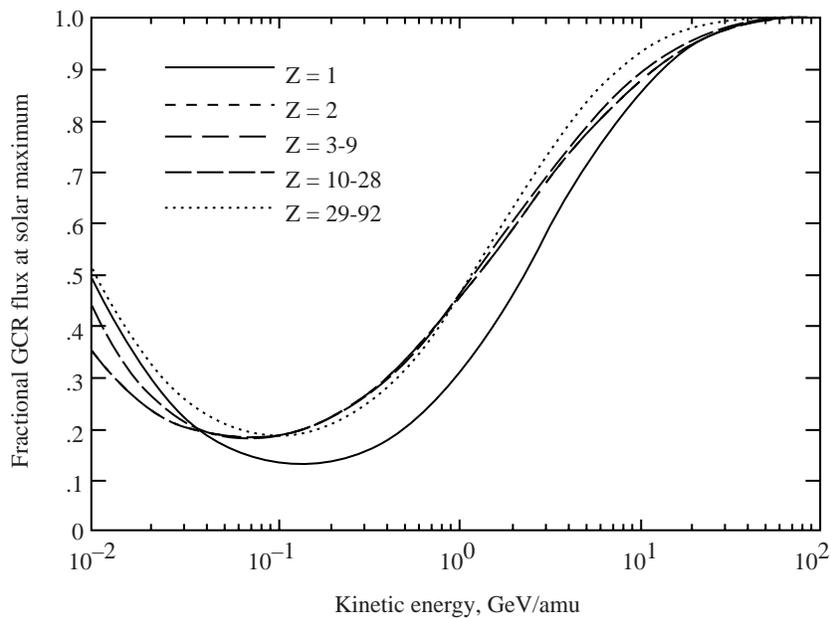
(b) Flux Reduction Ratios at Solar Maximum.

Figure 1. Galactic Cosmic Ray Environment Data.
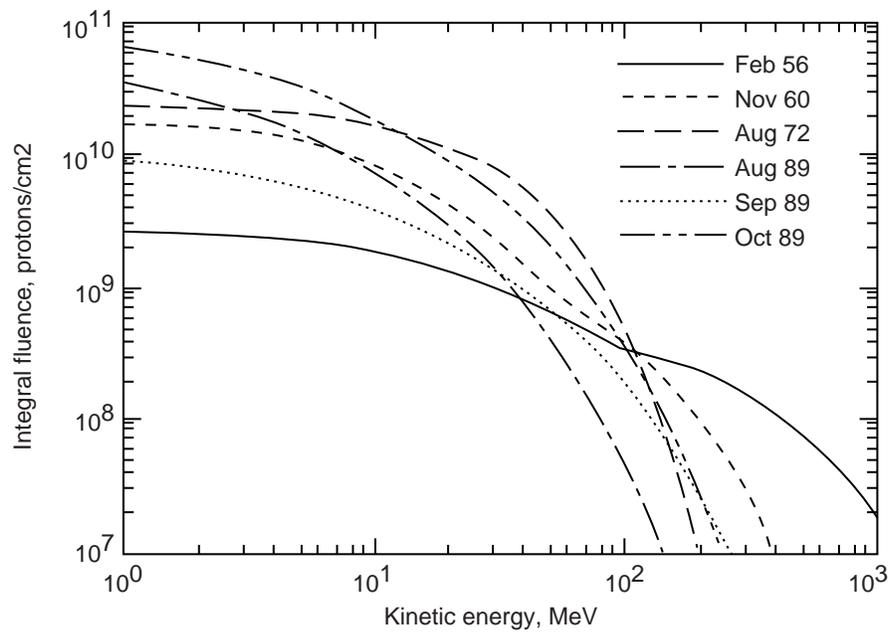
Figure 2. Large Solar Proton Flare Spectra at 1 AU.
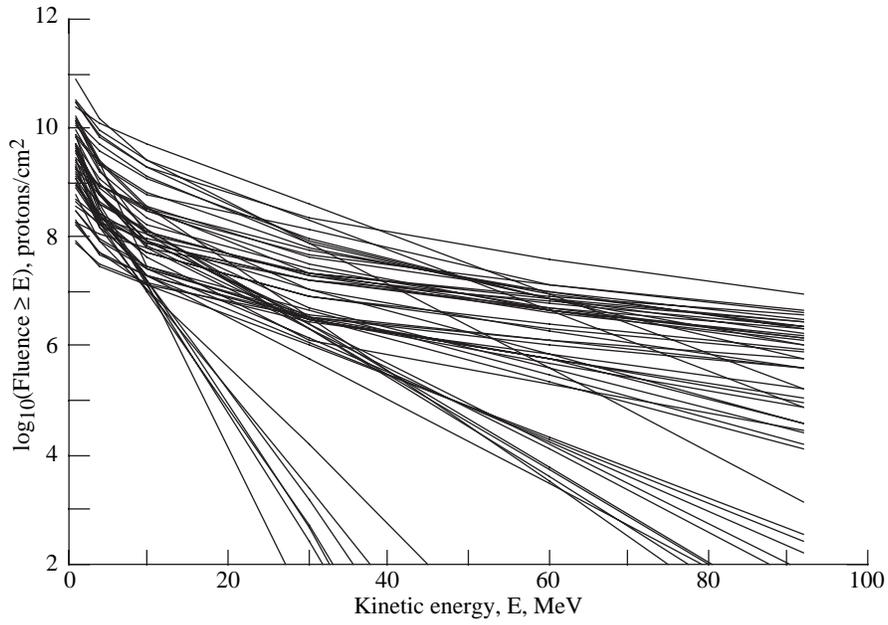
(a) Fluence Spectra.
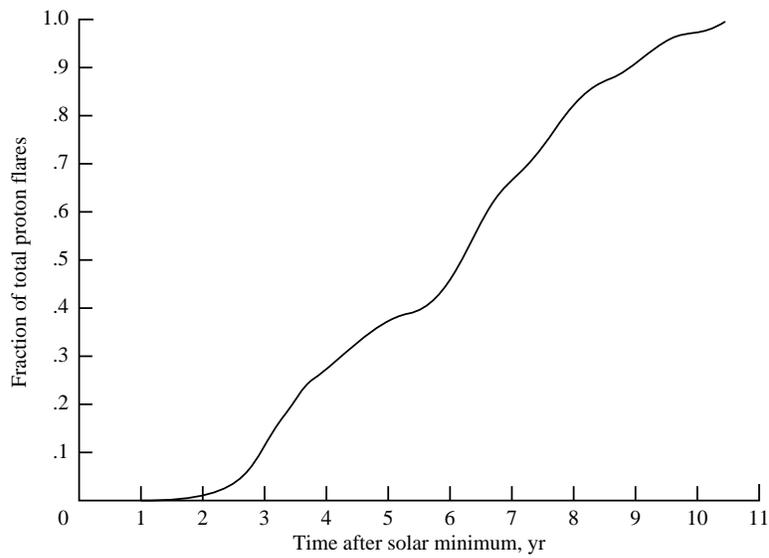
(b) Flare Occurrence Distribution Function.

Figure 3. Ordinary Proton Flare Characteristics for Solar Cycle XXI.
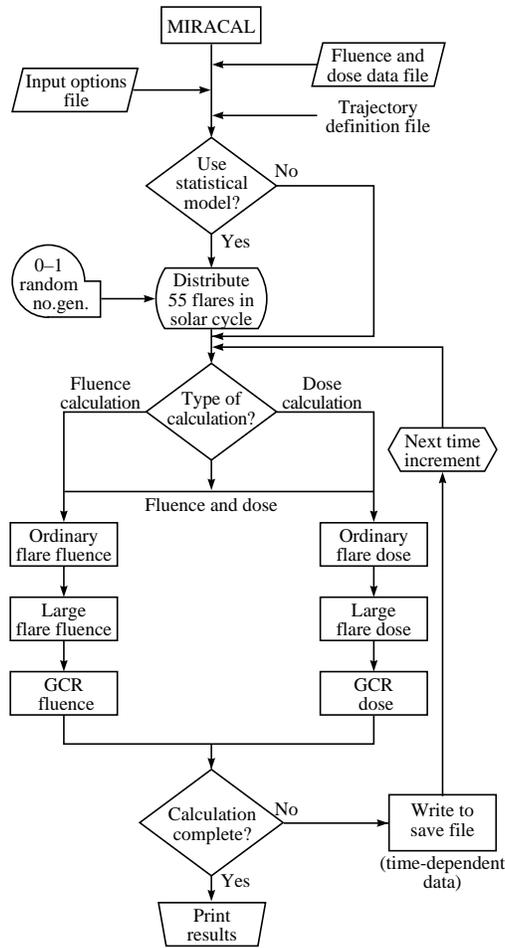
Figure 4. Computational Algorithm Flow Diagram.
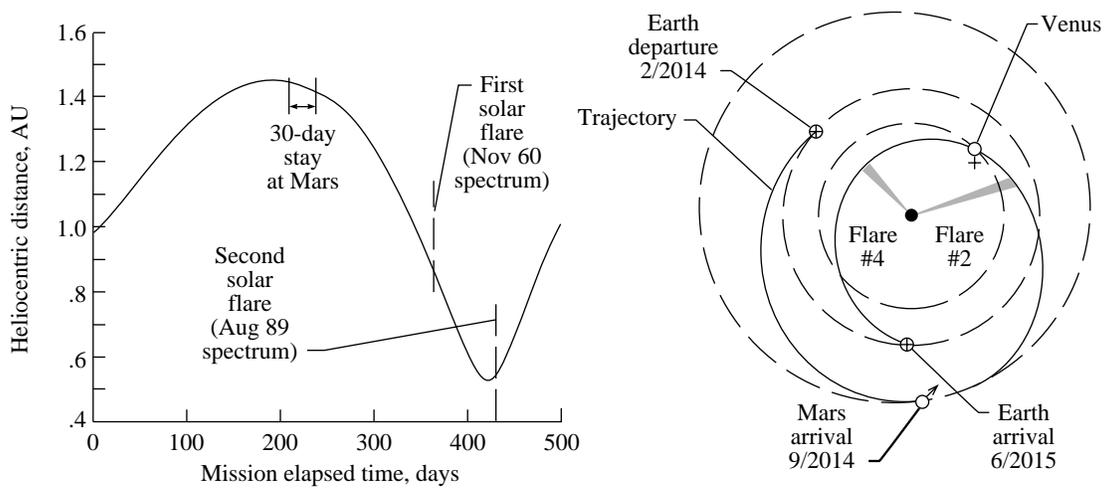
Figure 5. Mission Trajectory Details for Sample Calculation.
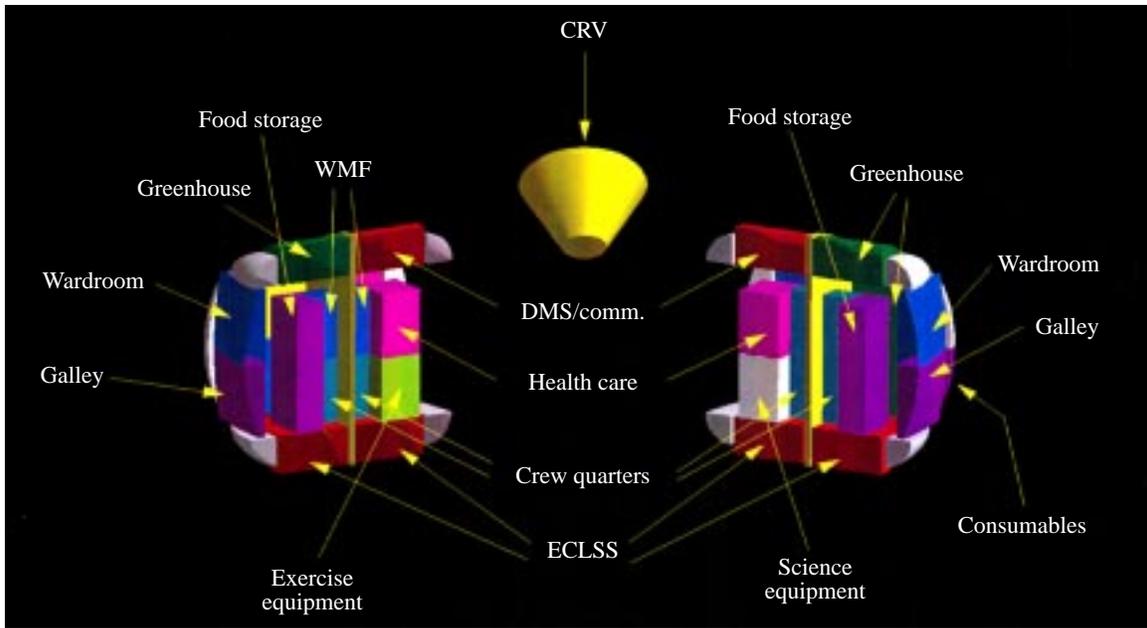
Figure 6. (a) Split View of CAD-modeled Mars Transfer Vehicle.
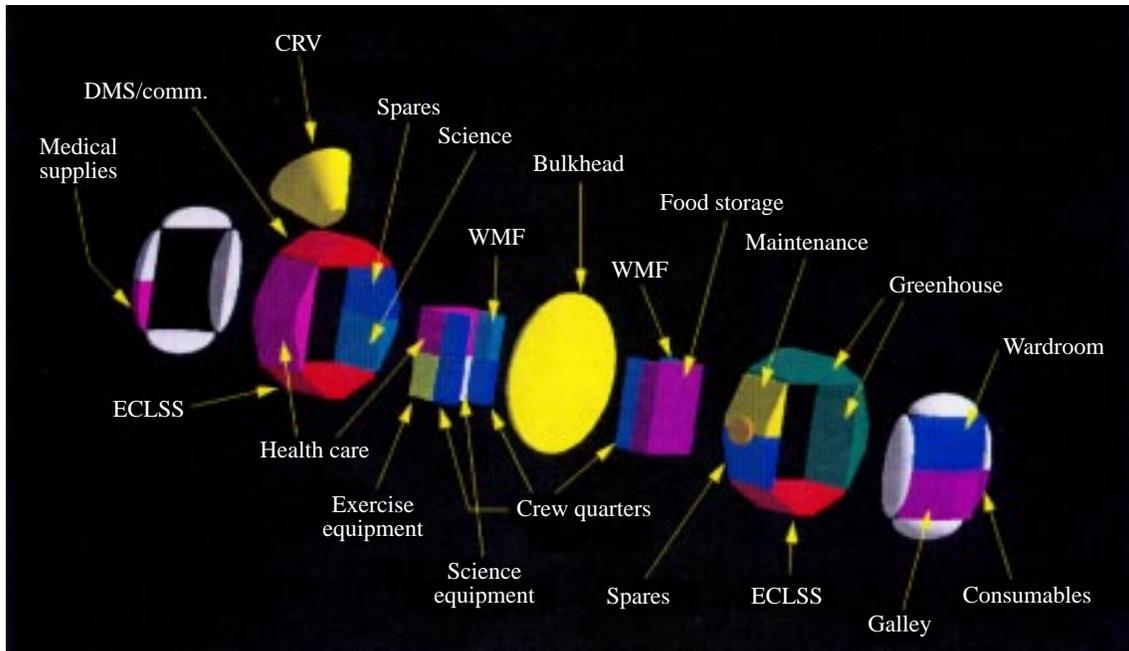

Figure 6. (b) Exploded View of CAD-modeled Mars Transfer Vehicle.
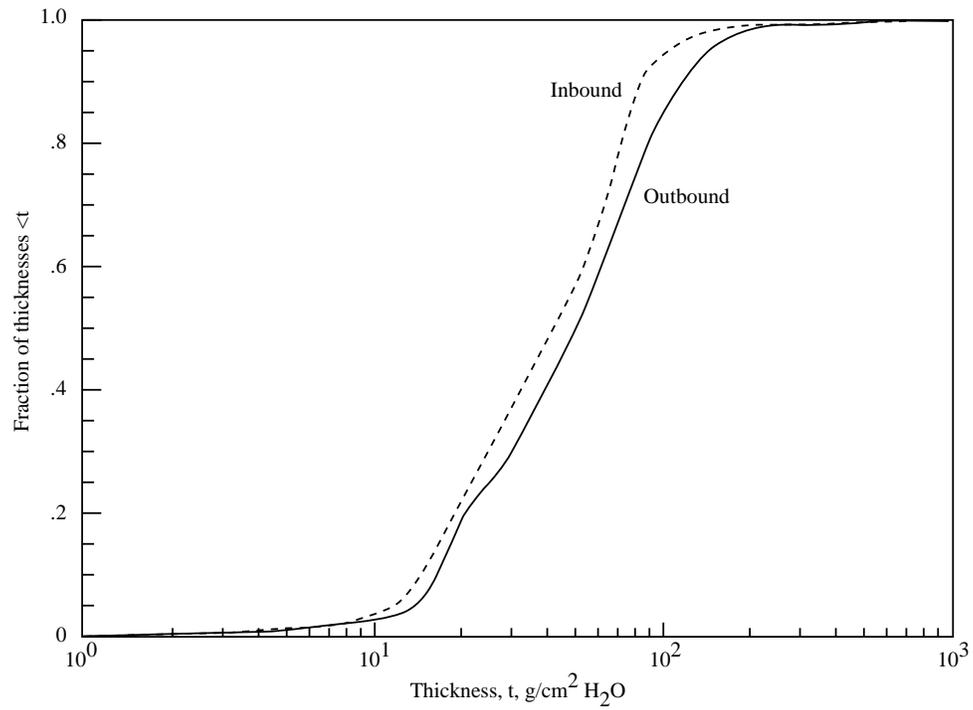
Figure 7. Cumulative Thickness Distributions for CAD-modeled Mars Transfer Vehicle.

CHAPTER 4

ANALYSIS OF LUNAR AND MARS HABITATION MODULES FOR THE SPACE EXPLORATION INITIATIVE (SEI)

by

Lisa C. Simonsen[1]

[1]NASA Langley Research Center, Hampton, Virginia 23681

Chapter 4

ANALYSIS OF LUNAR AND MARS HABITATION MODULES FOR THE SPACE EXPLORATION INITIATIVE (SEI)

SUMMARY

A summary of radiation protection assessments performed for advanced SEI Lunar and Mars manned missions are presented to illustrate radiation shielding estimation techniques. The Langley cosmic ray transport code HZETRN and nucleon transport code BRYNTRN are used to quantify the transport and attenuation of galactic cosmic rays and solar proton flares through various shielding media. Galactic cosmic radiation at solar maximum and minimum, as well as various flare scenarios are considered. Propagation data for lunar regolith (soil), carbon dioxide and Martian regolith are included. Shield thickness and shield mass estimates required to maintain incurred doses below 30-day and annual limits (as set for Space Station Freedom and used as a guide for space exploration) are presented for candidate lunar base habitats shielded with lunar regolith. On the surface of Mars, dose estimates are presented for crews with their only protection being the carbon dioxide atmosphere. Surface doses are estimated using both a low-density and a high-density carbon dioxide model of the atmosphere for altitudes of 0, 4, 8, and 12 km above the surface. A solar modulation function is incorporated to estimate the GCR dose variation between solar minimum and maximum conditions over the 11-year solar cycle. Using current Mars reference design missions, doses are estimated on the Martian surface for both short- and long-duration stay times throughout the solar cycle. Doses are also estimated for crew members inside a candidate habitat protected by additional shielding provided by Martian regolith.

INTRODUCTION

The most critical aspect of manned lunar and Mars exploration missions is the safety and health of the crew. One of the major health concerns is the damaging effects of ionizing space radiation. Once the crew leaves the Earth's protective environment, they will be bombarded by radiation of varying energies and ranges of intensity. Adequate shielding will be required to protect the crew from this environment both in transit to and from the moon and Mars and while on the planetary surfaces. Shielding for transfer vehicles has been addressed in other analyses [1–11]. Here, the radiation protection analysis will focus on lunar and Martian surface habitation issues.

For the surface analysis considerations, radiation doses from galactic cosmic rays (GCR) and solar proton flares are of the most concern.

The constant bombardment of high-energy GCR particles delivers a lower steady dose rate compared with large solar proton flares which can deliver a very high dose in a short period of time (on the order of hours to days). The GCR contribution to dose becomes more significant as the mission duration increases. For the long duration missions, the GCR dose can become career limiting. In addition, the biological effects of the GCR high-energy and high-charge particles are not well understood and lead to uncertainties in the biological risk estimates. The amount of shielding required to protect the astronauts will depend on the time and duration of the mission.

Solar proton flares are also a radiation hazard for crew members on the lunar or Martian surfaces. Very large solar proton events are relatively rare with one or two events per solar cycle. The largest flares observed in the past are the November 1949, the February 1956, the July 1959, the November 1960, the August 1972 event, and the August, September, and October 1989 events. A solar flare event can be very dangerous if a spacecraft/habitat is inadequately shielded because of its potentially high dose. For relatively short duration missions (2–3 months), the most important radiation hazard is the possibility of an unusually large solar proton event. The amount of shielding required for protection will depend on the nature of the energy spectrum of the flare and the intensity of the event.

Habitation shielding strategies on the lunar surface will differ from those employed on the Martian surface due to the differences in their environments. Final shielding requirements must be coupled with the anticipated doses incurred in transit (especially when considering the long Mars travel time) for a total mission dose estimation. It is this total mission dose that must be compared with the exposure limits established for exploratory-class missions.

This paper summarizes some of the past radiation analyses performed under NASA's Space Exploration Initiative for lunar and Martian surface habitation. There have been significant advancements in the field since these studies were performed; such as transport code improvements, combined solid modeling shielding capabilities, improved atomic and nuclear data base models, biological risk assessment techniques, improved environmental models, etc. However, this work is a valuable starting point to continue the effort towards addressing radiation concerns for manned space exploration. Although, the final dose and shielding estimates may differ using the improved capabilities the methodology presented here remains valid.

SYMBOLS AND ABBREVIATIONS

ALARA	as low as reasonably achievable
BFO	blood-forming organ
BRYNTRN	a baryon transport code
CREME	cosmic ray effects on microelectronics
Gray (Gy)	1.0 cGy equals 1.0 rad

GCR	galactic cosmic rays
GOES-7	Geostationary Operational Environmental Satellite
HZETRN	a heavy-ion/nucleon transport code
ICRP	International Commission on Radiological Protection
LEO	low-Earth orbit
LET	linear energy transfer
MIRACAL	Mission Radiation Calculation program
NCRP	National Council on Radiation Protection and Measurements
NOAA	National Oceanic and Atmospheric Administration
NRL	Naval Research Laboratory
Q	quality factor
SEI	Space Exploration Initiative
Sievert (Sv)	1.0 cSv equals 1 rem
Z	atomic number

SHIELD ASSESSMENT METHODOLOGY

The design process flow chart used for preliminary shield and dose estimates is illustrated in figure 1. The basic flow chart consists of the mission requirements feeding into the two separate branches which then combine into one for a preliminary shield design estimate. The desired mission information includes the time frame of the mission, the mission duration, candidate habitat configurations, transfer vehicle design and trajectory, possible shield material types, etc. As with any conceptual analyses, certain assumptions are made as required when not specified by the mission model. The left-hand branch consists of the transport calculations. Based on an assumed environmental model consistent with the reference mission time frame, transport calculations are performed to obtain dose as a function of depth for various shield materials. The right-hand path consists of modeling the candidate configuration, including shielding and equipment location, to calculate a shielding thickness distribution for specified points within the habitat/spacecraft. The directional shielding thickness distribution contains the amount of shield materials traversed by a series of rays covering a 4π (free space) or 2π (planetary surface) solid angle which emanate from a specified target point. An interpolation routine is then used to combine the two paths to calculate the directional and integrated dose. Once a shielding and subsequent dose estimates are made, they are then compared with the radiation exposure guidelines/limits and the ALARA principle to determine if an adequate shield design has been accomplished. If the shielding is considered insufficient, the habitat/spacecraft equipment and/or shielding can be increased or relocated until sufficient shielding is obtained as part of the design process.

From the simplified procedure shown in figure 1, a more advanced procedure evolved and is used for current shield design studies. This method is discussed by Nealy [12] and Qualls [13]. The most recent advances includes the incorporation of computer aided design solid modeling and ray tracing techniques to calculate the shield thickness distribution rather than relying on analytical calculations. The additional shielding provided by the habitat structure and supporting equipment, which can be significant, can now be easily included in the preliminary analyses.

In the following sections, the features of the shield design flow chart will be discussed. The design methodology will be implemented to illustrate preliminary shielding requirement calculations for lunar and Martian surface habitation modules.

DESIGN REFERENCE MISSIONS

The mission will be designed in such a way as to provide enough shielding from the radiation environment in order to keep crew members doses within specified exposure limits and as low as reasonably achievable. Mission scenarios for the Nation's Human Exploration Initiative have been described in The 90-Day Study [14]. The final goal of the Initiative is to establish two permanent operational outposts on both the Moon and Mars.

Lunar Surface Mission

After a 3-day trip from Earth to the Moon, crew rotation times on the surface are described as starting with a 30-day stay, to a 6-month stay, to a 12-month stay, and finally growing to 600 days. Early lunar habitats have been described as a Space Station Freedom derived module and an inflatable/constructible sphere [15]. The Space Station derived module is assumed to be 4.6 m in diameter and 12.2 m in length and situated lengthwise on the surface. The spherical habitat is 15.2 m in diameter and is modeled as a half-buried sphere with the portion above ground level requiring shielding. Local resources, such as lunar regolith, will be available for use as protective shielding to cover the habitats.

Mars Surface Mission

The flight time to Mars is estimated to take from 7 months to over a year each way. Crew rotations on the Martian surface are described as starting with a 30-day stay, to a 90-day stay, up to a 600-day stay. Thus, an entire Mars mission is estimated to take anywhere from 500 to 1,000 days round trip. Relief from the harsh free-space radiation environment can be found on the surface of Mars. Although Mars is devoid of an intrinsic magnetic field strong enough to deflect charged particles, it does have a carbon dioxide atmosphere which will help protect surface crews from free-space radiative fluxes.

Because exploration crews are likely to incur substantial doses in-transit to and from Mars and perhaps from other radiation sources (e.g., nuclear reactors), further increasing the amount of shielding, beyond that provided by the atmosphere, may be desirable if reasonably achievable. By utilizing local resources, such as Martian regolith, shielding materials can possibly be provided without excessive launch weight requirements from Earth. A candidate

habitat configuration was considered in order to assess the potential benefits of additional shielding provided by Martian regolith.

Similar to the lunar scenario, one early Martian habitat is described as a Space Station Freedom derived module 8.2 m in length and 4.45 m in diameter [14]. The cylindrical module is assumed to be lengthwise on the Martian surface. The shielded configuration is assumed to have various thicknesses of Martian regolith surrounding it while another configuration assumes the module is situated 2 m from a 10-m high cliff.

RADIATION EXPOSURE

Ultimately, the mission must be designed to maintain crew-incurred doses to acceptable levels. This is illustrated at the bottom of the flow chart (Figure 1). Currently, no radiation-exposure limits are established for exploratory-class Mars or lunar missions. However, the National Council on Radiation Protection and Measurements has recommended that the limits established for low-Earth orbit (LEO) operations be used as guidelines if the principle of ALARA (as low as reasonably achievable) is followed [16]. LEO limits are established for the skin, ocular lens, and blood-forming organs as shown in Table 1. The limits are included here only for discussion purposes. Exploratory class missions will most likely receive separate and individual consideration [16]. For high-energy radiation from GCR and solar proton flares, the dose delivered to the vital organs is the most important with regard to latent carcinogenic effects. This dose is often taken as the whole-body exposure and is assumed equal to the blood-forming organ (BFO) dose. When detailed body geometry is not considered, the BFO dose is conservatively computed as the dose incurred at a 5-cm depth in tissue (simulated in this analysis by water). A conservative estimate for the skin and eye dose is made using the 0-cm depth dose. Dose-equivalent limits are established for the short-term (30-day) exposures, annual exposures, and career exposure for astronauts in low-Earth orbit. Short-term exposures are important when considering solar flare events because of their high dose rate. Doses received from GCR on long-duration missions are especially important to total career limits, which are determined by the age and gender of the individual. A review of the NCRP-98 recommendations on risk limitations is discussed by Curtis [17].

Table 1. Ionizing Radiation Exposure Limits for Low-Earth Orbit (NCRP-98-1989)

Exposure Interval	BFO Dose Equivalent (cSv)	Ocular Lens Dose Equivalent (cSv)	Skin Dose Equivalent (cSv)
30-day	25	100	150
Annual	50	200	300
Career	100–400*	400	600

*Varies with age and gender

Standard dosimetric techniques used to evaluate health risks due to radiation exposures are uncertain, particularly with regard to latent effects due to the high-energy, low dose-rate exposure from the GCR heavy ions. Current methods for evaluating dose equivalents resulting from heavy-ion exposure utilize biological effectiveness quality factors (Q) which are specified as functions of linear energy transfer (LET) of the projectile particles to the biological system being traversed [18]. Thus, efforts are in progress toward better definition of risk assessment for GCR exposures. Newly proposed quality factors have been based on recent biological effects data [19]. Preliminary calculations with the latest Q-values indicate that previous evaluations may have been somewhat, but not dramatically, conservative [20]. Other recent studies have suggested abandoning the Q-value/LET system [21] and formulating more detailed models of cell destruction and transformation using radiosensitivity parameters derived from biological experiments [22]. Such direct biophysical models are expected to be a distinct improvement. However, evolution of such models is directly coupled to the available radiobiological effects data bases, which for GCR-type radiation, are very limited in number. Clearly, the relationship between heavy-ion exposure and health risk is in need of better definition.

Nonetheless, for illustrative purposes, the resultant doses for the mission model will be compared to the LEO limits at the end of the design process. This comparison can be used to estimate the magnitude of the shielding required and how it may affect mission parameters.

RADIATION ENVIRONMENT

The natural radiation environment encountered during a lunar or Mars mission will vary depending on the solar activity (measured by sunspot number). The solar dipole moment cycles approximately every 20–24 years leading to solar activity cycles of 10–12 years modulated by the direction of the dipole moment. The solar activity increases with the decline of the dipole moment with maximum activity occurring as the dipole switches hemispheres. Activity declines as the dipole moment maximizes along its new direction. With each activity cycle, there are approximately 3 1/2 to 4 years of active solar conditions. The greatest probability of a large solar proton event occurring is during this rise and decline in solar activity. The magnitude of the GCR flux varies over the 10–12 year solar cycle. The fluxes are greatest during solar minimum conditions when the interplanetary magnetic field is the weakest, allowing more intergalactic charged particles to gain access to our solar system. During maximum solar activity, the GCR fluxes are at their minimum, however, the probability of a large solar proton event increases significantly.

For these analyses, a conservative radiation environment was selected for initial shield estimates. Typically, a solar flare environment can be assumed which consists of the possibility of a single large solar proton flare or the three 1989 solar proton flares occurring during the mission. The GCR environment at solar minimum conditions can be selected for conservatism if specific mission times are not specified. If mission times are specified, a GCR modulation function can be incorporated to estimate the GCR dose for the mission duration. The environmental models used as inputs to the transport codes are discussed below.

Solar Flare Events

Except for the near certainty that large solar proton events take place during the years of elevated solar maximum, they are practically unpredictable with regard to their time of occurrence and spectral characteristics. The three large flares of August 1972, November 1960, and February 1956 are widely used to estimate flare shielding requirements. The fluence-energy spectra for these events are shown in figure 2 [23]. The flare of August 1972 produced the greatest number of protons above 10 MeV but had fewer protons than the other two events for energies greater than approximately 150 MeV. The February 1956 event produced approximately one-tenth as many protons above 10 MeV as the 1972 flare, but delivered far more protons of 200 MeV or greater than both other flares.

Recently, several flares larger than any recorded since the August 1972 event have occurred in the latter months of 1989. These flares have been recorded by the GOES-7 satellite and include the August 12, September 29, and the October 19, 1989 flares. Figure 3 shows the proton fluence energy spectra based on rigidity functions reported by Sauer *et al.* [24]. The magnitude of the October 1989 event is on the same order as the August 1972 event and has heightened concern over flare shielding strategies. The addition of these three flares can provide a fairly realistic estimate of a flare environment that may be encountered during missions taking place during active solar conditions.

There are also more frequently occurring smaller flares which will contribute to mission doses. These flares are not included in the analyses presented here, because the shielding required to minimize the dose from a large solar proton flare and from GCR will also minimize the doses from these smaller proton flares [25].

Galactic Cosmic Rays

Galactic cosmic radiation consists of the nuclei of the chemical elements that have been accelerated to extremely high energies outside the solar system. The natural GCR environment used in these analyses is the widely used Naval Research Laboratory (NRL) CREME model, which specifies ion fluxes for particles of atomic numbers between 1 and 28 (hydrogen through nickel) [26]. Figure 4 shows the GCR particle spectra at solar minimum conditions. The magnitude of GCR flux reductions at solar minimum for the various nuclei are shown in figure 5 in terms of the energy-dependent ratios of solar maximum to solar minimum fluxes according to the NRL model [26]. The flux reduction is most pronounced for the energy range between 1 and 10^3 MeV, while the particles of higher energies (greater than 10^4 MeV) are only slightly affected by solar cycle variation. The resulting dose varies by roughly a factor of two between the solar minimum and maximum extremes. There is growing evidence that the NRL model overestimates the modulation effect.

The rather comprehensive study of ground level measurements by Nagashima *et al*. [27] indicates an approximate sinusoidal behavior of the general cosmic ray intensity between the extrema within a cycle. For these analyses, this flux variation between the cycle extrema was calculated using a weighting or modulation function. The modulation function represents the reduction factor to be applied to the peak GCR flux as a function of time throughout an 11-year cycle. The modulation of the GCR flux depends directly on the intensity of the solar activity

which may be gauged by examining the intensity of the 10.7-cm microwave flux (F10.7 index). The intensity of the 10.7-cm flux is characteristically observed to return to approximately the same level at solar minimum for each cycle, but does vary from cycle to cycle. The modulation function has a reciprocal relationship to the magnitude of the 10.7-cm flux. The modulation function of figure 6 was derived from the F10.7 index variation during solar cycle XXI [28]. Since solar cycle XXI was a relatively weak cycle during active sun years, the GCR fluxes in the present model never attain their minimum values. Consequently, some degree of conservatism is present in the modeled GCR fluxes. The actual solar minimum fluxes have been observed to lag 10.7-cm flux [29]; an improved modulation function would incorporate a phase delay of 8 to 12 months.

Considerable uncertainty does exist in the energy distribution of the CREME model GCR ions. An overview of current deep space environment models and their associated uncertainties is discussed by Badhwar [30]. More recent GCR flux models have been developed by Badhwar and O'Neill [31] which may represent significant improvements over earlier models. The 1977 solar minimum GCR spectrum described by Badhwar and O'Neill [31] has a greater number of particles between 50 and 500 MeV and lacks a low energy anomalous component compared with the NRL CREME model. Although the dose versus depth estimates for the various materials may differ slightly depending on the GCR model used, the calculated depths required for long-term GCR shielding are illustrative of the magnitude of the required shielding.

TRANSPORT AND DOSIMETRY ANALYSIS

Selected radiation environments, based on the mission scenario, are now used as inputs to transport codes. The transport of high-energy nucleons and heavy-ions through condensed matter is calculated with the Langley-developed codes BRYNTRN [32, 33] and HZETRN [34, 33]. For solar proton flares, the baryon transport code BRYNTRN is used and for the galactic cosmic rays, HZETRN is used. Both programs implement combined numerical and analytical techniques to provide solutions to the one-dimensional Boltzmann transport equation for particle flux and energy. The solution methodology of this integrodifferential equation may be described as combined analytical-numerical technique [35]. The BRYNTRN code transports both primary and secondary nucleons and includes the effects of target nucleus recoil reactions. The energy loss by heavy target fragments and recoil nuclei is assumed to be deposited locally. The HZETRN code transports nuclear species with charge numbers between 0 and 28. Secondary products from nuclear fragmentation reactions are also transported. Both BRYNTRN and HZETRN evaluate dosimetric quantities based on the linear energy transfer of particles traversing the media. The dose, due to energy deposition at a given location by all particles, is evaluated in terms of cGy, or rad (100 ergs/g). For human exposure, the dose equivalent (in terms of cSv or rem) is defined by introducing the quality factor which relates the biological risk produced due to any ionizing radiation to the damage produced by soft X rays. In general, the quality factor is a function of linear energy transfer (LET), which in turn is a function of both particle type and energy. For the present calculations, the quality factors used are those specified by the International Commission on Radiological Protection [18]. These are the values used to specify radiation exposure limits for carcinogenic and mutagenic effects (see Table 1). The biological effects of HZE (high charge and energy)

particles, present in the GCR fluxes and to a lesser extent in the nuclear reaction products of GCR and solar flare protons [16] with material, are not well understood and lead to uncertainty in risk estimates [36].

Many uncertainties presently exist in high-energy, heavy-ion transport analyses; therefore, the results included herein should be considered as a means to scope the magnitude of the shielding problem for lunar and Mars missions. In addition, since these analyses were performed, many improvements to the transport codes have been incorporated including: improvements and additions to the existing nucleus-nucleus cross sections and their energy dependence, provisions for pion and muon contributions, improvements in target fragmentation treatment, and computational efficiency. These improvements should not greatly alter the current results which still provide a reasonable description of cosmic ray particle fluxes and the corresponding dose equivalent predictions.

PROPAGATION DATA

Basic propagation data can be generated for a variety of materials for both the GCR spectrum and different flare spectra using BRYNTRN and HZETRN. Results include slab calculations of the particle-flux energy distributions at various material thicknesses from which slab-dose estimates as a function of material thickness are determined. The slab calculations correspond to a monodirectional beam of particles normally incident on a planar layer of shield material. Both lunar and Martian regolith have been identified in mission scenarios as convenient candidate bulk shield materials. As previously mentioned, Mars has an atmosphere which will provide a significant amount of protection. The composition of the lower Mars atmosphere by volume is approximately 95.3% carbon dioxide, 2.7% nitrogen, and 1.6% argon. For simplicity in this analysis, the composition of the atmosphere was assumed to be 100% carbon dioxide. Thus, propagation data was generated for lunar regolith, carbon dioxide, and Martian regolith.

The regolith compositions are modeled using the mass-normalized concentrations of the five most abundant elements found in the soil. The lunar model composition is based on Apollo return samples [37], and the Martian model composition is based on Viking Lander data [38]. The normalized compositions used in the regolith shielding studies are given in Table 2 [39, 40]. Moderate changes in composition are found to have negligible effects on the overall shielding properties [39, 41]. As might be expected from the similarity of the Mars and lunar constituents, the regolith shielding characteristics are comparable.

Sample propagation results are presented here to illustrate the nature of the data used in the preliminary shield analysis. Both skin and BFO doses (cSv) were calculated as a function of depth. The BFO results represent the dose evaluated after traversing a given material thickness followed by a 5-cm tissue layer (simulated by water). Often times, the largest shield thicknesses are required to maintain the BFO doses to acceptable levels. Thus for conciseness, only the BFO dose results will be shown here to illustrate the methodology. Other relevant propagation results are given by Simonsen [42]; Simonsen and Nealy [4, 43]; Simonsen *et al.* [44]; Wilson *et al.* [33]; and Nealy *et al.* [39, 41].

Table 2. Composition of Lunar and Martian Regolith

	Composition, Normalized Mass Percentage	Density, g/cm^3
Lunar Regolith	52.6% SiO_2 19.8% FeO 17.5W% Al_2O_3 10.0% MgO	0.8–2.15
Martian Regolith	58.2% SiO_2 23.7% Fe_2O_3 10.8% MgO 7.3% CaO	1.0–1.8

Lunar Surface

The results of BFO dose versus depth in lunar regolith are given for the three large flares of February 1956, November 1960, and August 1972 in figure 7. The regolith results are very similar to those for aluminum, which is not surprising, since the mean molecular weight of the lunar regolith is comparable with the atomic weight of aluminum [4]. For incident solar flare protons, the variation of dose with shield amount is sensitive to the energy characteristics (differential flux spectra). For these flares, the proton fluences have an approximate coincidence close to 100 MeV. Consequently, this behavior is reflected in a corresponding cross-over of the dose-depth curves of figure 7, where the coincidence occurs at approximately 15 g/cm^2 of regolith.

Figure 8 shows the calculated propagation data for the GCR at solar minimum conditions. Although the code simulates the transport of particles 0, 1, 2, ...28 individually, the dose contributions are represented as five entities for illustration: neutrons, protons, alpha particles, lighter nuclei ($3 \leq Z \leq 9$), and heavier nuclei ($10 \leq Z \leq 28$). For very thin layers, the heaviest ion group ($10 \leq Z \leq 28$) contributes over half the dose equivalent. For increasing thicknesses, the heavier ions fragment and react with target nuclei to produce particles of lower mass (ultimately, nucleons) which then deliver the greater percentage of the dose. For the lunar soil, approximately 90 percent of the dose is estimated to result from nucleons (mostly secondaries) for shield layers greater than approximately 20 g/cm^2. For the very energetic GCR spectrum, most of the reduction in dose occurs in the first 20–30 g/cm^2, with the magnitude of the dose gradient decreasing at larger thicknesses.

Martian Surface

Radiation exposures on Mars differ considerably from radiation exposures on the lunar surface because of its carbon dioxide atmosphere. The basic carbon dioxide propagation data may be applied to the Martian atmosphere when gas density as a function of altitude is specified as will be illustrated later. Consequently, dose-depth functions are generated in carbon dioxide for the three large solar proton flares of 1956, 1960, and 1972. These results are shown in figure 9. The shielding effectiveness per unit mass of carbon dioxide is greater than the effectiveness of either aluminum or regolith results as shown previously [4]. The BFO dose equivalent as a function

of carbon dioxide absorber amount is shown in figure 10 for the 1989 solar proton events. The October 1989 flare will deliver the largest dose at the surface compared with the August and September flares as illustrated by the dose vs. depth curves where the October event delivers the largest dose of the three flares at equal absorber thicknesses.

The BFO dose equivalent rates as a function of carbon dioxide absorber amount are shown in figure 11 for GCR at solar minimum conditions and in figure 12 for GCR at solar maximum conditions. Again, the dose contributions are displayed as five entities. The GCR is not attenuated as quickly as the solar proton events due to the greater number of high-energy particles in the GCR spectrum. The shielding effectiveness per unit mass of carbon dioxide is greater than that of lunar regolith for the GCR dose attenuation. The annual BFO dose incurred during solar maximum conditions is roughly half of the dose incurred during solar minimum conditions.

When Mars regolith is considered as a protective shield medium, the transport calculations must be made for the atmosphere-regolith thicknesses combined. In this case, the detailed flux/energy spectra emergent from a specified carbon dioxide amount is used as input for the subsequent regolith calculation. Sample BFO dose results for such a procedure are given in figure 13, where fixed carbon dioxide amounts are used in conjunction with increasing regolith layer thicknesses. Three sample transport calculations are shown here: two GCR cases and the energetic February 1956 solar flare. For moderate carbon dioxide absorber amounts, the dose reductions from additional regolith layers are small compared to the dose reduction occurring in the first few g/cm^2 of carbon dioxide (figure 9 and figure 11).

EXAMPLES OF SHIELD ASSESSMENT METHODOLOGY

Considering once again the flow chart of figure 1, various radiation environment models have been used as input to the transport codes to generate propagation data in the form of dose as a function of depth in various materials (left-hand side). When the computed propagation data for the GCR and solar flare protons are applied to specific shield geometries (right-hand side), the dose at specified target points throughout a habitat can be evaluated (center). Examples using this methodology are presented for both lunar and Mars surface habitat modules as described by mission scenarios.

Lunar Surface Habitation

Dose calculations inside candidate habitats are estimated using the computed propagation data for solar flares and the GCR shown in figure 7 and figure 8. When mission dates are not available, a conservative estimate of the free-space environment is to assume the combination of GCR at solar minimum and the occurrence of one large proton event. The slab-dose results can be used as a first approximation of an appropriate shield thickness to select for further analysis. From figure 7 and figure 8, the regolith slab-dose estimates imply that a 50-cm (75 g/cm^2 assuming a regolith density of 1.5 g/cm^3) thickness will reduce the BFO dose-equivalent to approximately 40 cSv for the sum of the GCR and one large flare (February 1956). With the 2π solid angle shielding provided by the lunar surface and the additional 50-cm regolith layer, the annual dose for this environment is reduced to approximately 20 cSv. Thus, a minimum shield thickness of 50-cm is selected for analysis to reduce BFO dose levels to slightly

less than half of the annual limit. Shield thicknesses of 75 cm (112.5 g/cm^2) and 100 cm (150 g/cm^2) are also selected for analysis to determine the extent to which additional shielding can further reduce incurred doses.

As described in the mission scenario, one lunar habitat concept is a modified space station module. Here, the module is assumed to be lengthwise on the lunar surface and covered with either 50 cm or 100 cm of lunar regolith overhead. Along the sides, the regolith material is filled in around the cylindrical module to form a vertical wall up to the central horizontal plane. For the 50-cm layer, the shield thickness will vary from 230 cm to 50 cm from ground level up to this plane as shown in figure 14a. The spherical habitat concept, as described by Alred *et al.* [15], is 15.2 m in diameter and is modeled as a half-buried sphere with the portion above ground level shielded with either a 50-cm, 75-cm, or 100-cm regolith layer. See figure 14b.

To evaluate the dose at particular points within the habitats, the radiation from all directions must be determined. In free space, radiation will surround the crew from the full 4π solid angle. However, on a planetary surface, only a solid angle of 2π is considered because the mass of the planet protects the crew from half of the free-space radiation. The dose contribution attributed to particles arriving from a given direction is determined by the shield thickness encountered along its straight-line path to specified target points. For the shield assessments, the regolith thicknesses and the corresponding dosimetric quantities are evaluated for zenith angles between 0° and 90° in 5° increments and for azimuth angles of 0° to 360° also in 5° increments. The regolith shield thickness distributions were calculated using geometric models. For the cylindrical habitat, the top half of the habitat was modeled as two concentric cylinders while the bottom half was modeled as a cylinder within a rectangular box. The spherical habitat was modeled as two concentric spheres. The thicknesses in all directions at a target point were then calculated analytically, thus completing the right hand side of the flow chart of figure 1. The directional dose was subsequently estimated by interpolating/extrapolating a dose for each direction from the dose vs. depth propagation results based on the shield thickness encountered. The directional dose is then numerically integrated over the solid angle (2π for planetary surface) about the target point to determine the total dose at that point.

The integrated BFO dose estimates which would have been incurred from the three solar flare events using shield thicknesses of either 50 cm or 100 cm are shown in Table 3. These values represent the dose in the center of

Table 3. BFO dose comparison for three large solar flares for lunar habitats (Data from Nealy *et al.*, 1988)

Proton Flare Occurrence	Regolith Thickness (cm)*	Estimated Dose in Cylinder (cSv)	Estimated Dose in Sphere (cSv)
February 1956	50	7.5	7.0
	100	2.7	2.9
November 1960	50	1.6	1.9
	100	0.2	0.2
August 1972	50	0.3	0.3
	100	<0.1	<0.1

*Assumes regolith density of 1.5 g/cm^3.

the habitat for each flare event. The dose distribution was also calculated throughout each habitat. The BFO dose variations within these habitats for the November 1960 flare event are shown in figure 15 and figure 16. For the cylindrical module, the general dose levels show little change for heights above and below the center plane. The radiation field maxima occur at about two-thirds the distance between the center and end wall. For the spherical habitat, the field maximum occurs above the center point at positions closer to the top, while doses in the buried half are significantly reduced.

Dose estimates within the habitats were also calculated for the GCR at solar minimum conditions. The maximum integrated BFO doses estimated in each habitat for various regolith shield thicknesses are shown in Table 4. For the cylindrical habitat configuration, the dose variation throughout the configuration is relatively small (Figure 17). For the portion of the spherical habitat above ground level, the dose variation is also relatively small with a broad maximum dose rate observed directly above the center point (approximately 11 to 12 cSv/yr). Below ground level, a large gradient in dose rate is shown in the downward direction, with values in the lower section decreasing to less than 5 cSv/yr (Figure 18). With 75 cm overhead shielding, the dose rate maximum is reduced to 8 to 10 cSv/yr throughout the upper half of the sphere. This increased shielding is of even less significance in the regions below the ground where predicted doses approach the same low values as seen in the 50-cm calculation. Relatively little reduction in dose (less than 20 percent) occurs for a 50-percent increase in layer thickness, indicating that further substantial dose reductions would require very thick layers of regolith.

Table 4. GCR Integrated Annual BFO Dose Results for Lunar Habitats (Data From Nealy *et al.* 1989)

Habitat Geometry	Regolith Thickness (cm)*	BFO Dose Rate (cSv/yr)
Cylindrical	50	12
Spherical	50	12
	75	10

*Assumes regolith density of 1.5 g/cm^3.

Using the dose estimates calculated within the habitat, surface mission doses can be estimated. A conservative estimate of dose is to assume the crew receives the dose delivered from the GCR at solar minimum and the dose delivered from one large flare (in this case, the February 1956 flare since it delivers the largest dose in the shielded module). The surface habitat doses are shown in Table 5 for different stay times as specified by the mission scenario for the cylindrical habitat. Likewise, the mission doses can be estimated for the spherical habitat. As shown at the bottom of the flow chart of figure 1, the estimated doses can now be compared with established

Table 5. Surface Mission Dose Estimates Inside Cylindrical Habitat
Configuration of Figure 14a.

Stay Time	GCR Dose (cSv)	February 1956 Flare Dose (cSv)	Mission Surface Dose (cSv)
30 days	1	7.5	8.5
6 months	6	7.5	13.5
1 year	12	7.5	19.5

exposure criteria. All the surface dose estimates are well below the annual 50 cSv established guidelines for US astronauts. The 30-day limits, with regard to the flares, remain below the 25-cSv limit. The skin doses, not presented in this analysis, are also well below the established 30-day and annual limits. The above estimates have not taken into account the added shielding provided by the pressure vessel wall, supporting structures, or the placement of equipment in and around the module. It must also be emphasized that the dose in-transit to the moon and possible larger doses received during EVA's are not included. The complete mission doses must be compared with established criteria.

As seen in Table 5, the solar flare dose contribution dominates the shorter missions while the GCR contribution starts to dominate the longer missions. Shielding from solar flare events will be essential on the lunar surface whether in the form of heavily shielded areas (i.e., flare shelters) or overall habitat protection for any mission duration. For longer stay times on the surface, the shielding from GCR becomes necessary to reduce the crew member's annual exposures and overall career exposure. A regolith shield thickness on the order of 50 cm is estimated to provide adequate flare and GCR protection. However, further trade studies are required to investigate the ALARA philosophy. Before an optimum thickness and shielding strategy are selected, the complete mission scenario (including the lunar transport vehicle) must be studied in detail.

Martian Surface Habitation

Atmosphere shielding analysis. The amount of protection provided by the Mars atmosphere from free-space radiative fluxes must be evaluated prior to estimating if additional shielding will be required for crew members while on the surface. The composition and structure of the atmosphere as well as the crew member's altitude will determine the extent of the atmospheric protection. The Committee on Space Research has developed warm high- and cool low-density models of the atmospheric structure [38]. The low-density model and the high-density model assume surface pressures of 5.9 mb and 7.8 mb, respectively. The amount of protection provided by the atmosphere, in the vertical direction, at various altitudes is shown in Table 6 [44]. Dose predictions at altitudes up to 12 km are included in the analysis because of the great deal of topographical relief present on the Mars surface. Both atmosphere models are considered in order to estimate the possible variation in the radiation intensities found at the surface.

Table 6. Martian Atmospheric Protection in the Vertical Direction

Altitude (km)	Low-density model (g CO_2/cm^2)	High-density model (g CO_2/cm^2)
0	16	22
4	11	16
8	7	11
12	5	8

The surface doses at various altitudes in the atmosphere are determined from the computed propagation data for the GCR and solar flare protons in carbon dioxide. The dosimetric values at a given target point are computed for carbon dioxide absorber amounts along slant paths in the atmosphere. In these calculations, a spherical concentric atmosphere is assumed such that the amount of protection provided increases with increasing zenith angle as shown in figure 19. For a target point at altitude h above the surface, the distance s along a slant path with zenith angle θ is given by

$$s(z, \theta) = \sqrt{(R + h)^2 \cos^2 \theta + \left[2R(z - h) + z^2 - h^2 \right]} - (R + h) \cos \theta$$

where z is the vertical altitude. The absorber amount along the slant path is then

$$T(h, \theta) = \frac{M_{CO_2}}{N_A} \int_0^\infty c(s)\, ds \quad g/cm^2$$

where M is the molecular weight of CO_2, N_A is Avogadro's number, and c is the number density (particles/volume) as a function of altitude determined by the atmospheric model. For a given target point, the absorber amounts and the corresponding dosimetric quantities are evaluated for zenith angles between 0° and 90° in 5° increments. For example, on the surface (0 km) at a zenith angle of 0°, the low density model provides 16.0 g/cm^2 of protection directly overhead with the protection increasing to 59.6 g/cm^2 at 75°. The dose equivalents corresponding to each absorber thickness at each zenith angle are log-linearly interpolated/extrapolated from the basic carbon dioxide dose vs. depth propagation data. The calculated directional dose is then numerically integrated over a 2π solid angle to obtain the total dose at the point of interest (the dose from the other 2π solid angle is assumed zero because of planetary shielding).

Integrated total dose calculations are made for both the high- and low-density atmosphere models at altitudes of 0, 4, 8, and 12 km as shown in Table 7. Results include dose estimates for the GCR at solar minimum and maximum conditions and the solar proton flare events of 1956, 1960, 1972, and 1989. The range in doses indicated in the table is a result of the different atmospheric models used. As seen in Table 7, the incurred GCR dose during solar maximum conditions is approximately half of the dose incurred during solar minimum conditions. The GCR remains relatively constant with altitude compared with the range of estimated flare doses.

Table 7. Integrated BFO Dose (cSv) on the Surface of Mars Using Both High- and
Low-Density Atmosphere Models

Radiation Source	BFO Dose at 0 km	BFO Dose at 4 km	BFO Dose at 8 km	BFO Dose at 12 km
GCR at solar minimum (annual)	10.5 – 11.9*	12.0 – 13.8	13.7 – 15.8	15.6 – 18.0
GCR at solar maximum (annual)	5.7 – 6.1	6.2 – 6.8	6.7 – 7.4	7.3 – 8.1
Feb. 1956 flare	8.5 – 9.9	10.0 – 11.8	11.7 – 13.6	13.4 – 5.3
Nov. 1960 flare	5.0 – 7.3	7.5 – 10.8	10.6 – 14.8	14.4 – 19.1
Aug. 1972 flare	2.2 – 4.6	4.8 – 9.9	9.5 – 18.5	17.4 – 30.3
Aug. 1989 flare	0.1 – 0.3	0.3 – 0.6	0.6 – 1.3	1.2 – 2.6
Sept. 1989 flare	1.0 – 2.0	2.0 – 3.8	3.7 – 6.5	6.1 – 10.6
Oct. 1989 flare	1.2 – 2.7	2.8 – 5.9	5.7 – 11.4	10.6 – 20.5

*High-density model dose estimate—low-density model dose estimate

The flare doses were estimated using the fluence at 1 AU. In the vicinity of Mars (approximately 1.5 AU), the fluence of these flares is expected to be less. A reasonable estimate is that the radial dispersion of the flare particle flux is inversely proportional to the square of the distance from the Sun [45]. However, large variabilities in this behavior may be expected primarily due to inhomogeneities in the interplanetary magnetic field, anisotropic flux properties and the nature of the energy spectrum [46]. There is still much discussion on the dependence of the flare's radial dispersion with distance. It is left to the judgment of the reader as to whether the estimated flare doses should be multiplied by $1/r^2$ (where r is the distance from the sun in astronomical units; $r \approx 1.5$ AU for Mars).

The values in Table 7 can be used to estimate the total incurred dose while on the surface of Mars during a variety of proposed missions occurring at various times during the solar cycle. The GCR dose variation over the 11-year solar cycle can be evaluated using the modulation function described previously. The GCR dose equivalent rate H_{GCR} at time t (after last solar minimum) is evaluated as follows:

$$H_{GCR}(t) = w(t)H_{GCR}^{\text{solar min}} + [1 - w(t)]H_{GCR}^{\text{solar max}}$$

where $w(t)$ is the modulation function value (Figure 6) and $H^{\text{solar min}}$ and $H^{\text{solar max}}$ are the GCR doses listed in Table 7.

When mission dates are specified, surface GCR doses for different Mars mission scenarios can be calculated. The references for the selected mission stay times are compiled in Striepe *et al*. [5, 6]. Table 8 shows the calculated doses for short-duration stay times on the Mars surface and Table 9 shows the calculated doses for long-duration stay times on the surface. The GCR doses for a particular stay time are estimated by numerically integrating the

GCR variation with time in solar cycle as specified by the modulation function between the Mars arrival and departure dates. All calculations assume the stay is at an altitude of 0 km. (Likewise, these calculations may be performed at other altitudes; however, the GCR dose does not vary significantly with altitude). The calculations also assume that the crew member's only protection is the carbon dioxide atmosphere; i.e., the pressure vessel and other supporting equipment are not included as shielding. This approximation is only slightly conservative. It has been shown that moderate amounts of additional shielding will not provide substantial additional protection compared with that already provided by the atmosphere [40].

For illustrative purposes, the surface doses of Table 8 may be compared with the LEO limits; however, it must be realized that the doses incurred for the entire mission must remain below the limits (the LEO limits may differ from future limits or acceptable risks for exploratory missions). The estimated GCR doses for surface stays of 30 days do not contribute significantly to the 25 cSv BFO or to the 150 cSv skin limits; likewise, the GCR doses for short-duration missions over 30-days do not contribute significantly to the yearly skin and BFO limits of 300 cSv and 50 cSv, respectively. Similarly for the long-duration missions lasting over a year, the GCR doses listed in Table 9 do not surpass the yearly skin or BFO limits.

Table 8. Estimated GCR Dose for Short-Duration Stays on Surface of Mars
(Simonsen and Nealy 1993)

| Mission | Arrival | | Departure | | Stay time (days) | Dose equivalent, cSv | | | |
| | Date | Year after solar min. | Date | Year after solar min. | | Skin | | BFO | |
						High density	Low density	High density	Low density
1	7/11/2014	6.7	10/19/2014	6.9	100	2.1	2.3	1.9	2.1
2	2/15/2008	0.3	3/26/2008	0.4	40	1.2	1.4	1.1	1.3
3	7/1/2014	6.6	9/29/2014	6.9	90	1.9	2.1	1.7	1.9
4	11/18/2020	2.1	12/18/2020	2.2	30	0.9	1.1	0.9	1.0
5	8/4/2016	8.7	9/23/2016	8.9	50	1.4	1.6	1.3	1.4
6	9/27/2011	3.9	10/27/2011	4.0	30	0.8	0.9	0.7	0.8
7	4/11/2005	8.3	5/11/2005	8.4	30	0.8	0.9	0.7	0.8
8	3/24/2018	10.4	5/23/2018	10.5	60	1.9	2.2	1.7	2.0
9	2/26/2018	10.3	4/27/2018	10.5	60	1.8	2.2	1.7	1.9
10	6/11/2024	5.7	8/10/2024	5.8	60	1.3	1.4	1.2	1.3
11	7/13/2018	10.7	9/11/2018	10.8	60	1.9	2.2	1.7	2.0
12	8/27/2014	6.8	9/26/2014	6.9	30	0.6	0.7	0.6	0.6

Table 9. Estimated GCR Dose for Long-Duration Stays on Surface of Mars (Simonsen and Nealy 1993)

Mission	Arrival		Departure		Stay time (days)	Dose equivalent, cSv			
						Skin		BFO	
	Date	Year after solar min.	Date	Year after solar min.		High density	Low density	High density	Low density
1	3/17/2008	0.3	10/15/2009	1.9	577	17.9	20.9	16.7	18.9
2	6/10/2008	0.6	8/21/2009	1.8	437	13.6	15.9	12.6	14.3
3	4/29/2010	2.5	11/18/2011	4.0	568	15.7	18.1	14.5	16.4
4	8/13/2010	2.7	8/22/2011	3.8	374	10.3	11.9	9.6	10.8
5	6/1/2012	4.5	10/26/2013	6.0	512	11.1	12.5	10.2	11.3
6	6/4/2012	4.6	12/21/2013	6.0	565	12.2	13.7	11.3	12.5
7	7/1/2014	6.6	3/11/2016	8.3	619	13.8	15.6	12.8	14.1
8	8/29/2014	6.8	11/30/2015	8.0	458	10.0	11.3	9.3	10.3
9	8/31/2016	8.8	5/3/2018	10.5	610	17.7	20.6	16.5	18.6
10	10/1/2016	8.9	3/14/2018	10.3	529	15.3	17.8	14.3	16.1
11	10/1/2018	10.9	8/8/2020	1.8	677	21.2	24.7	19.7	22.3
12	1/7/2019	0.2	6/6/2020	1.7	516	16.0	18.7	14.9	16.9
13	12/12/2020	2.2	9/16/2022	3.9	643	18.1	21.0	16.9	19.0
14	2/19/2021	2.4	7/21/2022	3.8	517	14.6	16.9	13.5	15.3

The other main contributor to dose that should be taken into account is the dose from a large solar flare event. Listed in Table 8 and Table 9 are the arrival and departure dates in terms of years after the last solar minimum. For missions taking place during active solar conditions (approximately years 3–9), the occurrence of a large solar proton event may be taken into account such as the large flares of August 1972, November 1960, and February 1956. The 1989 large flare environment may be assumed. The September 29 flare occurred approximately 48 days after the August 12 flare, and the October 19 flare occurred approximately 20 days after the September event. Individually while on the surface of Mars, the 1989 flares do not contribute significantly towards the 30-day BFO and skin limits (assuming LEO limits) of 25 cSv and 150 cSv, respectively. The September and October doses may be added together and compared to the 30-day limit since they occur approximately 20 days apart. The sum of the September and October BFO doses of approximately 2.2–4.7 cSv are also shown not to contribute significantly towards the 30-day limits at a 0-km altitude. A solar flare can contribute more significantly to dose at higher altitudes. The only 30-day limit exceeded is the BFO limit of 25 cSv for the August 1972 event at the altitude of 12 km. However, as seen in figure 9, the August 1972 flare is rapidly attenuated by matter, and a few g/cm^2 of additional shielding should reduce the anticipated dose below this limit.

The doses incurred during transit to and from Mars will most likely dominate the total mission dose [2]. The surface dose estimates presented here have been incorporated into the MIRACAL program which can be used to

estimate doses for an entire Mars mission including transit to and from Earth [47]. Applications of the MIRACAL code for various Mars missions including surface stay doses are presented in Striepe *et al*. [5, 6].

Regolith Shielding Analysis. The atmosphere does provide a significant amount of protection. However, to follow the ALARA principal, the benefits of additional shielding should be addressed to determine if a significant amount of protection can be realized for little increased effort or expense. The shield effectiveness of Martian regolith will be examined here. The GCR particle flux at solar minimum and solar flare particle flux spectra obtained during the atmosphere calculations at 0-km and 8-km altitudes are now used as input conditions for regolith shield calculations. For a representative large solar flare contribution, the very penetrating spectrum of the February 1956 event is selected for further analysis. This event has the greatest flux of high-energy particles which results in the highest dose at the Martian surface. The subsequently calculated particle flux versus energy distributions in the regolith can then be used to determine the dose at specified locations in the shield media. The dose contribution attributed to particles arriving from a given direction is now determined by the amount of carbon dioxide traversed and then the shield thickness encountered along its straight line path to a specified target point within the habitat. An example of some of the basic propagation data required was shown in figure 13.

The candidate habitat configuration, as described by the mission scenario, is shown in figure 20. A series of calculations was performed for various regolith thicknesses covering the module. Again, no consideration is given to the added shielding provided by the pressure vessel and internal equipment. The largest integrated dose equivalent in a vertical plane through the center of the cylinder was plotted versus an effective regolith thickness in figure 21. As shown in the figure, the regolith does not provide much additional protection from the GCR or the flare event than that already provided by the carbon dioxide atmosphere. The slope of each curve is relatively flat after 20 g/cm^2, with most of the BFO dose reductions occurring in the first 20 g/cm^2. For 20 g/cm^2 of regolith protection, the annual BFO dose equivalent due to GCR is reduced from 11.9 cSv/yr to 10.0 cSv/yr at 0 km, and from 15.6 cSv/yr to 11.2 cSv/yr at 8 km. For 20 g/cm^2 of regolith, the BFO dose equivalent due to the solar flare is reduced from 9.9 rem/event to 6.3 cSv/event at 0 km.

A possible way to further reduce the dose equivalent received on the Martian surface would be to locate the habitat next to a cliff as shown in figure 20b. The cliff further reduces the BFO dose equivalent by approximately 2 to 3 cSv/yr for the GCR at 0 km, and by approximately 1 to 1.5 cSv/event for the February 1956 flare at 0 km as shown in figure 21. The shielding provided by the cliff and atmosphere alone result in a BFO dose equivalent of 9.1 cSv/yr due to GCR at solar minimum and 7.4 cSv/event due to the February 1956 event.

From this analysis, it is seen that moderate thicknesses of Martian regolith do not provide substantial additional protection to that already provided by the carbon dioxide atmosphere. If regolith is used as shielding material, the largest reduction in dose equivalent occurs in the first 20 g/cm^2 (or approximately 15 cm assuming a regolith density of 1.5 g/cm^3). Thus, if additional protection using Martian regolith is desired, a shield thickness on the order of 15 to 20 cm should be considered. If additional protection using 15 cm of Martian regolith is provided at an altitude of

0 km, the blood forming organ dose equivalent (yearly solar minimum GCR plus Feb. 1956 flare) will be reduced from 22 to 16 cSv/yr, respectively [40].

For radiation protection provided by regolith on the surface of Mars, mission planners must decide if the radiation doses anticipated warrant the added equipment and time required for crew members to "bury" themselves. For the shorter stay times of 30 to 90 days, the additional requirements placed on a Mars mission to cover a module may be unnecessary, especially if a flare shelter is provided. A logical alternative to massive shielding efforts is to take advantage of local terrain features found on the surface of Mars. Regolith shielding may become more attractive for the longer stay times of 600 days or for futuristic permanent habitation.

CONCLUDING REMARKS

A shield design methodology has been developed and implemented to estimate shield requirements and subsequent doses for both lunar and Mars surface missions. The results presented here should be considered best estimates made with the tools available at the time SEI studies were being initiated. Many advancements have developed in nuclear physics, environmental models, transport phenomena, radiobiology, and risk assessment techniques. There still remain many uncertainties which must be reduced in order to evaluate the shield effectiveness of materials and the effects of radiation on humans before the most affordable shield design strategy can be selected. In these studies, conventional dosimetry (quality factors) and LEO limits were used to assess material shield effectiveness. The definition of new quality factors relating dose to biological damage will have an impact on these results as well as the movement away from conventional dosimetric limits and techniques in assessing the risks of heavy-ion exposure. In most instances, these advancements can be incorporated into the current methodology as minor modifications. Available biological response models, as well as other subsystem response models (electronic, optical, etc.) can be incorporated into the design methodology. The particle fluence as a function of depth in material would be used instead of dose as a function of depth. The directional particle fluences would be extrapolated from the propagation data and integrated to obtain the total particle fluence as a function of energy at the target point of interest. The particle spectrum can then be used as input to the response model. Current techniques also incorporate computer aided solid modeling of the shielding and advanced ray tracing techniques to calculate the shield thickness distribution. With this capability, radiation shielding can easily become part of the conceptual design process for transfer vehicle, habitat, and satellite configurations. The studies and methodology presented here provide an excellent starting point for further shielding analyses for manned lunar and Mars missions.

REFERENCES

1.   J. E. Nealy: SEI Analysis of Deep Space Vehicle Shielding. Shielding Strategies for Shielding Exploration Workshop, NASA Johnson Space Center, Dec. 6–8, 1995.

2. J. E. Nealy, L. C. Simonsen, J. W. Wilson, L. W. Townsend, G. D. Qualls, B. G. Schnitzler, and M. M. Gates: Radiation Exposure and Dose Estimates for a Nuclear-Powered Manned Mars Sprint Mission. 8th Symposium on Space Nuclear Power Systems, Albuquerque, NM, 1991, pp. 531–536.

3. J. E. Nealy, L. C. Simonsen, and S. A. Striepe: Natural Radiation Environment Fluence and Dose Predictions for Missions to the Moon and Mars. ANS New Horizons in Radiation Protection and Shielding, Pasco, Washington, April 26–May 1, 1992a.

4. L. C. Simonsen and J. E. Nealy: Radiation Protection for Human Missions to the Moon and Mars. NASA TP-3079, 1991.

5. S. A. Striepe, J. E. Nealy, and L. C. Simonsen: Radiation Exposure Predictions for Short-Duration Stay Mars Missions. *Journal of Spacecraft and Rockets*, **29**, No. 6, Nov.–Dec. 1992, pp. 801–807.

6. S. A. Striepe, L. C. Simonsen, and J. E. Nealy: Radiation Exposure for Long-Duration-Stay Mars Missions. *Journal of the Astronautical Sciences*, **42**, No. 2, April–June 1994, pp. 131–142.

7. L. W. Townsend, J. E. Nealy, J. W. Wilson, and W. Atwell: Large Solar Flare Radiation Shielding Requirements for Manned Interplanetary Missions. *Journal of Spacecraft and Rockets*, **26**, No. 2, March–April 1989a, pp. 126–128.

8. L. W. Townsend, J. W. Wilson, and J. E. Nealy: "Space Radiation Shielding Strategies and Requirements for Deep Space Missions." SAE Paper No. 891433. 19th Intersociety Conference on Environmental Systems, San Diego, CA, 1989b.

9. L. W. Townsend, J. L. Shinn, and J. W. Wilson: Interplanetary Crew Exposure Estimates for the August 1972 and October 1989 Solar Particle Events. *Radiation Research*, **126**, 1991, pp. 108–110.

10. L. W. Townsend, J. W. Wilson, J. L. Shinn, and S. B. Curtis: Human Exposure to Large Solar Particle Events in Space. *Adv. Space Res.*, **12**, 1992a, (2)339–(2)348.

11. L. W. Townsend, F. A. Cucinotta, and J. W. Wilson: Interplanetary Crew Exposure Estimates for Galactic Cosmic Rays. *Radiation Research*, **129**, No. 1, January 1992b, pp. 48–52.

12. J. E. Nealy: Integrated Shield Design Methodology. Shielding Strategies for Shielding Exploration Workshop, NASA Johnson Space Center, Dec. 6–8, 1995.

13. G. D. Qualls: Simulation of Shield and Human Geometry. Shielding Strategies for Shielding Exploration Workshop, NASA Johnson Space Center, Dec. 6–8, 1995.

14. Report of the 90-Day Study on Human Exploration of the Moon and Mars: NASA Johnson Space Center, 1989.

15. J. Alred, A. Bufkin, J. Graf, K. Kennedy, J. Patterson, A. Petro, M. Roberts, J. Stecklein, and J. Sturm: "Development of a Lunar Outpost: Year 2000–2005," Lunar Bases and Space Activities of the 21st Century, Symposium Paper No. LBS-88-240, 1988.

16. National Council of Radiation Protection and Measurements: Guidance on Radiation Received in Space Activities. NCRP Report No. 98, July 31, 1989.

17. S. Curtis: Human Risk Models and Risk Uncertainty. Shielding Strategies for Shielding Exploration Workshop, NASA Johnson Space Center, Dec. 6–8, 1995.

18. Recommendations of the International Commission on Radiological Protection, ICRP Publ. 26, Pergamon Press, Jan. 17, 1977.

19. International Commission on Radiation Units and Measurements: The Quality Factor in Radiation Protection, ICRU Publ. 40, Pergamon Press, 1986.

20. J. W. Wilson, J. L. Shinn, and L. W. Townsend: "Nuclear Reaction Effects in Conventional Risk Assessment for Energetic Ion Exposure." *Health Physics*, **58**, No. 6, June 1990, pp. 749–752.

21. R. Katz, : "Biological Effects of Heavy Ions from the Standpoint of Target Theory." *Adv. Space Res.*, **6**, No. 11, 1986, pp. 191–198.

22. F. A. Cucinotta, R. Katz, J. W. Wilson, L. W. Townsend, J. E. Nealy, and J. L. Shinn: Cellular Track Model of Biological Damage to Mammalian Cell Cultures from Galactic Cosmic Rays. NASA TP-3055, 1990.

23. J. W. Wilson: Environment Geophysics and SPS Shielding. Workshop on the Radiation Environment of the Satellite Power System, Walter Schimmerling and Stanley B. Curtis, eds. (Contract W-7405-ENG-48), Univ. of California, 1978.

24. H. H. Sauer, R. D. Zwickl, and M. J. Ness: Summary Data for the Solar Energetic Particle Events of August through December 1989. NOAA-Space Environment Laboratory, Feb. 21, 1990.

25. J. E. Nealy, L. C. Simonsen, L. W. Townsend, and J. W. Wilson: Deep Space Radiation Exposure Analysis for Solar Cycle XXI (1975–1986). SAE Paper No. 901347, 20th International Conference on Environmental Systems, Williamsburg, VA, 1990.

26. J. H. Adams Jr., R. Silberberg, and C. H. Tsao: Cosmic Ray Effects on Microelectronics. Part I—The Near-Earth Particle Environment. NRL Memo. Rep. 4506-Pt. I, U.S. Navy, Aug. 1981 (Available from DTIC as AD A103 897.)

27. K. Nagashima, S. Sakakibara, K. Murakami, and I. Morishita: "Response and Yield Functions of Neutron Monitor, Galactic Cosmic Ray Spectrum and Its Solar Modulation, Derived from All the Available World Wide Surveys." Nuovo Cimento, No. l. 12C, Ser. 1, No. 2, March–April 1989, pp. 173–209.

28. G. L. Withbroe: Solar Activity Cycle: History and Predictions, *J. of Spacecraft and Rockets*, **26**, No. 6, Nov.–Dec. 1989, pp. 394–402.

29. D. F. Smart and M. A. Shea: Solar Proton Events During the Past Three Solar Cycles. *J. of Spacecraft and Rockets*, **26**, No. 6, Nov.–Dec. 1989, pp. 403–415.

30. G. D. Badhwar: Deep Space Radiation Sources, Models, and Environmental Uncertainty. Shielding Strategies for Human Space Exploration Workshop, NASA Johnson Space Center, Dec. 6–8, 1995.

31. G. D. Badhwar, P. M. O'Neill: An Improved Model of GCR for Space Exploration Missions. *Nucl. Tracks Radiat. Meas.*, **20**, pp. 403–410, 1992.

32. J. W. Wilson, L. W. Townsend, J. E. Nealy, S. Y. Chun, B. S. Hong, W. W. Buck, S. L. Lamkin, B. D. Ganapol, F. Khan, and F. A. Cucinotta: BRYNTRN: A Baryon Transport Model. NASA TP-2887, 1989.

33. J. W. Wilson, L. W. Townsend, W. S. Schimmerling, G. S. Khandelwal, F. Khan, J. E. Nealy, F. A. Cucinotta, L. C. Simonsen, J. L. Shinn, and J. W. Norbury: Transport Methods and Interactions for Space Radiations. NASA RP-1257, 1991b.

34. J. W. Wilson, S. Y. Chun, F. F. Badavi, L. W. Townsend, and S. L. Lamkin: HZETRN: A Heavy Ion/Nucleon Transport Code for Space Radiations. NASA TP-3146, 1991a.

35. J. W. Wilson: "Analysis of the Theory of High Energy Transport," NASA TN D-8381, 1977.

36. F. A. Cucinotta, R. Katz, J. W. Wilson, L. W. Townsend, J. Shinn, and F. Hajnal: Biological Effectiveness of High-energy Protons: Target Fragmentation. *Radiation Research*, **127**, 1991, p. 130.

37. C. Dalton and E. Hohmann, eds.: Conceptual Design of a Lunar Colony. NASA CR-129164, 1972.

38. R. E. Smith and G. S. West, compilers: Space and Planetary Environment Criteria Guidelines for Use in Space Vehicle Development, 1982 Revision (Volume 1). NASA TM-82478, 1983.

39. J. E. Nealy, J. W. Wilson, and L. W. Townsend: Solar-Flare Shielding with Regolith at a Lunar-Base Site. NASA TP-2869, 1988.

40. L. C. Simonsen, J. E. Nealy, L. W. Townsend, and J. W. Wilson: Space Radiation Shielding for a Martian Habitat. SAE Tech. Paper Ser. 901346, 1990b.

41. J. E. Nealy, J. W. Wilson, and L. W. Townsend: Preliminary Analysis of Space Radiation Protection for Lunar Base Surface Systems. SAE Paper No. 891487. 19th Intersociety Conference on Environmental Systems, San Diego, CA, 1989.

42. L. C. Simonsen: Construction Technologies: Prefabricated vs. In Situ in Lunar Studies. NASA Workshop on "Shielding Strategies for Human Space Exploration." Houston, TX, December 6–8, 1995.

43. L. C. Simonsen and J. E. Nealy: Mars Surface Radiation Exposure for Solar Maximum Conditions and 1989 Solar Proton Events. NASA TP-3300, 1993.

44. L. C. Simonsen, J. E. Nealy, L. W. Townsend, and J. W. Wilson: Radiation Exposure for Manned Mars Surface Missions. NASA TP-2979, 1990a.

45. Interplanetary Charged Particle Models. NASA SP-8118, 1975.

46. Zdenek Švestka: Solar Flares. D. Reidel Publ. Co., Inc., 1976.

47. J. E. Nealy, S. A. Striepe, and L. C. Simonsen: MIRACAL: A Mission Radiation Calculation Program for Analysis of Lunar and Interplanetary Missions. NASA TP-3211, 1992b.
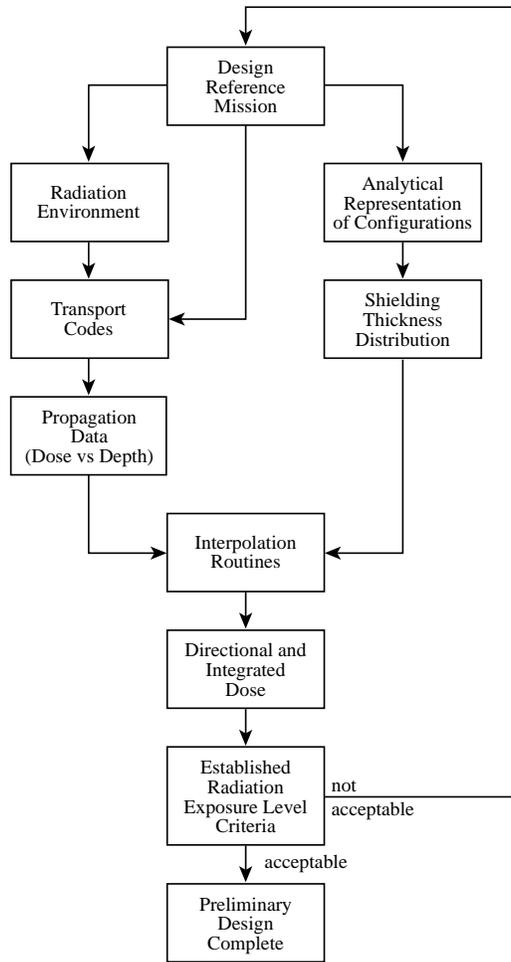
Figure 1.   Flow chart of radiation shield design methodology.
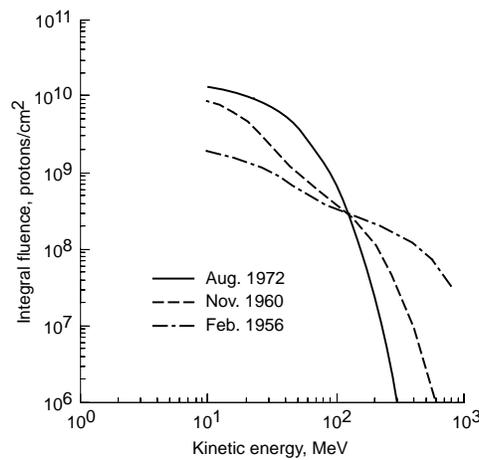
Figure 2.   Integrated fluence spectra for the three large solar proton flares of February 1956, November 1960, and August 1972 (Wilson 1978).
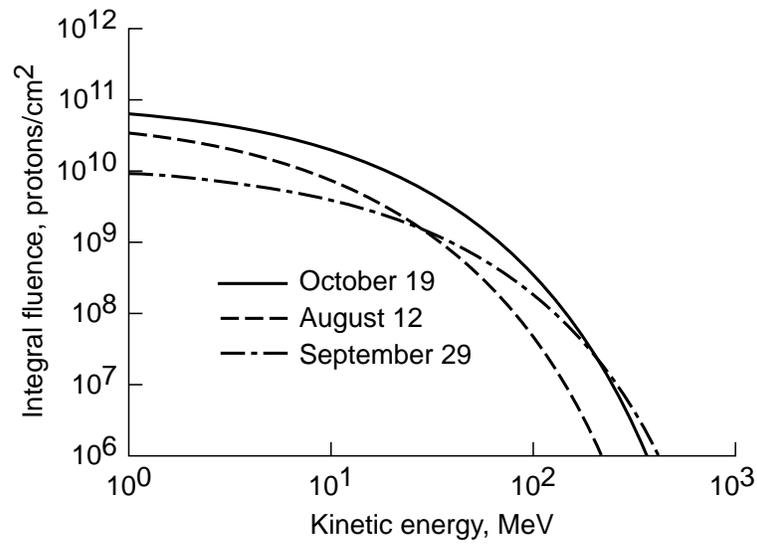
Figure 3.   Three large solar proton flare integral fluences based on 1989 GOES-7 data (Sauer *et al.* 1990).
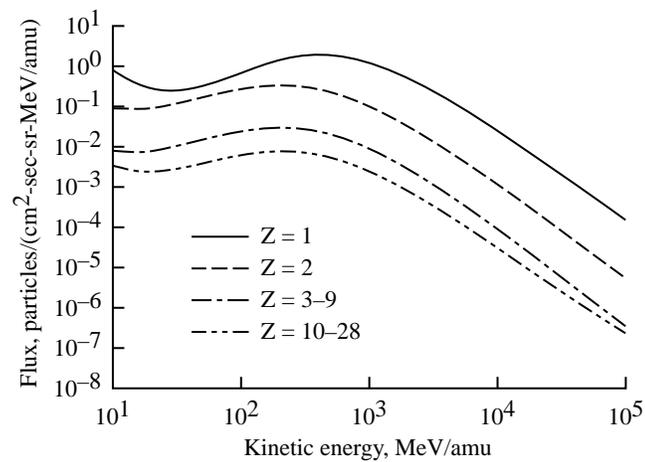
Figure 4.   Galactic cosmic ray differential flux spectra for solar minimum conditions for selected elemental groups.
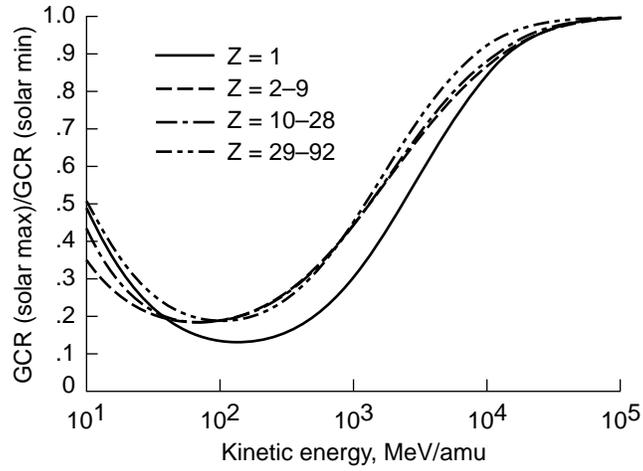
Figure 5.   Ratios of GCR differential flux at solar maximum conditions to corresponding flux at solar minimum for selected elemental groups.
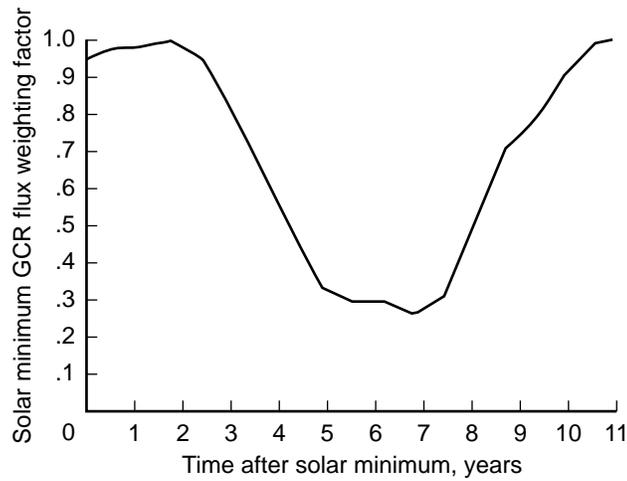
Figure 6.   Modulation function for GCR flux as derived for solar cycle XXI in terms of a weighting factor for observed peak (solar minimum) flux.
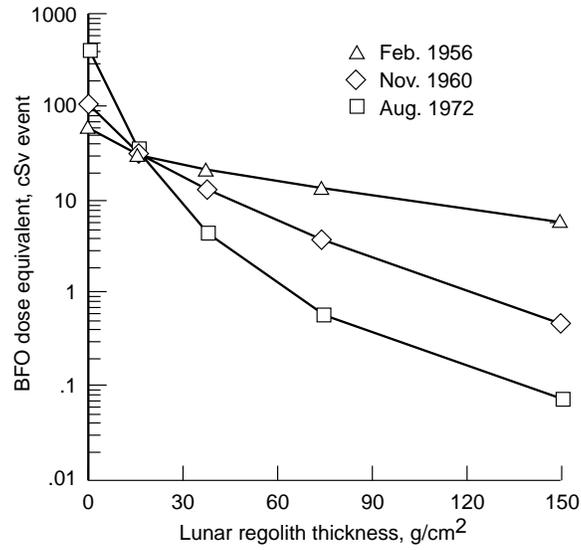
Figure 7.   Estimated BFO dose equivalent as a function of lunar regolith thickness for three large solar proton events (Nealy *et al.* 1988).
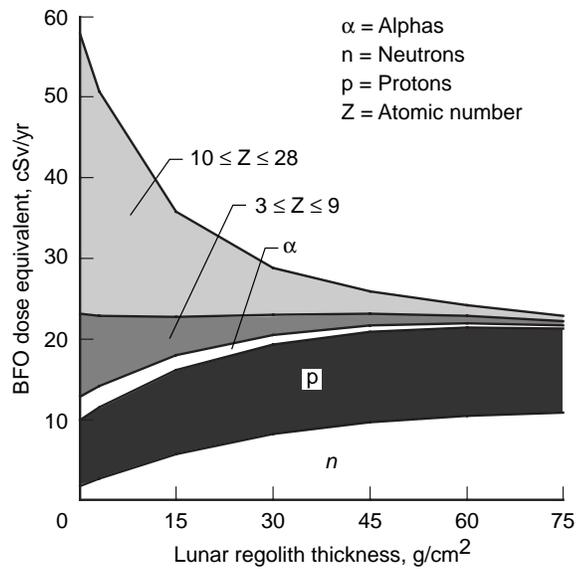
Figure 8.   BFO annual dose-equivalent contributions from specified particle constituents as a function of lunar regolith thickness for GCR at solar minimum conditions (Nealy *et al.* 1989).

71
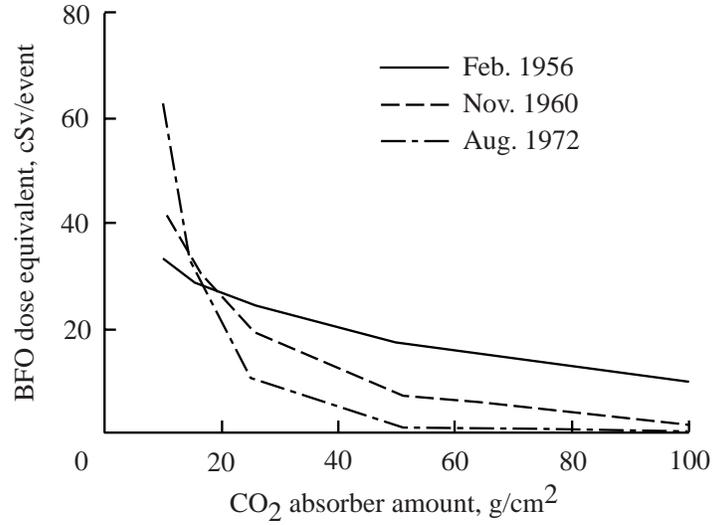
Figure 9.   BFO dose equivalent as a function of carbon dioxide absorber amount for the solar proton events of February 1956, November 1960, and August 1972 (Simonsen *et al.* 1990a).
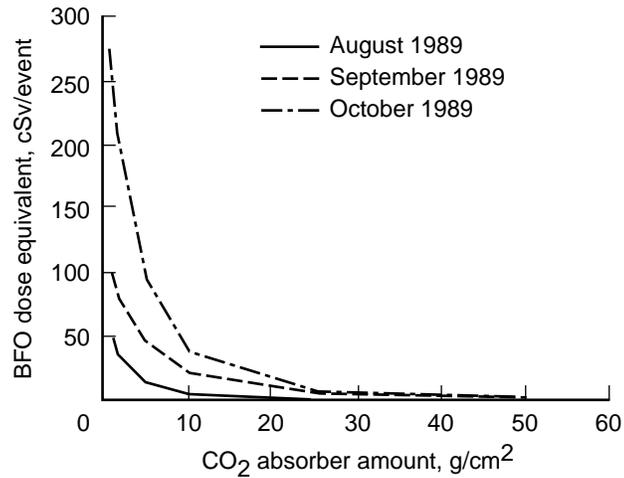
Figure 10. BFO dose equivalent as a function of carbon dioxide absorber amount for the three 1989 solar proton events (Simonsen and Nealy, 1993).
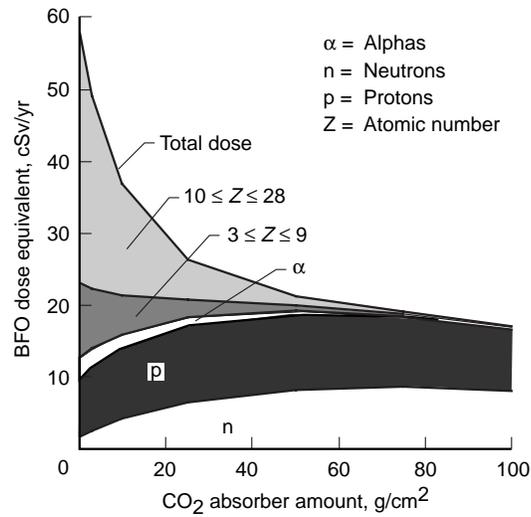
Figure 11. BFO annual dose-equivalent contributions from specified particle constituents as a function of carbon dioxide absorber amount for GCR at solar minimum conditions (Simonsen *et al.* 1990a).
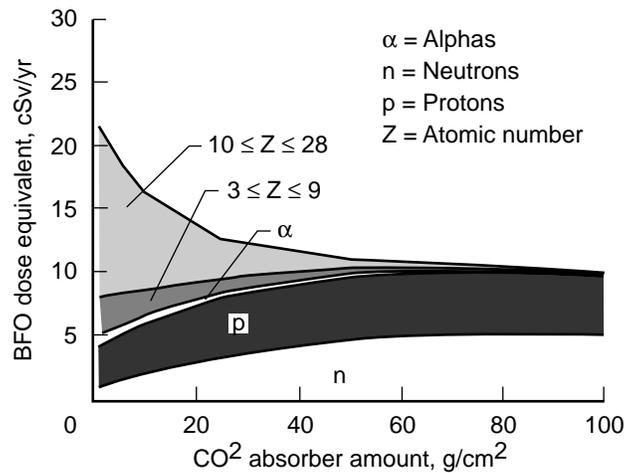
Figure 12. BFO annual dose-equivalent contributions from specified particle constituents as a function of carbon dioxide absorber amount for GCR at solar maximum conditions (Simonsen and Nealy, 1993).
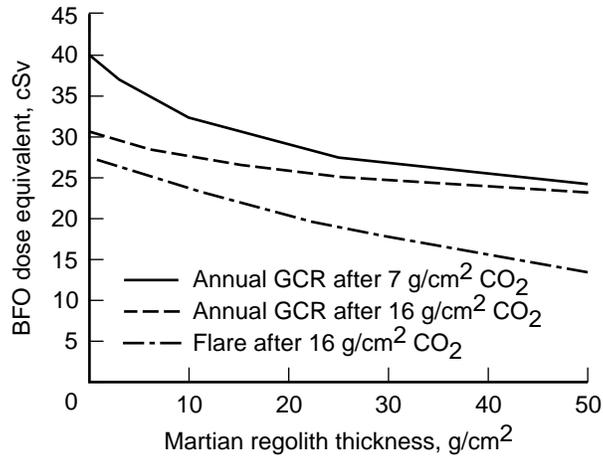
Figure 13. BFO dose equivalent as a function of regolith thickness after transport through the Martian atmosphere in the vertical direction (Simonsen *et al.* 1990b).

(a)   (b)
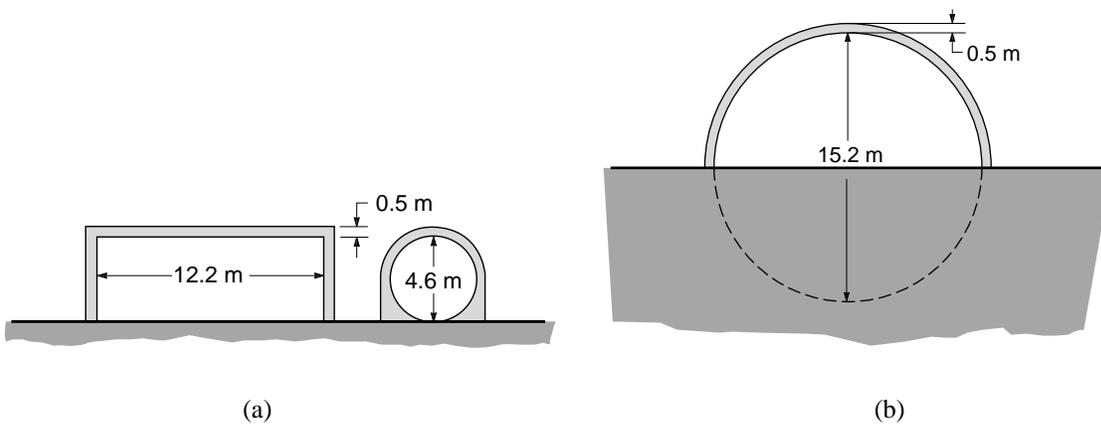
Figure 14. Modeled shielded configurations of candidate lunar habitat modules (Nealy *et al.* 1989).
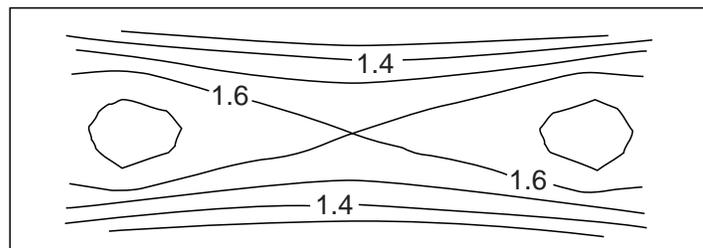
Figure 15. BFO dose-equivalent (cSv) variation resulting from the November 1960 flare event within the shielded cylindrical configuration of Figure 14a for the central horizontal plane (Nealy *et al.* 1988).
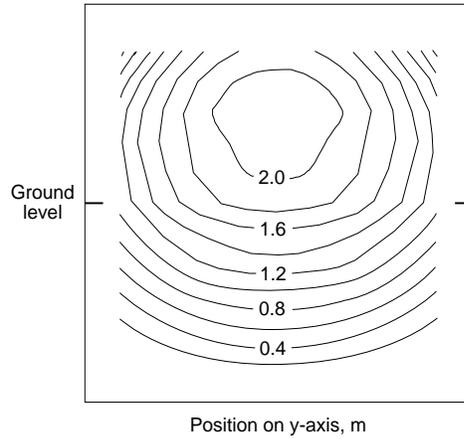
Figure 16. BFO dose-equivalent (cSv) variation resulting from the November 1960 flare event within the half-buried sperical configuration of Figure 14b for a central vertical plane (Nealy *et al.* 1988).


Figure 17. Annual BFO dose-equivalent (cSv) variation resulting from GCR at solar minimum within the shielded cylindrical configuration of Figure 14a for central horizontal plane (Nealy *et al.* 1989).
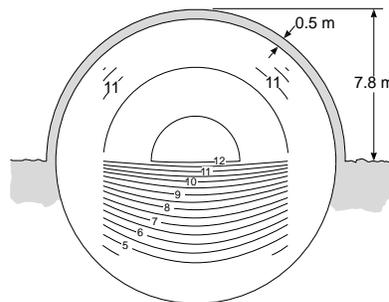
Figure 18. Annual BFO dose-equivalent (cSv) variation resulting from GCR at solar minimum within the half-buried spherical configuration of Figure 14b for a central vertical plane (Nealy *et al.* 1989).
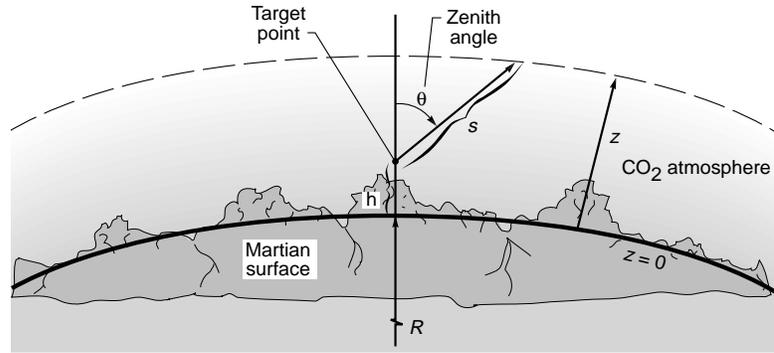
Figure 19. Martian atmosphere geometry and parameters associated with dose calculations at target point
(Simonsen *et al.* 1990a.)
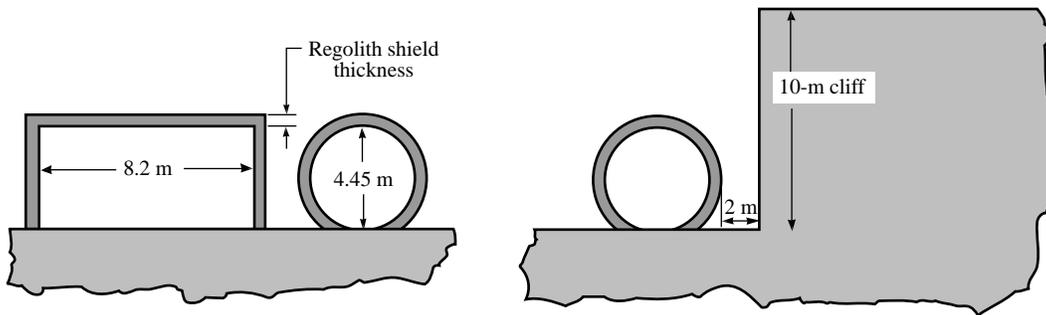
(a) Side and end views.   (b) Module next to cliff.

Figure 20. Cylindrical habitat module with regolith shielding for Mars (Simonsen *et al.* 1990b).
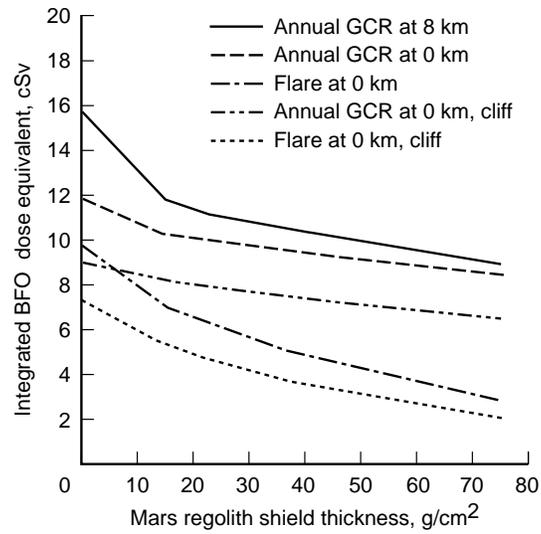
Figure 21. Maximum BFO dose in central across sectional plane of module as a function of effective regolith shield thickness (Simonsen *et al.* 1990b.)

CHAPTER 5

HUMAN RISK MODELS AND RISK UNCERTAINTY

by

Stanley B. Curtis[1]

---

[1] Fred Hutchinson Cancer Research Center, Seattle, Washington 98104

Chapter 5

HUMAN RISK MODELS AND RISK UNCERTAINTY

SUMMARY

This presentation is a brief review of current methods of relating the galactic cosmic radiation environment in space to the estimated risk of radiation-induced cancer in space travelers on extended space missions. In the following discussion, only cancer will be addressed since it is presently assumed to be the most important late radiation effect to travelers on extended missions outside the magnetosphere. The hazard from large solar particle events will not be considered here. Uncertainty considerations will be discussed.

CURRENT GUIDELINES

First, we define terms and present current guidelines for earth-orbiting spacecraft such as Shuttle and Space Station. We must emphasize that concepts and even risk numbers for conventional radiation (i.e., low-LET radiation) are evolving and changing with time. The concept used in the radiation protection community up to 1991 was the *dose equivalent.* The dose equivalent is defined as the dose of low-LET radiation (usually taken to be gamma rays) that is necessary to produce the same biological effect (i.e., risk) as the radiation environment in question. It is defined for use only in radiation protection and only for low dose and dose-rate situations, where linearity of risk response vs. dose is expected. Thus, dose equivalents from radiations of different quality (i.e., from different LET's) can be added:

$$H = \sum_i H_i \tag{1}$$

where the sum is over the different LET radiations in the environment. For a mixed-LET radiation environment, the dose equivalent can be calculated:

$$H = \int D(L)Q(L)dL \tag{2}$$

where $D(L)dL$ is the dose deposited in the LET interval $[L, L + dL]$, and $Q(L)$ is a weighting factor that converts absorbed dose into dose equivalent at a given LET. It is called the *quality factor* and is decided upon (by committee) after a study of relevant Relative Biological Effectiveness (RBE) factors obtained at low dose and dose-rate (or in fractionated experiments). The units of dose equivalent are sieverts (Sv). The exposure by 1 Sv of any

radiation is equivalent to 1 Gy of low-LET radiation (i.e., for $Q = 1$). Older units for the dose equivalent and absorbed dose are rem (1 rem = 0.01 Sv) and rad (1 rad = 0.01 Gy), respectively. The present guidelines [1] for career limits (assuming an excess cancer risk of 3%) recommended by the National Council for Radiation Protection (NCRP) for low earth-orbiting missions (Shuttle and Space Station) and accepted by NASA and OSHA are given in Table 1. These numbers, however, are presently under revision by NCRP Committee 75 due to a revision in the low-LET risk coefficients by the ICRP [2] and NCRP [3]. Inclusion of this revision would be to lower the career limits given in Table 1 by about a factor of two.

Table 1. Career Whole-Body Dose Equivalent Limits (Sv) for a
Lifetime Excess Risk of Fatal Cancer of 3%[1]

Age	25	35	45	55
Male	1.5	2.5	3.25	4.0
Female	1.0	1.75	2.5	3.0

[1]From NCRP Report #98 [1].

In addition to the revision of the values of the low-LET risk coefficients mentioned above, other changes were recommended in the ICRP60 report [2] including the introduction of a new concept (equivalent dose) and a change in the dependence of the quality factor on LET. The unit of equivalent dose is the same as for dose equivalent (Sv), but a different calculation is used to arrive at the new quantity. The definition of equivalent dose is

$$H_T = \sum w_R D_{R,T} \tag{3}$$

where the w_R are the *radiation weighting factors*, $D_{R,T}$ are the average absorbed doses from radiation R in tissue T, and summation is over all the different types of radiation. The radiation weighting factors for various radiations are given in Table 2 [2]. More recently, concern has been shown that the value in this table for protons with energies greater than 2 MeV ($w_R = 5$) is too high [4], and the proton value has been lowered to 2 and further qualified in the most recent NCRP publication dealing with limitations of exposure to ionizing radiation [5]. An alternative method to calculate equivalent dose suggested for those radiations not covered in the table is

$$H_T = \overline{Q} \cdot D_{T,R} \tag{4}$$

where

$$\overline{Q} = \frac{1}{D} \int_0^\infty Q(L)D(L)dL \tag{5}$$

and *D(L)* is the distribution in dose from the radiation environment in question *at a point 10 mm deep within the ICRU sphere* (a sphere of tissue-equivalent material 30 cm in diameter). In this case, $\overline{Q}$ is considered

Table 2. Radiation Weighting Factors[1]

Type and energy range	w_R
Photons, all energies	1.0
Electrons and muons	1.0
Neutrons, energy < 10 keV	5.0
10 – 100 keV	10.0
100 keV – 2 MeV	20.0
2 – 20 MeV	10.0
> 20 MeV	5.0
Protons, other than recoils, E > 2 MeV	5.0
Alpha particles, fission frag., heavy nuclei	20.0

[1]From ICRP60 [2].

an "approximation" of the radiation weighting factor w_R.   The new dependence of the quality factor on LET is given in Table 3, and both the new and old dependencies are shown for comparison in figure 1. Therefore, in evaluating radiation risks that have been calculated in recent years, it is important to be aware of which (new or old) risk coefficients and Q vs. LET expressions were used, and whether dose equivalent or equivalent dose was calculated.

Table 3. Table of Quality Factor in Various Regions of LET[1]

Unrestricted LET, L, in water (keV / μm)	$Q(L)$
< 10	1
10 –100	$0.32 L - 2.2$
>100	$300 / L^{1/2}$

[1]From ICRP60 [2].

EFFECTS OF SHIELDING

It is of some interest to note what increasing the shield thickness might do to the relative contributions of high- and low-LET radiation caused by the galactic radiation. Figures 2 and 3 show LET-distributions of the galactic cosmic radiation (at solar minimum) behind aluminum shielding thicknesses of 1 and 10 g/cm^2 weighted by the new (1990) quality factor. The two maxima on the left are from the proton and helium-ion components and the large portion between 15 and 1000 keV/μm is contributed by carbon through iron ions. It is clear that the 9 g/cm^2 of

aluminum decreases the carbon through iron component appreciably while the proton and helium-ion contributions remain almost the same. Included in the figures are the physical dose distributions in LET; they are seen as dashed lines at the bottom of the figures. Below 10 kev/μm, $Q = 1$, so the "biologically weighted" and physical dose distributions are identical.

The process can be taken one step further by introducing a Computerized Anatomical Man (CAM) and calculating the risk of cancer in a particular organ being induced by the galactic cosmic rays. To do this, the risk coefficients for the radiosensitive organs of the body are used. They are given in Table 4 and come directly from ICRP60 [2]. The total risk of radiation-induced cancer is considered to be 4% per Sv for an adult population. The numbers in this table come from a reevaluation of the epidemiological data obtained from the atomic bomb survivors of Hiroshima and Nagasaki. Several steps, however, have been taken to arrive at these values. First, the data for cancer mortality have been projected out to the end of life to arrive at lifetime mortality risks because many of the survivors are still alive, and probabilities as a function of age are not yet completely known. Secondly, the risks were transferred across populations, since the Japanese people have organ sensitivities different from populations in other countries of the world. Finally, a factor of one-half was introduced to decrease the risk coefficients (which were obtained at high dose-rate) to those considered to apply to a low dose-rate situation. The numbers in the second column of the table are those assumed to apply to the various organs of the body. Using those numbers, the risk distribution in LET can be calculated for each organ of the body behind 10 g/cm^2 of aluminum for a galactic cosmic ray spectrum at solar minimum. This is shown in figure 4 [6]. Here we see that all the distributions have similar shapes; the heights of the distributions are affected by (1) how much self-body shielding is available, and (2) the value of the risk coefficient from Table 4. The results of the integrations of these curves are given in Table 5. Here we see the risks per year of exposure to the galactic cosmic rays from radiation-induced tumor mortality to astronauts at solar minimum behind 10 g/cm^2 aluminum shielding.

UNCERTAINTIES

Several sources of uncertainty have been identified in the risk evaluation process. They can be divided into two distinct categories: (1) uncertainty in the physical determination of the radiation environment inside the space traveler's body and (2) the uncertainty in the risk *given* the radiation environment within a tissue in the body. The first uncertainty can be broken into two components: uncertainty in the radiation environment itself to be found outside the spacecraft (or habitat), and the uncertainty involved in transporting the radiation through the available shielding and the bodies of the space travelers. The uncertainty in the risk for a given radiation exposure within the tissues of interest can also be broken into two components. Since the risk is presently anchored to the risk from low-LET radiation, one component arises from the uncertainty in the low-LET risk coefficients and the other from the uncertainty in the risk from the high-LET components relative to that from the low-LET components (i.e., the radiation weighting factors or quality factor as a function of LET). One attempt to estimate the uncertainties from

Table 4. Low Dose-rate Cancer Mortality Risk Coefficients

Organ/Tissue	Probability of Excess Fatal Cancer[1] (Percent / Sv)
Stomach	0.88
Colon	0.68
Lung	0.68
Bone Marrow	0.4
Bladder	0.24
Esophagus	0.24
Breast	0.16
Liver	0.12
Ovary	0.08
Thyroid	0.06
Bone Surface	0.04
Skin	0.02
Remainder	0.4
TOTAL	4.0

[1]From ICRP Report #60 [2].

these various sources is shown in Table 6. We note that the overall uncertainty is dominated by the biological uncertainties in the low-LET coefficient and the high-LET quality factor. The uncertainties in the low-LET risk coefficient has been addressed in some detail [7], and the contributions are identified in Table 7. Estimates have been made in the table as to the magnitudes of the various contributions as well as the direction that errors would move the risk coefficient (i.e., to greater or less risk).

NCRP COMMITTEE ON THE STUDY OF A FLUENCE-BASED RISK METHODOLOGY

The NCRP has appointed a committee to study various methodologies of radiation protection for space activities outside the magnetosphere, including one based on the fluence spectra of charged particles found in organs of interest. It is presently too early to report the final conclusions of this study, but it appears that available experimental data do not support an introduction of a totally fluence-based system at the present time. The committee is unanimous, however, in recommending that more well-chosen biological experiments be performed to define the dependence of end points (relevant to human risk) on the important particles and energies making up the space radiation environment.

Table 5. Risk Quantities for Seven Radiation-induced Cancers[a]

Organ	Risk per yr of exposure to GCR	Yearly absorbed dose (Gy)	Yearly dose equivalent (Sv)
BFO	1.28×10^{-3}	0.12	0.32
Bladder	6.25×10^{-4}	0.12	0.26
Breast[b]	1.2×10^{-3}	0.12	0.38
Colon	2.04×10^{-3}	0.12	0.30
Esophagus	8.42×10^{-4}	0.12	0.35
Lung	2.07×10^{-3}	0.12	0.30
Stomach	2.27×10^{-3}	0.12	0.26
Total yearly risk	10.3×10^{-3} (for females)		
	9.1×10^{-3} (for males)		

[a] Conditions: One year exposure to GCR at solar minimum conditions behind 10 g/cm^2 aluminum shielding, assuming Computerized Anatomical Male (CAM) or Female (CAF) model .

[b] Applicable to female crew only.

Table 6. Uncertainties

$$\text{Risk} = R_\gamma \int Q(L)\, L\, \overline{\Phi}(L)\, dL$$

Source	R_γ	$Q(L)$	$\overline{\Phi}(L)$
Physical			
Particle Environment			$\pm(10-15)\%$
Transport through shielding			$\pm 50\%$
Biological			
DDREF, extrapolation across nationalities, risk projection to end-of-life, dosimetry, etc.	200 – 300% (mult.)		
Radiation quality dependence of human cancer risk		200 – 500% (mult.)	

Table 7. Uncertainties in the Low-LET Risk Coefficient[1]

Uncertainties	Approximate Contribution
Supporting higher risk estimates	
Dosimetry bias errors	+10%
Under-reporting	+13%
Projection directly from current data	+ ?%
Supporting lower risk estimates	
Dosimetry: more neutrons at Hiroshima	− 22%
Projection, i.e., by using attained age (?)	− 50%
Either way	
Transfer between populations	? ± 25–50%
Dose response and extrapolation	? ± 50%

[1]From [7].

REFERENCES

1. NCRP98, Guidance on Radiation Received in Space Activities, NCRP Report No. 98, National Council on Radiation Protection and Measurements, Bethesda, MD, 1989.

2. ICRP Publication 60, *Annals of the ICRP,* **21**, (No. 1–3), Pergamon Press, Oxford, 1991.

3. NCRP115, Risk Estimates for Radiation Protection, NCRP Report No. 115, National Council on Radiation Protection and Measurements, Bethesda, MD, 1993.

4. S. B. Curtis, Are radiation weighting factors relevant for protons and heavier charged particles? In: *Radiation Research* 1895–1995, *Congress Proceedings*, Volume 2 (Eds.: V. Hagen, D. Harder, H. Jung and C. Streffer), Würzburg, Germany, pp. 161–164 (1995).

5. NCRP116, Limitation of Exposure to Ionizing Radiation, NCRP Report No. 116, National Council on Radiation Protection and Measurements, Bethesda, MD, 1993.

6. S. B. Curtis, J. E. Nealy and J. W. Wilson, Risk cross sections and their application to risk estimation in the galactic cosmic ray environment, *Radiat. Res.* **141**, 57–65 (1995).

7. W. K. Sinclair, *Science, Radiation Protection and the NCRP*, Lauriston Taylor Lecture, Proceedings of the 29th Annual Meeting, April 7–8, 1993, NCRP, Proceedings No. 15, 209–239, 1994.
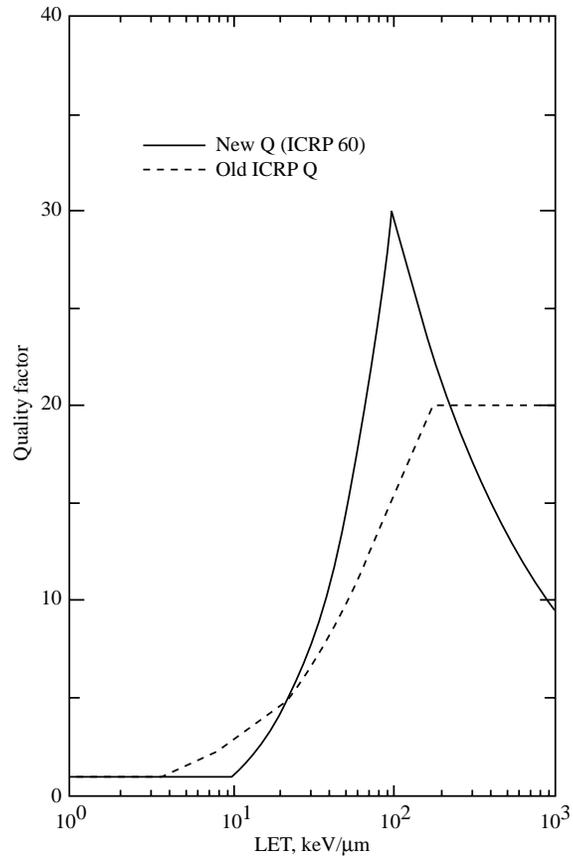
Figure 1. The new and old quality factors as a function of LET.
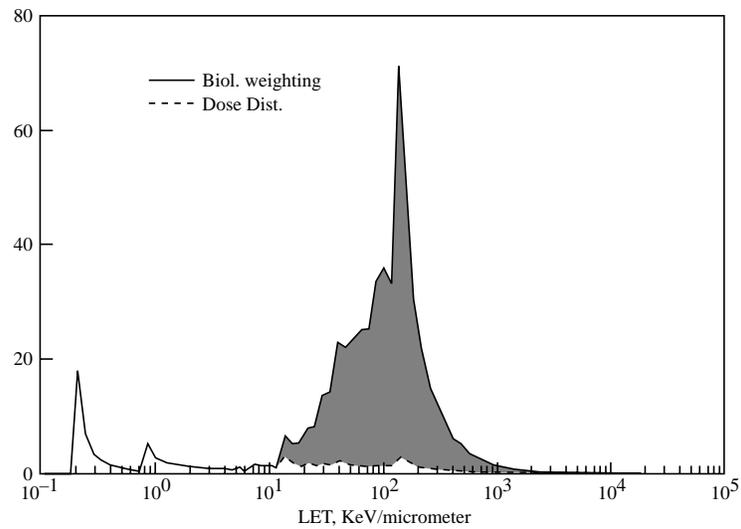
Figure 2. Dose equivalent and physical dose distributions for the galactic cosmic rays at solar minimum behind 1 g/cm^2 aluminum shielding. The shaded area denotes the difference between the distributions with and without the ICRP60 quality factor included.
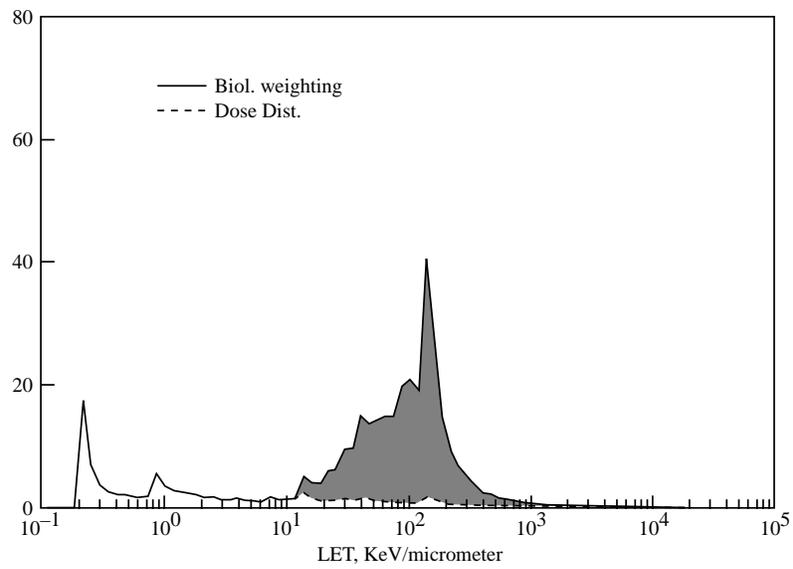
Figure 3. Dose equivalent and physical dose distributions for the galactic cosmic rays at solar minimum behind 10 g/cm^2 aluminum shielding. The shaded area denotes the difference between the distributions with and without the ICRP60 quality factor included.
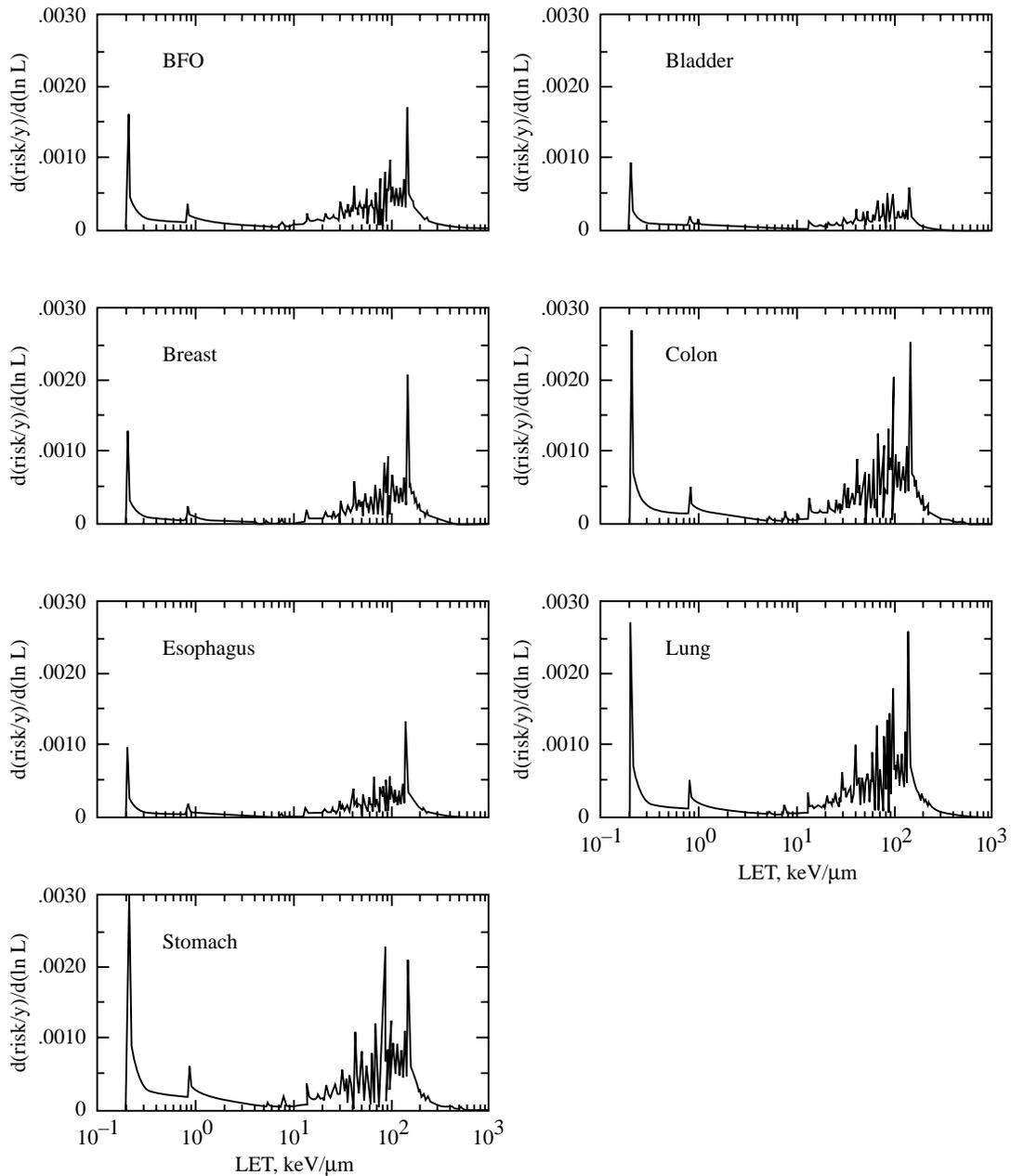
Figure 4.   Differential risks per logarithmic interval of LET for one year's exposure to the galactic cosmic rays at solar minimum behind 10 g/cm^2 aluminum shielding plotted semi-logarithmically against LET for seven radiation-sensitive organs. The plots show the relative importance of the various components of LET to the total risk (from [6]).

CHAPTER 6

BIOLOGICAL RESPONSE TO HEAVY ION EXPOSURES

by

Tracy Chui-hsu Yang[1]

Laurie M. Craise[2]

[1]NASA Johnson Space Center, Medical Sciences Division, Houston, Texas 77058
[2]Lawrence Berkeley Laboratory, Life Sciences Division, University of California, Berkeley, CA 94720

Chapter 6

BIOLOGICAL RESPONSE TO HEAVY ION EXPOSURES

SUMMARY

Studies on the biological responses to heavy ion radiation began early in the 20th century. As accelerator technologies advanced, biological research moved gradually from the effects of low-energy to high- energy heavy ions. Although radiotherapy was the main focal point of research, significant findings were obtained from basic studies of heavy ion effects. Most experimental results showed that high-Linear Energy Transfer (high-LET) heavy ions can be more effective than low-LET radiation in causing various biological effects, including cell inactivation, mutation, and carcinogenesis. Basic studies of types of DNA damage and chromosome aberrations suggested that the high ionization density of the heavy particle track might be the reason that heavy ions have relatively high Relative Biological Effectiveness (RBE).

Further investigations, however, have indicated that certain type(s) of chromosome damage, such as sister chromosome exchange, may be independent of LET. In addition, studies of low-energy charged particles have suggested that the biological effectiveness of heavy ions may depend on both the energy and the LET of the particle, i.e., its track structure. Fragmentation of primary particles and/or target can be important in the biological response to heavy ions, since limited data on the induction of chromosome aberrations with very high energy charged particles showed RBEs greater than one.

Although substantial amounts of data have been obtained during the past several decades, many important questions remain unanswered. Many more studies are needed to complete our understanding of the various potential biological effects of heavy ions and its mechanisms. In the past, the availability of radiation sources limited the range of heavy-ion energies that could be studied. Most investigations were conducted with 10–600 MeV/u heavy ions; very few experimental data exists on the biological effects of very-low-energy (less than 1 MeV/u) and very-high-energy particles (greater than 1 GeV/u). Within the next few years, it is expected that exciting heavy ion research will be continued and that new data will be obtained from very-low- and very-high-energy charged particle studies.

INTRODUCTION

Since the discovery of cosmic rays early in the 20th century, many scientists have studied the physics of high energy charged particles [1]. Advances in accelerator technology and increasing emphasis on human health problems during the past thirty years have greatly stimulated biological and medical research with heavy ions. The new era of human space flight program demanded further investigations of heavy-ion radiobiology to assess the health risks from space radiation.

The space environment includes several sources of ionizing radiation, including trapped radiation belts around the Earth, the solar particle events, and the galactic cosmic rays. These types of radiation are different from gamma rays and neutrons. They are high-energy charged particles with energy in the MeV/u to GeV/u range and charges ranging from one (protons) to many (e.g., uranium nuclei). For long-term space flight, especially missions to the moon and Mars, the crew members will unavoidably be exposed to ionizing radiation as they travel through the inner trapped proton belt, the outer trapped electron belt, and through the galactic cosmic rays of interplanetary space. In addition, outside the Earth's magnetosphere, there is the possibility for exposure to charged-particle radiation from solar particle events. The potential biological effects of these kinds of space radiation must be understood and countered where possible to ensure the safety of the crew members and the success of their missions. Intensive studies of the effectiveness of both low- and high-energy charged particles in inducing cellular as well as tissue injuries are urgently needed. Understanding the molecular mechanisms of radiation damage is essential for developing countermeasures and for building biophysical models that can be used to project risks for a given space radiation environment.

This paper briefly reviews early studies and recent advances in heavy-ion radiobiology. Clearly, large amounts of data have been obtained and from these data some insights have been gained on the basic mechanisms of heavy ion effects. However, many basic questions remain to be answered, and far more information is needed on the biological effects of heavy ions with energies less than 1 MeV/u or greater than 1 GeV/u. A complete set of data on biological effects of charged particles with various charges and energies is essential for shielding design of spacecraft and for radiation risk assessment.

BIOLOGICAL RESPONSES TO HZE PARTICLES

As early as 1932, alpha particles were found to be more effective in killing cells than X or gamma rays [2, 3]. Shortly after World War II, the biological effectiveness of accelerated helium ions was shown to depend on the kinetic energy of the particle in yeast cultures [4]. Studies of chromosomal aberrations in plants indicated that fast particle beams produced aberrations in a linear fashion with dose, whereas X rays produced chromosome aberrations with quadratic kinetics [5]. From the late 1950's to the 1960's, many investigations were performed using heavy-ion linear accelerators (HILAC). A detailed study was completed on the relative biological effectiveness (RBE) of low-energy heavy ions (10 MeV/u) on human cells, and the low oxygen effect of high-LET heavy ions was demonstrated [6].

From 1970 to present, investigators in various countries have been able to characterize the relationships between LET and various biological effects, such as cell killing, mutation, carcinogenesis, and tissue damage, using high-energy heavy ion beams. From these studies, the RBE and LET relationships have been determined. For most normal mammalian cells, the RBE determined at 10% survival level increased with LET, reaching a peak at about 100–200 keV/μm, and decreasing with further increases of LET [7–9]. From the dose-response curves, the target size or cross section can be calculated. The calculated cross-section for inactivation under aerobic and hypoxic condition shows an increase of size with an increase of LET and reaches a plateau value close to the geometric area of the cell nucleus. For high-LET radiation, normal cells in general have a greater RBE value than repair-deficient cells, suggesting that heavy ions are effective in producing irreparable lethal lesions [10]. Experiments with confluent mouse embryonic cells exposed to heavy ions yielded results indicating that the production of irreparable lethal lesions depended on both LET and track structure [8], as shown in figures 1, 2, and 3. Analysis of these data suggests that more than one heavy particle must pass through the cell nucleus to inactivate a mammalian cell in culture (Figures 4 and 5).

The RBE and LET relationships for somatic mutation and neoplastic transformation also have been obtained by several groups [11–14]. The general pattern of the RBE and LET relationships for these two biological effects are similar to that for cell inactivation. Heavy ions having LET of less than 200 keV/μm can be more effective in causing somatic mutation and neoplastic transformation [13–15]. High-LET heavy ions also produced more potentially oncogenic lesions that are irreparable in cells, and the RBE value for cells for which plating was delayed was greater than that for cells plated immediately after irradiation [16].

Studies of early and late effects of radiation in animals revealed RBE and LET relationships similar to those for cellular effects. Effects studied to date include the colony-forming ability of spleen cells, the inactivation of proliferative cells in the testes and intestine, and the reduction in life span. Peak position and RBE values vary to some extent, however. In general, high-LET charged particles can be much more effective than low-LET radiation in generating these effects. These results have been summarized in several reports [17,18].

In addition to these studies of cells and animals, many experiments sought to reveal the basic mechanisms by which heavy ions exerted their effects. Studies of free radical scavengers showed that heavy-ion damage may be induced through direct action. For example, mammalian cells treated by 2M DMSO were about three times less sensitive to X rays but had the same responses to high-LET iron particles in terms of cell inactivation, mutation, and transformation [7, 16]. This difference in protection by DMSO was taken to indicate possible difference in track structures of heavy ions versus X rays. High-LET heavy ions can produce tracks with dense ionization, which increases the probability of direct damage to cellular DNA. A heavy-ion track with dense ionization that passes through DNA is likely to cause double-strand breaks. This idea was confirmed in other experiments in which increasing LET led to an increase in double-strand breaks, with no change or decreases in single-strand breaks [19, 20]. Moreover, high-LET particles were much more effective in producing nonrejoining DNA breaks, and the relationship between percent of nonrejoining DNA strand breaks and LET was very similar to that between RBE and

LET for cell survival [21, 22]. DNA double-strand breaks can lead to breaks in chromatin and chromosomes; several studies have verified that high-LET radiation was more effective than photons in causing chromatin breaks [23, 24] and chromosome aberrations [25, 26].

Since 1990, significant and exciting studies have been done with accelerated heavy ions and low-energy alpha particles. Interest in the potential health effects from radon spurred many investigations of biological effects of low energy alpha particles. Also, advances in cellular and molecular biology in recent years have enabled scientists to explore fundamental questions that could not be addressed before.

After many years of research, sufficient data were generated on the carcinogenic effects of radiation with different qualities to allow definition of the relationship between RBE and LET [27, 28]. For a long time, it was unclear if the RBE will stay the same at LETs over 100 keV/μm [29]. From the dose-response curves generated for gamma rays, protons, helium, neon, iron, niobium, and lanthanum ions, which cover LET ranging from about 0.3 to 1000 keV/μm, RBE values were obtained from the initial slope and tumor prevalence at 25%.

Figure 6 illustrates the RBE-to-LET relationship for Harderian tumor induction; this relationship is very similar to that for neoplastic cell transformation. The peak RBE for Harderian tumors, however, was about four times higher than that for cell transformation. This big difference in RBE values might be due to the fact that one heavy ion can traverse through many cells in the body. The cross section for carcinogenesis, calculated from the initial slope of the dose-response curves as a function of LET, becomes larger as the LET increases and reaches a plateau at about 500 keV/μm. The maximum cross section is about 100 μm^2, close to the geometric nuclear area of the cell. This interesting result suggests that all DNA in the nucleus might be the target for carcinogenesis. Since a diploid mammalian cell contains about one million genes, and since only limited genes, less than one hundred, have been identified as important in cancer formation, these results suggest that one heavy ion traversing through the body could hit targets in more than ten thousand cells. Although possible, the probability of such interactions is very small, and other mechanisms probably play roles in heavy ion carcinogenesis. For example, heavy ions may kill a certain number of cells in the tissue where they hit, thereby allowing transformed cells to proliferate and thus having promotional effect. It is well known that promotion is an important step in carcinogenesis.

Unlike photons, heavy ions at low dose rates can be more effective in transforming cells than at high dose rates. This so called "inverse dose-rate effect" has been shown recently to depend on LET and be limited to LET between 30 and 130 keV/μm [30]. Similar results have been found for fractionated doses of 4.3 MeV alpha particles (LET = 101 keV/μm) [31]. Brenner and colleagues [32] have proposed a cell cycle-dependent model to explain this inverse dose rate effect. According to this model, the inverse dose-rate effect disappears at high LET because fewer cells are being hit, and disappears at LETs below about 30 keV/μm because most of the dose is deposited at low specific energies, which can not produce the saturation effect central to this phenomenon. Inverse dose-rate effect, however, has also been detected in confluent mouse embryonic cells [33]. Mechanisms other than cell cycle need to be sought.

Tsuboi and others [14] have reported results from a detailed study on the mutagenic effects of heavy ions in human diploid fibroblasts. For all types of radiation studied (gamma rays, neon, argon, iron, and lanthanum ions), mutation frequency increased linearly with dose. The RBE-to-LET relationship is shown in figure 7. Notably, at LET above 500 keV/μm, the RBE for survival seems to be higher than that for mutation, suggesting that very high-LET particles may be more effective in inactivating cells than in inducing mutation.

Figure 8 shows calculated cross sections for mutation and inactivation of human diploid fibroblasts. The maximum cross section for inactivation was about ten thousand times greater than that for mutation. Since only one gene (HPRT) was studied, these results suggest that the target for HPRT mutation can be larger than the gene itself. Molecular analyses have verified that radiation can induce mutation by deleting DNA that is larger than the HPRT gene.

Chromosome studies also have produced interesting results. Nagasawa *et al.* [34] examined the induction of chromosomal aberrations by 3.7 MeV alpha particles or gamma-ray irradiation in Chinese hamster cells. Their results of chromosomal breaks show that the RBE values for chromosomal breaks ranged from about 10 at low doses to 5 for high doses. Gamma rays seemed to produce breaks, rings, and dicentrics in approximately equal numbers; several data points, however, indicated that gamma rays might be slightly more effective in causing rings and dicentrics. Alpha particles, on the other hand, seemed to induce breaks more often than rings or dicentrics.

Durante *et al*. [35, 36] provided additional evidence that chromosomal aberrations produced by high-LET radiation may be different from those produced by photons. This group scored dicentrics, breaks, interstitial deletions, gaps, rings, and chromatid aberrations separately in mouse embryonic cells and in human mammary epithelial cells. X rays were found to be most effective in causing dicentrics in confluent mouse embryonic cells and that helium ions were most effective in inducing breaks in this cell type. Similar results were found with the epithelial cells. Why photons and heavy ions should produce different chromosomal aberrations is unclear at present.

Although most investigations have shown that high-LET heavy ions can be more effective than low-LET radiation in causing biological effects, one suggested otherwise [37]. In this study, high-LET alpha particles (120 keV/μm) were found to be less effective than deuterons (40 keV/μm) in inducing sister chromatid exchanges (SCE). When the frequency of SCE was normalized with that of the control, alpha particles clearly induced fewer SCE than deuterons for a given dose. At low fluence, i.e., less than one particle per nucleus, the induction of SCE was independent of LET. These responses seem to preclude DNA double-strand breaks as the origin of radiation-initiated SCE; since DNA single-strand breaks also are independent of LET, these results suggest that they may provide the origin.

Raju and others [38] have systematically examined the effectiveness of low-energy alpha particles (0.4 to 3.5 MeV) in cell killing. As alpha-particle energy decreases, their effectiveness in killing cells decreases as well. The maximum RBE value was found to extend to LET values as high as 180 keV/μm. Alpha particles that

penetrated the cell nucleus were more effective than those that stopped inside the nucleus. The terminal tracks of alpha particles were less effective in causing cell death. These results, taken together, indicate a track-structure effect.

Track-structure effects also have been observed by other investigators using different cell systems and endpoints. For LET between 20–30 keV/μm, the RBE for protons was higher than that for deuterons and helium ions [39]. At 31 keV/μm, cell inactivation is similar for protons and deuterons, and at higher LETs the RBE values for protons were less than that for helium ions. In studying the induction of DNA strand breaks by low-energy heavy ions at GSI in Darmstadt, Germany, Heilmann *et al.* [40] found that for a given particle, both the LET and the particle energy determined the efficiency of inducing DNA lesions. Similar track structure effects for cell inactivation and chromosomal aberrations in mammalian cells have been observed and reported [25, 41, 42]. Goodwin *et al.* [43] also found that the RBEs for both cell inactivation and chromosome damage decrease as particle energy increases, using helium, neon and argon beams with the same LET (120 keV/μm).

At present, the reason for the reduction of the biological effects at very high LET near the stopping point of the particles is unclear. One possibility is that in mammalian cells at very high energy densities, radical recombination occurs at a high rate, thus reducing the ability of free radicals to incur biological damage. An alternative explanation would be to assume that the DNA in the mammalian cell nucleus is not distributed uniformly, since nuclear DNA has helical structures and accounts only for about 6% of the nuclear volume. There can be spaces in the nucleus free of DNA molecules. Therefore, a very low energy particle, which has a very small track, may be able to traverse the nucleus but miss the DNA. Nevertheless, a track structure repair kinetic model developed by Wilson *et al.* [44] gives a good fit to these data.

Chatterjee and Schaefer [45] proposed a model for microdosimetric structure of heavy ion tracks in tissue. This model distinguishes the particle track into two regions: core and penumbra. The core is a narrow central zone with a radius in tissue far below 1 μm where energy deposition occurs mainly in processes of excitation and electron plasma oscillation. The penumbra is a peripheral zone enveloping the core where energy deposition occurs mainly in ionization events by energetic secondary electrons released by the primary particle in the center of the core traveling at rather high speed, thus spreading laterally. About half of the total energy deposits in each region. The local energy density in the core is assumed to be uniform, and the local energy density in the penumbra decreases with the square of increasing radius. The radius of the core (Rc) is directly proportional to the speed of the particle: $Rc = 0.0116$ (v/c) μm, where v is the velocity of particle and c the speed of light. The radius of penumbra (Rp) can be calculated from the formula: $Rp = 0.768 E – 1.925(E)1/2 + 1.257$ μm, where E is the kinetic energy of the particle in MeV/u. The core radius increases rapidly with energy at low energies and reaches a maximum value of 0.01μm at about 1000 MeV/u. Unlike the core, the radius of penumbra continues to increase with energy. At 1000 MeV/u, the radius of penumbra can be over 500 μm. The importance of core or penumbra in producing DNA damages may depend on the energy and charge of the particle.

FUTURE DIRECTIONS

Since the discovery of cosmic rays, many scientists have studied the biological effects of heavy ions, and much quantitative information has been obtained on the RBE-to-LET relationships for DNA breaks, chromosomal aberrations, cell inactivation, somatic mutation, neoplastic transformation, tumor induction in animals, and normal tissue responses. These experimental data have generated significant insights as to how heavy ions cause various biological effects and have provided a scientific basis for protecting humans from space radiation. Most of these studies, however, involved heavy ions having energies in the range of 1 to 1000 MeV/u. Very limited data indicate that multi-GeV charged particles with relatively low LET can be more effective than *X* or gamma rays in inducing chromosomal aberrations in human cells (Table 1). For a complete understanding of heavy ion effects, we need to study the biological effects of heavy ions with very low energies (less than 1 MeV/u) and very high energies (greater than 1 GeV/u).

Table 1. Relative Biological Effectiveness (RBE*) Coefficients of Accelerated Charged Relativistic Particles.

	Radiation Type, Energy and LET		
Biological Test	Helium Ions 4 GeV/u 0.80 keV/μm	Protons 9 GeV/u 0.23 keV/μm	Deuterons 4 GeV/u 0.21 keV/μm
Number of aberrant cells	1.8 ± 0.2	1.4 ± 0.2	1.8 ± 0.2
Total no. aberrants	1.7 ± 0.2	1.6 ± 0.2	1.6 ± 0.2
No. dicentrics & rings	1.9 ± 0.2	1.4 ± 0.2	1.9 ± 0.2
Average value of RBE coefficient	1.8 ± 0.2	1.47 ± 0.2	1.77 ± 0.2

*[60]Co gamma rays as the reference radiation for RBE determination. Human blood lymphocytes were irradiated in culture. (Data from V. N. Gerasimenko *et al.* (1986) Radiobiologiya **27**: 743–747.)

Table 2 shows a summary of biological responses to HZE particles or to X or gamma rays. At present, the mechanisms by which heavy ions exert their biological effects are incompletely understood, and much remains to be learned. Findings discussed here lead to still more challenging questions: Can a single heavy ion induce mutation and neoplastic transformation? And is it energy and charge dependent? Do high-LET heavy ions produce genetic alterations different from that by photons? If so, what mechanisms underlie there differences? Do initial lesions induced by photons differ at the molecular level from lesions induced by heavy ions? How do repair enzymes handle these different types of lesions? Do heavy ions induce unique damage to DNA, membranes, or both? Answers for these questions will be essential for the fundamental understanding of radiation effects, as well as for shielding design to protect humans from space radiation on long-term missions.

Table 2. Radiation Responses of Mammalian Cells to Charged Particle.

	X or Gamma Rays	HZE Particles
RBE		
—inactivation	1	> 1
—mutation	1	> 1
—oncogenic transformation	1	> 1
—chromosomal aberrations	1	> 1
Nonrejoining DNA Breaks	less	more
Dose Rate	Effects reduced at low dose rates	Effects enhanced or unchanged at low dose rates
Cell Cycle	Radiosensitivity highly depends on cell stage	Effects less depend on cell stage
Oxygen	Radiosensitivity decreases under hypoxic condition	Radiosensitivity about the same under hypoxic condition
Free Radical Scavenger	Highly effective in reducing radiosensitivity	Not very effective in reducing radiation effects
Repair Inhibitors	Significantly increase radiosensitivity	Not effective in increasing radiation responses

SUMMARY

1. Most experimental results showed that high-LET heavy ions can be more effective than low-LET radiation in causing various biological effects, including chromosomal aberrations, cell inactivation, mutation, and carcinogenesis.

2. The biological effectiveness of heavy ions depends on both the energy and the LET of the particle, i.e., its track structure.

3. The RBE values of accelerated relativistic charged particles, which have low LET, can be much greater than 1.

4. Biological effects induced by high-LET heavy ions can be qualitatively different from that by low-LET radiation.

5. Research studies on biological effects of particle or target fragmentation are needed.

6. For radiation protection, both quantitative and mechanistic studies with low- and high-energy charged particles are essential.

REFERENCES

1. Tobias, C. A.: Faila Memorial Lecture: The future of heavy-ion science in biology and medicine. *Radiat. Res.* **103**: 1–33, 1985.

2. Zirkle, R. E.: Some effects of alpha radiation upon plant cells. *J. Cell Comp. Physiol.* **2**: 251–274, 1932.

3. Zirkle, R. E. and C. A. Tobias: Effects of ploidy and linear energy transfer on radiobiological survival curves. *Arch. Biochem. Biophys*. **47**: 282–306, 1953.

4. Tobias, C. A.: The dependence of some biological effects of radiation on the rate of energy loss. In: *The Basic Aspects of Radiation Effects on Living Systems* (J. J. Nickson, Ed.), pp. 357–392, Wiley, New York, 1952.

5. Giles, N. H. and C. A. Tobias: Effect of linear energy transfer on radiation-induced chromosome aberrations in Tradescantia microspores. *Science* **120**: 993–994, 1954.

6. Todd, P.: Reversible and irreversible effects of ionizing radiation on the reproductive integrity of mammalian cells cultured *in vitro*. Ph.D. Thesis, University of California, Berkeley, 1964.

7. Yang, T. C. and C. A. Tobias: Neoplastic cell transformation by energetic heavy ions and its modification with chemical agents. *Adv. Space Res*. **4**: 207–218, 1984.

8. Yang, T. C., Craise, L. M., Mei, M., and C. A., Tobias: Neoplastic cell transformation by high-LET radiation: Molecular mechanisms. *Adv. Space Res*. **9**: 131–140, 1989.

9. Blakely, E. A., Tobias, C. A., Yang, T. C., Smith, K. C., and J. T. Lyman: Inactivation of human kidney cells by high-energy monoenergetic heavy-ion beams. *Radiat. Res*. **80**: 122–160, 1979.

10. Tobias, C. A., Blakely, E. A., Chang, P. Y., Lommel, L., and R. Roots: The response of x-ray sensitive and resistant human cell lines to accelerated heavy ions. Br. J. Cancer 49 (Suppl. IV): pp. 175–185, 1984.

11. Kronenberg, A. and J. B. Little: Locus specificity for mutation induction in human cells exposed to accelerated heavy ions. *Int. J. Radiat. Biol.* **55**: 913–924, 1989.

12. Kronenberg, A. and J. B. Little: Molecular characterization of thymidine kinase mutants of human cells induced by densely ionizing radiation. *Mutation Res*. **211**: 215–224, 1989.

13. Yang, T. C., Craise, L. M., Mei, M., and C. A. Tobias: Neoplastic cell transformation of heavy charged particles. *Radiat. Res*. **104**: S-177–S-187, 1985.

14. Tsuboi, K., Yang, T. C., and D. J. Chen: Charged-particle mutagenesis: I. Cytotoxic and mutagenic effects of high-LET charged iron particles on human skin fibroblasts. *Radiat. Res*. **129**: 171–176, 1992.

15. Mei, M., Craise, L. M., and T. C. Yang: Induction of proline prototrophs in CHO-k1 cells by heavy ions. *Int. J. Radiat. Biol*. **50**: 213–224, 1986.

16. Yang, T. C., Mei, M., George, K. A., and L. M. Craise: DNA damage and repair in oncogenic transformation by heavy ion radiation. *Adv. Space Res*. **18,** No. 1/2, pp. 49–58, 1996.

17. Ainsworth, E. J.: Early and late mammalian responses to heavy charged particles. *Adv. Space Res.* **6**: 153–165, 1986.

18. Rodriguez, A., Alpen, E. L., and P. Powers-Risius: The RBE-LET relationship for rodent intestinal crypt cell survival, testes weight loss, and multicellular spheroid cell survival after heavy-ion irradiation. *Radiat. Res*. **132**: 184–192, 1992.

19. Kampf, G. and E. Eichhorn: DNA strand breakage by different radiation qualities and relations to cell killing: further results after the influence of alpha particles and carbon ions. *Studia Biophysica*, **93**: 17–26, 1983.

20. Roots, R., Kraft, G. and E. Gosschalk: The formation of radiation-induced DNA breaks: The ratio of double-strand breaks to single-strand breaks. *Int. J. Radiat. Oncology, Biology, Physics* **11**: 259–265, 1985.

21. Roots, R., Yang, T. C., Criase, L., Blakely, E. A. , and C. A. Tobias: Impaired repair capacity of DNA breaks induced in mammalian cellular DNA by accelerated heavy ions. *Radiat. Res*. **78**: 38–49, 1979.

22. Roots, R., Holley, W., Chatterjee, A., Irizarry, M. and G. Kraft: The formation of strand breaks in DNA after high-LET irradiation: A comparison of data from *in vitro* and cellular systems. *Int. J. Radiat. Biol*. **58**: 5569, 1990.

23. Goodwin, E.: The LET dependence of interphase chromosome breakage and rejoining in two mammalian cell lines, Ph.D. thesis, University of California, Berkeley, 1988.

24. Goodwin, E. H. and E. A. Blakely: Heavy ion-induced chromosomal damage and repair. *Adv. Space Res*. **12**: 81–89, 1992.

25. Kraft, G.: Radiobiological effects of very heavy ions: Inactivation, induction of chromosome aberrations and strand breaks. *Nucl. Sci. Appl*. **3**: 1–28, 1987

26. Yang, C. H., Criase, L. M., Durante, M., and M. Mei: Heavy-ion induced genetic changes and evolution processes. *Adv. Space Res*. **14**: 373–382, 1994.

27. Alpen, E. L., Powers-Risius, P., Curtis, S. B., and R. DeGuzman: Tumorgenic potential of high-LET, charged particle radiations. *Radiat. Res*. **136**: 382–392, 1993.

28. Alpen, E. L., Powers-Risius, P., Curtis, S. B., DeGuzman, R., and R. J. M. Fry: Fluenced based relative biological effectiveness for charged particle carcinogensis in mouse harderian gland. *Adv. Space Res*. **14**: 573–582, 1994.

29. Fry, R. J. M., Powers-Risius, P., Alpen, E. L., and E. J. Ainsworth: High-LET radiation carcinogenesis. R*adiat. Res.* **104**: 188–195, 1985.

30. Miller, R. C., Randers-Pehrson, G., Hieber, L., Marino, S. A., Richards, M., and E. J. Hall: The inverse dose-rate effect for oncogenic transformation by charged particles is dependent on linear energy transfer. *Radiat. Res*. **133**: 360–364, 1993.

31. Bettega, D., Calzolari, P., NorisChiorda, G., and L. Tallone-Lombardi: Transformation of C3H10T1/2 cells with 4.3 MeV alpha particles at low doses: Effects of single and fractionated doses. *Radiat. Res*. **131**: 66–71, 1992.

32. Brenner, D. J., Hall, E. J., Randers-Pehrson, G., and R. C. Miller: Mechanistic considerations on the dose-rate/LET dependence of oncogenic transformation by ionizing radiations. *Radiat. Res*. **133**: 365–369, 1993.

33. Yang, T. C., Craise, L. M., Mei, M., and C. A. Tobia: Dose protraction studies with low- and high-LET radiations on neoplastic cell transformation *in vitro*. *Adv. Space Res*. **6**: 137–147, 1986.

34. Nagasawa, H., Little, J. B., Inkret, W. C., Carpenter, S., Raju, M. R., Chen, D. J., and G. F. Strnist: Response of x-ray-sensitive CHO mutant cells (xrs-6c) to radiation: II. Relationship between cell survival and the induction of chromosomal damage with low doses of alpha particles. *Radiat. Res*. **126**: 280–288, 1991.

35. Durante, M., Grossi, G. F., Napolitano, M., Pugliese, M. and G. Gialanell: Chromosome damage induced by high-LET alpha particles in plateau-phase C3H10T1/2 cells. *Int. J. Radiat. Biol.* **62**: 571–580, 1992.

36. Durante, M., Grossi, G. F., and T. C. Yan: Radiation-induced chromosomal instability in human mammary epithelial cells. *Adv. Space Res.* **18**, No. 1/2, pp. 99–108, 1996.

37. Geard, C. R.: Induction of sister chromatid exchange as a function of charged-particle linear energy transfer. *Radiat. Res.* **134**: 187–192, 1993.

38. Raju, M. R., Eisen, Y., Carpenter, S., Jarrett, K., and W. F. Harvey: Radiobiology of alpha particles. IV. Cell inactivation by alpha particles of energies 0.4–3.5 MeV. *Radiat. Res.* **133**: 289–296, 1993.

39. Belli, M., Cera, F., Cherubini, R., Goodhead, D. T., Haque, A. M. I., Ianzini, F., Moschini, G., Nikjoo, H., Sapora, O., Simone, G., Stevens, D. L., Tabocchini, M. A., and P. Tiveron: Inactivation induced by deuterons of various LET in V79 cells. *Radiat. Protection Dosimetry* **52**: 305–310, 1994.

40. Heilmann, J., Rink, H., Taucher-Scholz, G., and G. Kraft: DNA strand break induction and rejoining and cellular recovery in mammalian cells after heavy-ion irradiation. *Radiat. Res***. 135**: 46–55, 1993.

41. Kraft, G., Kramer, M., and M. Scholz: LET, track structure and models. *Radiat. Environmental Biophysics* **31**: 161–180, 1992

42. Scholz, M. and G. Kraft: Calculation of heavy ion inactivation probabilities based on track structure, x-ray sensitivity and target size. GSI-93-17 Preprint. Gesellschaft fur Schwerionenforschung mbH, Darmstadt, Germany, 1993.

43. Goodwin, E. H., Bailey, S. M., Chen, D. J., and M. N. Cornforth: The effect of track structure on cell inactivation and chromosome damage at a constant LET of 120 keV/μm. *Adv. Space Res.* **18**, No. 1/2, pp. 93–98, 1996.

44. Wilson, J. W., Kim, M., Schimmerling, W., Badavi, F. F., Thibeault, S. A., Cucinotta, F. A., Shinn, J. L., and R. Kiefer: Issues in space radiation protection: Galactic cosmic rays. *Health Physics* **68**: 50–58, 1995.

45. Chatterjee, A. and H. J. Schaefer: Microdosimetric structure of heavy ion track in tissue. *Rad. and Environm. Biophys.* **13**: 215–227, 1976.
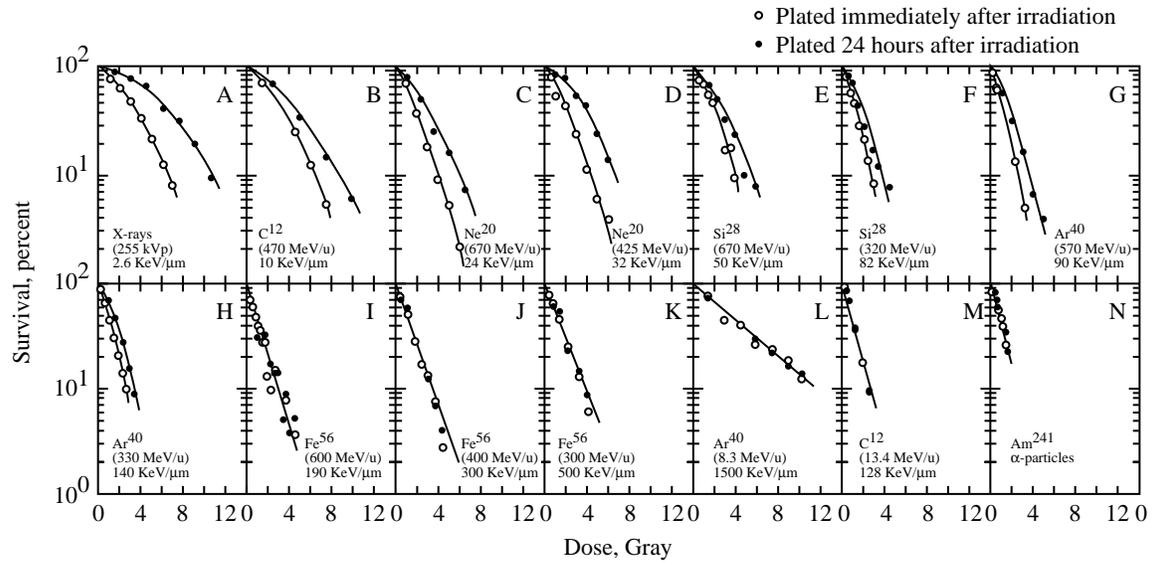
Figure 1. Dose-response curves for survival of confluent mouse embryonic cells (C3H10T1/2) exposed to heavy ions with various charges and energies.
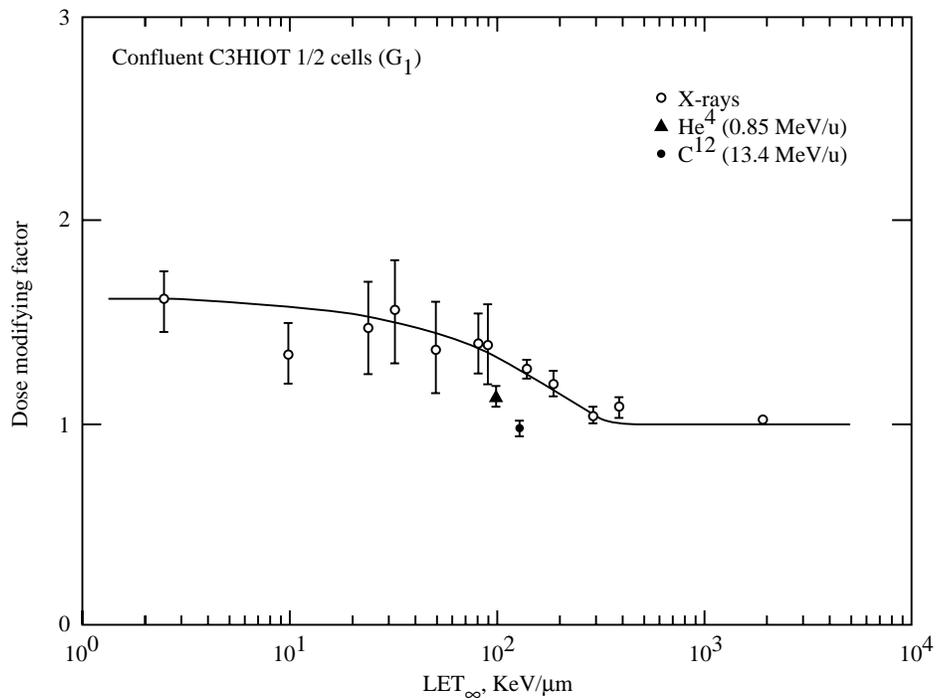
Figure 2. Dose modifying factor as a function of LET for confluent C3H10T1/2 cells.
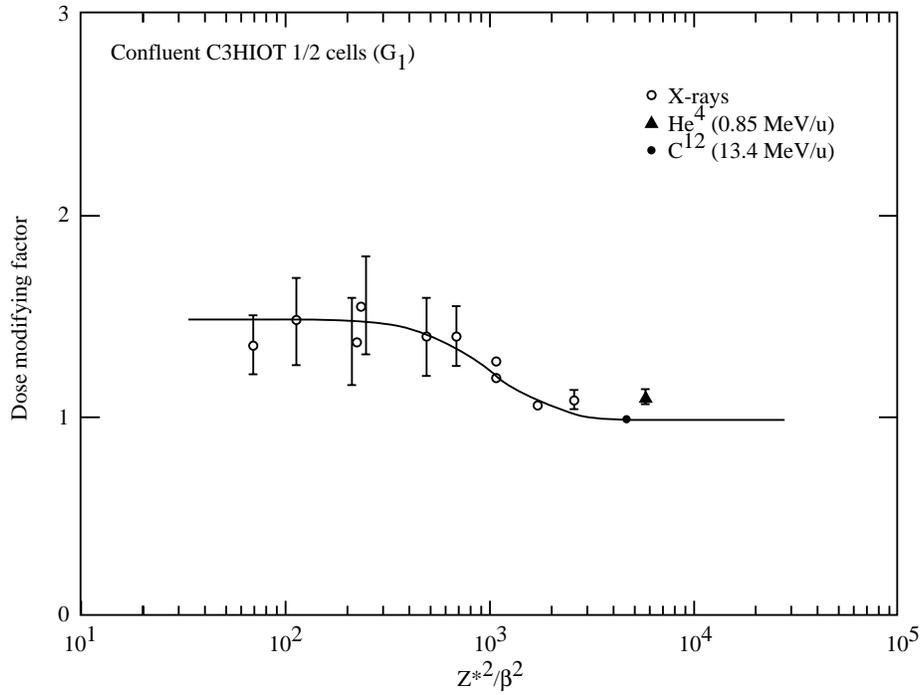
Figure 3. Dose modifying factor as a function of $Z*^2/ß^2$ for confluent C3H10T1/2 cells.
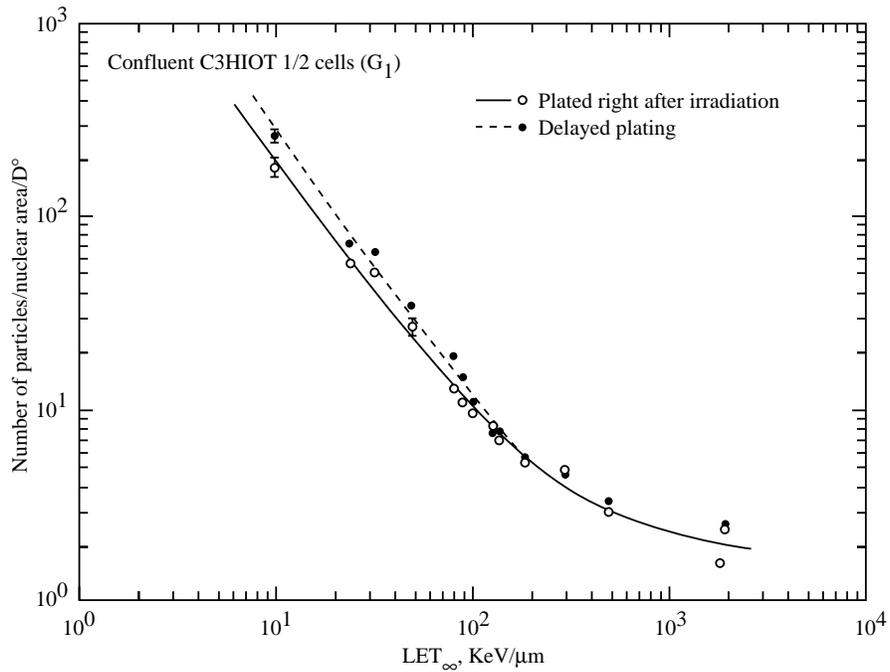

Figure 4. Number of particles per nucleus for cell inactivation as a function of LET.
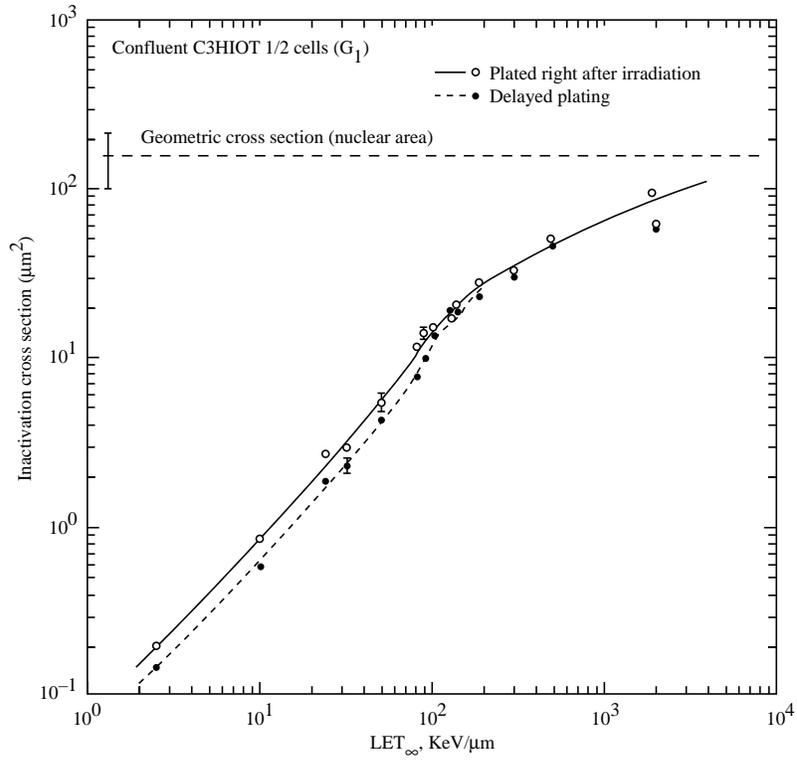
Figure 5.   Inactivation cross section as a function of LET for C3H10T1/2 cells.
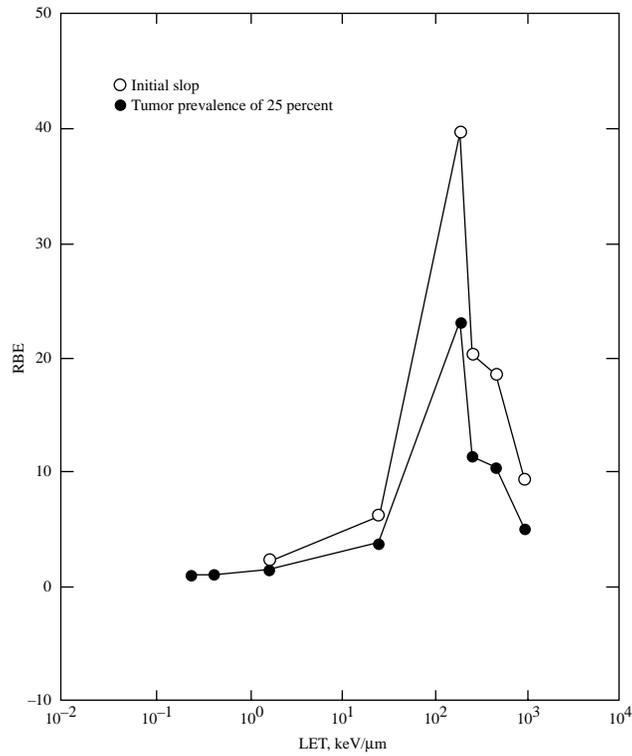
Figure 6. The RBE-to-LET relationship for Harderian tumor induction.
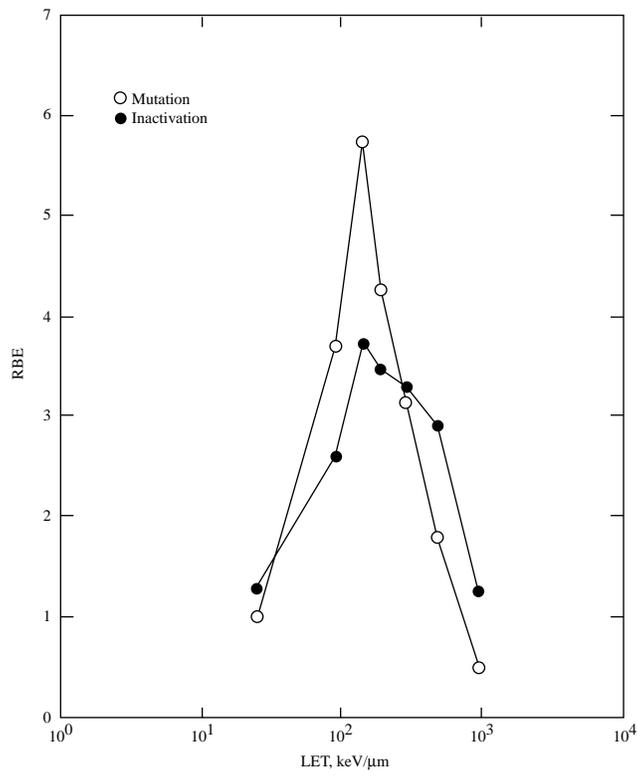
Figure 7. The RBE-to-LET relationship for HPRT gene mutation in human diploid fibroblasts.
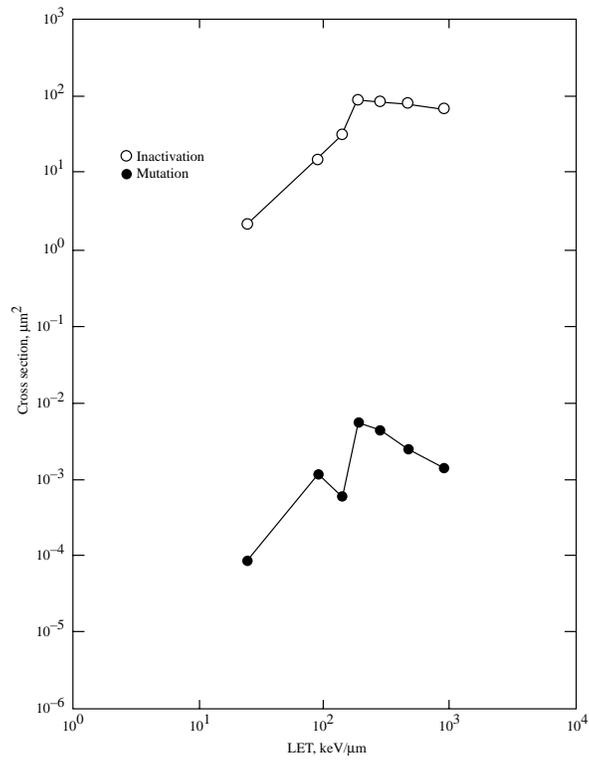
Figure 8. The calculated cross sections for mutation and inactivation of human diploid fibroblasts.

CHAPTER 7

RADIATION SHIELDING DESIGN ISSUES

by

John W. Wilson[1]

Francis A. Cucinotta[1]

Sheila A. Thibeault[1]

Myung-Hee Kim[2]

Judy L. Shinn[1]

Francis F. Badavi[3]

[1]NASA Langley Research Center, Hampton, Virginia 23681
[2]National Research Council—NASA LaRC Research Associate
[3]Christopher Newport University, Newport News, VA 23601

Chapter 7

RADIATION SHIELDING DESIGN ISSUES

INTRODUCTION

Within a few years of the discovery of particles of high charge and energy (HZE) as components of the Galactic Cosmic Rays (GCR), the unique pattern of energy deposit on the microscopic scale raised issues with respect to effects on living cells as discussed by Schaefer [1]. Although radiobiological knowledge has greatly improved, still our ability to estimate risk to the astronaut from such exposures is uncertain [2] by a factor of 4 to 15 [3]. Even a crude estimate using the Linear Energy Transfer (LET) dependent quality factor [4] results in as much as 1.2 Sv/yr exposures depending on shielding near solar minimum showing a large potential impact on the career of a space worker or a deep space explorer.

It is clear that 1.2 Sv/yr is an important number but one must hesitate in applying it to astronaut risk in the usual sense of extrapolation from the human database for late somatic effects which are based primarily for X-ray and γ-rays exposures [3, 5]. There is growing evidence of biological endpoints which are peculiar to high-LET exposures (including HZE) that are not produced by X-rays or γ-rays for which Relative Biological Effectiveness (RBE) is infinite or undefined [2, 6–8]. Thus, new methods to predict the risk resulting from exposure to GCR radiation may need to be developed which are not simple extrapolations of the present human database.

The biological response of living tissues depends (in part) on the temporal and spatial fluctuations of the energy deposits within the tissue system. Such fluctuations depend not only on the specific environment to which the astronaut is exposed but how that environment is modified by interaction with the astronaut's body in reaching the specific tissues. Only by knowledge of the specific radiation types and their physical properties at the tissue site can a basis for estimating astronaut risk be found. Even if the environment to which the astronaut is exposed is known precisely, the energy deposit within specific tissues deep in the astronaut's body are largely known through theoretical estimates and therefore are limited by the uncertainty in the calculational models. Clearly, an accurate conversion of the astronaut's environment to estimates of exposure fields at specific tissue sites is a high priority in the space radiation protection problem [2].

Apart from the issues of the astronaut's self-shielding factors and uncertainty in human response to the HZE particles, radiation shielding implies some control over the interior radiation environment to which the astronaut is exposed. The traditional structural material within the space program has been aluminum and the dose at solar

minimum (1977) from an annual GCR exposure within an aluminum shield increases from the free space value of 190 mGy/yr to a maximum 210 mGy/yr at 3–4 g/cm^2 and declines to the free space value at about 30 g/cm^2. Clearly no shielding advantage is found in reduction of the energy absorbed by the astronaut, and if any protection is provided it results from changes in the microscopic pattern of the energy absorption events [9, 10].

Herein we examine the modification of the physical parameters of the attenuated GCR environment in various materials to develop an understanding of the qualitative changes in environmental components as a function of shield composition (including tissue equivalent shields). In this context one begins to appreciate the role of nuclear reactions in modifying the interior environment and the associated microscopic fluctuation in the energy absorption events at local tissue sites. Furthermore, we will begin to understand the effects of nuclear cross section uncertainty as it applies to the change in the estimated microscopic energy absorption fluctuations. We will assess the importance of these environmental modifications on biological systems in terms of conventional dosimetry using defined quality factors for stochastic effects and several track structure dependent biological response models. We are not suggesting that a clear relationship between these biological models and astronaut cancer risk are known, and the use of an LET dependent quality factor has specifically not been recommended [5]; the present study will only allow us to evaluate the relative merits of an LET dependent quality factor and tract structure dependent risk models in shield estimates.

BIOLOGICAL RESPONSE MODELS

The astronaut excess cancer risk from a dose D_γ with low LET and low dose rate is represented by a sensitivity coefficient k_γ as

$$R_\gamma = k_\gamma D_\gamma \tag{1}$$

The concept of dose as a physical or chemical insult per unit mass of tissue is a carryover from the concepts of pharmacology and assumes dose is a measure of effects on individual cells [11]. Tissue cells are not all equal at low exposures because the energy deposits are quantized, and energy is deposited in only a fraction of cells; similarly, volumes within a given cell are not all equally sensitive. In general, absorbed dose D is not a good measure of biological damage for charged ions since the energy deposit is highly localized near the particle trajectory and relatively few cells are in fact hit for ordinary exposures and high LET. Consider the decomposition of the dose as follows [11].

$$D = \frac{\sum \varepsilon_i}{V N_E} = \frac{\sum \varepsilon_i}{V N_H} \frac{N_H}{N_E} = \frac{\bar{\varepsilon}}{V} \frac{N_H}{N_E} \tag{2}$$

where the average energy deposition event size (hit size) $\bar{\varepsilon}$ is

$$\bar{\varepsilon} = \frac{\sum \varepsilon_i}{N_H} \tag{3}$$

and V is the sensitive site volume (unit density is assumed), ε_i is the energy absorbed by the site of the ith hit, N_H is the number of site hits, and N_E is the number of sites exposed. The site size for biological injury is not precisely known. A single chromatin strand and its immediate environs on the order 0.1 µm may provide an important site size. The mean hit size, $\bar{\varepsilon}$, and the fraction of sites hit, N_H/N_E, in exposed 0.1 µm sites is shown for 1 Gy exposure with several ions in figure 1. The maximum biological effects are expected for LET values on the order of 100 keV/µm, for which less than one per thousand sites are in fact hit. These results can only be understood if cancer induction results from transforming only one or a few cells which ultimately produce the tumor and that high LET particles are the most effective in forming a transformed cell. The average hit size and fraction of sites hit for a 5 µm cell nucleus is shown in figure 2. Again we see for the most effective exposures at 100 keV/µm that about 50 percent of the nuclei are hit and only a small fraction of hit cells are in fact transformed. This maximal biological effectiveness at high LET values is introduced by factors depending on the quality of the radiation (the term quality is taken herein to refer to energy loss per unit path length and its radial distribution).

CONVENTIONAL RISK ASSESSMENT

Human excess cancer risks are estimated according to eq. (1) based on coefficients derived from X-ray and γ-ray exposures. The conventional method of extrapolating the human database to high-LET exposures is to replace D_γ in eq. (1) by the dose equivalent H given by

$$H = QD \tag{4}$$

where Q is the LET dependent quality factor. Equation (4) follows from analogy with the relative biological effectiveness given for γ-ray and ion exposure levels (D_γ and D_i) which result in the same biological endpoint by

$$\text{RBE} = D_\gamma/D_i \tag{5}$$

We note that the quality factor is a defined quantity (not given by a measurement) and represents trends of measured RBE in cell culture, plant, and animal experiments. The RBE values depend on endpoint, dose, dose rate, and quality of the radiation usually represented by LET. It is usually assumed that RBE reaches a maximum value (denoted RBE_m) at sufficiently low dose as related to the initial slopes of the response curves of each radiation type [5]. The current uncertainties in risk estimates derive from uncertainty in the gamma-ray risk coefficient k_γ for low dose rates and the appropriate value for RBE (including dose rate effects). Conventional estimates of risk in radiation protection rely on the defined quality factor and risk coefficient k_γ. The quality factor recommended by the ICRP [4] is shown in figure 3.

CELLULAR TRACK-STRUCTURE REPAIR MODEL

Although the use of quality factors may give some indication of the attenuation of biologically important components, their use in space protection against HZE particles has specifically not been recommended [5]. We consider herein an alternate approach utilizing biological systems which have been characterized in laboratory tests

using HZE ion beams. The limitations of the laboratory data are the limited number of ion types and energies available in the test and that the tests are done at relatively high dose rates as opposed to the low dose rates experienced in space exposure. Thus we are required to have a dynamic model in which the extrapolation to low dose rate is made by knowing dynamic information on the repair rates, the repair efficiencies, and information on tissue dynamic processes [12, 13].

Such a dynamic model must represent the processes within the tissue system which occur at both the cellular level and the systemic level. Cancer is a multistep process in which a cell is transformed or initiated into a precancerous state but not engaged in tumor formation. At least one added stage of development is required to promote the cell into a growing tumor [14, 15]. The initiation stage is thought to be a cellular event inducible by ionizing radiation in a process known as transformation. Cellular repair of radiation induced injury is important in relating to space exposure and the repair rates and repair efficiencies need to be understood. These are obtained in fractionated exposures within the cellular repair period (such repair occurs over several minutes to several hours) in which recovery is measured by comparison with single exposure data. An example study is the split dose recovery with a variable recovery interval [16] as shown in figure 4. The second step (and possible subsequent steps) to promote tumor growth may be systemic or may also be promoted by subsequent exposure and accounts for the delay between exposure and tumorgenesis. The radiation promotion of transformed cells is an important issue to space exposure and can only be studied in fractionated exposures over time periods of the tissue dynamic response of days to several weeks [17].

The first alternate test biological system considered herein is a track-structure repair model for inactivation and cell transformation of the C3H10T1/2 mouse cell which has been well characterized in HZE ion beams by Yang and coworkers [18, 19] for the comparative study of space shield properties. Ionizing radiation interacts with matter through the formation and interaction of radicals which we call the nascent lesions. These highly active chemical species may result in structural change or restore the cell to its initial state but are finally consumed. If these structural changes occur within the DNA and cannot be repaired by enzymatic processes, then subsequent generations may exhibit new phenotypes (for example, transformed) or the cell may be unable to undergo cell division for which clonogenic death occurs (inactivation).

The track structure model of Katz [20] attributes biological damage from energetic ions to the secondary electrons (δ-rays) produced along the ion's path. The effects caused by energetic ions are correlated with those of gamma-rays by assuming the injury at sensitive sites near the ion's path is the same as for gamma-rays at the same dose. The injury due to single ion effects is then approximately related to the gamma-ray response and the delta-ray dose surrounding the ion's path. For a multitarget cell response with target number m, the inactivation (or transformation) of cells by gamma-rays is assumed to follow a Poisson distribution reflecting the random accumulation of sublethal damage [4], with a radiosensitivity parameter D_0. Such inactivation (or transformation) may occur by the passage of a single ion with sufficiently dense ionization spread laterally over the cells' sensitive sites.

In exposures to galactic cosmic rays, the dose rate is very small ($D \approx 0.3\mu$ Gy/min) for which the nonsurviving (or transformed) fraction after a time t is [12]

$$\frac{n_m(t)}{n_0} \simeq \frac{\alpha_{m_1}}{\alpha_1} 6^{\frac{1}{3}} \frac{(1-P)D}{D_0} + \frac{\sigma}{L}D. \tag{6}$$

In eq. (6) the parameters D_0, σ, and P are the usual Katz model values and $6^{\frac{1}{3}}$ results from a binomial coefficient for a 3 hit system.

The inactivation (or transformation) cross section for a sensitive site is determined as

$$\sigma = \int_0^\infty 2\pi t dt \left(1 - e^{-\overline{D}/D_0}\right)^m \tag{7}$$

where $\overline{D}$ is the average dose at the sensitive site from the ion's delta rays. The evaluation of the cross section is separated by Katz [20] into a so-called grain-count regime, where inactivation (transformation) occurs randomly along the path of the particle and into the so-called track-width regime, where many inactivations (transformations) occur and are said to be distributed like a "hairy-rope" (these descriptive terms come from the track appearance in nuclear emulsion). The transition from the grain-count regime to the track-width regime is observed to take place at a value of $Z*^2/\kappa\beta^2$ of about 4; (at lower values we are in the grain-count regime and at higher values the track-width regime) where the effective charge number is given by

$$Z* = Z\left(1 - e^{-125\beta/Z^{2/3}}\right) \tag{8}$$

and κ is a parameter related to the radius of the sensitive site, by

$$D_0 a_0^2/\kappa \cong 2 \times 10^{-7} \text{ erg/cm} \tag{9}$$

The cross section exhibits an inflection at this boundary where σ attains a saturation value of σ_0. In the grain-count regime, σ may be approximated as

$$\sigma = \sigma_0\left(1 - e^{-Z*^2/\kappa\beta^2}\right)^m \tag{10}$$

and is the source of some approximations to radiation quality in terms of $Z*^2/\beta^2$ as opposed to LET [21]. In general, one should use eq. (7) for accurate cross-section values [22].

The fraction of the cells damaged in the ion-kill (ion-transformation) mode is $P = \sigma/\sigma_0$, and note that in the track-width regime $\sigma > \sigma_0$, it is assumed that $P = 1$. The track model assumes that a fraction of the ion's dose, $(1 - P)$, acts cumulatively (at least at high dose rate) with that for other particles to inactivate (transform) cells in the gamma-kill (gamma-transform) mode. These intertrack processes are closely related to gamma-ray or X-ray exposure response and show strong dose rate dependence depending on the enzymatic repair efficiencies. At low

dose and low dose rate the inactivation and transformation do not compete and eq. (6) applies. At high dose and high dose rate the competition yields a more complex formalism [12]. We identify m (taken as 3 in eq. (6)) with the number of lesions for which adequate enzyme repair is no longer possible. Note that α_{m_1}/α_1 is the probability that a single lesion is not properly repaired. The repair efficiency is $\left(1 - \alpha_{m_1}/\alpha_1\right)$. The kinetic parameters found from the cell survival and transformation experiments of Yang *et al.* [18, 19] are given in Table 1. Examples of model comparisons are shown in figures 5 and 6 with added details given elsewhere [12].

Table 1. C3H10T1/2 Cellular Track Structure and Repair Parameter

	σ_0, cm^2	κ	D_0, G$_y$	α_{m_1}/α_1
Survival	5×10^{-7}	750	2.8	0.03
Transformation	7×10^{11}	475	150	0.002

The RBE at low dose and low dose rates (denoted as RBE$_m$ since it is maximized) for the cell model of an exponentially growing population is found from eq. (6) as

$$\mathrm{RBE}_m = 1 - \frac{\sigma}{\sigma_0} + 6^{\frac{-1}{3}} D_0 \frac{\alpha_1 \sigma}{\alpha_{m_1} L} \tag{11}$$

where the RBE of HZE ions $(\sigma \neq 0)$ can be large if the repair efficiency is high $\left(\alpha_{m_i} \ll \alpha_1\right)$. Furthermore, strong track structure dependent factors enter through σ. In the $Z*^2/\beta^2$ approximation given by eq. (10), the RBE$_m$ for C3H10T1/2 survival is shown in figure 7. The results in figure 7 are in fact somewhat misleading since the cross section given by eq. (7) is more complex as seen by comparing the cross-section values of eq. (7) with that of eq. (10), as shown in figure 8. In actual practice, eq. (7) appears reasonably accurate as shown by the comparison with experimental data [22] for V79 cell inactivation and HGPRT mutation, as shown in figures 9 and 10. The study of the effects of simplified models of risk such as $(\mathrm{RBE} \approx Q)$, as given by eqs. (4) and (5), or as related to $Z*^2/\beta^2$, as given by eqs. (10) and (11) in comparison with the more accurate values given by eqs. (7) and (11) would be of interest in understanding the shield attenuation characteristic dependence on the biological model used to estimate risk. At least to the extent that risk is related to cellular events.

TISSUE CANCER RISK MODEL

The initiation promotion model describes the time development of initiated cell populations which once promoted leads to formation of tumors [17]. There are naturally occurring initiations described by

$$\dot{n}_I(t) = \mu_I n_0(t) - \left(\mu_p + \beta_I - \alpha_I\right) n_I(t) \tag{12}$$

where $n_0(t) \approx s$ is assumed to be a stable population of normal target cells in mature animals, μ_I is the natural initiation rate, β_I is the rate of initiated cell loss through (immunological) death, α_I is the rate of initiated cell

division, and μ_p is the rate at which initiated cells are promoted. Tumor prevalence is scored as the fraction of animals in which a neoplasm is found at time (t). The rate of tumor appearance (hazard function) is given as

$$h(t) = \dot{n}_p\left(t - t_g\right) \tag{13}$$

where t_g is the minimum growth time to an observable tumor. The prevalence is related to the distribution of tumors among the control group assuming Poisson statistics as

$$P(t) = 1 - \exp\left[-\int_0^t h(t)d\tau\right] \tag{14}$$

The initiated cell population is given as

$$n_I(t) = \frac{\mu_I s}{g_I + \mu_I - \mu_p}\left\{\exp\left[\left(g_I - \mu_p\right)t\right] - \exp\left(-\mu_I t\right)\right\} \tag{15}$$

where we have set $g_I = \alpha_I - \beta_I$. The rate of growth is controlled by g_i if $g_I \gg \mu_I$ or μ_p. The parameters in eqs. (12)–(15) are determined by experimental observation [13, 17] and shown in Table 2.

Table 2. Natural incidence parameters for Harderian tumors in B6CF, mouse

	μ_I, day^{-1}	μ_p, day^{-1}	g_I, day^{-1}	σ
Survival	0.5×10^{-7}	0.5×10^{-7}	8×10^{-3}	6.7×10^6

Harderian gland tumor induction was studied by Alpen *et al.* [23, 24] with various ion beams. These experiments were analyzed by Cucinotta [13] in which the number of initiated cells from the high dose rate exposure at age t_r is added to the result of eq. (15) as

$$n_I(t_r) = \frac{\mu_I s}{g_I + \mu_I - \mu_p}\left\{\exp\left[\left(g_I - \mu_p\right)t_r\right] - \exp\left(-\mu_I t_r\right)\right\} + \left\{\frac{\alpha_{m_1}}{\alpha_1} 6^{\frac{1}{3}} \frac{(1 - P)D}{D_0} + \frac{\sigma}{L}D\right\}s \tag{16}$$

where α_{m_1}, α_1, P, D_0, σ have the usual meaning as cellular parameters but with values fit to the data of Alpen *et al.* [23, 24]. The analysis by Cucinotta [13] and the resulting prevalence is shown in figure 11 in comparison with Alpen's data with the cell induction parameters in Table 3. Cucinotta has solved the cell/tissue dynamic equations

Table 3. Radiation induction parameters for Harderian gland

	σ_0, cm^2	κ	m	D_0, G$_y$	α_{ri} / α_i
Survival	3.2×10^{-7}	550	3	3.2	0.990
Initiation	3.5×10^{-10}	480	3.0	225.0	0.995

for low dose rate exposures appropriate to GCR exposures [17] and has found the following form if radiation promotion of initiated cells is ignored. The probability of excess tumors at age t is

$$P = \sum_j \int F_j\left(Z_j,\ E,\ t\right) \phi_j(E)\ dE \tag{17}$$

where

$$F_j\left(Z_j, E, t\right) = f\left(s, \mu_p, g_I, t, tr\right)\left\{ \sigma + \frac{\alpha_{m_1}}{\alpha_1} 6^{\frac{1}{3}} \frac{\left(1 - \frac{\sigma}{\sigma_0}\right)}{D_0} \right\} \tag{18}$$

t_r is the age at time of flight, t is the age at observation, and the remaining parameters were fit to the Alpen *et al.* data. The expression in the base of eq. (18) is the cross section for initiating a target cell in the Harderian gland

$$\sigma_I = \sigma + \frac{\alpha_{m_1}}{\alpha_1} 6^{\frac{1}{3}} \frac{\left(1 - \frac{\sigma}{\alpha_0}\right)}{D_0} \tag{19}$$

and clearly shows the relation between cell and tissue responses. The initiation cross section for the Harderian gland tumor induction is shown in figure 12 and compares favorably with the C3H10T1/2 transformation cross section found from the data of Yang *et al.* shown in figure 8. The comparison is interesting in that the track structure effects are quite similar and the magnitude of the initiation cross section is reasonable in spite of uncertainty in the model parameters, including the number of target cell *s*. The limitation of the $Z*^2/\beta^2$ model to represent cellular data may be judged by comparing figures 8, 10 and 12.

Clearly the above mentioned models show greatly varied dependence on radiation quality expressed in terms related to the particle track. The effects of these differences will now be examined as to their importance to shield design.

SHIELD MATERIAL CHARACTERISTICS

Shielding the work area of an astronaut crew will always result in a wall thickness (given in cm) that is small in comparison with the linear dimension of the crew compartment. The shield mass is then proportional to the areal density (given in g/cm^2), which we use as the appropriate measure of shield thickness.

The shield properties depend on the basic atomic/molecular and nuclear cross sections. Atomic/molecular stopping cross sections depend on the number of electrons per unit volume, the electronic mean excitation energy, and tight binding corrections for the inner shell electrons. The stopping range in units of areal density are shown in figure 13 for several ions and greatly differing materials. Materials with the most electrons per unit mass, the least

mean excitation energy, and the least tight binding corrections make the best energy absorbers. Thus, liquid hydrogen is a favored material and lead is less efficient as an energy absorber.

The nuclear cross sections relate not only to the free paths for nuclear reaction but to the nature of the reaction products. The projected nuclear cross section per unit mass of material is the appropriate parameter as shown in figure 14. Equally important is the nature of the reaction products produced. The production cross sections per unit mass of shield at high energy are shown in figure 15. Although the low atomic number shields are favored by the short free paths of figure 14, the effects of the products produced in figure 15 are unclear.

The microscopic fluctuations in the energy absorption events of several ions are represented parametrically as a function of LET in figure 1. Although LET is a less-than-perfect indicator of the microscopic patterns, it is a useful physical quantity to indicate radiation quality; it remains the focus of many biological investigations and serves as the basis of conventional radiation protection practice [4, 5]. The transmitted differential LET spectra for the year 1977 (solar minimum) through four shield materials are shown in figure 16. The fluence in 1977 is the largest fluence observed over the last 40 years and provides a conservative estimate [25]. The left-hand discontinuities are associated with the minimum ionization at relativistic energies for each ion type. The far-left discontinuity consists of hydrogen isotopes followed by helium isotopes and so on through N_i isotopes. The smaller right-hand discontinuities are associated with maximum ionization in the stopping region. At one time these stopping ions were suspected of being the primary hazard [1].

One should keep in mind that uncertainties in nuclear cross sections limit the accuracy of the attenuation characteristics. An uncertainty factor of 2 to 3 was estimated a few years ago for the LET region above 100 keV/μm because of an uncertainty in the projectile nuclear fragmentation cross sections [26]. Even adding energy dependence in the nuclear cross sections resulted in a 50-percent increase above 100 keV/μm [27] at 15 g/cm^2. Current efforts are being made to improve our nuclear data and reevaluation of the uncertainties seems appropriate. A second means is to consider the succession of databases which is a converging sequence for which the last two iterates provide an estimation of uncertainty. Thus we would compare NUCFRG1 with NUCFRG2, including target knockout processes [28, 29, 30]. We will further discuss this issue in a subsequent section.

In each case, we see the attenuation of the highest LET components in each material with liquid hydrogen being the most efficient and lead the least efficient. When viewing the transmission curves for aluminum (figure 16(c)), one notes that the spectral changes are minimum in the range of several keV/μm and that the LET spectrum attenuates at higher LET and amplifies at lower LET. This pivotal LET value, which is a function of the shield composition, increases to 40 to 50 keV/μm for lead and decreases to less than 1 keV/μm for liquid hydrogen. The pivotal LET value is associated with the loss of a given species because of attenuation being matched by the production of a similar species of equal LET in nuclear events. The location of the pivotal LET value is critical to the changes in the microscopic fluctuations in energy-absorption events which ultimately affect the biological response. Clearly, the shield effectiveness is intimately related to the nature of the nuclear cross sections through the change in the microscopic fluctuations in biological exposure. How effective these changes are in reducing

biological risk depends on the nature of the dependence of the risk model on specific transmitted components as we now demonstrate.

ILLUSTRATIONS OF SHIELD EFFECTIVENESS

We examine the aforementioned concepts in terms of three biological models. The first model is the conventional risk-assessment method [4,5] using the quality factor as a function of LET. The second model is a track-structure-repair kinetic model [12] for the C3H10T1/2 mouse cell using the Z^{*2}/β^2 approximation of eq. (10). We will evaluate the effectiveness of these materials to reduce the biological effects as a function of shield mass.

The distribution of particle fluence at 5 g/cm^2 is converted to the distribution of absorbed dose over the same LET intervals in figure 17a. Also in figure 17a is the dose-equivalent distribution obtained by multiplying the absorbed dose at each LET by the corresponding quality factor (as shown in figure 3). A large contribution to the dose equivalent results from ions in the LET interval ranging from 10 to 10^3 keV/μm. Shown in figure 17b are the geometric hit frequency, the initial level of cell injury (nearly proportional to dose), and the unrepaired cell injury leading to clonogenic death in a C3H10T1/2 mouse cell population as calculated by Wilson *et al*. [12].

The attenuation of dose equivalent as a function of areal density is shown in figure 18(a). The modification of the LET distribution as it depends on shield composition is obviously a critical issue. Lead shielding with the LET pivot point near the peak of the LET contributions to dose equivalent is a poor shield material for the GCR environment. Clearly the lowering of the LET pivot point enhances the shield performance of the materials, with liquid hydrogen being an optimum selection. Liquid hydrogen, is of course, a difficult material to use because it is a very low temperature cryogenic liquid. Evaluation of the relative gain made by the use of off-optimum shield materials that are more useful in construction is a critical issue. Furthermore, the adequacy of results derived using quality factors to represent biological systems is still questionable for HZE particles.

A second illustration is found using a model for neoplastic transformation of the C3H10T1/2 mouse cell for which sufficient experimental data exist for developing a reasonable model [12]. The repair kinetics model was solved at a low dose rate for a 1-year exposure behind the shields materials in figure 16. Figure 17b shows that although the cell is most often hit by protons and helium ions, the probability of injury is small and the repair efficiency is high with little permanent injury. Conversely, a high probability of injury and near-zero efficiency of repair occur from hits of silicon and iron ions. As a consequence, most clonogenic death from GCR exposure comes from ions with an LET above 10 keV/μm (ions above relativistic carbon). Radiation injury from these ions shows minimal cellular repair. As a result, dose protraction (an extended exposure period at the same accumulated dose) for GCR exposure will be less effective in reducing the biological response.

The change in radiation-induced transformations for a 1-year exposure in space for the Z^{*2}/β^2 model (eq. (10)) is shown in figure 18b. Although the attenuation characteristics for various shield materials are qualitatively similar to attenuation of dose equivalent shown in figure 18a, important quantitative differences exist.

This is best seen in terms of the attenuation of the transformation rate in a given material compared with attenuation of the dose equivalent in the same material. The relative attenuation for the transformation rate and dose equivalent are shown in figure 19 for the data shown in figure 18.

The rates of attenuation of biological effects as estimated by the LET and $Z*^2/\beta^2$ risk models are similar only for the liquid hydrogen shield. This implies that the quality factor in ICRP-60 represents in some way the dependence on radiation quality in this case, or at least the general decline of the high LET spectrum in hydrogen targets results in similar attenuation characteristics in each model. The quality factor is less useful in representing cell transformation for shields containing nonhydrogenous components and is a poor indicator for lead shields. Very similar results are found as well for clonogenic death of the C3H10T1/2 cells [12]. What is very clear from figure 18 is that the use of local materials (such as regolith) for a lunar base or for Martian exploration shielding designs based on quality factors remains in great doubt.

The third illustration uses the Harderian gland tumor model which was fit to the data of Alpen *et al.* using eq. (7) for the action cross section. The attenuation of tumor incidence after a one year exposure behind various shield materials is shown in figure 20. The curves are qualitatively similar to the corresponding transformation curves in figure 18 in which the $Z*^2/\beta^2$ approximation was used. Had the more accurate values of action cross section for transformation given by eq. (7) been used, then the attenuation curves for C3H10T1/2 cell transformation and the corresponding curves for Harderian gland tumors would be nearly indistinguishable. Thus the three models may exhibit some degree of universality as models based on LET, $Z*^2/\beta^2$, and track structure and their relative attenuation characteristics. The correlation of the Harderian gland tumor in the track structure model with the attenuation of dose equivalent is shown in figure 21. Clearly, the lack of correlation is further accentuated in the more accurate track structure model.

PROPOSED SHIELD-PERFORMANCE INDEX

In an attempt to assign a quantitative measure of shield performance, we consider a track-structure kinetics model of the C3H10T1/2 cell system for clonogenic death and transformation using the $Z*^2/\beta^2$ approximation to the action cross section in eq. (10). Results of this model for a 1-year exposure behind a 5 g/cm^2 aluminum shield is shown in figure 17b. We have further evaluated this model for various shield materials used in the present study at the various depths in figure 18b. We note that the depths in units of areal density are proportional to the total shield mass of a large shielded region. The exposure conditions assume a stationary G_1 phase exposure for a constant dose rate over the 1-year period. We compare the cell transformation behind an aluminum shield $\left(T_{Al}(x)\right)$ of areal density x with the cell transformation for a different material $\left(T_m(x)\right)$ of the same areal density. Thus, the cell transformation shield performance index $p_T(x)$ is

$$p_T(x) \equiv \text{Cell} - \text{transformation ratio} = \frac{T_{Al}(x)}{T_m(x)} \tag{20}$$

as a measure of the relative biological protection of the two materials.

As shown previously, the cell-transformation ratio does not correlate well with the dose equivalent. (See ref. 10 and figure 19 herein.) Although the attenuation of dose equivalent may be quite different from that of cell transformation for a specific material, a dose equivalent based performance index $p_H(x)$ given as

$$p_H(x) = \frac{H_{Al}(x)}{H_m(x)} \tag{21}$$

will show similar relative merit of specific materials relative to aluminum shielding. One would similarly define a performance index based on Harderian gland tumor prevalence as

$$p_{HG}(x) = \frac{P_{Al}(x)}{P_m(x)} \tag{22}$$

We will now examine these performance indices to evaluate the relative merit of various shield materials relative to aluminum, which is predominately used in space construction.

The three performance indices $p_H(x)$, $p_T(x)$, and $p_{HG}(x)$ are shown in figures 22–24 for several shield materials. It is clear from figures 22–24 that liquid hydrogen has the potential of very high shield performance as does methane or lithium hydride. Using liquid hydrogen as the limiting high performance material, then the high performance limit achievable can be set using the three biological models as shown in figure 25. Clearly, there is an enormous potential for developing high performance shield materials, and the challenge is to develop these materials to approach the limiting region as closely as possible.

Thus far in this presentation, we have examined the effects of uncertainty resulting from the three biological response models. A second source of uncertainty results from the cross-section data used to evaluate the transmission properties.

NUCLEAR ATTENUATION AND SHIELD PERFORMANCE

The transmission properties are represented by the LET distribution in figure 16 which is related to biological response models as in figure 17 and the shield attenuation characteristics in figure 18. Relating any particular LET interval with any particular species of the radiation field or to the specific nuclear processes by which the field composition is altered is difficult because of the large number of particle types contributing. The nuclear data are represented by two aspects as they affect the radiation field. The first aspect is the mean free paths of individual species to a nuclear reaction site given in figure 14, and the second aspect is the array of secondary products of the reactions as given in figure 15.

The nuclear free paths are among the best-known nuclear parameters. Although the physical measurements of free paths are limited in the number of projectile-target combinations and beam energies, theoretical calculations can be made without a detailed knowledge of the nuclear excitation spectra and corresponding wave functions because free paths are calculated from the elastic channel amplitudes and are little affected by coupling to inelastic

processes. Confidence is gained in that the limited experimental nuclear-absorption cross sections agree well with theoretical calculation, as will be discussed in detail by Dr. Cucinotta. In distinction, the nuclear breakup depends on the details of the nuclear excitation spectra (both discrete and continuous) and theoretical calculations are not as yet possible (with the exception of very light nuclei).

The effects of the fragment distributions can be studied by looking at the physical limits of the fragmentation event. These limits are expressed as an extreme peripheral collision in which a single nucleon is removed from the projectile per collision to extreme central collisions in which the projectile is completely dissociated into nucleonic components. There are important target constituent knockout events which can strongly affect the shield transmission properties. The effects of these physical limits on several shield types are shown in figure 26 along with results from several nuclear databases.

In the figure are shown dose equivalent relative attenuation curves $\left(H(x)/H(0)\right)$ using several nuclear models. The use of relative attenuation in part corrects for the fact that the NUCFRG2, soft, and hard spectrum results used a different environmental model that mainly affects the absolute magnitude, but the shape is dominated by the nuclear database. The peripheral and central collision limits result from the application of unitarity requirements on the projectile states while ignoring target knockout and fragmentation products. The curve labeled Letaw *et al.* [31] is for the database developed by the Naval Research Laboratory (NRL) in common use until a few years ago and still used extensively in electronic hardening. NUCFRG1 is the first database developed by Langley Research Center [28] as a result of concerns over the NRL database in comparison with experiments performed by Dr. Schimmerling [32] and atmospheric airshower data [33]. The NUCFRG2 database [29] is the result of the last series of validation experiments at the Bevalac by the NASA funded experiments to be further discussed by Dr. Miller. As a result of the recent comparisons with shuttle flight studies using a particle telescope, to be discussed by Dr. Badhwar, we have recently added target knockout contributions to the database which yields attenuation curves higher than the peripheral collision limit. The hard spectrum database is the addition of target knockout components approximated by available data in the literature extrapolated to high energies [30]. The soft spectrum is a high energy extrapolation correction factor compared to the shuttle measurements [30]. The NRL database is still commonly used in electronic hardening applications, and cosmic ray studies. The NUCFRG1 and NUCFRG2 database codes are mainly used in radiation health applications. The addition of target knockout contributions yields results above the peripheral collision limit and is the current step towards a new nuclear database. Clearly, the curves represent in some way our current level of uncertainty in dose equivalent attenuation. The track structure biological response models are even more sensitive to nuclear database modifications.

A similar analysis using the $Z*^2/\beta^2$ cell transformation model is shown in figure 27 for four different materials. The two materials of lower atomic number than aluminum show good attenuation characteristics for each of the three databases shown whereas aluminum shows good attenuation for the central collision limit (similar good attenuation is expected for NUCFRG1 and Letaw *et al.* databases), the NUCFRG2 database shows a substantial increase in cell transformation rate with increasing shield thickness and emerging databases mainly resulting from

the shuttle flight experiments carry us well above the peripheral collision limit indicating that aluminum construction may be harmful to the astronaut's health. Clearly, these effects of nuclear database modifications need to be resolved.

As a final note of our current nuclear database uncertainties, the relative effects of $Z*^2/\beta^2$ and the track structure model given by eq. (7) are shown for aluminum in figure 28 for the NUCFRG2 database. The addition of target knockout contributions is shown for the track structure model (using eq. (7)) as well. The possible hazard poised by aluminum space construction is clear. While the experimental database on nuclear reaction products in space and the biological response models are uncertain, these issues beg for resolution because of the current use of aluminum as the basic space construction material. This is especially true in a Mars or Lunar mission design where excess shield mass has such a large impact on mission cost as noted in the introduction to this workshop. It would be ironic to add substantial aluminum to the wall structure on the basis of reducing dose equivalent for these missions at substantial cost, while increased health risk to the astronaut is the result.

SPACE RADIATION RISK VALIDATION EXPERIMENTS

Although ground based testing can provide data for the development of biological response models, there remains concern that biological response to radiations in space may be modified by space related stress factors, the most obvious being microgravity [2, 34, 35]. The specific testing of radiation risk models based on ground experiments can be used in a null hypothesis with space flight validation [34]. The risk model is relatable to the cellular response model and tissue systems dynamic factors. The cellular response model parameters depend not only on the tissue in which they reside but on overall specific stress factors which modify the cell response and the tissue dynamics as well [35]. These factors can only be tested in whole mammalian systems.

The demands for space flight validation require a detailed understanding of the biological response of specific particle types which initiate the biological events leading to tumor development (for example, figures 9–12). A broad dynamic range of particle type and energies are ultimately related to the space biological response, and the null hypothesis requires not only an adequately developed ground tested biological response model but an adequate understanding of the physical radiation components present at specific tissue sites during the space flight test. This last requirement is likely only to be met by well defined computational procedures and corresponding validated database in conjunction with adequate radiation monitoring during the validation test. The combination of computational procedures and measurement is required to define the particle fields within the biological test systems to allow evaluation of unmeasured components, the mapping of the fields into test sites outside the measured locations, and to correct for measurement errors of specific measuring devices. For example, during the German Spacelab mission (D1), the radiation was monitored by CR-39 detectors. The measured LET spectrum (Δ) is compared with the evaluated LET spectrum (- -) in figure 29. The measured results are understood only if the processing of the CR-39 foil is modeled (—), for which reasonable agreement is obtained. Clearly, the LET spectrum inferred from the CR-39 measurement alone may differ from the actual LET spectrum by up to an order of

magnitude above the 100 keV/ μm and has an important impact on space risk model validation. It is likely that computational procedures will provide the essential link in risk model validation and will place great demands on the accuracy of the computational procedures and databases.

CONCLUDING REMARKS

Radiation risks to astronauts depend on the microscopic fluctuations of energy absorption events in specific tissues. These fluctuations depend not only on the space environment but on the modifications of that environment by the shielding of the astronaut's surrounding structures and the attenuation characteristics of the astronaut's body. The effects of attenuation within the shield and body depends on the tissue biological response to these microscopic fluctuations. In the absence of an accepted method for estimating astronaut risk, we examined the attenuation characteristics using conventional LET dependent quality factors (as one means of representing RBE) and track-structure repair models fit to cell transformation (and inactivation) data in the C3H10T1/2 mouse cell system and the Harderian gland tumor system obtained for various ion beams. Although the usual aluminum spacecraft shield is effective in reducing dose equivalent with increasing shield depth, cell transformation rates are increased for thin aluminum shields and provide no or little added protection to rather large depths in aluminum. Clearly, the exact nature of the biological response to LET and track width is critical to evaluation of biological protection factors provided by a shield design. A significant fraction of the biological injury results from the LET region above 100 keV/ μm. Since uncertainty in nuclear cross sections results in a factor of 2–3 uncertainty in the transmitted LET spectrum beyond depths of 15 g/cm^2, even greater uncertainty is due to the combined effects of uncertainty in biological response and nuclear parameters. This is especially true for the track-structure dependent models which are sensitive not only to LET but the individual particle type as well. Clearly, these uncertainties must be reduced before the shield design can be made.

Even within these current limitations, one can evaluate shield performance relative to aluminum as the space construction standard material. It is clear that low atomic number materials are good performers, although degree of increased performance for lesser atomic number is different for each biological model used in the present study. The limiting maximum performance material is liquid hydrogen, for which the performance is about an order of magnitude improvement over a pure aluminum shield. Clearly, such materials related factors are important to reducing mission costs. The challenge is to produce functional shields which are structurely sound, thermally stable, and resistant to degradation over the mission lifetime, which approach these high shield performances. Clearly, a materials development program to develop shielding technology is highly desirable.

REFERENCES

1. H. J. Schaefer: Evaluation of present-day knowledge of cosmic radiation at extreme altitude in terms of hazard to health. *J. Aviation Med*., **21**: 375–394, 1950.

2. W. Schimmerling: Radiobiological problems in space—An overview. R*adiat. Environ. Biophys*., **31**: 197–203; 1992.

3. S. B. Curtis, J. E. Nealy, and J. W. Wilson: Risk cross sections and their applications to risk estimates in the galactic cosmic-ray environment. *Radiat. Res*., **141**: 57–65, 1995.

4. International Commission on Radiological Protection: 1990 Recommendations of the International Commission on Radiological Protection. Pergamon Press Inc., ICRP Report No. 60, 1991.

5. National Council on Radiation Protection and Measurements: Guidance on radiation received in space activities, Bethesda, MD NCRP Rep. No. 98, 1989.

6. S. Z. Aghamohammadi, D. T. Goodhead, and J. R. Savage: Induction of sister chromatid exchanges (SCE) in G0 lymphocytes by plutonium-238 alpha-particles. *Int. J. of Radiat. Biol. Relat. Stud. Phys., Chem. Med*., **53**: 909–915, 1988.

7. M. A. Kadhim, D. A. Macdonald, D. T. Goodhead, S. A. Lorimore, S. J. Marsden, and E. G. Wright: Transmission of chromosomal instability after plutonium α-particle irradiation. *Nature*, **355**: 738–740, 1992.

8. G. Kraft, Radiobiological effects of very heavy ions: Inactivation, induction of chromosome aberrations and strand breaks. *Nucl. Sci. Appl*., **A3**: 1–28, 1987.

9. J. W. Wilson, J. S. Wood, J. L. Shinn, F. A. Cucinotta, and J. E. Nealy: A proposed performance index for galactic cosmic ray shielding materials. Washington, DC, NASA TM-4444, 1993.

10. J. W. Wilson, M. Kim, W. Schimmerling, F. F. Badavi, S. A. Thibeault, F. A. Cucinotta, and J. L. Shinn, and R. Kiefer: Issues in space radiation protection: Galactic cosmic rays. *Health Physics*, **68**: 50–58, 1995.

11. V. P. Bond, M. N. Varma, and C. A. Sondhaus: The RBE Concept, its inadequacies and a suggested replacement. Mechanisms of radiation interaction with DNA: Potential implications for radiation protection, U.S. Dept. of Energy, Washington, DC, CONF-870163, 31–38, 1988.

12. J. W. Wilson, F. A. Cucinotta, and J. L. Shinn: Cell kinetics and track structure. Biological Effects and Physics of Solar and Galactic Cosmic Radiation, C. E. Swenberg, G. Horneck, G. Stassinopoulos, eds., Plenum Press, 295–338, 1993.

13. F. A. Cucinotta, and J. W. Wilson: An initiation promotion model of tumor prevalence from high change and energy radiations. *Phys. Med. Biol*., **39**: 1811–1831, 1994.

14. P. Armitage, and R. Doll: A two-stage theory of carcinogenesis in relation to age distribution of human cancer. *Br. J. Cancer*, **11**: 161–169, 1957.

15. S. H. Maologavkar, and A. G. Knudson, Mutation and cancer: A model for human carcinogenesis. *J.N.C.I.*, **66**: 1037–1051, 1981.

16. J. M. Nelson, L. A. Braby, N. F. Metting, and W. C. Roesch: Multiple components of split-dose repair in plateau-phase mammalian cells: A new challenge to phenomenological modelers. *Radiat. Res*., **121**: 154, 1990.

17. F. A. Cucinotta, and J. W. Wilson: Initiation promotion mode of tumor prevalence in mice from space exposures. *Radiat. Environ. Biophysics*, **34**: 145–149, 1995.

18. T. C. Yang, L. M. Craise, M. T. Mei, and C. A. Tobias: Neoplastic cell transformation by high-LET radiation: Molecular mechanisms. *Adv. Sp. Res*., **9(10)**: 131, 1989.

19. T. C. Yang, L. M. Craise, M. T. Mei, and C. A. Tobias: Neoplastic cell transformation by heavy charged particles. *Radiat. Res*., **104**: S-177–S-187, 1985.

20. R. Katz, B. Ackerson, M. Homayoonfar, and S. C. Sharma: Inactivation of cells by heavy ion bombardment. *Radiat. Res*., **47**: 402–425, 1971.

21 S. B. Curtis, F. F. Badavi, and J. W. Wilson: Using $Z*^2/\beta^2$ as a predictive parameter biological effects for radiation protection purposes. 43rd annual meeting of the radiation research society, April 1–6: 218, 1995.

22. F. A. Cucinotta, J. W. Wilson, M. R. Shavers, and R. Katz: The effects of track structure and cell inactivation on the calculations of heavy ion mutation rates in mammalian cells. *Internat. J. Radiat. Biol*., **69**: 593–600, 1996.

23 E. L. Alpen, P. Powers-Risius, S. B. Curtis, and R. DeGuzman: Tumorgenic potential of high LET, charged particle radiations. *Radiat. Res*., **136**: 382–391, 1993.

24. E. L. Alpen, P. Powers-Risius, S. B. Curtis, R. DeGuzman, and J. M. Fry: Fluenced based relative biological effectiveness for charged particle carcinogenesis in mouse harderian gland. *Adv. Sp. Res*., **14**: 573–582, 1994.

25. G. D. Badhwar, F. A. Cucinotta, and P. M. O'Neill: An analysis of interplanetary space radiation exposure for various solar cycles. *Radiat. Res*., **138**: 201–208, 1994.

26. L. W. Townsend, F. A. Cucinotta, and J. W. Wilson: HZE reactions and data base development in *Biological Effects and Physics of Solar and Galactic Cosmic Rays*, C. E. Swenberg, G. Horneck, G. Stassinopoulos, eds. Plenum Press, New York, 787–810, 1993.

27. J. L. Shinn, S. John, R. K. Tripathi, J. W. Wilson, L. W. Townsend, and J. W. Norbury: Fully energy-dependent HZETRN (A galactic cosmic ray transport Code). Washington, DC, NASA TP-3243, 1992.

28. J. W. Wilson, L. W. Townsend, and F. F. Badavi: A semiempirical nuclear fragmentation model. *Nucl. Inst. Methods Phys. Res*., **B18**: 225–231, 1987.

29. J. W. Wilson, J. L. Shinn, L. W. Townsend, R. K. Tripathi, F. F. Badavi, and S. Y. Chun: NUCFRG2: A semiempirical nuclear fragmentation model. *Nucl. Inst. Methods Phys. Res*., **B94**: 95–102, 1995

30. F. A. Cucinotta, L. W. Townsend, J. W. Wilson, J. L. Shinn, G. D. Badhwar, and R. R. Dubey: Light ion components of the galactic cosmic rays: Nuclear interactions and transport theory. *Adv. Sp. Sci*., **17(2)**: 77–86, 1996.

31. J. R. Letaw, R. Silberberg, and C. H. Tsoo: Radiation hazards on space missions outside the magnetosphere. *Adv. Sp. Res*., **9(10)**: 285–291, 1989.

32. J. W. Wilson, L. W. Townsend, H. B. Bidasoria, W. Schimmerling, M. Wong, and J. Howard: ^{20}Ne depth-dose relations in water. *Health Phys*., **46**: 1101–1111, 1984.

33. J. W. Wilson, L. W. Townsend, F. F. Badavi, Galactic HZE propagation through the Earth's atmosphere. *Radiat. Res*., **109**: 173–183, 1987.

34. W. Schimmerling, Space and radiation protection: Scientific requirements for space research. *Radiat. Environ. Biophys.*, **34**: 133–137, 1995.

35. D. R. Morrison, Cellular changes in microgravity and the design of space radiation experiments. *Adv. Space Res.*, **14**(**10**): 1005–1019, 1994.
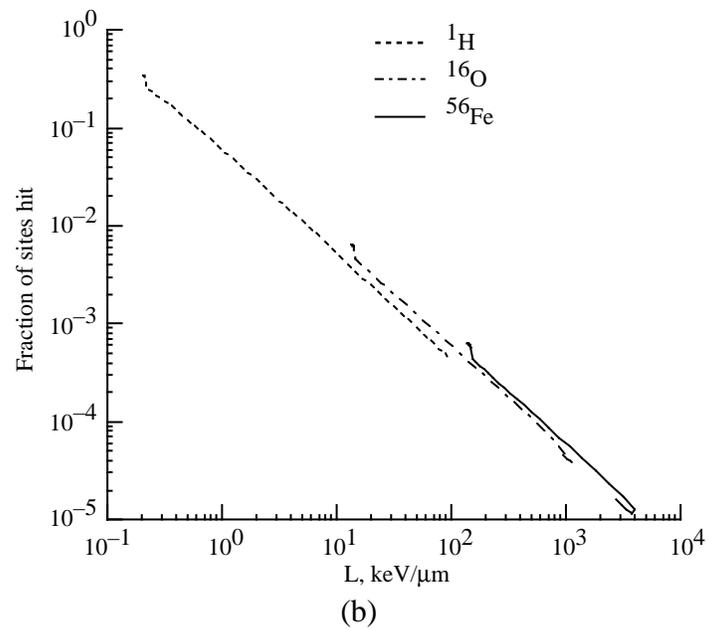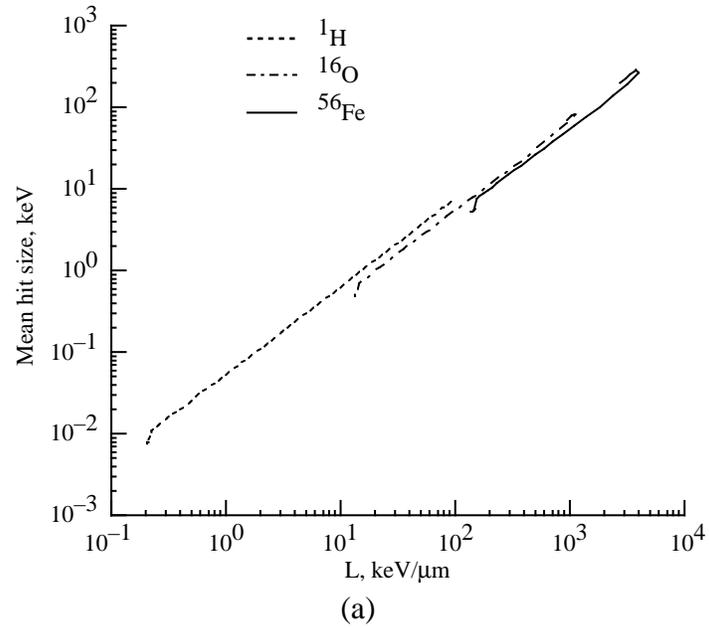
Figure 1.   Microscopic fluctuations in 0.1 µm sites represented by (a) mean hit size and (b) number of sites hit.
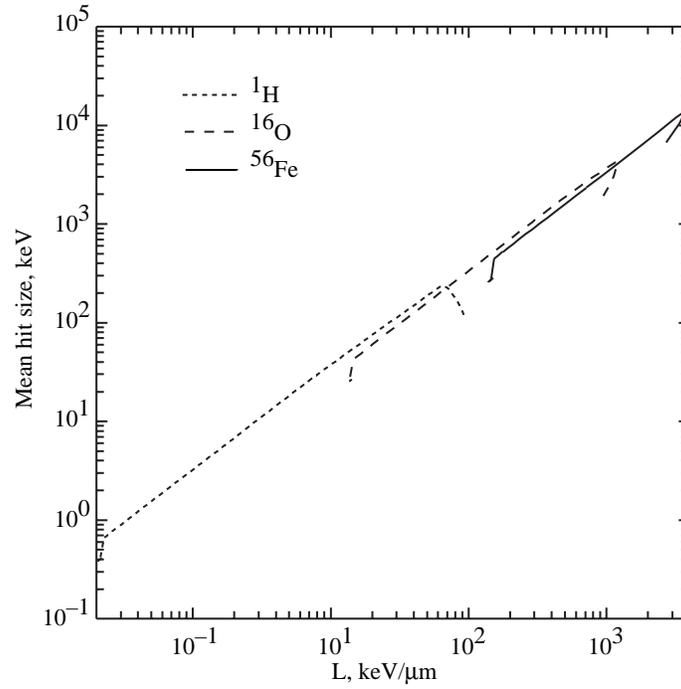
(a)
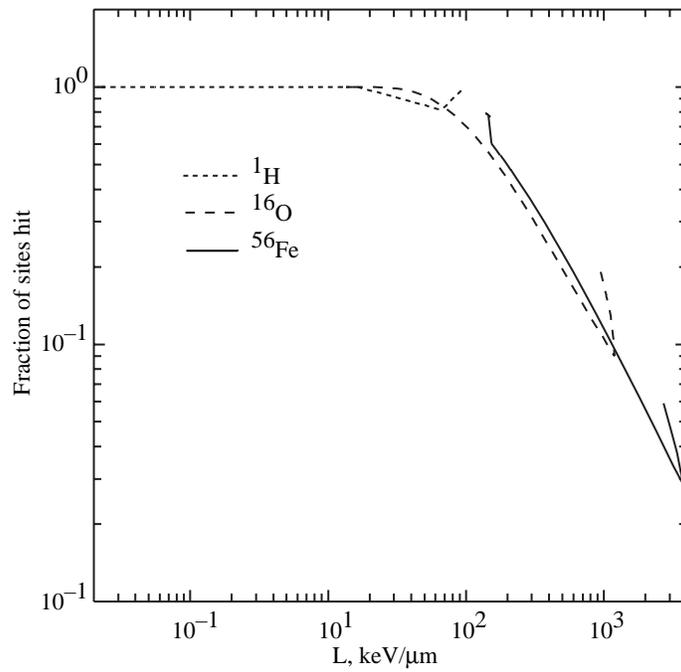
(b)

Figure 2.   Microscopic fluctuations in 5 μm sites represented as (a) mean hit size and (b) number of sites hit.
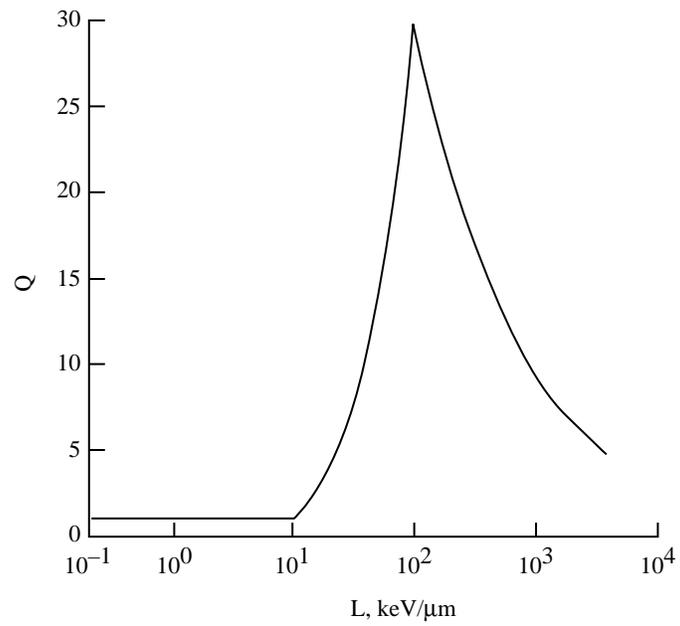
Figure 3.   ICRP-60 Recommended Quality Factor.
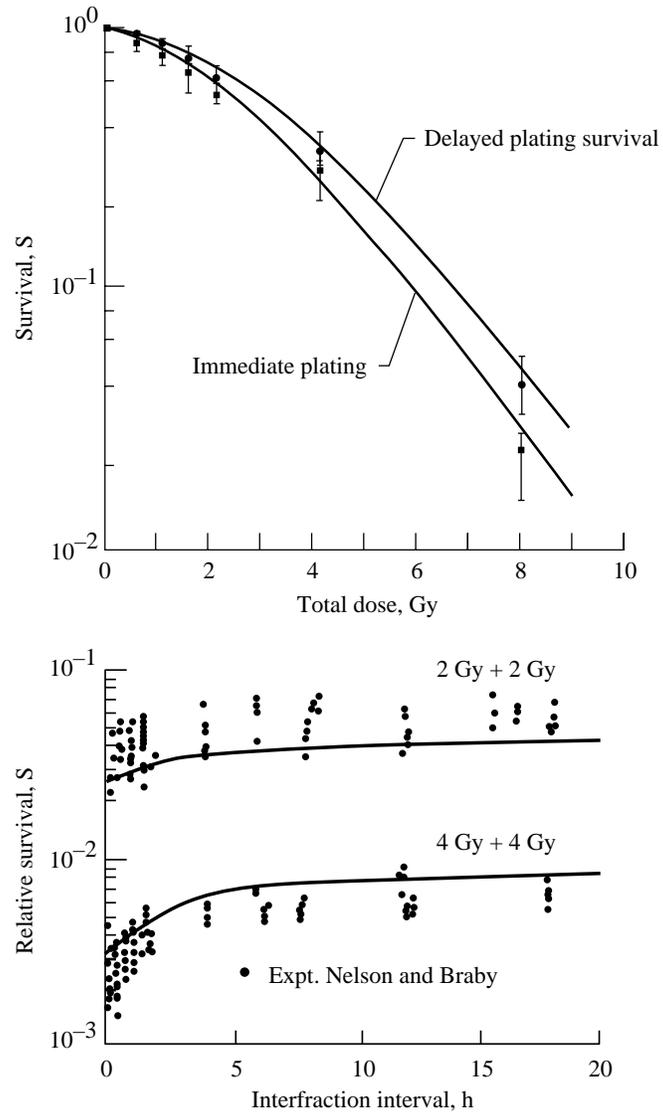
Figure 4.　　CHO cell kinetic response studies.

^{20}Ne, 425 MeV amu^{-1}, 32 keV μm^{-1}

^{28}Si, 670 MeV amu^{-1}, 50 keV μm^{-1}

^{28}Si, 320 MeV amu^{-1}, 82 keV μm^{-1}

^{56}Fe, 600 MeV amu^{-1}, 190 keV μm^{-1}
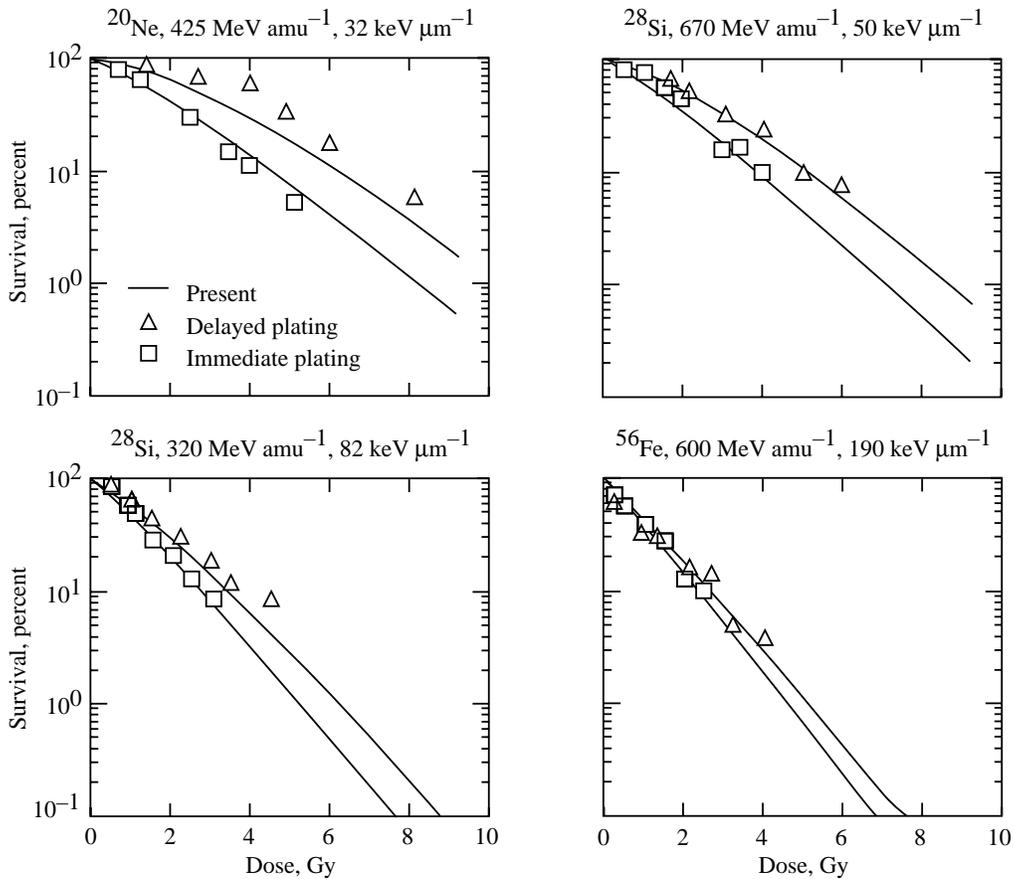
Figure 5.   Cell survival of C3H10T1/2 for delayed and immediate plating data of Yang *et al.*
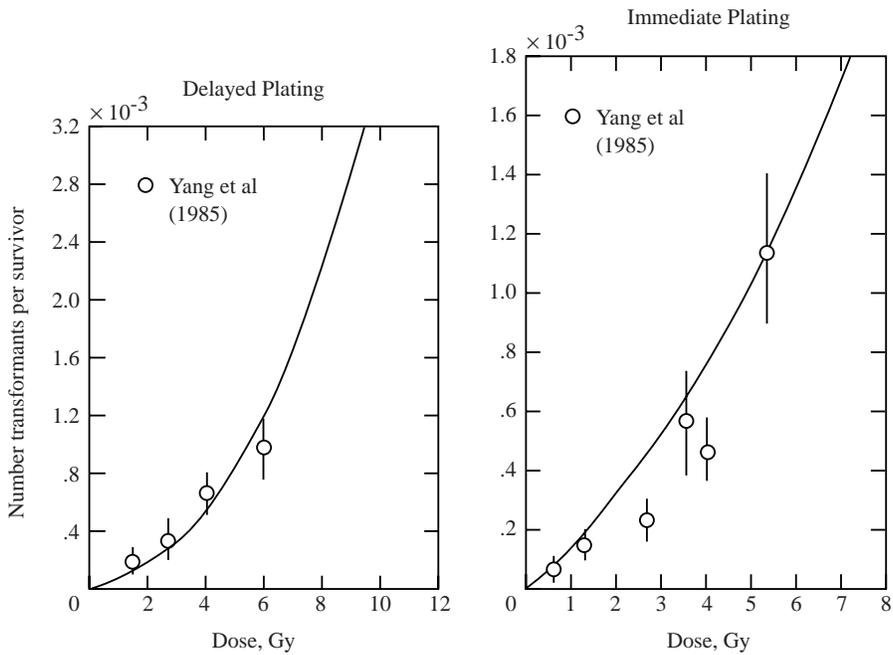
Figure 6.   Transformation of C3HT10T1 1/2 cells compared with experiment for Ne^{20} (425 MeV/amu).
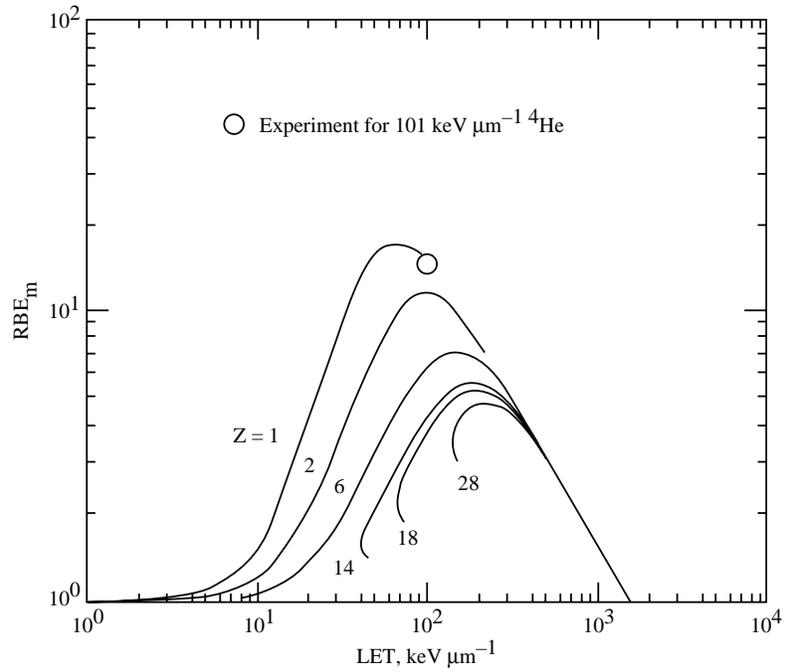
Figure 7. RBE$_m$ for cell survival of a C3H10T1/2 exponential population. The (☐) is the value measured by Bettega, *et al*. (1990) for low energy ^{4}He ions at 0.01 Gy.
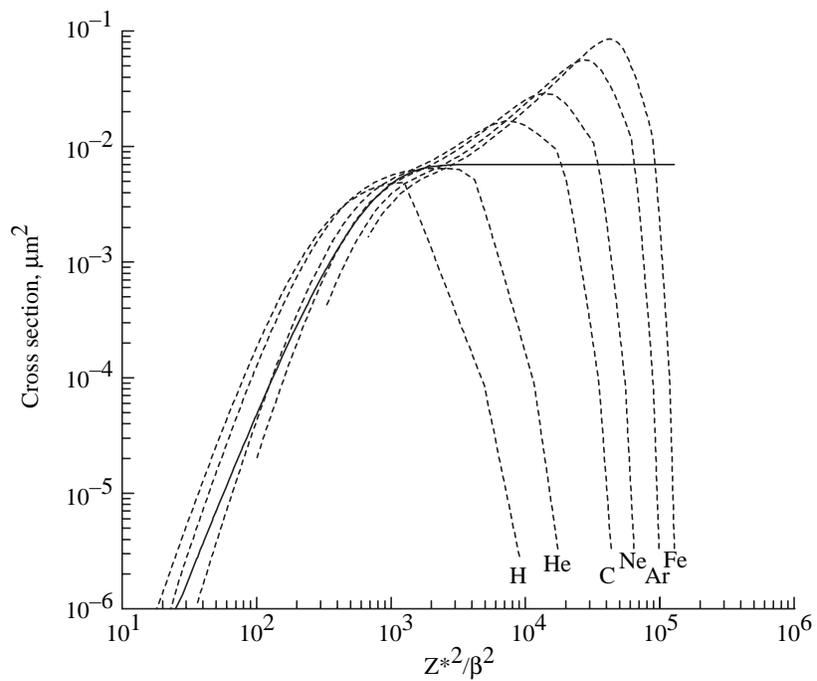
Figure 8. Cell transformation cross section in C3H10T1/2 according to $Z*^2/\beta^2$ model and track structure model.
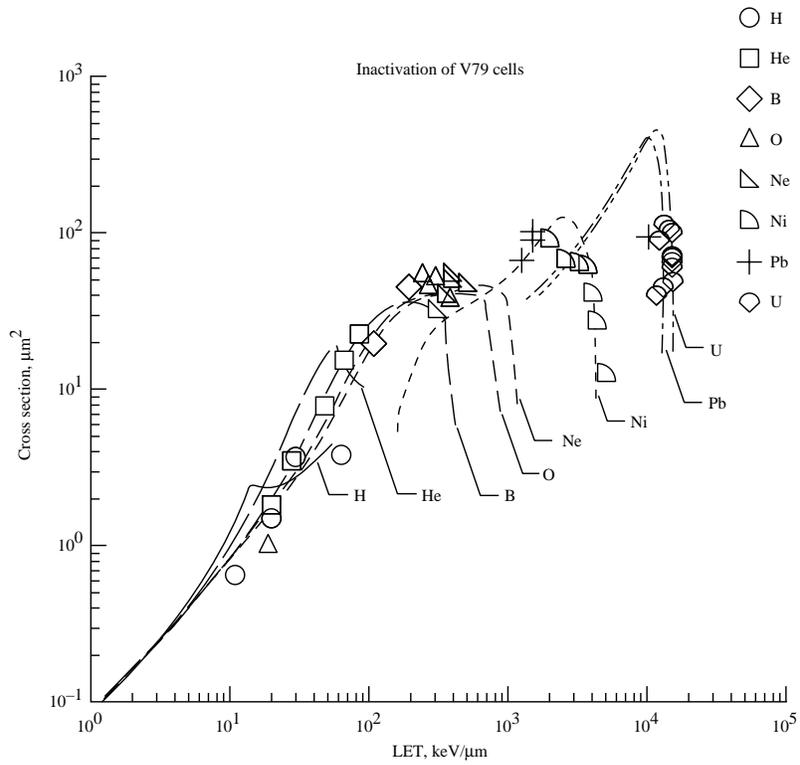
Figure 9.   Track structure model inactivation cross section comparison to experimental data.
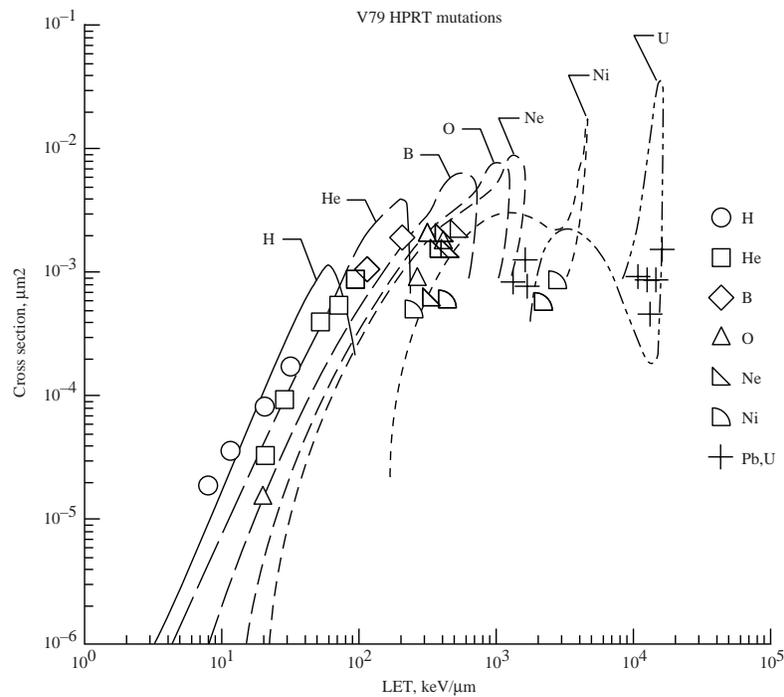
Figure 10. Track structure model mutation cross section compared to experimental data.
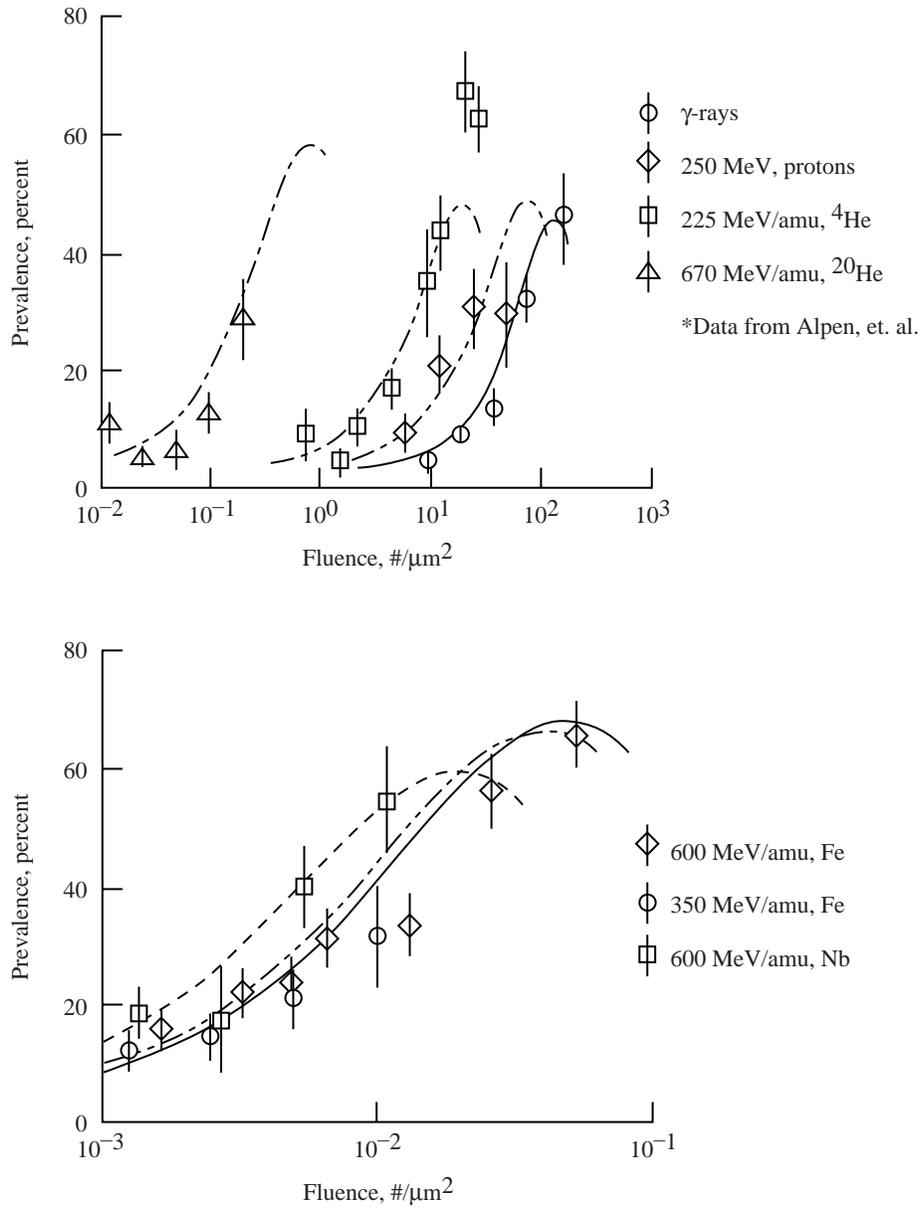
Figure 11. Fluence response for Harderian gland tumors.
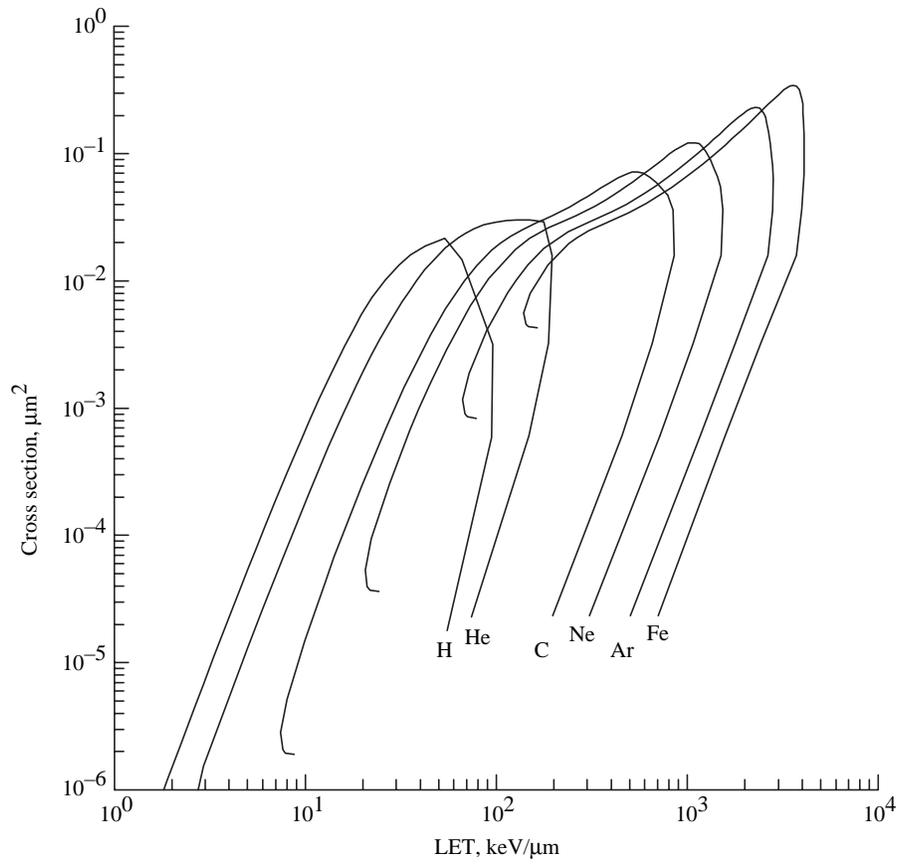
Figure 12. Cancer initiation cross section for Harderian gland target cells.

(a) Liquid hydrogen.

(b) Water.
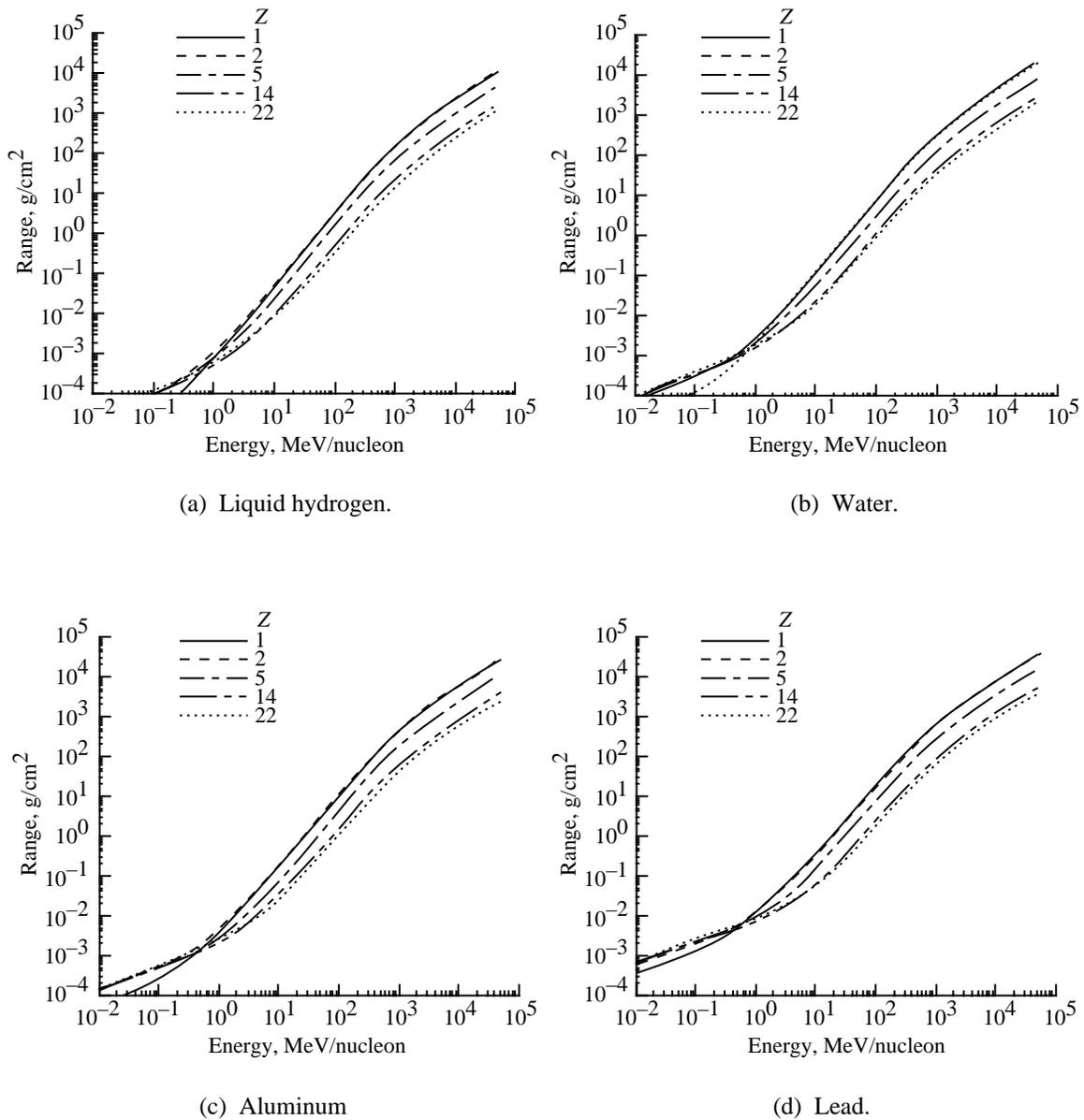
(c) Aluminum

(d) Lead.

Figure 13.   Stopping ranges of selected ions in four diverse materials.
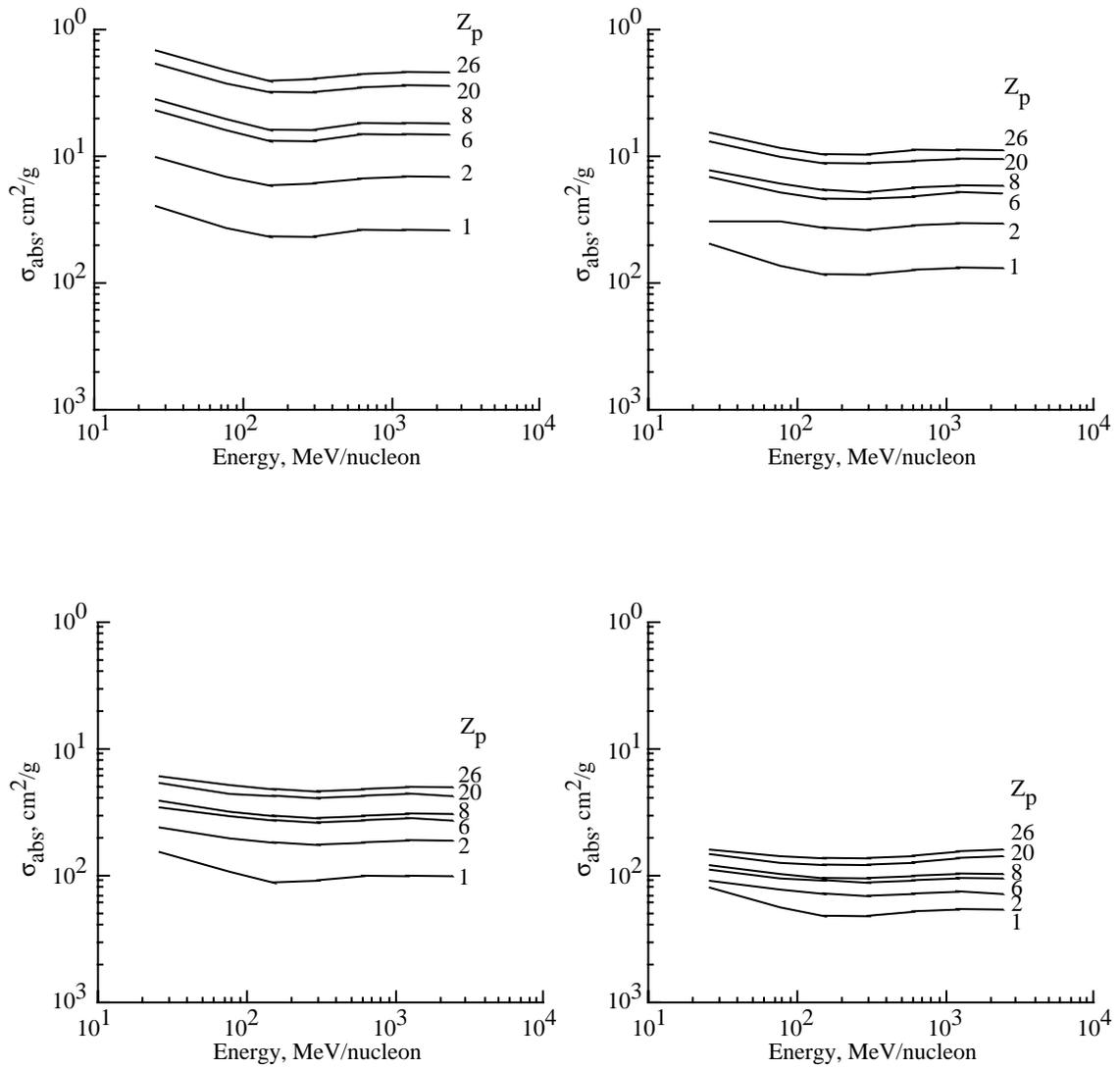
Figure 14.   Nuclear absorption cross sections per unit mass for selected ions in four diverse materials.
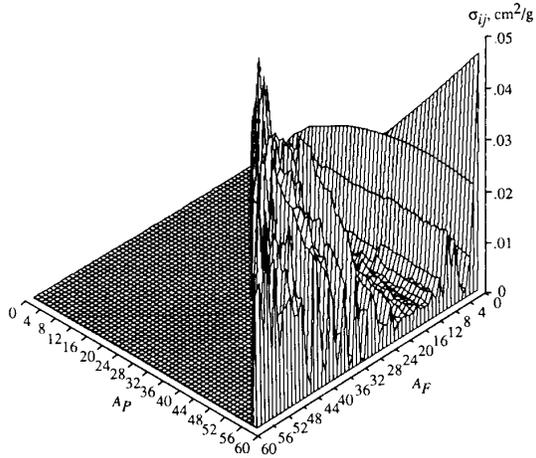
(a) Liquid hydrogen   (b) Water.
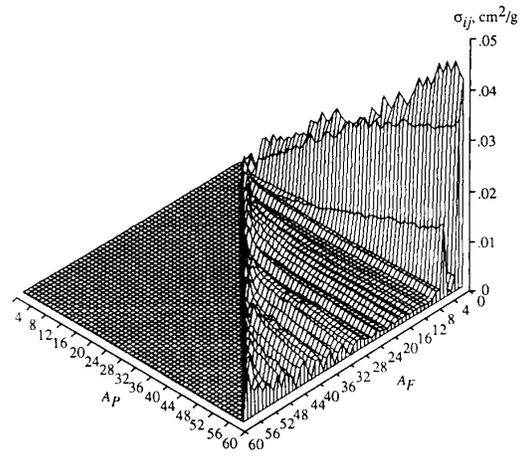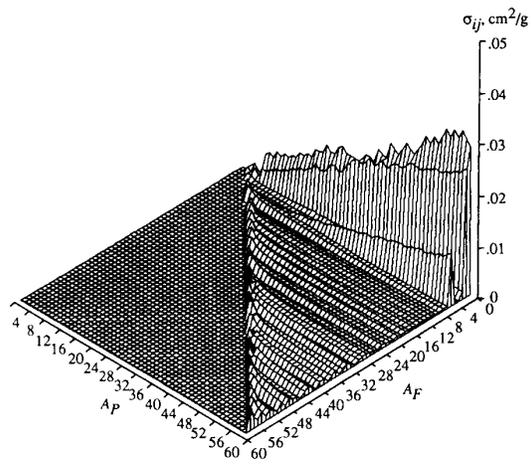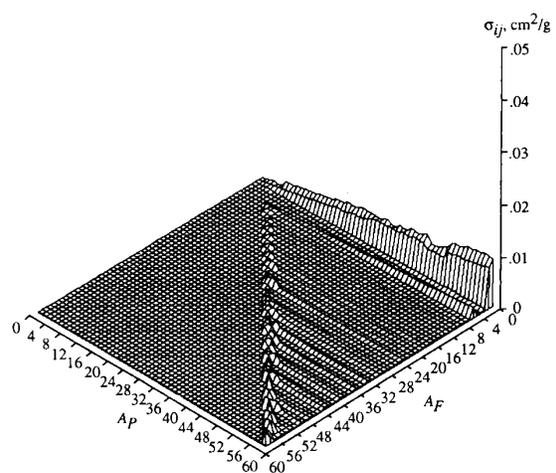
(c) Aluminum.   (d) Lead.

Figure 15. Fragment production cross sections per unit mass for ions transported in the shielding code in four
            diverse materials.
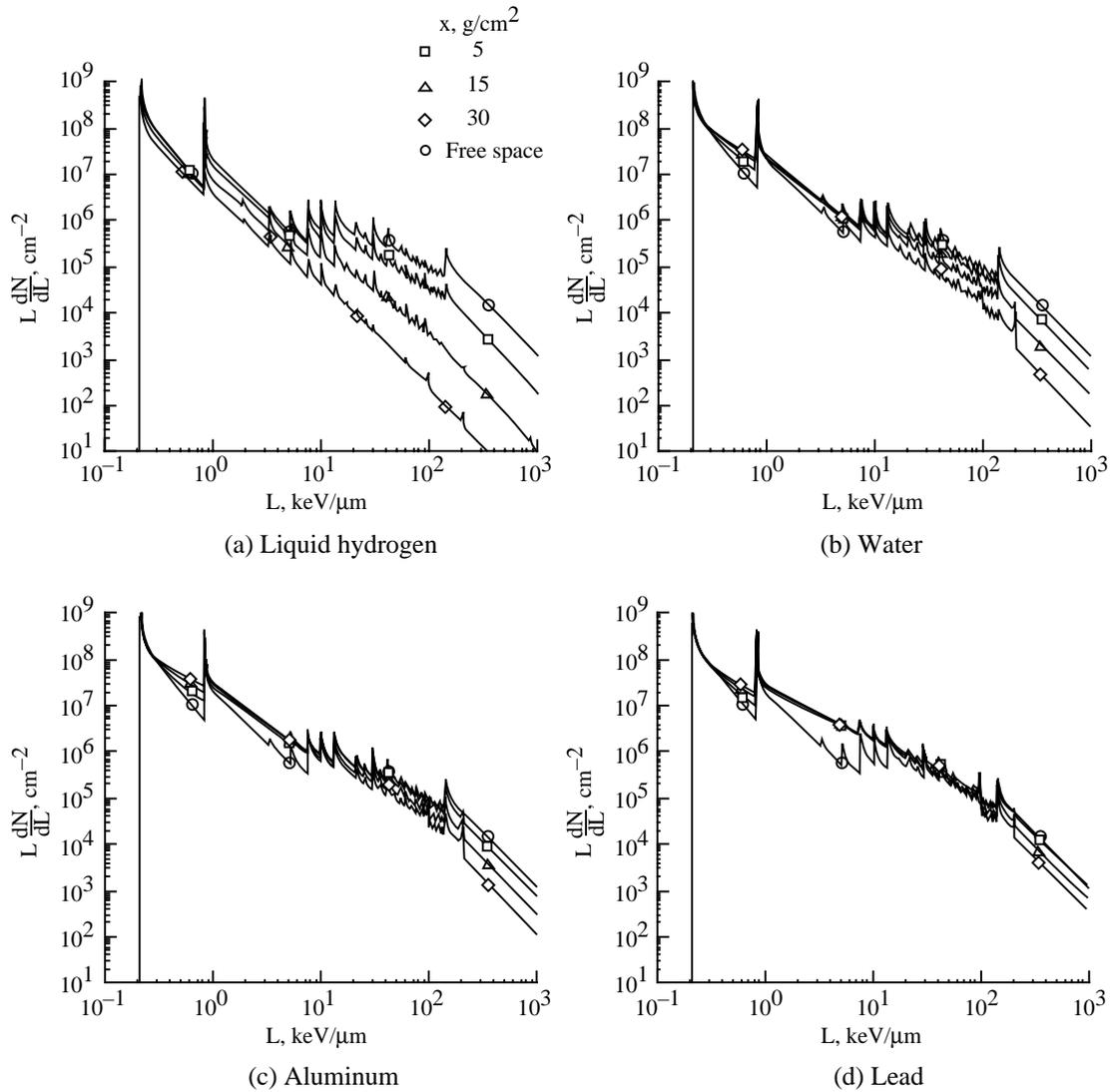
Figure 16.   Annual transmitted 1977 solar minimum GCR differential LET spectrum in four materials.

(a) Dose equivalent

(b) Cell transformation
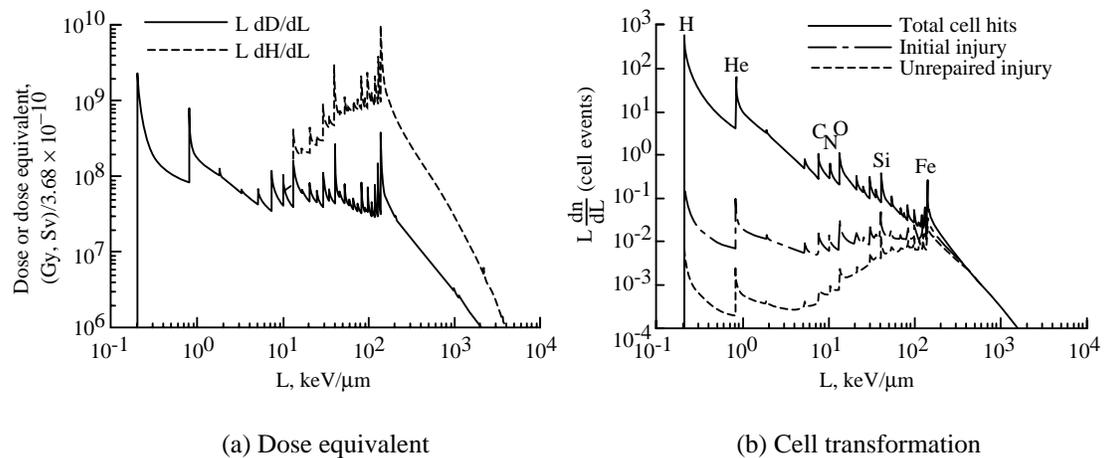
Figure 17.   Distribution of biological injury behind 5 g/cm^2 of aluminum according to two biological models

141
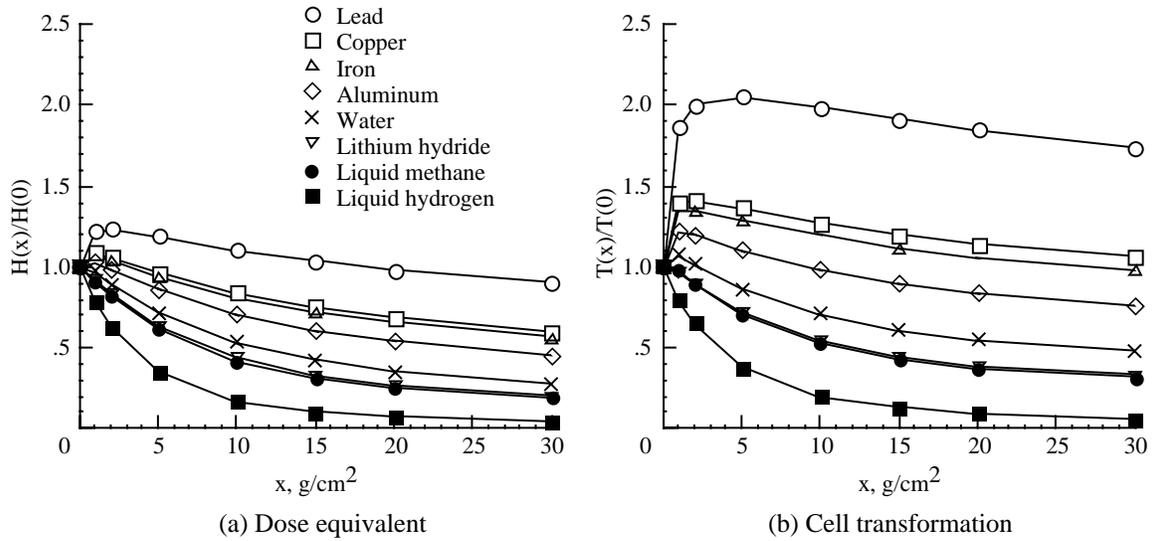
Figure 18. Attenuation of dose equivalent and cell transformation in one year exposure behind several shield materials.
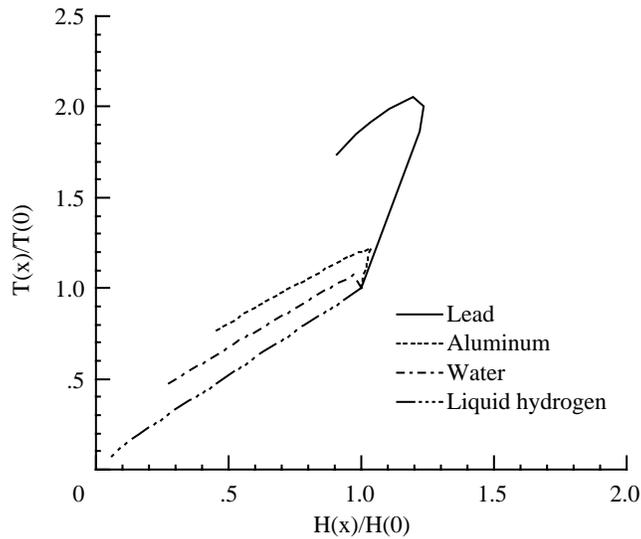
Figure 19. Correlation of cell transformation and dose equivalent behind several shield materials.
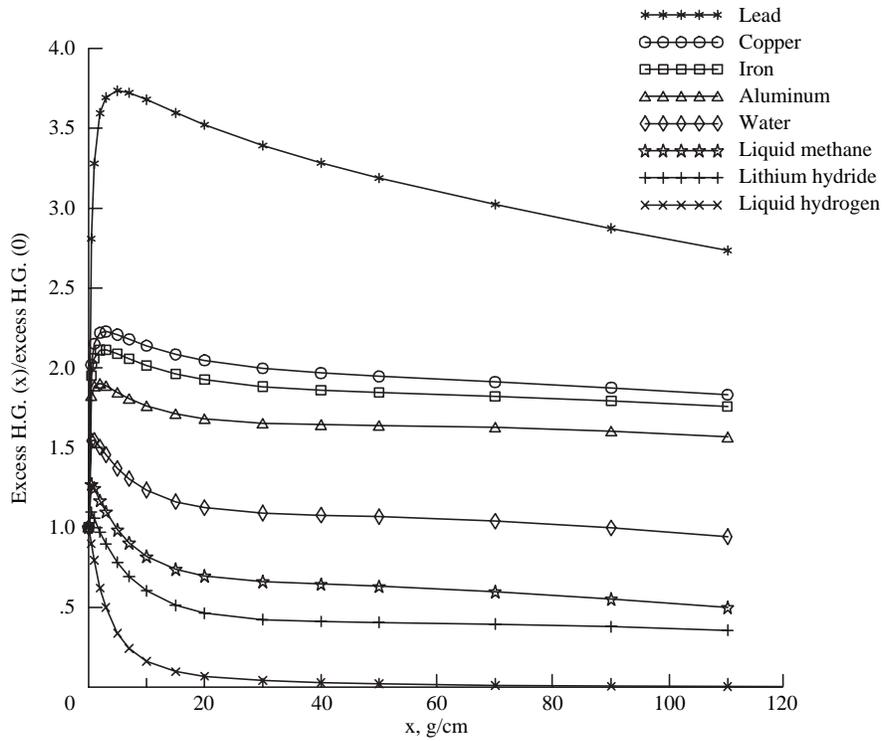
Figure 20. Attenuation of excess Harderian gland tumors for an annual exposure to cosmic rays behind various shield materials.
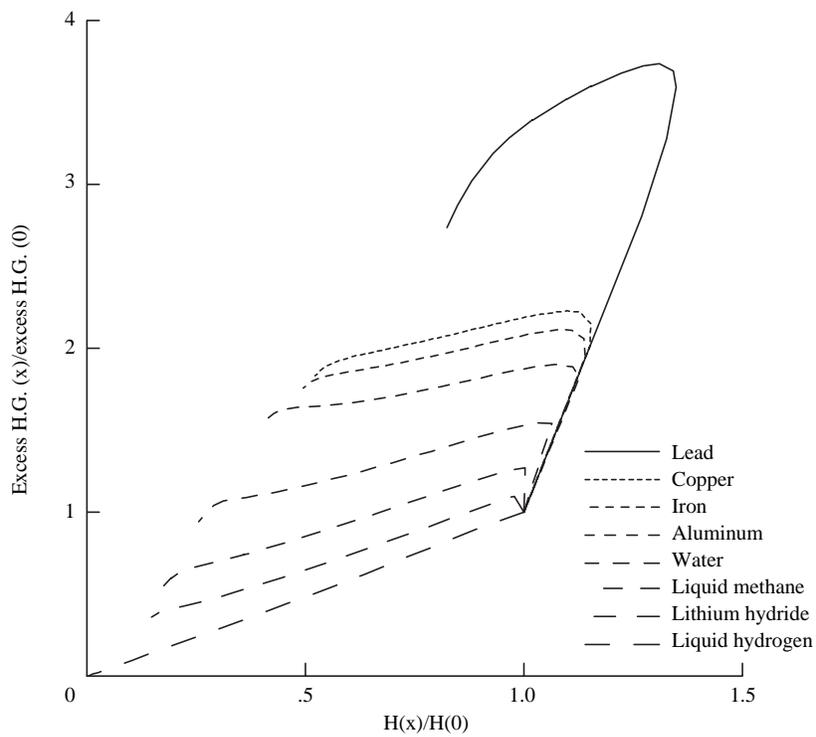
Figure 21. Correlation of excess Harderian gland tumors with dose equivalent behind various shield materials.
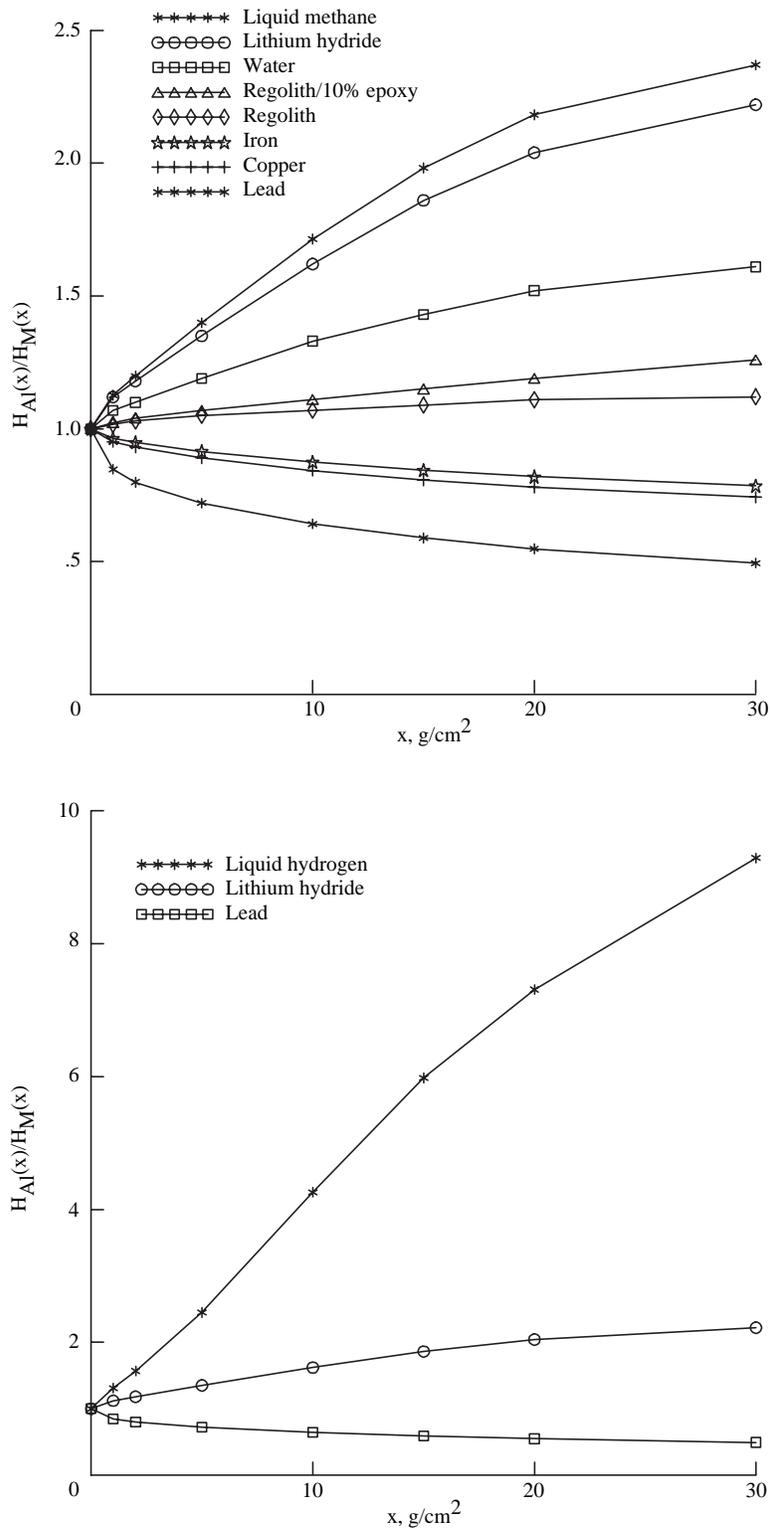
Figure 22.   Dose equivalent based relative shield performance factors for several materials relative to aluminum.
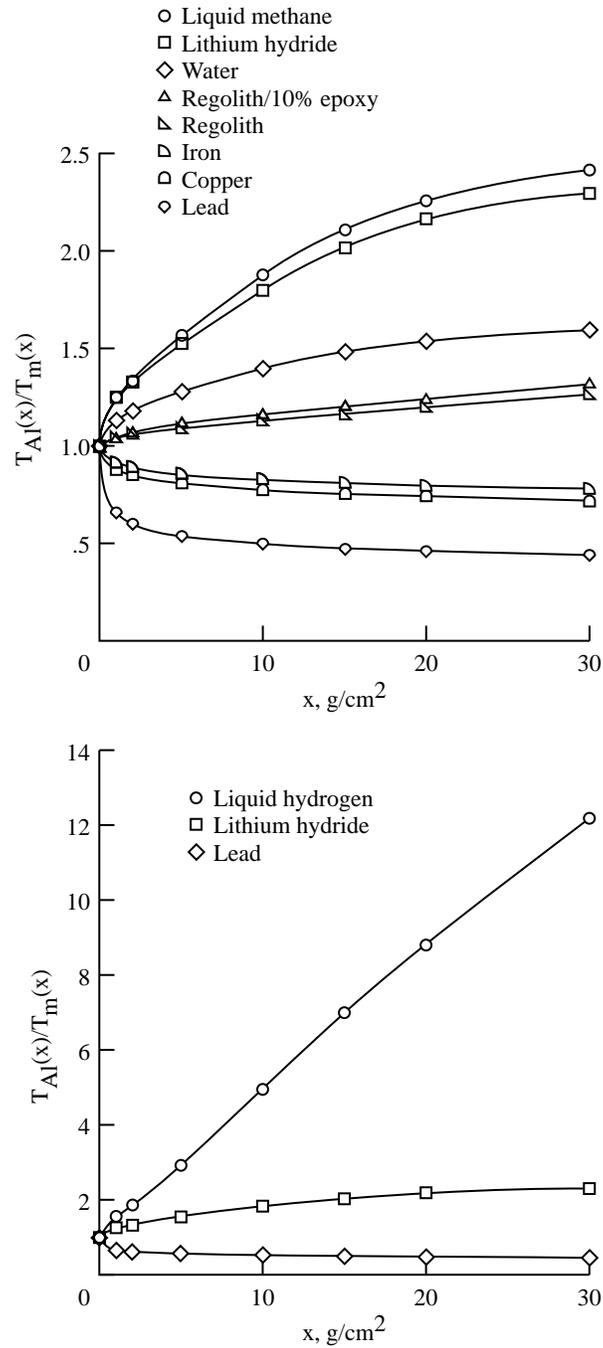
Figure 23. Cell-transformation based relative shield performance factors for several materials relative to aluminum
standard.
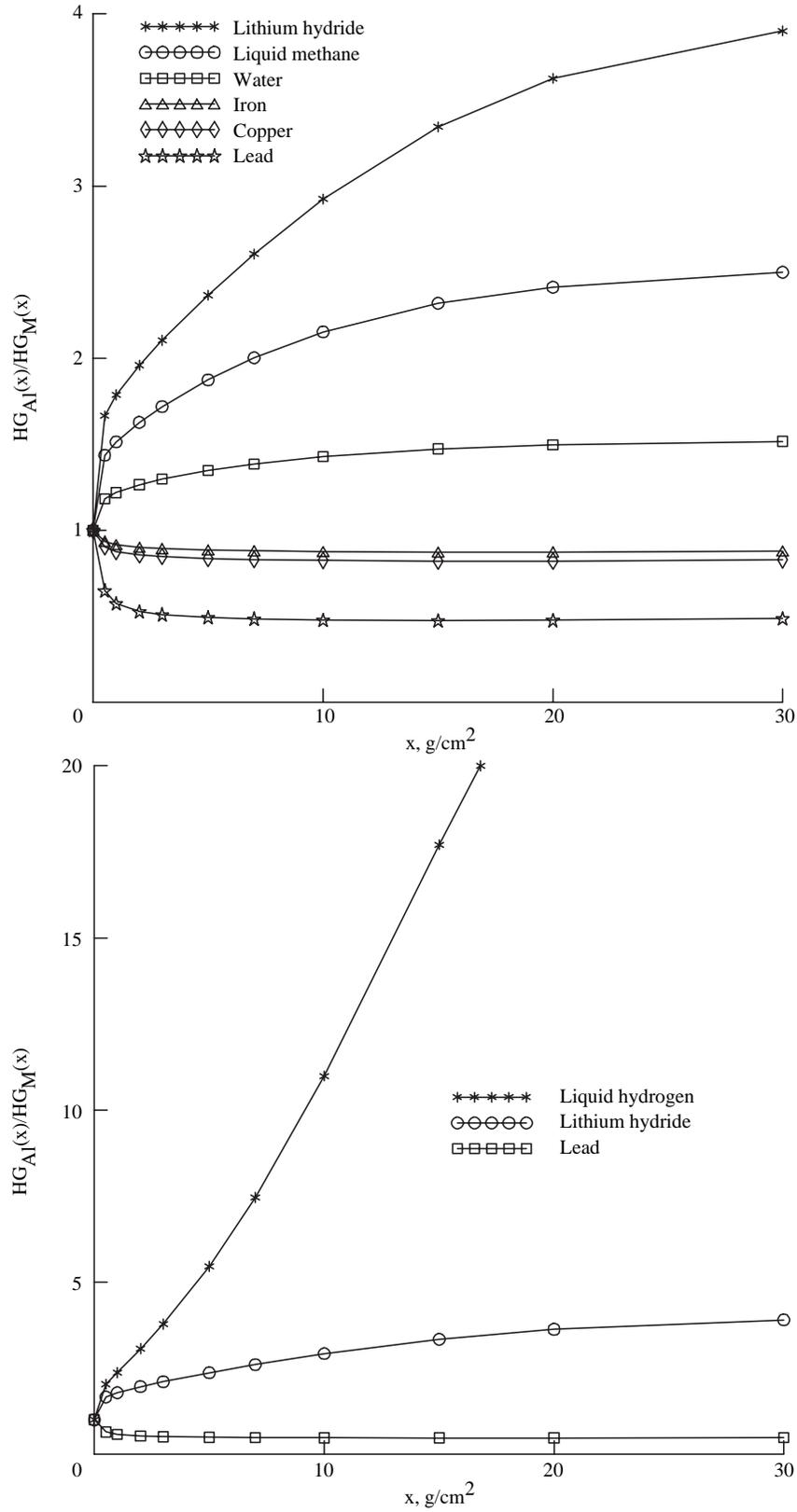
Figure 24. Excess Harderian gland tumor based relative shield performance factor for several materials relative to aluminum.
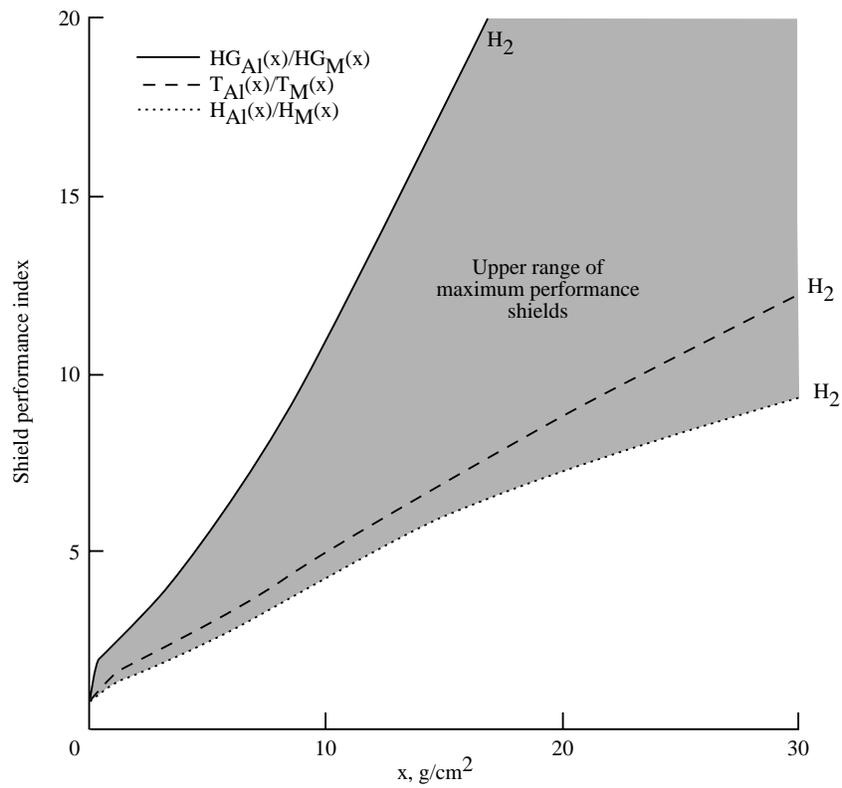
Figure 25. Maximal relative shield performance factors relative to aluminum with various biological models.
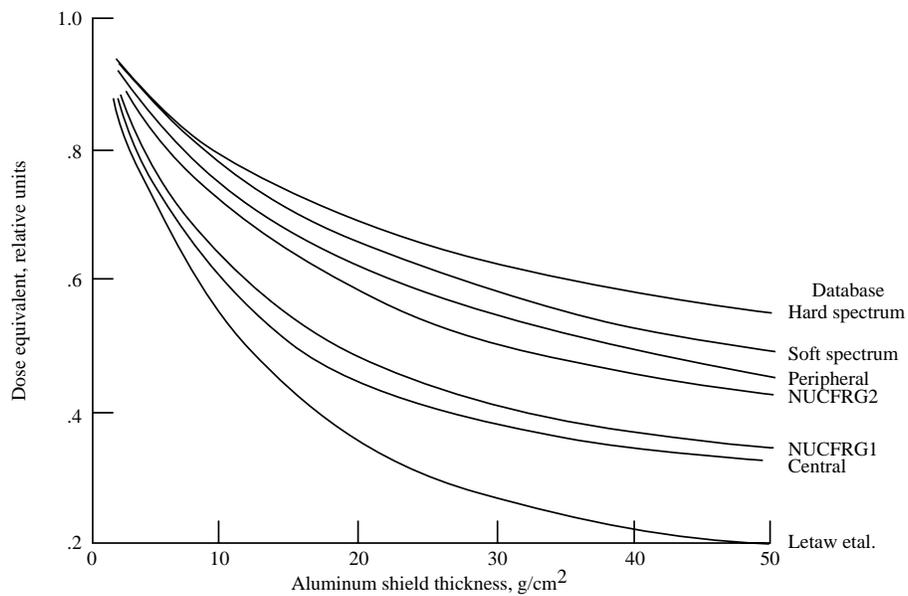
Figure 26. Shield attenuation for solar minimum galactic cosmic ray dose equilvalent resulting from nuclear fragmentation models.

(a) Liquid Hydrogen.

(b) Water.

(c) Aluminum.

(d) Lead.
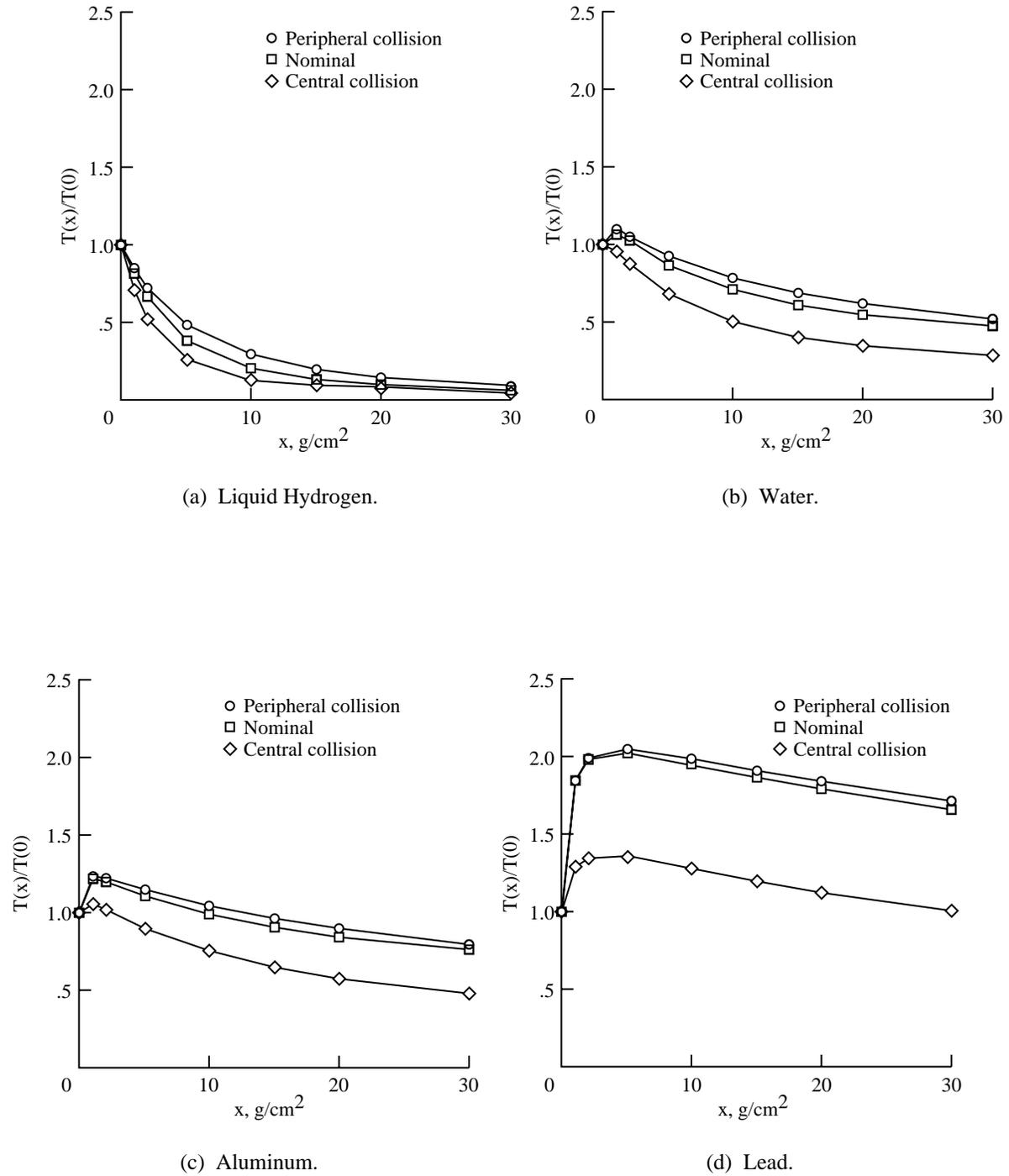
Figure 27.   Effects of physical limits on several shield types.
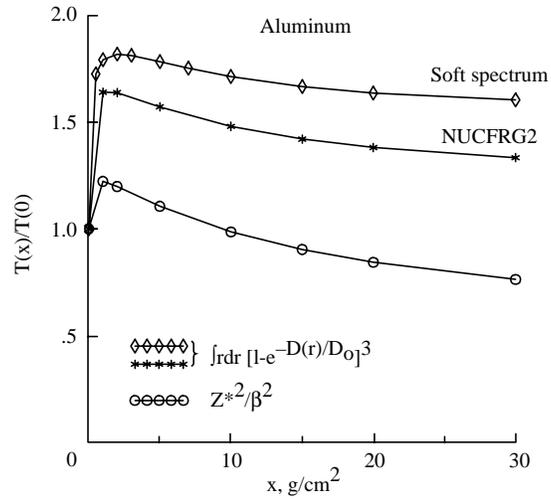
Figure 28.   Effects of recent nuclear database charges on various biological models.
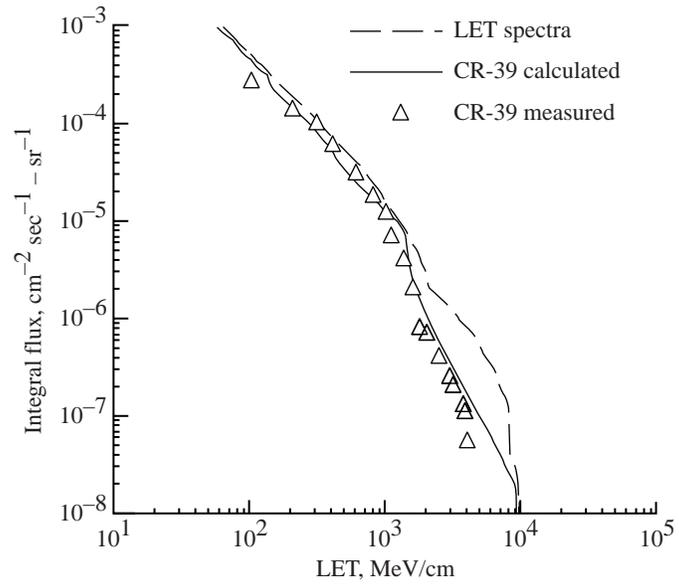
Figure 29.   Calculated LET spectra, predicted CR-39 response, and measured CR-39 response for the DI mission.

CHAPTER 8

COMPUTATIONAL PROCEDURES AND DATABASE DEVELOPMENT

by

F. A. Cucinotta[1]
J. W. Wilson[1]
J. L. Shinn[1]
R. K. Tripathi[2]
K. M. Maung[2]
F. F. Badavi[3]
R. Katz[4]
R. R. Dubey[5]

_____

[1]NASA Langley Research Center, Hampton, VA, 23681
[2]Hampton University, Hampton, VA 23669
[3]Christopher Newport Univeristy, Newport News, VA 23601
[4]University of Nebraska, Lincoln, NE 68558
[5]Old Dominion University, Norfolk, VA 23508

Chapter 8

COMPUTATIONAL PROCEDURES AND DATABASE DEVELOPMENT

SUMMARY

The development of the theory of high charge and energy (HZE) ion transport and the associated atomic and nuclear databases are reviewed. The basic solution behavior and approximation techniques will be described. An overview of the light ion and HZE transport codes currently available at the NASA Langley Research Center will be given. The near-term goal of the Langley program is to produce a complete set of one-dimensional transport codes. The ultimate goal is to produce a set of complete three-dimensional codes which have been validated in the laboratory and can be applied in an engineering design environment which implies high computational efficiency and ease in interfacing with computer aided design (CAD) software. Recent progress toward completing these goals is discussed. The transfer of energy from the radiation fields to materials and biological tissues is dominated by the local production of electrons by the moving ions, and methods of representing the highly correlated electron fields are discussed. The development of nuclear databases relies heavily on quantum multiple scattering theories. Progress in the development of these models is discussed.

INTRODUCTION

Propagation of galactic ions through matter has been studied for the past 40 years as a means of determining the origin of these ions [1, 2, 3]. The "solution" to the steady-state equations is given as a Volterra equation by Gloeckler and Jokipii [4], which is solved to first order in the fragmentation cross sections by ignoring energy loss. They provide an approximation to the first-order solution with ionization energy loss included that is only valid at relativistic energies. Lezniak [5] gives an overview of cosmic-ray propagation and derives a Volterra equation including the ionization energy loss, which he refers to as a solution "only in the iterative sense" and evaluates only the unperturbed term. The main interest among cosmic-ray physicists has been in first-order solutions in the fragmentation cross sections, since path lengths in interstellar space are on the order of 3–4 g/cm^2. Clearly, higher order terms cannot be ignored in accelerator or space shielding transport problems [6–10].

Several approaches to the solution of high-energy heavy ion propagation including the ionization energy loss have been developed over the last 20 years [7–19]. All but one have assumed the straight-ahead approximation and velocity conserving fragmentation interactions [7]. Only two have incorporated energy-dependent nuclear cross sections [7, 10]. The approach by Curtis, Doherty, and Wilkinson [15] for a primary ion beam represented the first-generation secondary fragments as a quadrature over the collision density of the primary beam. Allkofer and Heinrich [16] used an energy multigroup method in which an energy-independent fragmentation transport approximation was applied within each energy group after which the energy group boundaries were moved according to continuous slowing down theory ($-dE/dx$). Chatterjee, Tobias, and Lyman [17] solved the energy-independent fragment transport equation with primary collision density as a source and neglected higher order fragmentation. The primary source term extended only to the primary ion range from the boundary. The energy-independent transport solution was modified to account for the finite range of the secondary fragment ions.

Wilson [8] derived an expression for the ion transport problem to first order (first collision term) and gave an analytic solution for the depth-dose relation. This was followed by examination of the more common approximations used in solving the heavy ion transport problem [7]. Errors generated by assuming conservation of velocity on fragmentation and the straight-ahead approximation were found to be negligible for cosmic-ray applications. Methods of solution for the energy-dependent nuclear cross sections have been developed [7]. Letaw, Tsao, and Silberberg [18] approximated the energy loss term and ion spectra by simple forms for which energy derivatives were more explicitly evaluated (even if approximately). This approximation results in a decoupling of motion in space and a change in energy giving rise to a separable solution [11]. In Letaw's formalism, the energy shift was replaced by an effective attenuation factor. Wilson added the next higher order (second collision) term [9]. This term was found to be very important in describing ^{20}Ne beams at 670 MeV/nucleon. The three-term expansion of Wilson [9] was modified to include the effects of energy variation of the nuclear cross sections [10]. The integral form of the transport equation [7] was further used to derive a numerical marching procedure to solve the cosmic-ray transport problem [11]. This method can easily include the energy-dependent nuclear cross sections within the numerical procedure. Comparison of the numerical procedure [11] with an analytic solution to a simplified problem [12] validates the solution technique to about 1 percent accuracy. Several solution techniques and analytic methods have been developed for testing future numerical solutions to the transport equation [19]. More recently, an analytic solution for the laboratory ion beam transport problem has been derived assuming a straight-ahead approximation, velocity conservation at the interaction site, and energy-independent nuclear cross sections [13]. These analytic techniques were used to derive the Green's function to be used for space or laboratory exposure [20].

In the previous overview of past developments, the applications generally split into two separate categories according to a single ion species with a single energy at the boundary versus a broad host of elemental types with a broad, continuous energy spectrum. Techniques requiring a representation of the spectrum over an array of energy values require vast computer storage and computation speed for the laboratory beam problem to maintain sufficient energy resolution. On the other hand, analytic methods [7, 8, 13] are probably best applied in a marching

procedure [11], which again has within it a similar energy resolution problem. This is a serious limitation because we require a final High Charge and Energy (HZE) Code for cosmic-ray shielding that has been validated by laboratory experiments. In the present report we will review our current status in the development of computational procedures and databases for the evaluation of particle fields within materials and the corresponding energy transfer processes to the material media including the highly correlated electron fields about individual ion trajectories.

TRANSPORT THEORY

The massive particle transport equations are derived by balancing the change in particle flux as it crosses a small volume of material with the gains and losses caused by nuclear collision. The resulting equations for a homogeneous material are given by [21]

$$\left[\Omega\cdot\nabla - \frac{1}{A_j}\frac{\partial}{\partial E}S_j(E) + \sigma_j(E)\right]\phi_j(\mathbf{x},\Omega,E)$$
$$= \sum_k \int dE' \ d\Omega' \sigma_{jk}(E,E',\Omega,\Omega')\phi_k(\mathbf{x},\Omega',E') \tag{1}$$

where $\phi_j(\mathbf{x},\Omega,E)$ is the flux of ions of type j with atomic mass A_j at $\mathbf{x}$ with motion along Ω and energy E in units of MeV/nucleon, $\sigma_j(E)$ is the corresponding macroscopic cross section, $S_j(E)$ is the linear energy transfer (LET), and $\sigma_{jk}(E, E', \Omega, \Omega')$ is the production cross section for type j particles with energy E and direction Ω by the collision of a type k particle of energy E' and direction Ω'. The term on the left side of equation (1) containing $S_j(E)$ is a result of the continuous slowing-down approximation, whereas the remaining terms of equation (1) are seen to be the usual Boltzmann terms. The solutions to equation (1) exist and are unique in any convex region for which the inbound flux of each particle type is specified everywhere on the bounding surface. If the boundary is given as the loci of the two-parameter vector function $\Gamma(s,t)$ for which a generic point on the boundary is given by Γ, then the boundary condition is specified by requiring the solution of equation (1) to meet

$$\sigma_j(\Gamma,\Omega,E) = f_j(\Gamma,\Omega,E) \tag{2}$$

for each value of Ω such that

$$\Omega\cdot n(\Gamma) < 0 \tag{3}$$

where $n(\Gamma)$ is the outward-directed unit normal vector to the boundary surface at the point Γ and f_j is a specified boundary function.

The fragmentation of the projectile and target nuclei is represented by the quantities $\sigma_{jk}(E, E', \Omega, \Omega')$, which are composed of three functions:

$$\sigma_{jk}(E,E',\Omega,\Omega') = \sigma_k(E')\nu_{jk}(E')f_{jk}(E,E',\Omega,\Omega') \tag{4}$$

where $\nu_{jk}(E')$ is the average number (which we loosely refer to as multiplicity) of type j particles being produced by a collision of a type k of energy E', and fjk (E, E', Ω, Ω') is the probability density distribution for producing particles of type j of energy E into direction Ω from the collision of a type k particle with energy E' moving in direction Ω'. For an unpolarized source of projectiles and unpolarized targets, the energy-angle distribution of reaction products is a function of the energies and cosine of the production angle relative to the incident projectile direction. The secondary multiplicities $\nu_{jk}(E')$ and secondary energy-angle distributions are the major unknowns in ion transport theory.

The spectral distribution function is found to consist of two terms that describe the fragmentation of the projectile and the fragmentation of the struck nucleus as follows [22, 23]:

$$\sigma_{jk}(E, E', \Omega, \Omega') = \sigma_K(E')\left[\nu_{JK}^P(E')f_{jk}^P(E, E', \Omega, \Omega') + \nu_{jk}^T(E')f_{jk}^T(E, E', \Omega, \Omega')\right] \tag{5}$$

where ν_{jk}^P and f_{jk}^P depend only weakly on the target and ν_{jk}^T and f_{jk}^T depend only weakly on the projectile. Although the average secondary velocities associated with f^P are nearly equal to the projectile velocity, the average velocities associated with f^T are near zero. Experimentally, Heckman [22] observed for massive fragment (A $\geq$ 4) that

$$
\begin{aligned}
f_{jk}^P(E, E', \Omega, \Omega') &\approx \left[\frac{m}{2\pi\left(\sigma_{jk}^P\right)^2}\right]^{3/2} \sqrt{2E} \exp\left[-\frac{(\mathbf{p} - \mathbf{p}')^2}{2\left(\sigma_{jk}^P\right)^2}\right] \\
&\approx \left[\frac{m}{2\pi\left(\sigma_{jk}^P\right)^2}\right]^{3/2} \sqrt{2E} \exp\left[-\frac{\left(\Omega\sqrt{2mE} - \Omega'\sqrt{2mE'}\right)^2}{2\left(\sigma_{jk}^P\right)^2}\right]
\end{aligned}
\tag{6}
$$

where $\mathbf{p}$ and $\mathbf{p}'$ are the momenta per unit mass of j and k ions, respectively, and

$$f_{jk}^P(E, \mathbf{E}', \Omega, \Omega') \approx \left[\frac{m}{2\pi\left(\sigma_{jk}^T\right)^2}\right]^{3/2} \sqrt{2E} \exp\left[-\frac{\mathbf{p}^2}{2\left(\sigma_{jk}^T\right)^2}\right] \tag{7}$$

where σ_{jk}^P and σ_{jk}^T are related to the root-mean-square (rms) momentum spread of secondary products. These parameters depend only on the fragmenting nucleus. Feshbach and Huang [24] suggested that the parameters σ_{jk}^P and σ_{jk}^T depend on the average square momentum of the nuclear fragments as allowed by Fermi motion. A precise formulation of these ideas in terms of a statistical model was obtained by Goldhaber [25].

The notation is simplified by introducing a vector of flux fields as

$$\phi = \left[\phi_j(\mathbf{x}, \Omega, E)\right] \tag{8}$$

the linear Boltzmann operator

$$\mathbf{B} = \left[\Omega \cdot \nabla - \frac{1}{A_j}\frac{\partial}{\partial E}S_j(E) + \sigma_j(E)\right]$$

(9)

and the integral collision operator

$$\Sigma\phi = \left[\sum_k \int dE'\, d\Omega'\, \sigma_{jk}(E, E', \Omega, \Omega')\, \phi_k(\mathbf{x}, \Omega', E')\right]$$

(10)

Each component of the field vector ϕ corresponds to a given particle type and by convention we place the most massive particle to the top of the vector and least massive to the bottom. The Boltzmann operator $\mathbf{B}$ representing field drift and collisional losses (atomic and nuclear) is diagonal and the collisional operator Σ tends to be lower triangular. There exists an integrating factor for $\mathbf{B}$; we will refer to its inverse as the Boltzmann propagator $\mathbf{G}_O$ and it has been found using the method of characteristic [6,7] as a solution of

$$\mathbf{B}\mathbf{G}_o = 0$$

(11)

The general solution to the Boltzmann equation is then [6, 7]

$$\phi = \mathbf{G}_o\,\phi_B + \mathbf{B}^{-1}\Sigma\phi$$

(12)

and satisfies the boundary conditions (2) provided $\mathbf{G}_O$ reduces to the identity operators at the boundary (note: we choose the constants of integration for equation (11), so this is true). A number of approximate methods have been developed based on equation (12).

A Newman series [6, 7, 20] may be developed for equation (12) as

$$\phi = \mathbf{G}_o\,\phi_B + \mathbf{B}^{-1}\Sigma\mathbf{G}_O\,\phi_B + \mathbf{B}^{-1}\Sigma\mathbf{B}^{-1}\Sigma\mathbf{G}_O\,\phi_B + \dots$$

(13)

which we rewrite in terms of the complete propagator $\mathbf{G}$ as [20]

$$\phi = \mathbf{G}\,\phi_B$$

(14)

It is clear from equation (13) that the complete propagator is given by

$$\mathbf{G} = \mathbf{G}_O + \mathbf{B}^{-1}\Sigma\,\mathbf{G}$$

(15)

Clearly, $\mathbf{G}$ depends on the bounding surface and the physical properties of the media [26]. There are two streams of development in solving the transport problem. The first is to establish solutions to equation (12) according to some computational procedure [6–11] and the second is to develop methods for evaluation of the complete propagator of equation (15) for application to specific input spectra [20, 26].

APPROXIMATION PROCEDURES

In the remainder of this report, we will discuss a progression of development towards increasing levels of sophistication in evaluation methods of particle fields within complex geometric objects. We will not discuss methods for which the relation to the previously discussed formalism is at best tenuous [11]. Nor shall we dwell on strictly finite difference procedures or Monte Carlo simulation, although they shall at times provide insight into the accuracy of the final methodology [6, 14, 19, 26].

Decoupling of Target Fragments

The separation of the interaction cross sections into projectile and target fragment contributions as in equations (5) to (7) provides a basis of simplifying the computation procedure. We may separate the fields as $\phi = \phi_P + \phi_T$ in which

$$\mathbf{B}\phi_P = \Sigma_P \left(\phi_P + \phi_T\right) \tag{16}$$

$$\mathbf{B}\phi_T = \Sigma_T \left(\phi_P + \phi_T\right) \tag{17}$$

In that the second term on the right-hand side of equations (16) and (17) is negligible since the range of the multiple charged target fragments is small compared to the nuclear mean free paths, we may take

$$\mathbf{B}\phi_P = \Sigma_P \ \phi_P + O\left[\sigma_k \ R_j\left(\sigma_{jk}^{T2} \big/ 2m\right)\right] \tag{18}$$

$$\mathbf{B}\phi_T = \Sigma_T \ \phi_P + O\left[\sigma_k \ R_j\left(\sigma_{jk}^{T2} \big/ 2m\right)\right] \tag{19}$$

where $R_j(E)$ is the range energy relation for ion type j. Equation (18) must be yet evaluated after which equation (19) becomes a simple quadrature [7, 27]. The remainder of this report will focus on the solution of equation (18) neglecting terms to the order of $\sigma_k \ R_j\left(\sigma_{jk}^{T2} \big/ 2m\right) \approx 10^{-3}$. In the remainder, we will drop the subscript P from equation (18) to simplify notation so that ϕ will refer to the projectile fields only and ϕ_T will refer specifically to target fragments.

Conservative Field Estimates

A guiding principle in radiation protection practice is that if errors are committed in risk estimates they should be overestimates. The presence of strong scattering terms in the collision terms in equation (10) provides lateral diffusion along a given ray. Such diffusive processes result in leakage at near boundaries [26]. If $\phi_T(\Gamma)$ is the

solution of the Boltzmann equation for a source of particles on the boundary surface Γ, then the solution for the surface source on Γ within a region enclosed by Γ' denoted by $\phi_{\Gamma'}(\Gamma)$ has the property

$$\phi_{\Gamma'}(\Gamma) = \phi_{\Gamma}(\Gamma) + \varepsilon_{\Gamma'} \tag{20}$$

where $\varepsilon_{\Gamma'}$ is positive definite provided Γ' completely encloses Γ. The most strongly scattered component is the neutron fields for which $\varepsilon_{\Gamma'} \approx 0.2$ percent for an infinite media for most practical problems [26]. Standard practice in space radiation protection replaces G as required at some point on the boundary and along a given ray by the corresponding G_N evaluated for normal incidence on a semi-infinite slab. The errors in this approximation are second order in the ratio of beam divergence and radius of curvature of the object and rarely exceed a few percent and are always conservative [26].

Straight-Ahead Approximation

The adequacy of the straight-ahead approximation in shielding from space protons was demonstrated by Alsmiller and coworkers many years ago [28]. The straight-ahead approximation for multiple charged ions is accomplished by approximating equation (6) as

$$f_{jk}^P(E, E', \Omega, \Omega,) \approx f_{jk}^P(E, E')\delta(\Omega \cdot \Omega' - 1) \tag{21}$$

The error term generated [7] by the replacement of equation (21) is

$$\varepsilon_\delta \approx \sigma_{jk}^{P^2} \Big/ 2m\sqrt{EE'} \tag{22}$$

and is quite small provided the angular distributions of the fields at the boundary are relatively uniform [7] since the width σ_{jk}^P of the fragment momentum spectrum is small compared to the projectile momentum. Furthermore, the straight-ahead approximation overestimates the transmitted flux and is therefore conservative in most space shielding applications. The success of the straight-ahead approximation results in part from the small increase in attenuation for lateral diffusion through angles as large as 30° [21].

Velocity Conserving Interactions

The multiple charged fragments formed by nuclear interaction are mainly the spectators of the collision process which conceptually lead Goldhaber [25] to suggest that the momentum spread σ_{jk}^P in the fragment spectrum is related to the spectators random Fermi motion at the time of collision. The final fragment velocity is then the collective spectator velocity prior to collision and is nearly equal to the velocity of the projectile. The velocity conserving interaction is affected by replacing

$$f_{jk}^P(E, E') \simeq \delta(E - E') \tag{23}$$

in equation (21). The error term generated [7] by the replacement is

$$\varepsilon_\nu \approx \sigma_{jk}^P \Big/ \sqrt{2mE} \tag{24}$$

Although this error is small when energy variation in the fields is modest as for space radiations, the velocity conserving interaction is an inferior approximation to the straight-ahead approximation for space radiations as seen by comparing equations (22) and (24).

ONE-DIMENSIONAL THEORY

This section will deal with evaluation of the particle fields under approximations given by equations (18) and (21). There is no lateral spread so that the surviving spatial variable is the depth of penetration and the integral operator Σ is reduced to a simple integral operator over the energy variable only. The transmitted flux in this approximation is always conservative but the degree of error is small for space radiation exposure estimates [28]. We now consider methods by which equation (18) can be solved under the approximation given by equation (21).

Perturbation Theory

The integral form of equation (18) is given as

$$\phi = \mathbf{G}_o \phi_B + \mathbf{B}^{-1} \Sigma \phi \tag{25}$$

and has the Neuman series given by equation (13). The first two terms of the Neuman series have been used by various workers to implement an approximate solution for low penetration depths [4, 5, 8, 15, 17]. An iterative procedure was developed by Lamkin and Wilson [6, 7, 29] which is continued until convergence. The charged particle fields were found to converge rapidly while the neutral neutron component required a greater number of terms [30]. Although these methods showed promise as a very efficient shielding code compared to Monte Carlo procedures, the computational demands were considered excessive compared to marching procedures.

Numerical Marching Procedures

As a consequence of the straight-ahead approximation, the integral equation (25) is a Volterra equation and may be solved using marching procedures. Considering any point on the boundary, the solution can be propagated from the boundary Γ_0 to an interior surface Γ_1 using equation (13) as

$$\phi\left(\Gamma_1\right) = \mathbf{G}_o \, \phi\left(\Gamma_0\right) + \mathbf{B}^{-1} \Sigma \mathbf{G}_o \, \phi\left(\Gamma_0\right) + O\left(\left|\Gamma_1 - \Gamma_0\right|^2\right) \tag{26}$$

where the error term is on the order of the square of the distance between Γ_0 and Γ_1 which can be made arbitrarily small. Equation (26) may be used repeatedly to cover the solution domain as

$$\phi\left(\Gamma_{n+1}\right) = \mathbf{G}_o \, \phi\left(\Gamma_n\right) + \mathbf{B}^{-1} \Sigma \mathbf{G}_o \, \phi\left(\Gamma_n\right) \tag{27}$$

The propagated error at the nth step is

$$\varepsilon_n \le \frac{\varepsilon(h)}{h\sigma}\left[1 - \exp\left(-\sigma n h\right)\right] \tag{28}$$

where h is the distance between Γ_{n+1} and Γ_n and $\varepsilon(h)$ is the maximum error committed on any step. The truncated error of equation (26) is on the order of $(\sigma h)^2$ giving reasonable error propagation in equation (28) for most components except the low energy neutrons. This method is the basis of the BRYNTRN and HZETRN codes [11, 14, 21] and provides adequate solutions where low energy neutrons are of minor importance.

For convenience of notation and to simplify the computational procedures, we scale the flux vector by multiplying by the proton stopping power as

$$\Psi\left(\Gamma_{n+1}\right) = S_P\,\phi\left(\Gamma_{n+1}\right) = G_o\,\Psi\left(\Gamma_n\right) + B^{-1}\,\Sigma'\,G_o\,\Psi\left(\Gamma_n\right) \tag{29}$$

where B, Σ', G_O are new operators corresponding to $\boldsymbol{B}, \boldsymbol{\Sigma}, \boldsymbol{G_O}$. The component equations of equation (29) are written along a given ray as

$$\begin{aligned}
\Psi_j(x+h,r) = {} & e^{-\sigma_j(r)h}\,\Psi_j\left(x, r+v_j h\right) + \sum_k \int_o^h dz\, e^{-\sigma_j(r)z} \int_{r+v_j z}^{\infty} \bar{f}_{jk}\left(r+v_j z, r'\right) \\
& \times \quad e^{-\sigma_k(r')(h-z)}\,\Psi_k\left[x, r'+v_k(h-z)\right]\,dr'
\end{aligned} \tag{30}$$

where E has been replaced by proton residual range and v_j the ion range scale parameter Z_j^2/A_j. It was shown by Lamkin et al. [29] that the integrals of equation (30) may be evaluated as (for $Z_j, Z_k, \le 2$)

$$\begin{aligned}
\Psi_j(x+h,r) = {} & e^{-\sigma_j(r)h}\,\Psi_j\left(x, r+v_j h\right) + \sum_k \int_{r+v_j h/2}^{\infty} e^{-\left[\sigma_j(r)+\sigma_k(r')\right]\frac{h}{2}} \\
& \times \Psi_k\left(x, r'+v_k\frac{h}{2}\right)dr'\bar{F}_{jk}\left(r, v_j h, r'\right) + O\left(h^3\right)
\end{aligned} \tag{31}$$

where

$$\bar{F}_{jk}\left(r, v_j h, r'\right) = \int_0^h \bar{f}_{jk}\left(r+v_j z, r'\right)\,dz \tag{32}$$

Equations (31) and (32) are the bases for the BRYNTRN code for nucleon transport. The $\bar{F}_{jk}\left(r, v_j h, r'\right)$ is related to the integral spectrum of particles produced by the nuclear collision.

The ions with $Z > 2$ can be written as

$$\begin{aligned}
\Psi_j(x+h,r) \approx {} & e^{-\sigma_j(r)h}\Psi_j\left(x, r+v_j h\right) \\
& + \sum_k \int_0^h dz\, e^{-\sigma_j(r)z - \sigma_k(r)(h-z)}\Psi_k\left[x, r+v_j z + v_k(h-z)\right]
\end{aligned} \tag{33}$$

and may be reduced to

$$\Psi_j(x+h,r) = e^{-\sigma_j(r)h}\Psi_j\left(x,r+v_jh\right)$$
$$+ \sum_i \sigma_{jk}(r)\left[\frac{e^{-\sigma_j(r)h} - e^{-\sigma_k(r)h}}{\sigma_k(r)-\sigma_j(r)}\right]\Psi_k\left(x,r+v_jh\right) \tag{34}$$

Note that this formula is similar to the prescription of Allkofer and Heinrich [16]. Equation (34) for $Z \le 2$ coupled to equation (31) provides the source for the HZETRN code.

As a method of validation, we show in figure 1 a comparison of BRYNTRN with a three-dimensional Monte Carlo simulation (HETC) for a rather thick aluminum shield (20 g/cm^2) in front of a 30-cm tissue slab (phantom). The HZE propagation of equation (34) compares to a converged numerical solution [19] of equation (18) under approximations (21) and (23) to within 2 percent. Further attributes of these codes are described elsewhere [21].

Green's Functions

Although the numerical procedures discussed above are adequate when the primary particles have broad continuous spectra, the problem of code validation would be limited to space flight experiments in which the primary particle environmental models are only approximately known, the spacecraft geometry is to a degree uncertain, and detector response is only partly understood. Code validation is ultimately to be achieved in particle accelerator experiments where the primary particle type is known with certainty, its energy is well defined, and the highest quality detection systems can be employed under optimal configuration design to measure the reaction products transmitted through shield materials. We now discuss methods which are efficient tools for space shield design and may be validated in a laboratory environment.

The content of the Green's function method is when $\phi(\Gamma)$ defined on a closed boundary Γ is related to ϕ in the interior region as

$$\phi = \mathbf{G}_\Gamma\ \phi(\Gamma) \tag{35}$$

where $\mathbf{G}_\Gamma$ is the Green's function which reduces to the identity on the boundary and satisfies

$$\mathbf{G}_\Gamma = \mathbf{G}_{o\Gamma} + \mathbf{B}^{-1}\ \Sigma\ \mathbf{G}_\Gamma \tag{36}$$

We noted in connection with equation (20) that $\mathbf{G}_\Gamma$ could be replaced at each point on the boundary by the Green's function for a semi-infinite slab value $\mathbf{G}_{p\Gamma}$ and that a conservative estimate of $\mathbf{G}_{p\Gamma}$ within the interior is found by using the straight-ahead approximation of equation (21). We therefore consider a conservative approximate solution of equations (35) and (36) by using $\mathbf{G}_{p\Gamma}$ in place of $\mathbf{G}_\Gamma$ but must yet develop $\mathbf{G}_{p\Gamma}$ for the semi-infinite slab.

The propagator $\mathbf{G}_p$ relates solutions in a semi-infinite slab to any arbitrary flux $\phi(\mathbf{p})$ at the planar boundary p as

$$\phi_\mathbf{p} = \mathbf{G}_\mathbf{p}\ \phi(\mathbf{p}) \tag{37}$$

Suppose we evaluate $\phi_p(\mathbf{p}')$ at a plane p' parallel to p which is chosen such that

$$\mathbf{G}_p \approx \mathbf{G}_{op} + \mathbf{B}^{-1}\Sigma\mathbf{G}_{op} + \mathbf{B}^{-1}\Sigma\mathbf{B}^{-1}\Sigma\mathbf{G}_{op} \tag{38}$$

Then the solution beyond p' is given as

$$\phi_{p'} = \mathbf{G}_{p'}\,\phi_p(p') = \mathbf{G}_{p'}\,\mathbf{G}_p(p')\,\phi(p) \tag{39}$$

If we denote $\mathbf{G}_p(\mathbf{p}')$ as the propagator from $\mathbf{p} \to \mathbf{p}'$ and $\mathbf{G}_{p'}$ as the propagator beyond $\mathbf{p}'(\mathbf{p}' \to \infty)$, while $\mathbf{G}_p$ is the propagator from $\mathbf{p} \to \mathbf{p}' \to \infty$, then equations (37) and (39) yield

$$\mathbf{G}_p = \mathbf{G}_{p'}\mathbf{G}_p(p') \tag{40}$$

Since $\mathbf{G}_p(\mathbf{p}')$ and $\mathbf{G}_p$ differ only by a translation they are functionally equal and equation (38) can be used to cover a restricted region of the space while equation (40) is a nonperturbative relation which can be used to cover the entire space.

Approximate Green's Functions

The scaled Green's functions in residual range space are given by

$$G_{jm}\left(x, r_j, r'_m\right) = \tilde{S}_j(E)\, G_{jm}(x, E, E') \tag{41}$$

where r_j, r'_m are the residual ranges. This Green's function may be approximated by

$$G_{jm}\left(x, r_j, r'_m\right) = e^{-\sigma_j x}\delta_{jm}\delta\left(x + r_j - r'_m\right) + \frac{\sigma_{jm}}{\Delta^{(1)}}\left(\frac{e^{-\sigma_j x} - e^{-\sigma_m x}}{\sigma_m - \sigma_j}\right)$$
$$+ \left[g_{jm}(x) - e^{-\sigma_j x}\delta_{jm} - \sigma_{jm}\left(\frac{e^{-\sigma_j x} - e^{-\sigma_m x}}{\sigma_m - \sigma_j}\right)\right] \Big/ \Delta^{(2)} \tag{42}$$

where

$$\Delta^{(1)} = x\left(\frac{v_m}{v_j} - 1\right) \simeq \Delta^{(2)} \tag{43}$$

The function $g_{jm}(x)$ is a solution to the energy independent problem and is approximated by

$$g_{jm}(x) = \delta_{jm}\, e^{-\sigma_j x} + \sigma_{jm}\left[\frac{e^{-\sigma_j x} - e^{-\sigma_m x}}{\sigma_m - \sigma_j}\right] + 0\left(x^2\right) \tag{44}$$

where higher order terms are discussed elsewhere [13, 20]. The perturbation series may be used to cover a portion of the space and the nonperturbative equation to cover the remaining space is

$$g_{jm}(x) = \sum_{k} g_{jk}(x-y)g_{km}(y) \qquad (45)$$

These nonperturbative techniques hold great promise for accurate and efficient computational methods for evaluation of the HZE particle fields in space or laboratory problems. They are yet to be extended to light ion and especially neutron fields.

Values for the collision related terms of $G_{jm}\left(x, r_j, r'_m\right)$ are shown in figure 2. The x is depth in a water medium, Z_p is the charge of the incident projectile, and specifically produced species are noted in the figure label. Clearly the production of any given species is dominated by the projectiles of nearly the same but greater charge. The multiple collision terms are mostly important for those projectiles whose charge is far removed from the specific species. These Green's functions are used to evaluate the composition of a 600 MeV/nucleon iron beam in a water column at several depths with results in figure 3. These types of solutions are amenable to experimental validation by HZE ion beams. By way of example, the calculated unchanged charge fluence of 674(±2) A MeV beams of ^{12}C, ^{14}N, and ^{16}O is compared to experiments at the GSI accelerator [32] in figure 4. The single charge removed fluence is shown in figure 5. To achieve this level of agreement required the addition of clusters knockout in the projectile fragmentation of ^{16}O and ad hoc corrections for shell structure effects indicating the level of detail required for predictive nuclear models.

OVERVIEW OF NUCLEAR MODELS AND DATABASES

The database of nuclear interaction cross sections required for galactic cosmic ray transport is enormous when one considers the energy and charge spectrum of the incident ions and the materials of interest in spacecraft and aircraft design, biological tissues, and planetary atmospheres and surfaces. The large number of reaction species combinations, secondary types, and primary energies makes an experimental determination of the cross section database unlikely because of the large number of measurements required. Nuclear reaction models must then be developed which are both accurate and diverse in predictability. The final reaction models to be used for transport code databases must be computationally efficient in order to be practical as input to transport codes to be used by a design engineer.

The reaction cross sections necessary for GCR transport are the inclusive ones, which are a function of the primary type and energy, secondary energy and angle, and the target atom. For transport codes utilizing the straight-ahead approximation, the angular dependence is not required. There have been two main approaches to the development of databases for high energy ion transport: 1) Monte Carlo simulation, and 2) Quantum Multiple Scattering Theories (MST). Monte Carlo simulation is used extensively in proton or neutron reactions on target nuclei, as well as particle production processes such as pions, muons, and gamma-rays [31, 33]. Cugnon [34] has developed the Monte Carlo approach for heavy ion reactions; however, only light particle production has been

extensively studied. Early on, Bertini [33] had noted the lack of any diffractive nature in most particle production processes, making a Monte Carlo simulation which relied only on classical physics and including the Pauli principle, advantageous.

The manifestation of diffraction is not the only signature of quantum effects in nuclear reactions. The optical theorem relates the absorption cross section to the elastic amplitude which is very diffractive in nature, pointing to a quantum description. Also, there are other quantum effects which become important and make the quantum MST approach more favorable. These include the non-diagonal components of the nuclear response function important for describing the quasi-elastic peak in proton, neutron, and alpha particle scattering; the spin effects important in nucleon induced reactions; the discrete nature of low lying states in lighter mass nuclei (A < 16); and the importance of nuclear structure such as shell effects and clustering and correlation effects in the nuclear wave function. The rich variety of quantum effects expected to be manifest in nuclear reactions favors the use of the MST approach, which we next describe.

A non-relativistic MST [35–39] proceeds from the Schrodinger equation and the corresponding integral form in the Lippman-Schwinger or Faddeev equations. A relativistic MST is now available based on meson exchange theory [40–42], while a more general relativistic treatment awaits further theoretical understanding of the non-abelian theory, quantum chromodynamics. The elastic channel can be described through the derivation of an optical (one-body) potential. The inelastic channels, including particle production and fragmentation, are more difficult to treat since several relative motions become important, such that a one-body integral equation is not useful. Approaches for treating the inelastic channels are through a perturbative type solution of a Faddeev like equation and the use of the Eikonal model or Glauber models to reduce the MST to a solvable form. The quantum approach relies heavily on models of nuclear structure for treating excited state wavefunctions, cluster wavefunctions, and also of the nuclear response function. We next describe several developments in the theoretical framework for database development. We also discuss the relation between the quantum models and the semi-empirical NUCFRG model which has been used in the past for the heavy ion fragmentation database in the HZETRN code.

Inclusive Scattering Cross Sections

The scattering amplitude for the heavy ion collision is related to the cross section by the phase space of each particle that appears in the final state. We consider inclusive reactions where a fragment originating in the projectile is measured. For simplicity, the final target state is not considered and will use closure on these states with a single momentum vector denoted $\mathbf{p}_X$ used to represent these states. The cross section is then determined by

$$d\sigma = \frac{(2\pi)^4}{\beta} \sum_X d\mathbf{p}_X \, d\mathbf{p}_{F*} \sum_{n=1} \prod_{j=1}^{n} \left[d\mathbf{p}_j \right] \delta\left(E_i - E_f \right) \delta\left(\mathbf{p}_i - \mathbf{p}_f \right) \left| T_{\mathrm{fi}} \right|^2 \tag{46}$$

where β is the relative projectile-target velocity, $F*$ represents the pre-fragments formed in the projectile-target interaction, n is the number of nucleons knocked out of the projectile in the overlap region with the target, and i and

f label the initial and final states, respectively. The pre-fragment will decay through particle emission if sufficient energy is available. To include the phase space of decay products of F^*, we write

$$d\mathbf{p}_{F^*} = d\mathbf{p}_F \prod_{r=0} d\mathbf{p}_r \tag{47}$$

where the r is the ions (if any) emitted in the decay of the F^*. In considering nucleon production from the decay, we would study the $\mathbf{p}_r$. We use the momentum conserving delta-function in (46) to eliminate $\mathbf{p}_F$ or of the $\mathbf{p}_{j_1}$ from equation (46).

The total momentum transfer is related to p_X through

$$\mathbf{q} = \mathbf{p}_T - \mathbf{p}_X \tag{48}$$

where p_T is the initial target momentum. The inclusive cross section for producing and ion F is then

$$\frac{d\sigma}{d\mathbf{p}_F} = \frac{-(2\pi)^4}{\beta} \sum_x \int d\mathbf{q} \, d\mathbf{p}_F \prod_{r=0} d\mathbf{p}_r \sum_{n=1} \prod_{j=1}^{n} \left[d\mathbf{p}_j \right] \delta\left(E_i - E_f\right) \delta\left(\mathbf{p}_i - \mathbf{p}_f\right) |T_{\text{fi}}|^2 \tag{49}$$

For elastic scattering on the excitation of discrete states, the relation between the transition matrix T_{fi} and the inclusive cross sections is trivial. For fragmentation reactions, where several to many particles are present in the final state, the integrals in (49) then become intractable and approximations must be introduced. One approach is to use a closure approximation on all unobserved projectile fragments. Such approximation is made at the expense of losing information on final state interactions among the projectile fragments. Real progress in reducing the multi-particle momentum integrals to a computationally feasible form is achieved only after studying the structure of the nucleus-nucleus transition matrix, which we next discuss.

NUCLEUS-NUCLEUS TRANSITION MATRIX

The equations of motion for nuclear scattering are expressed in terms of the transition operator which represents an infinite series for the multiple scattering of the constituents of the projectile and target nucleon. The strong nature of the nuclear force requires a non-perturbative solution to the scattering problem. A relativistic theory is of interest for the space radiation databases, because of the high energies of the particles and the large number of production processes which are naturally included in a relativistic theory. In relativistic field theory, the non-abelian nature of the strong force precludes a formulation of the transition matrix for nuclear scattering using the Lagrangian of quantum chromodynamics. A relativistically covariant formulation of the problem has been put forth by Maung and co-workers using meson exchange theory [40–42]. The basic approach, in both relativistic and non-relativistic multiple scattering theories, is to re-sum the multiple scattering series, which is expressed in terms of the irreducible and reducible exchange diagrams in the RMST or the nuclear potential in the NRMST, in terms of the transition matrix for the constituents of the projectile and target nuclei. This avoids having to deal directly with the highly

singular behavior of the nuclear potential at short distances, and instead the constituent transition matrix is used, which is often known from experimental determinations.

The integral equation approach is quite successful for studying elastic scattering where a one-body integral equation can be found using an optical potential. For studying knockout and fragmentation reactions, the Eikonal approximation is useful in order to reduce a many component integral equation to a manageable form. The importance of final state interactions between projectile fragments suggests the use of a Faddeev type integral equation where the interactions between projectile constituents are treated [43, 44].

In the RMST the infinite sum of meson exchange diagrams is written as an integral equation of the Bethe-Salpeter form [42]. The Bethe-Salpeter equation is reduced to a three-dimensional form using a covariant three-dimensional relativistic propagator. The propagator of Maung et al. [41] is most useful for performing the three-dimensional reduction, since it treats the target and projectile constituents on an equal footing, avoiding non-physical singularities that occur with other propagators. The transition operator derived in the RMST [42] is written as

$$T = K + KGT \tag{50}$$

where G is the Bethe-Salpeter propagator representing the two nuclei in intermediate states and the kernel K is the sum of all irreducible diagrams based on meson exchange theory for scattering of the projectile and target constituents. The kernel is decomposed into various terms corresponding to one meson exchange between constituents, two meson exchange between constituents, two meson exchange between more than one constituent, etc.

$$K = K_1 + K_2 + K_{2X} + \dots \tag{51}$$

This infinite sum of irreducible diagrams is described in [42]. The three-dimensional reduction of the RMST is found by introducing an approximate propagator g to obtain the coupled integral equations:

$$T = V + VgT \tag{52}$$

$$V = K + K(G - g)V \tag{53}$$

The three-dimensional reduction is chosen to represent the best approximation to an exact propagator G. In application, the approximation $V \cong K_1$ is often evoked.

The effects of nuclear clustering are considered in the MST by assuming the constituent interactions are those between clusters rather than the choice of nucleons [42–44]. The RMST with clusters has been treated in [42] and involves complicated summations over irreducible diagrams among the cluster constituents. The choice of which cluster configuration is chosen is determined by reaction channel and nuclear cluster considerations. The convergence of a cluster expansion series should be more rapid than the nucleon one when the kernel is known; however, more detailed bound state properties may be involved for performing such calculations.

The NRMST is obtained from equations (50)–(53) by approximating the full kernel by the leading order term corresponding to one-meson exchange diagrams and using a non-relativistic reduction of the three-dimensional propagator g. The potential term is then the sum of the interactions of the constituents [37]

$$V = \sum_{j=1}^{A_p} \sum_{a=1}^{A_T} \tau_{\alpha j} \tag{54}$$

and the non-relativistic propagator is given by

$$g_{NR} = \left(E - H_p - H_T\right)^{-1} \tag{55}$$

where H_P and H_T are the projectile and target internal Hamiltonians, respectively. The constituent interactions involve the full many-body problem as seen from the integral equation

$$\tau_{\alpha j} = V_{\alpha j} + V_{\alpha j} \, g_{NR} \, \tau_{\alpha j} \tag{56}$$

where V is the nucleon-nucleon potential and the propagator includes the effects of nuclear binding. At high energies the impulse approximation is invoked, which assumes that the relative kinetic energy of the constituents is much larger than the binding energies such that the propagator is approximated by (impulse approximation)

$$g_o = \left(E - T_p - T_T\right)^{-1} \tag{57}$$

and the constituent interactions are replaced by the free interactions which are truly of the two-body form. For high energy reactions, the scattering is often confined to the forward direction. Here the Eikonal approximation is useful for reducing the scattering problem to a closed form expression. There are several approaches for deriving the Eikonal form of the MST [45, 46]. Here we continue our considerations of the nucleus-nucleus propagator and introduce the Eikonal propagator [45]

$$g_{eik} = \left(\frac{\mathbf{k} \cdot (\mathbf{k} - \mathbf{k}')}{p_\alpha}\right) \delta\left(\mathbf{k} - \mathbf{k}'\right) \tag{58}$$

The insertion of the Eikonal propagator into the MST allows for a summation of the series into a closed form expression. Calculations using the Eikonal model are considered next.

THE ELASTIC CHANNEL AND NUCLEAR ABSORPTION

The evaluation of the nuclear absorption cross section proceeds from the elastic scattering amplitude and the optical theorem. In the Eikonal coupled channels (ECC) model [46, 47], the matrix of scattering amplitudes for all possible projectile-target transitions is given by

$$\bar{f}(\mathbf{q}) = \frac{ik}{2\pi} \hat{Z} \int d^2 b \, e^{i\mathbf{q}\cdot\mathbf{b}} \left\{ e^{i\bar{x}(\mathbf{b})} - \bar{1} \right\} \tag{59}$$

where barred quantities represent matrices and bold quantities represent vectors. Here, $\mathbf{b}$ is the impact parameter vector, $\mathbf{q}$ is the momentum transfer vector, and k is the projectile-target relative wave number. In equation (59), $\hat{Z}$ is an ordering operator for the z-coordinate which is necessary only when noncommuting two-body interactions are considered. The phase elements of $\bar{X}$ are defined by matrix elements of arbitrary projectile-target states of the operator

$$\bar{X}(\mathbf{b}) = \sum_{\alpha,j} \frac{-\mu}{2k} \int_{-\infty}^{\infty} dz\, t_{\alpha j}\left(\mathbf{r}_\alpha - \mathbf{r}_j + \mathbf{x}\right) \tag{60}$$

where μ is the nucleus-nucleus reduced mass, α and j label the projectile and target constituents, respectively, $\mathbf{r}$ is the internal coordinate, $\mathbf{x}$ is the relative coordinate with $\mathbf{x} = (\mathbf{b}, z)$, and $t_{\alpha j}$ is approximated by the free two-body scattering amplitude in the overall center-of-mass frame. For a projectile transition from quantum state n to n' and target transition from ν to ν' we write

$$X_{n\nu, n'\nu'}(\mathbf{b}) = \sum_{\alpha,j}^{A_P, A_T} \frac{-\mu}{2k} \int_{-\infty}^{+\infty} dz'\, \langle n\nu |\, t_{\alpha j}\, | n'\nu' \rangle \tag{61}$$

where A_P and A_T denote the mass numbers of projectile and target, respectively. Equation (61) is written in terms of transition densities ρ as

$$X_{n\nu, n'\nu'}(\mathbf{b}) = \frac{-\mu}{2k} \sum_{\alpha,j} \int_{-\infty}^{\infty} dz \int d\mathbf{r}_\alpha\, d\mathbf{r}_j\, \rho_{\nu\nu'}\left(\mathbf{r}_j\right) \rho_{nn'}\left(\mathbf{r}_\alpha\right) t_{\alpha j}\left(\mathbf{r}_\alpha + \mathbf{r}_j - \mathbf{x}\right) \tag{62}$$

or in terms of transition form factors as

$$X_{n\nu, n'\nu'}(\mathbf{b}) = \frac{-\mu}{2k(2\pi)^3} \sum_{\alpha,j} \int_{-\infty}^{\infty} dz \int d\mathbf{q}\, e^{i\mathbf{q}\cdot\mathbf{x}}\, F_{nn'}(-\mathbf{q})\, G_{\nu\nu'}(\mathbf{q})\, t_{\alpha j}(\mathbf{q}) \tag{63}$$

where F and G are the projectile and target one-body form factors, respectively. The two-body amplitudes must be related to their values in the nucleon-nucleon (NN) center-of-mass (CM) frame where the physical amplitude f_{NN} is determined by experiments. Making this transformation and noting that the z-integration in equation (63) can be performed formally if commuting interactions are assumed reduces equation (63) to

$$X_{n\nu, n'\nu'}(\mathbf{b}) = \frac{1}{2\pi k_{NN}} \sum_{\alpha,j} \int d^2 q\, e^{i\mathbf{q}\cdot\mathbf{b}}\, F_{nn'}(-\mathbf{q})\, G_{\nu\nu'}(\mathbf{q}) f_{NN}(q) \tag{64}$$

where f_{NN} is the two-body scattering amplitude in the NN CM frame. Equation (64) is convenient for calculations since it is essentially a one-dimensional integration if the form factors are known.

The second-order approximation to the elastic (EL) amplitude is obtained by including all transitions between the ground and excited states and assuming that transitions between excited states are negligible. Furthermore, the

density of all excited (EXC) states is approximated by an average excited-state density. The phase matrix is then of the bordered form

$$X(\mathbf{b}) = \begin{pmatrix} X_{EL} & X_{00,01} & X_{00,10} & X_{00,11} & \cdots \\ X_{01,00} & X_{EXC} & 0 & 0 & \cdots \\ X_{10,00} & 0 & X_{EXC} & 0 & \cdots \\ X_{11,00} & 0 & 0 & X_{EXC} & \cdots \\ \vdots & \vdots & \vdots & \vdots & \end{pmatrix} \tag{65}$$

where $X_{EL} = X_{00,00}$. The characteristic equation of this bordered matrix is

$$\left(X_{EXC} - \lambda\right)^{N_0 - 2}\left[\left(X_{EL} - \lambda\right)\left(X_{EXC} - \lambda\right) - \mathrm{Y}^2\right] = 0 \tag{66}$$

where N_0 is the order of $\bar{X}$, λ is the eigenvalue, and Y^2 is defined by

$$\mathrm{Y}^2(\mathbf{b}) = \sum_{n \text{ or } \nu \neq 0} X_{00,n\nu} X_{n\nu,00} \tag{67}$$

The eigenvalues are given by

$$\lambda_{1,2} = \frac{1}{2}\left(X_{EL} + X_{EXC}\right) \pm \left\{\left[\frac{1}{2}\left(X_{EL} - X_{EXC}\right)\right]^2 + \mathrm{Y}^2\right\}^{1/2} \tag{68}$$

with all others taking the value X_{EXC}. The form of the eigenvalues allows us to treat the scattering system as an effective two-channel problem with

$$X = \begin{pmatrix} X_{EL} & \mathrm{Y} \\ \mathrm{Y} & X_{EXC} \end{pmatrix} \tag{69}$$

Then, from employing Sylvester's theorem we find that

$$f_{CC}^{(2)}(\mathbf{q}) = \frac{-ik}{2\pi} \int e^{-i\mathbf{q}\cdot\mathbf{b}} \left[\cos\left(X_{DIF}^2 + \mathrm{Y}^2\right)^{1/2} + iX_{DIF}\frac{\sin\left(X_{DIF}^2 + \mathrm{Y}^2\right)^{1/2}}{\left(X_{DIF}^2 + \mathrm{Y}^2\right)^{1/2}} - 1\right] d^2b \tag{70}$$

where the subscript CC denotes coupled channels and the difference (DIF) is given as

$$X_{DIF} = \frac{1}{2}\left(X_{EL} - X_{EXC}\right)$$

An expansion of equation (70) reveals, as expected, that X_{EXC} appears only in third-order and higher order terms in $f_{NN}(\mathbf{q})$. A reasonable approximation to X_{EXC} is to assume the ground-state density for the excited states [47]. If X_{EXC} is set equal to X_{EL} we find

$$f_{CC}^2(\mathbf{q}) \approx \frac{-ik}{2\pi} \int \exp(-i\mathbf{q} \cdot \mathbf{b}) \left[\exp(iX_{EL})\cos Y - 1\right] d^2b \tag{71}$$

The coherent approximation [46] is recovered in the limit of small Y.

By using closure to perform the summations in equation (67), Y^2 is given as

$$Y^2(\mathbf{b}) = A_P A_T \left(\frac{1}{2\pi k_{NN}}\right)^2 \int d^2q \; d^2q' \; e^{-i\mathbf{q}\cdot\mathbf{b}} \; e^{-i\mathbf{q}\cdot\mathbf{b}} f_{NN}(\mathbf{q}) \; f_{NN}(\mathbf{q}')$$
$$\times \left[-A_P A_T \; F^{(1)}(\mathbf{q}) \; F^{(1)}(\mathbf{q}') \; G^{(1)}(-\mathbf{q}) \; G^{(1)}(-\mathbf{q}') + (A_P - 1)(A_T - 1) \; F^{(2)}(\mathbf{q}, \mathbf{q}') \; G^{(2)}(-\mathbf{q}, -\mathbf{q}') \right. \tag{72}$$
$$\left. + (A_T - 1) \; F^{(1)}(\mathbf{q} + \mathbf{q}') \; G^{(2)}(-\mathbf{q} - \mathbf{q}') + (A_P - 1) \; F^{(2)}(\mathbf{q}, \mathbf{q}') \; G^{(1)}(-\mathbf{q}, -\mathbf{q}') \right]$$

where $F^{(1)}$ and $F^{(2)}$ ($G^{(1)}$ and $G^{(2)}$) are the projectile (target) one- and two-body, ground-state form factors, respectively.

Townsend [48] has considered Pauli correlation effects between projectile and target nucleons. Here, the first-order elastic phase is written as

$$X_{EL}(\mathbf{b}) = X_{DIR}(\mathbf{b}) - X_{EX}(\mathbf{b}) \tag{73}$$

The direct (DIR) term is written as

$$X_{DIR}(\mathbf{b}) = \frac{A_P A_T}{2\pi k_{NN}} \int d^2q \; e^{i\mathbf{q}\cdot\mathbf{b}} \; F^{(1)}(-\mathbf{q}) \; G^{(1)}(\mathbf{q}) f_{NN}(\mathbf{q}) \tag{74}$$

and the exchange (EX) term is written as

$$X_{EX}(\mathbf{b}) = \frac{A_P A_T}{2\pi k_{NN}} \int d^2q \; e^{i\mathbf{q}\cdot\mathbf{b}} \; F^{(1)}(-\mathbf{q}) \; G^{(1)}(\mathbf{q}) \; \frac{1}{(2\pi)^2} \int d^2q' \; e^{i\mathbf{q}'\cdot\mathbf{b}} \; f_{NN}(\mathbf{q} + \mathbf{q}') \; C(\mathbf{q}') \tag{75}$$

We use the parameterization of f_{NN} as

$$f_{NN}(q) = \frac{\sigma(\rho + i)}{4\pi} k_{NN} \; \exp\left(-\frac{1}{2} Bq^2\right) \tag{76}$$

where k_{NN} is the relative wave number in the two-body system, σ is the two-body scattering cross section, B is the slope parameter, and ρ is the ratio of the real part to the imaginary part of the forward two-body scattering amplitude. Values for the energy-dependent σ, B, and ρ are found in [48]. The correlation factor is found as

$$C(q) = \frac{1}{4}\frac{\pi}{d}\, e^{-q^2/4d^2} \tag{77}$$

in [48] with $d = 1.85$ fm^{-1}.

The total (TOT) cross section is found from the elastic amplitude by using the optical theorem as follows:

$$\sigma_{TOT} = \frac{4\pi}{k}\, \text{Im}\, f(\mathbf{q}=0) \tag{78}$$

Equations (71) and (79) show that

$$\begin{aligned}
\sigma_{TOT} = 4\pi \int_0^\infty b\, db & \left\{ 1 - \frac{1}{2}\exp\left[-\text{Im}\,(X_{EL}+Y) \right] \cos\left[\text{Re}(X_{EL}+Y) \right] \right. \\
& \left. - \frac{1}{2}\exp\left[-\text{Im}\,(X_{EL}-Y) \right]\cos\left[\text{Re}(X_{EL}-Y) \right] \right\}
\end{aligned} \tag{79}$$

where Im and Re denote imaginary and real quantities, respectively. The total absorption (ABS) cross section is found by using

$$\sigma_{TOT} = \sigma_{ABS} + \sigma_{EL} \tag{80}$$

where σ_{EL} is the total elastic cross section. Integrating equation (71) by using $d\Omega \approx d^2q/k^2$ and equations (79) and (80) yields

$$\sigma_{ABS} = 2\pi \int_0^\infty b\, db \left\{ 1 - \frac{1}{2}\exp\left(-2\ \text{Im}\ X_{EL} \right) \left[\cosh\left(2\ \text{Im}\ Y \right) + \cos\left(2\ \text{Re}\ Y \right) \right] \right\} \tag{81}$$

For low-energy ions, the impulse approximation and the forward scattering assumption are not expected to be valid. However, here the effects of Coulomb Repulsion on the scattering becomes important and may dominate other effects. The Eikonal model is connected for the Coulomb trajectories by modifying the impact parameter surface as [49]

$$d^2b \rightarrow d^2b \left(1 - \frac{V_{coul}(\mathbf{b})}{E_{CM}} \right) \tag{82}$$

where V_{coul} is the Coulomb potential between projectile and target nuclei and E_{CM} is the total C. M. kinetic energy.

Light Ion Interactions

For proton or neutron induced knockout of nucleons or light clusters and the fragmentation of light nuclei, such as cosmic ray helium, the multiple scattering series is written in the Faddeev form in order to include the effects of final state interactions in the formalism [50–51]. An alternate approach would be to consider a distorted wave form for the knocked-out particles. The three-body approach of the Faddeev formalism allows for a convergent series if the transition matrix for the light particles incident on nuclei is known. The leading order terms to the knockout series are represented by the overlap functions for the virtual decay of the nucleus and the quasi-elastic scattering of the participants. For heavy ions the overlap functions are represented by the single particle wave functions.

We consider the breakup of a light ion into a two-body final state as

$$P + T \rightarrow a + b + X \tag{83}$$

The transition matrix can be written as a three-body problem of $a - T$, $b - T$, and $a - b$ interactions when rearrangement channels are neglected and with the understanding that all target final and intermediate states must be summed. Using the Faddeev method we consider the multiple scattering series generated by the coupled set of integral equations [51]

$$\tilde{T} = \tilde{T}^a + \tilde{T}^b + \tilde{T}^T \tag{84}$$

with

$$\tilde{T}^a = \tilde{T}_{bT} + \tilde{T}_{bT} G_o \left(\tilde{T}^b + \tilde{T}^T \right) \tag{84a}$$

$$\tilde{T}^b = \tilde{T}_{aT} + \tilde{T}_{aT} G_o \left(\tilde{T}^a + \tilde{T}^T \right) \tag{84b}$$

$$\tilde{T}^T = \tilde{T}_{ab} + \tilde{T}_{ab} G_o \left(\tilde{T}^a + \tilde{T}^b \right) \tag{84c}$$

where $\tilde{T}_{aT}$, $\tilde{T}_{bT}$, and $\tilde{T}_{ab}$ are the "two-body" amplitudes which are the transition operators for aT, bT, or ab scattering, respectively, in the PT Hilbert space and where the Green's function in the impulse approximation is

$$G_o = \left(E - \frac{\mathbf{k}_a^2}{2m_a} - \frac{\mathbf{k}_b^2}{2m_b} - \frac{\mathbf{k}_X^2}{2m_X} + i\eta \right)^{-1} \tag{85}$$

We consider the leading order corrections to the pole approximation by truncating (84) as

$$\tilde{T} = \left(1 + \tilde{T}_{ab} G_o \right) \left(\tilde{T}_{aT} + \tilde{T}_{bT} + \tilde{T}_{aT} G_o \tilde{T}_{bT} + \tilde{T}_{bT} G_o \tilde{T}_{aT} \right) \tag{86}$$

and replacing T_{aT} and T_{bT} by their on-shell values. Equation (86) allows for all orders of multiple scattering, however, assuming the dominance of the *ab* cluster in the projectile and that *ab* final state interactions (FSI) occur

only after interactions with the target. A comparison of the light ion breakup model to experiment for ^{3}H production $\alpha-^{12}C$ reactions is shown in figures 6.

The MST of (86) has been applied to α-particle knockout, as well as to the knockout of nucleons from target nuclei by incident nucleons. For the target knockout case

$$N + T \rightarrow N_1 + N_2 + X \tag{87}$$

a series similar to (84) is introduced as

$$\tilde{T} = \tilde{T}^{N_1} + T^{N_2} + T^x \tag{88}$$

The evaluation of the inclusive cross sections for the α-particle breakup or light particle knockout from nucleon induced reactions involves the quasi-elastic scattering of the fragments. The quasi-elastic distributions have been described by Cucinotta et al. [52–54] in the Eikonal model and are further described below. For the reaction (87) the identity of N_1 and N_2 may be the same (e.g., for p and n production) and the quasi-elastic scattering of the incident nucleon (p or n) may overlap with the knockout distribution. These individual contributions are written

$$\left(\frac{d\sigma}{d\mathbf{p}}\right)_{p,n} = \left(\frac{d\sigma}{d\mathbf{p}}\right)_{K.O.} + \left(\frac{d\sigma}{d\mathbf{p}}\right)_{QE} + \left(\frac{d\sigma}{d\mathbf{p}}\right)_{EVAP} \tag{89}$$

where we have also included a contribution from the decay of highly excited target recoils. The quasi-elastic term in (89) may have a contribution from charge-exchange [54] or nucleon resonances.

QUASI-ELASTIC SCATTERING SERIES

We next consider the quasi-elastic scattering or energy loss distributions for light particles. When treating inelastic scattering, we assume that the off-diagonal terms in $\bar{X}$ (denoted by $\bar{X}_o$) are small compared with the diagonal ones [46], $\bar{X}_D$; then we expand $\bar{f}$ in powers of $\bar{X}_o$ to

$$\bar{f}(\mathbf{q}) = \frac{ik}{2\pi} \int d^2 b \, e^{i\mathbf{q}\cdot\mathbf{b}} e^{i\bar{X}_D(\mathbf{b})} \sum_{m=1} \left\{\frac{[i\bar{X}_O(b)]^m}{m!}\right\} \tag{90}$$

We also will make the assumption that all the diagonal terms are represented by the ground-state elastic phase. Using equation (90), we sum over target final states X (continuum) to find the inclusive angular distribution for the projectile when its mass remains unchanged as in

$$\frac{d\sigma}{d\Omega}\Big)_{IN} = \frac{k^2}{(2\pi)^2} \int d^2 b \, d^2 b' \, e^{i\mathbf{q}\cdot(\mathbf{b}-\mathbf{b}')} \, e^{i\left[X_D(\mathbf{b})-X_D^\dagger(\mathbf{b}')\right]}$$

$$\times \sum_{X\neq 0} \sum_{m=1} \frac{1}{(m!)^2} \langle 0_P 0_T | [i\hat{X}_O(\mathbf{b})]^m | 0_P X \rangle \langle X 0_P | [i\hat{X}_O^\dagger(\mathbf{b}')]^m | 0_P 0_T \rangle \tag{91}$$

Equation (91) only allows for a study of the momentum transfer spectra of the projectile. However, in any consideration of the projectile energy loss, energy conservation must be treated. Based on continuum states for the target final state, energy conservation leads to

$$\left.\frac{d^2\sigma}{d\Omega\,dE_{P'}}\right)_{IN} = \frac{k^2}{(2\pi)^2}\int d^2b\;d^2b'\;e^{i\mathbf{q}\cdot(\mathbf{b}-\mathbf{b}')}\;e^{i\left[X_D(\mathbf{b})-X_D^\dagger(\mathbf{b}')\right]}\sum_{m=1}^{A_T}W_m(\mathbf{b},\mathbf{b}',\omega) \tag{92}$$

and

$$\left.\frac{d\sigma}{dE_{P'}}\right)_{IN} = \int d^2b\;e^{-2\;\mathrm{Im}\,X_D(\mathbf{b})}\sum_{m=1}^{A_T}W_m(\mathbf{b},\mathbf{b},\omega) \tag{93}$$

where $E_{P'}$ is the energy of the projectile in the final state, ω is the projectile energy loss, and we define

$$W_m(\mathbf{b},\mathbf{b}',\omega) = \frac{1}{(m!)^2}\int\prod_{j=1}^{m}\left[\frac{d\mathbf{k}_j}{(2\pi)^3}\right]\delta\left(E_f-E_i\right)\langle 0_P 0_T|\left[\hat{X}_O(\mathbf{b})\right]^m|0_P\mathbf{k}_j\rangle\langle\mathbf{k}_j 0_P|\left[\hat{X}_O^\dagger(\mathbf{b}')\right]^m|0_P 0_T\rangle \tag{94}$$

where $\mathbf{k}_j$ is the wave number vector of a knocked-out target nucleon. We first consider the evaluation of the collision terms W_m using plane waves for the final continuum states of the target. The projectile motion is treated in the coherent approximation. The first collision term is written [54]

$$W_1(\mathbf{b},\mathbf{b}',\omega) = \frac{A_P^2 A_T}{(2\pi)^4 k_{NN}^2}\int_{-\infty}^{\infty}dz\int_{-\infty}^{\infty}dz'\int d\mathbf{q}\,d\mathbf{q}'\,e^{i\mathbf{q}\cdot\eta}\,e^{-i\mathbf{q}'\cdot\eta'}$$
$$\times F(\mathbf{q})F(\mathbf{q}')f_{NN}(\mathbf{q})f_{NN}^\dagger(\mathbf{q}')\int\frac{d^3k}{(2\pi)^3}\delta\left(\omega-E_k\right)G_{0_T\mathbf{k}}(\mathbf{q}')\,G_{\mathbf{k}_{0_T}}^\dagger(\mathbf{q}') \tag{95}$$

where $G_{0_T\mathbf{k}}$ is the transition form factor of the target and A_P and A_T are the projectile and target mass numbers, respectively. Changing variables as

$$\alpha = \frac{1}{2}(\mathbf{q}+\mathbf{q}') \tag{96}$$

$$\beta = \mathbf{q}-\mathbf{q}' \tag{97}$$

$$\mathbf{x} = \mathbf{r}-\mathbf{r}' \tag{98}$$

$$\mathbf{y} = \frac{1}{2}(\mathbf{r}+\mathbf{r}') \tag{99}$$

Also,

$$\mathbf{R} = \eta-\eta' \tag{100}$$

$$S = \frac{1}{2}(\eta + \eta') \tag{101}$$

with the transverse parts denoted $\mathbf{R}_\perp$ and $\mathbf{S}_\perp$, respectively. The first collision term is rewritten

$$W_1(\mathbf{R}_\perp, \mathbf{S}_\perp, \omega) = \frac{A_P^2 A_T}{(2\pi)^4 k_{NN}^2} \int dz\, dz'\, d^3\alpha\, d^3\beta\, e^{i\alpha \cdot \mathbf{R}}\, e^{i\beta \cdot \mathbf{S}} \times A\left(\alpha + \frac{\beta}{2}\right) A^\dagger\left(\alpha - \frac{\beta}{2}\right) R_1(\alpha, \beta, \omega) \tag{102}$$

where we have defined

$$A(\mathbf{q}) = F(\mathbf{q}) f_{NN}(\mathbf{q}) \tag{103}$$

and

$$R_1(\alpha, \beta, \omega) = \int \frac{d^3k}{(2\pi)^3}\, \delta(\omega - E_k)\, G_{0k}\left(\alpha + \frac{\beta}{2}\right) G_{k0}^\dagger\left(\alpha - \frac{\beta}{2}\right) \tag{104}$$

Introducing the Fourier transform pair

$$R_1(\alpha, \beta, \omega) = \int \frac{dt}{(2\pi)} e^{i\omega t} \tilde{R}_1(\alpha, \beta, t) \tag{105}$$

and

$$\tilde{R}_1(\alpha, \beta, t) = \int d\omega\, e^{-i\omega t} R_1(\alpha, \beta, \omega) \tag{106}$$

allows us to evaluate the energy-conserving delta function in equation (104). For the target nucleons, we use

$$E_{\mathbf{k}} = \frac{\mathbf{k}^2}{2m_N} + \varepsilon_{B_1} \tag{107}$$

where m_N is the nucleon mass, ε_{B_1} is the binding energy, and equation (106) is

$$\tilde{R}_1(\alpha, \beta, t) = \int \frac{d\mathbf{k}}{(2\pi)^3}\, d\mathbf{x}\, d\mathbf{y}\, e^{i\varepsilon_{B_1} t}\, e^{-ik^2 t/2m_N}\, e^{i\mathbf{k} \cdot \mathbf{x}}\, e^{i\alpha \cdot \mathbf{x}}\, e^{i\beta \cdot \mathbf{y}}\, \rho\left(\mathbf{y} + \frac{\mathbf{x}}{2}, \mathbf{y} - \frac{\mathbf{x}}{2}\right) \tag{108}$$

where the density matrix is $\rho(\mathbf{r}, \mathbf{r}')$ and is defined by

$$\rho(\mathbf{r}, \mathbf{r}') = \Phi(\mathbf{r})\, \Phi^\dagger(\mathbf{r}') \tag{109}$$

and Φ is the ground-state single-particle wave function. We then find

$$R_1(\alpha, \beta, \xi) = \frac{m_N \xi_1}{(2\pi)^2} \int d^3x\, d^3y\, e^{i\alpha \cdot \mathbf{x}}\, e^{i\beta \cdot \mathbf{y}}\, j_o(\xi_1 x) \rho\left(\mathbf{y} + \frac{\mathbf{x}}{2}, \mathbf{y} - \frac{\mathbf{x}}{2}\right) \Theta\left(\omega - \varepsilon_{B_1}\right) \tag{110}$$

where j_o is a spherical Bessel function, Θ is the unit step function, and

$$\xi_1 = \sqrt{2m_N\left(\omega - \varepsilon_{B_1}\right)} \tag{111}$$

The higher order terms are more difficult to treat because of the enumeration of projectile and target intermediate states. A first approximation is to assume that the projectile remains in the ground state throughout the collision (coherent projectile approximation).

Using similar coordinate changes as described above, we find the mth-order collision term as [54]

$$
\begin{aligned}
W_m\left(\mathbf{R}_\perp, \mathbf{S}_\perp, \omega\right) = {} & \frac{A_P^{2m} A_T^m}{(m!)^2 k_{NN}^{2m} (2\pi)^{(2m+2)}} \int dz\ dz' \int \prod_{j=1}^m \left[d^3\alpha_j\ d^3\beta_j \right. \\
& \times\ e^{i\alpha_j \cdot \mathbf{R}}\, e^{i\beta_j \cdot \mathbf{S}}\, A_j\left(\alpha_j + \frac{\beta_j}{2}\right) A_j^\dagger\left(\alpha_j - \frac{\beta_j}{2}\right)\Bigg] \\
& \times\ R_m\left(\alpha_1, \ldots, \alpha_m, \beta_1, \ldots, \beta_m, \omega\right)
\end{aligned}
\tag{112}
$$

where

$$
\begin{aligned}
R_m\left(\alpha_1, \ldots, \alpha_m, \beta_1, \ldots, \beta_m, \omega\right) = {} & \frac{m_N}{2}\left(\frac{1}{2\pi}\right)^{3m/2} \int \prod_{j=1}^m \left[d^3 x_j\ d^3 y_j\ e^{i\alpha_j \cdot \mathbf{x}_j}\, e^{i\beta_j \cdot \mathbf{y}_j} \right. \\
& \times \rho\left(\mathbf{y}_j + \frac{\mathbf{x}_j}{2}, \mathbf{y}_j - \frac{\mathbf{x}_j}{2}\right) \Bigg] \frac{\xi_m^{3m/2-1}}{\left(\sum_j x_j^2\right)^{3m/4-1/2}} \\
& \times J_{3m/2-1}\left[\sqrt{2m_N\left(\omega - \varepsilon_{B_m}\right)\sum_{j=1}^m x_j^2}\right] \Theta\left(\omega - \varepsilon_{B_m}\right)
\end{aligned}
\tag{113}
$$

where $R_m = 0$ for $\omega < \varepsilon_{B_m}$. The solutions for the mth-order terms in equation (113) result from the Fourier transform of the temporal response. For forward-peaked wave functions, we approximate

$$
R_m\left(\alpha_1, \ldots, \alpha_m, \beta_1, \ldots, \beta_m, \omega\right) \cong C_m\left(\omega - \varepsilon_{B_m}\right)^{m-1} \prod_{j=1}^m R_1\left(\alpha_j, \beta_j, \frac{\xi_m}{\sqrt{m}}\right) + O\left(\xi_j^4 x_j^4\right)
\tag{114}
$$

such that

$$
W_m\left(\mathbf{R}_\perp, \mathbf{S}_\perp, \omega\right) = \frac{C_m\left(\omega - \varepsilon_{B_m}\right)^{m-1}}{(m!)^2}\left[W_1\left(\mathbf{R}_\perp, \mathbf{S}_\perp, \frac{\xi_m}{\sqrt{m}}\right)\right]^m
\tag{115}
$$

where $C_1 = 1$, $C_2 = \dfrac{\pi}{4}$, $C_3 = \dfrac{\pi}{105}$, and $C_4 = \dfrac{\pi^2}{240}$. Equation (114) is found by considering the Taylor series for

$J_{3m/2-1}$. We then have, for the energy loss spectra (eq. (92)) in a coherent projectile model,

$$
\left.\frac{d^2\sigma}{d\Omega\, dE_{P'}}\right)_{IN} = \frac{k^2}{(2\pi)^2} \int d^2R\ d^2S\ e^{i\mathbf{q}\cdot\mathbf{R}_\perp}\ e^{i}\left[X(\mathbf{R}_\perp + \mathbf{S}_\perp/2) - X^\dagger(\mathbf{R}_\perp - \mathbf{S}_\perp/2) \right]
$$

$$
\times \sum_{m=1}^{A_T} \frac{C_m\left(\omega - \varepsilon_{B_m}\right)^{m-1}}{(m!)^2} \left[W_1\left(\mathbf{R}_\perp, \mathbf{S}_\perp, \frac{\xi_m}{\sqrt{m}}\right) \right]_n^m
$$

(116)

and

$$
\frac{d\sigma}{dE_{P'}} = \int d^2S\ e^{-2\ \mathrm{Im}\, X(\mathbf{S}_\perp)} \sum_{m=1}^{A_T} \frac{C_m\left(\omega - \varepsilon_{B_m}\right)^{m-1}}{(m!)^2} \left[W_1\left(0, \mathbf{S}_\perp, \frac{\xi_m}{\sqrt{m}}\right) \right]^m
$$

(117)

The coherent approximation assumes that the projectile remains in the ground state throughout the scattering. The leading-order correction to the coherent terms occurs in the collision term W_2 and corresponds to the following replacement of W_2 [53]:

$$
A_P^4 F\left(\alpha_1 + \frac{\beta_1}{2}\right) F\left(\alpha_1 - \frac{\beta_1}{2}\right) F\left(\alpha_2 + \frac{\beta_2}{2}\right) F\left(\alpha_2 - \frac{\beta_2}{2}\right)
$$

$$
\to A_P^2\left\{\left[F(2\alpha_1) + (A_P - 1)\, F\left(\alpha_1 + \frac{\beta_1}{2}\right) F\left(\alpha_1 - \frac{\beta_2}{2}\right)\right]\right.
$$

(118)

$$
\left.\times \left[F(2\alpha_2) + (A_P - 1)\, F\left(\alpha_2 + \frac{\beta_2}{2}\right) F\left(\alpha_2 - \frac{\beta_2}{2}\right)\right]\right\}
$$

which follows from using closure on the projectile intermediate states. Physically, equation (118) allows the projectile to dissociate in the intermediate state. Further modifications are necessary when correlation effects are treated.

The target transition form factors will describe the effects of the FSI between the unobserved ejected nucleons and the recoiling target nucleus. The transition form factor of the target appearing in the first-order response is given by

$$
G_{0_T \mathbf{k}_1}(\mathbf{q}) = \langle 0_T | e^{i\mathbf{q}\cdot\mathbf{r}} | \psi_{\mathbf{k}_1}^{(-)} \rangle
$$

(119)

where $\psi_{\mathbf{k}_1}^{(-)}$ is the outgoing scattering state. With the Moller operator $\hat{\Omega}_{\mathbf{k}_1}^{(-)}$, the transition form factor is written, using plane-wave states, as

$$
G_{0_T \mathbf{k}_1}(\mathbf{q}) = \langle 0_T | e^{i\mathbf{q}\cdot\mathbf{r}} \hat{\Omega}_{\mathbf{k}_1}^{(-)} | \mathbf{k}_1 \rangle
$$

(120)

The Moller operator is related to the Green function $\hat{g}_o^{(-)}$ and to the transition operator $\hat{T}$ as

$$\hat{\Omega}_{\mathbf{k}_1}^{(-)} = 1 + \hat{g}_o^{(-)}\hat{T} \tag{121}$$

Using equations (120) and (121), we can separate the first-order response function into three terms corresponding to the plane-wave response, elastic distortion in the FSI, and inelastic reaction in the FSI (cascade). Thus [54],

$$R_1(\mathbf{q},\mathbf{q}',\omega) = R_1^{PW} + R_1^{DW} + R_1^{IN} \tag{122}$$

The plane-wave term was described above. For the DW term, we have

$$R_1^{DW} = \int \frac{d^3k_1}{(2\pi)^3} \delta\left(\omega - E_{\mathbf{k}_1}\right) \Big[\langle 0_R | e^{i\mathbf{q}\cdot\mathbf{r}} \hat{g}_o^{(-)}\hat{T} | \mathbf{k}_1 \rangle \langle \mathbf{k}_1 | e^{i\mathbf{q}'\cdot\mathbf{r}'} | 0_R \rangle$$
$$+ \langle 0_R | e^{i\mathbf{q}\cdot\mathbf{r}} | \mathbf{k}_1 \rangle \langle \mathbf{k}_1 | \hat{g}_o^{(-)\dagger}\hat{T}^\dagger e^{i\mathbf{q}'\cdot\mathbf{r}'} | 0_R \rangle \Big] \tag{123}$$

where $| 0_R >$ is the ground-state wave function of the recoil nucleus. The cascade term describes a new inelastic collision series of the ejected nucleon with $\mathbf{k}_1$ reacting on the target recoil given by

$$R_1^{IN} = \sum_{\ell=2}^{A_T} \int \frac{d^3k_1}{(2\pi)^3} \prod_{j=2}^{\ell} \left[\frac{d^3k_j}{(2\pi)^3} \right] \delta\left(\omega - E_{\mathbf{k}_1} - \sum_{j=2}^{\ell} E_{\mathbf{k}_j}\right)$$
$$\times \langle 0_R | e^{i\mathbf{q}\cdot\mathbf{r}} \hat{g}_o^{(-)}\hat{T} | \mathbf{k}_1 \prod_{j=2}^{\ell} \mathbf{k}_j \rangle \tag{124}$$
$$\times \langle \mathbf{k}_1 \prod_{j=2}^{\ell} \mathbf{k}_j | \hat{g}_o^{(-)\dagger}\hat{T}^\dagger e^{-i\mathbf{q}'\cdot\mathbf{r}'} | 0_R \rangle$$

The evaluation of the response functions is considered in [54, 55] using the harmonic oscillator shell model wave function and the Eikonal approximation. Comparisons of the model for proton scattering on ^{27}Al and $\alpha - \alpha$ reactions are shown in figures 7 and 8, respectively.

Heavy Ion Fragmentation Models

The abrasion-ablation models describe nuclear fragmentation as a two-step process of abrasion, where the projectile and target overlap at various impact parameters leading to the shearing of the nucleons in the overlap region, followed by ablation where the projectile or target remnants denoted the pre-fragments that were outside the overlap zone are assumed to have received excitation energy due to the collision and subsequent decay through particle emission. The theoretical calculation of the fragmentation cross sections involves 4 areas: (1) the description of the probability of removing a given amount of mass and charge, (2) the description of the distribution of pre-fragment excitation energies formed in the abrasion step, (3) the description of the statistical decay of the pre-fragments to form the final fragment distribution, and (4) the description of the momentum distributions of light

particles (p, n, d, t, h, and α) created both in initial overlap of projectile and target and the statistical decay of the pre-fragments.

The earliest abrasion-ablation models [56] considered a geometrical formulation of the abrasion-ablation model. Following Bowman, Swiatecki, and Tsang [56] the cross section for removal of ΔA nucleons is given by

$$\sigma(\Delta A) = \pi b_2^2 - \pi b_1^2 \tag{125}$$

where b^2 is the impact parameter for which the volume of intersection of the projectile contains Δ_{abr} nucleons and the resulting exciting energies release additional Δ_{abl} nucleons at the rate of 1 nucleon for every 10 MeV of excitation such that

$$\Delta_{abr}(b_2) + \Delta_{abl}(b_2) = \Delta A - \frac{1}{2} \tag{126}$$

and similarly for b_1

$$\Delta_{abr}(b_1) + \Delta_{abl}(b_1) = \Delta A + \frac{1}{2} \tag{127}$$

Wilson, et al. [57–58] have considered modifications of the original model for both Δ_{abr} and Δ_{abl}. The impact parameter dependence of the Δ_{abr} now includes an energy dependent attenuation factor and a correction for Coulomb trajectories. The mass removal for abrasion is given by

$$\Delta_{abr} = F A_P \left[1 - \exp\left(\frac{-C_T}{\lambda} \right) \right] \tag{128}$$

where C_T is the chord lengths of the intersecting surface in the target at the separation which maximizes the interaction potential [58]. The expressions for F differ depending on the nature of the collision (peripheral versus central) and the relative sizes of the colliding nuclei. The functional dependence for F is given in [58, 59, 60]. The charge ratio of removed nuclear matter is assumed to be that of the parent nucleus.

The mass removal for ablation assumes that a nucleon is removed for every 10 MeV of excitation energy with the excitation energy having contributions from surface distortion and frictional spectator interactions [60–62]. The mass removal in ablation is then

$$\Delta_{abl} = \frac{E_s + E_x}{10 \; MeV} \tag{129}$$

The surface distortion energy is modeled by considering the difference in surface area between a misshapen sphere and a perfect sphere of equal volume [59, 60]. The excitation energy associated with surface energy is taken as 0.95 MeV/fm^2 such that

$$E_s' = 0.95\Delta S \tag{130}$$

where formulas for the change in surface area are given in [59, 60]. Wilson et al. [57, 58] have considered corrections to (129) for large numbers of nucleons removed, represented by

$$f = 1 + 5F + \left[1500 - 320(A_P - 12)\right]F^3 \tag{131}$$

which approaches 1 when the impact parameter is large but increases the excess excitation when large portions of the nuclei are removed in the collisions and when grossly misshapened nuclei are formed. The term in brackets is limited to positive values. The total excitation energy is then

$$E_s = E_s' f \tag{132}$$

It is also assumed that all fragments with a mass of 5 are unbound, that 90 percent of the fragments with a mass of 8 are unbound, and that 50 percent of the fragments with a mass of 9 (^{9}B) are unbound.

A secondary contribution to the excitation energy is the transfer of kinetic energy of relative motion across the intersecting boundary of the two ions. The rate of energy loss of a nucleon when it passes through nuclear matter [63] is taken at 13 MeV/fm, and the energy deposit is assumed to be symmetrically dispersed about the azimuth so that 6.5 MeV/nucleon-fm at the interface is the average rate of energy transfer into excitation energy. This energy is transferred in single particle collision processes, and on half of the events, the energy is transferred to excitation energy of the projectile and the remaining half of the events leaves the projectile excitation energy unchanged. The first estimate of this contribution is to use the length of the longest chord C_1 in the projectile surface interface. This chord length is the maximum distance traveled by any target constituent through the projectile interior. The number of other target constituents in the interface region may be found by estimating the maximum chord C_t transverse to the projectile velocity which spans the projectile surface interface. The total excitation energy from spectator interaction is then

$$E_x' = 13C_1 + \frac{1}{3}13C_1(C_t - 1.5) \tag{133}$$

where the second term only contributes if $C_t > 1.5$ fm. It is assumed that the effective longitudinal chord length for these remaining nucleons is one third the maximum chord length.

In accordance with the previously discussed directionality of the energy transfer, E_x is double valued as

$$E_x = \begin{cases} E_x' & \left(P_x = \dfrac{1}{2}\right) \\ 0 & \left(P_{\bar{x}} = \dfrac{1}{2}\right) \end{cases} \tag{134}$$

where P_j is the corresponding probability of occurrence of each value in collisions. The charge distribution of the final projectile fragments are evaluated using the Rudstam empirical formula [61]. Selection rules within the code

assume the most tightly bound structures are removed first in the excitation decay process subject to overall mass and charge conservation.

The geometric model is useful for its computation efficiency (a complete nuclear database for cosmic ray transport requires about 20 minutes on a VAX4000), while including some of the physics of the abrasion-ablation process. It thus offers some advantage over empirical fits to fragmentation data such as Silberberg and Tsao [64] in that charge and mass are conserved and extrapolation into regions where no experimental data on fragmentation exist is guided by physics of the model. However, many aspects of the physics are considered only in a simplified manner or not at all. These include the diffuseness of the nuclear surface, nuclear structure effects that are apparent in the single particle wavefunctions, and statistical decay properties such as fluctuations in ground-state masses and level densities. Also, not included are clustering effects, such as α-particles. These effects are next considered through a microscopic formulation of the abrasion model.

MICROSCOPIC ABRASION MODEL

We next discuss the derivation of the abrasion cross section using the nuclear scattering operator including its relationship to the excitation spectrum of the pre-fragment nuclei. The work of Hufner, Schaffer, and Schurman [65] first discussed this problem in a microscopic context and further related to the optical model formalism by Townsend [66]; however, closure approximations were invoked on both the projectile knockout and pre-fragment final states resulting in complete loss of information on the momentum spectrum of knockout or pre-fragment excitation spectrum, respectively. Herein we discuss the excitation spectrum of the pre-fragments and its relationship to the abrasion cross section and the relation to the momentum distribution of the knockout protons [67, 68] and neutrons [69]. The excitation spectrum following cluster abrasion of alpha particle was treated by Cucinotta and Dubey [44].

The excitation spectrum is treated by considering energy conservation in the projectile-target overlap. This is done only approximately, due to the complexity of the reaction. The two main approximations introduced at this time are the neglect of the longitudinal momentum transfer in the high energy model and the use of a closure approximation on the target final states. We also have the problem of treating final state interactions (FSI) between the projectile knockouts and the prefragment where further energy is expected to be deposited in the prefragment. Methods for treating this interaction have been considered [54].

In the Glauber model the scattering operator for nucleus-nucleus collisions is written

$$f(\mathbf{q}) = \frac{ik}{2\pi} \int d^2b \, e^{i\mathbf{q}\cdot\mathbf{b}} \Gamma(\mathbf{b}) \tag{135}$$

where k is the projectile-target relative wave number, $\boldsymbol{b}$ is the impact parameter, $\boldsymbol{q}$ the momentum transfer, and the profile function is

$$\Gamma(\mathbf{b}) = 1 - \prod_{\alpha, j} \left(1 - \Gamma_{\alpha j}\left(\mathbf{b} - \mathbf{s}_\alpha - \mathbf{s}_j\right)\right) \tag{136}$$

where α and j label the target and projectile constituents, respectively. In equation (136), $\Gamma_{\alpha j}$ is the two-body profile function with the internal coordinate having components $\mathbf{r} = (\mathbf{s}, z)$.

The scattering amplitude of equation (135) is related to the production cross section for a projectile nucleon from the abrasion process by

$$\frac{d\sigma}{d\mathbf{k}} = \sum_x \frac{1}{(2\pi)^2} \int dE_{F*} d^2q \, d^2b \, d^2b' \exp\left[i\mathbf{q} \cdot (\mathbf{b} - \mathbf{b}')\right] \delta(E_i - E_f)$$
$$\times \int \prod_{j=2}^n \left[\frac{d\mathbf{k}_j}{(2\pi)^3}\right] \langle TP|\Gamma^\dagger(\mathbf{b}')|XF*\mathbf{k}_j\rangle \langle \mathbf{k}_j F*X|\Gamma(\mathbf{b})|PT\rangle \tag{137}$$

where the $\mathbf{k}_j$ are the wave numbers of the abraded nucleons, $F*$ is the pre-fragment, with $A_{F*} = A_P - n$, and in equation (137) we have inserted initial and final states. The excitation spectrum of the pre-fragments is given by

$$\frac{d\sigma}{d\varepsilon_{F*}} = \sum_x \frac{1}{(2\pi)^2} \int d^2q \, d^2b \, d^2b' \exp\left[i\mathbf{q} \cdot (\mathbf{b} - \mathbf{b}')\right] \delta(E_i - E_f)$$
$$\times \int \prod_{j=2}^n \left[\frac{d\mathbf{k}_j}{(2\pi)^3}\right] \langle TP|\Gamma^\dagger(\mathbf{b}')|XF*\mathbf{k}_j\rangle \langle \mathbf{k}_j F*X|\Gamma(\mathbf{b})|PT\rangle \tag{138}$$

Equations (137) and (138) show the direct relationship between the momentum spectrum of the nucleons produced in P-T overlap and the spectrum of the pre-fragments. However, the momentum distribution is expected to have only a weak dependence on the residual spectrum and a closure approximation on the $F*$ states will be accurate. In contrast, the prediction of the excitation of specific levels will require construction of these states. Previous abrasion-ablation models [65,66] which used average excitation energies for the $F*$ suggest a statistical model for the reduction of (138) would be useful, especially for $n >> 1$. At high energies a closure approximation over the target states is accurate which reduces (138) to

$$\frac{d\sigma}{d\varepsilon_{F*}} = \langle T| \int d^2q \, d^2b \, d^2b' \exp\left[i\mathbf{q} \cdot (\mathbf{b} - \mathbf{b}')\right] P_{FF*}(\mathbf{b}, \mathbf{b}') \Lambda_n(\mathbf{b}, \mathbf{b}', \mathbf{q}, E_{F*})|T\rangle \tag{139}$$

where the abrasion response function is defined

$$\Lambda_n(\mathbf{b}, \mathbf{b}', \mathbf{q}, E_{F*}) = \binom{A_P}{n} \int \prod_{j=1}^n \left[\frac{d\mathbf{k}_j}{(2\pi)^3}\right] \langle \phi_n \left| \prod_{j=1}^n Q_j^\dagger(\mathbf{b}') \right| \mathbf{k}_j\rangle \langle \mathbf{k}_j \left| \prod_{j=1}^n Q_j(\mathbf{b}) \right| \phi_n\rangle \delta(E_i - E_f) \tag{140}$$

and the pre-fragment excitation is described by

$$P_{FF*}(\mathbf{b}, \mathbf{b}') = \langle F \left| \prod_{l=n+1}^{A_P} Q_l^\dagger(\mathbf{b}') \right| F*\rangle \langle F* \left| \prod_{l=n+1}^{A_P} Q_l(\mathbf{b}) \right| F\rangle \tag{141}$$

In Eq's (140) and (141) we have used the factorization of the projectile coordinates into pre-fragment and abraded nucleon terms as

$$\Gamma(\mathbf{b}) = 1 - \prod_{l=n+1}^{A_P} Q_l(\mathbf{b} - \mathbf{s}_l) \prod_{j=1}^{n} Q_j(\mathbf{b} - \mathbf{s}_j) \tag{142}$$

where

$$Q_j = \prod_{\alpha=1}^{A_T} (1 - \Gamma_{\alpha j}). \tag{143}$$

Also, we have used a simplified model of the projectile wavefunction. Here the orbits of the pre-fragments are assumed to be nearly the same as those of the projectile. This is consistent with the use of the impulse or frozen nucleus approximations at high energies. A completely factored form in the participant and spectator coordinates is assumed for the projectile wavefunction such that

$$|P\rangle = |F\rangle|\phi_n\rangle \tag{144}$$

The antisymmetrization is ignored in (144) which should be accurate if the mass of F is much larger than the knockouts. Antisymmeterization in the sub-systems of $|F\rangle$ and $|\phi_n\rangle$ may still be included. A more accurate form of the projectile wavefunction which includes configuration mixing could be included using the same formalism as described above. The reduction of the momentum spectrum (137) is described in [67, 68]. A comparison of the model for proton production in $^{12}C - A_T$ reactions is shown in figure 9a and for $^{40}Ar - A_T$ in figure 9b. In Fig. 10 we show a similar comparison for neutron production [69] where the evaporation neutrons have been included.

The reduction of (140) follows closely the developments of equations (94)–(114) which show the direct relationship between the quasi-elastic response of fast projectiles and the response of the knockouts in both cases as they multiple scatterer on the target. As shown in [67] the spectrum described above reduces to the optical [62] or Glauber model [65] forms of the abrasion cross section when energy conservation is not considered and closure is assumed on the projectile subsystems.

The reduction of the core-excitation function (141) is difficult to treat due to the detailed dependence on the pre-fragment wavefunctions. For few nucleon (or cluster) removal direct evaluation using model wavefunctions is useful. For large numbers of knockouts a statistical model is warranted. The fragment cross sections are found as a convolution of the abrasion cross sections with the probability for decay as

$$\sigma_F = \int d\varepsilon_{F*} \frac{d\sigma}{d\varepsilon_{F*}} P(F* \to F, E_{F*}) \tag{145}$$

Statistical Decay of Pre-Fragments

The pre-fragment nuclei are assumed to decay through particle emission to a stable nucleus. Many studies have employed a Monte-Carlo simulation computer code for describing the decay cascade. A Master Equation has been used to describe the decay and solved in closed form under approximate conditions [70]. An alternative approach is to solve the Master Equation in a perturbative fashion at low to medium excitation energies as has been studied in [71]. The approximate closed-form solutions may be used at large excitation energies to improve convergence. A further improvement on the accuracy and convergence of this approach is to test the strength of the pre-fragment cross section, using the more accurate solution above a cut-off in the pre-fragment formation cross section and the approximate solution below the cut-off.

The de-excitation of the pre-fragments into a stable configuration is described by the Master Equation [70]

$$\frac{df^b\left(E_b^*,t\right)}{dt} = \sum_j \int dE\, f^a\left(E_a^*,t\right) P_j^a(E) - \sum_k \int dE\, f^b\left(E_b^*,t\right) P_k^b(E) \tag{146}$$

where $f^b\left(E_b^*,t\right)$ is the probability of finding the nuclei b at time t with excitation energy E_b^*, and $P_k^b(E)$ is the probability that an ion k will be emitted by b with energy E. The first term on the right-hand side of (146) corresponds to gains by the decay of nuclei a as $a \to b + j$. (We use subscripts $j,k,l\dots$ to label the light ions in a decay and superscripts $a,b,c\dots$ to label the parent and daughter nuclei.) The second term on the right-hand side of (146) corresponds to losses through $b \to c + k$.

Campi and Hufner [70] have solved equation (146) by keeping only the first-order derivatives in the energy loss and second-order in the neutron excess, while using only average values for these quantities, thus ignoring nuclear structure effects and the change in these quantities in the cascade. The resulting closed-form solutions to the statistical decay are quite convenient and resemble closely the parametric model of Rudstam [61]. For both light to medium mass nuclei (A < 60) and lower regions of excitation energy ($E^* < 100$ MeV), nuclear structure effects in the nuclear level density are known to be important. Here a perturbative solution to (146) is convergent and has been described in [71]. The decay probabilities are modeled using an energy dependent formation cross section which includes coulomb barrier and tunneling effects. Also, the level density model of Ignatyuk et al. [72], which includes pairing effects, shell structure, and energy gaps, is used for A > 11. For lighter nuclei (A $\leq$ 11), decay probabilities are coded using experimentally determined properties of nuclear levels and decay branches.

The probability of finding the nuclei b at time t with E_b^* can be divided into stable and unstable parts depending on the lowest excitation energy of $E_b, \min\left[S_j^b\right]$

$$f^b\left(E_b^*,t\right) = g^b\left(E_b^*,t\right) + h^b\left(E_b^*,t\right) \tag{147}$$

where g^b are stable and h^b are unstable. As $t \to \infty$, we have $h^b \to O$ such that

$$\lim_{t \to \infty} f^b\left(E_b^*, t\right) = g^b\left(E_b^*, t\right) \tag{148}$$

The corresponding probabilities for a one-step decay are defined as

$$F_j^a = \int_0^{E^* - S_j^a} P_j^a(E)\, dE \tag{149}$$

$$G_j^a = \int_{E_a^* - S_j^a - \min\left[S_k^b\right]}^{E_a^* - S_j^a} P_j^a(E)\, dE \tag{150}$$

and

$$H_j^a = \int_0^{E_a^* - S_j^a - \min\left[s_k^b\right]} P_j^a(E)\, dE \tag{151}$$

with

$$F_j^a = G_j^a + H_j^a \tag{152}$$

and

$$\sum_j F_j^a = 1 \tag{153}$$

The effects of nuclear structure on the decay probabilities G_j^a and H_j^a were studied in [70] and found to be quite important in describing the final fragment distributions in heavy ion reactions.

The integral equation of (148) can be separated into two parts using (147) and (148) as

$$g^b\left(E_b^*, \infty\right) = g^b\left(E_b^*, 0\right) + \sum_j \int_0^\infty dt \int dE f^a\left(E_a^*, t\right) P_j^a(E) \tag{154}$$

and

$$0 = h^b\left(E_b^*, 0\right) + \sum_j \int_0^\infty dt \int dE\, f^a\left(E_a^*, t\right) P_j^a(E) \tag{155}$$

The solutions of (154) and (155) in terms of the G_j and H_j proceed by testing the available excitation energies and thresholds for parent and daughter nuclei to determine how many terms in their iterations occur for forming each stable product based on the initial conditions. An alternative approximate analytic solution is considered in [70]. Comparisons of the microscopic abrasion-ablation model to the NUCFRG2 model and experiments for ^{24}Mg [73], ^{32}S [74], and ^{56}Fe [75, 76] projectile fragmentation are shown in figures 11–15. The use of the statistical decay model with a nuclear level density that includes structure effects reproduces much of the odd-even dependence of the experimental elemental cross sections; however, further work on determining the pre-fragment excitation

energies is needed. Initial development of a complete GCR fragmentation database using the HI model described above suggests c.p.u. times on a VAX_{4000} of 22 hr for a specific material which are stored for later use by the HZETRN code. For the first time, an alternate to the NUCFRG database generator code is available with sufficient computational efficiency for use in shielding studies.

NUCLEAR CLUSTERING EFFECTS IN HEAVY ION FRAGMENTATION

For many light to medium mass nuclei, specific light ion configurations (d, t, h, α) have a large probability to appear in relative motion with a core configuration in the ground-state wavefunction. Physically this clustering effect occurs through the shell structure of the nucleus which favors a closed-shell core configuration and due to the favorable binding properties of the alpha particle. Nuclei, where clustering effects are expected to be important, include many of the most abundant GCR primaries and the constituents of tissue. Clustering effects will lead to an enhanced probability for populating specific final fragments of the projectile similar to the dominant role of one nucleon removal in the fragment population. Also, the energy spectrum of the light ions produced by direct knockout will be more energetic than the evaporation components of light ions since their distributions will be indicative of the fermi motion of the nucleus rather than the temperature of a nuclear resonance, thus leading to a buildup of secondary radiations in shielding materials. The development of an abrasion cross section for clusters was considered in [44] and follows closely the development of the nucleon abrasion cross section as is summarized here.

We next consider the formulation of the abrasion cross section for α-particle knockout [44]. The profile function is factored into clusters of alpha particles rather than nucleons leading to the introduction of the cluster wavefunction in the model. For a projectile nucleus with a number, N_C, of α clusters we introduce

$$Q_{j_c\beta} = \prod_{j=1}^{4} \left[1 - \Gamma_{j\beta}\left(\mathbf{b} - \mathbf{s}_j - \mathbf{s}_\beta \right) \right] \tag{156}$$

such that the profile function becomes

$$\Gamma(\mathbf{b}) = 1 - \prod_{j_c=1}^{N_c} \prod_{\beta=1}^{A_T} Q_{j_c\beta}. \tag{157}$$

The cluster model wave function is an antisymmetrized product of the intrinsic wave function of a core nucleus and an alpha particle, and their wave function of relative motion $\phi(r)$ such that

$$\Psi_{A_P} = A\left\{ \Phi_c\left(\mathbf{r}_c \right) \Phi_\alpha\left(\mathbf{r}_\alpha \right) \phi(\mathbf{r}) \right\} \tag{158}$$

In describing the fragmentation of a projectile through α-abrasion ($P \rightarrow n\alpha$ reactions) we will neglect multistep contributions where α particles are dissolved and reformed in intermediate states. The profile functions are then averaged over the intrinsic α-particle wave functions in equation (157) in a rigid α-particle model defining

$$Q_{\alpha N}\left(\mathbf{b} - \mathbf{s}_{j_c} - \mathbf{s}_\beta \right) = \left\langle \Phi_\alpha \left| \prod_{j=1}^{4}\left[1 - \Gamma_{\beta_j}\left(\mathbf{b} - \mathbf{S}_{j_c} - \mathbf{s}'_j - \mathbf{s}_\beta \right) \right] \right| \Phi_\alpha \right\rangle \tag{159}$$

where we have introduced projectile coordinates r'_j relative to the cluster coordinates R_{j_c} with S_{j_c} the transverse component of R_{j_c}. Only the relative part of the projectile wave function is then indicated in the remainder of this paper. The abrasion cross section that is similar to (139) with multiple scattering of the α-particle on the target and the pre-fragment (core) excitation occurring predominantly through the rotation bands favored by the $P - \alpha F^*$ configurations are used. Results in figure 16 for ^{12}C production from ^{16}O projectiles studied experimentally by Olson et al. [83] versus target mass number indicate an important role for α abrasion process. In figure 17 we show comparison [82] for projectile fragmentation through leading to a final fragment with charge and neutron number, $Z_P - 2$ and $N_P - 2$, respectively. The results indicate the large contribution for α-abrasion relative to the multi-step nucleon abrasion and ablation. These calculations require a large number of cluster wavefunctions and further developments in this area will be needed to improve the accuracy of the calculations and to consider other systems.

TRACK STRUCTURE MODELS

The development of track structure models to describe the spatial distribution of ionizations about the path of heavy ions originates from the paper of Butts and Katz in 1967 [84]. These authors considered the radial distribution of dose from secondary electrons produced in the medium by the passing ion. A more comprehensive approach is to consider the spatial distribution of ionizations produced by the ion tracks. These calculations require large Monte-Carlo simulations in order to follow the paths of individual electron tracks [85, 86] as they transverse a medium. The accuracy of both approaches depends on the production cross sections of the primary electrons released and their subsequent transport properties. We next review the radial dose model of Katz which is advantageous due to its rapid generation of spatial ionization properties for all ions. The success of the radial dose model is based on efficient representation of secondary electron energy depositions at the expense of loss of information on fluctuations in individual energy depositions.

Radial Dose Model

For calculations of cross sections the radial dose from secondary electrons based on the model of Kobetich and Katz [87] is used. We have updated some of the physical inputs in this calculation [88], including the use of the secondary electron spectrum from proton impact in water from Rudd [89], a revised angular distribution ansatz, and the electron range-energy and stopping power formula from Tabata et al. [90]. Also, we have included a contribution for excitations to the radial dose model using the ansatz of Brandt and Ritchie [91], normalized such that the summed contributions from excitations and delta-rays (from modified Kobetich and Katz model) conserves the LET for each ion where

$$LET = 2\pi \int_0^{T_{\max}} t \, dt \left[D_\delta(t) + D_{exc}(t) \right] \tag{160}$$

We have not considered the effects of nuclear stopping power which should become important at low energies (< 1 MeV/u). The radial dose model used in calculations is based on the model of Koebetich and Katz [87] using

recent models for secondary electronic production and the electron range-energy formula and stopping power (Tabata et al. [90] and Rudd [89]). In this model the radial dose $D(t)$ is a function of the radial distance t from the center of the ion's path and including an angular distribution for the ejected electrons with energy ω at an angle θ is given by

$$D_\delta(t) = \frac{-1}{2\pi t} \sum_i \int d\Omega \int_{\omega_t(\theta)}^{\omega_m - I_i} d\omega \frac{\partial}{\partial t}\left[\eta\,(t,\omega,\theta)\,W\,(t,\omega,\theta)\right]\frac{dn_i}{d\omega d\Omega} \tag{161}$$

ω_m is the maximum secondary electron energy, I_i is the ionization energy for an electron, η is the transmission function, and ω is the residual energy of the electrons. In equation (161) the summation is over all atoms. The range-energy formula assumed is from Tabata et al. [90] and the transmission functions from Kobetich and Katz [92].

A qualitative model for the angular distribution of the secondary electrons is to assume a distribution peaked about the classical ejection value, such as

$$\frac{dn}{d\omega d\Omega} = \frac{dn}{d\omega}f(\theta) \tag{162}$$

with

$$f(\theta) = \frac{N}{\left[\theta - \theta_c(\omega)\right]^2 + \dfrac{A}{\omega}} \tag{163}$$

with $\theta_c(\omega)$ determined as the root of

$$\cos^2\theta = \frac{\omega}{\omega_m} \tag{164}$$

with N a normalization constant, and A a constant found to be about 0.015 keV to simulate the data of Rudd et al. [93] and Toburen [94]. The Eq. (162)–(164) will not reproduce any forward or backward peaks in the production specturm. For the single differential distribution in equation (162) we use the model of Rudd [89] scaling to heavy ions using effective change. Extensive comparisons of the model described above to experiments for radial dose from heavy ions are described in Cucinotta et al. [88]. The use of the model of Rudd and the angular distribution of equations (162)–(164) generally reduce the estimated dose in the core region.

The model for the radial dose from δ rays described above can be parameterized by utilizing the $1/t^2$ fall off dependence at intermediate distances and introducing functions that modify the distribution at small and large distances. The radial dose in water is then

$$D_\delta(t) = \left(Z^{*2}/\beta^2\right)\left(Ne^4/mc^2\right)f_s(t)\left(1/t^2\right)f_L(t) \tag{165}$$

where β_c is the ion's velocity, Z^* is the effective charge, and m the electron mass. The function $f_s(t)$ modifies the short distance behavior and is represented by

$$f_s(t) = \left(1/t + c_1\right)^{-1} \tag{166}$$

with

$$c_1 = 0.6 + 1.7\beta \tag{167}$$

The function $f_L(t)$ modifies the long distance behavior and is represented by

$$f_L(t) = \exp{-\left(t/0.37T_{\max}\right)^2} \tag{168}$$

where $T_{\max}$ is the maximum radial penetration distance for δ rays of an ion at speed β_c.

The radial dose from excitations is assumed of the form [92]

$$D_{exc}(t) = \frac{Ce^{-t/d}}{t^2} \tag{169}$$

where C is determined by Eq. (160) and $d = \beta/2W_r$ with $W_r = 13\ eV$ for water. The radial dose contribution from excitations is then contained to small radii of less than a few 10's of nm.

The result of our calculations, for 1 MeV protons in water using different assumptions (to display problems encountered close to and remote from the ions' path) and ^{20}Ne at 377 MeV/amu, and in which the excitation functions of Brandt and Ritchie [91] are incorporated, are shown in figures 18a and 18b, in comparison with measurements by Wingate and Baum [95] for protons and measurements of Varma and Baum [96] for Ne, respectively. The present calculations made for other ions (adjusted from calculations for protons by multiplication with the square of the effective charge) are here used for the evaluation of action cross sections. Typically different assumptions yield major differences close to the ion's path (most important for latent tracks and possibly for consideration of damage to crystalline structure) and remote from the ion's path (most important for considerations of "thin down," the decrease in the inactivation cross section while the ion's LET increases, as the ion approaches the end of its range). A comparison of the parametric Eqs. (165)–(168) to the model of Eqs. (162)–(164) is shown in figure 19 with good agreement found.

REFERENCES

1. B. Peters, The Nature of Primary Cosmic Radiation. *Progress in Cosmic Ray Physics*, J. G. Wilson, ed., Interscience Publ. Inc., pp. 191–242 (1958).

2. Leverett Davis, Jr., On the Diffusion of Cosmic Rays in the Galaxy. P*roceedings of the Moscow Cosmic Ray Conference, International Union of Pure and Applied Physics (Moscow)*, pp. 220–225 (1960).

3. V. L. Ginzburg and S. I. Syrovatskii (H. S. H. Massey, transl., and D. Ter Haar, ed.), *The Origin of Cosmic Rays*. Macmillan Co. (1964).

4. G. Gloeckler and J. R. Jokipii, Physical Basis of the Transport and Composition of Cosmic Rays in the Galaxy. *Phys. Review Lett.*, vol. 22, no. 26, pp. 1448–1453 (1969).

5. J. A. Lezniak, The Extension of the Concept of the Cosmic-Ray Path-Length Distribution to Nonrelativistic Energies. *Astrophys. & Space Sci.*, vol. 63, no. 2, pp. 279–293 (1979).

6. J. W. Wilson and S. L. Lamkin, Perturbation Theory for Charged-Particle Transport in One Dimension. *Nucl. Sci. & Eng.*, vol. 57, no. 4, pp. 292–299 (1975).

7. J. W. Wilson, *Analysis of the Theory of High-Energy Ion Transport*. NASA TN D-8381 (1977).

8. J. W. Wilson, Depth-Dose Relations for Heavy Ion Beams. *Virginia J. Sci.*, vol. 28, no. 3, pp. 136–138 (1977).

9. J. W. Wilson, *Heavy Ion Transport in the Straight Ahead Approximation*. NASA TP-2178 (1983).

10. J. W. Wilson, L. W. Townsend, H. B. Bidasaria, W. Schimmerling, M. Wong, and J. Howard, ^{20}Ne Depth-Dose Relations in Water. *Health Phys.*, vol. 46, no. 5, pp. 1101–1111 (1984).

11. J. W. Wilson and F. F. Badavi, Methods of Galactic Heavy Ion Transport. *Radiat. Res.*, vol. 108, pp. 231–237 (1986).

12. J. W. Wilson and L. W. Townsend, A Benchmark for Galactic Cosmic-Ray Transport Codes. *Radiat. Res.*, vol. 114, no. 2, pp. 201–206 (1988).

13. J. W. Wilson, S. L. Lamkin, H. Farhat, B. D. Ganapol, and L. W. Townsend, *A Hierarchy of Transport Approximations for High Energy Heavy (HZE) Ions*. NASA TM-4118 (1989).

14. J. W. Wilson, L. W. Townsend, J. E. Nealy, S. Y. Chun, B. S. Hong, W. W. Buck, S. L. Lamkin, B. D. Ganapol, F. Khan, and F. A. Cucinotta, *BRYNTRN: A Baryon Transport Model*. NASA TP-2887 (1989).

15. S. B. Curtis, W. R. Doherty, and M. C. Wilkinson, *Study of Radiation Hazards to Man on Extended Near Earth Missions*. NASA CR-1469 (1969).

16. O. C. Allkofer and W. Heinrich, Attenuation of Cosmic Ray Heavy Nuclei Fluxes in the Upper Atmosphere by Fragmentation. *Nucl. Phys. B*, vol. B71, no. 3, pp. 429–438 (1974).

17. A. Chatterjee, C. A. Tobias, and J. T. Lyman, Nuclear Fragmentation in Therapeutic and Diagnostic Studies With Heavy Ions. *Spallation Nuclear Reactions and Their Applications*, B. S. P. Shen and M. Merker, eds., D. Reidel Publ. Co., pp. 169–191 (1976).

18. J. Letaw, C. H. Tsao, and R. Silberberg, Matrix Methods of Cosmic Ray Propagation. *Composition and Origin of Cosmic Rays*, M. M. Shapiro, ed., D. Reidel Publ. Co., pp. 337–342 (1983).

19. B. D. Ganapol, L. W. Townsend, S. L. Lamkin, and J. W. Wilson, *Benchmark Solutions for the Galactic Heavy-Ion Transport Equations With Energy and Spatial Coupling*. NASA TP-3112 (1991).

20. J. W. Wilson and F. F. Badavi, New Directions in Heavy Ion Shielding, Proceedings of New Horizons in Radiation Protection and Shielding, ANS Topical Conference, Pasco, Washington, April 26–May 1, 1992.

21. J. W. Wilson, L. W. Townsend, W. Schimmerling, G. S. Khandelwal, F. Khan, J. E. Nealy, F. A. Cucinotta, L. C. Simonsen, J. L. Shinn, and J. W. Norbury, *Transport Methods and Interactions for Space Radiations*. NASA RP-1257 (1991).

22. H. H. Heckman, D. E. Greiner, P. J. Lindstrom, and F. S. Bieser, Fragmentation of ^{14}N Nuclei at 29 GeV: Inclusive Isotope Spectra at 0°. *Phys. Review Lett.*, vol. 28, no. 14, pp. 926–929 (1972).

23. G. M. Raisbeck and F. Yiou, Production Cross Sections of Be Isotopes in C and O Targets Bombarded by 2.8 GeV α Particles: Implications for Factorization. *Phys. Review Lett.*, vol. 35, no. 3, pp. 155–159 (1975).

24. H. Feshbach and K. Huang, Fragmentation of Relativistic Heavy Ions. *Phys. Lett.*, vol. 47B, no. 4, pp. 300–302 (1973).

25. A. S. Goldhaber, Statistical Models of Fragmentation Processes. *Phys. Lett.*, **53B**, 306–308 (1974).

26. J. W. Wilson and G. S. Khandelwal, Proton Dose Approximations in Arbitrary Convex Geometry. *Nucl. Technol.* **23**, 298–305 (1974).

27. F. A. Cucinotta, F. Hajnal, and J. W. Wilson, Energy Deposition at the Bone-Tissue Interace From Nuclear Fragments Produced by High-Energy Nucleons. *Health Physics* **59**: 819–825 (1990).

28. R. G. Alsmiller, Jr., D. C. Irving, W. E. Kinney, and H. S. Moran, *The Validity of the Straightahead Approximation in Space Vehicle Shielding Studies*, Second Symposium on Protection Against Radiations in Space, Arthur Reetz, Jr., ed. NASA SP-71, 177–181, 1965.

29. S. L. Lamkin, G. S. Khandelwal, J. L. Shinn, and J. W. Wilson, Numerical Methods for High Energy Nucleon Transport. ANS Topical Meeting, New Horizons in Radiation Protection and Shielding, Pasco, WA, April 26–May 1, 1992, pp. 165–170.

30. S. L. Lamkin, A Theory for High-Energy Nucleon Transport in One Dimension. Thesis, Old Dominion University, Norfolk, Virginia, December, 1974.

31. J. L. Shinn, J. W. Wilson, L. W. Townsend, F. A. Cucinotta, S. Y. Chun, and F. F. Badavi, Computationally Efficient Space Radiation Codes. ANS Topical Meeting, New Horizons in Radiation Protection and Shielding, Pasco, WA, April 26–May 1, 1992, pp. 171–180.

32. D. Schardt, I. Schall, H. Geissel, H. Irnich, G. Kraft, A. Magel, M. F. Mohar, G. Münzenburg, F. Nickel, C. Scheidenberger, W. Schwab, and L. Silver, Nuclear fragmentation of high-energy ions in water. *Adv. Space Res.* **15**: (1995).

33. H. W. Bertini, M. P. Guthrie, and A. H. Culkowski, *Nonelastic Interactions of Nucleons and π-Mesons With Complex Nuclei at Energies Below 3 GeV*. ORNL-TM-3148, U. S. Atomic Energy Commission, 1972.

34. J. Cugnon, Monte Carlo Calculation of High-Energy Heavy-Ion Interactions. *Phys. Rev. C*, vol. 22, no. 5, pp. 1885–1896, Nov. 1980.

35. K. M. Watson, Multiple Scattering and the Many-Body Problem—Applications to Photomeson Production in Complex Nuclei. *Phys. Rev.*, vol. 89, no. 3, pp. 575–578, Feb. 1953.

36. A. K. Kerman, H. McManus, and R. M. Thaler, The Scattering of Fast Nucleons From Nuclei. *Ann. Phys.* (N. Y.), vol. 8, no. 4, pp. 551–635, Dec. 1959.

37. J. W. Wilson, Multiple Scattering of Heavy Ions, Glauber Theory, and Optical Model. *Phys. Lett.*, vol. B52, no. 2, pp. 149–152, Sept. 1974.

38. R. J. Glauber, Potential Scattering at High Energies. *Phys. Rev.*, vol. 91, p. 459, Sept. 1953.

39. L. D. Faddeev, Scattering Theory for a Three-Particle System. *Sov. Phys. JETP*, vol. 12, no. 5, pp. 1014–1019, May 1961.

40. K. M. Maung and F. Gross, Covariant Multiple Scattering Series for Elastic Projectile-Target Scattering. *Phys. Rev. C*, vol. 42, no. 4, pp. 1681–1693, Oct. 1990.

41. K. M. Maung, J. W. Norbury, and D. E. Kahana, Quark Confinement and the Hadron Spectrum, World Scientific, ed. Brambilla, N. (1995).

42. T. L. Christian, K. M. Maung, and F. A. Cucinotta, Relativistic Two-Body Amplitudes, Cluster Model and Multiple Scattering Theory. Submitted.

43. K. M. Maung, *J. Phys. G: Nucl. Part. Phys.* vol. 20, L99 (1994).

44. F. A. Cucinotta and R. D. Dubey, Alpha Cluster Model of ^{12}C (^{12}C, 3 α)X at 2.1 A·GeV. *Phys. Rev. C*, vol. 50, pp. 974–984 (1994).

45. J. W. Wilson, Proton-Deuteron Double Scattering. *Phys.Review C*, vol. 10, no. 1, pp. 369–376, 1974b.

46. J. W. Wilson, Composite Particle Reaction Theory, Ph.D dissertation, 1975.

47. F. A. Cucinotta, G. S. Khandelwal, L. W. Townsend, and J. W. Wilson, Correlations in α – α Scattering and Semi-Classical Optical Models. *Phys. Lett.*, vol. B223, no. 2, pp. 127–132, June 8, 1989.

48. L. W. Townsend and J. W. Wilson, *Tables of Nuclear Cross Sections for Galactic Cosmic Rays—Absorption Cross Sections*. NASA RP-1134 (1985).

49. J. Hufner, C. Sander, and G. Wolschin, On the Similarity of Fragment Yields in Heavy Ion Reactions at 20 MeV/A and 2100 MeV/A. *Phys. Lett.*, 73B, no. 3, pp. 289292, Feb. 1978.

50. F. A. Cucinotta, L. W. Townsend, and J. W. Wilson, *Description of Alpha-Nucleus Interaction Cross Sections for Cosmic Ray Shielding Studies*. NASA TP-3285, April 1993.

51. F. A. Cucinotta, et al., Light Ion Component of the Cosmic Rays: Nuclear Interactions and Transport Theory. *Adv. in Space Res.*, vol. 17, pp. 77–86 (1995).

52. F. A. Cucinotta, L. W. Townsend, and J. W. Wilson, Inclusive Inelastic Scattering of Heavy Ions in the Independent Particle Model. *J. Phys. G: Nucl. Particle Phys.*, vol. 18, no. 5, pp. 889–901, May 1992.

53. F. A. Cucinotta, L. W. Townsend, and J. W. Wilson, Multiple-Scattering Effects in Quasi-elastic α–^{4}He Scattering. *Phys. Rev. C*, vol. 46, no. 4, pp. 1451-–1456, Oct. 1992.

54. F. A. Cucinotta and R. R. Dubey: *Final State Interactions and Inclusive Nuclear Collisions*. NASA TP-3353 (1993).

55. F. A. Cucinotta, L. W. Townsend, and R. D. Dubey: *Energy Loss Cross Sections for Inclusive Charge Exchange Reactions at Intermediate Energies*. NASA TM-4522, Oct. 1993.

56. J. D. Bowman, W. J. Swiatecki, and C. F. Tsang, *Abrasion and Ablation of Heavy Ions*. LBL-2908, Lawrence Berkeley Lab., Univ. of California (1973).

57. J. W. Wilson, L. W. Townsend, and F. F. Badavi, A Semiempirical Nuclear Fragmentation Model. *Nuclear Instrum. & Methods Phys. Res.*, vol. B18, no. 3, pp. 225–231 (1987b).

58. J. W. Wilson, J. L. Shinn, L. W. Townsend, R. K. Tripathi, F. F. Badavi, and S. Y. Chan, NUCFRG2: a semiempirical nuclear fragmentation model. *Nuclear Instrum. & Methods Phys. Res.* B94, pp. 95–102; 1994

59. D. J. Morrissey, W. R. Marsh, R. J. Otto, W. Lovel, and G. T. Seaborg. *Phys. Res.* C18, p. 1267 (1978).

60. J. Gosset, H. H. Gutbrod, W. G. Meyer, A. M. Poskanzer, A. Sandoval, R. Stock, and G. D. Westfall, Central Collisions of Relativistic Heavy Ions. *Phys. Review*, vol. 16, ser. C, no. 2, pp. 629–657 (1977).

61. G. Rudstam, Systematics of Spallation Yields. *Zeitschrift fur Naturforschung*, vol. 21a, no. 7, pp. 1027–1041 (1966).

62. L. W. Townsend, J. W. Wilson, and J. W. Norbury, A Simplified Optical Model Description of Heavy Ion Fragmentation. *Canadian J. Phys.*, vol. 63, no. 2, pp. 135–138 (1985).

63. G. D. Westfall, L. W. Wilson, P. J. Lindstrom, H. J. Crawford, D. E. Greiner, and H. H. Heckmann. *Phys. Rev.* C19, p. 1309 (1979).

64. R. Silberberg, C. H. Tsao, and M. M. Shapiro, Semiempirical Cross Sections, and Applications to Nuclear Interactions of Cosmic Rays. *Spallation Nuclear Reactions and Their Applications*, B. S. P. Shen and M. Merker, eds., D. Reidel Publ. Co., pp. 49–81 (1976).

65. J. Hüfner, K. Schäfer, and B. Schürmann, Abrasion-Ablation in Reactions Between Relativistic Heavy Ions. *Phys. Review*, vol. 12, ser. C, no. 6, pp. 1888–1898 (1975).

66. L. W. Townsend, O*ptical-Model Abrasion Cross Sections for High-Energy Heavy Ions*. NASA TP-1893 (1981).

67. F. A. Cucinotta, Forward Production of Protons From ^{12}C in Heavy Ion Collisions. *J. Phys. G.*, vol. 20, pp. 1811–1831 (1994).

68. F. A. Cucinotta, *Multiple Scattering Model for Inclusive Proton Production in Heavy Ion Collisions*. NASA TP-3470 (1994).

69. F. A. Cucinotta, J. W. Wilson, and L. W. Townsend*, Abrasion-Ablation Model for Neutron Production in Heavy Ion Collisions*. NASA TM-4656 (1995).

70. X. Campi, and J. Hufner, Nuclear Spallation-Fragmentation Reactions Induced by High-Energy Projectiles. *Phys. Rev.* C24, pp. 2199–2209, Nov. 1981.

71. F. A. Cucinotta and J. W. Wilson, *Study of Analytic Statistical Decay Model of the Decay of Light and Medium Mass Nuclear Fragmentation*. NASA TP-3594, 1996.

72. A. Ignatyuk, G. Smirenkin, and A. Tishin., *Sov. J. Nucl. Phys.*, vol. 21, pp. 255–261, (1975).

73. O. Sampsondis, et al., Fragmentation Cross Sections of ^{16}O, ^{24}Mg, and ^{32}S Projectiles at 3.65 GeV/nucleon. *Physic. Rev. C*, vol. 1, no. 6, pp. 3304–3308 (1995).

74. C. Brechtmann, and W. Helnrich, Fragmentation Cross Sections of ^{32}S at 0.7, 1.2, and 200 GeV/nucleon. *Z. Phys. A*, 331, pp. 463–472 (1988).

75. G. D. Westfall, L. W. Wilson, P. J. Lindstron, H. J. Crawford, D. E. Greiner, and H. H. Heckman, Fragmentation of Relativistic ^{56}Fe. *Phys. Rev. C.*, vol. 19, no. 4, Apr. 1979, pp. 1309–1323.

76. J. R. Cummings, W. R. Binns, T. L. Garrard, M. H. Israel, J. Klarmann, E. C. Stone, and C. J. Waddington, Determination of the Cross Sections for the Production of Fragments From Relativistic Nucleus-Nucleus Interactions. I. Measurements. *Phys. Rev. C.*, vol. 42, no. 6, Dec. 1990, pp. 2508–2529.

76. J. J. Butts and R. Katz, Theory of RBE for Heavy Ion Bombardment of Dry Enzymes and Viruses. *Radiat. Res.*, vol. 30, no. 4, pp. 855–871, Apr. 1967.

77. L. Anderson et al., Inclusive Particle Production at Forward Angles from Collisions of Light Relativistic Nuclei: Nuclear Fragmentation, *Phys. Rev.* C. 28, pp. 1224–1245 (1993).

78. V. G. Ableev, et al., Proton and Triton Momentum Distributions from 4-He Fragmentation at Relativistic Energies. *Few-Body Syst.* 8, pp. 137–144 (1990).

79. R. E. Chrien et al., Proton Spectra from 800 MeV Protons on Selected Nuclides. *Phys. Rev.* C 21, pp. 1014–1029 (1980).

80. J. Banaigs et al. *Phys. Rev.* C 35, p. 1416 (1987).

81. J. Gosset, J. L. Kapusta, and G. D. Westfall, Calculations with the Nuclear Firestreak Model. *Phys. Rev.* C 18, pp. 844–855, 1978.

82. W. R. Webber, J. C. Kish, and D. A. Schrier, Individual Charge Changing Fragmentation Cross Sections of Relativistic Nuclei in Hydrogen, Helium, and Carbon Targets. *Phys. Rev. C: Nucl. Phys.*, vol. 41, no. 2, Feb. 1990, pp. 533–546.

83. D. I. Olson, B. L. Berman, D. E. Greiner, H. H. Heckman, P. J. Lindstrom, and H. J. Crawford, Factorization of Fragment-Production Cross Sections in Relativistic Heavy-Ion Collisions. *Phys. Rev. C.*, vol. 28, no. 4, Oct. 1983, pp. 1602–1613.

84. J. J. Butts and R. Katz, Theory of RBE for Heavy Ion Bombardment of Dry Enzymes and Viruses. *Radiat. Res.*, vol. 30, no. 4, pp. 855–871, Apr. 1967.

85. H. G. Paretzke, Comparison of Track Structure Calculations with Experimental Results. *Proceedings of the 4th Symposium on Microdosimetry*, J. Booz, H. G. Ebert, R. Eickel, and A. Walker, eds., Commission of the European Communities, pp. 141–168, (1974).

86. H. Nikjoo, O. T. Goodhead, O. F. Charlton, and H. G. Paretzke. *Phys. Med. Biol.*, vol. 34, pp. 691–705 (1989).

87. E. J. Kobetich, and R. Katz, Width of Heavy-Ion Tracks in Emulsion. *Phys. Rev.*, vol. 170, no. 2, pp. 405–411, June 10, 1968.

88. F. A. Cucinotta, R. Katz, J. W. Wilson, and R. R. Dubey, *Heavy Ion Track Structure Calculations of Radial Dose in Arbitrary Materials.* NASA TP-3497 (1995).

89. M. E. Rudd, User-Friendly Model for the Energy Distribution of Electrons From Proton or Electron Collisions. *Nucl. Tracks Radiat. Meas.*, vol. 16, no. 2/3, pp. 213–218 (1989).

90. T. Tabata, R. Ito and S. Okabe, Generalized Semiempirical Equations for the Extrapolated Range of Electrons. *Clear Instrum. & Methods*, vol. 103, pp. 85–91, 1972.

91. W. Brandt and R. H. Ritchie, Primary Interactions in the Physical Stage, In: Physical Mechanisms in Radiation Biology, eds., R. D. Cooper and R. W. Wood, TIS, USAEC, pp. 20–50 (1974).

92. E. J. Kobetich, and R. Katz, Electron Energy Dissipation. *Nucl. Instrum. Methods*, vol. 71, no. 2, pp. 226–230, June 1, 1969.

93. M. E. Rudd, L. H. Toburen, and N. Stolterfoht, Differential Cross Sections for Ejection of Electrons From Helium by Protons. *Atomic Data and Nucl. Data Tables*, vol. 18, no. 5, pp. 413–432 Nov. 1976.

94. L. H. Toburen, Distribution in Energy and Angle of Electrons Ejected From Xenon by 0.3- to 2.0-MeV Protons. *Phys. Rev. A*, vol. 9, no. 6, pp. 2505–2517, June 1974.

95. C. L. Wingate and J. W. Baum, Measured Radial Distributions of Dose and LET for Alpha and Proton Beams in Hydrogen and Tissue-Equivalent Gas. *Radiat. Res.*, vol. 65, pp. 1–19 (1976).

96. M. N. Varma and J. W. Baum, Energy Deposition in Nanometer Regions by 377 MeV/Nucleon ^{20}Ne Ions. *Radiat. Res.*, vol. 81, pp. 355–363 (1980).
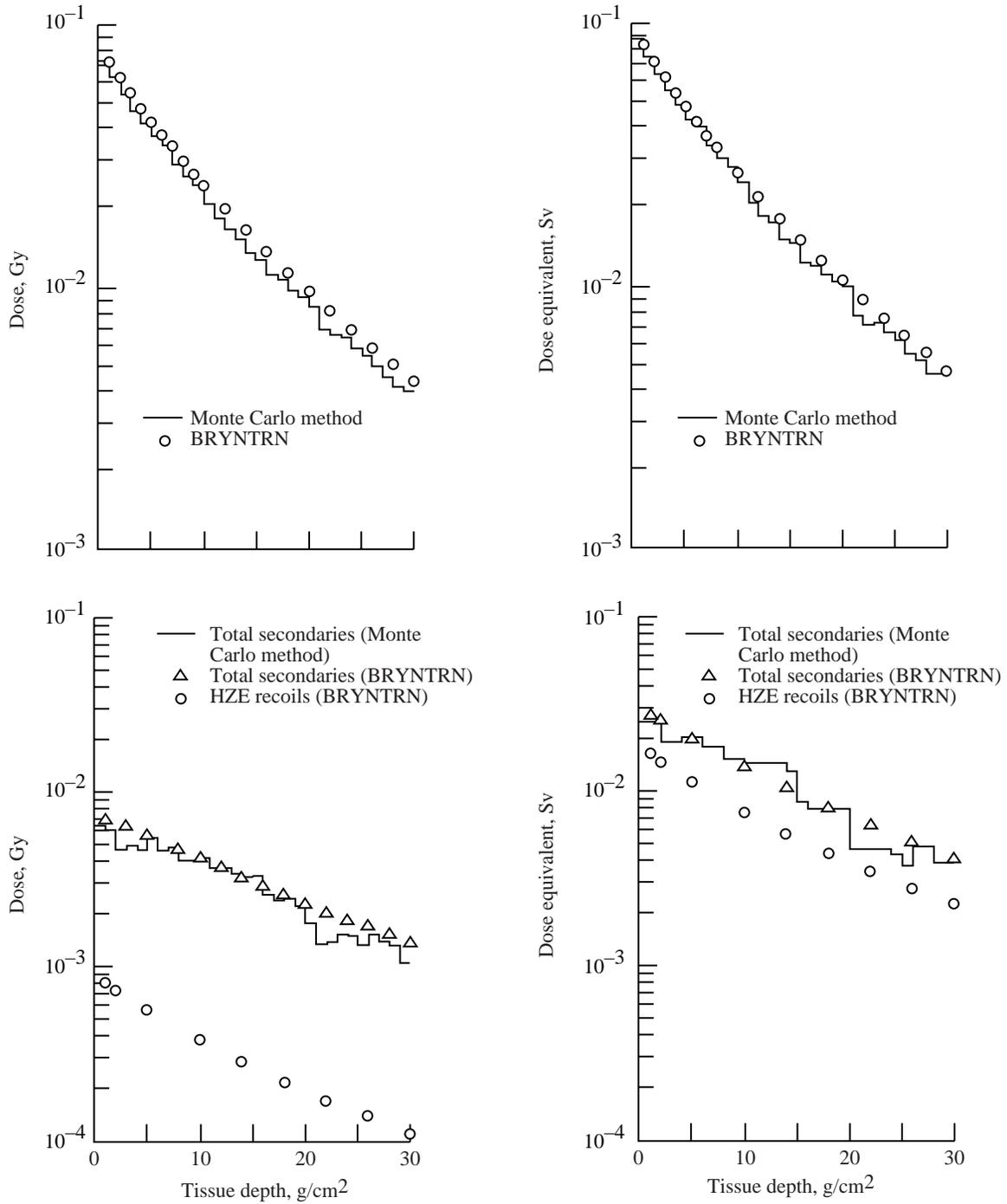
Figure 1.   Comparison of the BRYNTRN code with Monte Carlo calculations.
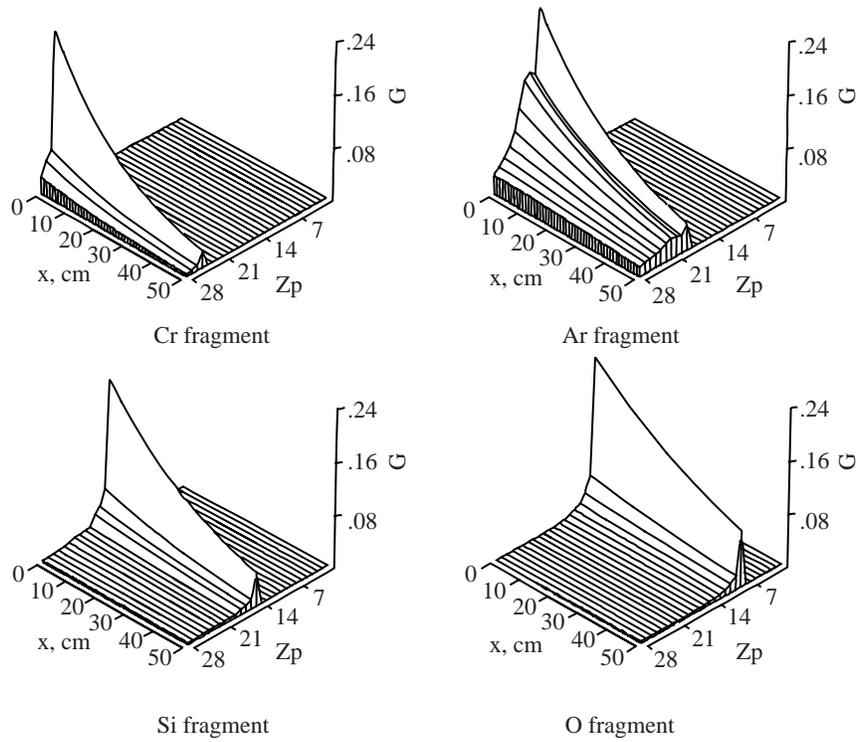
Figure 2.   Scaled Green's function for specific species produced in water shield.
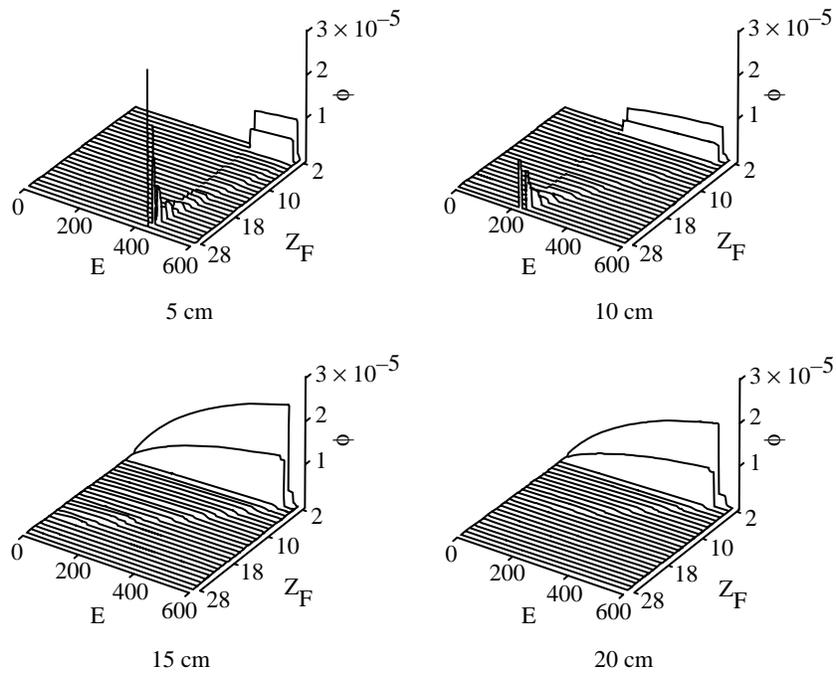
Figure 3.   Composition of a 600 MeV/nucleon Fe beam in water shield. The $Z_F > 2$ flux is scaled by $1/Z_F$. The $Z_F - 1, 2$ flux is scaled by $1/10$.
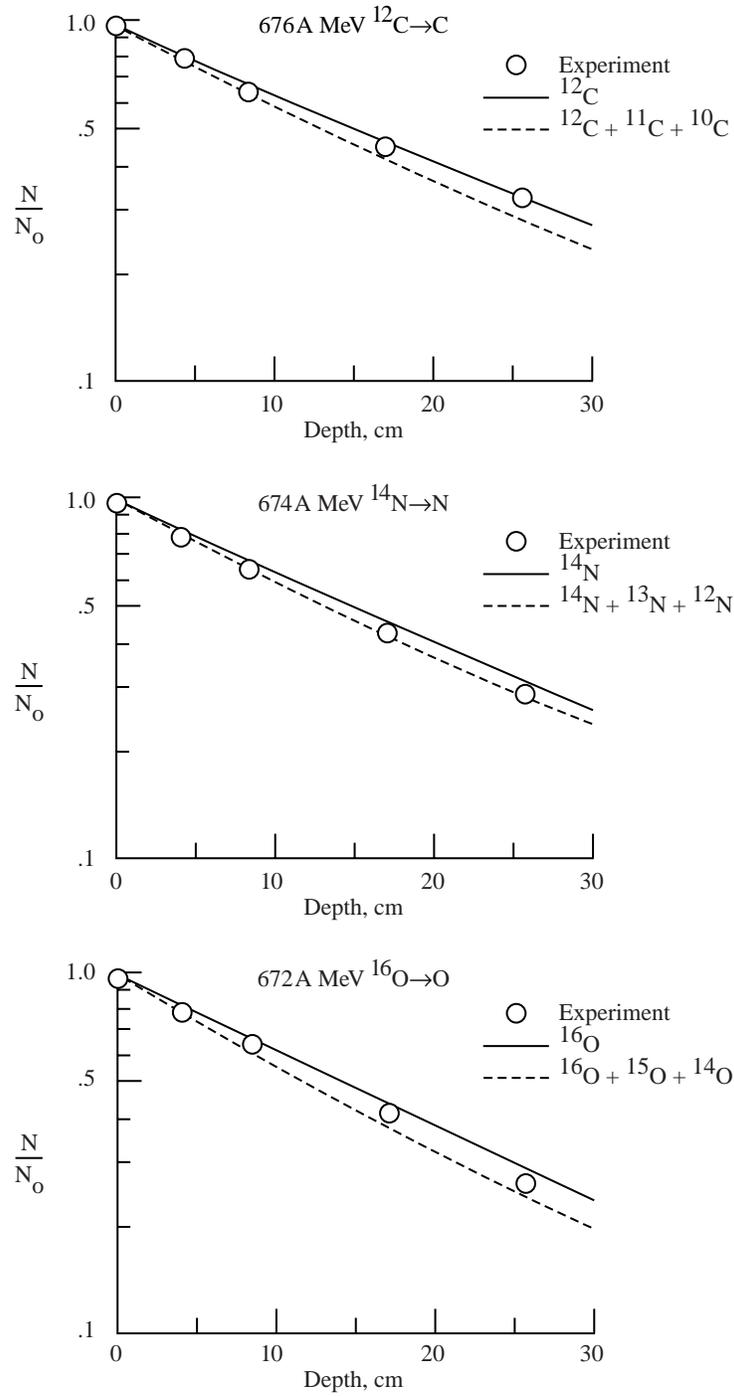
Figure 4.   Comparison of calculations with NUCFRG2 database experiments [32] for attenuation of C, N, and O beams in water. Calculations are with GRNTRN code and include secondaries of same charge as beam.
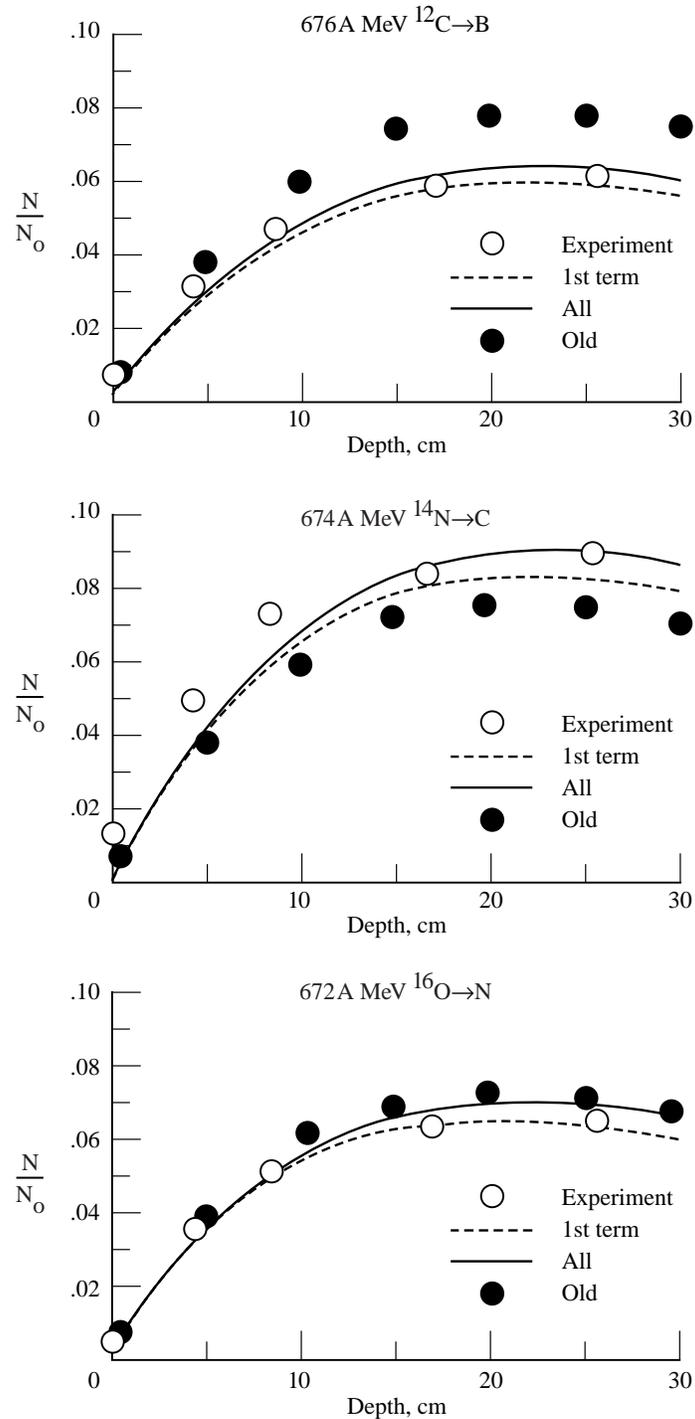
Figure 5.   Comparisons of calculations with NUCFRG1 database (•) and NUCFRG2 database (---, —), to experiments [32] for total flux of 2 charge removal fragments. Comparisons are as a functions of depth in water.
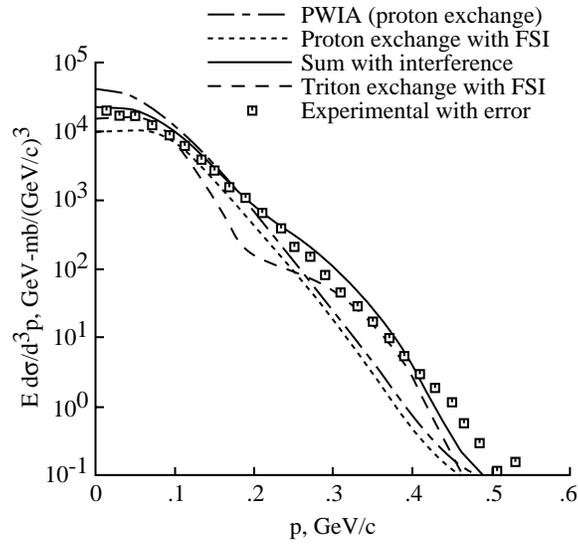
Figure 6a. Comparison of calculations to experiments [77] for longitudinal momentum distribution of tritons from alpha-C collisions at 1.9 A GEV.
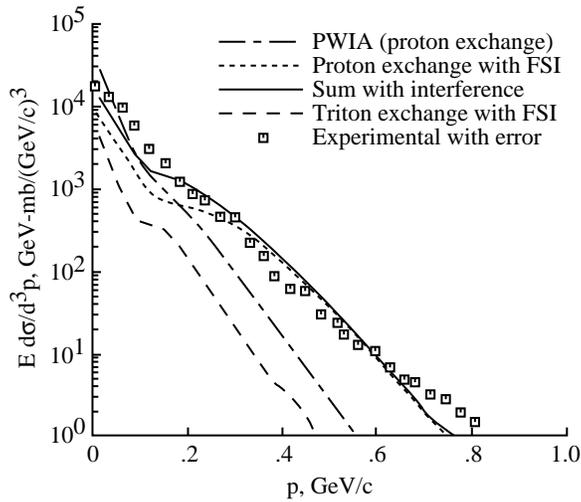
Figure 6b. Comparison of calculations to experiments [78] for transverse momentum distribution of tritons from alpha-C collisions at 2.1 A GEV.
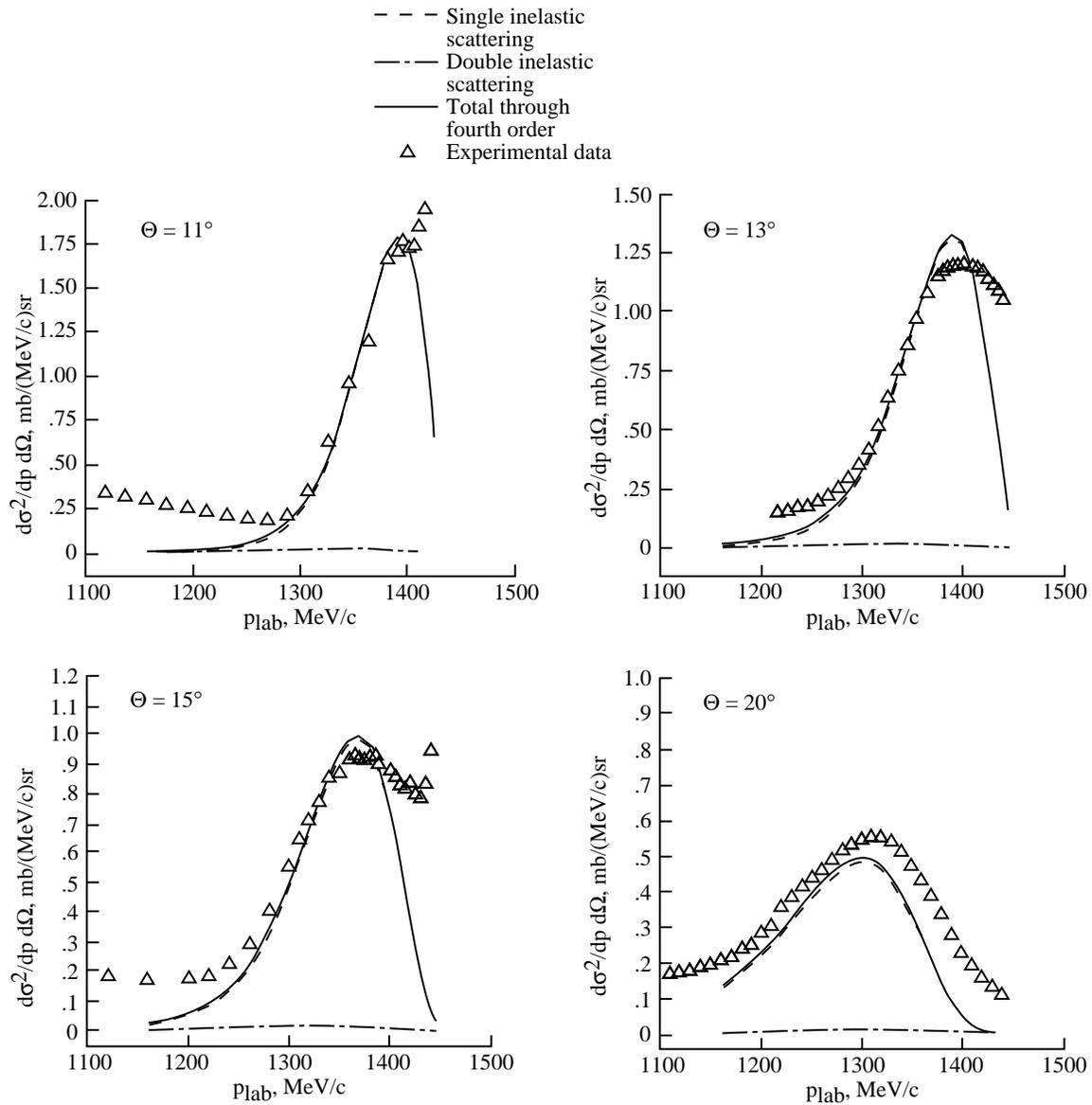
Figure 7.   Comparisons of calculations to experiments [79] for double differential cross sections for secondary protons in p-Al reactions at several angles.
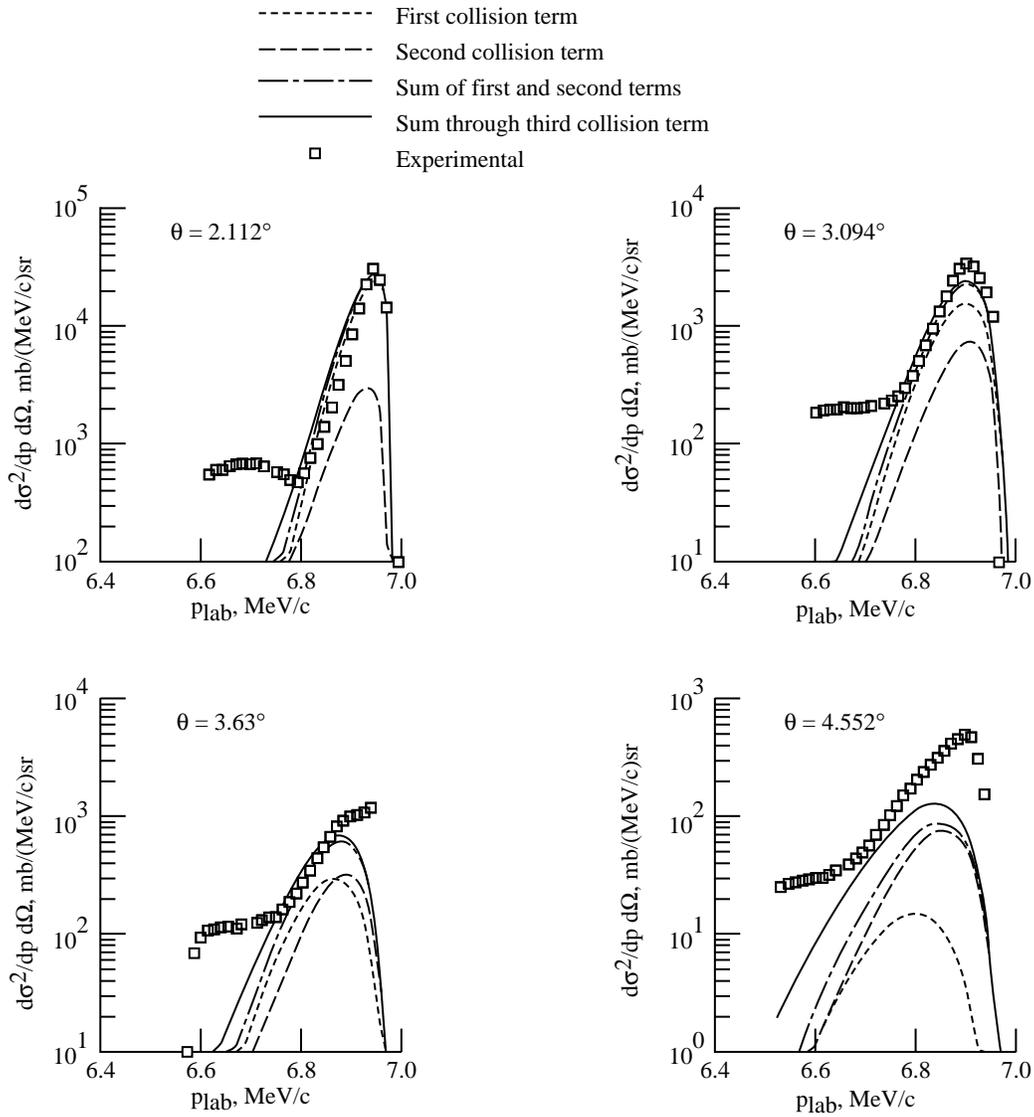
Figure 8. Momentum spectra of α particles in α-^{4}He collisions at 1 A GeV for scattering angles of 2.112° ($q = 1.31$ fm^{-1}), 3.094° ($q = 1.92$ fm^{-1}), 3.63° ($q = 2.25$ fm^{-1}), and 4.552° ($q = 2.82$ fm^{-1}). Experimental data are from Ref. [80]. The dotted line is the first collision term, the dashed line is the second collision term, the dot-dashed line is the sum of the first and second collision term, and the solid line includes the third collision term.
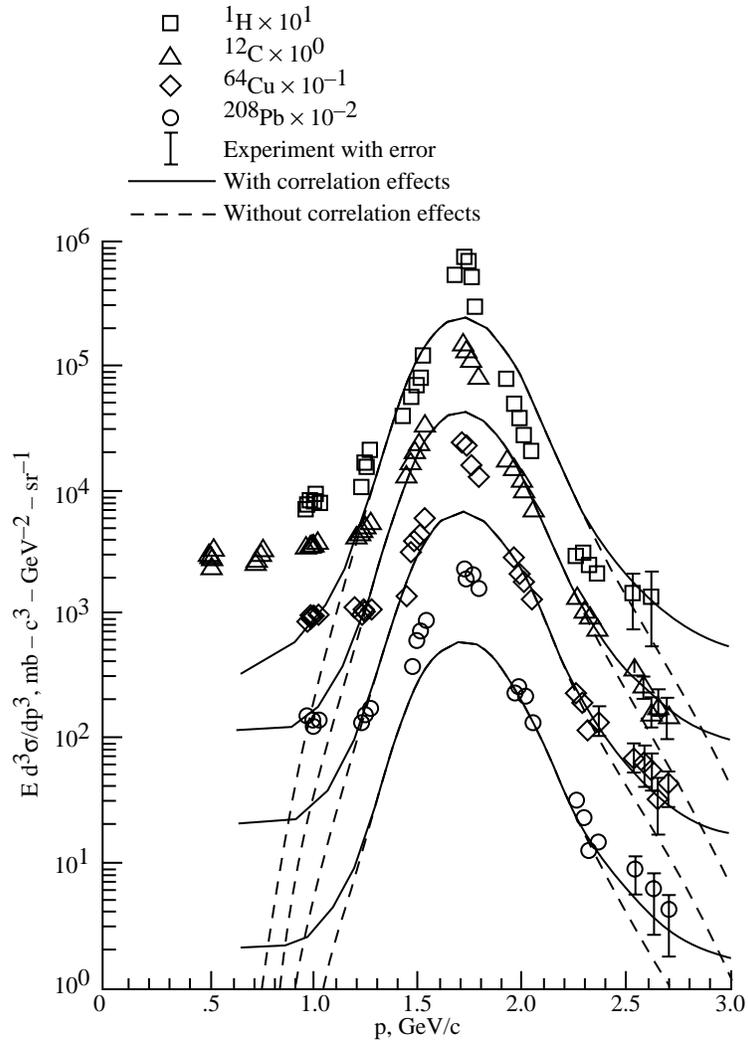
Figure 9a.　Comparison of calculation with experiments of [77] for proton production at 0 deg from C collisions on several target nuclei at 1.028 A GeV.
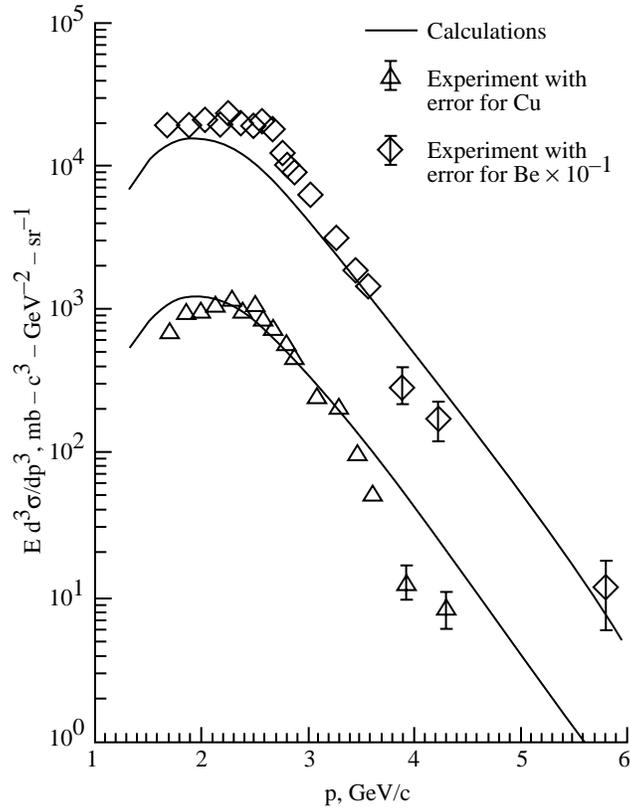
Figure 9b. Comparison of calculation with experiments of [81] for proton production at 5 deg from Ar collisions on several target nuclei at 1.8 A GeV.
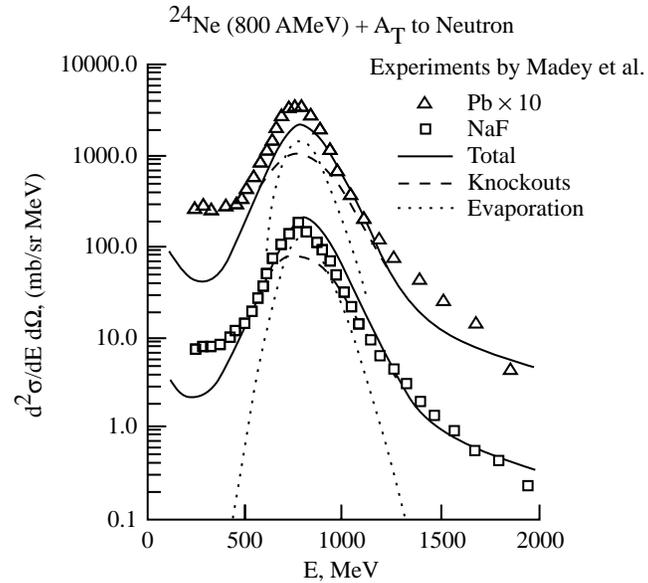
Figure 10. Comparison of calculation with experiments for neutron production at 0 deg from Ne collisions on several target nuclei at 0.8 A GeV.
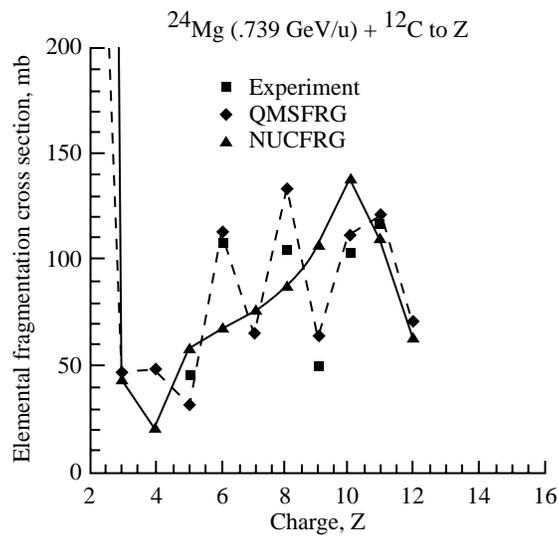
Figure 11. Comparisons of model calculations to experiments [82] for projectile fragmentation of ^{24}Mg on 12C at .739 A GeV.

206
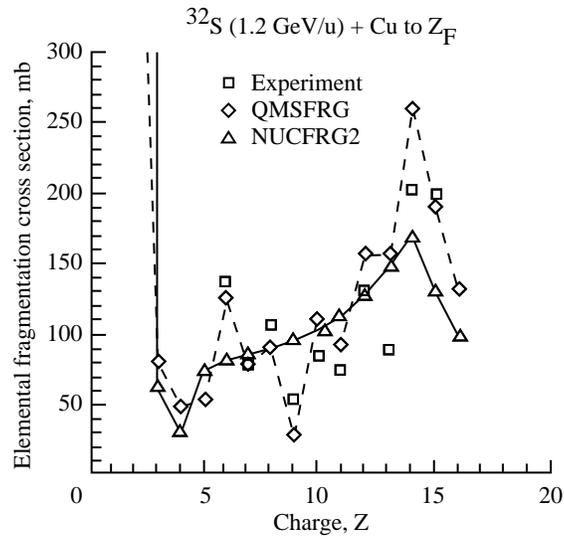
Figure 12. Comparisons of model calculations to experiments [74] for projectile fragmentation of ^{32}S on Cu at 1.2 A GeV.
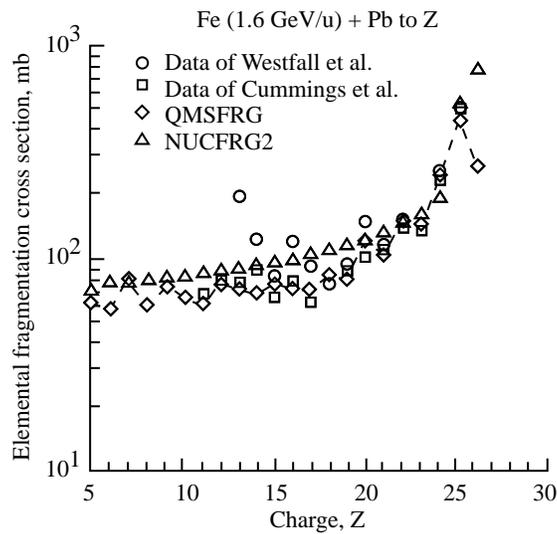
Figure 13. Comparisons of model calculations to experiments [75, 76] for projectile fragmentation of ^{56}Fe on Pb at 1.6 A GeV.
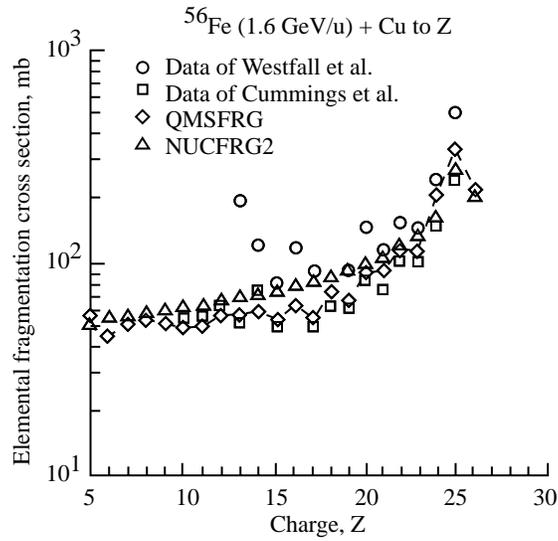
Figure 14. Comparisons of model calculations to experiments [75,76] for projectile fragmentation of ^{56}Fe on Cu at
1.6 A GeV.
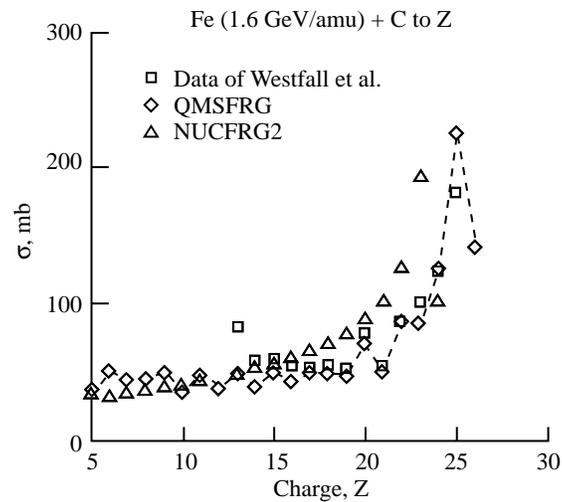
Figure 15. Comparisons of model calculations to experiments [75] for projectile fragmentation of ^{56}Fe on C at
1.6 AGeV.
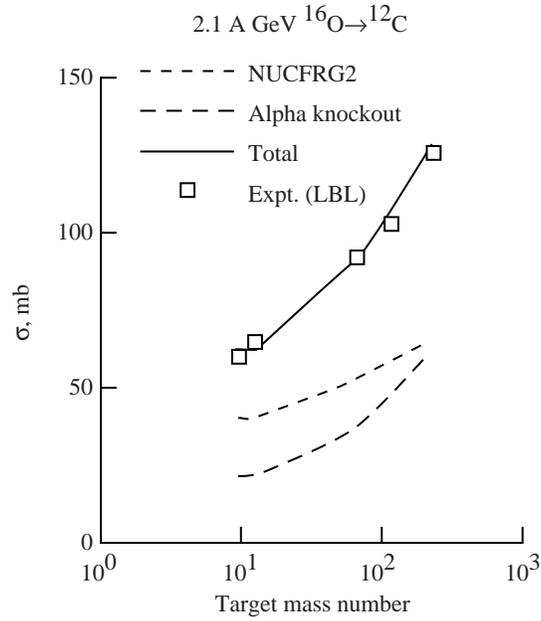
Figure 16. Comparisons of model calculations to experiments [83] for ^{12}C for ^{16}O on several targets. Model calculations include cluster knockout and multiple nucleon knockout contributions.
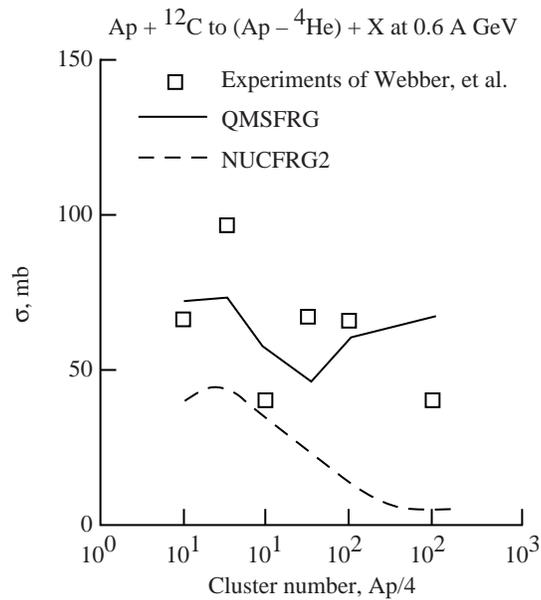
Figure 17. Comparisons of model calculations to experiments [82] for fragment production from alpha cluster nuclei at 600 A MeV.
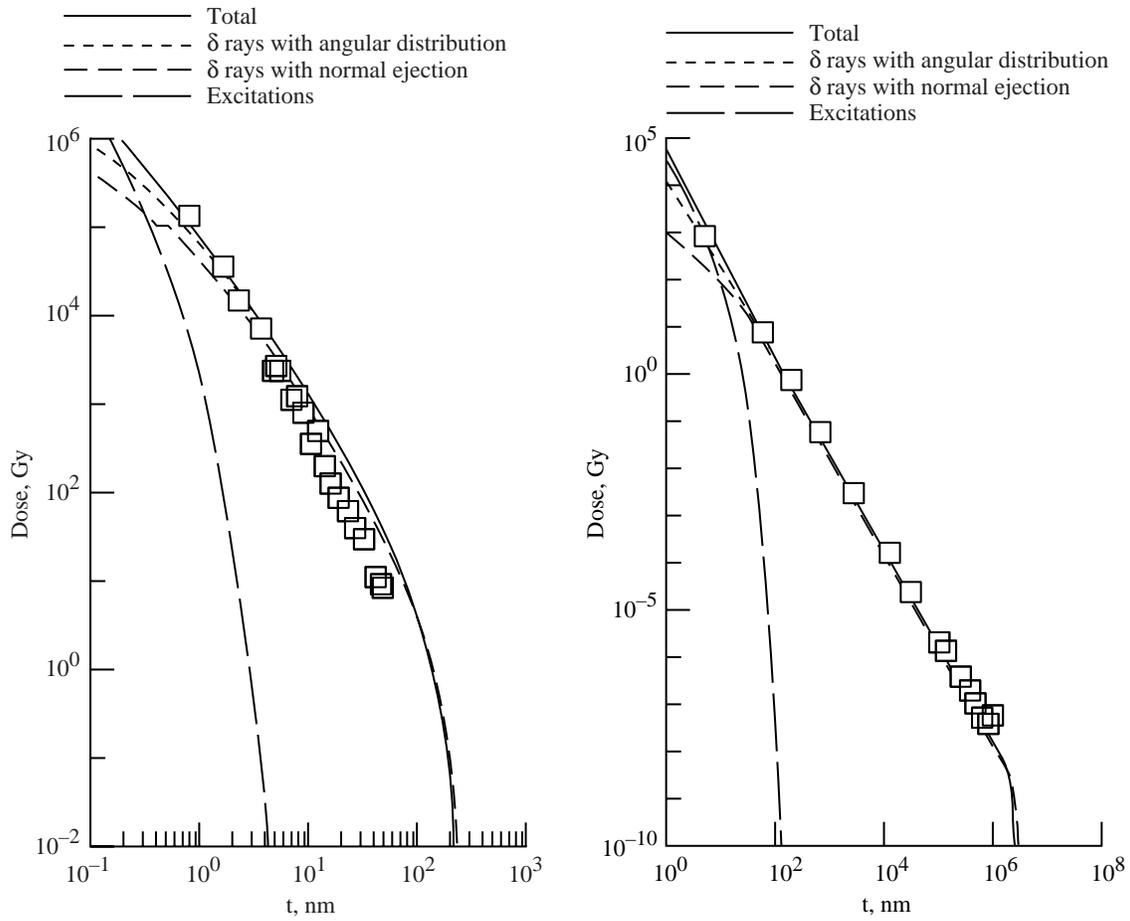
Figure 18.   Comparison of radial dose distributions from model calculations with experiments [95, 96].
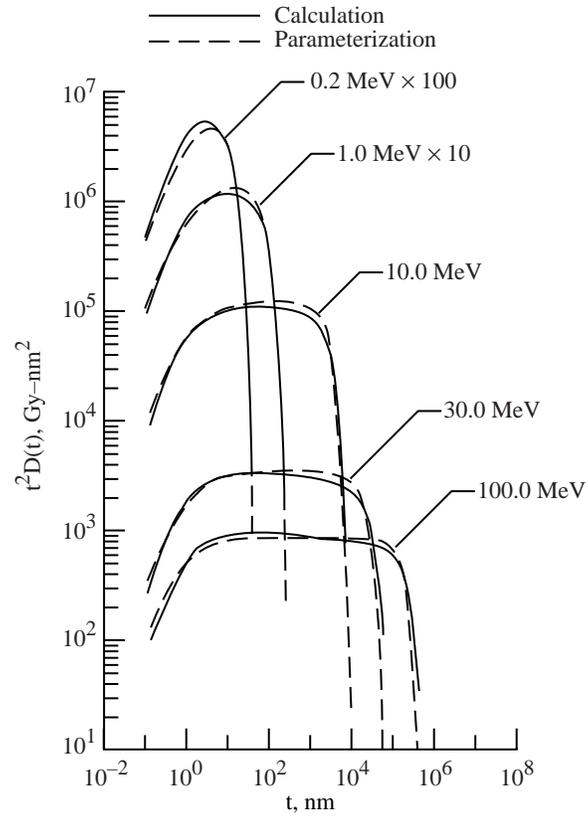
Figure 19.   Comparison of parametrized dose distribution to model calculations.

CHAPTER 9

HZE INTERACTIONS IN BIOLOGICAL MATERIALS

by

M. Eugene Rudd[1]

[1]Department of Physics and Astronomy, University of Nebraska, Lincoln, Nebraska 68588

Chapter 9

HZE INTERACTIONS IN BIOLOGICAL MATERIALS

SUMMARY

It is shown that most of the energy deposited by fast charged particles traversing matter occurs through ionization, i.e., the ejection of electrons during the atomic collision. The important mechanisms of ionization are identified and several methods of calculating the relevant differential and total cross sections are described. These include both classical and quantum theoretical methods and two semi-empirical models. The calculational methods were intended only for light, bare-ion projectiles, and care must be exercised in extending them to heavy, dressed projectiles.

IMPORTANCE OF IONIZATION

Fast charged particles traversing matter lose energy in successive collisions through three main processes: excitation, charge transfer, and ionization. Since ionization is not only the most probable of the three processes but also the one that involves the largest energy transfer, it is the one that contributes most to the stopping power. Energy must be transferred to overcome the binding energy (or ionization potential) in addition to that which provides the kinetic energy of the ejected electron or electrons. Furthermore, a sizable fraction of the ejected electrons (roughly half) have a high enough energy to cause further ionization. For these reasons, an understanding of radiation effects caused by fast charged particles requires data on ionization. Figure 1 shows the contributions to the stopping power by the three processes for proton impact on water vapor. At high energies, where charge transfer has dropped off to a negligible value, the sum of the fractions due to secondary electron kinetic energy F_ε and overcoming binding F_B account for over 80% of the stopping power with excitation contributing the rest. Thus, to make a comprehensive model of energy deposition, the systematics of electron production must be known.

INFORMATION NEEDED

To model the deposition of energy by charged particle interactions with matter, the following information is required:

1. The angular distributions of secondary electrons are needed to determine the spatial pattern of energy deposition.

2. The energy distributions of secondary electrons are needed to find the energy loss per ionization event, i.e., the stopping power.

3. Total ionization cross sections are required to calculate the mean free paths between ionizing events.

Unfortunately, ionization is a complex process, even for simple incident particles such as electrons and protons and is more complex for heavy, bare-nucleus projectiles. Heavy, dressed projectiles (i.e., those carrying electrons) have additional complications. We begin with a description of light ion (mostly proton) impact ionization because (a) many processes are the same as for heavy ions, and (b) most of the existing data and theories are for light ions, but these can often be extrapolated to apply to heavy ions.

CROSS SECTIONS

To make information on collisions useful we need to know the probabilities for various collision events. The quantitative measure of probability in atomic physics is the cross section which is a measure of how large the target looks to an incoming beam of ions for a given process. The total ionization cross section (or TICS) is measured in area units such as cm^2 or m^2. We also define singly differential cross sections (SDCSs) which are measured in units of area per unit ejected electron energy or area per unit solid angle, and doubly differential cross sections (DDCSs) measured in units of area per unit energy per unit solid angle. By integration, one can calculate the SDCSs and the TICSs from the DDCSs. Measurements of DDCSs are available for protons on many gases from a few keV to several MeV energy and for some heavy ions up to about 1000 MeV.

MECHANISMS OF ELECTRON EMISSION

The process of ionization can take place through one or more of several mechanisms. Some of the most important of these are:

1. Distant, soft collisions produce a peak at zero in the energy spectrum of electrons and an almost isotropic angular distribution.

2. Close, hard collisions are binary or billiard-ball-type interactions with a single electron in the target. Such collisions yield a peak in the spectrum of electrons at a secondary energy related to the angle of ejection through momentum and energy conservation.

3. Autoionization and Auger emission are processes that involve transitions between sharply defined energy levels and therefore yield sharp peaks in the energy spectra. Except in certain spectral regions, these mechanisms do not contribute much to the cross sections.

4. Projectile ionization (electron loss). A dressed ion (or atom) incident on a target may be thought of as a set of loosely bound electrons moving with the projectile which are easily detached, making elastic collisions with the target. While they may come off at any angle, they are found mostly in the forward directions. They produce a broad peak in the spectrum centered at the speed of the projectile.

Figure 2, showing energy spectra at different emission angles for electrons from 30-MeV O^{5+} + O_2 collisions, illustrates these mechanisms and their dependence on angle.

THEORETICAL METHODS

Several classical and quantum mechanical methods have been used to calculate electron ejection cross sections. Most of them account only for the soft, distant collision mechanism and the binary collision mechanism. The more elaborate methods generally yield better accuracy than the simple ones and are often more widely applicable. However, we will consider only a few of the simpler, more widely used methods.

Rutherford Equation

The Rutherford equation [1] was derived classically on the assumption that the electron in the target is initially at rest but held by a binding energy B. The total cross section is

$$\sigma_R = \frac{4\pi a_0^2 R^2}{TB} \tag{1}$$

where $T = m_e v^2/2$, m_e is the mass of the electron, v is the velocity of the projectile, a_0 is the Bohr radius (=0.529 Å), and R is the Rydberg of energy (=13.6 eV). The differential form of the equation is

$$\sigma_R(\varepsilon) = \frac{d\sigma}{d\varepsilon} = \frac{4\pi a_0^2 R^2}{TQ^2} \tag{2}$$

with $Q = B + \varepsilon$ where ε is the kinetic energy of the ejected electron. This form of the equation is often used with the kinematic cutoff at $\varepsilon = 4T = 2m_e v^2$.

Binary Encounter Approximation or BEA

The binary encounter approximation (BEA) takes account of the initial orbital motion of the electrons [2], but assumes that all electrons in the same shell have the same energy, U. The SDCS is

$$\sigma(\varepsilon) = \sigma_R(\varepsilon)\left(1 + \frac{4U}{3Q}\right), \qquad B \le Q \le Q_- \tag{3}$$

$$\sigma(\varepsilon) = \sigma_R(\varepsilon)\frac{U}{6Q}\left[\left(\frac{4T}{U}\right)^{3/2} + \left(1 - \sqrt{1 + \frac{Q}{U}}\right)^3\right], \qquad Q_- \le Q \le Q_+ \tag{4}$$

where $Q_{\pm} = 4T \pm 4(TU)^{1/2}$.

Binary Encounter Approximation With Fock Distribution

If one assumes a Fock hydrogenic distribution of velocities of the orbital electron and integrates over that distribution, the result is called the BEA-F equation [3]. It is stated in terms of the quantities $\alpha = Q/B$, $\phi = \left(T/\overline{U}\right)^{1/2}$ and $\beta = (\alpha/4\phi - \phi)^2$, where $\overline{U}$ is the average orbital kinetic energy.

$$\sigma(Q) = \sigma_A + \sigma_B, \quad \text{for} \quad B \leq Q \leq 4T \tag{5}$$

$$\sigma(Q) = \sigma_B, \quad \text{for} \quad Q \geq 4T \tag{6}$$

where

$$\sigma_A = \sigma_R(Q)\frac{\overline{U}}{\pi Q}\left[\frac{32\beta^{3/2}\alpha}{3(1+\beta)^3} + (4/3 + \alpha)(\pi - 2R_1)\right] \tag{7}$$

$$\sigma_B = \sigma_R(Q)\frac{\overline{U}}{\pi Q}\left[\frac{16}{3(1+\beta)^3}\left(\frac{4\phi^3}{3} - \beta^{3/2}\alpha - \frac{\alpha(\alpha+\beta)^{3/2}}{1-\alpha}\right) + \left(\frac{4}{3}+\alpha\right)R_1 - \left(\frac{4}{3} - \frac{\alpha}{1-\alpha}\right)R_2\right] \tag{8}$$

with

$$R_1 = \tan^{-1}\beta^{-1/2} + \frac{\beta^{1/2}}{(1+\beta)^3}\left(1 + \frac{8}{3}\beta - \beta^2\right) \tag{9}$$

and

$$R_2 = R_3 + (1-\alpha)^{-3/2}\tan^{-1}\left(\frac{1-\alpha}{\alpha+\beta}\right)^{1/2}, \quad \text{for} \quad \alpha < 1$$

$$= R_3 + (\alpha-1)^{-3/2}\ln\frac{(\alpha+\beta)^{1/2} - (\alpha-1)^{1/2}}{(1+\beta)^{1/2}}, \quad \text{for} \quad \alpha > 1 \tag{10}$$

and

$$R_3 = \left(2 + \frac{14}{3}\beta + \frac{8}{3}\alpha\right)\frac{(\alpha+\beta)^{1/2}}{(1+\beta)^3} - \frac{(\alpha+\beta)^{1/2}}{(1+\beta)(1-\alpha)} \tag{11}$$

Although this appears somewhat complicated, it is an analytic equation and can easily be programmed on a desk computer to produce cross sections for any given target, projectile energy, and secondary electron energy. The quantities B and U needed for the computation are given in the literature for a wide range of atomic and molecular targets [4]. In multishell targets the computation on these models is made for each shell, using the proper B and U

values, and then added. Usually only the outermost two or three shells contribute much to the cross section. There is a comparison of the Rutherford, BEA, and BEA-F equations with experimental data in Fig. 3.

Plane-wave Born Approximation

This is a quantum mechanical treatment which has been widely used. It assumes that the incident ion is deflected only slightly in its interaction with an electron in the target and also assumes a hydrogen wave function, scaled by the effective charge. It is generally fairly accurate at high energies (>500 keV/u) for relatively simple targets and projectiles.

$$
\sigma(\varepsilon,\theta) = \frac{2^8 m_p^2}{k^2} \int_{q_m}^{q} \max \frac{1}{q} \frac{\mu^6 \exp\left\{-2\mu\big/\kappa \tan^{-1}\left[2\kappa\mu\big/\left(q^2 - \kappa^2 + \mu^2\right)\right]\right\}}{q\left[(q+\kappa)^2 + \mu^2\right]\left[(q-\kappa)^2 + \mu^2\right]\left[1 - \exp(-2\mu/\kappa)\right]}
$$
$$
\times \frac{CD^3 + 4CDE^2 - 4BD^2E - BE^3 + 2AD^3 + 3ADE^2}{\left(D^2 - E^2\right)} dq,
\tag{12}
$$

where

$$
\begin{aligned}
A &= q^2 - 2q_m\kappa\cos\theta + \left(\kappa^2 + \mu^2\right)\left(q_m/q\right)^2 \cos^2\theta \\[4pt]
B &= 2\left(q^2 - q_m^2\right)^{1/2}\kappa\sin\theta - \left(\kappa^2 + \mu^2\right)\left(2q_m/q^2\right)\left(q^2 - q_m^2\right)^{1/2}\sin\theta\cos\theta \\[4pt]
C &= \left(\kappa^2 + \mu^2\right)\left[\left(q^2 - q_m^2\right)/q^2\right]\sin^2\theta \\[4pt]
D &= q^2 - 2q_m\kappa\cos\theta + \kappa^2 + \mu^2 \\[4pt]
E &= 2\kappa\left(q^2 - q_m^2\right)^{1/2}\sin\theta
\end{aligned}
\tag{13}
$$

θ is the angle of ejection of the electron, $q_m \approx (m/2)\left(\kappa^2 + \mu^2\right)\big/k$, k is the wave vector for the incident ion in the laboratory system, κ is the wave vector of the ejected electron, $\mu = \left(B/R\right)^{1/2}$, and $q_{max} \approx 2\kappa$. Cross sections are obtained by doing the integration over q numerically. Figure 4 shows a comparison of measured DDCSs with those calculated on the Born approximation and on the BEA. The agreement is good at intermediate angles but at the lower ejected energies, there are large discrepancies at small and large angles. The Born approximation is better for the large angles than the BEA, but still much too low. Both do poorly at small angles. These faults have been corrected in more sophisticated theoretical treatments.

SEMI-EMPIRICAL ANALYTICAL MODELS

Many users of cross section data are less interested in a rigorously derived theoretical equation than in a simple method of obtaining reasonably accurate cross sections. Many semi-empirical analytical models provide relatively simple equations or methods which yield such cross sections. Most analytical models require either some experimental data as input or values of a number of adjustable parameters. If the parameters have already been

determined from experiment, the model immediately yields the needed cross sections. Two such models will be described.

The Miller Model

The Miller model [5] is based on the Bethe equation which may be written

$$\sigma(\varepsilon) = \frac{4\pi a_0^2 R}{T}\left[\frac{R}{Q}\frac{df}{dQ}\ln\frac{4T}{R} + b(\varepsilon)\right] \tag{14}$$

where $Q = B + \varepsilon$, B is the ionization potential, ε is the ejected electron energy, and df/dQ is the differential optical oscillator strength. Quite accurate values of the latter quantity can be obtained from photoionization measurements. The first term of the Bethe equation is the "soft-collision" term; the second is the "hard-collision" term. Since the quantity $b(\varepsilon)$ is independent of projectile properties, it can be determined by subtracting the first term from one experimental spectrum of $\sigma(\varepsilon)$ at one incident energy. Then $b(\varepsilon)$ can be used for all incident energies. The model is most useful for large projectile energies. Figure 5 shows the good agreement between calculations using the Miller model and experimental energy distributions.

The Rudd Model

The Rudd model [6], which is based on Bethe equation, the BEA, and on molecular promotion theory, is useful at all incident energies and all electron energies. To obtain an electron spectrum at one incident energy, one needs to know 3 parameters, F_1, F_2, and α. To obtain spectra at all incident energies requires 10 parameters. The SDCS is given by

$$\sigma(w) = \frac{S}{B}\frac{F_1 + F_2 w}{(1 + w)^3\left\{1 + \exp\left[a(w - w_c)/v\right]\right\}}$$

where $w = \varepsilon/B, v^2 = T/B, w_c = 4v^2 - 2v - R/4B, S = 4\pi_0^2\,a_o^2 N(R/B)^2$, N is the number of electrons, and where

$$F_1 = L_1 + H_1 \qquad\qquad F_2 = L_2 H_2/(L_2 + H_2)$$

$$L_1 = C_1 v^{D1}/\left(1 + E_1 v^{D1+4}\right) \qquad L_2 = C_1 v^{D2}$$

$$H_1 = A_1\ln\left(1 + v^2\right)\left(v^2 + B_1/v^2\right) \qquad H_2 = A_2/v^2 + B_2/v^4$$

Values of the ten parameters, A_1, B_1, ...E_1, A_2, B_2, ...D_2, and α for many of the simple atomic and molecular gases are given in Table 1.

A sample of the fit of the Rudd model is given in Fig. 6 showing the energy spectra of electrons from $H^+ + H_2O$ collisions at 15–1000 keV. The quantity $Y = \sigma(\varepsilon)/\sigma_R(\varepsilon)$, which is the ratio of the SDCS to the corresponding Rutherford cross section, is plotted instead of the SDCS itself in order to reduce the large range of values and to make a more compact graph. The solid lines represent the model and the circles and crosses are measured values.

HEAVY BARE PROJECTILES

Most theoretical treatments yield collision cross sections which are proportional to Z^2, where Z is the charge of the projectile. This allows easy scaling from proton calculations, e.g., to any heavy bare ion projectile. Unfortunately, there are limitations to Z^2 scaling, especially for very high Z projectiles. There are at least three reasons for this: (1) for a given impact parameter, the probability of an ionization increases for increasing Z, but as the probability approaches unity, saturation limits its increase, (2) multiple ionization, which is an important contribution to the overall ionization cross section for heavy incident ions, does not scale as Z^2, and (3) simple theories do not account for two-center effects, that is, emission of electrons in which the fields of both the residual target ion and the incident ion affect the trajectories of emitted electrons.

The criterion for Z^2 scaling to hold is that $Zv_0/v \ll 1$ where v is the projectile velocity and v_o is the Bohr velocity. The failure of Z^2 scaling is illustrated in Fig. 7, where the total ionization cross sections for heavy bare-ion impact divided by the corresponding proton cross sections and by Z^2 are plotted against the energy per unit mass of the incident ion. The dotted line at unity indicates the results expected if Z^2 scaling held. At low incident velocities and especially for high Z projectiles, the cross sections fall off from the expected values.

A further example of Z^2 scaling failure is shown in Figure 8 for 25-MeV Mo^{40+} ions incident on helium. The energy spectra of electrons emitted at a forward angle, 20°, and a backward angle, 150°, are shown. The cross

Table 1. Parameters for fitting SDCSs to the Rudd Model

	He	Ne	Ar	Kr	H_2	N_2	0_2	H_2O	CO_2	CH_4	Inner Shells
A_1	1.02	0.58	1.20	1.46	0.96	1.05	1.02	0.97	1.09	1.15	1.25
B_1	2.4	65	8.0	5.7	2.6	12.0	50	82	25	14	0.50
C_1	0.70	0.23	0.86	0.65	0.38	0.74	0.40	0.40	0.75	0.35	1.00
D_1	1.15	0.55	0	−0.55	0.23	−0.39	0.12	−0.30	0.75	0.50	1.00
E_1	0.70	0.16	0.80	1.00	2.2	0.80	0.30	0.38	0.65	3.0	3.0
A_2	0.84	1.40	0.90	1.30	1.04	0.95	1.00	1.04	0.78	0.60	1.10
B_2	6.0	0	2.7	22	5.9	1.20	5.0	17.3	3.0	3.8	1.30
C_2	0.70	0.72	0.75	0.95	1.15	1.00	0.55	0.76	0.70	1.20	1.00
D_2	0.50	1.35	0.80	−1.00	0.20	1.30	0	0.04	0.85	0.45	0
α	0.86	0.57	0.71	0.78	0.87	0.70	0.59	0.64	0.53	0.61	0.66

sections have been divided by 1600 times the equal velocity proton cross sections. Thus, if Z^2 scaling held, the result should be unity as shown by the dashed line. However, the high-Z projectile evidently drags some of the electrons initially directed in the backward direction into the forward direction. Such two-center effects are important for electron emission in all directions. Furthermore, they are most important for $v_e \cong v_{ion}$. Also plotted in Fig. 8 are calculations made on the continuum-distorted wave–Eikonal-initial-state (CDW-EIS) theory, a relatively recent quantum mechanical model that takes the effects of both collision centers into account.

HEAVY DRESSED PROJECTILES

There are additional complications if the incident ion carries electrons. Some of these are: (1) The emission of projectile electrons. This was already discussed briefly earlier. (2) The possibility of simultaneous excitation and ionization. This provides an additional channel for the emission of electrons and in any calculation of cross sections it must be taken into account. An example is given in Fig. 9 showing the angular distributions of 218-eV electrons from 0.5-MeV/u He$^+$ + He collisions. In the calculation four reactions are combined to approximate the experimental distribution. The four are: (a) projectile ionization with the target remaining in the ground state, (b) projectile ionization with simultaneous target excitation, (c) target ionization with the projectile remaining in the ground state, and (d) target ionization with simultaneous projectile ionization. Note that all four contribute substantially to the total. (3) Screening effects. The nuclear charge of a dressed projectile is partially screened by the electrons it carries. When a projectile of nuclear charge Z carrying N electrons passes a target at a large distance, it looks to the target like an ion of charge Z-N. However, if it makes a very close collision the full charge Z is effective. This difference of screening has to be considered in calculating cross sections for dressed-ion collisions. An example of the effect of this change in screening is shown in Fig. 10 which compares the energy spectra of electrons for 0.5-MeV/u H$^+$, He$^+$, and He^{2+} ions incident on helium atoms. Consider the He$^+$ curve. The low energy ejected electrons come primarily from distant collisions for which the projectile's electron provides almost complete screening, making the projectile look like a proton. The high energy electrons, however, come mostly from very close collisions for which the nucleus is not screened and therefore yields a cross section close to that of the He^{2+}.

TWO USEFUL REPORTS

There are two extensive reports, both recently published, which review the subject of electron emission by charged particle interactions with matter. These should be especially useful to those who need cross sections for modelling the interaction of charged particle radiation with matter. One is *Atomic and Molecular Data for Radiotherapy and Radiation Research*, IAEA-TECDOC-799, May 1995, 754 pages. This is obtainable from Nuclear Data Section, International Atomic Energy Agency, Wagramerstrasse 5, P.O. Box 100, A-1400 Vienna, Austria. The other is *Secondary Electron Spectra from Charged Particle Interactions*, ICRU Report 55. This may be obtained from the International Commission on Radiation Units and Measurements, 7910 Woodmont Avenue, Bethesda, MD 20814.

REFERENCES

1. E. Rutherford: The scattering of α and β particles by matter and the structure of the atom. *Phil. Mag.* **21**: 669–688; 1911.

2. L. H. Thomas: The effect of orbital velocity of the electrons in heavy atoms on their stopping of α-particles. *Proc. Cambr. Phil. Soc.* **23**: 713–716; 1927.

3. M. E. Rudd, D. Gregoire, and J. B. Crooks: Comparison of experimental and theoretical values of cross sections for electron production by proton impact. *Phys. Rev.* A **3**: 1635–1640; 1971.

4. M. E. Rudd, Y. -K. Kim, D. H. Madison, and T. J. Gay: Electron production in proton collisions with atoms and molecules: energy distributions. *Rev. Mod. Phys.* **64**: 441–490 and W. Hwang, Y. -K. Kim and M. E. Rudd; New model for electron-impact ionization cross sections of molecules. *J. Chem Phys.* **104**: 2956–2966; 1996.

5. J. H. Miller, L. H. Toburen, and Steven T. Manson: Differential cross sections for ionization of helium, neon, and argon by high-velocity ions. *Phys. Rev.* A **27**: 1337–1344; 1983.

6. M. E. Rudd: Differential cross sections for secondary electron production by proton impact. *Phys. Rev.* A **38**: 6129–6137; 1988.

7. W. E. Wilson: Stopping power partition and mean energy loss for energetic protons in hydrogen. *Radiat. Res.* A **49**: 36–50; 1972.

8. N. Stolterfoht, D. Schneider, D. Burch. H. Wiemann, and J. S. Risley: Mechanisms for electron production in 30-MeV $O^{n+} + O_2$ collisions. *Phys. Rev. Lett.* **33**: 59–62; 1974.

9. M. E. Rudd and J. H. Macek: Mechanisms of electron production in ion-atom collisions. Case Studies in Atomic Physics **3**: No. 2, 47–136; 1972.

10. J. H. Miller, L. H. Toburen, and Steven T. Manson: Differential cross sections for ionization of helium, neon, and argon by high-velocity ions. *Phys. Rev.* A **27**: 1337–1344; 1983.

11. M. E. Rudd, Y. -K. Kim; D. H. Madison, and T. J. Gay: Electron production in proton collisions with atoms and molecules: Energy distributions. *Rev. Mod. Phys.* **64**: 441–490; 1992.

12. P. D. Fainstein, V. H. Ponce, and R. D. Rivarola: Electron emission for multielectronic atoms by ion impact at intermediate and high energies. *J. Phys.* B **20**: 1207–1215; 1991.

13. N. Stolterfoht, D. Schneider, J. Tanis, H. Altevogt, A. Salin, P. D. Fainstein, R. Rivarola, J. P. Grandin, J. N. Scheurer, S. Andriamonje, D. B. Ertault, and J. F. Chemin: *Europhys. Lett.* **4**: 899–904; 1987.

14. S. T. Manson and L. H. Toburen: Energy and angular distributions of electrons from fast $He^+ + He$ collisions. *Phys. Rev. Lett.* **46**: 529–532; 1981.
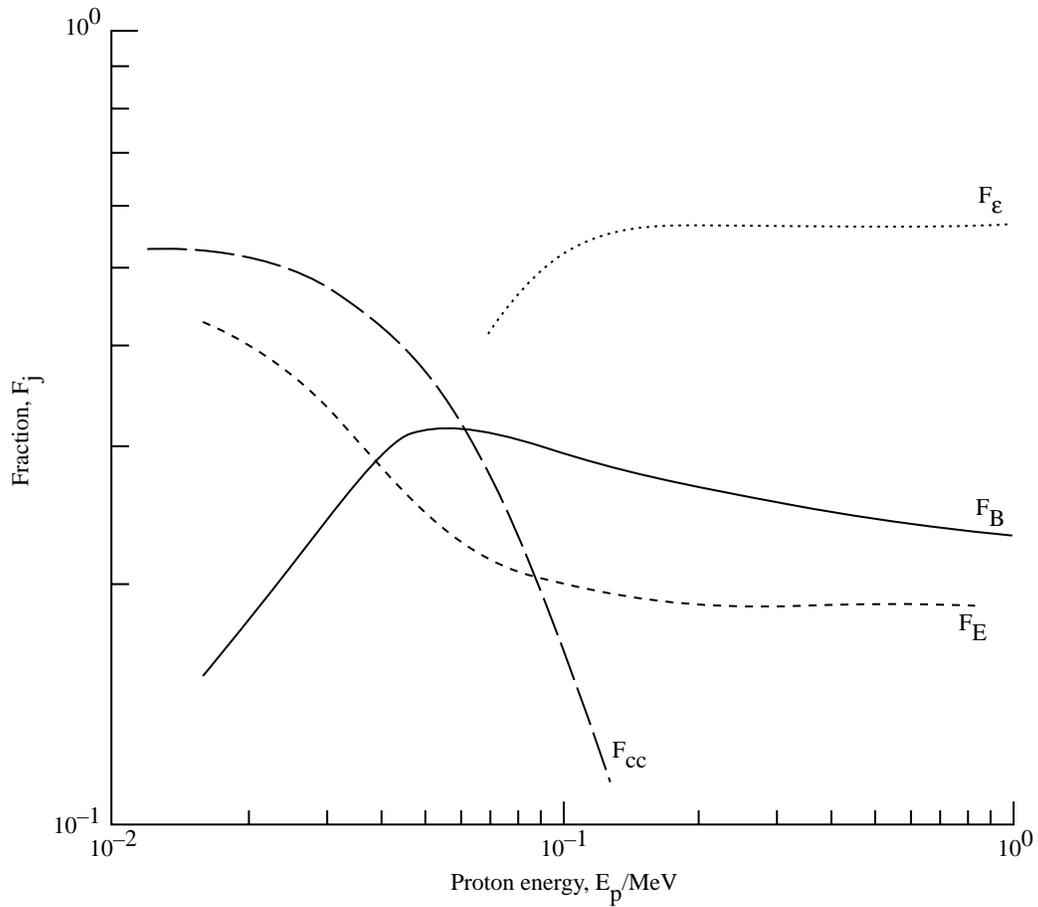
Figure 1.   Graph showing the fractions of the stopping power for protons incident on water vapor due to various processes: F_E excitation; F_{cc} charge transfer; F_B, overcoming binding energy of electrons; F_ε, kinetic energy given to ejected secondary electrons. The total fraction due to ionization is the sum $F_\varepsilon + F_B$. (Taken from Wilson, 1972.)
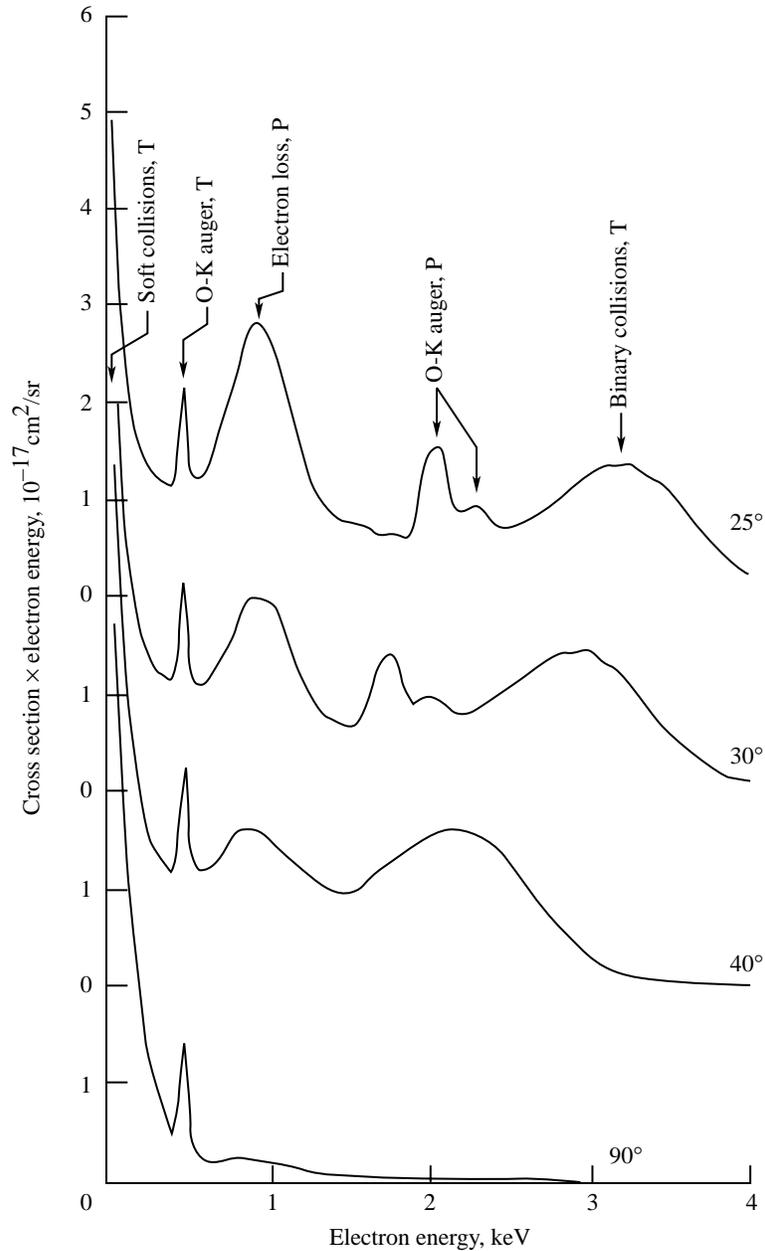
Figure 2. Energy spectra of electrons ejected at various angles from 30-MeV $O^{5+} + O_2$ collisions. *T* stands for emission from the target, *P* from the projectile. The binary collision peak comes at different energies for different angles. The Auger peak from the projectile also shifts with energy because of the kinematic effect of the moving source. (Taken from Stolterfoht, et al., 1974.)
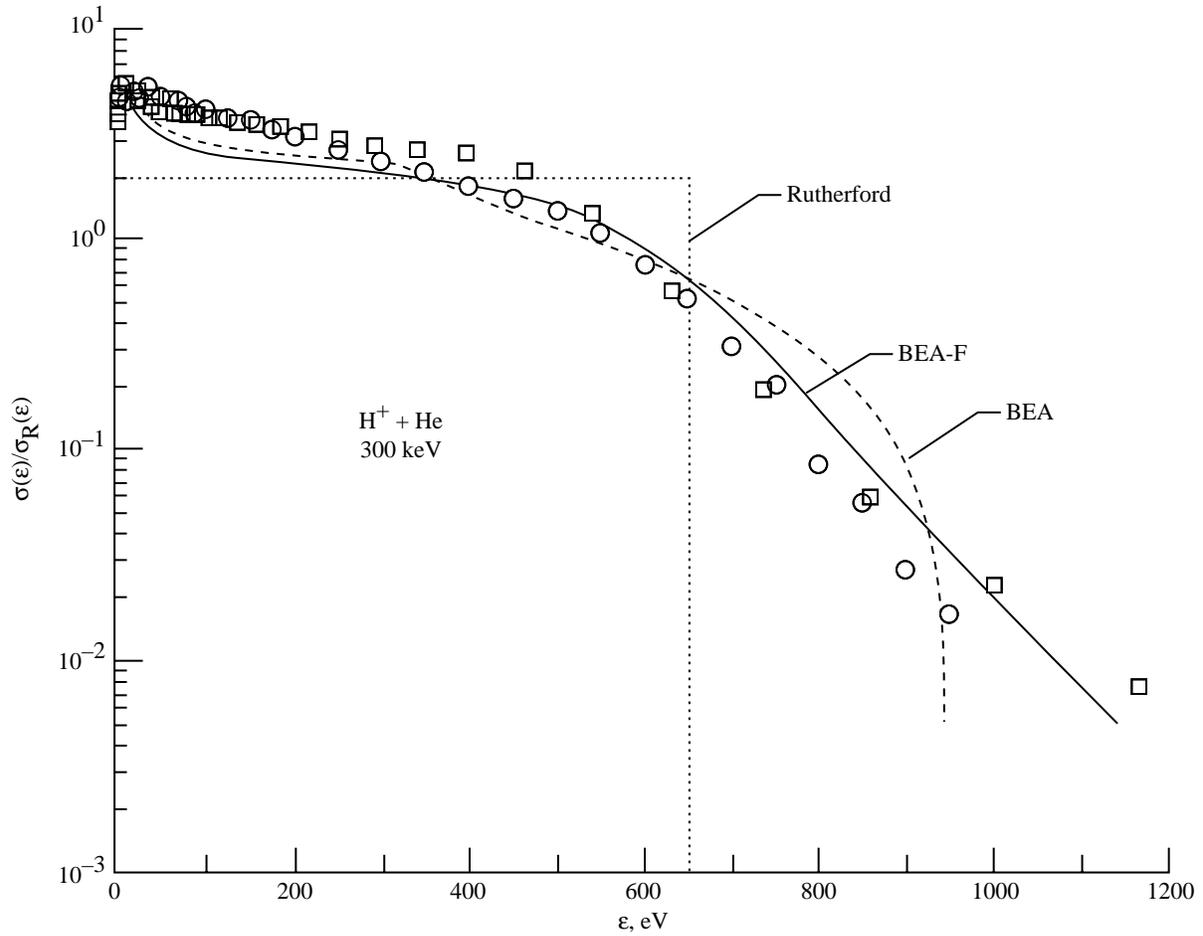
Figure 3. Comparison of the Rutherford, the BEA, and the BEA-F equations with experiment for the energy spectrum of electrons from 300-keV H^+ + He collisions.
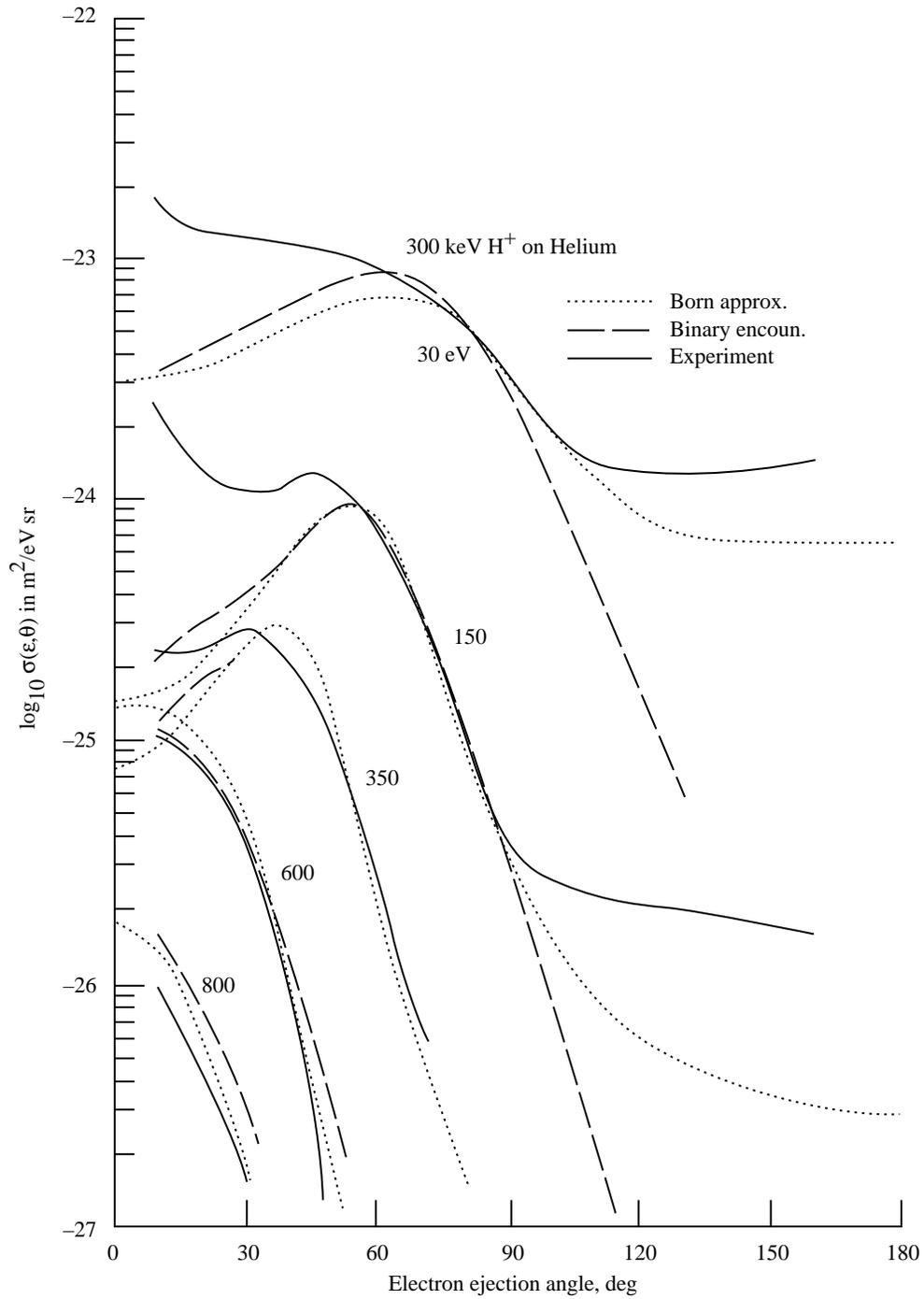
Figure 4.   Comparison of the Born approximation and the BEA with experiment for angular distributions of electrons of 30 to 800 eV from 300-keV H$^+$ + He collisions. (Taken from Rudd and Macek, 1972.)
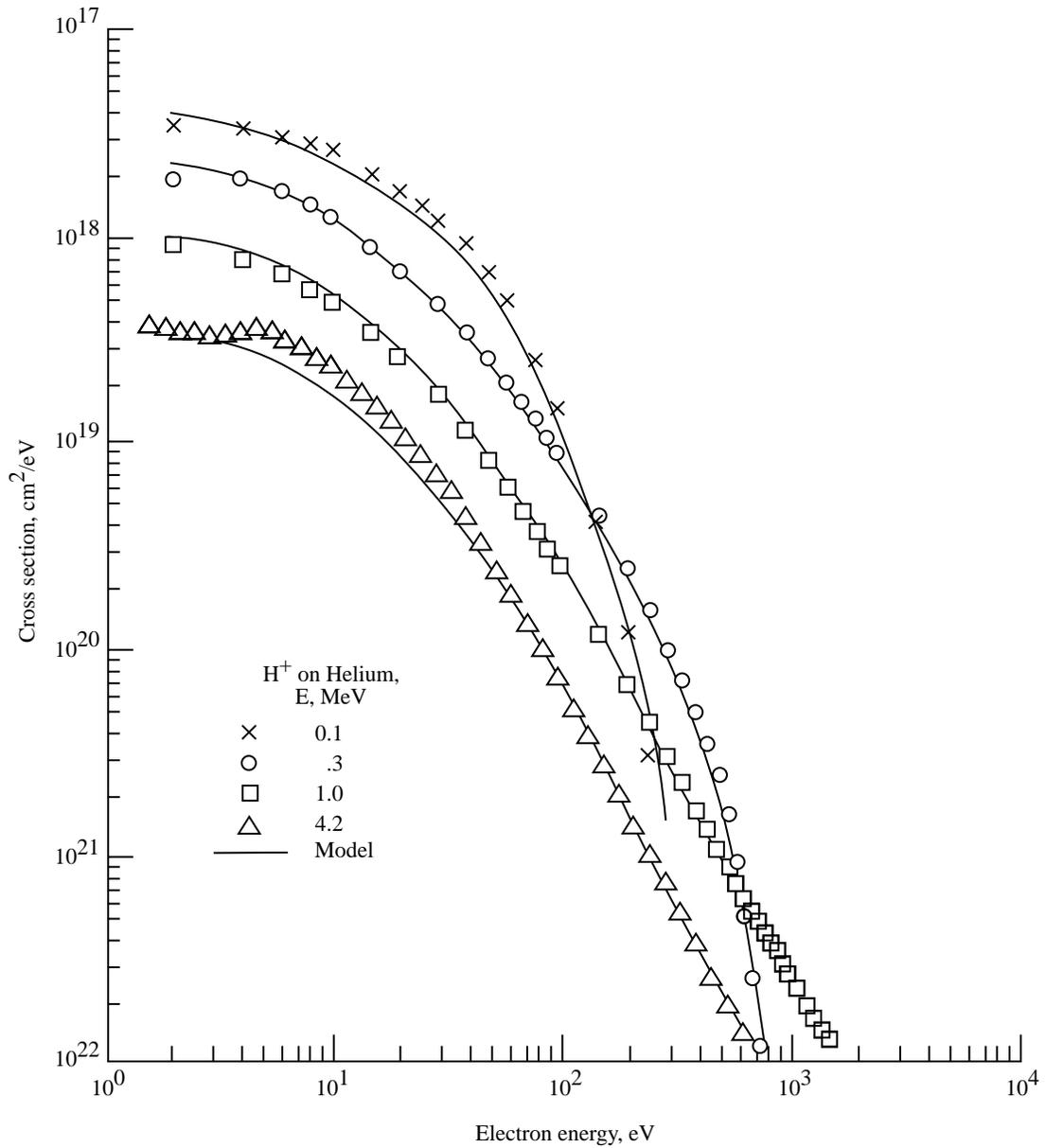
Figure 5.   Comparison of energy spectra calculated using the Miller model with experiment for four energies of protons on helium. (Taken from Miller et al., 1983.)
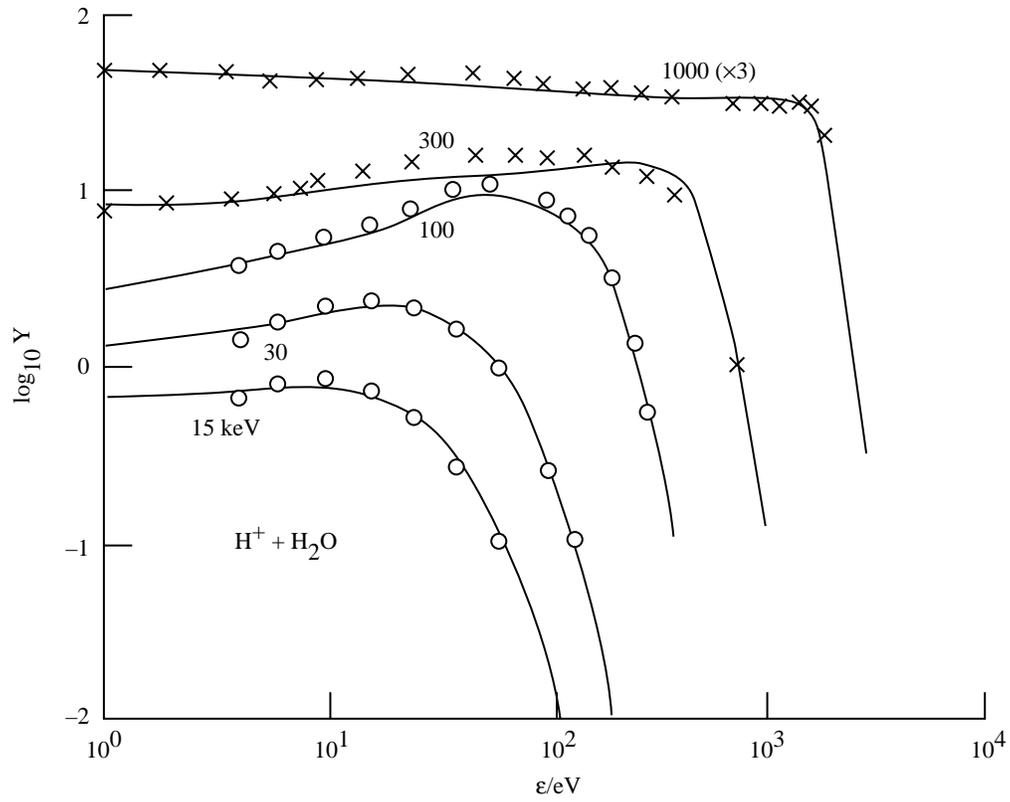
Figure 6.   Comparison of the Rudd model with experimental values of cross sections for 15 keV to 1 MeV $H^+ + H_2O$ collisions. (Taken from Rudd et al., 1992.)
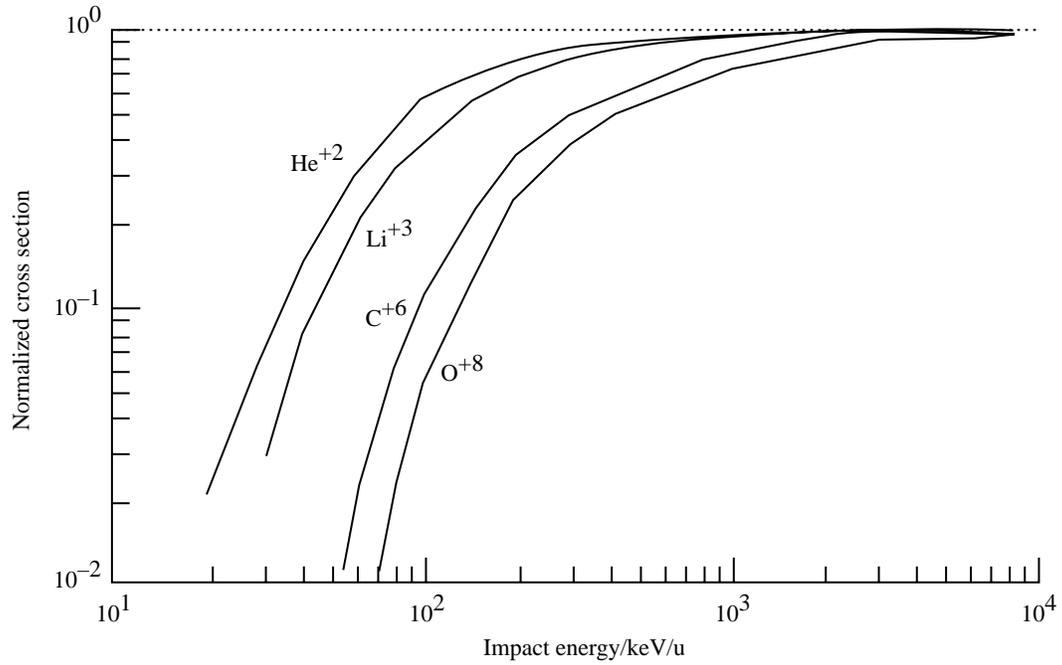
Figure 7.   The total ionization cross sections (TICSs) vs. impact energy per unit projectile mass. The TICSs have been normalized by dividing by Z^2 times the corresponding proton cross sections. The dotted line indicates expected results if Z^2 scaling held. (Taken from Fainstein, 1991.)
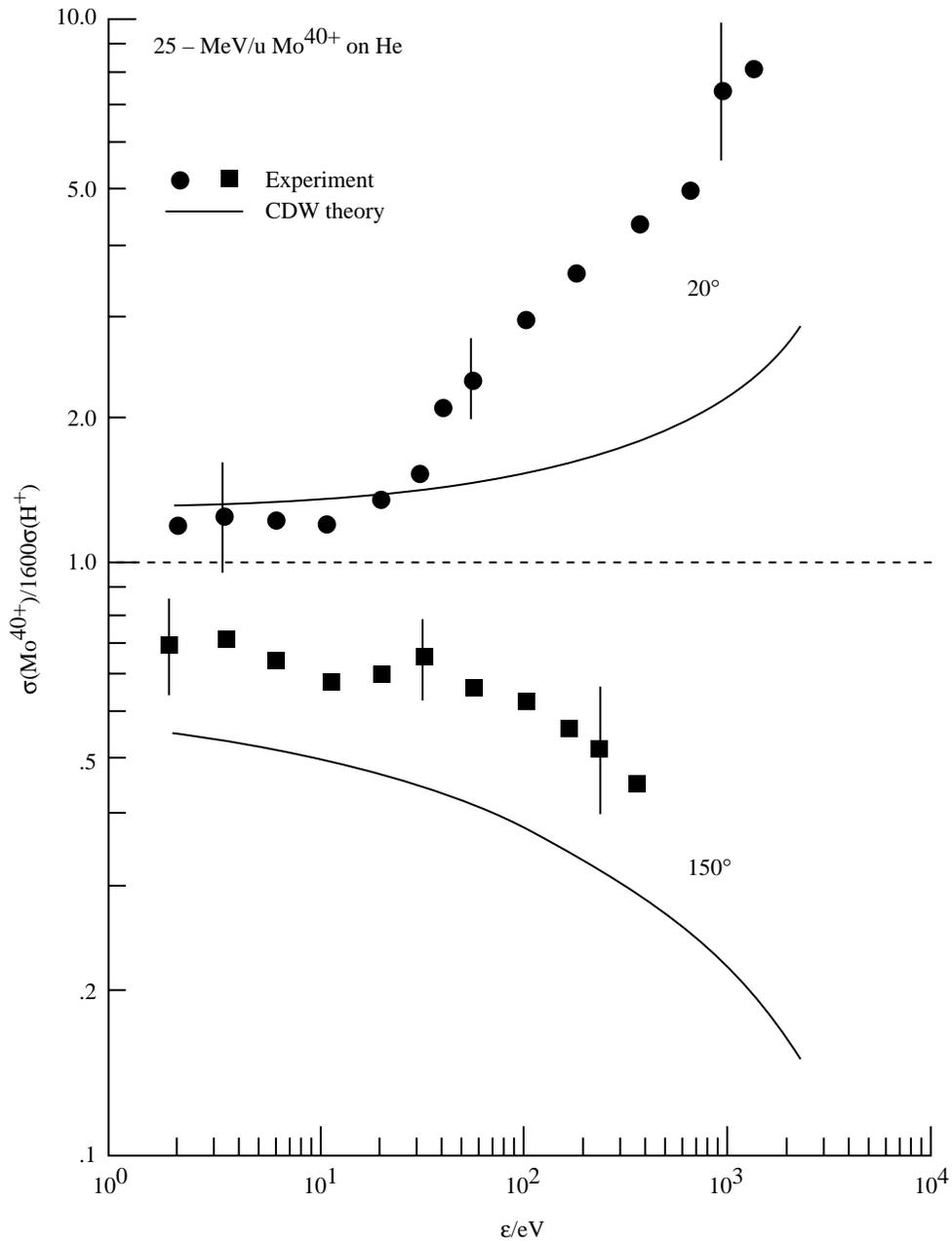
Figure 8. Energy spectra of electrons at two emission angles for 25-MeV/u Mo^{40+} + He collisions. The cross sections have been normalized by dividing by 1600 times the equal-velocity proton values. The dashed line indicates the expected result if Z^2 scaling held. The solid line gives calculations using the CDW-EIS theory (see text). (Taken from Stolterfoht et al., 1987.)
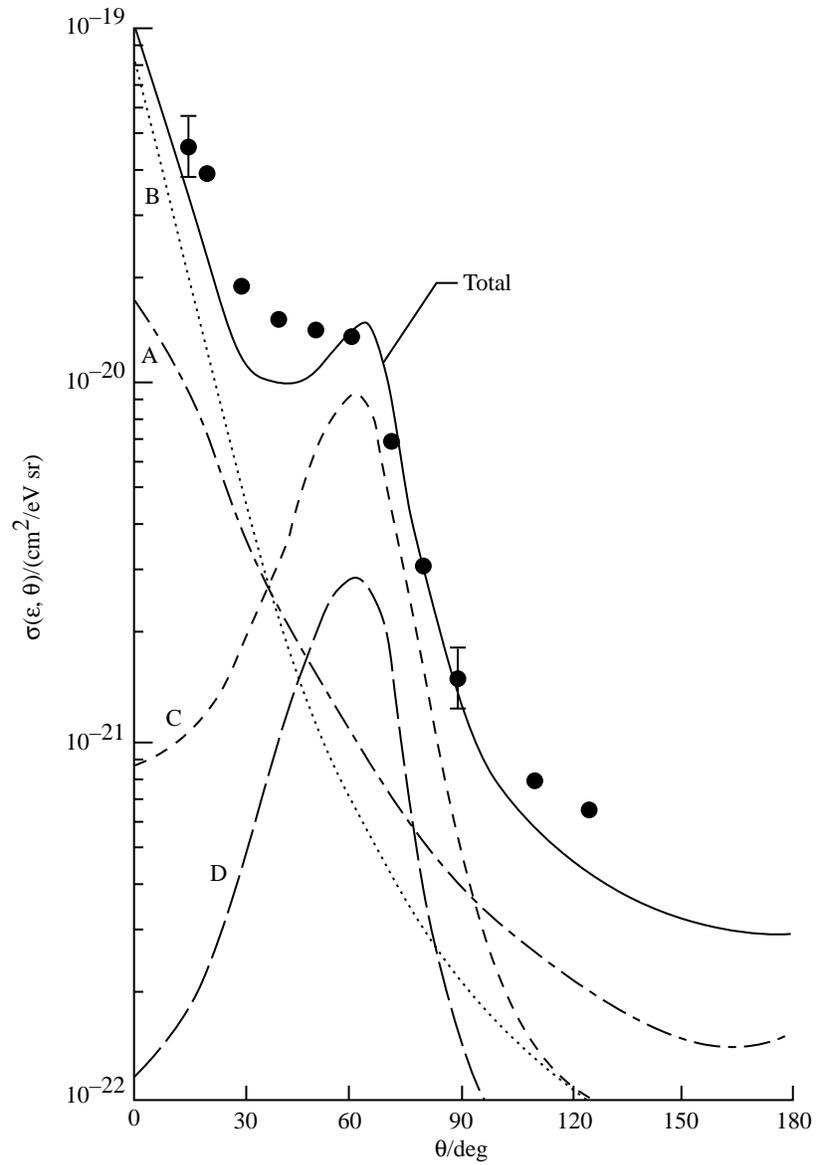
Figure 9.   Angular distribution of 218-eV electrons from 0.5 MeV/u He$^+$ + He collisions. Calculated values of four processes (see text) are added to give the total which is in fairly good agreement with experiment. (Taken from Manson and Toburen, 1981.)
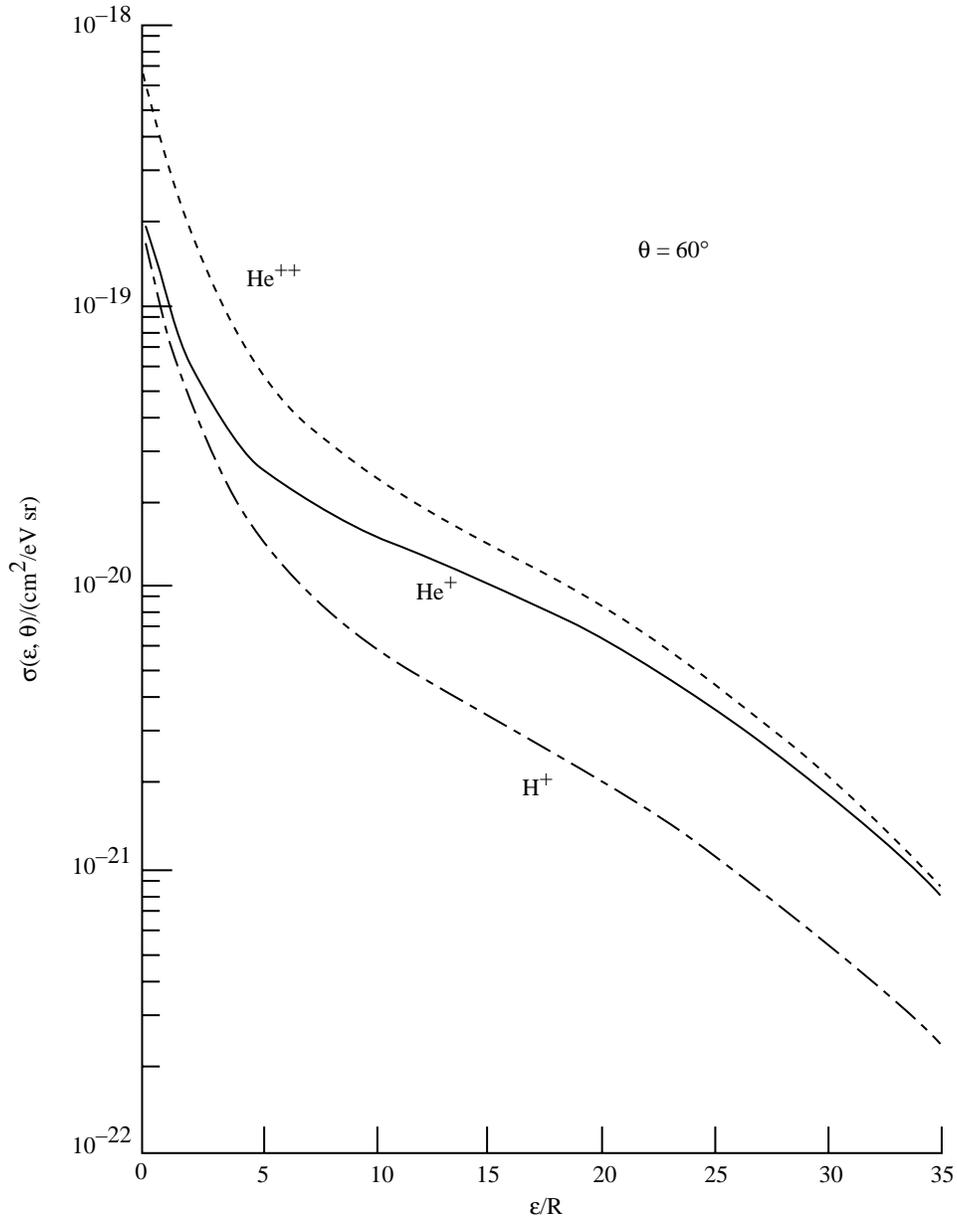
Figure 10. Energy spectra of electrons ejected at 60° from H$^+$, He$^+$, and He^{2+} collisions with helium to show how screening of the He$^+$ varies with ejection energy. (Taken from Manson and Toburen, 1981 [14].)

CHAPTER 10

DATABASE DEVELOPMENT AND LABORATORY VALIDATION

by

J. Miller[1]

_____
[1]Lawrence Berkeley Laboratory, Berkeley, CA 94720

Chapter 10

DATABASE DEVELOPMENT AND LABORATORY VALIDATION

SUMMARY

The two types of measurements needed for shielding applications, thin target cross sections and thick target fluence spectra, were defined. The existing database was discussed. Some basic principles of nuclear fragmentation and the detector systems used in accelerator experiments were outlined, with illustrative examples. The available heavy ion accelerator facilities were discussed. Estimates of accelerator beam time required to acquire data were presented.

INTRODUCTION

Data on heavy ion fragmentation and transport in shielding and tissue are needed for input to and validation of heavy ion transport models, and for direct evaluation of selected shielding materials. The data required are of two general kinds: *cross sections*, which are probabilities that an ion with a given charge, mass and energy incident on a given target nucleus will produce a fragment with a particular set of properties (charge, mass, energy, angle); *fluences*, which are numbers of fragments produced at depth in the material. The measurements involved in the two cases are similar, the principal difference being the target thickness. A cross section is the probability for a particular interaction to take place, and therefore must be measured with as thin a target as practical, in order to minimize the likelihood of secondary or higher order interactions affecting the final state of the measured fragment. Cross sections as a function of fragment energy are particularly critical for transport model development. A fragment fluence measurement can be made, in principle, behind any target thickness, and is deliberately designed to measure the cumulative effects of all the nuclear and electromagnetic interactions which can affect the final products. Cross sections more directly reflect the dynamics of the high energy nucleus-nucleus interactions, and are fundamental information which must be incorporated in heavy ion transport models. Fluence measurements are used to test the ability of a given model to account for the many different interactions which can occur in a thick target such as a spacecraft wall or the human body.

The energy range of greatest interest for space radiation applications (roughly 0.1-1 GeV/nucleon) is fortuitously similar to what has been available for over 20 years at heavy ion accelerators, and a number of heavy ion reaction cross sections have been measured (Figs. 1 and 2). However, since the choice of projectiles, targets, energies, and parameters measured has been motivated, for the most part, by basic questions in nuclear physics, the matrix of fragmentation cross section data which include fragment energies (Fig. 1) is still somewhat sparsely populated in some regions of particular interest for space radiation, for example, for iron projectiles ($Z = 26$). Note that measurements have been made at only a few beam energies. The beam energy dependence of fragmentation is a critical piece of information needed for accurate modeling. Similarly, until recently most of the measurements with thick targets were driven by the needs of the charged particle radiotherapy community, and thus have been largely confined to relatively light ions and tissue-equivalent targets such as water and polyethylene. However, the experimental methods developed for use in heavy ion nuclear physics and radiotherapy are directly applicable to space radiation. In this paper I will briefly review some of the methods and facilities which have been and are being used in database development and model validation.

NUCLEAR FRAGMENTATION

Nuclear fragmentation measurements may be somewhat arbitrarily divided into three regions (Fig. 3): target fragmentation, projectile fragmentation and mid-rapidity, or intermediate in velocity between target and projectile. Projectile fragments are the most numerous and most penetrating, and are concentrated in the forward direction. Mid-rapidity fragments tend to be light fragments emitted at large angles in the laboratory, and are detected using the same techniques as projectile fragments, but with the detector designed or positioned to cover angles well away from the projectile direction. Target fragments are slow and lose energy rapidly. Although many of them will stop very near where they are produced, they cannot be neglected—especially when they are produced within the human body.
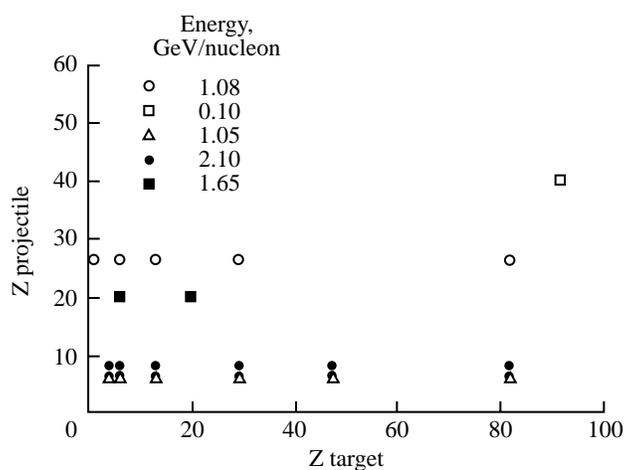
Figure 1.   Fragmentation cross section measurements which include fragment energy spectra. Symbols denote projectile energies in GeV/nucleon. Open square: 0.1; Open triangles: 1.05; Open circles: 1.08; Filled squares: 1.65; Filled circles: 2.1 (Data from refs. [1–4].)
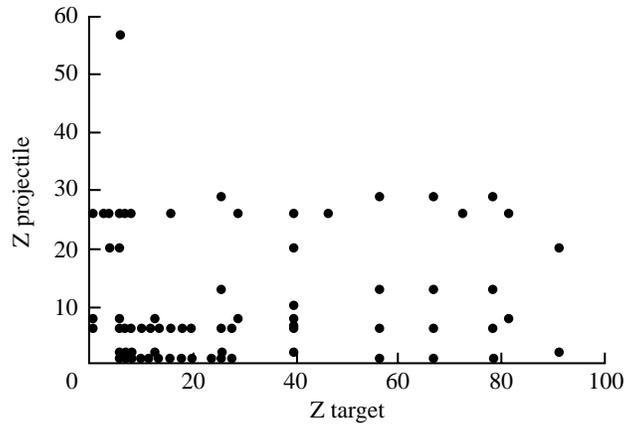
Figure 2.   Data for fragmentation cross section measurements where the fragment energy was not directly measured. (Data from refs. [5–17].)
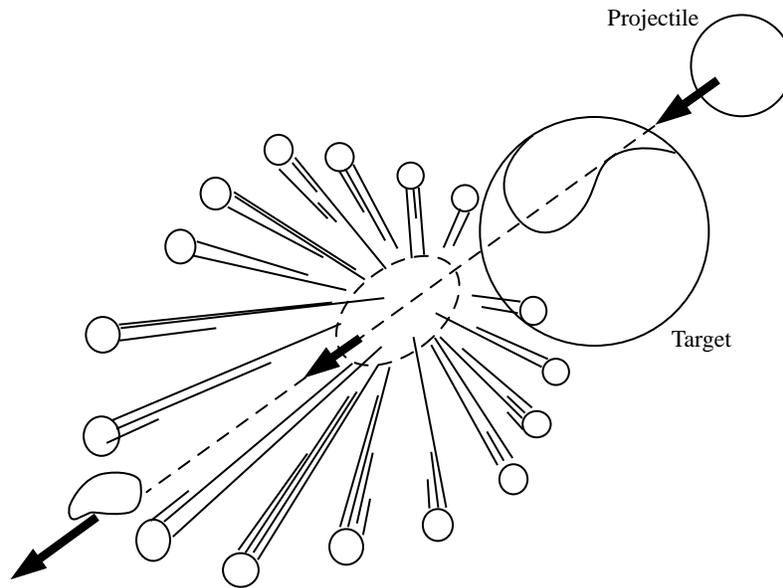

Figure 3.   Schematic representation of a high energy nucleus-nucleus collision. Target fragments are boiled off from the target remnant (second from right). "Mid-rapidity" fragments are emitted from the central interaction zone. The most energetic fragments are the one or more projectile remnants (left) that continue in the forward direction.

Target fragmentation presents unique detection problems because of the tendency of the particles of interest to be absorbed before they reach the detector. The majority of penetrating particles produced by GCR heavy ion interactions in shielding are projectile fragments, and I will focus on projectile fragmentation here.

DETECTORS

Table 1 lists some detector types and the observables which they can be used to measure. All particle physics experiments use one or more detector elements in combination with readout and data acquisition devices to record information about the particles of interest. The number and types of detectors varies according to the properties and

Table 1

Observable	Detector
energy loss ΔE, $\Delta E/\Delta x$	ionization chamber
	scintillation counter
	bubble chamber
	solid state
	nuclear emulsion
	plastic nuclear track detector (PNTD)
	calorimeter
velocity (or time of flight)	Cerenkov counter
	scintillator
position	multi-wire proportional chamber
	drift chamber
	TPC
	position-sensitive solid state
	bubble chamber
	emulsion
	PNTD

multiplicities of the particles to be measured. Two extreme examples are detecting cosmic rays in the laboratory and finding the top quark. Muons which are the end products of the interactions of cosmic rays with nuclei high in the atmosphere arrive at the Earth's surface at a rate of approximately $1/sec/cm^2$. Top quarks are produced in the laboratory in high energy proton-anti-proton collisions along with hundreds or even thousands of other particles in a fraction of a second. A table top experiment to count cosmic rays can be done with two plastic scintillation counters, whereas the large detectors recently used to identify the top quark from among the huge background contain hundreds of detectors of many different designs.

Detection systems to measure projectile fragmentation are typically of small to moderate size, depending upon the angular range covered. Figure 4 is a schematic of a detector configuration which our group has used to measure the fragmentation of 1.08 GeV/nucleon ^{56}Fe in a variety of materials at the Brookhaven National Laboratory Alternating Gradient Synchrotron (AGS) [3]. A series of solid state detectors record the energy deposited by charged particles traversing them. Convoluting the energy losses in two or more detectors makes it possible to
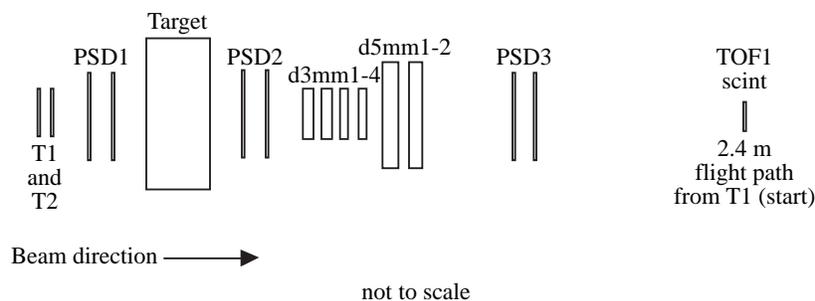
Figure 4. Detectors used to measure fragmentation cross sections and fragment fluences from 1.08 GeV/nucleon ^{56}Fe incident on a variety of targets. The detectors include plastic scintillation counters (T1, T2, TOF1), position sensitive solid state detectors (PSD1,2,3), and 3 and 5 mm solid state energy loss detectors (d3mm1–4, d5mm1–2).

calculate the particle's charge and energy. The solid state detector stack was augmented in this case by plastic scintillation counters to measure the time of flight between two points. This information is needed to supplement the energy loss information in the case of the lighter charged particles.

Figures 5 and 6 illustrate part of the process of converting signals from the detectors into useful information. (These data were taken using a detector similar to the one depicted in Figure 4, and using 510 MeV/nucleon ^{56}Fe at the LBL Bevalac [18].) Figure 5 is a plot of energy loss, measured in a 3-mm silicon detector, for fragments produced by iron beams interacting in 2 cm of polyethylene (CH_2). The abscissa is the energy loss in MeV. The lower energy peaks are from the lower Z fragments, with energy deposition falling with decreasing charge. Nuclei ranging from $Z = 26$ down to at least $Z = 13$ can already be discerned even in the raw data. Figure 6 is the same
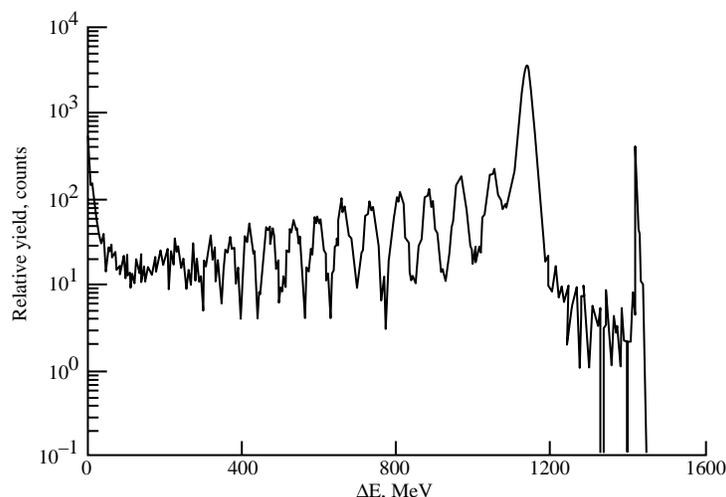
Figure 5. Energy loss spectrum for charged fragments produced by 510 MeV/nucleon ^{56}Fe incident on 2 cm CH_2. This measurement was made by a single 3mm thick solid state detector.
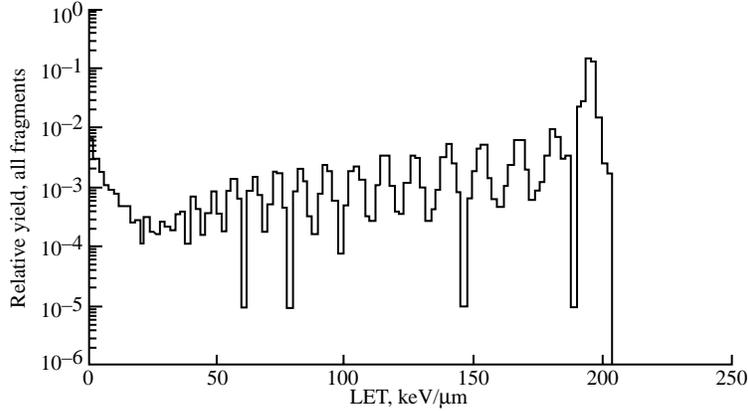
Figure 6.   Data in Fig. 5, converted to an LET spectrum.

distribution, converted to an LET (linear energy transfer) spectrum. The full charge identification is done using an analytic procedure [19]. In this case, charges in the range $Z = 7 - 26$ were identified. The lower limit for fluence measurements has now been extended to $Z = 2$, and in some cases to $Z = 1$. Figure 7 shows data for the cross section for production of fragment charges 12–25 by 1.08 GeV/nucleon ^{56}Fe in graphite. In this case, also, the lower limit of the measured charge will decrease with further data analysis.

FACILITIES

Table 2 is a list of the available high energy heavy ion accelerators. At the present time, the only facility which can provide iron projectiles at energies above 200 MeV/nucleon, and which has beam time available, is the AGS. The AGS Booster is at present used exclusively as a pre-accelerator for the AGS, and lacks a system for delivering beams to experimental areas. Beam time at SIS-18 is extremely limited.

Table 2

Facility	Z_{proj} (max)	E_{proj} (GeV/nucleon)	E_{proj} (^{56}Fe) (GeV/nucleon)
AGS (BNL)	79	1–10	1–10
AGS Booster (BNL)	79	0.1–1.5	0.1–1.25
SIS-18 (GSI-Darmstadt)	92	1–4.5	l–2
SATURNE (CEN-Saclay)	36	1.1	—
Synchrophasotron (JINR-Dubna)	16	4	—
Nuclotron (JINR-Dubna)	26	6	?
HIMAC (NIRS-Chiba)	20	0.1–0.8	—
SPS (CERN-Geneva)	82	200	—
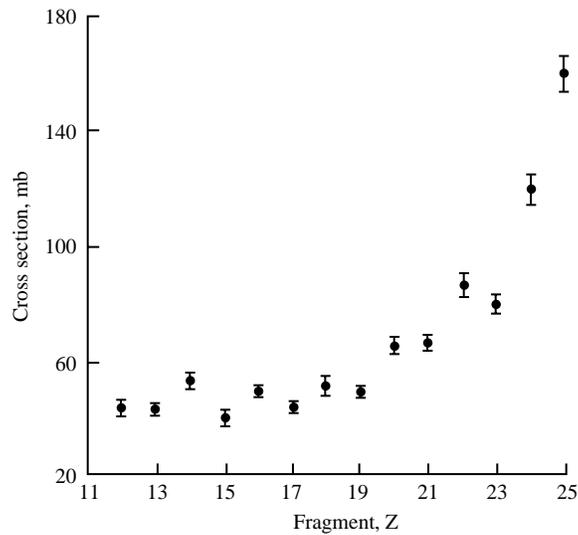
Figure 7.   Cross section for production of fragment charges 12–25 by 1.08 GeV/nucleon ^{56}Fe in carbon. (From ref. [3].)

BEAM TIME

How many hours of beam time are required for each data point for cross section and fluence measurements?

Define a single data point as: 1 projectile, Z_p

1 beam energy, T_p

1 target, A_t

1 angle, θ

all fragment charges, $Z = 1 \rightarrow Z_p$

Assume that the LET distribution is relatively flat (within an order of magnitude) as a function of energy and charge, except for light fragments and the primary, which dominate the statistics. This is supported by AGS and Bevalac data.

For zero-degree measurements, the rule-of-thumb relation is:

$$\text{No. hrs.} \ = \ \frac{N_{\text{bin}} \cdot N_{\text{evt}} \cdot N_{\text{frag}}}{R \cdot P \cdot \varepsilon}$$

where

N_{bin} = number of bins (energy intervals)

N_{evt} = number of events/bin

N_{frag} = number of fragments to measure

R = evt. rate (hr^{-1})

P = probability of producing one of N_{frag} fragments

ε = analysis efficiency

N_{evt} is determined by the precision desired.

The event rate, R, is a function of the detector, the data acquisition, the spill rate, and the spill structure. For recent measurements at Brookhaven [3],

$$R = (100/\text{spill}) \cdot (1800 \text{ spill/hr})$$
$$= 1.8 \times 10^5 \text{ hr}^{-1}$$

For all but the thickest targets, P is roughly e^{-x_{tgt}/λ_I}, where λ_I is the nuclear interaction length, and since the reaction products are dominated by primaries, $N_{\text{frag}} = Z_{\text{p}} - 1$. (This will give somewhat higher-than-needed statistics for protons and light fragments.)

Example: for a 20% interaction length target, 10 fragment energy bins with 10% statistics and $\varepsilon = 0.5$:

$$\text{No. hrs.} = \frac{10 \cdot 100 \cdot 25}{1.8 \times 10^5 \cdot 0.2 \cdot 0.5}$$
$$= \frac{2.5 \times 10^4}{1.8 \times 10^4}$$
$$= 1.4$$

This is consistent with the measured data rate at the AGS in 1995 of about 1 hour per data point for (near-) zero degree iron cross sections and fluences with 10% statistics.

This number is obviously sensitive to many parameters. For example, N_{bin} and N_{evt} are likely candidates to change over time according to the requirements of the theorists and others in the space radiation community. Obtaining data at higher angles will greatly increase the beam time required—by an order of magnitude, at least.

In accelerator experiments, one must also take into account beam time for detector setup and tests, which is typically between 8 and 48 hours—but can and occasionally will be greater. It can also take a number of hours for the accelerator to change ions and energies, limiting the number of different data sets which can be taken in a single running period.

CONCLUSIONS

For the most part, the facilties and detectors needed to generate the fragmentation database are available. What is required now—especially given the limited accelerator resources—is to determine what the critical data points are, and to assign priorities to the measurements, a process of which this workshop is a part. This is to some extent an iterative process: e.g., accelerator-based tests of model predictions often dictate what cross sections need to be measured, and with what precision.

ACKNOWLEDGEMENTS

REFERENCES

1. D. E. Greiner et al., Phys. Rev. Lett. **35**, 152 (1975).

2. C. E. Tull, Ph.D. thesis, Lawrence Berkeley Laboratory report No. LBL-29718, 1990 (unpublished).

3. C. J. Zeitlin et al., Phys. Rev. C., **56**, 388 (1997).

4. K. A. Frankel and J. D. Stevenson, Phys. Rev. C **23**, 1511 (1981).

5. H. H. Gutbrod et al., Phys. Rev. Lett. **37**, 667 (1976).

6. H. H. Heckman et al., Phys. Rev. C **17**, 1735 (1978).

7. Y. P. Viyogi et al., Phys. Rev. Lett. **42**, 33 (1979).

8. G. D. Westfall et al., Phys. Rev. C **19**, 1309 (1979).

9. J. D. Stevenson and P. B. Price, Phys. Rev. C **24**, 2102 (1981).

10. M. L. Webb et al., Phys. Rev. C **36**, 193 (1987).

11. J. M. Kidd, et al., Phys. Rev. C **37**, 2613 (1987).

12. W. R. Webber, J. C. Kish and D. A. Schrier, Phys. Rev. C **41**, 520, 533 and 547, (1990).

13. J. R. Cummings et al., Phys. Rev. C **42**, 2508 (1990).

14. S. E. Hirzebruch et al., Phys. Rev. C **46**, 1487 (1992).

15. V. E. Dudkin et al., Nucl. Phys. **A568**, 906 (1994).

16. C.-X. Chen et al., Phys. Rev. C **49**, 3200 (1994).

17. F. P. Brady, et al., Phys. Rev. C **50**, R525 (1994).

18. C. J. Zeitlin et al., Rad. Meas. **23**, 65 (1994).

19. C. J. Zeitlin et al., Radiat. Res., **145**, 655 (1996).

CHAPTER 11

PRODUCTION OF NEUTRONS FROM INTERACTIONS OF GCR-LIKE PARTICLES

by

L. Heilbronn [1]

[1]Lawrence Berkeley Laboratory, Berkeley, CA 94720

Chapter 11

PRODUCTION OF NEUTRONS FROM INTERACTIONS OF GCR-LIKE PARTICLES

INTRODUCTION

In order to accurately determine the radiation risk to astronauts from GCR, the nature of the secondary radiation field created by the fragmentation of GCR in shielding and tissue must be understood. Due to their high penetrabilities, neutrons are an important component of the secondary radiation field, especially for astronauts protected by thick shielding on lunar or Martian bases [1]. Because of their relatively short lifetimes, free neutrons are not present in the primary GCR. The predominant source of neutrons, then, is interactions of GCR in shielding materials. These interactions span the full range of GCR ions (protons, helium, and HZE) and GCR energies (100 MeV/nucleon and up), and hence neutrons are produced from an enormous set of varied and different interactions. Some studies have been conducted at ground-based accelerator facilities in regards to the production of neutrons from GCR-like interactions, but because accelerator resources are limited and because neutron experiments require a large amount of the time available at those accelerators, the best approach to the problem of determining the amount of neutron radiation behind shielding is through a calculational approach, such as the ones reported in references [1] and [2]. The models used to calculate neutron production behind thick shields will need cross-section data as input and thick-target production data for verification of the models' output. From the viewpoint of the experimentalist, the key questions are (1) What are the important sets of data needed by theorists for the development and verification of their codes, and (2) What data sets already exist that are applicable to the problem? The answers to those questions will help in the development of an experimental program that best addresses the problems concerning the production on neutrons behind shielding in various deep-space mission scenarios.

In answer to question (1), the data will need to shed information on some of the properties of the neutron flux such as total neutron production, angular distributions, and energy distributions. In addition, details on the systematics of neutron production on projectile mass and energy and target mass will be needed. The projectiles include protons, helium, and heavy ions with atomic number as large as 26 (iron). The projectile energies should at least span the range of energies around the peak of the flux distributions, namely 100 MeV/nucleon to 2 GeV/nucleon. Target masses should include possible shielding materials such as aluminum, water, and regolith components, as well as tissue components such as water, carbon, and nitrogen.

In the following sections, we describe some of the experimental results which are pertinent to question (2). In addition to briefly describing those results and how they apply to the issues raised above, we also outline some of the missing gaps in the database which we feel need to be filled.

NEUTRON PRODUCTION FROM PROTON INTERACTIONS

Since protons make up close to 90% of the GCR flux, data in regards to the production of neutrons from proton interactions are needed. One research program has produced an extensive set of measurements of neutron production from proton interactions in a variety of targets, including both thick-target (stopping and near-stopping target) yields and thin-target cross sections [3–6]. The measurements were done with proton energies of 113 MeV, 256 MeV, and 597 MeV, and with targets including Be, C, O, Al, Fe, W, Pb, and U. Neutrons were measured at energies as low as 500 keV and as high as the incident beam energy. Measurements were done at laboratory angles of 7.5, 30, 60, 120, and 150 degrees. This set of data covers much of the data needed to describe neutron production from GCR-like protons. Additional data that may be needed include measurements at 0 degrees with the systems mentioned above, measurements with water targets, and measurements at higher proton energies (up to 2 GeV).

NEUTRON PRODUCTION FROM HELIUM AND HZE INTERACTIONS

Although helium makes up about 10% of the GCR flux and HZE makes up about 1% of the GCR flux, one calculation [2] predicts that about 15% of the neutron flux behind 50 g/cm^2 of water comes from helium interactions, and another 16% comes from HZE interactions. As is the case with neutron production from proton interactions, any model that predicts neutron production from helium and HZE interactions needs cross-section data and thick-target data for input and verification. However, unlike the case with protons, the heavy-ion neutron database has a scant amount of applicable data. To our knowledge, there is only one reference [7] on neutron production from heavy-ion GCR-like particles stopping in shielding materials (177.5 MeV/nucleon and 160 MeV/nucleon helium particles stopping in C, Pb, steel, and water). There are a few references in regards to thin-target neutron cross-section data (see, for example, references [8–14]) that are relevant to GCR-like interactions. More data are needed in order to determine the systematics of neutron production on heavy-ion projectile mass and energy and on target mass. In order to fill in some of the missing gaps in the heavy-ion neutron database we have done two sets of accelerator-based experiments that have measured neutrons from heavy-ion interactions. What follows is a brief description of the results from those experiments for the purpose of illustrating the issues relevant to neutron production from GCR-like heavy-ion interactions.

272 AND 435 MeV/NUCLEON Nb + Nb, Al SYSTEMS

This set of data was collected from experiments carried out at the Bevalac facility at Lawrence Berkeley Laboratory. The 435 MeV/nucleon Nb beam was stopped in a Nb target 1 cm thick (8.57 g/cm^2), and the 272 MeV/nucleon beam was stopped in targets of 1.27-cm thick Al (3.42 g/cm^2) and 0.51-cm thick Nb

(4.37 g/cm^2). Data were taken from 14 detectors placed between 3º and 80º in the laboratory. Neutrons were detected at energies starting from 20 MeV up to twice the beam energy per nucleon.

Figure 1 shows neutron energy spectra at 3º, 9º, 16º, 28º, 48º, and 80º for the 435 MeV/nucleon Nb + Nb system. The error bars represent statistical uncertainties only. The solid lines are BUU (Boltzmann-Uehling-Uhlenbeck) model calculations of the data.

The broad peak in Figure 1 at 3º between 200 MeV and 400 MeV indicates a strong contribution from projectile breakup due to peripheral collisions with the target nuclei. Since the projectile may have any energy between 435 MeV/nucleon and 0 MeV at the time of collision, projectile breakup occurs over a wide range of velocities, hence the broadness of the peak at 3°. The spectra at 16º, 28º, 48º, and 80º have an exponential behavior which is typical of evaporation of fragments and nucleons from a hot source created in the overlap region between the target and projectile. There may also be some contribution from target evaporation in these spectra, but the low energy cutoff (about 20 MeV) is too high to see most of the neutrons that come from such a source. At 9º there is a transition from neutron spectra dominated by projectile-like neutrons to spectra that are dominated by neutrons emitted from the decay of the overlap region. Note that neutrons with energies above the beam energy per nucleon are observed, even out to 48º. This is typical of the collective nature of heavy-ion collisions, where individual nucleons in the projectile and target may get a momentum boost at the time of collision due to the Fermi motion of nucleons inside a nucleus. Figure 2 shows the same set of spectra for the 272 MeV/nucleon Nb + Nb system. The
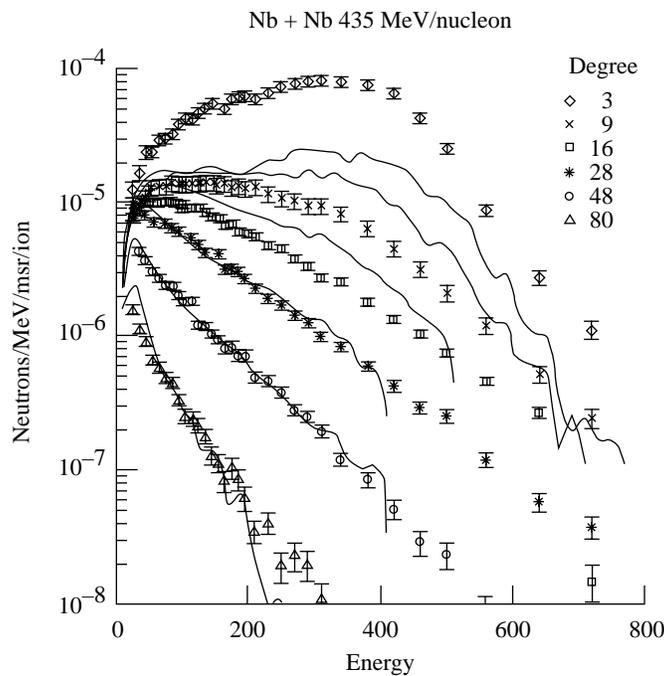

Figure 1.   Thick-target neutron spectra from the 435 MeV/nucleon Nb + Nb system at the indicated angles. The solid lines come from a fit to the data using BUU calculations.

same general features seen in Figure 1 are also seen in Figure 2, with the only significant change being the range of neutron energies at which these features occur. The shapes of the spectra for the 272 MeV/nucleon Nb + Al system are essentially identical to the 272 MeV/nucleon Nb + Nb system.

In order to predict the thick target neutron yields using BUU calculations [15], we have used a simple technique that builds up thick target yields using the cross sections calculated by the code. The physical dimensions of the detectors used in the experiment were included in the calculation of the thick target yield in order to account for any geometrical acceptance effects that may have affected the calculation.

The neutron cross sections were calculated at 50 MeV/nucleon intervals for each system. For the 272 MeV/nucleon Nb systems the calculations ran from 50 MeV/nucleon up to 250 MeV/nucleon, and for the 435 MeV/nucleon system the calculations ran from 50 MeV/nucleon up to 400 MeV/nucleon. Each separate calculation represented the neutron spectra produced by an incoming Nb ion in the target for a range of Nb energies. For example, the 200 MeV/nucleon Nb + Al calculation represented the neutron spectra produced by Nb ions ranging from 175 to 225 MeV/nucleon interacting in an Al target. All calculations represented a 50 MeV/nucleon span of Nb energies, except for the 400 MeV/nucleon calculation (which represented Nb energies between 375 and 435 MeV/nucleon) and the 50 MeV/nucleon calculation (used for Nb energies between 0 and 75 MeV/nucleon).
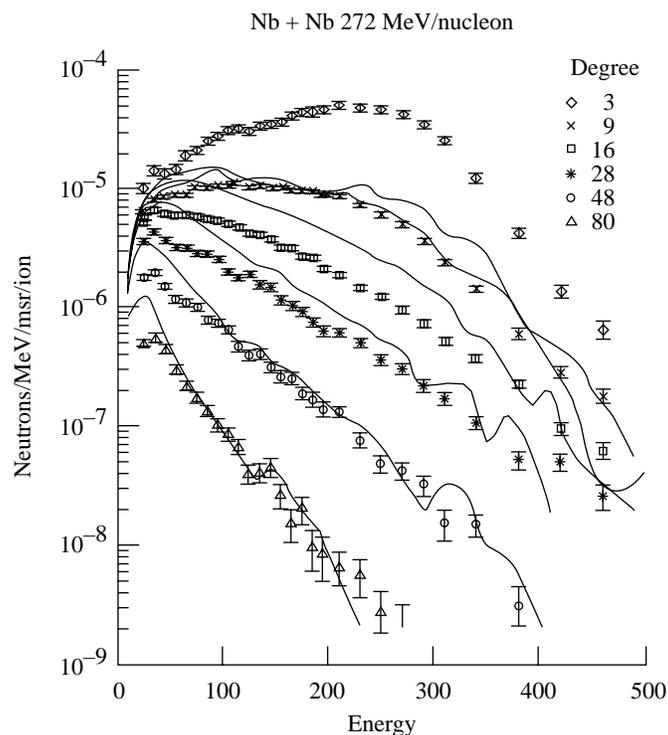
Figure 2.   Thick-target neutron spectra from the 272 MeV/nucleon Nb + Nb system at the indicated angles. The solid lines come from a fit to the data using BUU calculations.

The calculated cross sections were then put into a code that transported incoming Nb ions in the stopping target. The incoming Nb ion was passed through successive layers of the target, and at each layer the probability of undergoing a nuclear interaction was calculated using an energy-dependent geometric cross section. Then, using a Monte-Carlo method, it was determined whether or not the Nb ion underwent a nuclear interaction. If so, then the multiplicity of neutrons resulting from the interaction, as well as the distribution of neutron energies and angles, were determined by a Monte-Carlo method using the calculated neutron cross sections appropriate for the energy at which the Nb ion interacted. Each neutron produced was then followed to see if it made it within the geometrical acceptance of any of the detectors used in the experiment. Neutron interactions in the target were neglected. In this way, spectra for each neutron detector were built up by passing a large number of Nb ions through the target. A minimum of 10 million Nb ions were transported through the target in each of the simulations. The simulated thick target yields were then normalized for the number of Nb ions and for the solid angle of the detector, allowing for a direct comparison with the experimental data.

In general the BUU calculations do a good job of fitting the data at large angles, both in magnitude and shape. However, at the forward angles the BUU calculations either overpredict or underpredict the yield, depending on the angle and system. Even though the BUU calculation misses the magnitude of the forward angle spectra, it does a fairly good job in reproducing the shape of those spectra. Clearly, it would be helpful to have cross section data for the Nb + Nb and Nb + Al systems at a variety of Nb energies in order to find where the BUU calculations are not able to reproduce the data.

Figure 3 shows the angle-integrated energy distributions from all three systems. The solid lines show the fits to the data using BUU calculations. The BUU calculations fit the data well in the 435 MeV/nucleon Nb + Nb system, but underestimate the yield in the 272 MeV/nucleon Nb + Al system, and overestimate the yield below 100 MeV in the 272 MeV/nucleon Nb + Nb system. The disagreement between the model and data in the 272 MeV/nucleon Nb + Nb system indicates that the good agreement in the 435 MeV/nucleon Nb + Nb system may be fortuitous. Since the model overpredicts the yield below 100 MeV for incoming ion energies between 0 and 272 MeV/nucleon, it must underpredict that same yield for ion energies ranging between 272 and 435 MeV/nucleon in order to match the data for ion energies between 0 and 435 MeV/nucleon. This again points to the need for cross-section data in order to explore the finer details of the BUU calculations and find the points where the model can and cannot fit the data.

Table 1 shows the total neutron yield per incident ion for the indicated ranges in laboratory angle. The uncertainties shown include both statistical uncertainties and an assumed 10% systematic uncertainty in neutron detection efficiency. Also shown in Table 1 is the percentage of incident Nb ions that undergo a nuclear interaction in the stopping target, as calculated by stepping the incident beam ion through successive layers of the target and using the applicable energy-dependent geometric cross sections at each layer. For all three systems at least 80% of the total yield between 0º and 90º is contained in the forward 45º. Between 30% and 40% of the total neutron yield
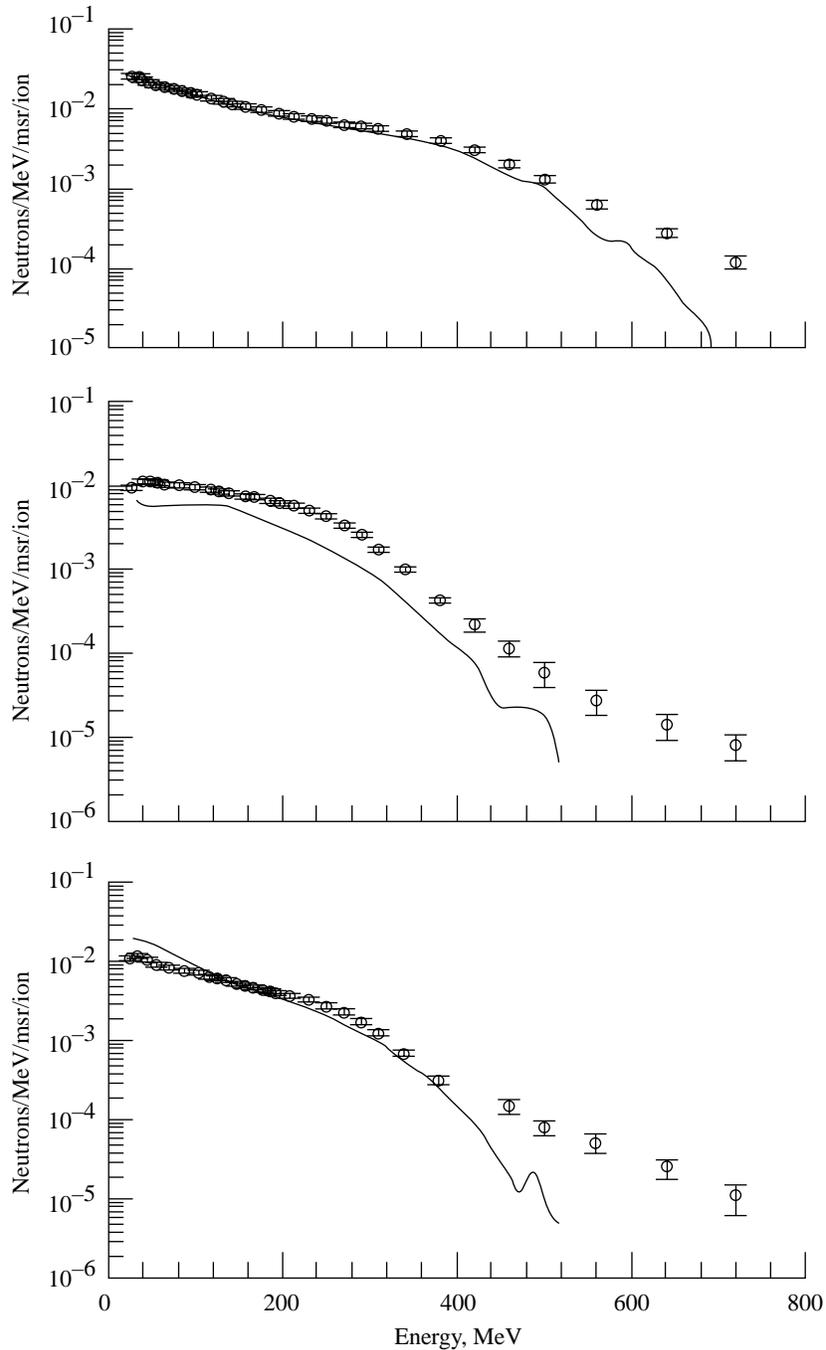
Figure 3.   Thick-target neutron energy distributions from all three systems. The solid lines show a fit to the data using BUU calculations.

is contained in the first 10º. Comparing the two Nb + Nb systems, one would expect from the % interacted calculation that the total yield from the 272 MeV/nucleon system would be about 1/2 of the total yield from the 435 MeV/nucleon system. In fact, the data show that the ratio of the two total yields is 0.38 ± 0.06. Keeping in mind that the data cut off below 20 MeV for both systems, that ratio may be closer to 1/2 if one could include data for neutrons between 0 and 20 MeV, since a larger fraction of the total 272 MeV/nucleon yield will be contained in

the first 20 MeV than it will for the 435 MeV/nucleon system's yield. One can argue, then, that to first order, the beam-energy dependence of the neutron yield scales as the number of interaction lengths seen by the projectile. Comparing the two 272 MeV/nucleon systems, one expects from the % interacted calculation that the Nb + Nb system's yield will be about 60% of the Nb +Al system's yield, and the data show the ratio to be 0.80 ± 0.13. It is difficult to extract any conclusions about the target dependence on the neutron yields from this data set since the lowest detected neutron energies are 20 MeV, which excludes a great deal of the neutron yield from target evaporation. It is interesting to note that Ref. [7], which also had neutron energies cut off around 20 MeV, found that the total neutron yield was independent of the target (about 0.5 neutrons per incident He). One can argue that here, too, the total neutron yield is independent of target for the same projectile, within uncertainties. Again, though, it is necessary to extend the measurements to neutron energies below 20 MeV in order to fully understand the target dependence on the total neutron yields.

Table 1. Neutron yields for the given systems and the given angular ranges in units of the number of neutrons above 20 MeV per incident ion. Numbers in the far right column indicate the estimated percentage of beam particles which undergo a nuclear interaction.

System	# neutrons 0–90 deg	# neutrons 0–10 deg	# neutrons 0–45 deg	% interacted
435A MeV Nb + Nb	4.45 ± 0.5	$1.3 \pm .15$	3.5 ± 0.4	23%
272A MeV Nb + Nb	1.68 ± 0.2	$0.54 \pm .06$	$1.38 \pm .15$	22.6%
272A MeV Nb + Al	$2.11 \pm .25$	0.8 ± 0.1	1.85 ± 0.2	19%

It is interesting to compare the neutron yields between the 256 MeV p + Al system and the 272 MeV/nucleon Nb + Al system. Figure 4 shows the yields from both systems at 7.5º, 30º, and 60º as a function of the atomic number of the projectile. At both 30º and 60º the yield from the Nb + Al system is about 10 times the yield from the p + Al system, whereas at 7.5º the yields differ by a factor of about 1000. This, along with the fact that there is an appreciable yield of neutrons above the beam energy per nucleon in HZE interactions with no such yield in proton interactions, best illustrates why the production of neutrons from HZE will need to be handled differently than in the case of production from proton interactions. The results shown here show that the production of neutrons from HZE interactions cannot be estimated reliably by a simple scaling of the neutron production from proton interactions.

155 MeV/NUCLEON He AND C + Al SYSTEMS

Thick target neutron yields from 155 MeV/nucleon He + Al and from 155 MeV/nucleon C + Al were measured at the National Superconducting Cyclotron Laboratory at Michigan State University. In addition to the thick target
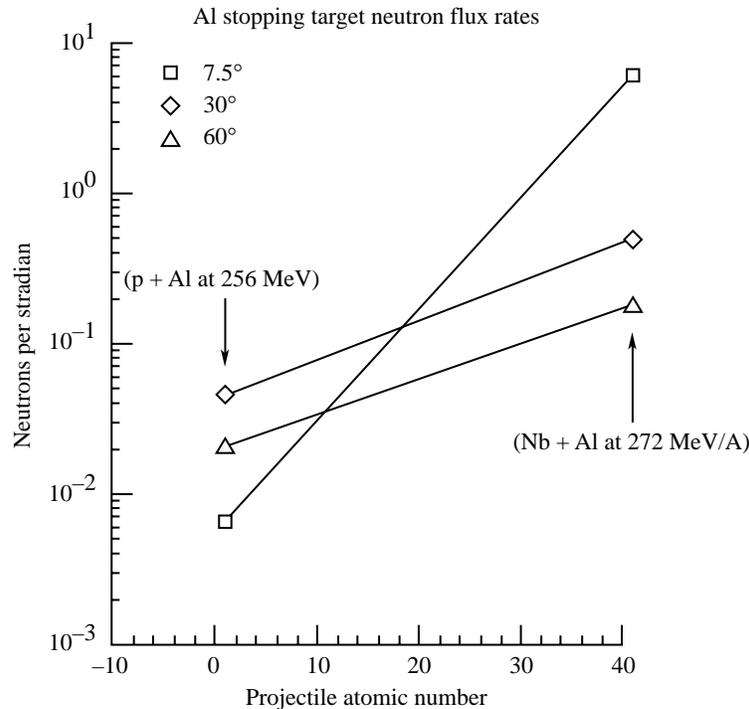
Figure 4. Comparison of neutron yields from 256 MeV p + Al and 272 MeV/nucleon Nb + Al interactions.

yields, cross section measurements were made for C + Al at 155 MeV/nucleon and 75 MeV/nucleon. Arrays of neutron detectors were placed from 4° to 160° in the laboratory. Analysis of the data is ongoing at this time. However, some preliminary thick-target spectra can be shown. Figure 5 shows unnormalized neutron spectra at 10º, 30º, 60º, 90º, 125º, and 160º for the 155 MeV/nucleon C + Al system.

As with the Nb systems, there is a strong contribution from projectile-like fragmentation in the forward direction, with neutron energies as high as twice the beam energy per nucleon. The spectra at the larger angles display the typical exponential behavior of the de-excitation of the overlap region of the beam-target collision. The data from these systems will be used to provide more information on the contribution to the yield from target evaporation.

CONCLUSIONS

The problem of determining the flux of neutrons produced by GCR interactions in shielding must ultimately be done using calculational techniques, which in turn require experimental data for verification of both the input and output of their calculations. To date the most complete data set available is with proton-induced interactions, although there are gaps in that data set which should be filled, such as extending the existing measurements to 0° and to higher incident proton energies. The set of data in regards to neutron production from heavy-ion induced interactions still requires a great deal of data in order to determine the systematics of neutron production on projectile mass and energy, target mass, production angle, and neutron energy. These systematics should cover a
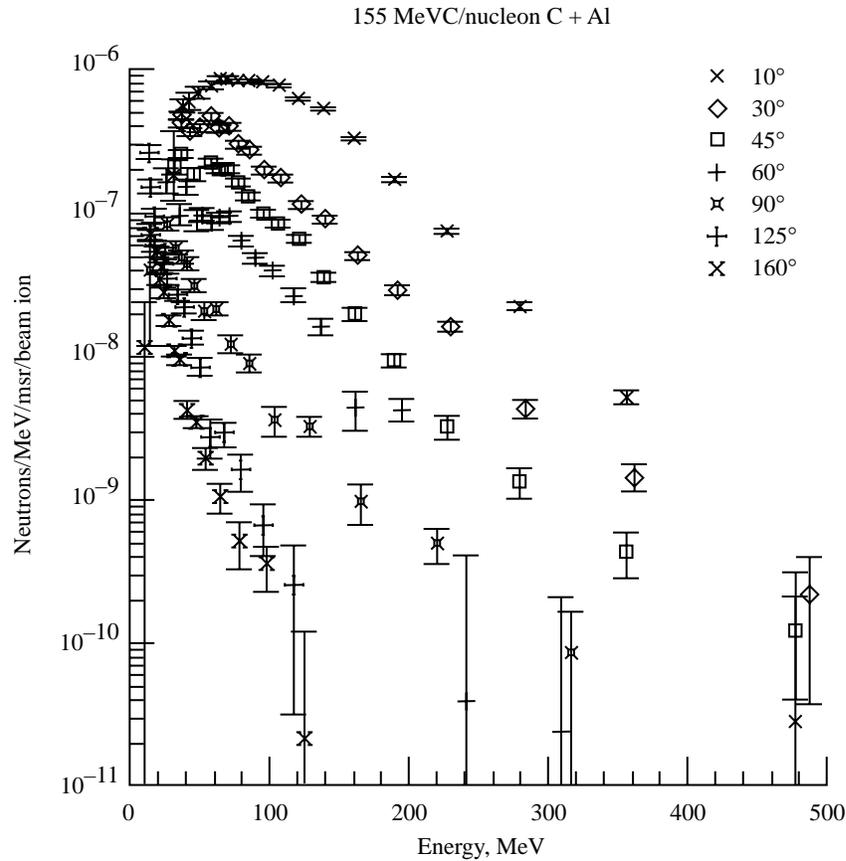
Figure. 5. Stopping-target neutron yields from 155 MeV/nucleon C + Al interactions at the indicated angles.

span of projectile energies from 100 MeV/nucleon up to 2 GeV/nucleon and projectile mass from He up to Fe. There is only one thick-target data set that looks at the dependence of the yield on projectile energy, and that set spans only a small part of the range (Nb + Nb reactions at 435 and 272 MeV/nucleon), and only looks at neutrons 20 MeV and above. There are two sets of data that look at the target-mass dependence on the yield (177.5 MeV/nucleon He + C, Al, Pb, and water, and 272 MeV/nucleon Nb + Nb and Al), and they have somewhat conflicting results. There is one set of thick-target data that looks at the projectile-mass dependence on the yield, and that only covers a small part of the range in mass (He and C interactions in Al at 155 MeV/nucleon). These measurements should also cover neutron energies down to 500 keV since neutrons in that range of energy still have large weighting factors in regards to their potential biological hazard. To our knowledge, no set of neutron production from heavy-ion thick-target interactions extends below 10 MeV. In addition, the comparison of the Nb + Nb and Nb + Al data with BUU calculations points to the importance of cross-section data for use in model calculations, and as is the case with thick-target data, there is an inadequate amount of cross-section data available.

ACKNOWLEDGMENTS

REFERENCES

1. L. C. Simonsen and J. E. Nealy, Radiation Protection for Human Missions to the Moon and Mars, *NASA Technical Paper 3079*, 1991

2. F. A. Cucinotta, Calculations of Cosmic-Ray Helium Transport in Shielding Materials, *NASA Technical Paper 3354,* 1993

3. M. M. Meier, D. A. Clark, C. A. Goulding, J. B. McClelland, G. L. Morgan, C. E. Moss, and W. B. Amian, Differential Neutron Production Cross Sections and Neutron Yields from Stopping-Length Targets for 113-MeV Protons, *Nucl. Sci. and Eng.* **102**, 310–321 (1989)

4. M. M. Meier, C. A. Goulding, G. L. Morgan, and J. L. Ullmann, Neutron Yields from Stopping-Length and Near-Stopping-Length Targets for 256-MeV Protons, *Nucl. Sci. and Eng.* **104**, 339–363 (1990)

5. M. M. Meier, W. B. Amian, C. A. Goulding, G. L. Morgan, and C. E. Moss, Differential Neutron Production Cross Sections for 256 MeV Protons, *Nucl. Sci. and Eng.* **110**, 289–298 (1992)

6. W. B. Amian, R. C. Byrd, D. A. Clark, C. A. Goulding, M. M. Meier, G. L. Morgan, and C. E. Moss, Differential Neutron Production Cross Sections for 597 MeV Protons, *Nucl. Sci. and Eng.* **115**, 1-12 (1993)

7. R. A. Cecil, B. D. Anderson, A. R. Baldwin, R. Madey, A. Galonsky, P. Miller, L. Young, and F. M. Waterman, Neutron angular and energy distributions from 710-MeV alphas stopping in water, carbon, steel, and lead, and 640-MeV alphas stopping in lead, *Phys. Rev. C* **21**, 2471–2484 (1980)

8. W. Schimmerling, J. W. Kast, D. Ortendahl, R. Madey, R. A. Cecil, B. D. Anderson, and A. R. Baldwin, measurement of the Inclusive Neutron production by Relativistic Neon Ions on Uranium, *Phys. Rev. Let.* **43**, 1985–1987 (1979)

9. R. A. Cecil, B. D. Anderson, A. R. Baldwin, R. Madey, W. Schimmerling, J. W. Kast, and D. Ortendahl, Inclusive neutron production by 337 MeV/nucleon neon ions on carbon, aluminum, copper, and uranium, *Phys. Rev. C* **24**, 2013–2029 (1981)

10. R. Madey, B. D. Anderson, R. A. Cecil, and P. C. Tandy, Total inclusive neutron cross sections and multiplicities in nucleus-nucleus collisions at intermediate energies, *Phys. Rev. C* **28**, 706–709 (1983)

11. R. Madey, J. Varga, A. R. Baldwin, B. D. Anderson, R. A. Cecil, G. Fai, P. C. Tandy, J. W. Watson, and G. D. Westfall, Inclusive Neutron Spectra at 0° from the Reactions Pb(Ne,n)X and NaF(Ne,n)X at 390 and 790 MeV per Nucleon, *Phys. Rev. Let.* **55**, 1453–1456 (1985)

12. R. Madey, W. -M. Zhang, B. D. Anderson, A. R. Baldwin, M. Elaasar, B. S. Flanders, D. Keane, W. Pairsuwan, J. Varga, J. W. Watson, G. D. Westfall, C. Hartnack, H. Stöcker, and K. Frankel, Inclusive neutron cross sections at forward angles from Nb-Nb and Au-Au collisions at 800 MeV/nucleon, *Phys. Rev. C* **46**, 1068–1076 (1990)

13. A. R. Baldwin, R. Madey, W. -M. Zhang, B. D. Anderson, D. Keane, J. Varga, J. W. Watson, D. Westfall, K. Frankel, and C. Gale, Inclusive neutron cross sections from Ne-Pb collisions at 790 MeV/nucleon, *Phys. Rev. C* **46**. 258–264 (1992)

14. H. R. Schelin, A. Galonsky, C. K. Gelbke, H. Hama, L. Heilbronn, D. Krofcheck, W. G. Lynch, D. Sackett, M. B. Tsang, X. Yang, F. Deak, A. Horvath, A. Kiss, Z. Seres, J. Kasagi, and T. Murakami, Neutron Production in Heavy-Ion Reactions at 35 and 50 MeV/Nucleon, *Nucl. Sci. and Eng.* **113**, 184–188, (1993)

15. P. Danielewicz and Q. Pan, Blast of light fragments from central heavy-ion collisions, *Phys. Rev. C* **46**, 2002–2011 (1992)

CHAPTER 12

HUMAN FACTORS IMPLICATIONS FOR SHIELDING

by

B. Woolford[1]

J. H. Connolly[1]

P. Campbell[2]

[1]Johnson Space Center, Houston, Texas 77058
[2]Lockheed Martin Space Mission Systems and Services, Houston, Texas 77058

Chapter 12

HUMAN FACTORS IMPLICATIONS FOR SHIELDING

INTRODUCTION

A number of human factors issues affect spacecraft and surface module design, and therefore shielding strategies and designs. First, the overall volume of the module ("module" will be used to refer either to the habitable portion of a spacecraft or to a surface habitable volume) depends on crew size and mission duration, and on the functions to be performed within it. Second, architectural features such as materials and layout within the volume are affected by gravity level, and by functional and habitability considerations. Finally, since the limiting factor is the total radiation exposure of the crewmember, the amount of extravehicular activity (EVA), in which less shielding is available, will drive the amount of radiation acceptable within the module. This allocation of crew time is partly mission driven, and partly driven by the use of technological alternatives to human EVA.

MISSION DURATION AND VOLUME

As demonstrated by the Gemini missions, relatively short durations (up to 2 weeks) can be endured by a person restrained to a couch or chair most of the time. The habitable volume per crewmember in Gemini was 0.57 cu m. [1,2]. However, the crew did perform EVAs, providing some relief. This level of restriction limits the functions a crewmember can perform to operating equipment and accessing supplies within reach from a relatively fixed position. It is also regarded as "tolerable," as opposed to a level permitting reasonable performance, much less an optimal level. For example, it does not permit reasonable levels of hygiene, allowing only for cleansing by wipes; it does not permit adequate access to medical facilities other than medication stored within reach, or to exercise countermeasures, recreation, waste management, or many other activities regarded as part of normal life. This level of restriction should be considered only as an extraordinary measure, for short periods, such as an EVA team being restricted to a heavily shielded rover during a solar particle event, when return to the habitat is impractical because of distance or equipment malfunction.

The Man-Systems Integration Standards, NASA-STD-3000, [3], recommends about 10 cubic meters of habitable volume per person as a minimal level at which performance can be maintained for mission durations of

four months or longer, and recommends about 20 cubic meters per person as optimal (Figure 1). Above four months,no significant increase in volume is needed for increased duration. Habitable volume should be interpreted as free volume, not volume occupied by equipment or stowage.

FUNCTIONAL ANALYSIS AND DESIGN

The functional analysis of the mission is essential to determining the amount and layout of the equipment and stowage. In μ-g, all parts of the volume are equally accessible for these, although a local vertical should be maintained in each module for crew efficiency and comfort. NASA-STD-3000 [3], Sec. 8.4, discusses orientation requirements. On the other hand, on the lunar or Martian surface, floor area becomes more significant than overall volume, and usable volume is limited to that which can be reached relatively easily. That is, all the volume of a 3-m high room may count towards "habitable volume" in μg, but not in a gravitational field. Shuttle crews routinely sleep in a variety of locations and orientations, but in a significant gravity environment, sleeping requires about a 2m x 1m horizontal area per person.

Functional adjacencies within the module may affect its shape, as well as being driven by it. Equipment used together, such as video displays and controls for teleoperators, or food stowage and preparation areas, should be in close proximity. On the other hand, some types of facilities must be widely separated. For example, the waste management and personal hygiene system should not be located next to the food preparation or dining areas for both hygienic and aesthetic reasons. The sleeping quarters should be acoustically isolated from the worst sources of noise during sleep periods, such as the waste management area. Again, the mission scenario drives design. When there is a small crew, operating on a single shift and sleeping at the same time, location of the sleep compartment is less important than when multiple shifts are planned, and noise from equipment and crew operations is always present. NASA-STD-3000 [3], Sec. 8.3.3, describes adjacency requirements.
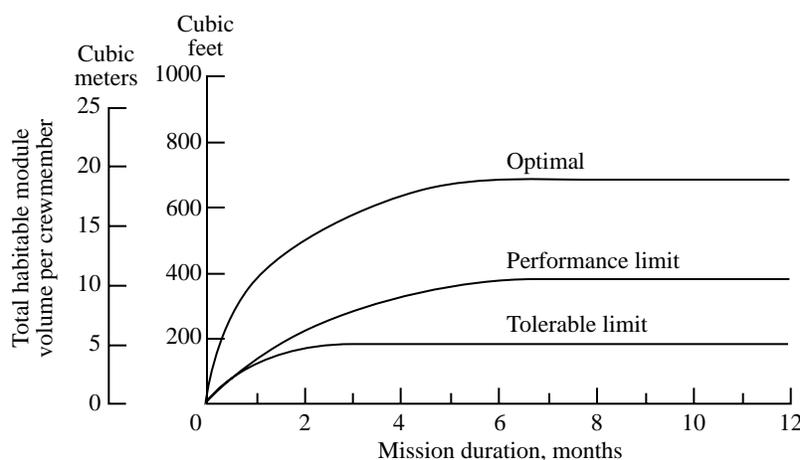

Figure 1.   Habitable Volume vs. Mission Duration

The significance of gravity in human biomechanics must also be considered in the issue of whether an interplanetary spacecraft can be used as a habitat on a planetary surface. In particular, the designation of local vertical must be made consistent with what will be the actual vertical on the surface. This may have design implications that result in a less than optimal layout for either environment. Another consideration in the spacecraft design for transit to Mars is the physical condition of the crew upon arrival. If the spacecraft is not designed to house the crew in a satisfactory manner for several days after landing, the crew will be required to don heavy extravehicular mobility units (EMUs) on their first encounter with gravity after several months in microgravity, and walk to the habitat. While some astronauts and cosmonauts have been able to stand and walk in Earth's gravity immediately after months in orbit, others have not been able to perform this task for a day or longer. Although Mars' gravity is significantly less than Earth's, the added mass of an EMU would decrease the effect of this difference. No conclusive data on means to reliably prevent this deconditioning are available.

MATERIALS AND DESIGN

Certain human factors considerations affect the materials used in module construction. First, since the Mercury flights, crewmembers have very strongly recommended windows. This requirement has been for both functional and psychological reasons. The International Space Station has windows integrated into the design, despite the increases in cost and the challenges in maintaining structural integrity. However, with the advent of high definition television and high resolution displays, and in view of the significantly increased radiation environment, it is likely that this requirement can be reduced, provided that the crew has access to high fidelity exterior views at all times. Trade-off studies and consultation with crewmembers may be required.

Another consideration is the design of airlocks for transit vehicles and particularly for surface habitats, where the hatches, and access to and from the outside, must be designed for quick, easy, reliable operation, and must not require excessive strength for operation. Possible scenarios include an EVA team returning with an injured member who must be carried into the habitat, or an EVA crew which has had to walk back from a broken rover, with resulting fatigue. This requirement for operation with minimal strength may affect the mass or other design features of the hatches.

Interior to the vehicle, some advantages in shielding may be obtained by the stowage of consumables in an enclosing arrangement around the habitable volume. Crew consumables include water, food, clothing, etc. The shielding properties of these materials will differ from each other. The amount of water will depend on the degree of recycling; the amount of food, on the use of plants grown for this purpose or for environmental control. However, equipment may also need to be arranged around the free space to allow room for operation by some crewmembers and a passageway for others to move from one area to another. Clearly, the design must permit access to the stowage areas without moving or disassembling equipment. Similarly, if plants are grown for food or environmental support in a habitable module that also serves other functions, the location of the trays and associated equipment (lights, liquids, and associated plumbing and pumps) should be planned both for any contribution

possible to increasing shielding and for easy access for care and harvesting. Another consumable, fuel, may be used for shielding outside the pressurized module, if precautions are taken to ensure that incidents such as a meteorite strike will not cause the fuel to either enter the module as a contaminant, nor, of course, burn the module.

Materials and layout of equipment and volume should also contribute to the habitability of the environment. Visual stimuli, including personal choices of pictures, variety of color and texture of the surfaces, etc., are necessary. Sound abatement is a very important criterion in interior design and layout, since prolonged exposure to high noise levels can cause permanent hearing damage, and even short durations of lower level noises can cause distraction, poor communications, and loss of productivity and efficiency. Such considerations affect any interior partitions which may be used for additional shielding.

MISSION OPERATIONS AND GOALS

Defining mission goals is logically the first step in spacecraft and habitat design. Until the purpose of the mission is clear, neither crew size nor duration can be meaningfully decided. Further, it determines the amount and types of equipment and supplies that must be available to the crew, from food to workstations to surface rovers. Sending humans to the Moon or Mars implies that there will be extensive extravehicular activity (EVA); However, the more time the crewmembers spend in EVA, the higher the exposure to radiation, and the lower the remaining budget for exposure inside the habitat. Separate discussions on EMUs and Rovers will address the shielding available from proposed EVA scenarios and equipment designs.

Exposure during EVA will also be affected by the design of any surface transportation, such as rovers. Since contingency planning requires assurance that the EVA team can return from any exploration, even if the rover malfunctions, sorties may be very limited in range unless redundancy is provided by a pair of rovers escorting each other, each with sufficient volume to accommodate all of the team. If lengthy or overnight expeditions are planned, the rovers should be designed to provide protection from normal levels of radiation, and a storm shelter in the case of solar particle event, either through intrinsic shielding or by being able to construct a shield from the lunar or Martian soil.

Within the habitat, the crew will spend more time in some areas and less in others, which again may affect shielding strategy. At least 8 hours per day are necessary for sleep; heavily shielded sleep compartments, or even protective coverings worn during sleep, could reduce total radiation exposure. Areas of lower shielding may include plant growth chambers. The design goal of current work in plant growth calls for minimal crew time requirements—a few hours per week, perhaps, after initial setup. Depending on the effects of radiation on the plants themselves, this would seem to be a candidate facility for less shielding. The time spent in the exercise area in transit may be a couple of hours per person per day. (Exercise requirements in lunar or Martian gravity are not known. Surface EVA will provide a significant amount of exercise of the load-bearing muscles and bones, due to the mass of the EMU.) Hygiene, dressing, and preparing for sleep require about another two hours. Food preparation and dining should be allocated about three hours per person per day, if Shuttle-type food is used,

requiring minimal preparation. For processing fresh food from a plant growth chamber, or preparing more elaborate meals for the group, one person may spend more time in the galley/wardroom. For long-duration missions, group meals, and in particular occasional "feasts" to mark special events or milestones, are recommended for psychological reasons [4]. The remaining time, about 10–12 hours per day, would be spent primarily on mission operations. Laboratories may therefore require significant shielding.

On missions exceeding a couple of weeks, rest days for personal recreation and activities are essential for the psychological well-being of the crew. If the sleeping quarters are adequately spacious and properly furnished with lights and a surface for writing, supporting a laptop computer or other audiovisual and communication equipment, members wishing privacy can use these locations. Other activities, such as group viewing of movies, might employ the displays used for external viewing. Conversations can be held in the wardroom or other work areas. Thus the recreational requirements can probably be fulfilled with dual use of areas required for mission operations.

CANDIDATE DESIGNS

The Johnson Space Center has developed a number of possible designs for surface modules over the last several years in conjunction with center and agency initiatives for lunar/Mars exploration. In a recent NASA Mars mission study, Weaver and Duke [5] proposed a cylinder, 7.5 m in diameter, vertically oriented with two levels, as a common module to be replicated, with modifications as necessary, for all mission phases. This concept is further developed in an in-house report by Weaver [6]. The integration of a plant growth subsystem into these modules is explored by Campbell and Moore [7]. These papers do not directly address the matter of shielding, but concentrate on mass, volume, and layout.

Proposals to construct a habitat separate from the transit vehicle, using local resources to build a shield, have also been presented. These include a design from the Lunar Outpost Study [8] to build a spherical, inflatable habitat partially underground, with a 1 m regolith-filled coil surrounding the aboveground portion. This particular design assumes a large crew, and estimates of the mass of atmospheric gases, interior equipment to be installed, construction equipment, etc., as well as the amount of crew time needed to erect and outfit the habitat and put the regolith shielding in place, make it questionable whether this design is as efficient as integrating multiple modules, assembled on Earth or in LEO.

MODELING TOOLS

The JSC Flight Crew Support Division (FCSD), in cooperation with other NASA divisions and program offices, has developed two tools which may be of use in estimating the mass and volume required for various crew sizes and mission durations. The Habitation Development Tool (HDT) is a habitable module parametric sizing tool described by Razzack, Campbell, and Bond [9]. The user inputs include crew size, mission length, technology choices for the various subsystems (life support, health care, thermal control, electrical power, etc.) and other variables, and the program computes the mass and pressurized volume for the habitable module. The HDT model can be used to estimate the size and mass of habitable modules for many different space flight missions. It is most

useful to personnel who are familiar with both flight crew support techniques and with the design of space flight missions, and is not generally distributed outside FCSD.

The Crew Habitable Element Estimation of Radiation Shielding (CHEERS) model is focused on radiation shielding requirements and mass estimates. Inputs include crew size, stay time, environment, radiation type of interest, allowable dose equivalent, shield material, and information about the habitable element. The outputs include an estimate of shield mass, of the inherent shielding provided by the habitable element, and of the additional shielding required. Multiple runs can be performed to generate plots showing shield mass versus allowable dose, or radiation dose equivalent versus mission elapsed time. This program is based primarily on data produced by the NASA Langley Research Center and is documented in Campbell [10]. The CHEERS model is integrated into the 1995 version of the HDT.

CONCLUDING REMARKS

Most of the questions regarding radiation shielding are not related to human factors at all - material properties, radiation sources and levels, the medical effects of different types and doses of radiation. However, when the shielding becomes integrated with the place people live and the functions they perform, human factors issues must be considered. The use of materials that are essential for human survival and performance to provide shielding is one example of the interaction of the two disciplines. Undoubtedly the optimal arrangement of consumables and equipment will differ for human factors criteria and for shielding criteria. If the crew sustains damaging or lethal radiation exposure, human factors are irrelevant. But if the shielding strategy prevents the crew from achieving the mission objectives, the same result could have been achieved by keeping the crew on Earth, at far less cost. It is in the interests of both disciplines to work together to achieve their mutual goals: a healthy crew performing its work effectively with minimum risk and difficulty.

REFERENCES

1. NASA, Project Gemini, A Chronology. The NASA Historical Series, 1969.

2. A. Nicogossian, S. R. Mohler, O. G. Gazenko, and A. I. Grigoryev (eds.): Space Biology and Medicine: Joint U.S./Russian Publication in 5 Volumes, **2(16)**, Astronaut Activity. American Institute of Aeronautics and Astronautics, Washington, D.C., 1994.

3. NASA, Man-Systems Integration Standards, NASA-STD-3000, Rev. B., **1**, 1995.

4. J. W. Stuster: The Modern Explorer's Guide to Long Duration Isolation and Confinement: Lessons Learned from Space Analogue Experiences, Report For NASA, JSC, 1995.

5. D. B. Weaver and M. B. Duke: Mars Exploration Strategies: A Reference Program and Comparison of Alternative Architectures. AIAA Space Programs and Technologies Conference, Huntsville, AL, 1993.

6. D. B. Weaver: A Mars Habitation System, in-house report, Flight Crew Support Division, Johnson Space Center, 1993.

7. P. D. Campbell and N. R. Moore: Integration of Plant Growth into a Mars Habitat. In-house report, Flight Crew Support Division, Johnson Space Center, 1994.

8. J. Alred, A. Bufkin, K. J. Kennedy, A. M. Roberts, J. Stecklein, and J. Sturm: Lunar Outpost, in-house report, Advanced Programs Office, Johnson Space Center, 1989.

9. A. Razzak, P. D. Campbell, and R. L. Bond: Habitation Development Tool, AIAA Number 95-3556, AIAA 1995 Space Programs and Technologies Conference, Huntsville, AL, 1995.

10. P. D. Campbell: Crew Habitable Element Space Radiation Shielding for Exploration Missions. LESC-30455, prepared for Flight Crew Support Division, Johnson Space Center, 1992.

CHAPTER 13

ROVERS

by

John F. Connolly[1]

[1]Johnson Space Center, Houston, Texas 77058

Chapter 13

ROVERS

INTRODUCTION

Planetary surface mobility is a key to increasing the range in which EVA astronauts are able to explore. Space suits are the primary means of surface mobility, but limit an astronaut's range of exploration to "walkback distance." Walkback distance is a function of the time which it takes to return to a place of safety, and can be limited by factors such as the amount of life support consumables carried on EVA or by the rise time of a solar particle event.

Rovers were first employed on Apollo 15 as a way to extend surface mobility range. Prior to the first Lunar Roving Vehicle (LRV), the maximum range an EVA crew traversed was only 1.1 km from the lunar module. With the addition of the LRV, crews increased their range to as much as 8.9 km from the LM. The increased range greatly increased the science content of the later Apollo missions, as it provided access to almost two orders of magnitude more surface area than prior surface missions.

Calculating the range (defined here as the accessible radial distance from a base or safe haven) which a rover allows crews to reach requires assumptions as to the average speed of both rovers and EVA crewmembers on foot. Along a straight-line path, nominal velocities of 2.5 km/hour for unaided EVA and 7.5 km/hour for rover traverses are consistent with Apollo experience. If EVA crewmembers carry 8 hours of life support consumables with them, a single, unpressurized rover would therefore be limited to a range of 15 km from the base. Multiple unpressurized rovers would increase this range to 26 km, and the addition of a single pressurized rover would increase the range to 60 km.

These ranges assume that life support consumables are the limiting factor in range calculation. In fact, radiation protection may be the limiting factor, and the maximum distance from a base or safe haven may be reduced to the distance which can be traversed before radiation flux or energy rises to a predetermined limit. For many of the lunar and Mars exploration studies performed between 1989 and 1995, an average SPE "rise time" of 2 hours was assumed, after which crews would need to be at a location with adequate radiation protection.

TYPES OF ROVERS

Crewed rovers are divided into two classes, pressurized and unpressurized [1]. Unpressurized rovers are characterized by an open crew cockpit which requires that each crewmember's EVA suit function as their only life support system for the duration of the sortie. Unpressurized rovers are usually thought of as lightweight, utilitarian and highly mobile. The Apollo LRV (figure 1) is an excellent example of an unpressurized rover. Although it has a mass of only 249 kg, its simple and robust design allowed it to carry 521 kg of crew and cargo.

Pressurized rovers are complete spacecraft on wheels. In addition to their mobility systems, they contain all the subsystems than any human-rated spacecraft such as the space shuttle or space station must contain. The fact that pressurized rovers are full-fledged spacecraft put them in a range of complexity and cost which is far above that of unpressurized rovers. Figure 2 shows a concept for a pressurized rover [2].

SORTIE TIME AND DISTANCE

As stated in the introduction, it is assumed that an EVA suited crewmember can traverse a radial path at approximately 2.5 km/hour, and that the addition of a rover increases surface velocity to approximately 7.5 km/hour. Speeds in excess of 7.5 km/hour were indeed attained on the lunar surface, but the low lunar gravity caused the LRV's wheels to increasingly lose contact with the surface as velocity was increased.
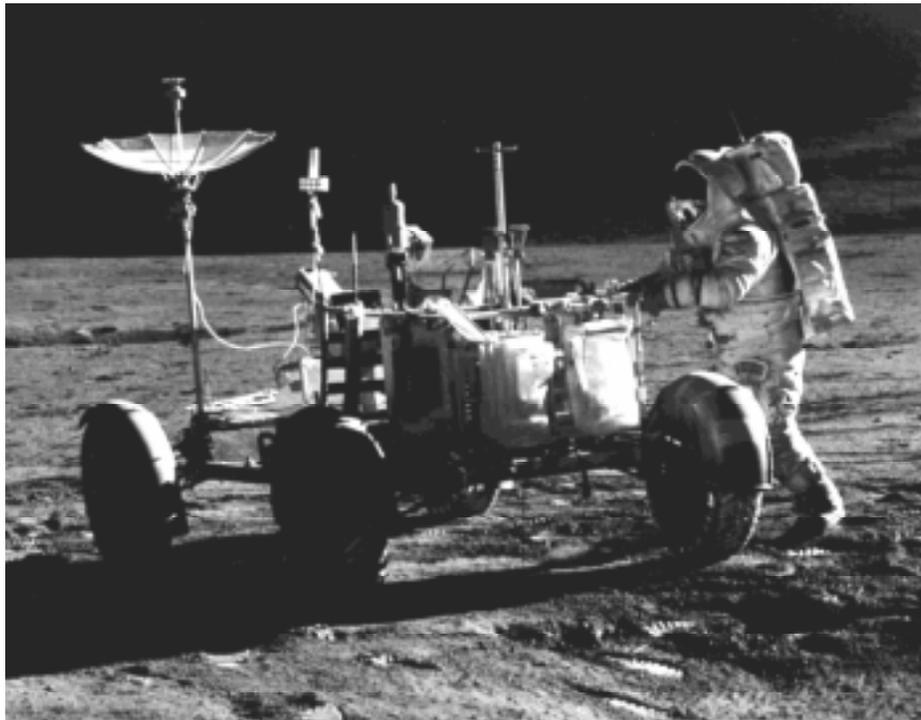
Figure 1.   Apollo Lunar Roving Vehicle
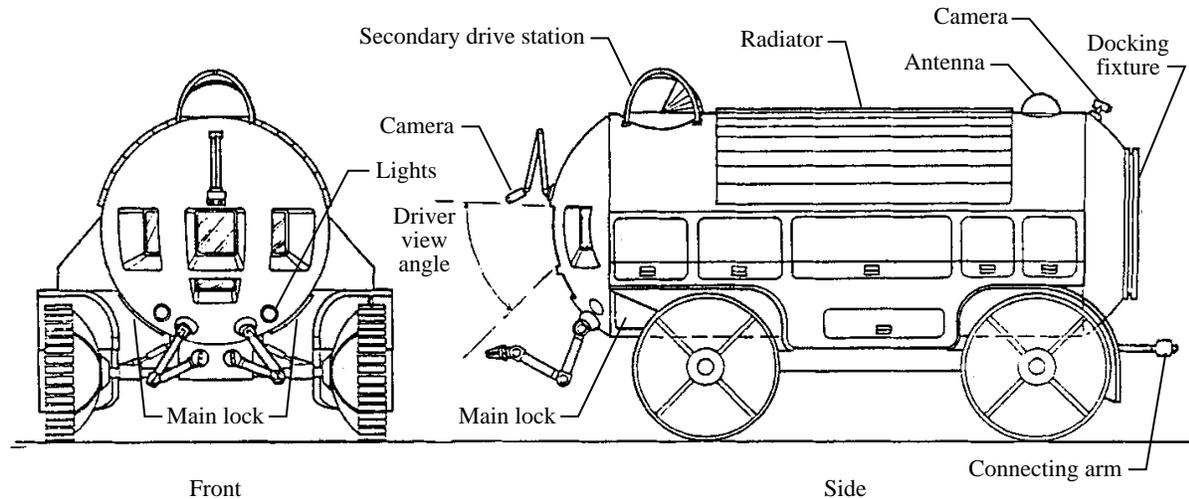
Figure 2.   Pressurized Rover concept

Life Support system lifetime, usually measured by the amount of consumables carried, is the second factor in computing sortie capability. Apollo moonwalkers carried enough consumables for approximately 8 hours of EVA, but were limited to three consecutive workdays on the lunar surface. Future crews, especially those traveling to Mars on conjunction-class missions, may have as many as 500 days to explore the planet. This may change the desired duration and scheduling of EVAs. Currently, mission planners are investigating 6-hour EVA durations as a better match for crew comfort.

Figure 3 shows a surface mobility continuum generated for NASA's 1992 "First Lunar Outpost" (FLO) Study. The Mare Smythii site is shown in the lower right with concentric arcs showing the limits of Apollo EVAs and the desired range for FLO exploration. The 20-km unpressurized rover range was possible only with two rovers delivered to the Outpost location. In a worst-case scenario, EVA astronauts begin their EVA by roving 20 km (2.67 hours) from the Outpost and then develop a rover failure. They begin to walk back to the Outpost at 2.5 km/hour, but will exceed their 8 hours of consumables before they arrive at the base. Therefore, the remaining two astronauts begin an EVA on a second rover, meet the first crew en route, and return them to the Outpost. The pressurized rover range shown is a lower limit and would eventually only be limited by consumables storage and crew time. A pressurized rover sortie of one week (168 hours) is estimated to cover a range of 135 km.

UNPRESSURIZED ROVERS

Pictures of the Apollo LRV bounding across the lunar surface give us a clear mental image of exactly what an unpressurized rover is. Many of the concepts for unpressurized rovers studied since Apollo have arrived at similar design solutions. In each case the rover held two primary crewmembers and some amount of cargo. The crewmembers wore only EVA suits as protection from the environment of the surface. Unpressurized rovers were typically powered by batteries or fuel cells, which were well suited for their limited service.
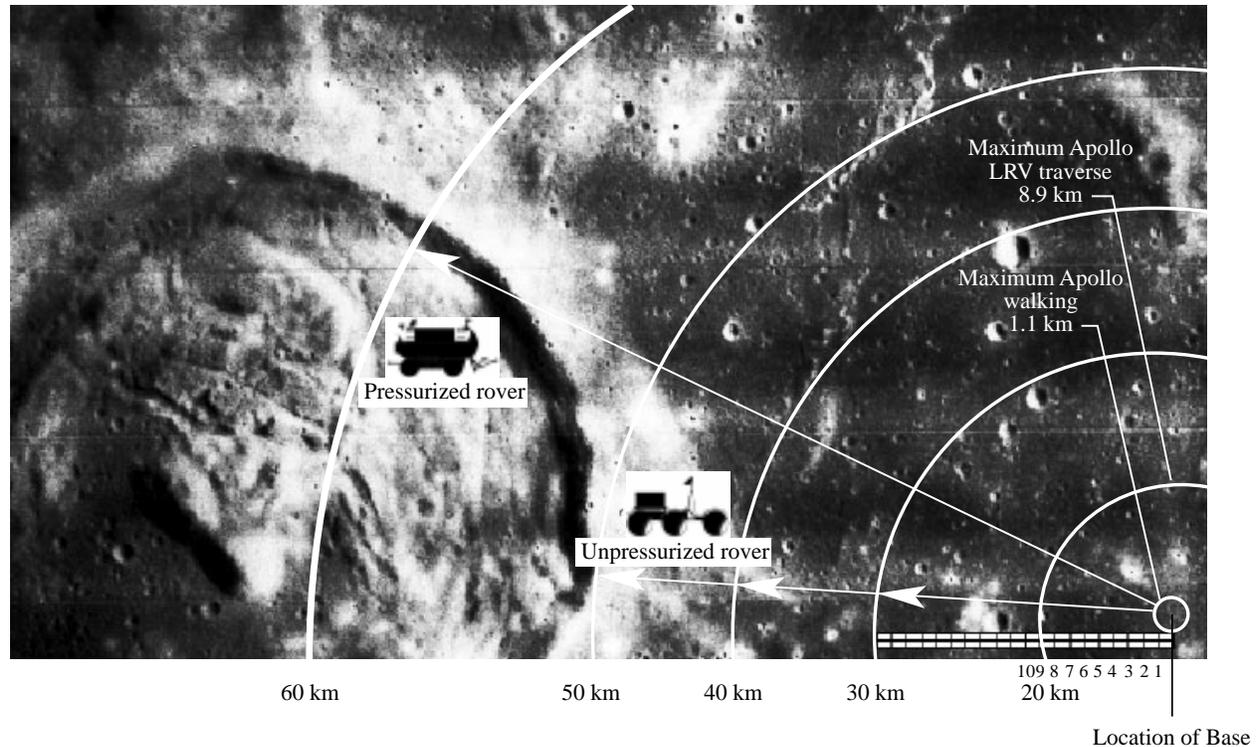
Figure 3.   Surface Mobility Continuum for the First Lunar Outpost Study

Unpressurized rovers offer no inherent radiation protection to their occupants, so an EVA crew 20 km from their Outpost may be almost 3 hours from a safe haven if a radiation event occurs. The only radiation protection available to the crew on an unpressurized rover is that which comes from their EVA suits.

Man-made radiation sources may also affect these crews. In a number of designs seen since 1989, radioisotope power supplies have been suggested for piloted rovers. One example is a FLO utility rover [3] shown in figure 4. In order to attain the power levels necessary for mobility systems, dynamic power conversion systems are matched with radioisotope heat sources. These Dynamic Isotope Power Supplies (DIPS) systems have the advantage of delivering constant power in the 1- to 3-kW range, but offer the distinct disadvantage of a radiation hazard.

The FLO utility rover was conceived to utilize a solid shadow shield to separate the crewmembers from the DIPS power system. The characteristic radiation field from an unshielded DIPS power source is shown in Figure 5. In the case of the FLO rover, the crew would be oriented in the "B" direction. Neutron and Gamma Ray attenuation for the DIPS is shown in figure 6, and a further mass breakdown of this rover is shown in figure 7. The lithium hydride shadow shield was sized to limit the crew's integrated radiation dose from the DIPS to about 0.01 rem/hour.
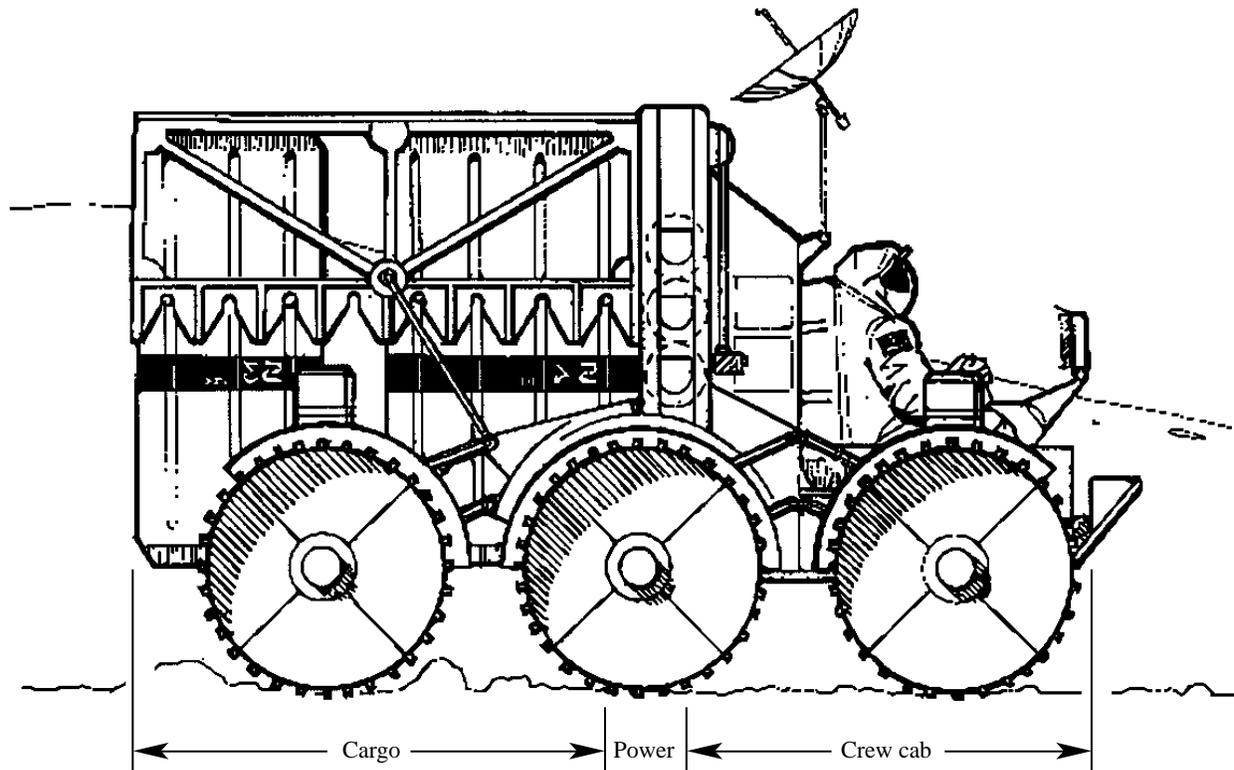
Figure 4.   First Lunar Outpost utility rover. This 922 kg rover is capable of carrying crew and cargo totaling 1000 kg. The DIPS power system is located behind the crew station and is separated by a shadow shield.

PRESSURIZED ROVERS

As early as 1964, NASA was considering pressurized rover designs for second generation Apollo lunar landings. The Mobile Lunar LABoratory (MOLAB) (Figure 8) would have been landed on a dedicated cargo lander and would have provided 2 crewmembers the ability to spend 14 days on the lunar surface traversing 400 km. The MOLAB concept progressed to the mockup and ground test phase before its future, and the Apollo program, in general, was cut short.

Pressurized rovers are still a goal of planetary exploration mission planners, and appear in every exploration study conceived since Apollo. Much more attention to radiation protection has been paid to pressurized rovers due to the long sortie durations associated with them. Because pressurized rovers are in fact complete spacecraft, with thermal, power, life support, crew accommodations, communications, guidance, navigation and propulsion (mobility) systems, there is greater opportunity to make use of their inherent systems as a first level of radiation protection.
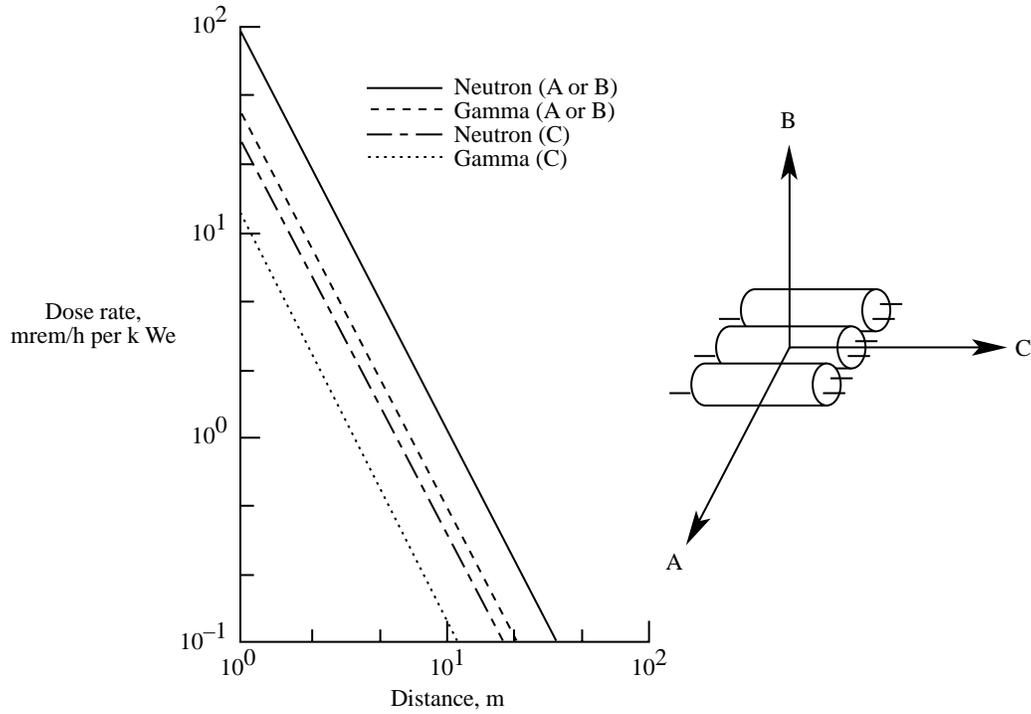
Figure 5.   Unshielded DIPS Radiation Field
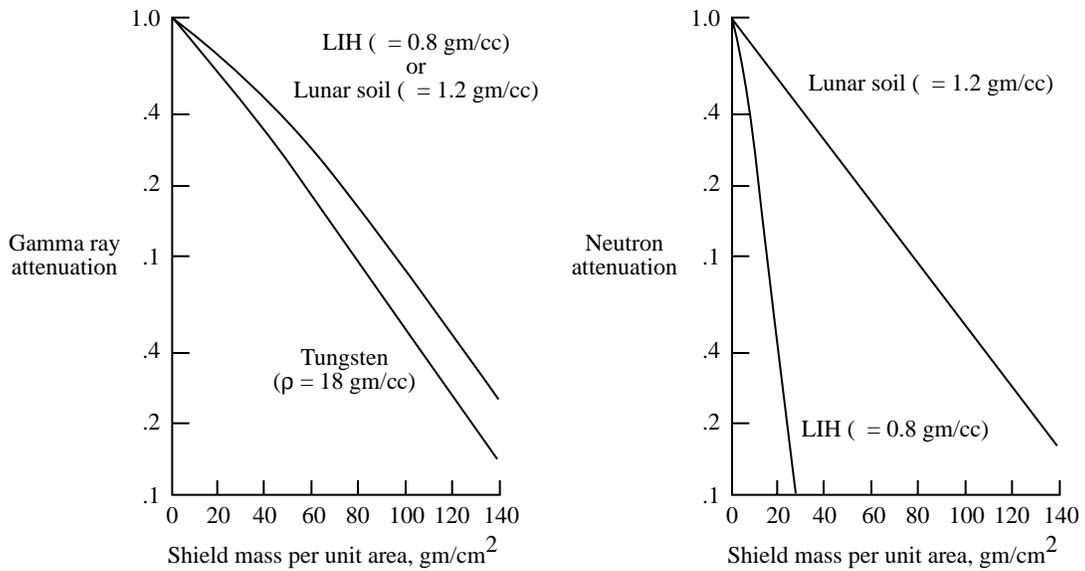
Figure 6. Radiation Attenuation Factors

| Chassis | 95 kg |
Mobility system	135 kg
Crew station	20 kg
Comm/data/nav	45 kg
Power/thermal	467 kg
Payload support	140 kg
Robotics package	30 kg
Total	922 kg
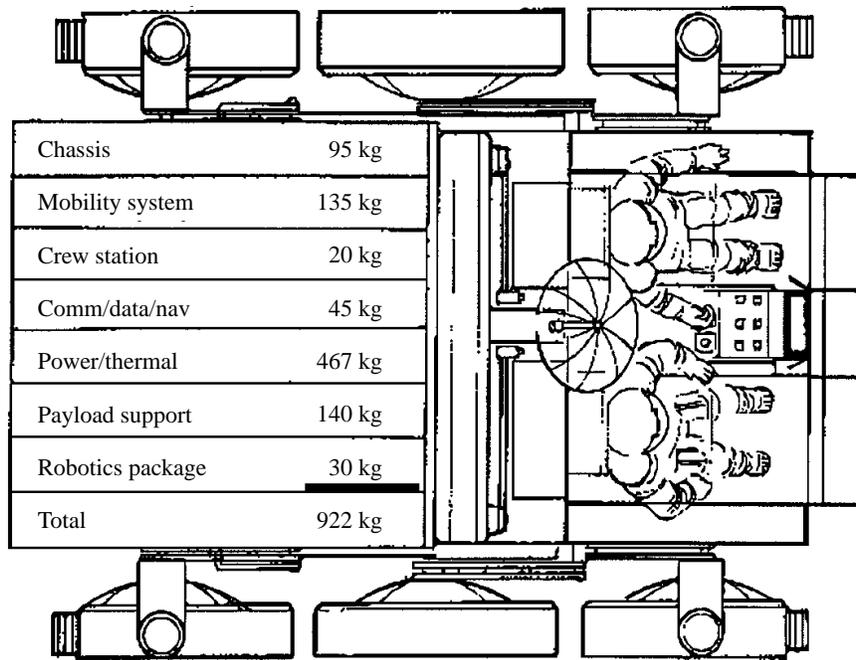
Figure 7. FLO utility rover mass breakdown.
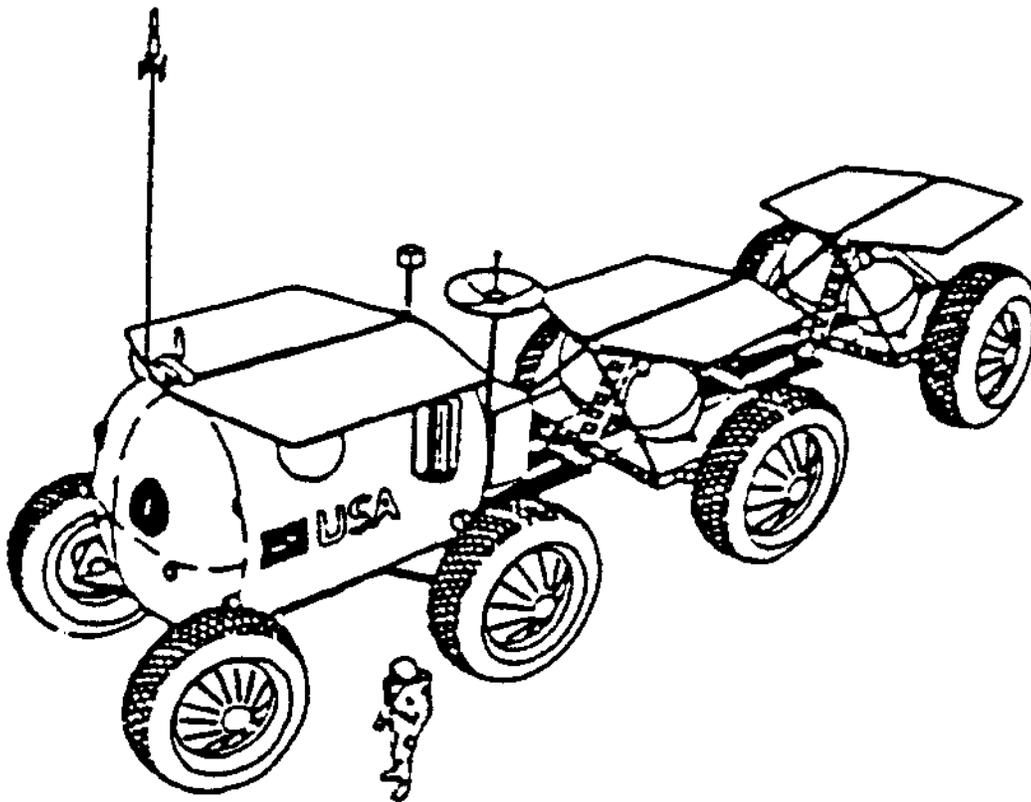
Figure 8. MOLAB Pressurized Rover concept.

279
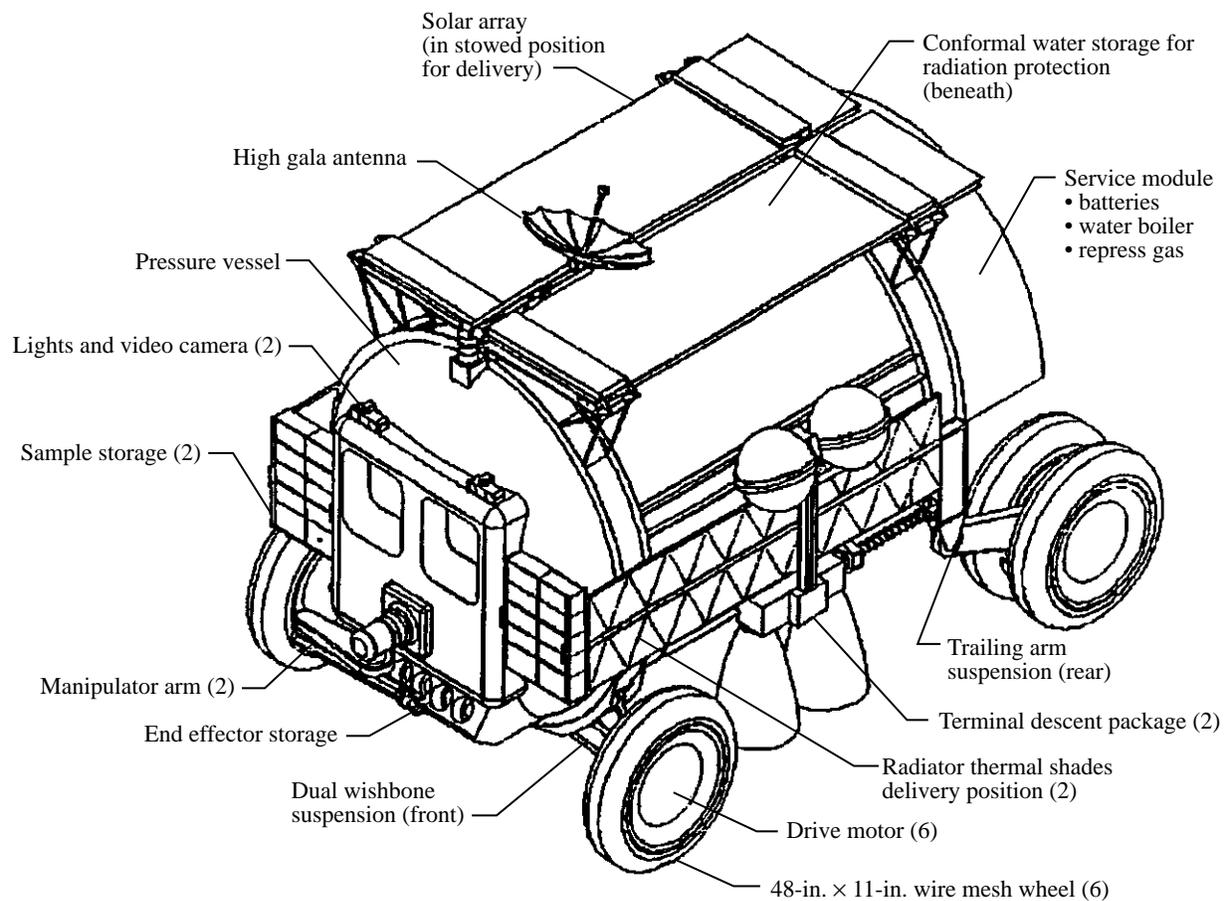
Figure 9.   Boeing "Rover First" Concept.

A small pressurized rover concept developed by Boeing [4] in 1992 is shown in Figure 9. Although this rover has a mass of only 4400 kg, it contains all the necessary subsystems to perform a 14-day, 240-km sortie with two crewmembers. Boeing calculated crew radiation levels within the rover by first optimizing the arrangement of the equipment racks and storage tanks. They generated contours and vector dose data utilizing the Boeing Radiation Exposure Model (BREM) analysis tool. The solid model was constructed utilizing the material densities shown in Figure 10, rack locations and equipment densities shown in Figure 11.

Without any additional radiation protection other than the inherent equipment, the Boeing design limited the crew radiation exposure for both skin and BFO to less than the NCRP limits in every case except the August 1972 SPE model. Some optimization of the internal equipment may improve the inherent shielding, but alternate protection for SPEs should also be investigated. These alternative methods include:

•   In-situ shielding options (lunar regolith)

•   Conformal water storage (fuel cell by-products or life support water storage)

•   Alternate materials (lightweight, low Z materials)

Material	Density, g/cm³	Material	Thickness, cm
Pressure vessel	2.86	2219 Al	0.318
Micrometeoroid shield	2.71	6061 Al	0.127
MLI blanket	0.192*	*	0.352
Modeled racks	**	**	**
Glass	2.20	Fused silica	variable

The MLI is configured in 21 layers. Sheldahl catalog data were used to calculate the nominal area of the layers at .068 g/cm². The MLI is composed of glass cloth, Teflon, Dacron, Mylar, Kapton, and Nomex, with microthin layers of vapor deposited aluminum. The compressed thickness of the MLI is estimated at .35 cm, leading to an average density of .192 g/cm³. Compositions for use in the model are as follows: C-47.2%, O-35.3%, Si-11.8%, H-3.7%, Al-1.0%, and N-1.0%.

**Rack densities have been assigned in accordance with individual rack mass and volumes. Rack mass and densities are proviced in the following chart.*

Comprised of Si-47% and 0.53%

Figure 10.   Solid Model Materials List
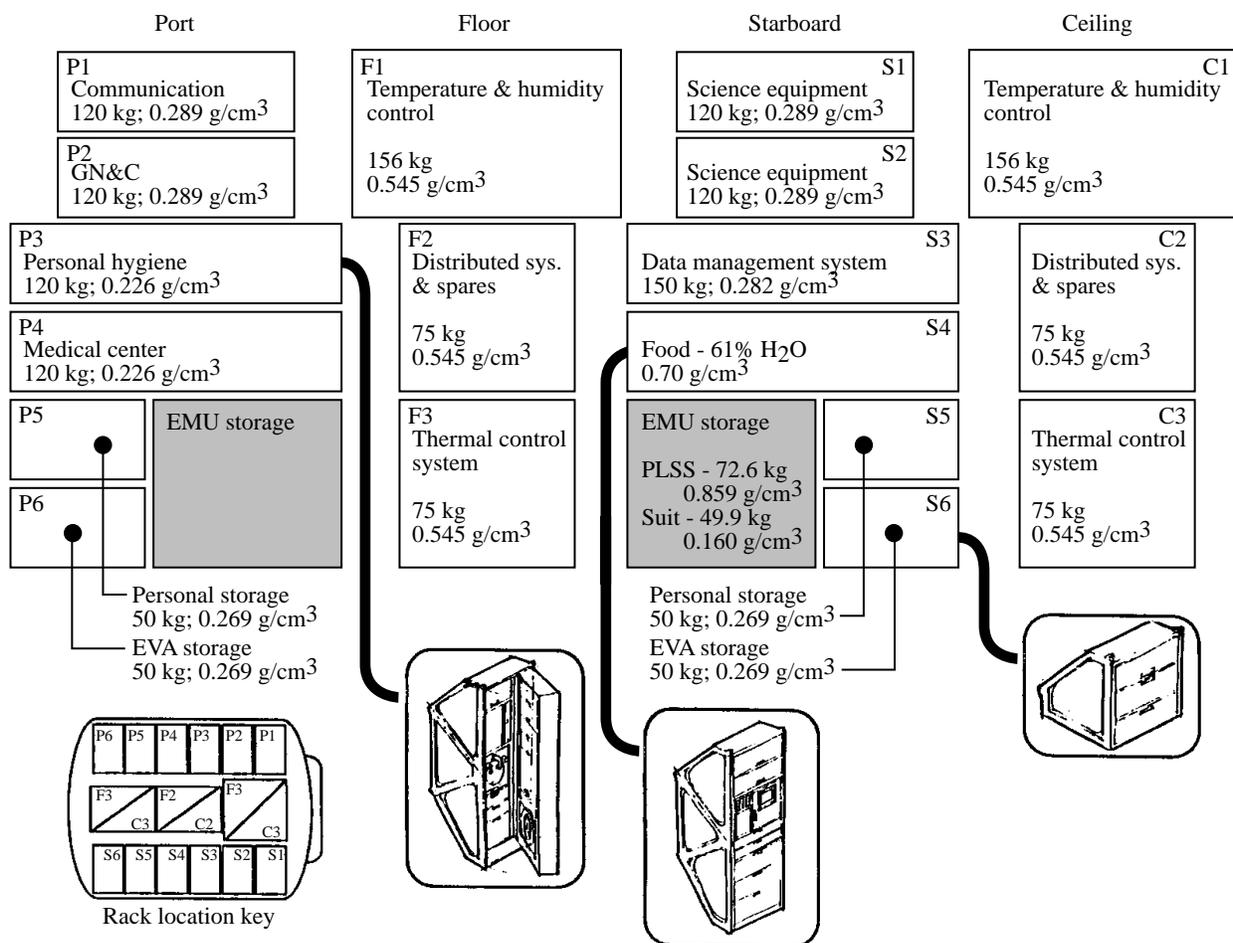
Figure 11.   Rack and Equipment Mass and Densities

The Boeing design is typical of pressurized rover designs and can generally be scaled to model larger pressurized rovers. Equipment rack densities should remain approximately constant, only volume will increase for larger rovers. The choice of power system may also change. The fuel cells which operate this rover will trade poorly with other power sources if longer sorties are attempted with larger rovers. If nuclear sources of power are employed (such as DIPS), then additional radiation protection measures need to be undertaken.

Pressurized rovers must carry their own radiation protection. The duration of their sorties is such that both active solar particle monitoring and integrated SPE shielding are a requirement. Tools which provide a thorough analysis of the rover configuration are necessary to model the radiation environment inside the rover during a radiation event.

REFERENCES

1. E. G. Cowart: Lunar Roving Vehicle: Spacecraft on Wheels, *The Institution of Mechanical Engineers Proceedings*, **187 45/73**: 463–491, 1973.

2. Anon.: Lunar Surface Transportation System Conceptual Design, Eagle Engineering, Inc., EEI Report 88-188, 1988.

3. Lee S. Mason, and Robert L. Cataldo: Nuclear Power Systems for the First Lunar Outpost, Tenth Symposium on Space Nuclear Power Systems, Albuquerque, NM, 1993.

4. Brand Norman Griffin: Pressurized Rovers, Essential for Effective Planetary Exploration, AIAA Paper # 93-4178, AIAA Space Programs and Technologies Conference, September 1993.

CHAPTER 14

SPACESUITS

by

Amy J. Ross[1]

Bruce Webbon[2]

Lisa C. Simonsen[3]

John W. Wilson[3]

_____

[1]NASA Johnson Space Center, Houston, TX 77058
[2]NASA Ames Research Center, Moffett Field. CA 94035-1000
[3]NASA Langley Research Center, Hampton, VA 23681-0001

Chapter 14

SPACESUITS

SUMMARY

The typical spacesuit allows up to 7.5 hours of maximum EVA (extravehicular activity) time spent outside the spacecraft in which the astronaut is with little protection. Nearly an hour is required to exit the normal living quarters while thirty minutes is spent in the airlock prior to re-entering the habitat. The spacesuit design can have a significant impact on exposure of some organs, depending on the environment spectral content.

INTRODUCTION

A spacesuit is required to protect the astronaut from the many environmental hazards of space during extra-vehicular activity EVA in low-Earth orbit, free-space, on the lunar surface, as well as activities within the tenuous Martian atmosphere. In addition to thermal, atmospheric, and micrometeoroid protection, the suit provides limited protection from space ionizing radiations. A description of the spacesuit's physical configuration is discussed in terms of the protection the suit provides from ionizing radiations which will impact the astronaut's exposure levels.

SPACESUIT USAGE

A typical shuttle EVA lasts 6–7 hours. The nominal maximum out-of-hatch time is 7.5 hours as limited by the suit consumables which is partially dependent on the metabolic rate of the astronaut. Eight hours per operation is regarded as a hard maximum upper limit as determined by the capability of the suit to operate under its own power.

Future spacesuit usage in space exploration will depend on the rover design. If an unpressurized rover is utilized, then the suit is the primary life support. If a pressurized rover is utilized, then the suit design may only support the astronaut for a few hours before a replenish/change-out cycle at a refill station. The use of such replenishment stations would greatly reduce the mass and volume of the portable life support systems.

For current shuttle operations, the time required in preparing for suit activity (once the liquid cooled ventilation garmet is donned) consists of:

- 20 minutes to suit up

- 8 minutes for suit purge

- 40 minutes for pre-breathe at 10.2 psi

- 10 to 15 minutes to exit the door

In returning to the shelter or habitat, the times required are:

- 10 minutes to close hatch

- 20 minutes to connect suit to the airlock

Planetary operations are expected to have a much different donning and doffing scenario. The goal of future space suit systems is a "10-minute out-the-door" preparation time.

SPACESUIT CONSTRUCTION

The basic spacesuit assembly (SSA) is shown in figure 1. It consists of an inner-liquid cooling ventilation garment (LCVG), communications carrier assembly (CCA), helmet, extravehicular visor assembly (EVVA), hard upper torso (HUT), arm assembly, gloves, and the lower torso assembly (LTA) which includes the boots. The helmet bubble (fig. 1) provides the pressure seal while the EVVA houses the various visors. Details on the EVVA visors and eyeshades are shown in figure 2. The 'protective visor' protects the helmet bubble from penetrations and scratches and remains physically closed. The 'sun visor' and 'center and side eyeshades' are movable within the EVVA and can be fully open or fully closed as the astronaut prefers. A thermal/meteoroid garmet covers only the EVVA shell with the front of the helmet protected by the various visor assemblies.

Although Shuttle and future spacesuit designs may have the same subassemblies, their construction varies with application. The construction of the spacesuit currently used on Shuttle missions is described in Tables 1 through 3. A similar suit design is planned for use at the International Space Station but will be strengthened (e.g., stitch patterns and primary axial restraint webbing) to increase usage to 25 EVA's. An advanced suit technology demonstrator, called the Mark III, is currently under development for exploration-type missions. It is similar in layup to the WETF-Qual suit analyzed elsewhere [1]. The construction of the Mark III suit assembly is described in Tables 4 through 6. The thermal/micrometeoroid garmet (TMG) of the Mark III suit is not yet designed and will probably be quite different from that of the shuttle suit due to the different micrometeoroid and thermal environments expected on lunar and Mars missions. The Shuttle suit TMG consists of an orthofabric cover, insulation, spacers, and an inner liner. For the material layups of the Mark III, the tables assume the usage of the shuttle suit TMG for completeness with the addition of a radiation shield layer. Likewise, the EVVA shell is not yet designed and the shuttle suit EVVA is assumed for the tables. The areal density estimates of the suit materials listed in the tables were partially compiled from reference 1. An illustration of a typical spacesuit assembly garmet cross section is shown in figure 3.

Several differences exist between the Shuttle suit design and the Mark III suit design. The Mark III suit may contain an additional layer of tungsten loaded silicone for radiation and meteoroid protection within the TMG. The usefulness and makeup of this layer is still being evaluated. More ionizing radiation protection is also afforded by

the increased thickness of the helmet bubble, protective visor, eye shades, and sun shade. The hard upper torso (HUT) of the advanced Mark III suit is currently designed using 6061T6 aluminum instead of the Fiberglas hard shell of the shuttle suit. Other candidate materials being considered for the Mark III HUT include carbon composite and urethane. The Mark III suit has an extended hard shell region, which not only includes the upper torso, but also the lower torso and the brief area to mid-thigh as indicated by Table 5. The shuttle lower torso and thighs are similar to the fabric for the arms and legs as indicated by Table 3. The proposed radiation protective layer is reduced in thickness in the Mark III suit for the arms and legs as shown in Table 6.

PRIMARY LIFE SUPPORT SUBSYSTEM

The Portable Life Support Subsystem (PLSS) is a complex array of equipment which performs many functions. One of the main goals of the Apollo PLSS design was to minimize weight while one of the main goals of the shuttle PLSS design was to minimize volume [2]. Aluminum could be used as the basic construction material for the Apollo PLSS for weight minimization because the short-duration Apollo missions incorporated nonreusable systems for which corrosion was not a concern. In contrast, the highly reusable PLSS of the Shuttle utilizes stainless steel construction to minimize corrosion. Consequently the mass and volume of the two PLS subsystems are different. A listing of subsystem mass, overall dimensions, and approximate material composition for the Apollo PLSS and the Shuttle PLSS are given in Table 7 and Table 8, respectively.

RADIATION EXPOSURES IN LEO

Calculations of the effects of spacesuit shielding in low-Earth orbit (LEO) were made by Kosmo et al. [1] for two suit configurations. The Shuttle suit assembly was assumed as listed in Tables 1 through 3 and an advanced suit configuration similar to the Mark III technology demonstrator suit described in Tables 4 through 6 was assumed. The advanced suit design was referred to as the 8.3 psi WETF (Weightless Environment Training Facility)-Qualified Space Assembly by Kosmo et al. [1]. This suit differed from the Mark III configuration assumed for Tables 4 through 6 in the TMG layer makeup. However, the tungsten loaded silicone layer as listed in the tables (4–6) was used for the analysis. The exact layering is listed in reference 1 and was converted therein to equivalent aluminum thickness for the analysis.

The EVA dose estimates are shown in Table 9. The EVA mission case conditions shown include a LEO orbit at 400 km and 28.5° and a LEO polar orbit at 250 km and 90°. The doses encountered in the LEO orbit are confined to protons and electrons in the South Atlantic Anomaly (SAA). An additional dose due to galactic cosmic ray exposure is included in the totals at all body locations at an exposure rate of 45 microSv/day for the 28.5° orbit. The LEO proton environment is similar to the spectral distribution of the solar cosmic rays in space so that these calculations are relevant to the effects in solar proton event exposures. The proton doses in polar orbit are confined to the SAA but the majority of the electron dose is encountered in the outer belts. At polar latitudes, a significant portion of the dose is from electrons for which the advanced suit design inclusive of a tungsten protective layer

provides a significant amount of protection. An additional dose due to galactic cosmic ray exposure is also included in the polar orbit totals at all body locations at an exposure rate of 100 microSv/day.

REMARKS

The material composition, configuration, and usage requirements of current and future spacesuit designs are presented to enable the evaluation of the radiation protection requirements for safe EVA's outside of spacecraft and surface structures. Several past radiation dose estimates are included to illustrate the added protection against electron doses provided by the tungsten loaded silicone layer while in LEO. Similar radiation analyses will be required for the radiation environments encountered during exploration missions outside the Earth's protective magnetosphere where galactic cosmic radiation will contribute more to the dose and where the hazards of solar proton events will be more prevalent. A more comprehensive spacesuit model is currently under development to estimate the shield mass distribution of suit designs while preserving the material composition of the layers (e.g., not equivalent aluminum) to aid in EVA analyses for exploration missions.

REFERENCES

1.   J. J. Kosmo, D. S. Nachtwey, A. Hardy, Candidate Space Station EVA Spacesuit Radiation Analysis, JSC document CTSD-SS-241, 1-24-89

2.   G. S. Thomas, Packaging Factors For Portable Life Support Subsystems Based On Apollo And Shuttle Systems, SAE Technical Paper 932182, 1993.

Table 1. Material layups (from exterior to interior) for the helmet/EVVA of the Shuttle spacesuit assembly.

Layer	Material	Areal density (g/cm^2)
Outer layer	Orthofabric cover -Teflon/Nomex/Kevlar	0.049
Insulation	Reinforced aluminized Mylar -5 plies	0.004
Spacer	Non-woven Dacron -5 plies	0.011
Inner liner	Teflon	0.028
EVVA shell	Polycarbonate	0.381
Sun visor	Polysulfone	0.190
Eye shades	Polysulfone	0.190
Protective visor	Polycarbonate	0.182
Helmet bubble	Polycarbonate	0.182

Table 2. Material layups (from exterior to interior) of hard upper torso (HUT) of the Shuttle suit assembly covering the torso area of the astronaut.

Layer	Material	Areal density (g/cm^2)
Outer layer	Orthofabric cover -Teflon/Nomex/Kevlar	0.049
Insulation	Reinforced aluminized Mylar - 5 plies	0.014
Inner liner	Neoprene coated nylon ripstop	0.028
Hard shell	Fiberglas	0.354
LCVG	Spandex/water/ Ethyvinylacetate	0.154

Table 3. Material layups (from exterior to interior) for the lower torso assembly (LTA), arms, and legs of the Shuttle suit assembly covering the brief area, arms, and legs of the astronaut.

Layer	Material	Areal density (g/cm^2)
Outer layer	Orthofabric cover -Teflon/Nomex/Kevlar	0.049
Insulation	Reinforced aluminized Mylar - 5 plies	0.014
Inner liner	Neoprene coated ripstop	0.028
Pressure restraint	Dacron	0.021
Pressure bladder	Urethane coated nylon ripstop	0.014
LCVG	Spandex/water/ethylvinylacetate	0.154

Table 4. Example of possible material layups (from exterior to interior) for the helmet/EVVA of the Mark III advanced technology demonstrator suit assembly.

Layer	Material	Areal density (g/cm^2)
Outer layer	Orthofabric cover - Teflon/Nomex/Kevlar	0.049
Insulation	Reinforced aluminized Mylar -5 plies	0.004
Spacer	Non-woven Dacron -5 plies	0.011
Radiation/meteoroid	Tungsten loaded silicone (75% by wt)	0.850
Inner liner	Teflon	0.028
EVVA shell	Polycarbonate	0.381
Sun visor	Polysulfone	0.570
Eye shades	Polysulfone	0.570
Protective visor	Polycarbonate	0.546
Helmet bubble	Polycarbonate	0.558

Table 5. Example of possible material layups (from exterior to interior) of hard upper torso (HUT) and the lower torso assembly (LTA) of the Mark III advanced technology demonstrator suit assembly covering the torso, brief and mid-thigh areas of the astronaut.

Layer	Material	Areal density (g/cm^2)
Outer layer	Orthofabric cover -Teflon/Nomex/Kevlar	0.049
Insulation	Reinforced aluminized Mylar - 5 plies	0.014
Radiation/meteoroid	Tungsten loaded silicone (75% by wt)	0.850
Inner liner	Neoprene coated nylon ripstop	0.028
Hard shell	6061T6 Aluminum	0.549
LCVG	Spandex/Water/Ethyvinylacetate	0.154

Table 6. Example of possible material layups (from exterior to interior) for the arms and legs of the Mark III advanced technology demonstrator suit assembly.

Layer	Material	Areal density (g/cm^2)
Outer layer	Orthofabric cover -Teflon/Nomex/Kevlar	0.049
Insulation	Reinforced aluminized Mylar - 5 plies	0.014
Radiation/meteoroid	Tungsten loaded silicone (75% by wt)	0.350
Inner liner	Neoprene coated ripstop	0.028
Pressure restraint	Polyester	0.021
Pressure bladder	Urethane coated nylon ripstop	0.014
LCVG	Spandex/water/ethylvinylacetate	0.154

Table 7. Approximate materials and dimensions of the Apollo primary life support system [2].

Subsystem	Materials	Mass* (lb.)	Dimension* (in.) (h,w,d)
Oxygen Ventilating Circuit			
regulators, vessels, fans.	Al, Cu..	14.0	–
LiOH assembly	LiOH, Al	9.5	–
Liquid transport			
pump, valves, sensors...	Al, Cu...	9.6	–
liquid	H, O, ...	?	–
Electrical systems			
electronics	Si, O, Cu,..	6.8	–
battery	ZnAgO	9.5	–
Oxygen purge system			
bottles	Al, O	9.5	–
regulator	Al, Cu	4.2	–
TOTAL		63.1	$26 \times 17.5 \times 10.25$

*From reference 2.

Table 8. Approximate materials and dimensions of the Shuttle primary life support system [2].

Subsystem	Materials	Mass* (lb.)	Dimension* (in.) (h,w,d)
Oxygen Ventilating Circuit			
regulators, vessels, fans..	Fe,Cr,Ni,Cu..	14.4	–
LiOH assembly	LiOH, Fe	6.4	–
Liquid transport			
pump, valves, sensors...	Fe, Cu...	6.5	–
liquid	H, O, ...	?	–
Electrical systems			
electronics	Si, O, Cu,..	15.1	–
battery	ZnAgO	10.0	–
Oxygen purge system			
bottles	Fe, O	8.6	–
regulator	Fe	4.2	–
TOTAL		65.2	$25 \times 23 \times 7$

* From reference 2.

Table 9. Exposure (microSv/day) of critical organs in LEO environments (proton, electron, and GCR) within two spacesuit designs [1].

	400 km $\times$ 28.5° Orbit			250 km $\times$ 90° Orbit		
	Dose from		Total	Dose from		Total
	protons	electrons	Dose[a]	protons	electrons	Dose[b]
Space shuttle suit						
Eye (sun visor up)	1010	1	1056	58	98	256
Eye (sun visor down)	960	1	1006	50	41	191
Skin (torso)	1140	9	1194	121	600	821
Skin (arms & legs)	1640	70	1755	626	3270	3996
BFO Depth	490	1	536	16	1	117
8.3 psi WETF-Qualified Space Assembly						
Eye (sun visor up)	870	1	916	41	4	145
Eye (sun visor down)	800	1	846	35	1	136
Skin (torso)	910	1	956	47	33	180
Skin (arms & legs)	1210	14	1269	158	896	1154
BFO Depth	470	1	516	14	1	115

[a]Includes 45 microSv/day from GCR for all body locations.
[b]Includes 100 microSv/day from GCR for all body locations.
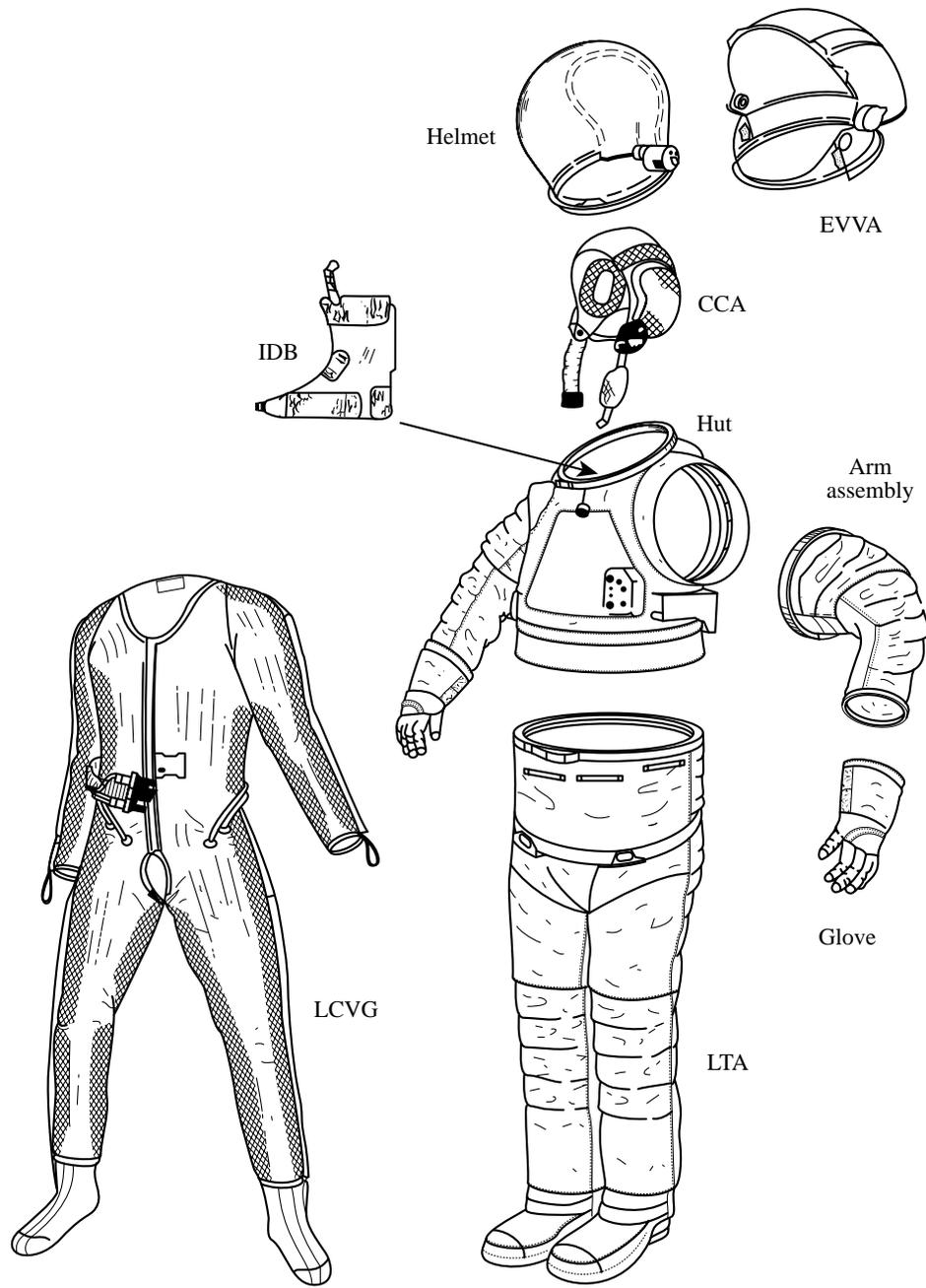
Figure 1. Basic components of a spacesuit assembly (SAA)
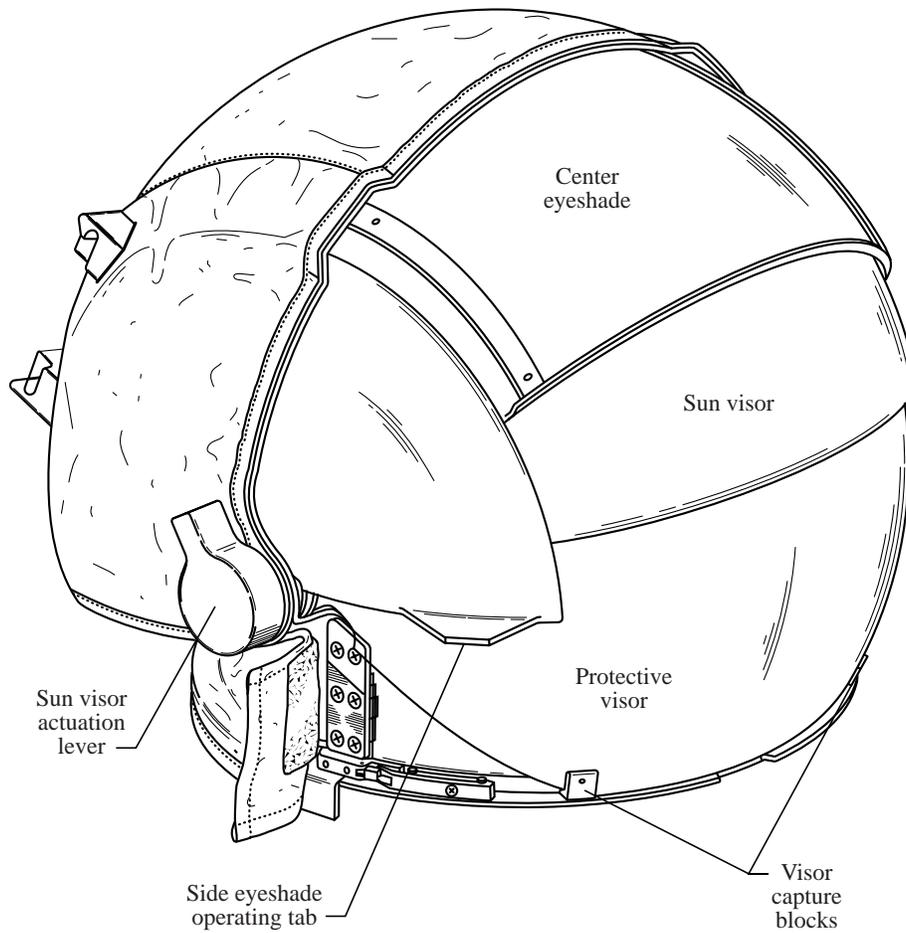
Figure 2. Illustration of helmet extravehicular visor assembly (EVVA) showing placement of visors and eyeshades.
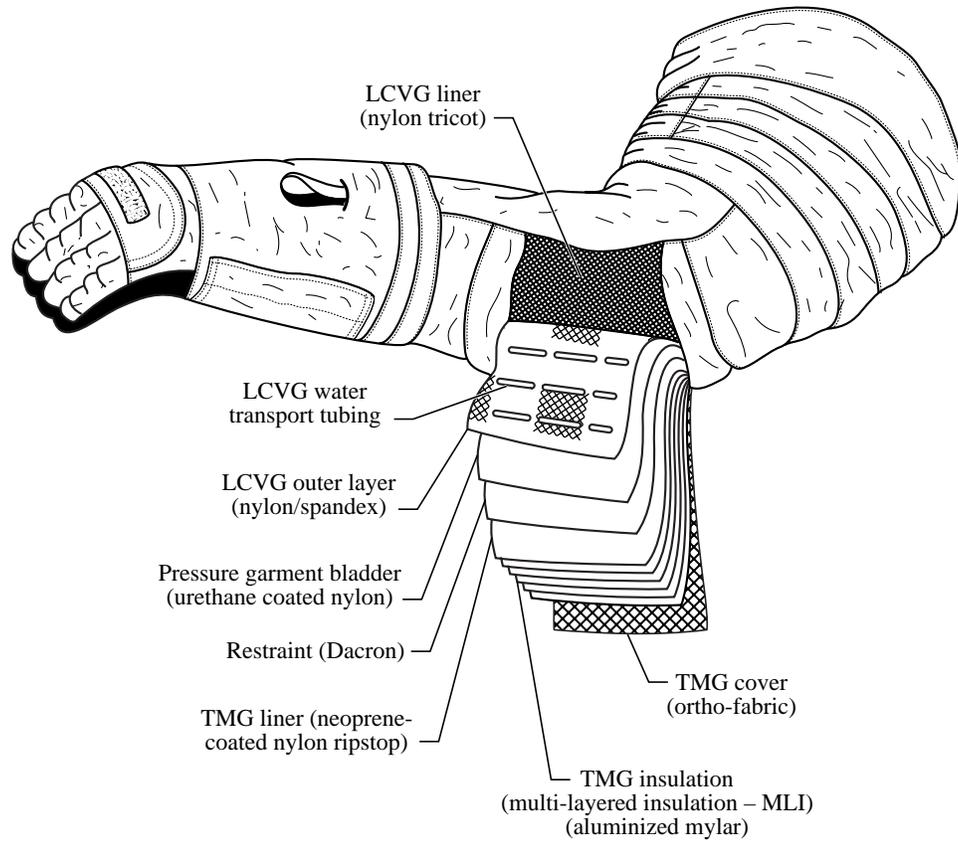
Figure 3. Cross section of material layup used for fabric for the arms and legs of the spacesuit.
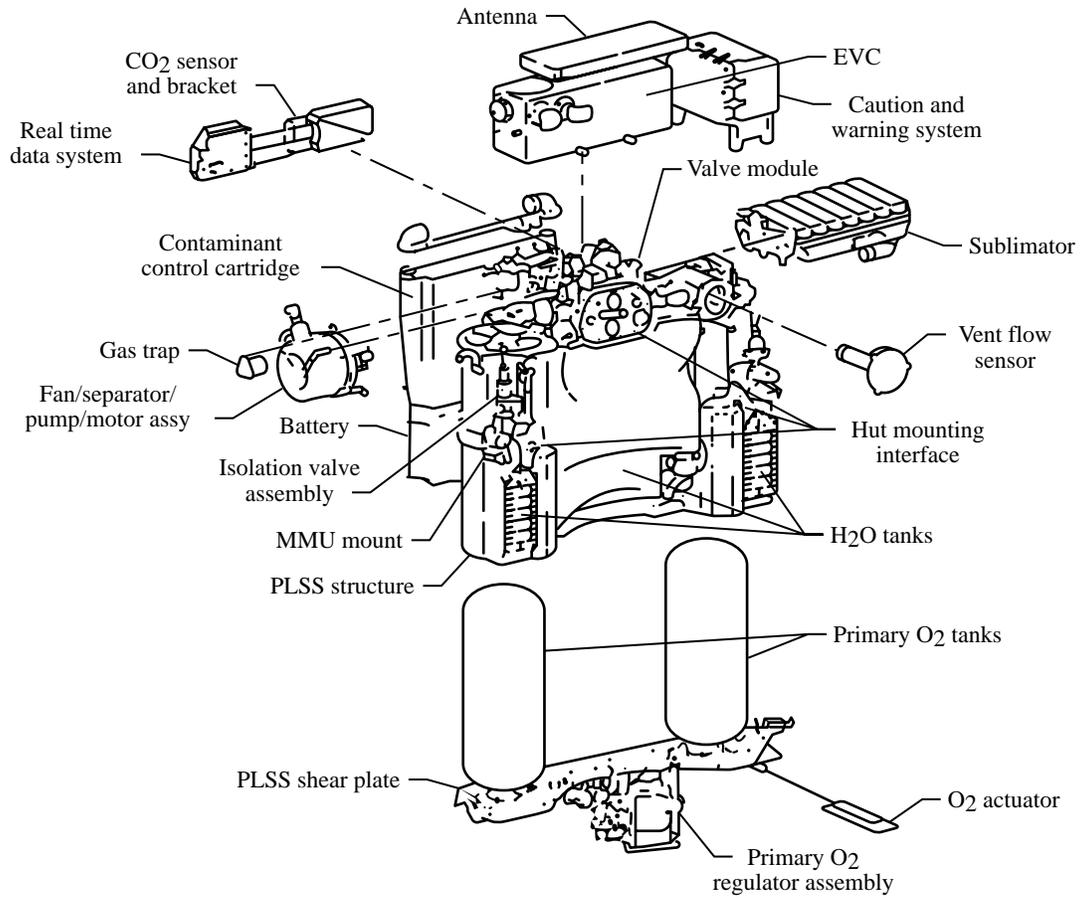
Figure 4. Space Shuttle extravehicular mobility unit (EMU) portable life support subsystem.

CHAPTER 15

CONSTRUCTION TECHNOLOGIES FOR LUNAR BASE:

PREFABRICATED VERSUS IN SITU

by

L. C. Simonsen[1]
W. Schimmerling[2]
J. W. Wilson[1]
S. A. Thibeault[1]

[1]Langley Research Center, Hampton, VA 23681-0001
[2]NASA Headquarters, Washington, D. C.

Chapter 15

CONSTRUCTION TECHNOLOGIES FOR LUNAR BASE: PREFABRICATED VERSUS IN SITU

ABSTRACT

The shield effectiveness of lunar regolith is compared with possible prefabricated shield materials from Earth, including commercially used shield materials in nuclear facilities. Several of the fabricated materials categorized as neutron absorbers and moderators exhibit favorable characteristics for space radiation protection. Although this effort is not intended to be a definitive trade study for specific shielding recommendations, attention is given to several factors that warrant consideration in such trade studies. For example, the transporting of bulk prefabricated shield material as opposed to the transporting of regolith-moving and processing equipment to the lunar surface is assessed on the basis of space Exploration Initiative (SEI) scenario studies. Other shielding strategies such as the processing of regolith with a composite material are considered to reduce the amount of bulk regolith required, to enhance its shielding characteristics, and to form a more structurally sound shield. Nevertheless, launching all the shield material from Earth may still be a viable alternative to the use of regolith from the standpoints of cost-effectiveness, EVA time required, and other risk factors.

INTRODUCTION

The protection of crewmembers from the harmful effects of ionizing radiation is an important issue that must be addressed during the development of lunar base mission scenarios. For the shorter duration missions, the possibility of an extremely large solar proton event occurring will drive the radiation protection requirements. As mission duration increases, the steady contributions to dose from galactic cosmic radiation will become more important. This study investigates the properties of various shielding materials for protection against both large solar proton events and galactic cosmic radiation (GCR).

Various strategies exist for the protection of crewmembers at an established lunar base. Popular concepts employ using in-situ materials to reduce launch mass requirements from Earth [1–4]. However, this will not reduce shielding launch requirements to zero mass because of the heavy equipment required to cover the habitats, although much of the equipment may serve multiple purposes. Other considerations of this strategy include the protection of

the crew from a potentially large solar proton event while they are in the process of covering their habitats and the logistics of such a covering operation on the lunar surface.

In this study, regolith shielding is compared with shields of aluminum, lithium hydride, magnesium hydride, various polymers and borated polymers, regolith-epoxy mixtures, and water. This information provides a materials database which is not only applicable to lunar surface operations, but also to cis-lunar and interplanetary space transfer vehicles. The amount of shielding required will ultimately be based on radiation exposure limits set forth by regulatory agencies for exploratory class missions.

RADIATION EXPOSURE

Currently, no limits have been recommended by the National Council on Radiation Protection and Measurement (NCRP) for exploration missions [5]. However, for planning purposes only, the NCRP suggests that the limits established for astronauts in low-Earth orbit (LEO) may be used as guidelines for other missions if the principle of ALARA (as low as reasonably achievable) is followed [5]. LEO limits for the skin, ocular lens, and vital organs are shown in table 1. The NCRP is currently in the process of revising the LEO recommendations as a result of larger estimates of cancer risk coefficients [6]. For high-energy radiation from GCR and solar proton events, the dose delivered to the vital organs is the most important with regard to latent carcinogenic effects. This dose is often assumed equal to the blood-forming organ (BFO) dose. When detailed body geometry is not considered, the BFO dose is usually computed as the dose incurred at a 5-cm depth in tissue (simulated by water in these analyses). Likewise, the skin and ocular lens dose can be conservatively approximated by the 0-cm dose.

Table 1. Ionizing radiation exposure limits for low-Earth orbit [5].

Exposure Interval	Dose Equivalent, cSv		
	Blood Forming Organ	Ocular Lens	Skin
30-day	25	100	150
Annual	50	200	300
Career	100–400[*]	400	600

[*]Varies with gender and age at initial exposure

LEO exposure limits are currently given as dose equivalents to specific organs for short-term (30-day) exposures, annual exposures, and total career exposure. The short-term exposures are important when considering solar flare events because they often deliver their total dose within several hours to a few days. It is believed that by adhering to the short-term limits, nonstochastic late effects as well as acute effects of the bone marrow, ocular lens, and skin can be held to acceptable levels [5]. Doses received from GCR on long duration missions are especially

important to total career limits, which are determined by the age and gender of the individual. For instance, career limits for typical 30-year old male and female astronauts are 200 cSv and 140 cSv, respectively.

For human exposure, the dose equivalent is defined by introducing the quality factor, Q, which relates the biological damage produced due to any ionizing radiation to the damage produced by soft x-rays. In general, Q is a function of linear energy transfer (LET), which in turn is a function of both particle type and energy. For the present calculations, the quality factors used are those specified by the International Commission on Radiological Protection (ICRP) [7]. The biological effects of HZE (high charge and energy) particles, present in the GCR fluxes and to a lesser extent in the nuclear reaction products of GCR and proton flares upon interaction with material, are not well understood and lead to uncertainty in risk estimates.

Three sets of quality factors have been published [6,7,8] to relate the deposition of energy to biological risk. Currently, the ICRP-26 quality factors are accepted by the United States regulatory bodies. The ICRU-40 quality factors have been pre-empted by the ICRP-60. However, neither the ICRU-40 or the ICRP-60 have as yet been accepted by any regulatory body in the United States. A system of weighting factors have been recommended by the ICRP which reflect the uncertainties in estimating the effects of the high LET radiations with the associated quantity referred to as equivalent dose [6]. The change in quality factors from ICRP-26 does not significantly affect the dose equivalents for 1989 solar proton flares [9], but larger differences are seen for the contributions to dose equivalent from the HZE particles of GCR. Future shield design studies should move away from dose limits based on quality factors and move toward emphasizing risk-based assessment methods based on biological response modeling [10].

LUNAR MISSION SCENARIO

There have been many habitat concepts proposed for future lunar outposts. However, analyses and trade studies must still be performed to clearly define the first outpost and the growth of the outpost to support crewmembers for longer stay times. One scenario envisions a crew of 5 on the surface for 14 days with stay times growing to a range of 45 days to 180 days for the more mature base [1]. Many concepts consider the use of existing technology modified for lunar operations, such as Space Station modules [1–3]. In order to compare radiation shield mass estimates, candidate concepts using station modules are selected for this analysis. The methodology of the shielding calculations presented here is also applicable to other habitat concepts.

Habitats composed of modified space station modules, as defined by Hypes et al. [2], are shown in figures 1 and 2. Concept 1 considers a 2/3 size module with dual airlocks while Concept 2 considers a full size module with dual airlocks. The use of multiple initial habitats was assumed to evolve into the permanent habitat for longer duration stay times. The individual habitat units could either be located as desired near base operational areas or be interconnected into a single base. Studies have shown that lunar regolith is a viable option for radiation protection. Estimates by Nealy et al. [11,12] have shown that 75 g/cm^2 of regolith will reduce the annual GCR dose during solar minimum and the dose due to large flares to within the limits established for LEO operations. Just as there are

many habitat concepts, there also are many regolith covering concepts, such as bagging the regolith, setting the regolith directly on the structure or on a standoff, construction of regolith concrete blocks, etc. The coverage technique selected for Concept 1 is a combination of regolith bags and direct application of regolith as shown in figure 3 [2]. Two coverage techniques for Concept 2 using direct application and standoffs are shown in figures 4 and 5 [2]. The minimum coverage of regolith is 75 g/cm^2 with increased protection in some areas as deduced from figures 4 and 5. The density of regolith varies from 1 g/cm^3 at the lunar surface to 1.5–2.0 g/cm^3 at depths of 10 to 20 cm [13]. Assuming a nominal regolith density of 1.5 g/cm^3, the regolith shield mass requirements can be calculated as shown in table 2.

Table 2. Regolith radiation shield requirements for candidate habitat concepts [2].

Concept	Coverage Technique	Volume of Regolith, m^3	Mass of Regolith, t[*]
1	fig. 3	556	834
2	fig. 4	481	722
2	fig. 5	693	1040

[*]1 metric ton = 1000 kg

The use of in-situ materials for the coverage of a lunar base does reduce the mass of shielding material that must be launched from Earth. However, heavy equipment, such as cranes, mining excavators, and haulers, must be available on the lunar surface to excavate the regolith, transport it to the base site, and place it on the habitat. Several examples of this type of equipment found in the literature [1,14,15] with their associated masses are shown in table 3. A list of this equipment is provided for an example of what kind of mass penalties may be involved in the coverage of the base. However, a direct trade-off of these mass requirements with the mass of prefabricated shielding is difficult because much of this equipment can serve multiple purposes, such as unloading cargo from landers and collecting regolith for the production of lunar liquid oxygen. Other matters which make a trade study difficult are estimating the EVA time required to cover a habitat, the cost of EVA, the risk of personal injury during EVA, how much of the coverage can be automated, etc.

NATURAL RADIATION ENVIRONMENT

The natural radiation environment encountered during a lunar mission will vary depending on the solar activity (measured by sunspot number). The solar dipole moment cycles approximately every 20–24 years leading to solar activity cycles of 10–12 years modulated by the direction of the dipole moment. The solar activity increases with the decline of the dipole moment with maximum activity occurring as the dipole switches hemispheres. Activity declines as the dipole moment maximizes along its new direction. With each activity cycle, there are approximately 3 1/2 to 4 years of active solar conditions. The greatest probability of a large solar proton event occurring is during the rise and decline in solar activity. The magnitude of the GCR flux varies over the 10–12 year solar cycle. The fluxes are greatest during solar minimum conditions when the interplanetary magnetic field is the weakest, allowing

more intergalactic charged particles to gain access to our solar system. During maximum solar activity, the GCR fluxes are at their minimum.

Table 3. Survey of proposed lunar outpost heavy-operation equipment.

Equipment	Description	Mass, t
Payload unloader /1/*	3-strut, teleoperated gantry crane	6.3
Miner hauler /1/	5 t load capacity	2.3
Miner loader /1/	Front-end type	4.6
Ripper/excavator/loader /14/	Loosens compact regolith, excavates and loads regolith	2.5
Regolith hauler /14/	Dump-truck type 7.7 t capacity	1.0
Payload unloader with excavator shovel assembly /14/	3-strut cargo unloader with ability to excavate and pile regolith	5.5
Drag-bucket excavator /15/	3-drum cable-way slusher excavates and loads regolith	5.5

*Denotes reference

Solar Proton Events

Very large solar proton events are relatively rare with approximately 0 to 3 events occurring within an 11-year solar cycle. The largest solar proton flares observed in the past are the February 1956, the November 1960, and the August 1972 events. The largest flares recorded since August 1972 occurred in the months of August through October 1989. Figure 6 shows the 1989 proton fluence energy spectra based on rigidity functions reported by Sauer et al. [16]. The magnitude of the October 1989 flare is on the same order as the widely studied August 1972 event. The addition of the three 1989 flare events, which occurred within 3 months of each other, can provide a fairly realistic estimate of the flare environment that may be encountered during missions taking place in the 3 or 4 years of active Sun conditions (solar maximum). There are also smaller, more frequently occurring solar proton events throughout a solar cycle. These events are not considered here since the shielding designed to reduce the GCR dose and a large solar proton event dose to within acceptable limits will dominate the shield design calculations. For the flare analysis, the transport calculations through various materials are performed for the sum of the three 1989 flares.

The forecasting of large solar proton events, such as the 1989 flares, will be of vital importance to warn crew-members of potentially lethal doses. Practically continuous monitoring of various aspects of solar activity (x-ray and radio emissions, sunspot number, etc.) during Solar Cycle XXI (1975–1986) to the present time has provided a valuable database for flare forecasting statistics. During recent years, the NOAA Space Environment Laboratory has examined the intensities of x-ray and radio emissions from the Sun and related them to the likelihood and severity of a subsequent energetic proton release. For 24-hr predictions during Solar Cycle XXI, the number of events which occurred without prediction of occurrence was about 10% of the total number predicted [17]. This resulted primarily because the initial x-ray and radio bursts were not on the visible portion of the Sun. The false

alarm rate was approximately 50%; that is, for every two flares predicted 24 hours in advance, one flare actually occurred.

Large solar proton events are preceded by strong x-ray bursts which may be detected a minimum of approximately 20 minutes before the arrival of energetic particles at 1 AU. Thus, the likelihood of a proton event is more accurately predicted with a 20-minute warning time, although the severity of the flare is still not predicted with much success. Therefore, it becomes important to consider the case where a crew may only have a 20-minute advance warning that energetic protons may arrive. The October 1989 flare was successfully predicted by NOAA from an x-ray burst that occurred approximately 1 hour before flare onset. The impact of a potentially large solar proton event during lunar activities away from the base is an operational concern that mission planners must address.

Galactic Cosmic Radiation

Galactic cosmic radiation consists of the nuclei of the chemical elements which have been accelerated to extremely high energies outside the solar system. The natural GCR environment used in this analysis is the widely used Naval Research Laboratory CREME model, which specifies ion flux spectra for particles of atomic numbers (Z) between 1 and 28 (hydrogen through nickel) [18]. Figure 7 shows the GCR particle spectra at solar minimum conditions. Protons account for nearly 91% of the total flux, alpha particles account for approximately 8%, and the HZE (high charge and energy for Z > 3) particles account for less than 1% of the total flux. Even though the number of HZE particles is relatively small, they contribute to 86% of the total dose equivalent (using ICRP-26 quality factors) [19]. Of the HZE particles, iron is the largest contributor to GCR dose equivalent, making up 26% of the total dose equivalent [19]. At solar maximum conditions, GCR fluxes are substantially reduced producing a dose of roughly one-half of that produced by the solar minimum GCR flux. In this analysis, the NRL solar minimum GCR flux will be used as the basis for shield material selections and dose estimates.

Considerable uncertainty does exist in the energy distribution of GCR ions. More recent GCR flux models have been developed by Badhwar and O'Neill [20] which may represent significant improvements over earlier models. The 1977 solar minimum GCR spectrum described by Badhwar and O'Neill [20] has a greater number of particles between 50 and 500 MeV and lacks a low energy anomalous component compared with the NRL CREME model. Although the dose versus depth estimates for the various selected materials may differ slightly, depending on the GCR model and quality factors selected, the basic ranking and depths required for long-term GCR shielding remain relatively consistent enough for our purposes.

TRANSPORT CODES

The transport of high-energy nucleons and heavy ions through condensed matter is calculated with the Langley-developed codes BRYNTRN [21] and HZETRN [22]. Both codes implement combined numerical and analytical techniques to provide solutions to the one-dimensional Boltzmann transport equation for particle flux and energy. The BRYNTRN code transports both primary and secondary nucleons and also includes the effects of target nucleus

recoil reactions. The GCR calculations are performed with the HZETRN code which transports nuclear species with charge numbers between 0 and 28. Secondary products from nuclear fragmentation reactions are also transported. Both codes evaluate dosimetric quantities based on the linear energy transfer of particles traversing the media. The dose is evaluated in terms of cGy, or rad (100 ergs/g). For calculations of dose equivalent, biological quality factors are combined with the particle LET to provide exposure in terms of cSv, or rem.

TRANSPORT CALCULATION RESULTS FOR SELECTED MATERIALS

Candidate Shield Materials

Several candidate shield materials are selected for analysis to examine their effectiveness for both GCR and solar proton flare protection. A brief description of the selected materials and their respective mass densities are listed in table 4. Aluminum and lunar regolith are selected for study because they can provide a convenient shield material on the lunar surface. Materials having high hydrogen content are selected because such substances are known to be most effective for high-energy charged particle shielding on a per-unit-mass basis. Magnesium hydride is interesting because of its potential use as a hydrogen storage medium. Remarkably, more hydrogen is contained per unit volume, noncryogenically, in MgH_2 than is found in pure liquid hydrogen [23]. Since hydrogen is not found naturally on the Moon, a convenient means of hydrogen storage may be of great importance. Furthermore, when any material used as a radiation shield can serve a dual purpose, mission costs can usually be reduced. Other examples of "dual use" materials are food stuffs, water, and waste water. Lithium hydride and borated polymers are considered for possible space applications because of their usage in nuclear reactor facilities for neutron moderation and absorption.

The addition of various weight percent loadings of boron to polyethylene and polyetherimide is considered because of the large thermal neutron cross section of boron-10. Both products of the $B^{10}(n,\alpha)Li^7$ reaction are quickly stopped in condensed matter, and consequently borated polymers are very effective in low-energy neutron control. Borated polyethylene is available commercially; however, the addition of boron to polyetherimide is relatively new [24,25]. Polyetherimide was selected because it is a space-qualified, advanced, high performance polymer. As opposed to polyethylene, polyetherimide can be used as the matrix resin for composite materials allowing for structural applications. Finally, regolith-epoxy mixtures are considered as a means to increase the shielding and structural properties of in-situ resources. Epoxy is the most used matrix resin in the aerospace industry with its behavior well understood. Epoxy mixtures can also be cured at standard temperature and pressure which may simplify the curing of regolith blocks on the lunar surface and are good for curing in thicker slabs.

The propagation results are evaluated as dose (or dose equivalent) versus areal density (in units of g/cm^2) which can be converted to a linear thickness (cm) by dividing by the density (g/cm^3) of the appropriate material. Displaying results in this manner is helpful in comparing the shield effectiveness of various materials because equal areal densities for a given large shielded volume will yield equal shield masses even though their linear thicknesses may differ.

Table 4. Candidate shield materials.

Material	Density, g/cm^3	Description
Lunar regolith (model 1)	1.0–2.0 (assume 1.5)	5 element model based on Apollo return samples /13/ (63 mol-%0, 17% Si, 10% Al, 6% Ca, 4% Mg)
Aluminum (Al)	2.7	Spacecraft/habitat structural components
Water (H_2O)	1.0	Also simulates waste water and food stuffs
Lithium hydride (LiH)	0.82	Commonly used reactor shield material for neutron moderation
Magnesium hydride (MgH_2)	1.6	Potential use as hydrogen storage medium
Polyethylene $(CH_2)_{-n}$	0.92	Composition typical of composite materials
Borated polyethylene	1.12	30 wt-% boron Commonly used reactor shield material for neutron absorption
Lunar regolith (model 2)	1.5	5 element model used in /27/ (61.5 mol-%0, 19.3% Si, 7.5% Al, 6.1% Fe, 5.5% Mg)
Regolith-epoxy mixture	1.48 1.46	10 wt-% epoxy additive 20 wt-% epoxy additive Mixture to bind regolith to enhance shielding and structural properties
Epoxy ($C_{36}H_{41}N_4O_6S$)	1.32	Commonly used as binder for composite mixtures
Polyetherimide ($C_{37}H_{24}N_2O_6$)	1.26 (pure)	Space-qualified, high performance polymer with 0–20 wt-% boron loadings

Solar Flare Calculations

The BRYNTRN nucleon transport code is used to compute the dose and dose-equivalent for the combined fluence spectra of the large proton fluxes that occurred in August, September, and October of 1989. A comparison of the shield effectiveness of selected materials is shown in figure 8 for shield thicknesses up to 25 g/cm^2. For thin layers (less than 2 or 3 g/cm^2) of all materials, the dose equivalents are high enough to be mission threatening. Substantial thicknesses of material (between 10 and 25 g/cm^2) are required to reduce the 5-cm depth dose equivalent to less than the 30-day guideline limit of 25 cSv. There is relatively little difference between the dose equivalents evaluated with the ICRP-26 and ICRP-60 quality factors [9].

As expected, the materials containing hydrogen are the most effective as solar proton flare shields, especially polyethylene, water, and lithium hydride. The present calculations also indicate that most secondary neutrons produced by interactions of solar flare particles are of energies too high to be significantly affected by the boron-10 thermal neutron cross section in the borated materials. In addition, the added boron may actually lessen the shield efficiency of polyethylene at the depths of interest. This may require further investigation since the BRYNTRN

code still needs improvement in the transport and modeling of low-energy neutrons as well as improvements in handling thermal neutron cross sections. The shielding differences between lunar regolith and polyethylene are illustrated in figure 9 where the particle spectra emergent from 10 g/cm^2 of lunar regolith and from 10 g/cm^2 of polyethylene are compared. In both cases, the primary flux of low energy protons (< 10 MeV) has been drastically reduced. However, the generation of secondary protons and neutrons emergent from the polyethylene are substantially less than that from the lunar regolith.

Galactic Cosmic Ray Calculations

The HZETRN code is used to compute the dose and dose equivalent for the CREME GCR flux at solar minimum conditions. The dosimetric values are generated for selected materials for shield amounts ranging between 0 and 50 g/cm^2. A comparison of the shielding effectiveness of the various materials is shown in figure 10 for the 5-cm depth dose. Aluminum and regolith behave similarly in general attenuation characteristics as seen from figure 10, with the regolith having slightly better shielding properties. Polyethylene and lithium hydride are also very similar in nature, and water and magnesium hydride are comparable materials of intermediate shield effectiveness in relation to the others. The better shielding characteristics for the materials containing hydrogen are also apparent, particularly in the case of polyethylene and lithium hydride. For the 50 g/cm^2 layers, the incurred dose equivalent is reduced by almost a factor of two by these more effective materials. Another factor influencing the estimated dose equivalents is the impact of imposing the new ICRP-60 quality factors. In most instances, the new quality factors tend to increase the dose equivalent compared with the ICRP-26 values, sometimes by more than 10 percent [26]. However, in general, the effect is not dramatic, and both dose equivalent evaluations appear to approach the same numerical values as shield amounts increase.

An examination of the particle fluxes obtained from the transport calculations helps to illustrate the contrast in behavior between hydrogenous lithium hydride and regolith. Figure 11 shows comparison spectra of the computed fluxes emergent from both 50 g/cm^2 of lunar regolith and lithium hydride. The heavy particle fluxes at all energies in LiH are substantially lower compared with the heavy particle fluxes in regolith where the Z = 10 to 28 fluxes do not appear on the LiH plot. This leads to a more rapid attenuation of the dose equivalent due to the heavy particles in the lighter material. The secondary neutron production is also substantially less in LiH.

Other studies have found similar results to those described here using modified input fluxes to an updated version of the transport code HZETRN [27]. As mentioned previously, iron is a large contributor to the total GCR dose equivalent and is widely used in laboratory beam experiments. The results of calculations investigating the effect of 0 to 20 wt-% boron loadings in polyetherimide are shown in figure 12 for a 33.88 GeV ^{56}Fe beam incident on 18 g/cm^2 of polyetherimide. As the boron loadings increase, the material's capacity to absorb secondary HZE particles diminishes. The decrease in shield effectiveness is illustrated by the increased fluence of projectile fragments. Thus, similar to the decrease in shield effectiveness seen with the addition of 30 wt-% boron to polyethylene for solar proton flare protection, a similar decrease in effectiveness against HZE particles is implied

here. The same caution should be exercised here with regard to HZETRN's modeling capability of low energy neutrons.

The addition of epoxy has been shown by Kim et al. [27] to improve the shielding characteristics of regolith. The dose is reduced by approximately 5 to 10% with the addition of 10–20 wt-% epoxy, respectively, as shown in figure 13. In figure 13, H(x) represents the annual 0-cm depth-dose in water at a shield depth of x from GCR and H(0) represents the annual free-space 0-cm depth dose both using the ICRP-60 quality factors. The calculation of the dose equivalents for these curves is similar to those shown in figure 10 with the following differences (1) the ICRP-60 quality factors are assumed instead of the ICRP-26 ; (2) the dose is at a 0-cm depth in water instead of at a 5-cm depth; (3) an updated version of HZETRN was used with an improved numerical solution methodology; (4) an updated nuclear cross-section database better modeling the energy dependence was used; (5) a slightly different regolith composition model was used as shown in table 4; and (6) the 1977 solar minimum GCR spectrum of Badhwar and O'Neill [20] was used instead of the CREME model solar minimum. Using the above methodology, the 0-cm free space GCR dose equivalent is calculated to be ~120 cSv/yr. It should be noted that an increase in the dose equivalent is seen at small thicknesses for the regolith materials (fig. 13) which are not seen in the results of figure 10. As noted, the results of figure 10 do include the traversal of an extra 5 cm of water. The GCR spectral differences affecting the buildup of secondary radiation also account for some of the differences. Despite these differences, this information can be used for a direct comparison with the shield calculations of figure 10.

As illustrated above, shield effectiveness can be examined by using the conventional risk assessment method incorporating quality factors as a function of LET. Another method is the use of a track structure repair kinetic model for the mouse cell C3H10T1/2 for which a large number of repair kinetic studies have been made with various ions and a track structure cell kinetics model derived [28]. The variation in the calculated cell transformation ratio T(x)/T(0) is shown in figure 14 where T(0) is the number of occurrences of neoplastic cell transformations resulting from a 1-year unshielded exposure to the 1977 solar minimum GCR and T(x) represents occurrences behind x g/cm^2 of shielding [27]. The results incorporate the same assumptions (excluding the use of quality factors) as those described for figure 13 and will vary depending on the biological model used. Although the attenuation characteristics for various shield materials are qualitatively similar to the attenuation of the dose equivalent shown in figure 13, there are important quantitative differences. Compared with the repair kinetics model incorporating track structure dependent injury coefficients, the quality factor may be misleading in the evaluation of attenuation characteristics in shields containing nonhydrogenous components [29]. This is best seen in terms of the attenuation of the transformation rate in a given material compared with the attenuation of the dose equivalent in the same material. Whereas the attenuation of dose equivalent [H(x)/H(0)] is correlated with that for cell transformation [T(x)/T(0)] in light shield materials, these quantities tend to be anti-correlated in more massive shield materials. The result is that the addition of some materials as shielding which reduces the dose equivalent may in fact increase the risk of cancer. Thus, the use of LET dependent quality factors for shield design studies using lunar regolith may not be the best approach. More of the issues regarding the use of quality factors versus the use of biological response

models for protection from galactic cosmic rays can be found in Wilson et al. [29]. However, until improved risk models and nuclear fragmentation parameters become available, conventional dosimetry in shield design studies is recommended to begin to understand the magnitude of lunar shielding requirements for protection against HZE particles.

COMPARISON OF SHIELDING OPTIONS

The materials data described in the previous section are used to approximate doses to crewmembers on the lunar surface for various shielded configurations. Ideally, a computer model can be generated to estimate the shielding thickness distribution around specific target points within the habitat. A detailed model will not only provide the thickness distribution of the shielding, but will also provide the added protection from the pressure vessel, tanks, consumables, and other structures. The directionally dependent dose contribution can then be interpolated/extrapolated from the material dose-vs-depth data for each thickness in each direction. In free space, radiation will surround the crew from the full 4π solid angle. However, on the lunar surface only a solid angle of 2π is considered because the mass of the planet protects the crew from half of the free-space radiation. The directional dose can then be numerically integrated over the solid angle about a target point to determine a total dose at that point.

Previously, such an analysis was performed for the regolith shielding configuration of figure 5 [2]. This analysis, as well as the other estimates in this section, consider only the protection of the added shielding and not of the basic habitat components. A series of target points were selected for a cross section of the module. The resulting dose equivalent (ICRP-26) distribution is shown in figure 15 for GCR at solar minimum (CREME model) and for the August 1972 flare (which is on the same order of magnitude as the October 1989 flare [9] which dominated the sum of the 1989 flare fluence spectrum). The maximum 5-cm depth dose incurred from GCR is approximately 8.2 cSv/yr while the dose incurred from the August 1972 event is approximately 0.6 cSv. When detailed geometry is not available, conservative approximations can be estimated directly from the dose-vs-depth data. For instance, for 75 g/cm^2 of regolith protection a 5-cm depth dose of 25 cSv/yr was estimated by Simonsen et al. [26] (a 25 cSv/yr dose equivalent can also be extrapolated from figure 10). On the lunar surface, the dose inside the habitat is estimated as half of the free-space dose or 12.5 cSv/yr. This is a fairly good approximation compared with the 8.2 cSv/yr considering that the natural slump line of the regolith provides significantly more protection than 75 g/cm^2 in many directions for the detailed calculations.

For long duration stays on the lunar surface, the GCR dose will tend to be the limiting dose that will drive the shielding requirements. In order to compare various shield materials with the habitat/regolith configuration using the dose-vs-depth data directly, a dose of 12.5 cSv/yr from GCR is assumed to be the design goal within the habitat. Lithium hydride and polyethylene, which are more effective in their attenuation of free-space radiative fluxes, are considered here for example purposes. For a 5-cm depth dose estimate inside the habitat of 12.5 cSv/yr, an areal density of 18 g/cm^2 of polyethylene and an areal density of 16 g/cm^2 of lithium hydride are log-linearly interpolated

from figure 10. These thicknesses of polyethylene and lithium hydride appear to be reasonable design choices since the dose-depth curves tend to flatten out between 15 to 20 g/cm^2 (fig. 10) with the addition of more shielding material providing less of a reduction in dose compared with the larger reductions at small thicknesses. Figure 16 shows the shielding configuration which assumes that Earth-transported shielding can be prefabricated to fit snugly around the module. The prefabricated shape greatly reduces the shielding volume requirements compared with the shielding volume requirements associated with just piling the regolith on top of the modules. However, the regolith volume requirements may also be reduced by techniques such as bagging (which may prove to be too labor intensive). Concept 1 requires approximately 40 m^3 of polyethylene and approximately the same of lithium hydride. Concept 2 requires approximately 59 m^3 of polyethylene and approximately the same for lithium hydride.

The processing of regolith with epoxy can reduce the amount of bulk regolith required because of its enhanced shielding characteristics and because the mixture can be cured into blocks that can fit snugly around the module similar to the shape of the prefabricated shield design of figure 16. For a rough approximation of the possible savings, assume that the addition of 20 wt-% epoxy decreases the estimated regolith shield thickness by 10% from 75 g/cm^2 to 68.5 g/cm^2 (see figure 13). The curing of the regolith blocks would be similar to the curing of borated epoxy as described by Thibeault et al. [30] except that the regolith-epoxy mixture can be cured at room temperature. Further study would be required to adapt an optimum processing technique that can be accomplished in the lunar environment. For a regolith-epoxy shield similar to the design of figure 16, Concept 1 would require approximately 100 m^3 and Concept 2 would require approximately 147 m^3. The epoxy, which is 20 percent of the shield mass, must be transported from Earth. The mass of required epoxy for Concept 1 is 29 t (1 t = 1000 kg) and for Concept 2 is 43 t. An overall summary of the shielded options are shown in table 5.

Table 5. Shield mass estimates for habitat concepts.

Material	Shield, Amount, g/cm^2	Shield Thickness, cm	Shield Volume, m^3		Mass, t	
			Concept 1	Concept 2	Concept 1	Concept 2
Regolith	75	50	556	481	834	722
Polyethylene	18	19	40	59	46	54
Lithium Hydride	16	19	40	59	32	48
Regolith -20 wt-% epoxy	68	46	100	147	146	215

For the selected regolith, polyethylene, and lithium hydride shield thicknesses, the sum of the 1989 flare doses can also be estimated. From figure 8, a 5-cm depth dose equivalent of 0.35 cSv for regolith, 7.6 cSv for polyethylene, and 11.0 cSv for lithium hydride shields is estimated. The increased thicknesses of shield material greatly reduces the flare contribution to dose because of the flare's softer or less-energetic particle spectrum compared with the GCR. Thus, the larger quantities of regolith appear favorable; however, doses for all materials are still within the 30-day guideline/limit of 25 cSv. The sum of the 1989 flare dose with the annual dose due to

GCR for the shielding options are also within the annual limit/guideline of 50 cSv. Skin and eye doses are also estimated to be within the limits/guidelines [26]. The flare data suggest that water, lithium hydride, or polyethylene may be excellent materials for a flare shelter which may be provided for protection while crewmembers are in the process of covering their habitat with regolith. Water would most certainly serve a dual purpose once the habitat was covered.

The mass estimates of the prefabricated shielding transported from Earth can be compared with the mass requirements of the heavy equipment for regolith coverage. From table 3, assuming the combination of regolith equipment from the ESDB [14], a total mass of 9.0 t is estimated. This is only approximately 20 to 30 percent of the prefabricated shield mass requirements. In addition, the payoff of the regolith equipment mass will increase as more habitats (which require coverage) are added to the base and much of the equipment will most likely be used for other base activities. The regolith-epoxy shield option will require both the regolith moving equipment plus the epoxy to be launched from Earth. Concept 1 and 2 would require 38 t and 52 t, respectively, of Earth-launched mass, which is on the same order of magnitude as the total requirement of the prefabricated shielding. However, more analysis of this shield design concept should be conducted before it is discounted. Caution should be exercised in comparing radiation shielding options on the basis of Earth launch mass alone. The habitat design and shielding concepts are intimately related, thus, although the shielding characteristics of the materials will remain the same, other factors of the habitat design (such as size and configuration) and base operations (such as EVA time constraints or available equipment) may drive the shielding selection.

OPERATIONAL CONCERNS

Mission planners must address a variety of operational parameters before large scale regolith moving activities, such as utilizing in-situ resources for radiation shielding, can be undertaken. Regolith mining equipment must be designed and qualified to withstand the harsh lunar environment and to minimize the creation of dust. Many of the tasks associated with regolith moving operations may prove too tedious and EVA time-consuming to be practical. The added risk of extensive EVA operations must also be addressed. With potentially long periods of time anticipated away from the lunar habitat, a plan must be developed to protect crewmembers during EVA and sortie missions in the event of a large solar proton flare.

Construction and Mining Equipment Design

Construction and mining equipment must be designed to withstand the lunar vacuum, large temperature extremes, 1/6 gravity, and the adherence of abrasive dust particles [31]. In the lunar vacuum, many of the terrestrial lubricants will break down and specialized bearings and motors may be required. The repair and maintenance of equipment will also be difficult if machines must be worked on in EVA suits or if they must be returned to a pressurized volume for work. In addition, the lunar dust will cause severe operating conditions. The abrasiveness of the dust will increase the wear and tear on all moving parts and seals. The electrostatic adherence of the particles to all surfaces will make it a difficult problem to avoid. Design tolerances must also address temperature extremes of

134 °C to -170 °C, which are far greater than terrestrial machine designs tolerances, as well as designing for a fast rate of temperature change as machinery passes in and out of shadows. The decreased gravity will affect the excavating force as well as the maneuverability of some machines. In addition, the mining equipment must be designed to achieve a high operating reliability in this environment which may also prove difficult. As stated by Gertsch [31], "Terrestrial mining is notoriously hard on equipment; even the most rugged components have a disconcerting habit of breaking despite decades of design experience. This history has forced a conservative approach to mining methods and machinery design. Lunar mining equipment must be at least as reliable while operating in an even more rugged, poorly understood, and risky lunar environment."

Dust Contamination

Dust creating tasks, such as regolith collection and moving, should be performed as far as reasonably possible from the habitat area. Dust will adhere to thermal rejection radiators and possibly other reflective surfaces and to solar panels creating decreased operational efficiency. All contaminated surfaces will require frequent cleaning. Dust will need to be cleaned off suits before entering the habitat to avoid contamination of the environmental control and life support system. Thus, a reliable means of dust contamination control should be developed prior to excavating and moving large quantities of regolith at a lunar base site.

EVA Requirements

EVA requirements will also be a strong mission driver. A rough approximation of the magnitude of the EVA requirements for regolith shielding activities is attempted here assuming the shielding methodology and rationale described in Appendix 1 of Little [4]. The analysis assumed that the regolith was collected, bagged, and stacked in place around a habitat similar to that of Concept 2 (but much larger). The analysis also assumed various degrees of automation throughout the shielding operations and relied heavily on the automation of the bagging, moving, and placement of regolith with varying degrees of human intervention for each task. Roughly 555 person-hours of EVA were estimated to cover the assumed habitat configuration with 4558 m^3 of regolith to a depth of 2 m (a shield thickness of 2 m was selected based on earlier shield requirement studies). In the analysis, a linear relationship existed between the volume of regolith required for shielding and the number of EVA hours required to shield the habitat. As shown in table 2, on the order of 481 m^3 to 556 m^3 of regolith are required for shielding the habitat concepts. Using the previous analysis as a basis, it is estimated that 68 EVA-hours are required to shield Concept 1 with 556 m^3 of regolith and 59 EVA-hours are required to shield Concept 2 with 481 m^3 of regolith. Further, assuming 4 workers are available and each one works one 6-hour EVA shift per day, then an estimated 2.5 to 3 days will be required. Although Concept 1 and Concept 2 do not require the bagging of all the regolith as did Little's analysis [4], the comparison does serve to illustrate the magnitude of the EVA time required.

In addition, the regolith excavation time must also be estimated. The duty cycle of a 7.7 t capacity front end loader (similar to the ripper excavation loader in Table 3) is estimated to have a yearly production rate of 33,000 t/yr with a 35% duty cycle [32]. In comparison, well-managed Earth-based operations have a daily production rate of 40

to 100 m^3 per 8 hours per person [33] which would equate to 22,000 to 55,000 t/yr of lunar regolith. Thus, 33,000 t/yr appears to be an ambitious production rate. Nonetheless, the 834 t (556 m^3) for Concept 1 would require just over 9 days to excavate and the 722 t (481 m^3) for Concept 2 would require approximately 8 days to excavate. Thus, the entire shielding operation is estimated to take between 10.5 to 12 days. Although it is not the purpose of this analysis to estimate EVA time and machinery design criteria for mission specifics, the above estimates do provide a rough magnitude of the required regolith moving operations and EVA activities. Likewise, there will be EVA requirements for the placement of prefabricated shielding.

Solar Proton Flares

During normal lunar base activities, it is anticipated that there will be many times during which crewmembers will venture from the habitat. Crewmembers may be relatively unprotected from the radiation environment during scientific sortie missions, during routine maintenance on external systems, during regolith excavation and moving, and during other in-situ radiation shielding operations. Scientific sortie missions and regolith moving activities will most likely take crewmembers furthest from the base. As mentioned earlier, if the solar flare can be predicted, crewmembers will have a minimum warning time of 20 minutes before the arrival of energetic particles. A time analysis of the development of the October 1989 flare was performed by Simonsen et al. [34]. The dose equivalent rate to the skin (0-cm depth dose), eye (0-cm depth dose), and BFO (5-cm depth dose) organs was estimated using the GOES-7 satellite time history data of the October flare as input to the BRYNTRN code. The dose equivalent rates (ICRP-26) were then compared with the LEO limits to determine if and when any limits were exceeded as shown in table 6. For missions away from the base, it was assumed that the EVA suit provided approximately 0.5 g/cm^2 of equivalent water protection. As shown in table 6, all the limits are exceeded except the BFO career limit (assumed to be 200 cSv) within the first 32.5 hr after receiving the flare warning. The limiting dose for the October 1989 flare is the 30-day ocular lens dose which is reached 17 hours after receiving warning. In comparison, one EVA shift may last between 6–8 hours. Most importantly, for flares like the October 1989 event, crewmembers will have a number of hours to seek shelter before any 30-day limits are exceeded. These times would then determine a safe distance a crewmember could venture from the protection of the habitat or flare shelter. The best possible scenario is that crewmembers reach the shelter as soon as possible to keep their doses as low as reasonably achievable.

Table 6. Time after start of October 1989 proton event for which limits are exceeded for a water shield thickness of 0.5 g/cm^2 on the lunar surface [34].

Exposure Limit	Time after which limit is exceed for		
	Blood Forming Organ, hr	Ocular Lens, hr	Skin, hr
30-day	21.5	16.8	21.0
Annual	32.5	22.2	23.3
Career	not exceeded (assuming 200 cSv limit)	24.4	28.1

The time development of flares can be very different. The October 1989 flare came in three main pulses and lasted on the order of 10 days. The February 1956 flare delivered its dose within hours; twenty minutes after the optical flare and radio noise were seen at Earth, energetic particles arrived. From the ground-based measurements, the February 1956 intensity was seen to have peaked 30 minutes later followed by a decay with a mean time of one hour [35]. Thus, the entire flare lasted only a few hours. Crewmembers would have had significantly less time to reach a flare shelter before limits were exceeded compared with the October event. The time development of the February event was also characteristically very different from the other recorded large flares of November 1960 and August 1972.

The August 1972 event series is an interesting set of events not only from the point of view of their seriousness of exposure, but also from the time occurrence and observation of related variables [36]. It was predicted on August 2, 1972, that there would be no major solar activity for the period of August 3 to August 9. However, it appears that even as this prediction was being officially released, the August 1972 flare sequence was in progress. During the class 3B flare of August 2, 1972, at 2005 UT, a large type IV radio burst was among the significant ground-based observations made. On the basis of these observed data, large dose rates were predicted for free space. However, the observed doses according to the IMP satellite data were found to be only 1.3 cGy at a 1-cm depth. A smaller 2B flare then occurred on August 4, 1972, at 0621 UT for which radio output records are lacking (presumably from observational selection). Whereas only minor doses in free space were predicted for this event, it was the largest event ever observed for space exposures. By 0700 UT, the accumulated dose at 1-cm depth was at 2.7 cGy, climbing rapidly to 10 Gy over the next several hours (1400 UT). Astronauts (nominally shielded in free space) would have had only ~3.5 hours to reach a flare shelter from the time of flare onset at 1AU to the time that 30-day exposure limits were exceeded. The second less conspicuous August 4, 1972, event may have led one to under react due to the "cry of wolf" only 34 hours earlier. However, if one did not react properly to this second event, in some ways a seemingly less important event, then severe exposures would have been received within several hours. For EVA missions on the lunar surface, the further examination of solar flare time development data and flare forecasting methods are required to quantify "safe" distances that crewmembers can venture away from their flare shelters during lunar operations.

CONCLUDING REMARKS

Although a definitive answer to "what is the best shielding option" cannot be made at this time, this analysis attempts to provide materials data which can be used for trade studies for various shield options. Examples of how to use the material dose-vs-depth data directly are provided to aid in quick comparisons of shield mass requirements. The materials data also provide valuable information for the selection of habitat components, for instance, the protection of crewmembers using potable and waste water or the selection of a polyetherimide composite as the internal structure of a habitat module. Various operational concerns associated with in-situ resource utilization, which must be examined before a shielding methodology is selected, are also discussed.

Lunar regolith still appears to be an attractive option for radiation protection for the habitat configurations considered in this analysis. However, if much smaller habitats are selected, then the mass of the regolith-moving equipment may approach the mass requirements of prefabricated shields launched from Earth. Some of the major trade-offs will be the EVA time requirements, EVA risk, and the design costs and reliability of regolith moving equipment. If it is deemed necessary to provide a flare shelter while the habitat is being covered, viable options appear to be polyethylene, lithium hydride, and water.

Future studies must emphasize the use of track-structure dependent biological response modeling for astronaut risk assessment instead of quality factors based on LET for protection from HZE particles. The adequacy of results derived using quality factors to represent biological systems is still in question for HZE particles. Thus, the optimization of shield designs must await an improved understanding of biological response. Space flight validation of shield design software, nuclear cross-section databases, transport codes, and environmental models are also required for shield design optimization. If advanced materials are selected, effort is required in the area of shield materials concept development and laboratory validation. The aforementioned advancements can be easily incorporated into the shield design methodologies described in this report.

REFERENCES

1. *Analysis of the Synthesis Group's Space Resource Utilization Architecture*. NASA Exploration Programs Office Document XE-92-002, February 7, 1992.

2. Hypes, W.D.; Butterfield, A.J.; King, C.B.; Qualls, G.D.; Davis, W.T.; Gould, M.J.; Nealy, J.E.; and Simonsen, L.C.: *Concepts for Manned Lunar Habitats*. NASA TM-104114, August 1991.

3. *Report of the 90-Day Study on Human Exploration of the Moon and Mars*. NASA Johnson Space Center, November 1989.

4. Arthur D. Little, Inc.: *Advanced Extravehicular Activity Systems Requirements Definition Study*. Final Report to NASA Johnson Space Center, Contract No. NASA-17894, Reference 60149, August 1988.

5. *Guidance on Radiation Received in Space Activities*. National Council on Radiation and Measurements. NCRP Report No. 98, July 31, 1989.

6. *1990 Recommendations of the International Commission on Radiological Protection*. ICRP Publ. 60, Pergamon Press, November 1990.

7. *Recommendations of the International Commission on Radiological Protection*. ICRP Publ. 26, Pergamon Press, Jan. 17, 1977.

8. International Commission on Radiation Units and Measurements: ICRU Report 40: *The Quality Factor in Radiation Protection*. Bethesda, MD, April 1986.

9. Simonsen, L.C.; Atwell, W.; Nealy, J.E.; and Cucinotta, F.A.: *Radiation Dose to Critical Body Organs for the October 1989 Proton Event*. NASA TP-3237, 1992.

10. Curtis, S.B.; Nealy, J.E.; and Wilson, J.W.: Risk Cross Sections and their Application to Risk Estimation in the Galactic Cosmic Ray Environment. *Radiation Research*, Vol. 141, pp. 57–65, 1995.

11. Nealy, J.E.; Wilson, J.W.; and Townsend, L.W.: *Solar-Flare Shielding with Regolith at a Lunar Base Site*. NASA TP-2869, 1988.

12. Nealy, J.E.; Wilson, J.W.; and Townsend, L.W.: Preliminary Analyses of Space Radiation Protection for Lunar Base Surface Systems. SAE Tech. Paper Ser. 891487, July 1989.

13. Smith, R.E.; and West, G.S., compilers: *Space and Planetary Environment Criteria Guidelines for Use in Space Vehicle Development, 1982 Revision (Volume 1)*. NASA TM-82478, 1983.

14. *Element/Systems Data Base (ESDB). Release 91.1*. Planet Surface Systems Office, NASA JSC-45107, May 1991.

15. Gertsch, R.E.: A Method for Mining Lunar Soil. Sixth Princeton/SSI Conference on Space Manufacturing, Paper No. AAS 83–234, 1988.

16. Sauer, H.H.; Zwickl, R.D.; and Ness, M.J.: *Summary Data for the Solar Energetic Particle Events of August through December 1989*. NOAA-Space Environment Laboratory, 1990.

17. Heckman, G.; Hirman, J.; Kunches, J.; and Balch, C.: The Monitoring and Prediction of Solar Particle Events—An Experience Report. *Adv. Space Res.*, Vol. 4 , No. 10, 1984, pp. 165–172.

18. Adams, J.H.; Silberberg, R.; and Tsao, C.H.: *Cosmic Ray Effects on Microelectronics. Part-I The Near-Earth Environment.* NRL Memo. Rep. 4506-Pt.-I, US Navy, Aug. 1981.

19. Wilson, J.W.; Townsend, L.W.; Schimmerling, W.S.; Khandelwal, G.S.; Khan, F.; Nealy, J.E.; Cucinotta, F.A.; Simonsen, L.C.; Shinn, J.L.; and Norbury, J.W.: T*ransport Methods and Interactions for Space Radiations*. NASA RP-1257, December 1991.

20. Badhwar, G.D.; and O'Neill, P.M.: An Improved Model of GCR for Space Exploration Missions. *Nucl. Tracks Radiat. Meas*., Vol. 20, pp. 403–410, 1992.

21. Wilson, J.W.; Townsend, L.W.; Nealy, J.E.; Chun, S.Y.; Hong, B.S.; Buck, W.W.; Lamkin, S.L.; Ganapol, B.D.; Khan, F.; and Cucinotta, F.A.: *BRYNTRN: A Baryon Transport Model*. NASA TP-2887, 1989.

22. Wilson, J.W.; Chun, S.Y.; Badavi, L.W.; Townsend, L.W.; and Lamkin, S.L.: *"HZETRN:" A Heavy-Ion/Nucleon Transport Code for Space Radiations*. NASA TP-3146, 1991.

23. Reilly, J.J.; and Sandrock, G.D.: Hydrogen Storage in Metal Hydrides. *Scientific American*, Vol. 242, Feb. 1980.

24. Stephens, J.M.; Glasgow, M.B.; Kiefer, R.L.; Orwoll, R.A.; and Long, S.A.T.: Radiation Effects on Films on Boron-Loaded Polymers. *Polymer Preprints*, Vol. 33 (1), pp. 1152–1153, 1992.

25. Kraus, W.B.; Glasgow, M.B.; Kim, M.Y.; Olmeijer, D.L.; Kiefer, R.L., Orwoll, R.A.; and Thibeault, S.A.: Boron Containing Polymers for Radiation Shielding. *Polymer Preprints*, Vol. 34 (1), pp. 592–593, 1993.

26. Simonsen, L.C.; Nealy, J.E.; and Townsend, L.W.: Concepts and Strategies for Lunar Base Radiation Protection: Prefabricated Versus In-Situ Materials. SAE Paper No. 921370. Society of Automotive Engineers International Conference on Environmental Systems Transactions, 1992.

27. Kim, M.Y.; Thibeault, S.A.; Wilson, J.W.; Kiefer, R.L.; and Orwoll, R.A.: Performance of Polymeric Materials as Shielding for Cosmic Radiation. *Polymer Preprints*, Vol. 35, No. 2, pp. 961–962, August 1994.

28. Wilson, J.W.; Cucinotta, F.A.; and Shinn, J.L.: Cell Kinetics and Track Structure. In *Biological Effects and Physics of Solar and Galactic Cosmic Radiation, Part A,* Edited by C.E. Swenberg et al., Plenum Press, New York, 1993.

29. Wilson, J.W.; Kim, M.; Schimmerling, W.; Badavi, F.F.; Thibeault, S.A.; Cucinotta, F.A.; Shinn, J.L.; and Kiefer, R.: Issues in Space Radiation Protection: Galactic Cosmic Rays. *Health Physics.* Vol. 68, No. 1, January 1995.

30. Thibeault, S.A.; Long, E.R., Jr.; Glasgow, M.B.; Orwoll, R.A.; and Kiefer, R.L.: Boron-Loaded Epoxy Material for Neutron Shielding. *Polymer Preprints*, Vol. 35 (2), pp. 954–955, 1994.

31. Gertsch, R.E.; and Gertsch, L.E.: Lunar Surface Mines and Mining Machinery: Design Criteria. In *Space 90: Engineering, Construction, and Operations in Space II*, *1990* (Edited by S.W. Johnson and J.P. Wetzel). pp. 274–283.

32. The Office of Exploration FY 1989 Annual Report. Exploration Studies Technical Report Volume III: Planetary Surface Systems. NASA TM-4170, 1989.

33. Sharp, W.R.; Steele, J.P.H.; Clark, B.C.; and Kennedy, E.R.: Mining and Excavating Systems for a Lunar Environment. In *Space 90: Engineering, Construction, and Operations in Space II*, *1990* (Edited by S.W. Johnson and J.P. Wetzel). pp. 294–304.

34. Simonsen, L.C.; Nealy, J.E.; Sauer, H.H.; and Townsend, L.W.: *Solar Flare Prediction for Manned Lunar Missions: Analysis of the October 1989 Proton Flare Event.* SAE Technical Paper Series No. 911351, 21st International Conference on Environmental Systems, San Francisco, California, July 15–18, 1991.

35. Foelsche, T.; Mendell, R.B.; Wilson, J.W.; and Adams, R.R.: *Measured and Calculated Neutron Spectra and Dose Equivalent Rates at High Altitudes; Relevence to SST Operation and Space Research.* NASA TN D-7715, October 1974.

36. Wilson, J.W. and Denn, F.M.: *Preliminary Analysis of the Implications of Natural Radiations on Geostationary Operations.* NASA TN D-8290, September 1976.
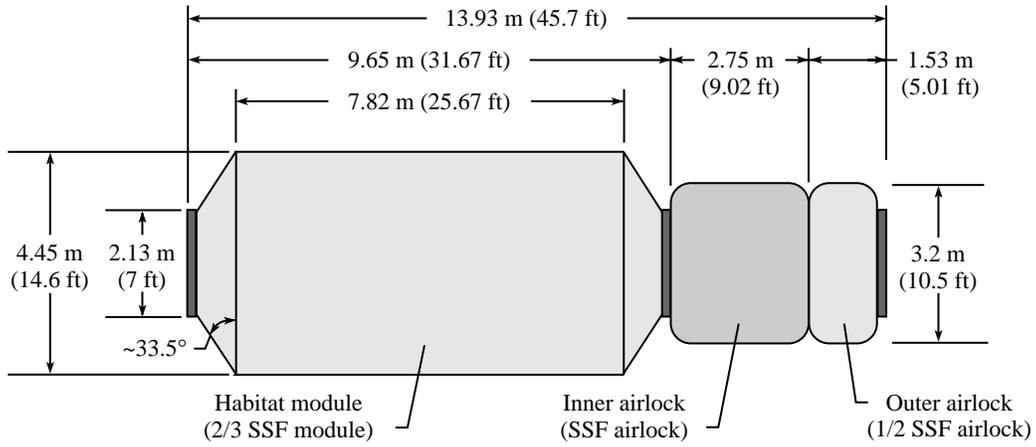
Figure 1.   Lunar outpost habitat Concept 1 [2].
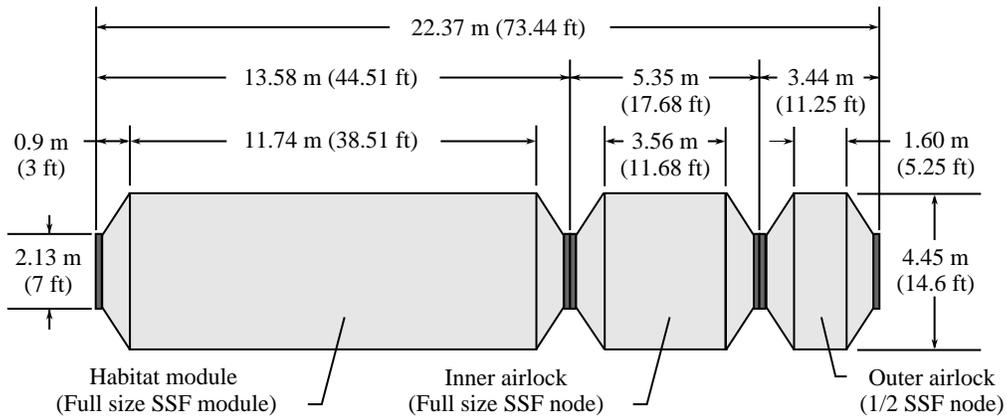
Figure 2.   Lunar outpost habitat Concept 2 [2].
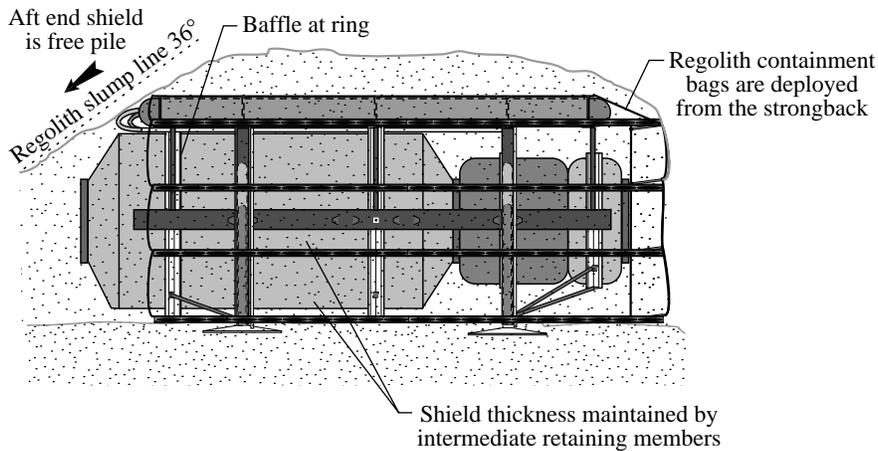
Figure 3.   Concept 1 habitat with regolith shield [2].
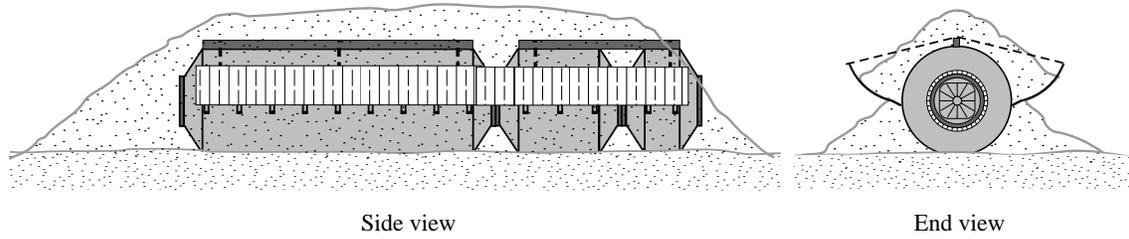
Figure 4.   Concept 2 habitat with regolith shield [2].
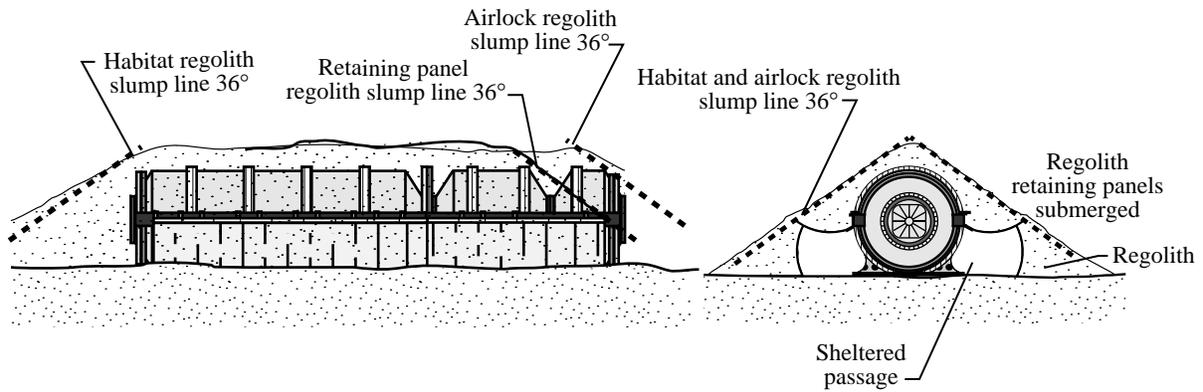
Figure 5.   Concept 2 habitat with regolith shield [2].
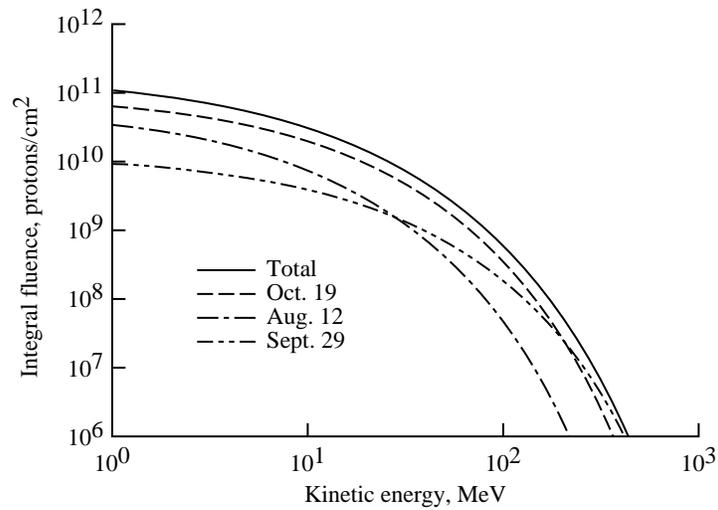
Figure 6.   Three large solar flare fluences based on 1989 GOES-7 data.
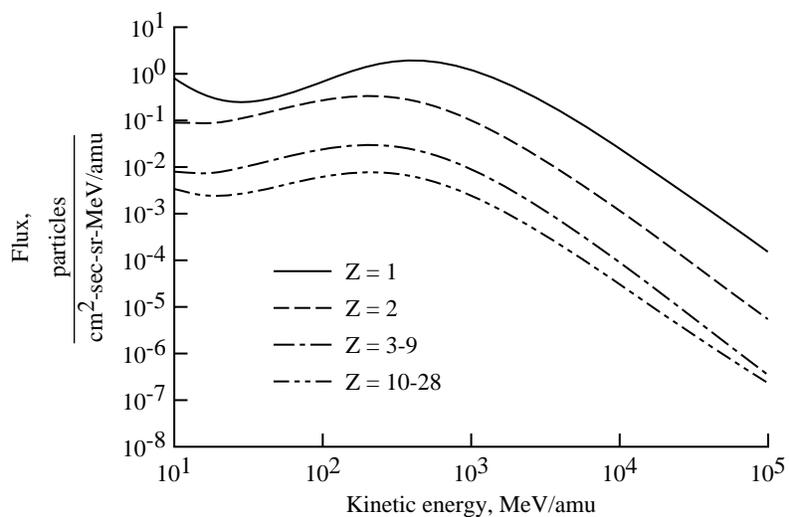
Figure 7.   Galactic cosmic ray differential flux spectra at solar minimum for selected elemental groupings.
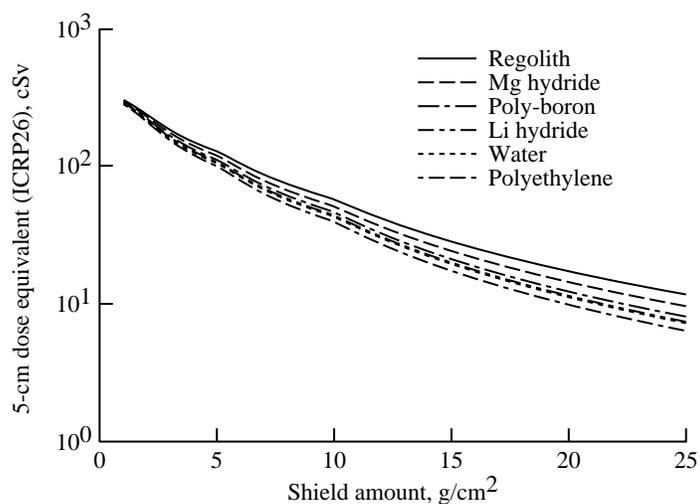
Figure 8.   5-cm depth dose for sum of 1989 flares as function of areal density for various materials.
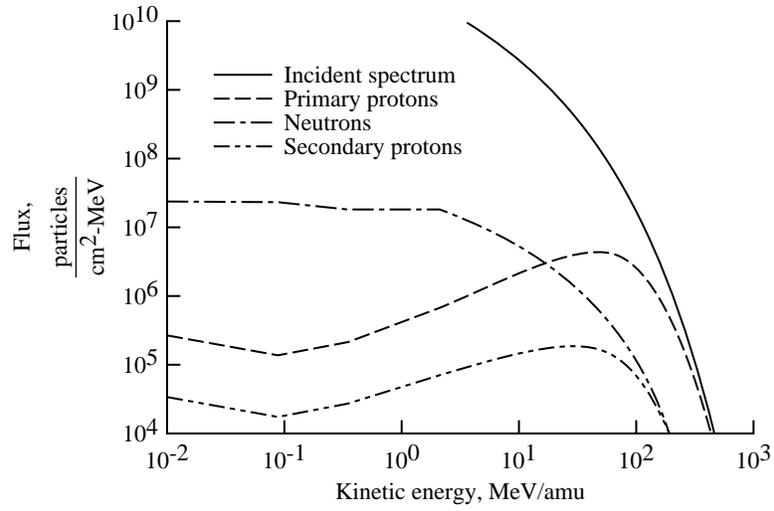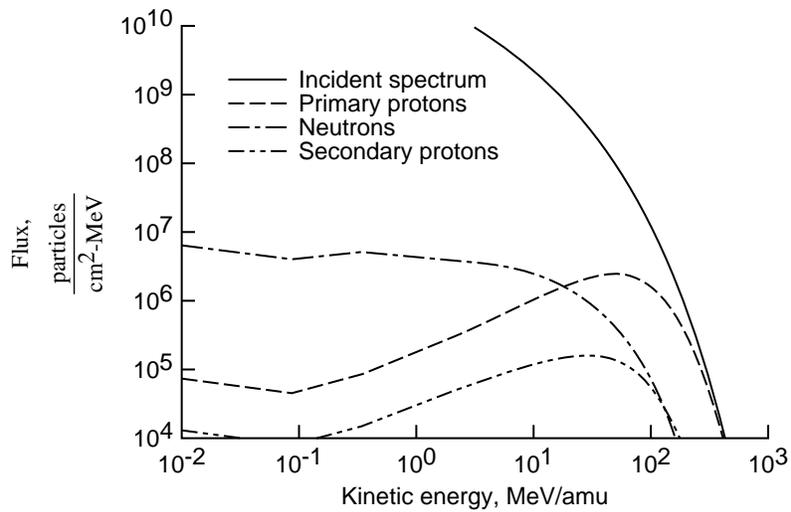
(a) Lunar regolith.

(b) Polyethylene.

Figure 9.   Nucleon flux spectra for 1989 flare exposures emergent from 10 g/cm^2 of lunar regolith and polyethylene.
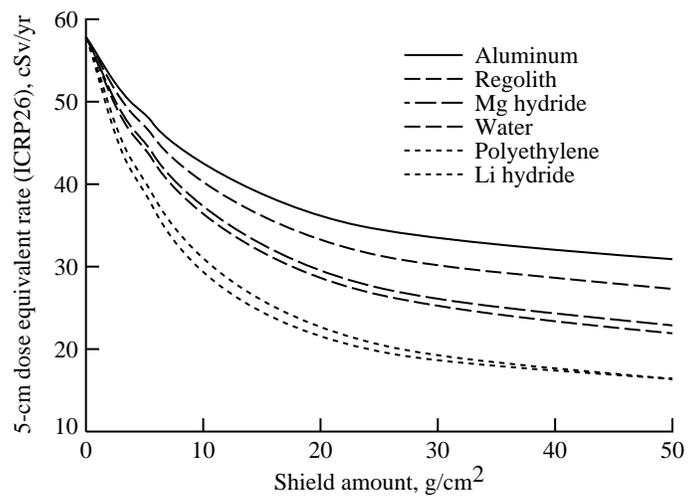
Figure 10.   5-cm depth dose for GCR at solar minimum as a function of areal density for various materials.
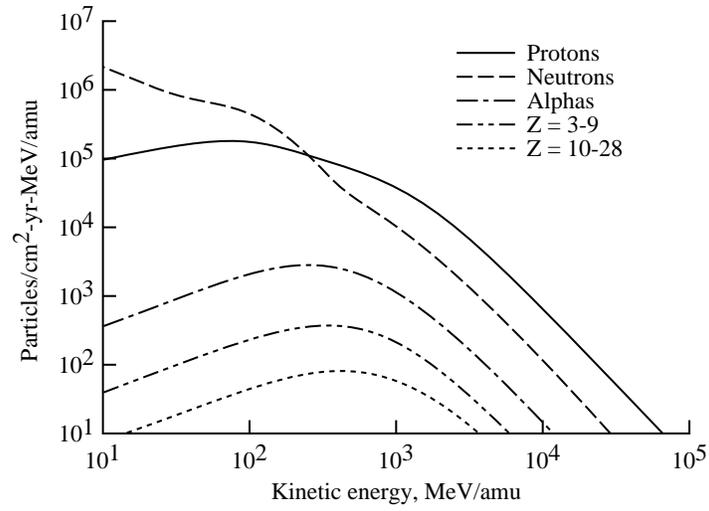
(a) Lunar regolith.

Figure 11. Energetic particle flux spectra for solar minimum GCR emergent from 50 g/cm^2 of lunar regolith and lithium hydride.
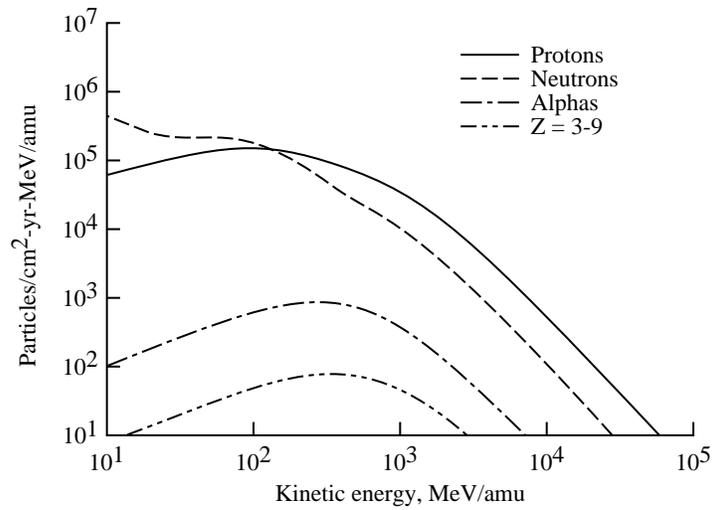
(b) Lithium hydride.

Figure 11. Concluded.
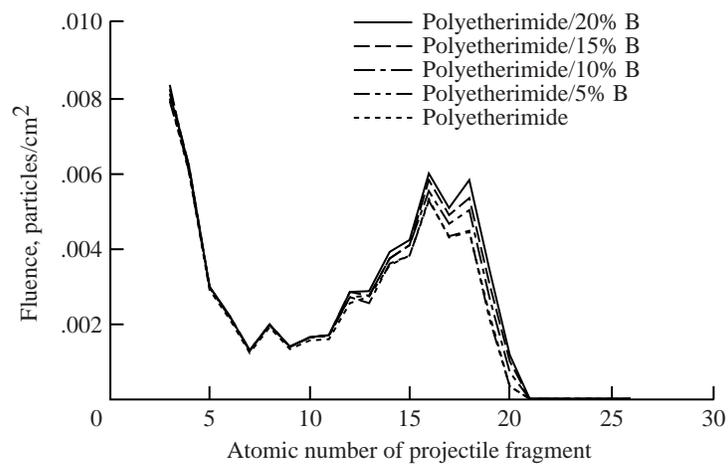
Figure 12. Calculated fluence of projectile fragments after traversal of 18 g/cm^2 thick polyetherimide shield irradiated with 33.88 GeV ^{56}Fe ions.
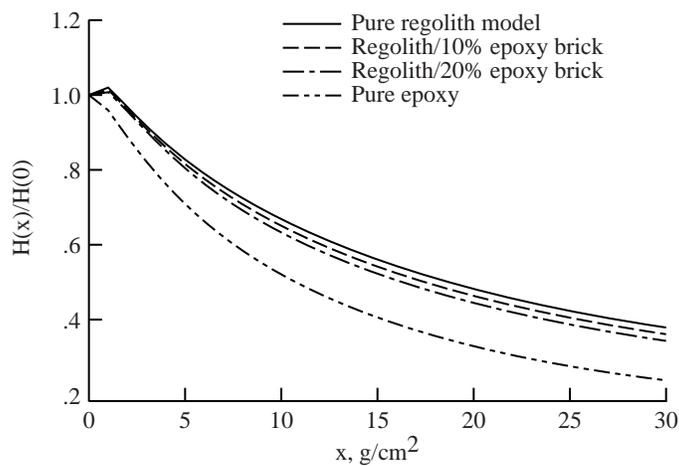
Figure 13. Attenuation of dose equivalent due to 1977 solar minimum GCR fluence behind regolith and regolith-epoxy shield as a function of areal density [27].
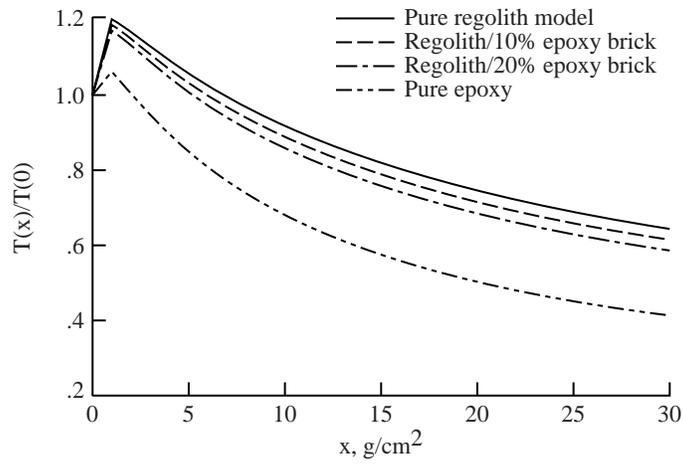
Figure 14. Attenuation of cell transformation due to 1977 solar minimum GCR fluence behind regolith and regolith-epoxy shields as a function of areal density [27].

(a) GCR at Solar Minimum   (b) August 1972 particle event
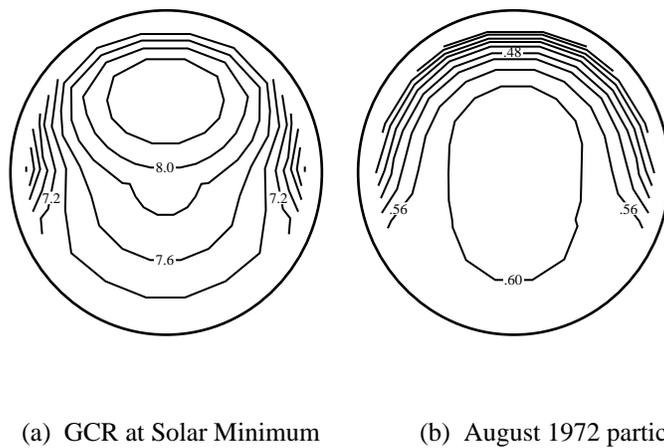
Figure 15. BFO dose equivalent distribution within the habitat module for the regolith shielding concept of figure 5.
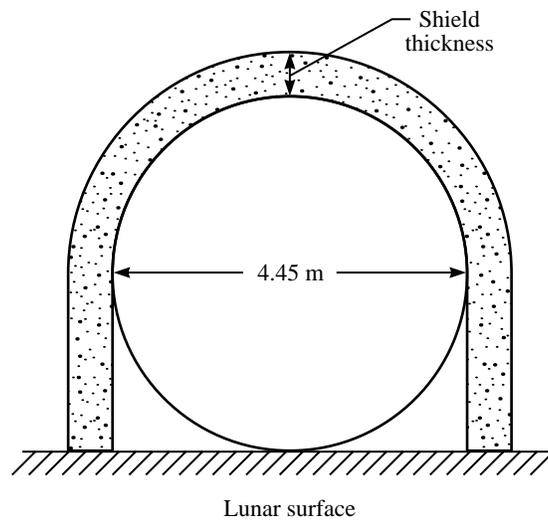
Figure 16.   Cross-sectional view of prefabricated shield concept around habitat module.

CHAPTER 16

EXCAVATING ON THE MOON AND MARS

by

Leslie Gertsch[1]

Richard Gertsch[2]

[1]Assistant Professor in the Mining Engineering Department and Director of the Center for Space Mining, Colorado School of Mines, Golden, CO 80401
[2]Rock Mechanics and Explosives Research Center, University of Missouri-Rolla, MO 65401

EXCAVATING ON THE MOON AND MARS

CHAPTER 16

INTRODUCTION

This paper briefly reviews terrestrial methods for excavating soil and rock, and discusses them with a view toward using the material as radiation shielding for initial human operations—reconnaissance missions—on the Moon and on Mars. Much of the equipment and techniques can be used also for mining, and would remain essentially the same whatever the end use of the material mined: local building material, resource export, or construction material for space operations. A small mining operation to provide shielding material for an outpost can form the nucleus of a larger scale effort in extraterrestrial manufacturing and supply for a permanent human presence.

All of the approaches to material excavation that are outlined here were developed on Earth. With rare exception, they have not been applied to any extraterrestrial environment (the exceptions are the robotic sample scoops on various lunar and martian landers, and the digging and coring performed by lunar astronauts). Consequently, many of the machine design criteria discussed here will have to be modified, often radically, for effective application on the Moon and Mars.

Although numerous effects of the nonterrestrial environments are discussed in this paper, all data regarding machine performance and mass trends are for present-day Earth-bound equipment. This paper is intended as background information source for planners, rather than a compendium of data that do not yet exist. To begin to obtain that data will require a well-planned, objective program of physical testing and evaluation of basic machine design criteria in the environments of the Moon and Mars.

SCENARIOS

Two basic shielding scenarios are possible for shielding human activity on the Moon and Mars from the harmful effects of cosmic radiation: tunneling into a rock mass to create living and working spaces, and heaping loose surface material over constructed habitats on the surface. Each scenario requires a different suite of equipment and techniques.

Tunneling

This approach would use the naturally occurring rock or regolith mass as a radiation shield, augmented perhaps by grouting the surrounding rock or lining the excavated spaces. The principal difference between this and the second scenario is the greater uncertainty of quality control with respect to the homogeneity of the shielding capability. Human fabrication of shield material would create a more certain product than reliance on variable properties of an imperfectly known rock mass.

On the other hand, a rock mass *in situ* already is in mechanical equilibrium on human time scales.

Unconsolidated Mass

This often-imagined scenario would construct habitats on or near the surface, with foundations seated perhaps a few meters deep. Regolith would be gathered and piled over the structures to an acceptable thickness. Variations on this theme include compaction of the regolith, masonry-like construction using manufactured regolithic bricks, and vitrification of the outer surface of the unconsolidated regolith shield.

Wilson et al. [1] estimate regolith thickness of 50 cm will be required to shield lunar habitats, 15 to 20 cm for martian habitats. The original studies ignored the angle of repose of unconsolidated regolith, although this has been rectified in other work (Simonsen et al. [2]). Incorporating the additional mass necessary to assure stability of the shielding material placement increases the radiation safety factor.

ENVIRONMENT

The environments of both the Moon and Mars are discussed in great detail elsewhere (Simonsen [3]). However, those aspects that will affect excavation processes are summarized here. The actual extent of these effects cannot be determined until physical trials are conducted.

Lunar

In terms of the energy needed for transport, the Moon and Mars are much closer to each other than they are to Earth, from where all support and supplies must come. Missions will have to be planned carefully and have a high degree of flexibility; sending home for a wider conveyor belt, for example, will be a very expensive option. This impacts directly on one of the major problems of excavation anywhere: the properties of natural materials vary in unexpected ways. Regardless of the degree of automation, it will be very difficult to micromanage an excavation operation successfully from Earth. This implies a high degree of autonomy, provided by humans or intelligent equipment or, more likely, a combination.

Both the Moon and Mars generate a gravitational acceleration that is significantly lower than accustomed to on Earth. Since nearly all mining and processing procedures rely heavily on the effects of Earth's gravity, this is expected to be one of the major differences. Lunar gravity is 17% that of Earth's.

The atmosphere of the Moon is essentially a vacuum. The few sparse gas molecules that do exist are insufficient to create the ubiquitous molecular layer on all surfaces that current industrial processes depend on. This will affect the flow of fragmented rock increasingly as the particle size becomes finer.

The lack of atmosphere and the two week day/night cycle create wide temperature extremes. Machines running in direct sunlight could tend to overheat, but night operation will be difficult due to the deleterious effects of cold on materials, including seals and lubricants.

Martian

In addition to the lower gravity (40% of Earth's) and the far remove from Earth cited for Lunar operations, Mars operations must deal with other factors.

The temperature swing between day and night is somewhat less than on the Moon, but the median temperature still is much colder than Earth activity (-123ºC to 26ºC). This depends also on the location of the operation, for Mars has an atmosphere. It is much thinner and of different composition (mostly carbon dioxide) than Earth's (mostly nitrogen) and so does not react in the same ways to external (solar) influences.

Martian soil is chemically reactive, containing a powerful oxidizing agent. If widespread, this would affect machine reliability to an unknown degree in both the short and long terms.

UNIT OPERATIONS

Mining projects are planned and conducted using the concept of unit operations that apply whether the operation is on the surface or underground, large or small, metal or nonmetal, or coal or industrial mineral. The mining unit operations are fragmentation, excavation, materials handling (transport), and ground support. The unit operations approach is a powerful tool; each unit operation can be a self-contained module of equipment and procedures. In practice, more than one unit operation often is incorporated in a single machine (Gertsch [4]). The techniques of accomplishing the unit operations can be either cyclic (e.g., drilling, blasting, removing the broken rock, ensuring rock mass stability, then starting all over again) or continuous (all unit operations underway at the same time).

Fragmentation

Fragmentation breaks the desired material from the surrounding mass by inducing fracturing. The method used may range from scraping to ripping to explosives to mechanical excavation. The distribution of fragment sizes and, to a lesser degree, shapes affects the performance of all subsequent handling of the material. These parameters are controlled mainly by the characteristics of the material, and to a lesser degree by the type of fragmentation method employed.

Excavation

Excavation is the process of removing the material from *in situ* after it has been fragmented. It often is combined with the fragmentation process (e.g., some mechanical excavators both fragment and excavate). For unconsolidated or weakly compacted materials, a separate fragmentation step often is unnecessary.

Transport

The transportation of the material to the processing plant or the placement location is an important aspect of mining. It can be the limiting factor in determining production rates. For example, current rock-cutting technology would allow mechanical tunnel boring machines to advance much faster than they actually do, but the broken rock has to be picked up from the excavation floor and removed at a rate no less than that at which it is produced.

Processing

Processing changes the form and/or content of the material in preparation for its final use. For producing shielding material, that could range from simple sizing (crushing, grinding, and sorting) to complex processes for element extraction and material manufacture. This aspect is not dealt with here.

Placement

Although not a traditional unit operation, placement is included here as the last step in the process of creating a radiation shield. It consists of either piling and compacting the regolith, or constructing a shield using more thoroughly processed material (i.e., manufactured building materials). It may be unnecessary in the tunneling scenario unless a lining is manufactured from native materials.

EQUIPMENT SELECTION

Equipment selection is a subject of great importance to terrestrial mining and civil engineers, as it has a profound influence on the financial success or failure of a project. Even so, it must account for so many variables, many of them imperfectly known, that it remains as much an art as a science. Martin et al. [5] and Atkinson [6] discuss this topic with respect to excavation equipment. Caterpillar Inc. [7] also publishes detailed information on selection criteria.

The production capacity of any machine is determined by the geometry of the machine, the cycle time, and the efficiency of the operation. The first parameter is determined by the machine design, including modifications made on-site (very common). The second is governed by the characteristics of the particular operation, including length of travel/haul; grade profile of the path; cohesiveness, bearing capacity, and angle of repose of the material; and times needed for fixed tasks (loading, dumping, turning, etc.). The third, efficiency, is a modifying factor that takes into account everything that affects the average production rate of the machine, such as moderate downhill grades (a help) or abrasive or sticky materials, night-time operation, etc. (hindrances). The efficiency of extraterrestrial excavation is expected to be very low by Earth standards.

Cycle times and machine efficiency on Earth are determined empirically, with time-and-motion studies of the actual or similar operations with the same or similar equipment. The more removed previous experience is from the situation at hand, the less reliable the prediction of machine efficiency (also called reliability or availability). In the instance of excavation on the Moon and Mars, terrestrial precedents are so different that only relative evaluations among different machines can be made. Even that is of limited usefulness since the nonterrestrial environments will affect different aspects of machine design, use, and maintenance.

The equipment selection process ranks all candidate machinery in terms of application severity and machine complexity to produce a relative score. Some of the issues of importance on Earth, such as the effect of wet weather, are not directly transferable off-planet. However, other issues will be of increased importance. What these are, and how they will affect equipment availability, can be determined with any degree of confidence only with empirical studies.

For example, for extraterrestrial projects, the shipping (launch) weight of the machine is of greater concern than usual. This will be exacerbated by the usual response of machine designers to abrasive conditions: thicken wear parts and make them more robust, thereby increasing the mass of the machine. Note that, although most of the plots in this paper concentrate on equipment mass and per-load capacity, many more factors must be taken into account for effective equipment selection.

A convenient measure for comparing excavation systems is the specific energy of excavation. This is the amount of energy required to fragment a unit volume of material. Figure 1 shows the relative specific energies of the different rock fragmentation methods in use on Earth. Subject to constraints of available power and machine strength, rock fragmentation is more efficient at lower specific energies; less fracture surface area is required to produce larger particles (fragmentation energy is directly proportional to fracture surface area created).

TUNNELING

Tunneling on Earth is accomplished either cyclically, with explosives, or continuously, with mechanical excavation equipment. This section describes the systems that are used to create underground openings.

Machine configurations, indeed the initial choice of machine type, depend on whether the tunnel is being driven in "soft ground"—poorly consolidated material—or hard rock. The choice on the Moon and Mars will depend on the location and the needs of the project. The relative radiation shielding characteristics of the two types of material also will play a part in equipment selection.

Cut-and-Cover

This actually is a surface method, in which a tunnel is created by digging it as a trench, erecting ground support for the sidewalls and roof, then backfilling the top. The depth of excavation could be calculated to provide just enough material for shielding the remaining height of the habitat, built as a surface structure.

This approach will require some sort of surface excavation system, such as a backhoe (see below), which is practical for depths to 6 m, although the process can be taken in stages to depths of 18 m (Morton [8]). Sheeting is installed to support the walls in all cases. The structural requirements (and therefore the mass) of the sheeting will have to be determined from more detailed study of lunar and martian materials. It must withstand inward flexure, bottom heave, and rupture.

Drilling and Blasting

This is the traditional method of excavating rock, and still consumes the lowest specific energy. It remains the fragmentation method of choice for many surface and underground mines. Material is fragmented by distributing an explosive agent in holes drilled into the rock volume. After detonation, the muck (broken rock) is removed by hand shovel or, more commonly, powered mucking machine. The cycle is repeated when the working area has been cleaned and made safe.

In terms of material volume fragmented versus launch mass, this approach is by far the most efficient. The specific energy for explosively fragmented material is much less than by any other method (Figure 1). With regard to transportation safety concerns, many explosives are available in binary form; that is, one component (the largest by mass or volume) is insensitive to normal shock, and can only be detonated by the second, initiator component (small volume). Additionally, Mars, and perhaps the Moon, may provide the appropriate raw materials to manufacture one or both components. This is an area of research that deserves increased attention, for it could provide enormous savings in program launch costs.

Drills will be needed to bore the blastholes for spreading the explosive throughout the rock volume to be fragmented. Numerous designs are in use today that operate by percussion, rotation, or a combination of the two. One design already has been adapted for obtaining core samples from the lunar regolith, with mixed success due in part to the unexpectedly high cohesion of the regolith below a few centimeters depth. This example points out the importance of detailed, accurate characterization of the target material prior to equipment design and mission planning.

Full-Face Mechanical Excavators

Also known as tunnel boring machines (TBMs), these are complex, dedicated fragmentation/excavation systems that create round tunnels one meter to 13 meters in diameter, to essentially unlimited length. Some of the smaller machines (microtunnelers, up to 3 m diameter) are designed to operate with no human presence in the tunnel, a feature that increases their usefulness in hazardous environments. TBM designs can be optimized for tunneling through rock of all strengths and conditions, by changing the cutting tools and the amount of support the machine gives the working face (Thon [9] and Handewith and Dahmen [10]).

TBMs and microtunneling machines operate by pushing a rotating cutterhead against the rock (Figure 2). The reaction forces for this are generated by gripping the walls of the just-excavated tunnel with hydraulic pads. Behind itself, the TBM pulls a short conveyor onto which it loads the muck (rock chips) created by the cutting tools

mounted on the cutterhead. This conveyor unloads the muck onto another conveyor, rail, or truck haulage for removal from the tunnel. Equipment for grouting the rock surrounding the tunnel, installing rock bolts (to prevent rockfalls), and installing tunnel lining also are mounted on the TBM frame, which can be 30 m long or more (Figure 3).

The smaller TBMs may be useful for creating living and working spaces within the regolith or the rock masses of the Moon and Mars. The stability of underground excavations too near the surface is poor, so increasing their depth will increase the mechanical stability of the opening as well as the radiation shielding effect.

Regolith would be considered "firm ground" in soft-ground tunneling parlance, in other words, non-rock material in need of support during the tunneling process, but not too prone to run-ins. TBMs for this condition support the ground immediately behind the working face with a shield that may extend around the entire periphery of the tunnel. The tunnel lining is installed immediately behind the shield. Drag-type bits (Figure 4) are most appropriate for tunneling in regolith, usually mounted on a broadly spoked cutterhead that leaves space for the material to fall through into the muck-collection system.

Tunneling through hard rock, such as lunar basalt, is similar, although the requisite thrust and torque on the cutterhead are much higher. Disc cutters (Figure 5) are mounted on a shrouded cutterhead (since advance rates are lower than in soft ground), probably without a shield. The mechanical processes remain the same. Table 1 lists some information from several recent hard rock tunneling projects in the northwestern United States with diameters appropriate for underground living spaces.

Table 1.   Performance data for some tunnel boring machines in hard rock (from Thon, [9]). Basalt is a crystalline rock similar to some granites in its excavatibility.

	site A	site B	site C	site D	site E
tunnel length (ft)	19,012	15,239	15,411	19,026	4,860
rock type	granitic gneiss, schist	diorite gneiss, schist	diorite gneiss, schist	granitic gneiss, schist	schistose gneiss
rock strength (lb/in^2)	2,000–14,000 (avg 8,000)	3,000–17,500 (90% 4,000–10,000)	3,000–17,500 (90% 4,000–10,000)	2,000–18,000 (avg 8,000)	8,000–10,000
tunnel diameter (ft)	19	19	19	19	21
revolution rate (rpm)	46	46	NA	NA	NA
total thrust (lb)	1,380,000	1,380,000	1,080,000	1,380,000	2,000,000
max power (hp)	900	900	720–1,080	900	1,000
advance (ft/day)	max 168 avg 82	max 125 avg 61	avg 148	avg 237	avg 81
availability	51%	39%	54%	50%	43%

In comparison to explosive fragmentation, where the specific energy is less than 2 kW-hr/m^3, disc cutters require about 10 kW-hr/m^3 and point attack cutters require about 30 kW-hr/m^3.

Partial-Face Mechanical Excavators

These mechanical excavators are more flexible and mobile than the full-face designs, but at the cost of increased complexity and decreased robustness. They fragment rock with a small-diameter rotating cutterhead mounted on the end of a boom (Figure 6). Movement of the boom during cutting allows openings of varied cross-sectional shape to be created. Machines of this type are known as roadheaders and continuous miners, and have been developed for varying purposes in underground mining. Muck is removed with gathering arms rotating continuously on an apron in front of the working face, forcing the muck to fall into a central chain conveyor that dumps, in turn, into a waiting shuttlecar or belt conveyor hopper.

Partial-face machines are used in many types of civil and mining engineering projects, but they cannot be used economically in rock with more than moderate strength. In abrasive rock, bit wear can become a problem. The more sophisticated roadheaders are so complex that they have to be operated under computer control to achieve their potential performance.

Muck Transport

On Earth, underground muck removal and transport systems have evolved to deal with the constant gravity vector. Fragmented rock falls immediately to the bottom (invert) of the working area, where it is picked up mechanically (e.g., rotating muck buckets, gathering arms, suspended clamshell buckets) and transferred to an external transport system. This traditionally consists of discrete units, such as railcars or mobile shuttlecars. Conveyor systems, which operate continuously, are being used increasingly, however (see below).

SURFACE MINING

The following descriptions briefly cover the major equipment types that might be considered for obtaining regolith for processing into shield material. Some types of machinery in common use are too large and complex to be feasible for startup or reconnaissance missions, but would be better suited for long-term and/or large-scale operations (e.g., dragline shovels, large bucketwheel excavators). Three representative equipment combinations have been examined previously with regard to their feasibility for lunar operations by Gertsch and Gertsch [11,12]. This section, as the previous one, deals primarily with the unit operations of fragmentation and excavation, leaving material transport to the next section. Some equipment, however, combines all three unit operations.

Drilling and Blasting

If the regolith or rock material is too cohesive to be excavated directly, explosives may provide the most efficient means to reduce its cohesion to the point where it can be removed by the equipment discussed below. The use of explosives is discussed above. If needed, "fluffing" could even be accomplished from orbit prior to landing, with a missile or series of small charges.

Slushers

This is the simplest and most flexible method of moving loose material, either on the surface (Figure 7) or underground. Proposed by Gertsch [13] for lunar regolith mining, it also would require the least mass to be launched from Earth for any excavation system. Slushers can handle relatively deep and steeply sided excavations well, and can be combined with other forms of material transport if the haul distance is greater than about 100 m (Ingersoll-Rand [14]).

Slushers come in several different forms (Figure 8). For cohesive, fine-grained regolith, a box or crescent-type blade will retain its load better than an open-sided, or hoe design. The crescent blade eliminates internal corners where sticky material can accumulate, which would reduce the effective payload and therefore the production rate of the system. However, if the regolith proves to be very abrasive, a blade design that covers load-bearing surfaces with a static layer of the material being excavated will reduce the wear. In this case a box design with a short loading lip may prove useful.

The key to successful slusher excavation is the system of wire ropes manipulated around pulleys and controlled by one, two, or three mechanical winches that are mounted on movable platforms (traveling bogies), as shown in Figure 7. Motion of the slusher blade is controlled by varying the tensions in the appropriate ropes. Combinations of rope tensions produce surprisingly subtle motions of the slusher blade. Slushers are amenable to remote control, provided the operator has a clear view. Automation may be possible in homogeneous materials such as stockpiles.

Slushers work well in material that already is fragmented. The size and to some extent the shape of the particles govern the achievable production rate. The cohesion of the material also affects performance. The top few centimeters of lunar regolith should present no problem to a conventional slusher arrangement. As the cohesion increases with depth, however, both the mass and the digging angle of the blade may have to be modified to break the material free from its surroundings if it has not been loosened by blasting or ripping (see below). Several interdependent aspects of slusher blade design will have to be investigated for this purpose. Figure 9 relates blade capacity of two types of box design to their shipping mass. Bear in mind that cycle times are as important as blade capacity in predicting performance, but since cycle times depend on minesite configuration, conclusions are difficult to draw at this stage.

Another problem will be oversized material (e.g., boulders) embedded in the regolith. If sparse, the blade can be worked around them. If too numerous, they can impact production severely. In the latter case a rake blade can be used to sift through the regolith, removing oversized material to a waste area at one side. Once the pit is cleaned up, then the excavation blade can be reinstalled and production resumed.

Dozers

The dozer is a crawler- or wheel-mounted tractor with a front-mounted blade used for digging and pushing loose material (Figure 10). They are used in excavation, fragmentation (ripping, digging), and short-range transport (Martin et al. [5]). Dozers with heavy duty shanks hinged on the back can rip apart weak consolidated material,

preparing it for removal. Dozers also push other equipment when that equipment's propel power needs to be increased temporarily.

Ripping—inserting and dragging a hardened steel prong through the material—works well in soils that are compacted or otherwise weakly consolidated, or bedded rocks with weak bonds between the bedding planes. With adequate traction, the largest dozers can disturb the soil as deep as 3.5 m. This may be required for regolith mining if the material proves to be too well-compacted for direct excavation. Caterpillar [7] has determined diagnostic ranges of seismic wave velocities for rippable material.

Ripper design is affected by the strength contrast between the matrix material (regolith) and embedded oversized fragments (boulders), available power, and the balance between traction and motive forces, among other factors. Long ripper tips work best in loose, abrasive materials because they offer the most wear material. However, if a great deal of oversized rock is mixed in the regolith, tip breakage may become a problem, necessitating a change to shorter, more robust tips.

Dozers come in two propel types: tracks (crawlers) and wheels. Crawler dozers tend to be more stable, have better traction, and exert lower pressure on the ground, but wheel dozers are two to four times faster. These comparisons may not change significantly on the Moon or Mars, but other factors will come into play. Crawler-mounted equipment, for example, tends to be more sensitive to abrasive materials than rubber-tired machines. The relative importance of this factor will depend on what technology replaces rubber tires off the Earth.

Commercially available dozers come in a very wide range of sizes and capabilities. Figure 11 illustrates the approximate relationship between machine mass and capacity. Terrestrial machine selection is based mainly on the blade capacity, with allowance for the swell factor of the material (10% to 65%).

Scrapers

Scrapers (Figure 12) excavate surface material in thin layers, transport it, and then discharge it with a spreading action. Their travel speed usually is rather fast. In terrestrial mines they are used for topsoil removal, general reclamation, overburden removal, thin seam mining, and general utility work. They do not have the fragmentation capability of dozers, but they are useful where thin layers of material must be removed from, and spread over, large areas (Martin [5] and Hays [15]).

Scheduling of auxiliary equipment, particularly pusher dozers, is crucial to the production rate of scrapers. Several different basic designs of scrapers are available, including one or two axles, one or two engines, and configurations for pull-, push-, or self-loading. Single-engine models are the most efficient design, with capacities about 45% of GVW. Other designs are somewhat lower. In hard-to-load materials they are pushed by one or more crawler dozers (usually outfitted with special pusher blades to prevent damage to either machine), or linked together in a push-pull arrangement. Self-loading machines are correspondingly heavier than other types. Dual-engine designs can move faster and have better traction than single-engine models. All designs have low centers of mass. Figure 13 shows how scraper capacity generally is related to machine size for several types of present-day scrapers.

Front-End Loaders

The front-end loader is a wheel or crawler mounted tractor with a bucket on the front (Figure 14). It is used for excavating, loading, and transporting material moderate distances and in some applications is known as a load-haul-dump (LHD). Tires are a major cost item, as they are for trucks (below).

Front-end loaders are very mobile, and are used often for small or intermittent load-and-carry applications (Martin et al. [5]). Larger models can be used as primary haulage for distances up to 183 m, if the grade of the path is low (Hays [16]). Figure 15 shows how bucket capacities generally increase with machine mass, although other factors also affect machine design. Some of the spread in the data is due to the interchangeability of buckets and the many aspects of bucket design that can be altered to match the excavating conditions.

Successful adaptation of front-end loaders to lunar and martian environments will depend on whether a prime mover as efficient and economical as the diesel engine can be developed. This will determine whether front-end loaders and, to a lesser extent, trucks, will be useful there. Truck haulage is easier to power externally (trolley-assist) due to its higher path-predictability. Front-end loaders, on the other hand, must be free to move about, to retain their flexibility.

Front-end loaders have been partially automated in some mines, although the interplay of forces required for loading the bucket is surprisingly subtle and difficult to automate completely. Some LHDs are successfully tele-operated underground where roof conditions are too dangerous for human presence on the machine. This compromise between full automation and on-site operator control is a promising alternative for extraterrestrial applications. The transmittal distance must be kept short enough, however, that time-lag remains negligible.

Hydraulic Excavators

Hydraulic excavators focus on excavation. When the material is weak and unconsolidated, they also can fragment, but usually this is accomplished by another system (e.g., blasting). Material transport is commonly by rail or truck.

This classification encompasses both hoes and shovels (Figure 16), which differ only in their bucket configurations (Martin et al. [5]). Backhoes also can be included (Figure 17). Units usually are diesel-powered, with hydraulics powering individual operating functions. The hydraulic system consequently is extremely complex. Hydraulic excavators can develop high crowding, prying, and breakout forces. Their advantages over front-end loaders include the absence of tire costs, lower specific energy, and greater ruggedness (Files [17]). They also permit highly selective excavating. For bulk mining of material where property variations are of less importance, selectivity may not be worth the additional mass and maintenance complexity. Figure 18 shows how machine mass varies with bucket capacity for many of the excavator models on the market today.

Electric Shovels

Originally operated by steam, then diesel, and now electric power, shovels operate in the mid-range capacity (front-end loaders and hydraulic excavators cover the low end, and draglines and bucketwheels cover the high end). Stripping shovels are the largest type, up to 140 m^3 bucket capacity (Files [18]). Loading shovels are in the 8 to 54 m^3 range (Sargent [19]), although 4 to 6 m^3 diesel-powered units are still used in very rugged applications (Martin et al. [5]). Electric power is supplied by a trailing cable, which often limits mobility and flexibility. However, the concept is readily transferable to environments where combustion engines will not operate. The production rates of equipment of this size probably will not be needed for some time, until after the demand for raw material has increased substantially over the needs of a reconnaissance mission.

MATERIAL TRANSPORT

Terrestrial practice makes extensive use of mobile conveyors, alone or in combination with transport vehicles such as scrapers, front-end loaders, etc. Trucks also are popular due to their flexibility. A possibility for extraterrestrial work is a ballistic transporter, which would throw material either directly into place or into an intermediate spreading system. Track (i.e., train) haulage, while formerly very popular in the mining industry, is not discussed here because of the need for an extensive infrastructure that will be beyond the needs of initial missions to the Moon and Mars.

Trucks

Trucks are limited to one unit operation: transport. Terrestrial off-highway mine trucks range in capacity from 35 to 350 tons, all larger than necessary for the envisioned startup on the Moon or Mars. The biggest single cost item in their maintenance is the tires. Pneumatic rubber tires provide the terrain flexibility that makes trucks so valuable on Earth. It is not clear how this aspect could be transferred successfully off-planet. Trucks are very flexible for transportation.

There are three types of off-highway trucks (Figure 19): conventional rear dump, tractor-trailer (bottom, side, and rear dump), and integral bottom dump. The conventional rear dump is the most common type used in terrestrial surface mines because it is the most flexible. It is suitable for a wide range of materials, including cohesive clays that resist flowing. Regolith also may not flow easily, although the effect of the excavation process on its cohesion is not yet well understood. Bottom dump truck designs are limited to free-flowing materials, and even side dumps do not have the quick unloading capability of a conventional rear dump truck. Rear dumps also can withstand severe loading impacts more easily, such as boulders. Rear dumps often are less economical for long-distance hauling, however, and their rated payload is lower than for other designs (Table 2). Figure 20 illustrates the average relationship between capacity and empty mass for conventional rear-dump trucks.

Table 2. Terrestrial mining truck capacities as functions of gross vehicle weight (GVW) (from Hays [20]).

	payload as % of GVW
conventional rear dump	55%–60%
tractor-trailer	60%–65%
integral bottom dump	60%–70%

Even off-highway trucks must have a relatively well prepared road surface in order to approach their production potential (Hays [20]). Road construction and maintenance are important parts of mining operations that use truck haulage. Road grades must be kept gentle; optimum grades on Earth for conventional rear dump trucks range from 7% to 10%, limited by the drive train, traction, and the ability to stop backward movement. Traction, the usable driving force developed by the truck tire on the road surface, will be less in reduced gravity. The radii of horizontal curves must be large enough that the trucks do not tip over at normal operating speeds. The tipping hazard will increase in low-gravity environments because the reduced weight will induce operators to forget that inertia remains the same. Adequate sight distance, determined by speed and stopping ability, always is important for safety reasons. Haulage roads also must have a stable roadbase that adequately supports the heavy weight of off-highway trucks. The road surface must not offer too much rolling resistance; this effect depends directly on gravity. Research will be required to determine the most effective ways of building adequate roads on the Moon and Mars.

Conveyors

While trucks are cyclic transporters of material, conveyors are continuous. This often makes conveyors more economical in mining applications. They are being used increasingly both underground and on the surface, for runs sometimes several miles in length (Duncan and Levitt [21]).

Conveyor belt capacity is determined mainly by the characteristics of the material to be transported (angle of repose, angle of surcharge, and flowability), in addition to belt speed and width (CEMA [22]). The angle of repose is the slope angle assumed by a freely formed pile of the material on a horizontal surface. The surcharge angle is the slope angle of the material on a moving conveyor belt, usually 5° to 15° less than the angle of repose (sometimes 20° less). Generally, as the angles of repose and surcharge increase, the flowability of the material decreases. Regolith is expected to have relatively high angles of repose and surcharge, indicating correspondingly low flowability. Again, these important parameters will have to be determined for planning purposes by direct physical measurements. Table 3 lists some examples of the mass capacity of standard troughed conveyor belt configurations, for selected belt widths, material densities, and side angles.

Conveyors are relatively complex machines, with a series of continuous belts (usually reinforced rubber-like material) stretched over freely rotating idlers spaced 2 m to 3 m apart. Figure 21 shows some of the aspects of basic conveyor design. The total mass of structural material needed to build a conveyor of any length adds up quickly.

Table 3.   Examples of normal bulk material capacity of troughed conveyor belts in tonnes/hr at 100 ft/min belt speed and a surcharge angle of 0.44 radians (Torre, [23]), under Earth-normal gravity. Idler roll angle is how far the sides of the belt are slanted up from horizontal, to reduce material spillage.

idler roll angle	material density	belt width (mm)				
(radians)	(kg/m^3)	762	1067	1372	1676	1829
0.47	481	54	114	195	299	358
	1201	136	285	489	752	896
	2002	227	475	815	1254	1493
0.61	481	59	120	203	309	370
	1201	146	298	506	773	925
	2002	244	498	845	1288	1542

Drive pulleys and tension pulleys are prone to wear, especially in abrasive environments or where the heat built up during operation cannot be dissipated quickly enough. Both factors may be problems on the Moon; the reactivity of Mars soils may enhance corrosion of moving parts, as well.

The infrastructure required for a conveyor system, although large, is less difficult to install than that for a rail haulage system. Railroads require carefully prepared base and sub-base courses. Like truck roads, railroads must be constantly maintained.

Some of these concerns may be ameliorated by advanced conveyor designs now being studied. Figure 22 shows a design being developed as one of several approaches to difficult situations.

Ballistic Transporters

An alternative to both cyclic haulage (front-end loaders, trucks, rail haulage) and continuous conveyor transport is the ballistic transporter. Similar to terrestrial snowblowers, this concept also could combine the fragmentation and excavation unit operations with transport if the distance was relatively short and the material poorly consolidated. Longer hauls would be possible by combining ballistic transporters with other forms of material transport, such as slushers at the input and/or output ends.

The production rate of this type of equipment depends on the excavatability of the material—whether undisturbed or stored in a bin or hopper—in addition to the diameter, lead angle, and rotational speed of the screw conveyor that mobilizes it, and the power of the thrower unit. A review of industrial snowblower design would be instructive, particularly locomotive-mounted sizes.

Airless environments offer the advantage of no breezes to disperse the product stream. Incorporating the effects of reduced gravity into the design should be a straightforward exercise. Like all machines, moving parts will suffer wear, especially when working in abrasive materials. However, the number of moving parts per unit volume of material is lower than any of the other transport concepts except slushers.

SHIELD CONSTRUCTION

Raw regolith material could be emplaced loose over surface structures, or it could be used to manufacture building materials with the appropriate shielding characteristics. The manufacturing process is beyond the scope of this paper, but placement of unconsolidated regolith is not.

Placement

Placing the loose regolith (or blasted rock fragments) around and over a habitat module will require strict control of rate and location. Depending on the size of the area to be covered, the following types of equipment could do the job:

- Slusher - small area. Working from a stockpile of mined material, this would allow one person to place regolith carefully and evenly. This system would exert little additional pressure on the area being covered.

- Front-end loader - small area. Although skilled operators can spread the material somewhat while dumping, the material will tend to form a hummocky surface that will have to be smoothed, if not compacted.

- Conveyor - small to large area. Elevate the output end of the conveyor over the center of the area to be covered, if it is small, or move the output end periodically, if the area is large. A slusher may be useful as an auxiliary spreader.

- Ballistic transporter - small to large area. The degree of control possible on the spread of the material stream will have to be evaluated. A sweeping motion of the output end of the transporter would tend to produce a relatively even layer of material, without the hummocky characteristics of cyclically unloaded material that must be counteracted during compaction.

- Scraper - large area. This approach would be feasible if the area to be covered can withstand the weight of a scraper passing over it, and if the area is relatively large. Consequently, it may be more appropriate at a later stage in human settlement.

Compaction

If the regolith must be compacted to increase its stability, any one or a combination of four techniques can be applied (Aulicino, [24]):

- Static weight, provided by surface rollers. Steel rollers, whether dual- or three-wheeled, operate best on granular soils that benefit from the crushing action of the weight. In less optimal conditions, waves of plastic deformation can be created in the material. The effects of vacuum, for lunar operations, and corrosive soils, for martian operations, remain to be evaluated.

- Kneading action, provided by sheepsfoot rollers. This is more appropriate for cohesive soils, on Earth. The penetrating feet spread the load in all directions within the material, and tend to pulverize lumps.

- Impact, provided by handheld tampers or rammers suited for small areas or confined spaces. These are differentiated from the vibratory compactors by their very low frequency and high amplitude.

- Vibration, provided by drum rollers and plate compactors. The latter also can be operated by hand, and are used for the bottoms of trenches, confined areas, and steep slopes. Both types of machines supply series of rapid impacts, and work best at some optimum moisture content. Dry material often does not compact well due to intergranular friction. This may be a problem on the Moon, where intergranular locking of the angular regolith particles will resist compaction.

All compaction techniques are applied to layers of the material, called lifts. Full compaction of a lift must be achieved before more material can be added, because the compaction forces penetrate only a limited depth. Therefore, the optimum lift thickness for achieving maximum shielding potential must be determined empirically.

Several possible problems will have to be evaluated before more detailed planning is possible. Increased machine mass will be needed to accomplish the same compaction in low gravity as under Earth-normal gravity. The compaction mechanisms familiar on Earth may operate differently where organic constituents, moisture, and atmospheric gases are not ubiquitous. The different compositions and structures of the lunar regolith and the martian soil will affect compaction as well.

CONCLUSIONS

At this early stage, with even the general configuration of the mine still unknown, the general consideration of minimizing specific energy at all stages of the fragmentation, excavation, and transport processes must guide recommendations. Launch mass must also be minimized, while maintaining maximum flexibility and robustness. Using these simple criteria, regolith for shield material should be obtained by:

- Primary excavation with a three-drum slusher system, after explosive loosening of the regolith if more than the top few centimeters are needed. Oversized rocks would be moved aside, with no additional (secondary) fragmentation.

- Transport with the slusher system, combined with a ballistic transporter if haul distance is on the order of a few hundred meters. If longer, a general-purpose truck or a series of ballistic transporters would be required.

- Placement with a slusher spreading the material over the area required.

For the tunneling scenario, two options are possible, depending on whether the openings are to be created in regolith (soft-ground tunneling) or basalt (hard rock tunneling). In regolith:

- Excavate the material with a semi-automated shielded tunnel boring machine mounted with drag-type bits and an open cutterhead.

- Load the material behind the machine into a general-purpose truck.

- Once the excavated material is on the surface, transport and place it as recommended for regolith mining.

For tunneling in basalt or any other strong, brittle rock, the same criteria lead to:

- Fragmentation of the rock by explosives.

- Excavation with a small powered mucker or a slusher.

- Muck transport with a robust truck.

Extraterrestrial mining to produce shielding material is possible using any one or a combination of all the techniques discussed in this paper.   They all are drawn directly from current terrestrial mining and construction practice. Little needs to be re-invented; instead, pre-existing technology can be comprehensively evaluated and adapted to the new challenges. This evaluation should be performed as much as possible in the space environment, for that will be the major source of obstacles. Creativity will be called for in designing modifications to equipment and techniques to overcome those obstacles while retaining the basic utility of their approaches.

These methods work because they have been tested under demanding field conditions continuously, in some cases for over one hundred years. This base of experience is a powerful tool that can help promote the goal of starting and maintaining a permanent human presence in space.

REFERENCES

1. J. W. Wilson et al., *Transport Methods and Interactions for Space Radiations*, NASA Reference Publication 1257, Dec, 1991.

2. L. C. Simonsen, et al., "Construction technologies for Lunar base: Prefabricated versus in-situ," this volume.

3. L. C. Simonsen, "Analysis of lunar and martian habitation modules for the Space Exploration Initiative (SEI)," this volume.

4. R. E. Gertsch, "Unit operations in lunar mining," Space Manufacturing 8, *Proc 10th Princeton/AIAA/SSI Conf*, American Institute of Aeronautics and Astronautics, Washington DC, Nov, 1991.

5. J. W. Martin, T. J. Martin, T. P. Bennet, and K. M. Martin, *Surface Mining Equipment*, 1st Ed., Martin Consultants Inc., Golden, Colorado, 455 pp, 1982.

6. Thomas Atkinson, "Selection and sizing of excavating equipment," Chap 13.3, *SME Mining Engineering Handbook*, 2nd Ed, Vol 2, Society of Mining Engineers of AIME, Littleton, CO, p 1311–1333, 1992.

7. Caterpillar Inc., *Caterpillar Performance Handbook*, 26th Ed (revised annually), Peoria, IL, 1995.

8. D. J. Morton, "Cut-and-cover construction," Chap 14, *Tunnel Engineering Handbook*, J. O. Bickel and T. R. Kuesel, eds, Krieger Publ Co., Malabar, FL, p 395–416, 1982.

9. J. George Thon, "Tunnel-boring machines," Chap 10, *Tunnel Engineering Handbook*, J. O. Bickel and T. R. Kuesel, eds, Krieger Publ Co., Malabar, FL, p 235–278, 1982.

10. Howard J. Handewith and Neil J. Dahmen, "Tunneling machines," Chap 9, *Underground Mining Methods Handbook*, W.A. Hustrulid, ed, Society of Mining Engineers of AIME, Littleton, CO, p 1104–1116, 1982.

11. L. E. Gertsch and R. E. Gertsch, "Application of lunar criteria to three terrestrial mining methods," *Engineering, Construction, and Operations in Space*, Proc Space 90, ASCE, Albuquerque, NM, 1990.

12. R. E. Gertsch and L. E. Gertsch, "Lunar surface mines and mining machinery: Design criteria," *Engineering, Construction, and Operations in Space*, Proc Space 90, ASCE, Albuquerque, NM, 1990.

13. R. E. Gertsch, "A method for mining lunar soil," *Space Manufacturing 1983*, Vol 53, Advances in the Astronautical Sciences, American Astronautical Society, 1983.

14. Ingersoll-Rand, *Modern Methods for Scraper Mucking and Loading*, Ingersoll-Rand Co., NY, 183 pp., 1939.

15. Ronald M. Hays, "Scrapers," Chap 6.5.5, *Surface Mining*, B. A. Kennedy, ed, p 709–714, 1990.

16. Ronald M. Hays, "Wheel loaders," Chap 6.5.6, *Surface Mining*, B. A. Kennedy, ed, p 715, 1990.

17. Thomas J. Files, "Hydraulic excavators," *Surface Mining*, B. A. Kennedy, ed, p 634–636, 1990.

18. Thomas J. Files, "Stripping shovels," *Surface Mining*, B. A. Kennedy, ed, p 636–638, 1990.

19. Fred R. Sargent, "Mining and quarry shovels," *Surface Mining*, B. A. Kennedy, ed, p 626–633, 1990.

20. Ronald M. Hays, "Trucks," Chap 6.5.2, *Surface Mining*, B. A. Kennedy, ed, p 672–691, 1990.

21. Larry D. Duncan and Brian J. Levitt, "Belt conveyors," Chap 6.5.3, *Surface Mining*, B. A. Kennedy, ed, p 692–705, 1990.

22. CEMA, *Belt Conveyors for Bulk Materials*, 4th Ed, Conveyor Equipment Manufacturers Association, 374 pp 1994.

23. Dominic C. Torre, "Underground belt conveyors," Chap 9, *Underground Mining Methods Handbook*, W. A. Hustrulid, ed, Society of Mining Engineers of AIME, Littleton, CO, p 1257–1262, 1982.

24. R. J. Aulicino, *Compaction Data Handbook*, Compaction Division, Ingersoll-Rand Co., 68 pp., 1974.

25. Levent Ozdemir, Leslie Gertsch, David Neil, and James Friant, *Performance Predictions for Mechanical Excavators in Yucca Mountain Tuffs*, report SAND91-7035, prepared for Sandia National Laboratories, Albuquerque, NM (contract 35-0039), 1991.

26. William A. Rhoades, "Slushers," Section 5, Chap 2, *Underground Mining Methods Handbook*, W. A. Hustrulid, ed, Society of Mining Engineers of AIME, Littleton, CO, p 1172–1178, 1982.

27. Thomas Atkinson, "Future concepts in surface mining," Chap 13.6, *SME Mining Engineering Handbook*, 2nd Ed, Vol 2, Society of Mining Engineers of AIME, Littleton, CO, p 1352–1363, 1992.
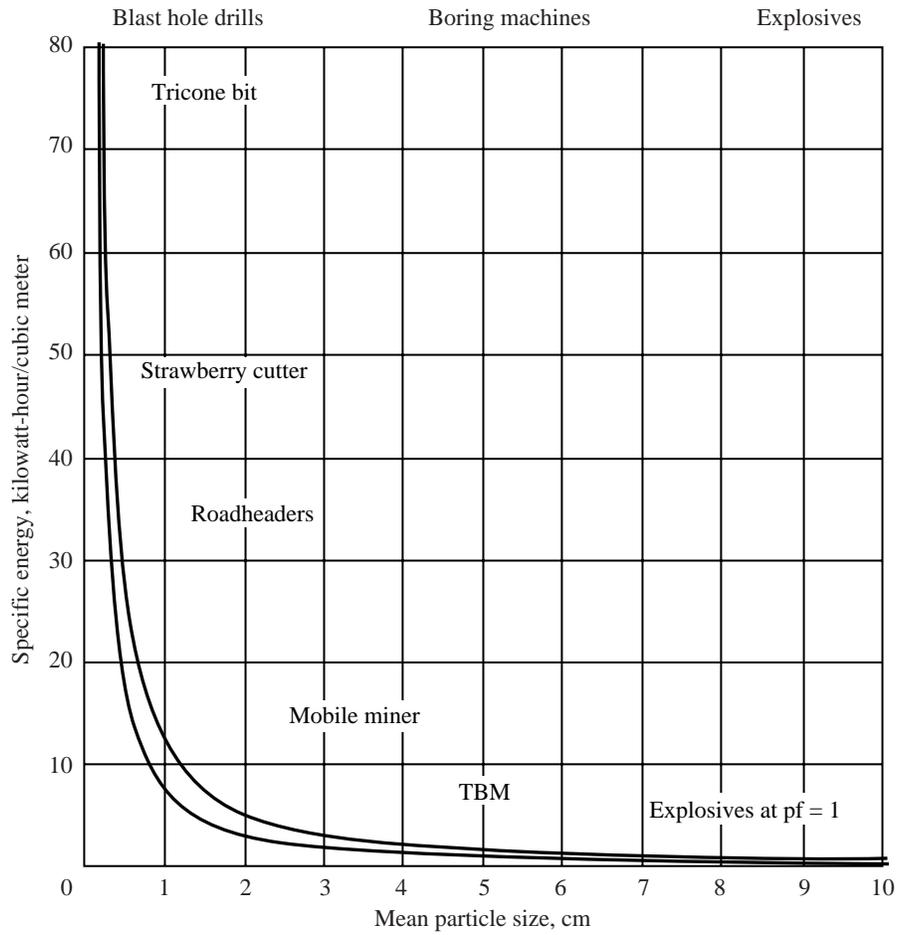
Figure 1.   Specific energy of excavation versus the average particle size produced, categorized according to technique. TBM = tunnel boring machine, pf = powder factor.
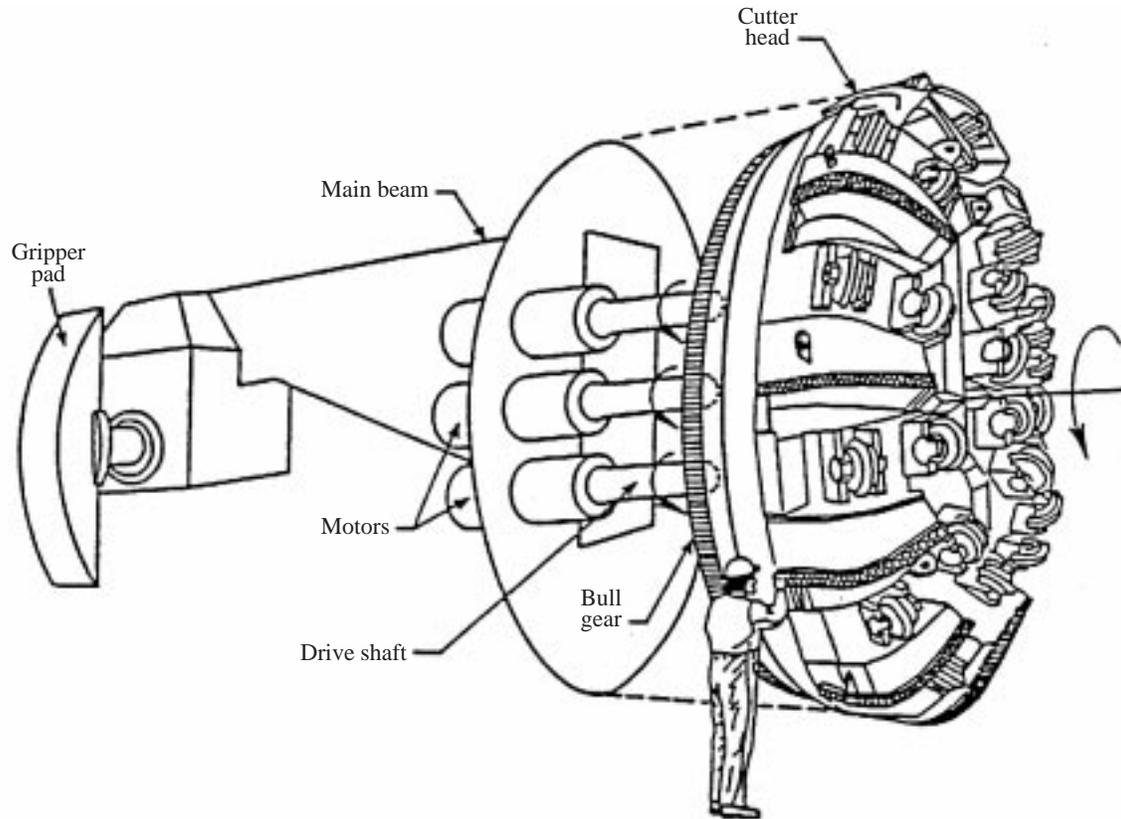
Figure 2.   Simplified schematic of a hard rock tunnel boring machine (Ozdemir et al. [25]).
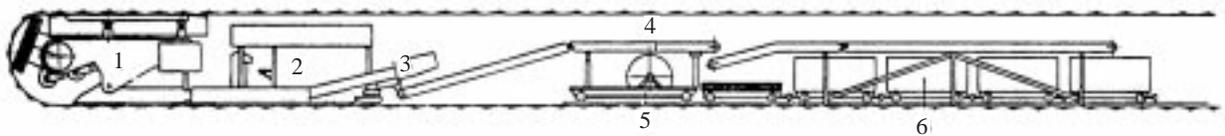
Figure 3.   A tunnel boring machine with its support system (from Handewith and Dahmen [10]). 1 = tunneling machine, 2 = trailer with the motors, 3 = machines's muck removal system, 4 = transfer conveyor, 5 = skid frame, 6 = railcars for transporting muck out of the tunnel.
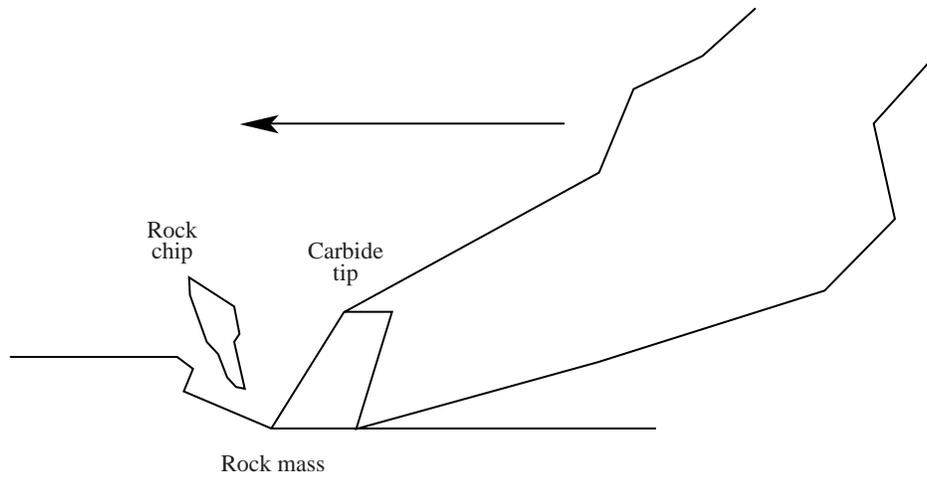
Figure 4. Drag bit chipping action in hard rock. In soft ground, drag bits both fracture and scrape the material off the working face.
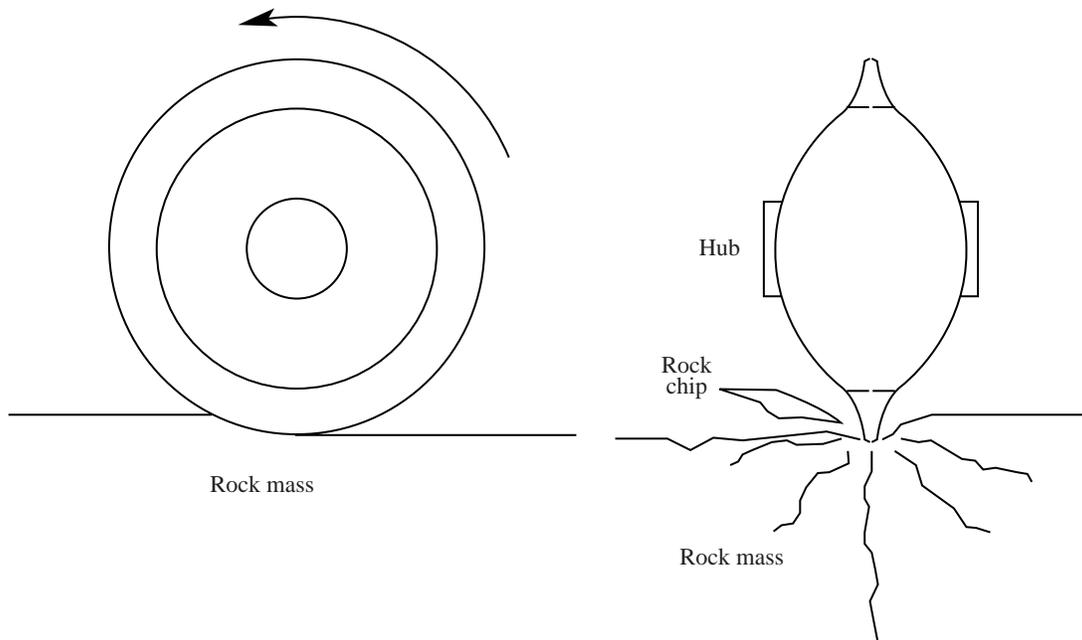
Figure 5.   Disc cutters fragment rock by chipping it. The arrow indicates the direction of motion as the cutter is rolled in a continuous circle. Machine advance is into the rock (downward on the page).
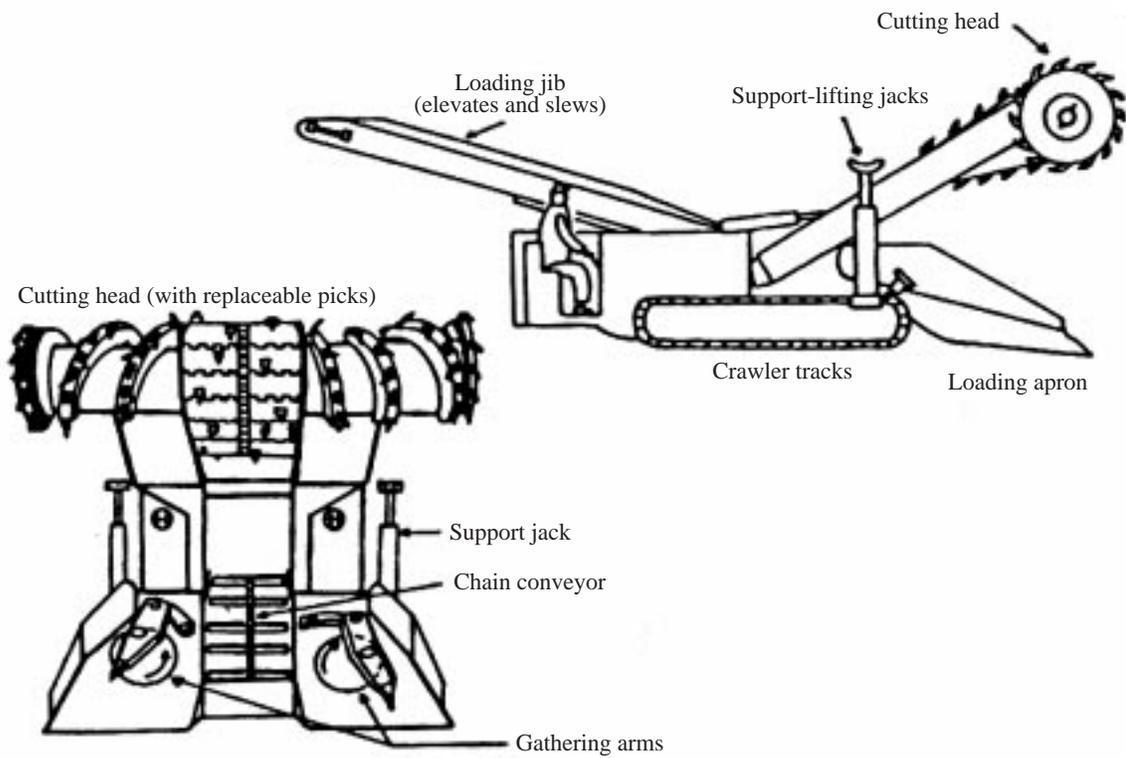
Figure 6.   A continuous miner, one type of partial-face excavator. The loading jib is a short conveyor that transfers muck to a series of shuttlecars. The machine derives part of its reaction forces from the support jacks, the rest from its own mass.
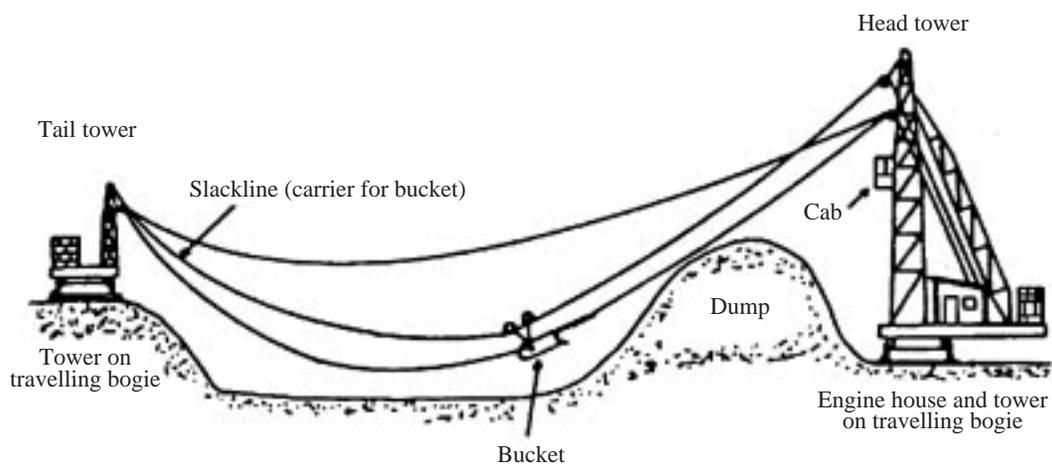
Figure 7.   Terrestrial surface mine setup using a slusher with the drums mounted on moving platforms.
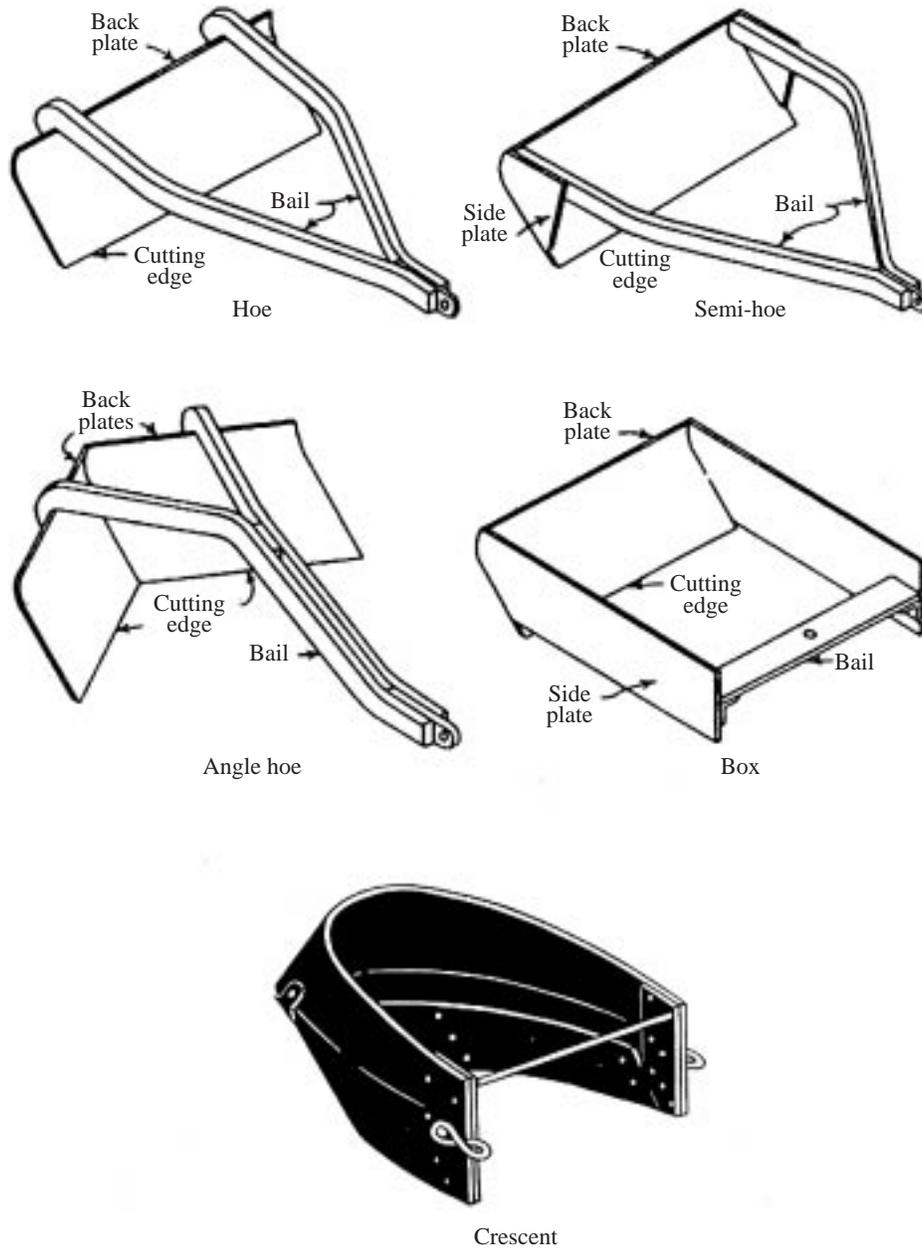
Figure 8. Basic slusher designs, illustrating different side lengths. (a) hoe, (b) semi-hoe, (c) angle hoe, (d) box, (e) crescent (Ingersoll-Rand [14]).
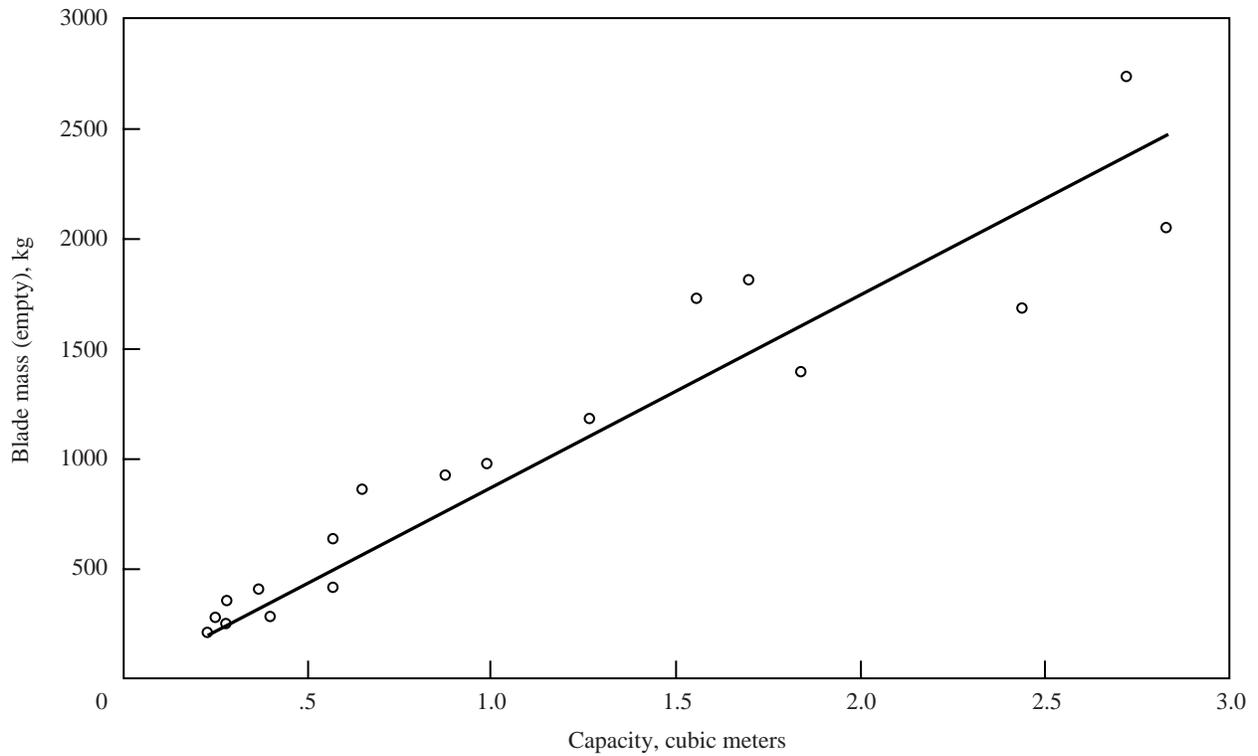
Figure 9.   Approximate relationship of slusher capacity to blade mass for box-hoe and folding-hoe designs (from Rhoades [26]).

Figure 10.   This model of dozer has an operating mass of nearly 37,000 kg, a height of 3.4 m, a length of 6.2 m, and a width of 3.4 m (excluding blade). Blade capacity varies form 4.7 m^3 to 11.7 m^3, depending on blade configuration (data from Caterpillar [7]).
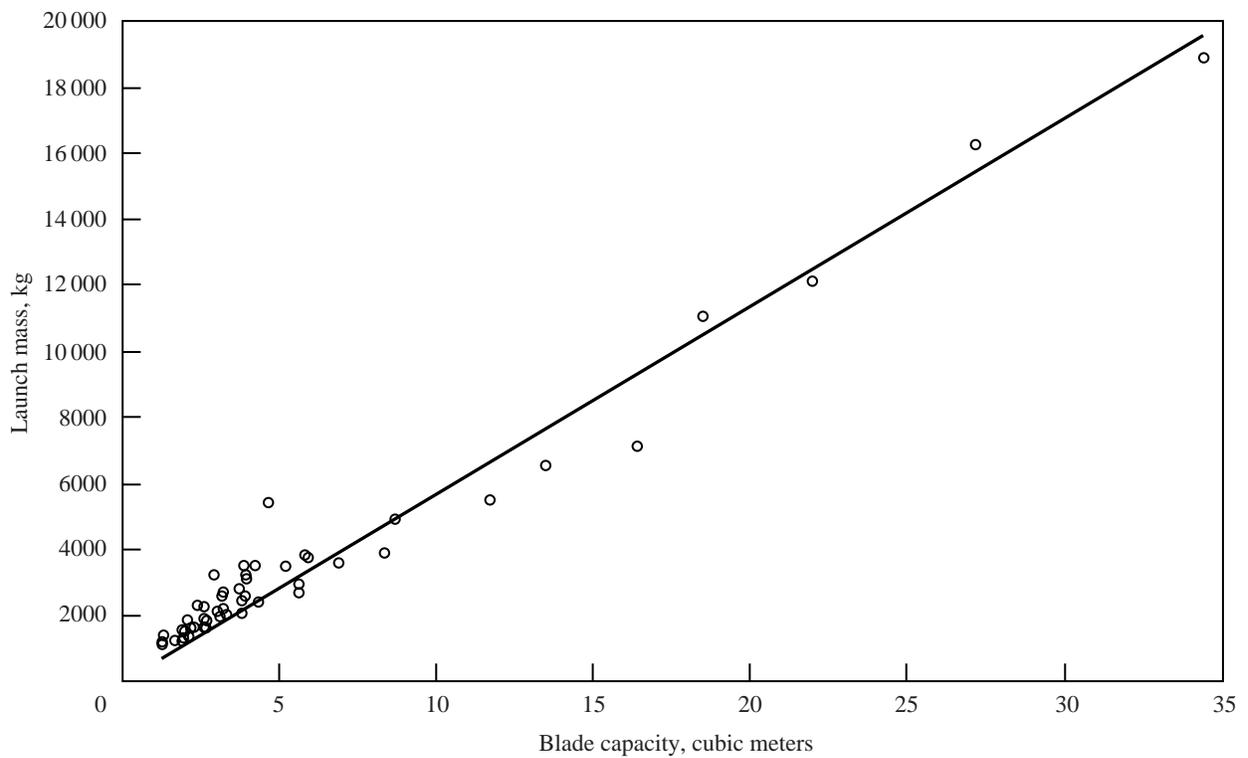
Figure 11. Approximate relationship of track-mounted dozer blade capacity to machine operating mass, including fluids (from Caterpillar [7]).

Figure 12.   This model of scraper has an operating mass of 44,000 kg, a height of 4.3 m, a length of 14.3 m, and a width of 3.9 m. Machine capacity is 23.7 m^3 (data from Caterpillar [7]).
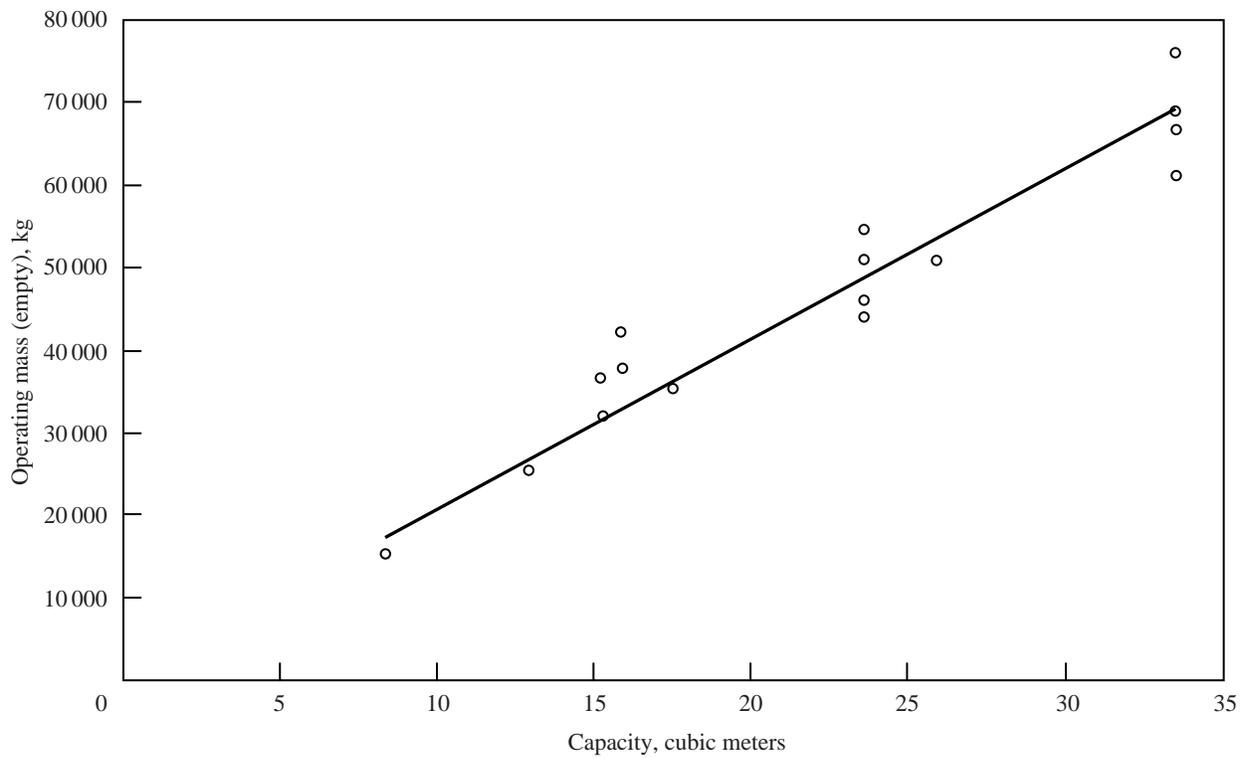
Figure 13. Approxiamte relationship of scraper capacity to machine operating mass (from Caterpillar [7]).

Figure 14.   This model of front-end loader has an operating mass of 9,000 kg, a height (with bucket raised) of 4.7 m, a length of 6.6 m, and a width of 2.4 m. Capacity varies form 1.4 m^3 to 1.7 m^3 depending on the bucket configuration (data from Caterpillar [7]).
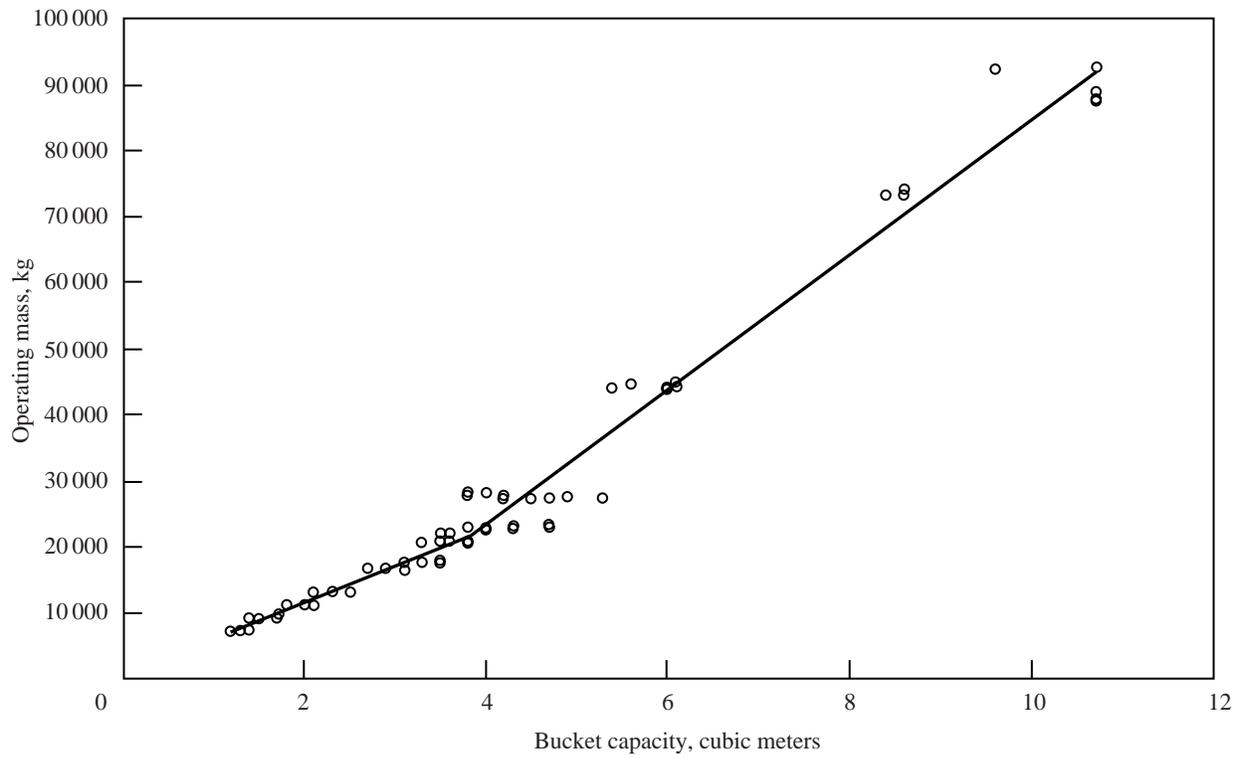
Figure 15. Approximate relationship of front end loader bucket capacity to machine operating mass (from Caterpillar [7]).

Figure 16. A small hydraulic shovel with a special gripping attachment on the bucket. Note the ability to dig below grade.

Figure 17. This type of backhoe masses about 450 kg and has a bucket capacity of 0.2 m^3 to 0.3 m^3.
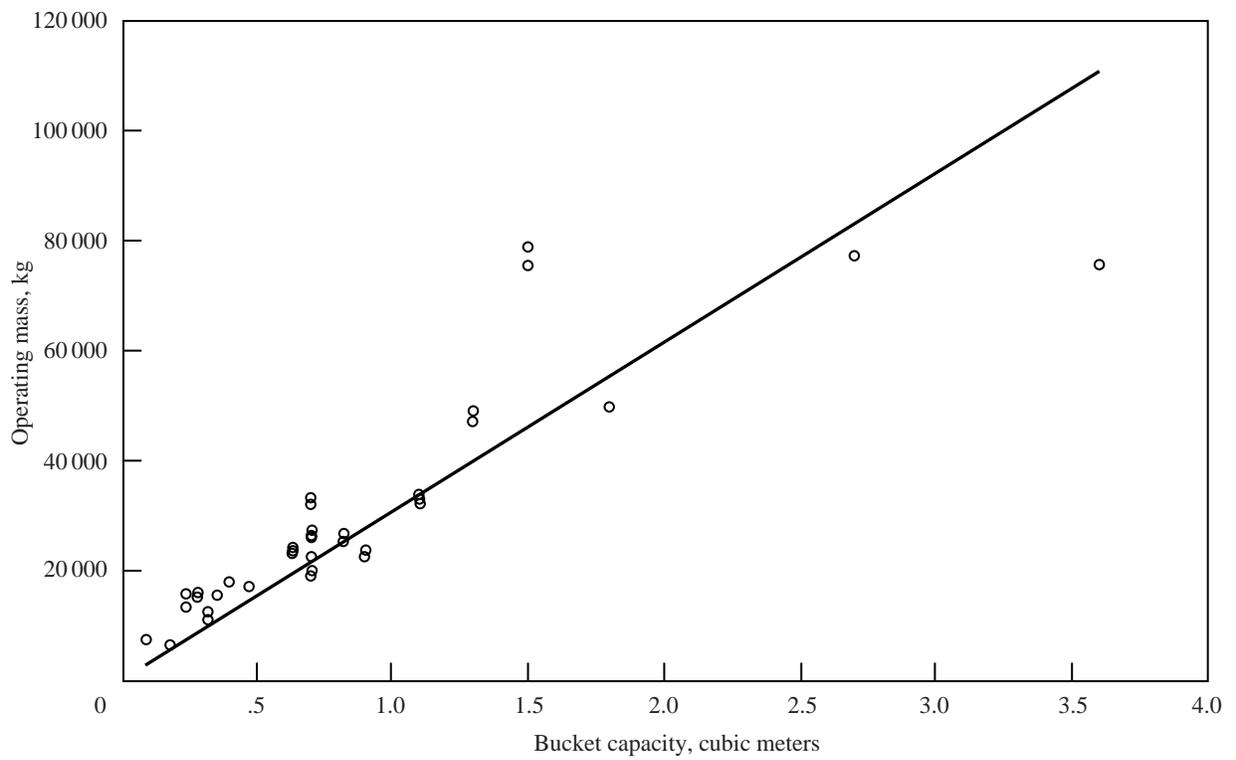
Figure 18. Approximate relationship of hydraulic excavator capacity to machine operating mass (from Caterpillar [7]).
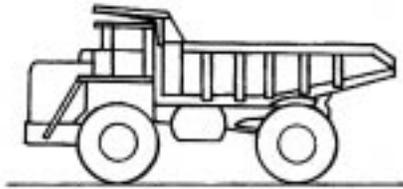
2-axle rear dump
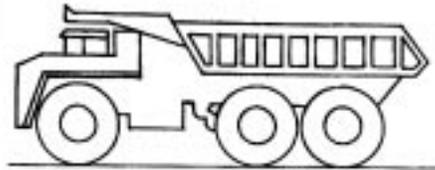
3-axle rear dump
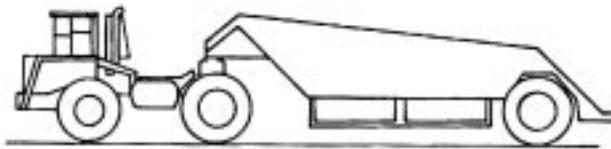
3-axle bottom dump
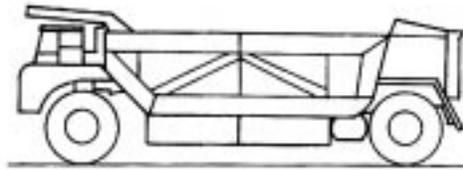
2-axle bottom dump

Figure 19. Basic designs of mining and construction off-highway trucks. Articulated trucks also can be side- or rear-dump.
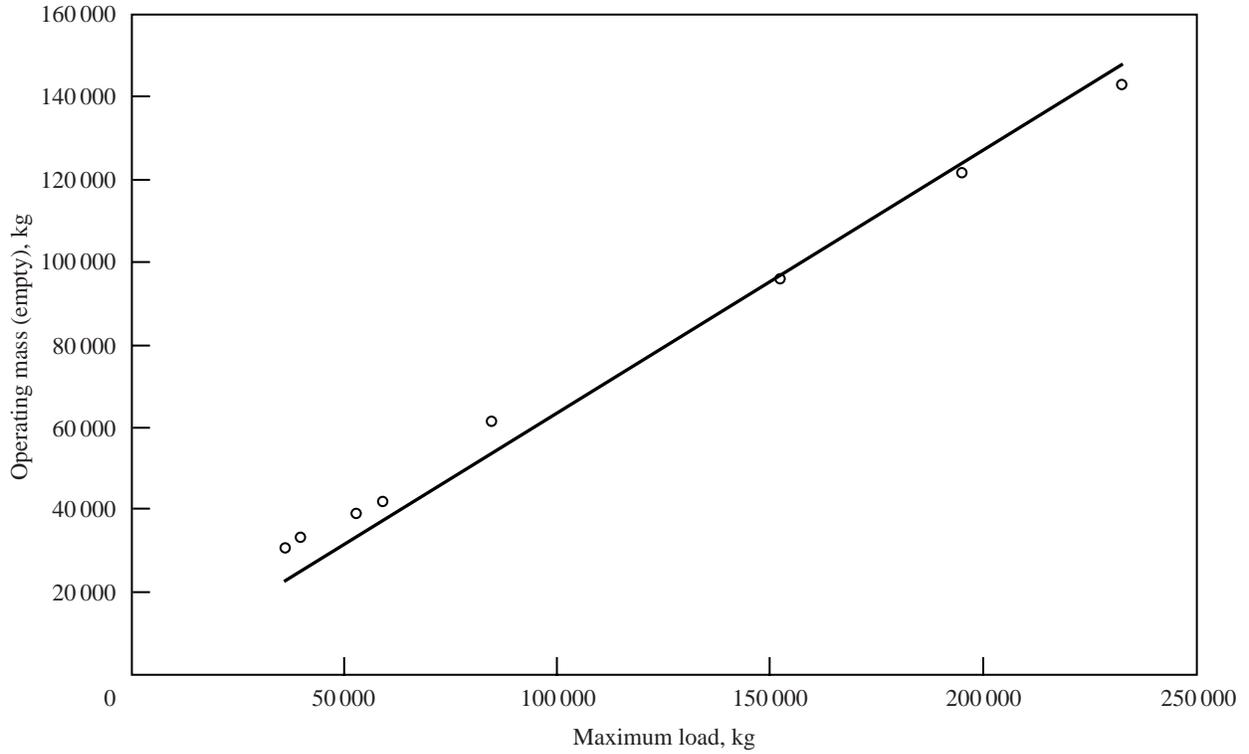
Figure 20. Truck capacity is normally given in terms of maximum load. In low-gravity environments, however, the volume of the bed may be the constraining factor (from Caterpillar [7]).
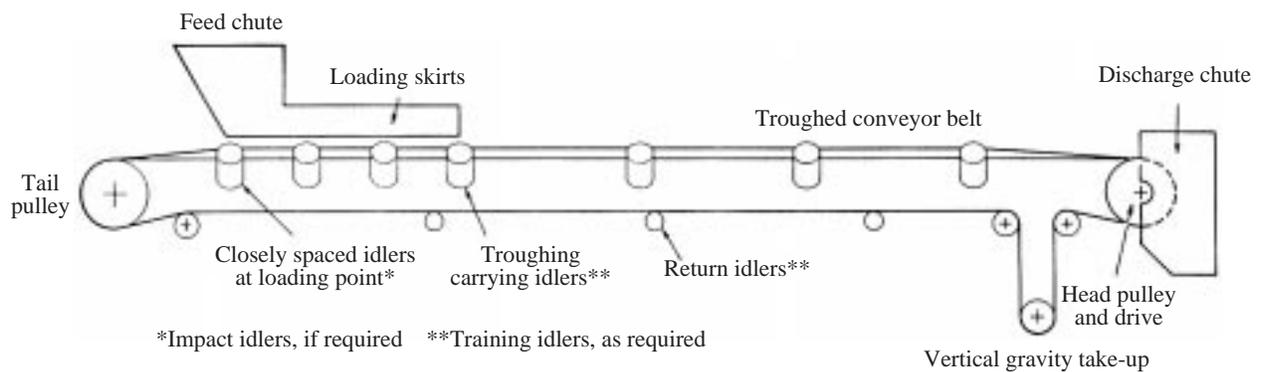
Figure 21. Schematic of a simplified belt conveyor, showing important components (CEMA [22]).

363
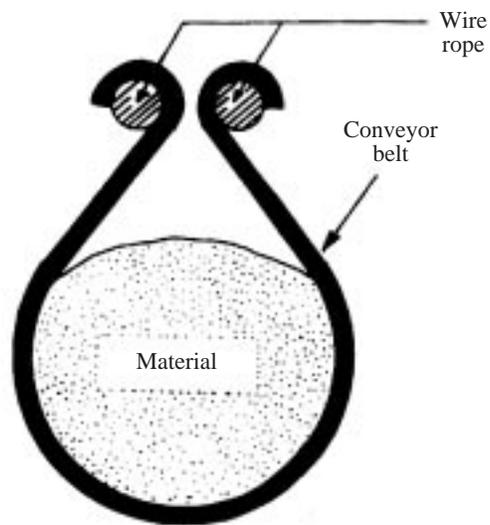
Figure 22. The pipe belt, an advanced belt conveyor concept for use on steep slopes (Atkinson [27]).

CHAPTER 17

SPACE RADIATION SHIELDING ANALYSIS BY CAD TECHNIQUES

by

G. D. Qualls[1]
Rick Boykin[2]

_____
[1]Analytical Services & Materials, Inc., Hampton, VA
[2]Computer Sciences Corporation, Hampton, VA

Chapter 17

SPACE RADIATION SHIELDING ANALYSIS BY CAD TECHNIQUES

SUMMARY

Analysis techniques have been developed and implemented in order to predict the amount of radiation shielding provided by matter surrounding a point in space. Computer-Aided Design (CAD) models are used to represent spacecraft components and materials so that the distance traversed by the radiation through each material may be calculated. Also, a full-body, human, Computed Tomography (CT) scan data set is being used to represent the amount of shielding provided by human body tissue to a point within the body. These two separate capabilites have been developed and integrated in order to provide a complete picture of a particular radiation shielding environment.

INTRODUCTION

Space is considered a hostile operating environment for many reasons, not the least of which are the effects of ionizing radiation. Whether the concern is for the health of an astronaut or the health of an electronic component, the extent of exposure to ionizing radiation in space can have a significant impact on mission duration, risk, and performance. For these reasons, it can significantly impact such large-scale design issues as spacecraft weight and overall configuration. It is, therefore, important to have a set of methods and tools which can accurately predict radiation doses for a component or crewmember operating in the space radiation environment.

In order to predict the radiation dose at a particular point in space, it is necessary to model both the external radiation environment and the surrounding matter which will shield the point from the environment. In general, given a particular directional distribution of radiation about a target point in space, a radiation shielding model would need to include the contributions of surrounding matter like the spacecraft structure, equipment, propellants, etc. For predicting the dose incurred by an astronaut in space, the shielding model is extended beyond the model of the physical hardware of the spacecraft to include the contribution of the body tissue surrounding the target point (Fig. 1). The tools and methods presented in this paper were developed in order to provide for the development and use of complex radiation shielding models for this purpose.

The two tools which are the primary focus of this paper were developed to give detailed information regarding the directional shielding distribution surrounding a target point in space. The first tool developed, RadICal, processes specially prepared CAD geometry models and calculates the directional thickness distributions about specified target points. The second tool developed, INT5, uses a Computed Tomography-scan (CT-scan) dataset to represent the body tissue of the 50th percentile USAF male. The shielding calculated with this software can then be combined with the output of RadICal to produce a total shielding model. A third computer program, XCSPH, is also presented, which displays this information graphically so that an analyst can evaluate and interpret results quickly and efficiently.

CAD GEOMETRY MODEL SHIELDING ANALYSIS

The RadICal program is used to process specially developed geometry models in a common format and produce directional shielding information for a set of specified target points. The flowchart in (Fig. 2) shows the input and output files associated with RadICal. The inputs consist of a geometry file, a material mapping file, a ray direction file, and a list of target points.

The geometry file contains all the physical components that RadICal will use for the shielding analysis. Each component in the model has a unique name and is associated with a particular material type as specified by the material mapping file. This mapping file lists each component of the model and its material type. The ray direction file is a list of direction cosines which defines the rays that will emanate from the target point. It is along these rays that the material thicknesses of each component will be calculated. These thicknesses, measured in each direction defined in the ray direction file, are sorted by material type and distance from the target point before being written to the output file. The following sections describe each of these files in more detail.

(a) RadICal Inputs: CAD Model

The format for the RadICal input geometry file was chosen to be compatible with some commonly available CAD tools and to provide a very simple format so that models which are created with incompatible CAD modelers can be easily translated into a format that is compatible with RadICal. Geometry models used by RadICal have surfaces represented by a mesh of flat faces or facets. These facets are defined by a series of points which define their edges (Fig. 3). The points are simply defined by their (x,y,z) coordinates. Typically, each collection of facets, which together form a closed volume or component, are put into a named group in the file. Only the facet groups which are referenced by the material mapping file are used as components by RadICal.

The restrictions on these groups of facets that represent components are:

- together they form a completely enclosed volume

- adjacent facets share points

- facet normals are consistent and oriented so that they are pointed "out" on outer surfaces and pointed "in" on interior surfaces

- there are no "cracks" in the facet connectivity

- each facet should be referenced by one and only one component

Also, to help ensure accuracy of the analysis and limit the growth of roundoff error, it is best to use triangular facets exclusively since they are inherently planar.

The primary CAD programs used to create shielding models used in the development of these analysis tools were the Solid Modeling Aerospace Research Tool (SMART) and the Wavefront Model program. SMART is a full-featured CAD program developed by the Vehicle Analysis Branch at NASA Langley Research Center. It is able to generate models in the required format directly. The Alias/Wavefront Model program is able to read and write models in the format used by RadICal in addition to performing many functions required to "clean up" a SMART output model so that it conforms to the restrictions outlined above.

The two biggest advantages of this simple, faceted, model representation are the fast calculation of the ray-facet intersections and the ability to easily translate models into this format which are based upon higher-order polynomial surfaces. This conversion from parametric surfaces to faceted geometry is often done by creating a triangle mesh based upon the intersection of isoparametric lines on the surface. This can be accomplished in most commercial CAD programs by exporting the geometry to a stereo lithography file format. Finite element modelers can also be quite useful for generating triangle meshes which meet the requirements for RadICal input.

Another consideration when constructing a shielding model for RadICal analysis is the level of detail. The two factors that most affect the contribution of a component to the total shielding are its thickness and the total angle it covers in a spherical coordinate system centered at the target point. If these two component attributes are modeled accurately, and the component is positioned properly with respect to the target point, modeling any further details generally will not increase the accuracy of the analysis. Further reduction in detail can be gained on components that are very far from the target point and cover a small solid angle. Often, even with a dense ray pattern, dense, compact components placed far from the target point will catch at most 1 ray out of roughly 2000. Modeling these components with attention to fine details will be a waste of time. Even close to the target point, component details which are small compared to the thickness of the component as a whole may be ignored.

Often when performing a shielding analysis of a preliminary design there will be a number of components about which only the outer dimensions and overall weight are known. For a simple analysis, it is often adequate to represent these components by only their outside shape and their total weight. This "smeared" approach to component modeling can provide adequate results when applied carefully.

(b) RadICal Inputs: Material Mapping File

The material mapping file is used by RadICal to determine the material type for each component in the model. The file format is simply the name of the component followed by an integer which identifies the material type. Often, each component is given a unique material number so that material types may be changed at a later date

without re-executing RadICal. Actual inclusion of the properties of the material as they relate to ionizing radiation occurs when a radiation analysis is performed using the RadICal output thicknesses as input.

(c) RadICal Inputs: Ray Direction File

The ray direction file is used to define which directions RadICal will use to calculate thicknesses. Any list of direction cosines are allowed; however, for the purposes of our development and analyses, an even distribution was thought to be the best in terms of computational efficiency and in terms of being able to understand the contributions of different components to the total shielding. The most common ray distribution used in RadICal is based upon a dodecahedron for which each pentagonal face has been divided into 5 identical triangles (Fig. 4). Each of these triangles is then recursively subdivided into more triangles to produce a finer mesh. Each vertex on the surface of this sphere is used to define a ray direction. A sphere which has been subdivided to the extent that it has 1922 vertices is usually adequate.

(d) RadICal Algorithms

In order to calculate the radial thicknesses of the faceted components, RadICal has a series of nested loops which, for each ray, checks for an intersection between the ray and each facet in the model. Any facets which are intersected by the current ray are then flagged as to whether the ray is going "into" or "out of" the facet. These intersections are then sorted by distance from the target point and material reference. Material thicknesses can then be calculated from the intersection locations and output in the order that the incoming radiation would encounter the different materials.

(e) RadICal Output

The output file for RadICal contains the sequence and thicknesses of the materials that are encountered by radiation as it approaches the target point. The format of the file is shown in (Fig. 5). This file is used in conjunction with radiation transport calculations through various thicknesses of ordered materials. Through the use of interpolation routines (used to reduce the number of transport calculations) the flux of particles at the target point can be calculated.

COMPUTED TOMOGRAPHY SCAN-BASED HUMAN BODY MODEL

The INT5 program uses a Computed Tomography scan (CT-scan) dataset as the basis for calculating the radiation shielding provided by body tissue surrounding a point within the body. The flowchart in (Fig. 6) shows the input and output files used by INT5. The inputs are the CT-scan data, a ray direction file, and a target point, about which the shielding will be calculated. There are 663 CT-scan data files, each containing a single, coronal, data slice. The ray direction input file is the same format as the one used in RadICal, described above. The target point is specified in millimeters, in the body coordinate system which has the positive X-axis pointing forward, the positive Y-axis pointing out of the right shoulder, and the positive Z-axis pointing down.

The raw CT-scan data are a three-dimensional, 256×256×663 array of data points. Each point represents the average radiodensity of the surrounding matter relative to the type of x-ray used in the scan. The original point spacing of the raw CT-scan data is 2.16×2.16 mm within each 256×256 data point slice and 3 mm between slices.

The ray direction file specifies the direction each ray points away from the specified target point. Body tissue density values are integrated along each ray to get the total shielding provided by body tissue in that direction, and these directional shielding values are stored for use with radiation dose prediction software. To aid in post-processing, the body tissue is also classified by density into several categories during the integration. This classification allows an analyst to view the shielding contribution of the body's fat, cartilage, bone, and/or soft tissue independently.

(a) CT-Scan Raw Data: Description

The raw CT-scan data used as the basis for this model were provided, courtesy of Dr. Elliot Fishman and Derrick Ney at Johns Hopkins Hospital. One portion of their studies was to produce a full-body, medium resolution, CT-scan of a fresh cadaver which had no obvious physical deviations from a healthy, living subject. This was done in order to aid in the development of new techniques in medical imaging. The high radiation dose incurred during the roughly five hours of beam exposure precluded the use of a live subject. Within two hours of the time of death, the CT-scan commenced with the subject lying flat on the scanning bed with his arms and hands placed in front of him. The subject was a male in his 50's who had died following a brain hemorrhage which was the result of a cerebral aneurysm. His height and weight place his body size near the 95th percentile. At the time of the scan, the subject was wrapped in sheets and had several tubes remaining in the body, which were left from various emergency medical procedures. These objects, the table which supported the subject, and a ring artifact due to the large size of the subject relative to the scanning equipment, are visible in the raw CT-scan data as delivered from Johns Hopkins.

The data values themselves were represented in an arbitrary system of units known as Hounsfield numbers. Hounsfield numbers (h) typically range from a value of -1000 to +1000 and the scale is typically calibrated so that water yields a value of 0 and compact bone is near +1000. To allow for efficient data storage, Johns Hopkins personnel shifted the Hounsfield numbers by an increment of 1024 so that they could be stored as positive (unsigned) integers.

(b) CT-Scan Raw Data: Preparation

The first step in processing the raw data received from Johns Hopkins was to remove the extraneous data artifacts described above. The table, ring artifact, and general noise were removed manually by setting values of data points which were outside the body to zero, slice by slice. Data artifacts which were internal to the body were left unchanged and later tests showed that they have a negligible impact on analysis results. The data values associated with the table and ring artifacts were quite high, however, and would have significantly skewed any results.

Another step in the processing of the raw CT-scan data was to determine scaling factors which would scale the original subject so that he would have the same physical dimensions as the U.S. Air Force 50th Percentile Male. Scaling the dataset to the dimensions of the 50th percentile male was desirable since most radiation calculations incorporating body geometry utilize the Computerized Anatomical Man (CAM) model [1] which is also based upon the 50th percentile male. Over 30 different physical measurements were taken from the CT-scan dataset and used to determine scaling factors which would scale the cadaver's physical size to that of the reference 50th percentile male [2]. Typical measurements used for this scaling ranged from chest circumference to foot length to head width. Software was written which could measure these dimensions directly from the data and store them in inches. Scaling factors were calculated in each direction (x, y, and z) for each part of the body where a clear size comparison could be made. These local scaling factors were then used to calculate three scaling factors for each slice in the dataset. If, for example, the y-direction scaling factor was 0.87 at the waist and 0.83 at the shoulder, the scaling factors for the slices in between would be linearly interpolated from these bounding values. This same approach was taken for scaling in all three directions. Since scaling factors in the Z (height) direction change the thickness of each slice, the slices were also individually translated in the Z direction so that there were no gaps between slices. These separate scaling factors were stored in a file which is used at runtime for each INT5 analysis.

In order to compute shielding values based upon the CT-scan data, the CT-scan data values were correlated with standard body tissue density values. A least squares curve fit for an equation in the form:

$$y = a\left(1 - e^{-bx}\right)$$

resulted in the plot shown in (Fig. 7) where y is tissue density and x is h + 1024. Points used for the correlation were the densities for the lungs, fat, liver, skeletal bone, and compact bone. The data point in the figure which identifies water is shown only for comparison. The equation obtained from the curve fit is used to convert the CT-scan Hounsfield numbers to tissue density values at runtime for integration. Except for the removal of the noise and scanning artifacts, all other processing and modification of the CT-scan data occurs at runtime so that the original tissue data are always stored in their original form.

(c) INT5 Inputs

INT5 inputs consist of the processed CT-scan data, a ray direction file, and the locations of the selected target points. Each of the 663 CT-scan slices from the processed dataset is stored in a separate, numbered file. These files are read into a single three-dimensional array at runtime and all calculations use this array, combined with the data from the scaling factors file, to represent the human body. The scaling factors file contains the X and Y point spacing for the data within each slice as well as the (x,y,z) location of the center of each slice.

The ray direction file used by INT5 is identical to the one used by RadICal. It contains a list of direction cosines which specify the direction of each ray along which the body tissue data will be integrated. Typically, an even distribution of rays is used. The selected target points are stored in a data file which is read at runtime. They

are specified in millimeters in the body coordinate system. In order to be consistent with existing human body radiation models, a right-handed, Cartesian coordinate system is used which has its origin at the top of the subject's head, X positive in the forward direction, Y positive out the right shoulder, and Z positive down, toward the feet.

(d) INT5 Algorithm

INT5 integrates along each ray specified in the ray distribution file, beginning at the target point and stopping when it reaches the edge of the dataset. At each integration step, it calculates the local body tissue density based on the correlation between Hounsfield numbers and tissue density described above. The data are interpolated in the plane of the slice (the X-Y plane) using the four surrounding data points. Due to the physics of Computed Tomography scanning, the data can be considered to be averaged already in the Z direction and no interpolation is necessary in that direction.

Integrating the tissue volumetric density along each ray produces an areal density for that direction which has the units mass/area. Also, depending on the value of the calculated tissue density at each point along the ray, INT5 classifies the tissue as either fat, organ, cartilage, or bone. Running totals of the amount of each tissue type are kept for each ray direction. These values are used during postprocessing to visualize the distribution of each type of tissue about the target point and to identify specific body structures which are contributing significantly to the shielding of the target point.

(e) INT5 Output

The output file for INT5 is written in the same format as the RadICal output file. It begins with a header identifying the file type and format. This is followed by the (x,y,z) location of the target point used. The data describing the calculated shielding distribution follow with the areal density values grouped with the direction cosines of the ray that they represent. As in RadICal, the first line of each group is the three direction cosines of the ray followed by an integer which specifies the number of "materials" which are related to that ray. For INT5 output, these different material numbers are used to represent the different tissue classifications described above. Material 1 is the total areal density in that direction considering all tissue encountered along the ray. Materials 2–5 represent the directional totals for fat, organ, cartilage, and bone, respectively. Using the same output format as RadICal allows for the use of the same postprocessing software as well as providing a straightforward way to combine RadICal results and INT5 results during any subsequent radiation analysis.

OUTPUT VISUALIZATION

The XCSPH program has been developed to postprocess the results of both RadICal and INT5. It has the capability to plot either calculated radiation shielding distributions or calculated directional doses and dose rates from other programs. It displays these data values as colors on the surface of a sphere. It is somtimes helpful to imagine this sphere centered on the analysis target point so that the color of a particular point on its surface will

represent the amount of shielding which is between the target point at its center and the external radiation environment.

The color spectrum used can be mapped linearly or logarithmically to the data values, depending on the user's preference. The user is also able to rotate the sphere interactively to clearly see how much shielding has been calculated in any particular direction from the target point. The data values displayed on the sphere can either represent the total shielding surrounding the target point or be restricted to particular materials (or combinations of materials) that are listed in the RadICal and INT5 output files.

An analyst or mission designer can gain many insights into the impact of the various spacecraft components on the overall shielding by examining RadICal output in this way. If, for example, each component has been assigned its own unique material ID, the contribution of each component to the overall shielding can be easily displayed and compared. It is clear what fraction of the 4π solid angle a component occupies and what level of shielding it provides relative to other components. This can be a great aid when configuration decisions must be made which are, in part, based upon shielding considerations.

CONCLUSIONS AND RECOMMENDATIONS

A suite of tools has been developed to calculate the radiation shielding provided by spacecraft components and biological tissue, represented by CAD models and a CT-scan dataset, respectively. Other specialized techniques and tools have been developed which allow an analyst to more easily understand and interpret the results of these analyses so that the impact of design changes can be quickly and easily understood both quantitatively and qualitatively.

Recommendations for furthering this work include a detailed comparison between the results calculated with the CT-scan model and those produced by the CAM model. Also, it would be useful to create other sets of scaling factors which could be used to represent a 5th percentile or 95th percentile male. Some effort has been given to identifying potential techniques for modifying the position of the appendages of the CT-scan dataset so that it is in a sitting or neutral bouyancy position, but software development for this purpose has not been initiated.

The INT5 software has been developed so that it may easily be adapted to use other CT-scan datasets as the basis of a radiation shielding body model. There are many opportunities for the acquisition and analysis of other CT-scan datasets, both animal and human. The same Johns Hopkins team which provided the CT-scan dataset used in this work has also scanned a variety of research animals which may be similar to animals which are flown on certain Space Shuttle experiments.

There are also two publicly available datasets available from the U.S. National Library of Medicine's Visible Human Project. In addition to photographic and Magnetic Resonance Imaging (MRI) datasets, this project has produced very high resolution CT-scans of a male and a female cadaver. These datasets would provide a higher level of fidelity when compared with the current CT-scan dataset.

Recommendations for further development of the RadICal program would include adding the capability to use parametric surfaces directly from high-end CAD packages instead of requiring that the model be converted to a faceted representation.

Another development area which should be pursued would be to transition any geometry related files for either input for output to use the more recently developed Virtual Reality Modeling Language (VRML) file format instead of the Alias/Wavefront object file format. This would allow for the geometry to be viewed and interacted with through a World-Wide-Web (WWW) browser instead of using specially written X-windows based interfaces which are often more costly and time-consuming to develop and maintain than WWW-based interfaces.

REFERENCES:

1. M. P. Billings and W. R. Yucker. *The Computerized Anatomical Man (CAM) Model*. NASA CR-134043, 1973.

2. R. W. Bailey. *Human Performance Engineering: A Guide for System Designers.* Prentice-Hall, Inc., New Jersey, 1985.
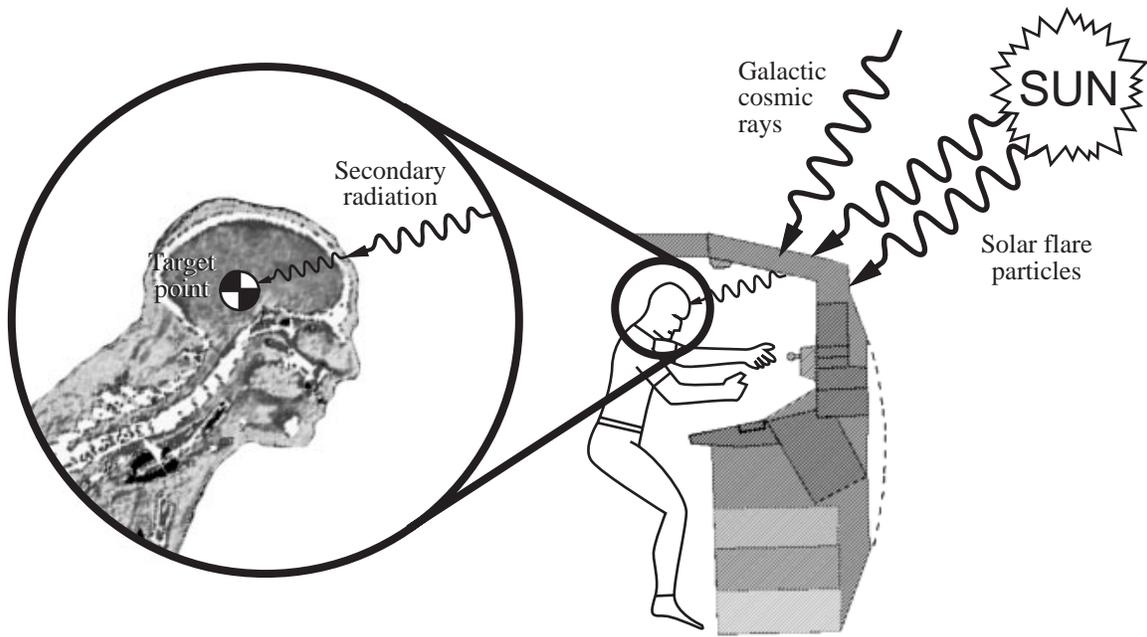
Figure 1.   Elements of Radiation Shielding Analysis.
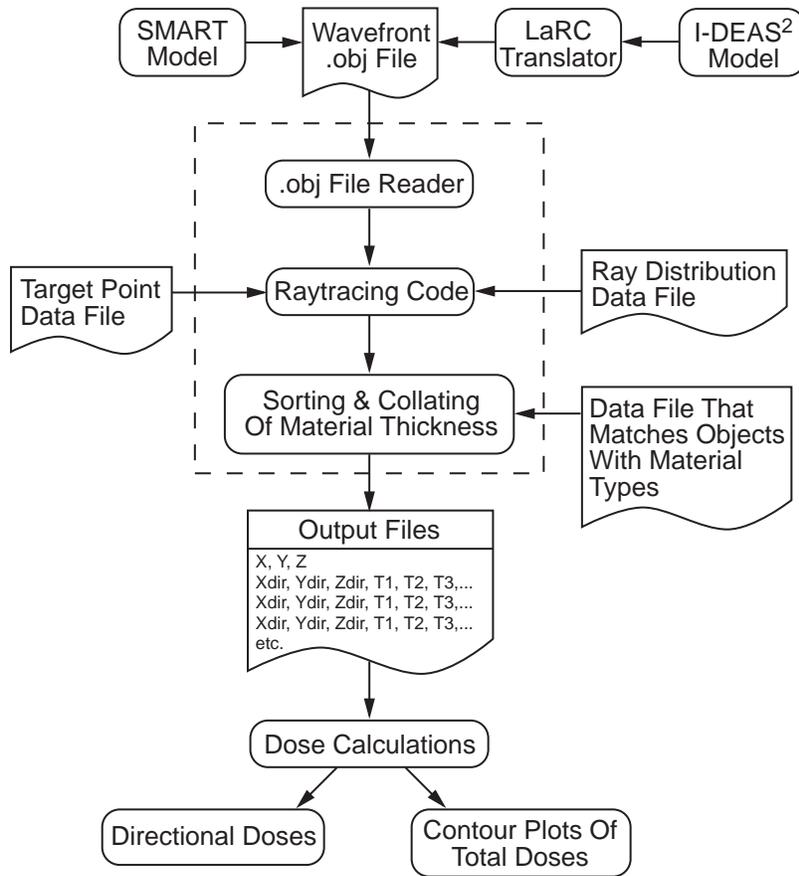
Figure 2.   RadICal Input and Output Files.

```
v    0.53486    0.21200    3.58775
v    2.34112    2.50000    3.58775
v    8.45452    3.23500    3.58775
v    3.26346    7.45347    3.75557
v    2.34543    4.23468    3.75557
v    6.98745    5.67454    3.75557
v    6.64563    3.34533    3.87343
v    6.00023    5.96788    3.87343
v    1.11584    7.52467    3.87343
g    component_1
f    1     2     3
f    2     3     4
f    3     4     5
f    4     5     1
f    5     1     2
g    component_2
f    6     7     8
f    7     8     9
f    8     9    10
f    9    10     6
f   10     6     7
```

Vertex locations

This facet references the first 3 vertices in this file

All facets in this region are in the group "component_1"

All facets in this region are in the group "component_2"

Facet normal is toward you when the numbering is counterclockwise

Figure 3.   Facet Definition for RadICal.
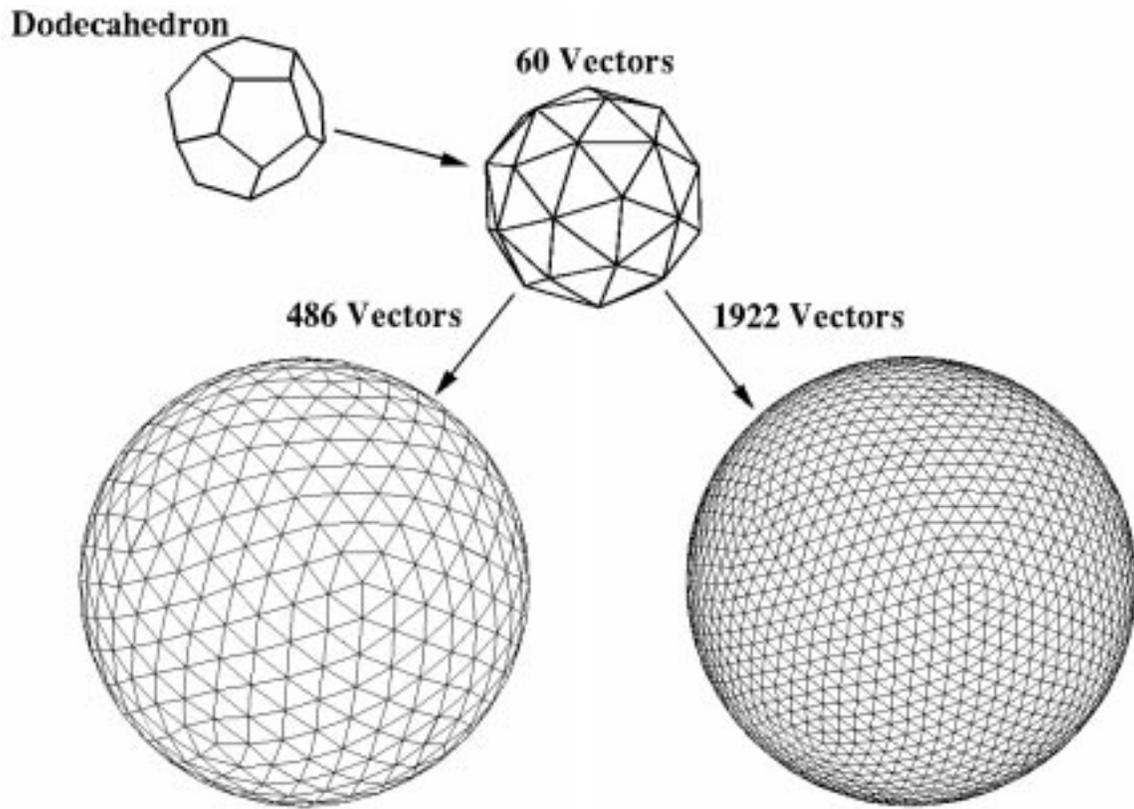
Figure 4. Generating Ray Distributions for Radical.
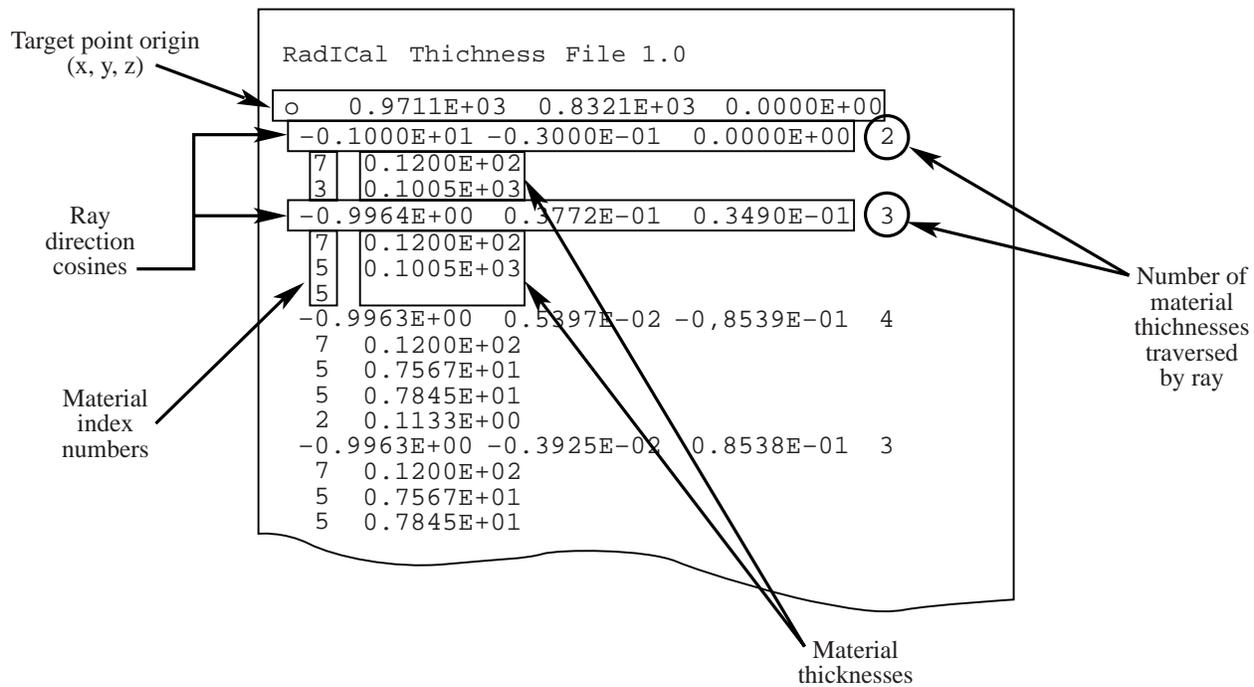
Figure 5.   RadICal Output File Format.
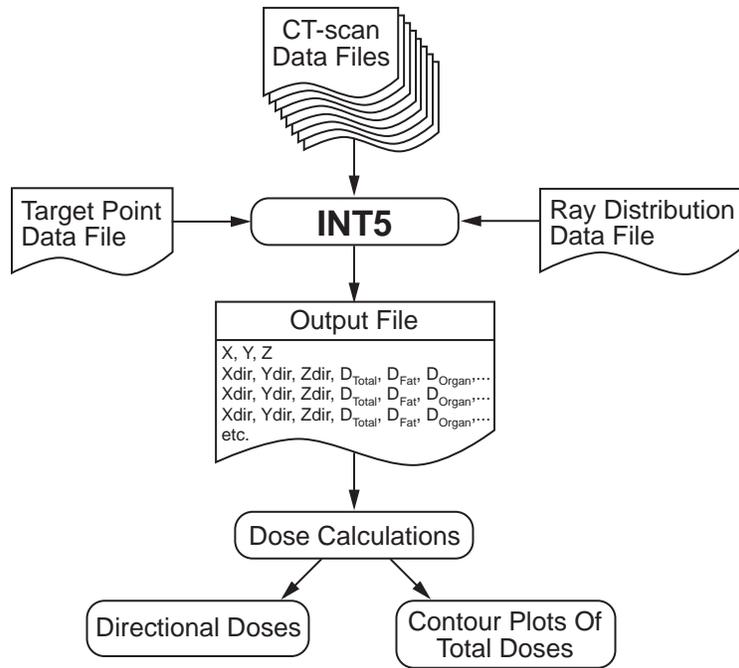
Figure 6. INT5 Input and Output Files.
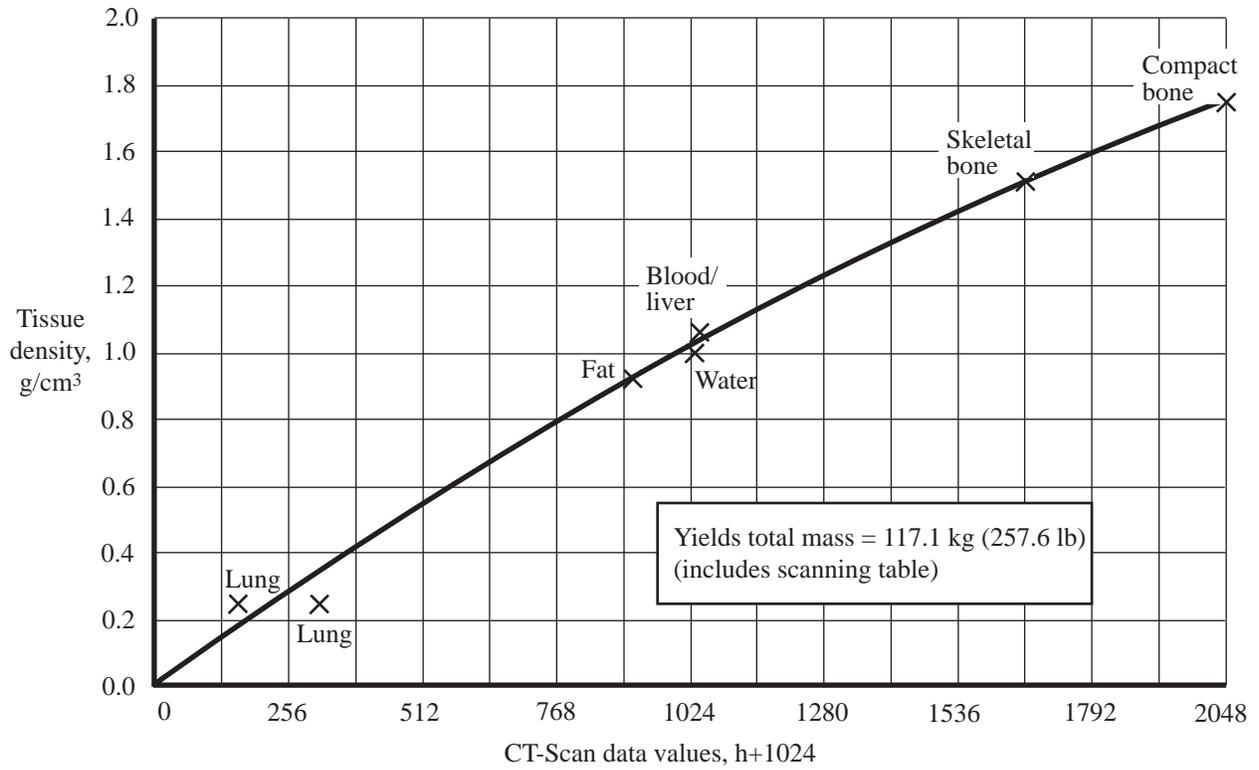
Figure 7.   Tissue density as a function of Hounsfield number.

CHAPTER 18

INTEGRATED SHIELD DESIGN METHODOLOGY:

APPLICATION TO A SATELLITE INSTRUMENT

by

John E. Nealy (Ret)[1]
Garry D. Qualls[2]
Lisa C. Simonsen[1]

[1] NASA Langley Research Center, Hampton, VA. 23681-0001
[2] AS & M, Inc., Hampton, VA 23681

Chapter 18

INTEGRATED SHIELD DESIGN METHODOLOGY: APPLICATION TO A SATELLITE INSTRUMENT

SUMMARY

A detailed analysis of the radiation exposure and subsequent effects on an environmental satellite charge-coupled device (CCD) photodetector has been performed for a 5-year mission in Sun-synchronous orbit at an altitude of 705 km. Estimates of energetic particle damage to the detector are based on presently available trapped radiation data, and also include contributions from large solar proton events and more numerous ordinary proton flares associated with solar activity. A representative computerized solid model of the spacecraft configuration has been developed, and detailed nucleon transport calculations have been made for the different spacecraft materials. Damage estimates have been made using currently accepted dosimetric techniques for these detector types. The present effort, while relating to a specific mission, also purports to describe a methodology more generally applicable to missions incorporating radiation-sensitive electronic components.

INTRODUCTION

Human efforts to explore and utilize extraterrestrial space have resulted in enormous benefits since the first crude satellites were placed in orbit during our own generations. In addition to the revolution in communications technology, a variety of instruments aboard orbiting platforms and deep space probes have brought about remarkable advances in our knowledge of the near-earth and interplanetary space environment. Knowledge of the environment, coupled with developments in instrument technologies, will enable the design and utilization of space platforms for measurements and observations of increasing detail and precision. One such platform instrument being designed for investigations related to the physics and chemistry of the Earth's atmosphere is the Stratospheric Aerosol and Gas Experiment (SAGE) III instrument, whose purpose is to provide accurate data on the temporal and spatial concentrations for a number of atmospheric species [1]. Consideration of the required accuracy of observation for some species indicate that spectrophotometric measurements of unprecedented precision are needed.

The SAGE instrument consists of a scanning Cassegrain telescope and diffraction grating spectrometer combination which examines spectral absorption of solar and lunar-reflected radiance in atmospheric occultation. A cross-section layout of the instrument indicating the location of optical components is shown in Fig. 1. The spectrometer utilizes the CCD as its optical detector. These devices consist of arrays of miniscule (~10 μm) silicon electrodes (pixels) and are currently used as general purpose optical imagers. Recently, techniques have been developed to accurately calibrate CCDs for measurement of absolute intensity of optical radiation. However, such calibrated CCDs are much more subject to both direct interference and long-term degradation as a result of exposure to high-energy nucleons and heavy ions found in the Earth-orbital and interplanetary space environment. Therefore, measures must be taken to provide adequate protection from these particles to ensure required instrument integrity. In order to approximate the useful lifetime of a CCD detector on a given mission, three factors must be considered: (1) the high-energy charged particle environment, which varies with solar activity and locale; (2) the transport and interaction of high-energy particles through spacecraft structural materials and supplied shielding; and (3) the ultimate exposure of the detector itself, which in the case of sensitive electronic devices is related to the number of lattice displacements produced in the active areas of the device.

MISSION ENVIRONMENT

The proposed orbit for this instrument mission is near-circular, with an altitude of 705 km in high inclination (98 deg.) so that on each revolution the platform crosses the equator twice and is in the vicinity of both poles. Such an orbit indicates that the instrument will be subjected to fluxes of trapped particles in the Van Allen belts while
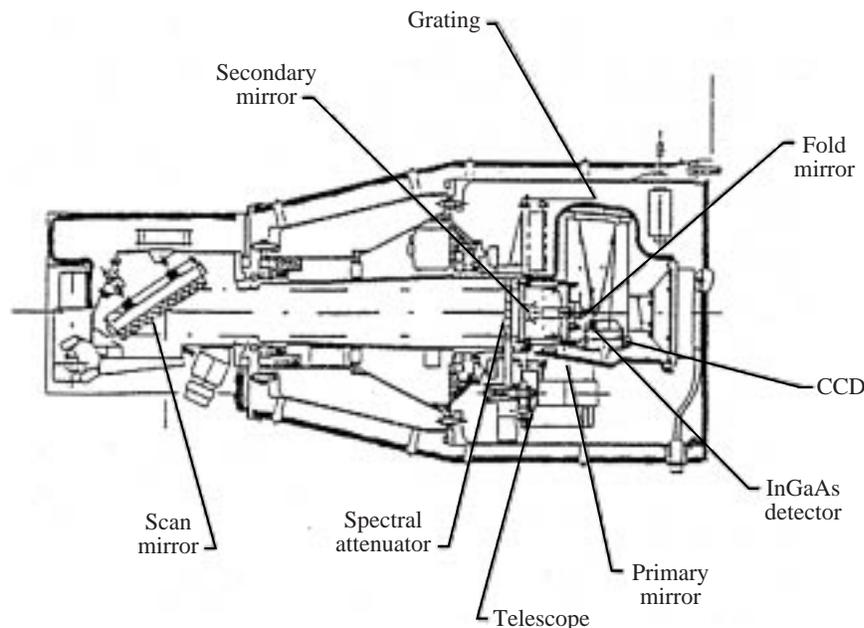
Figure 1.   Cross-section layout of SAGE instrument showing optical components.

over low and middle latitudes, and when crossing the polar regions, will be subject to exposure from solar proton flares and galactic cosmic rays. These latter constituents are substantially deflected by the geomagnetic field at lower latitudes. The design mission duration is five years.

The most important sources of radiation affecting the CCD are the protons in the trapped regions and particles from solar proton events. The low flux, high-energy galactic rays have been shown not to play a significant role in the general degradation of the detector [2]. The trapped proton environment is taken from the NASA AP8 model [3], and the five-year fluence has been computed previously for the appropriate orbital conditions [4]. The solar flare proton contribution consists of a combination of rare, large events and the more numerous ordinary flares [5]. The large flares selected for this mission correspond to the spectra observed by the GOES-7 satellite during Aug.– Oct. 1989 [6]. The ordinary flare constituent is based on the Explorer satellite measurements during Solar Cycle XXI [7], and represents the five-year fluence spectrum for these flares. The flare spectra have been modulated using a previously developed energy dependent magnetic cutoff model [8]. Transmission factors appropriate to the SAGE orbit have been applied to the free-space flare spectra. Fig. 2 shows the individual constituents and total five-year differential proton fluence ultimately chosen to represent total mission exposure. The trapped protons constitute most of the exposure at low and high energies, while the flare contribution is of greatest significance between 1 and 50 MeV. The total differential fluence spectrum has been used as direct input for the Langley transport code BRYNTRN [9] to compute the attenuation for spacecraft materials.
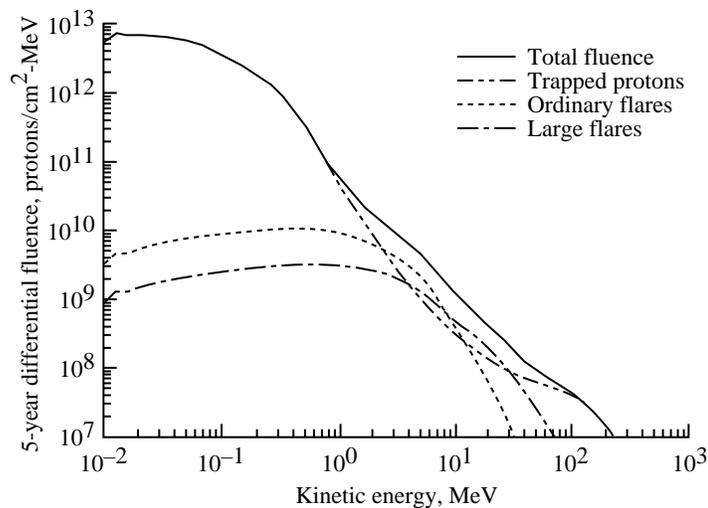
Figure 2. Modeled spectral proton environment for 5-year polar orbital mission at 705-km altitude.

CCD EXPOSURE ANALYSIS TECHNIQUES

Particle Transport

The ultimate particle flux incident on the CCD detector depends on the attenuation of the primary particles and on the generation and transport of secondaries produced by nuclear interactions. Individual material properties influence the manner in which the particles propagate. In addition, the order in which particles encounter various materials impacts the emergent spectra. The BRYNTRN code is ideally suited to performing transport calculations of this type, since it is an efficient, deterministic, high-energy nucleon transport program containing a relatively complete nuclear interaction database for many materials.

Sample flux spectra are given in Fig. 3 for emergent spectra through quartz-tantalum and tantalum-quartz combinations. The two calculations indicate the differences in emergent flux when the sequences of materials encountered are reversed; that is, the material slabs are not commutative with respect to the final spectrum. The most notable differences are observed in the transmitted primary protons, where at low energies (< 1 MeV), the Ta-quartz combination results in a proton flux of up to a factor of three less than the emergent proton flux from the quartz-Ta combination. Thus, it may be important to consider the spacecraft constituent materials and the manner in which they are distributed.

Instrument Solid Geometry Model

The detector, shield, and the important components of the SAGE III instrument have been modeled with Computer-Aided-Design (CAD) software using dimensions from scale drawings of the assembly. Fig. 4 shows a split view of the solid model and some of the more prominent components. Fig. 5 depicts the detector assembly in greater detail and indicates the shape and location of the aluminum block shield surrounding the CCD. The CAD model contains the information necessary to define directional thickness amounts around specified target points. In the present study, 1922 directed rays are defined at a target point and are regularly distributed so that all rays may be associated with a constant solid angle ($4\pi/1922$). For a target point in the center of the CCD detector, the distribution of shield amount in terms of linear density (g/cm^2) has been calculated. The values are sorted from minimum to maximum and plotted in Fig. 6 as a cumulative distribution function. The derivative of this function (shown in Fig. 7) may then represent a probability function of directional shield amounts. For the SAGE instrument, the probability distribution peaks at approximately 5 g/cm^2.

CCD Dosimetry

Permanent degradation of CCD performance from energetic particle radiation is thought to be primarily due to projectile-nucleus interactions leading to lattice displacements in the silicon crystal structure [10]. Several approaches are evolving to estimate these effects of the space radiation environment [10], [11], but presently, experimental testing of individual devices in high-energy accelerator beams is needed to provide accurate detector response characteristics.
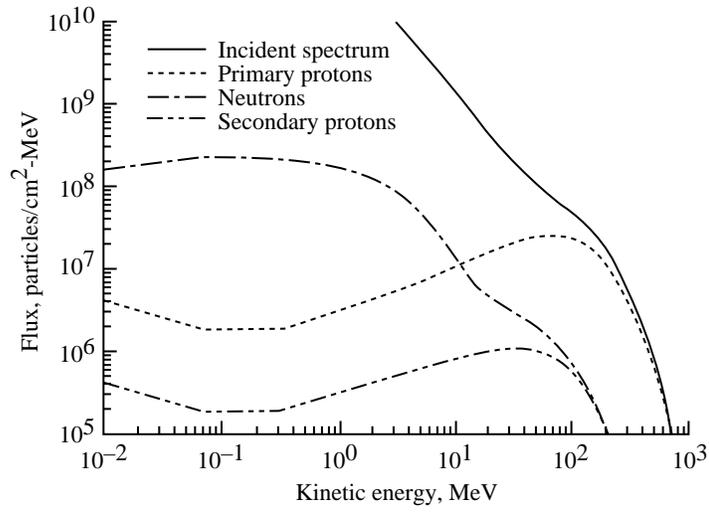
(a) 4 g/cm^2 SiO$_2$ + 4 g/cm^2 Ta.
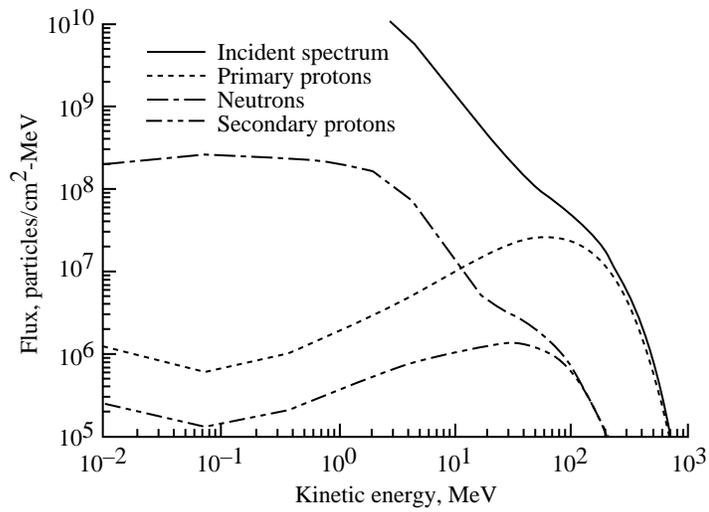
(b) 4 g/cm^2 Ta + 4 g/cm^2 SiO$_2$.

Figure 3. Calculated Flux Spectra for Quartz-Tantalum Material Combinations.
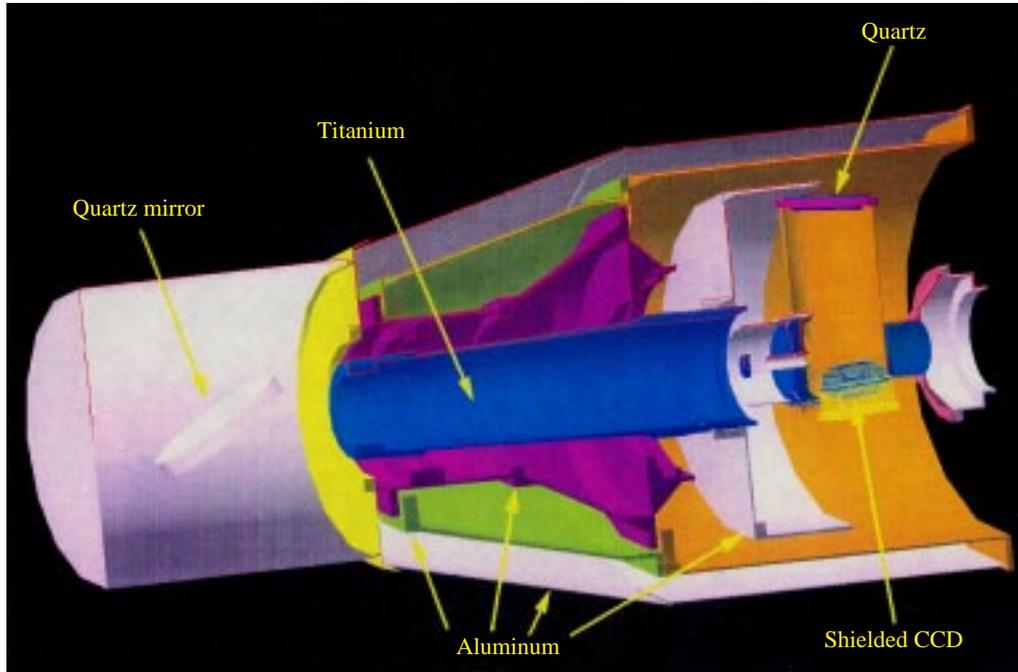
Figure 4.   CAD Model depiction of the SAGE III instrument.
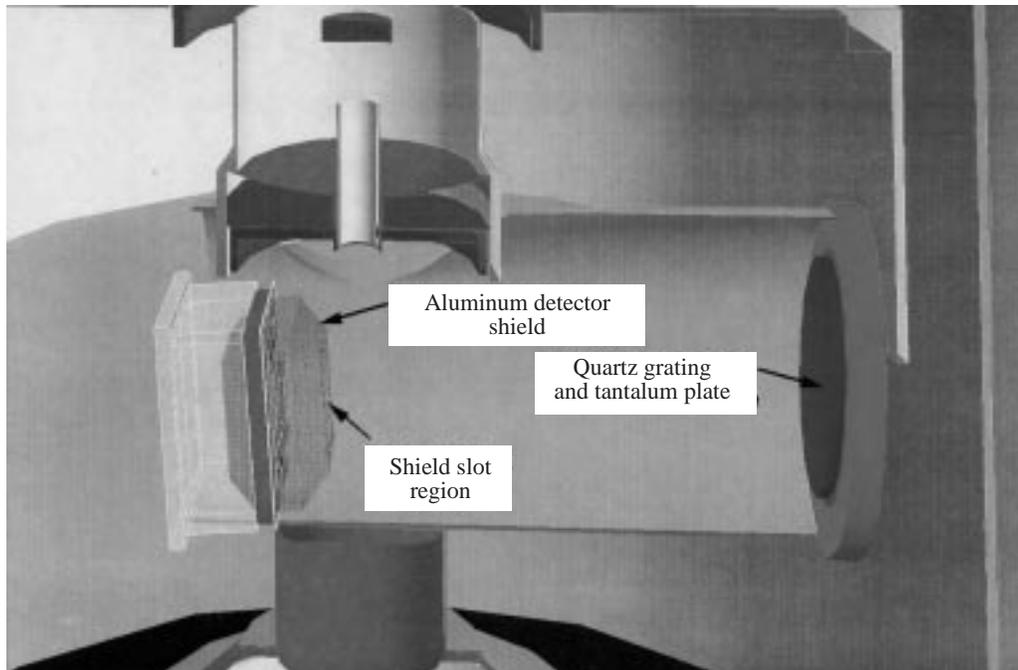
Figure 5.   CAD Model details of SAGE III detector and shield assembly.
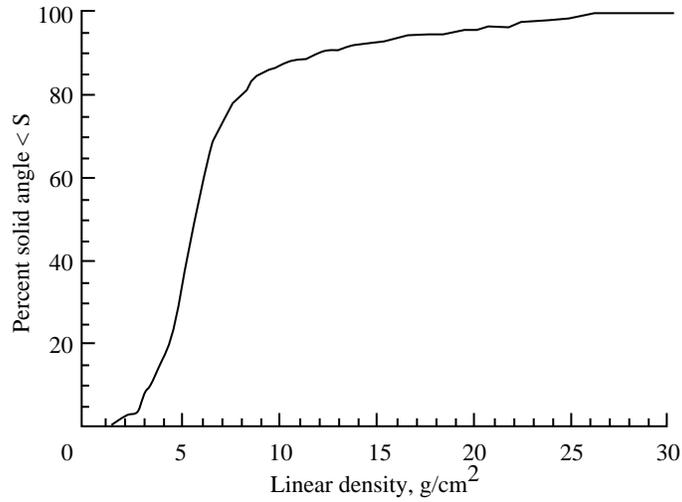
Figure 6.   Cumulative distribution of linear density for target point at detector location.
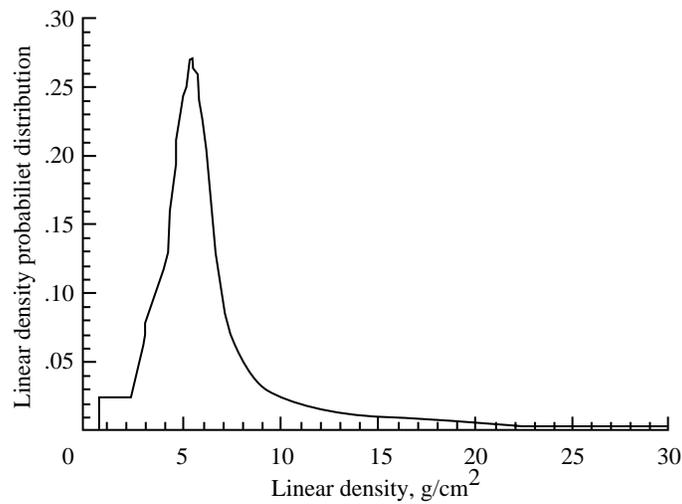

Figure 7.   Linear density probability distribution at detector location.

Radiation damage to CCDs may be related to the direct energy deposition, or dose, resulting from particle interactions in the silicon medium. The dose, D, may be calculated as

$$D = \int_0^\infty \phi(E)S(E)dE$$

where ϕ is the incident differential flux at energy E, and S is the stopping power, or energy loss per unit linear density of silicon (including both electronic and nuclear interactions). The proton stopping power for a silicon target is shown in Fig. 8, as extracted from the BRYNTRN atomic interaction database.
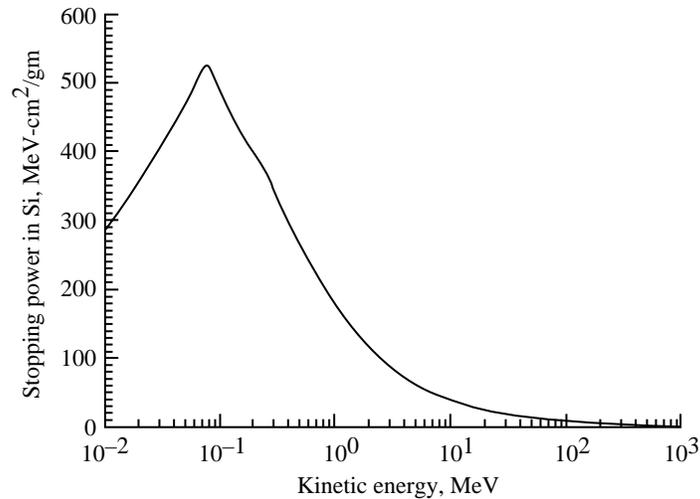
Figure 8.   Proton stopping power in silicon.

For protons, the conventional dose evaluation is dominated by the interactions with bound electrons; however, these interactions are not strongly related to permanent displacement damage. A dose evaluation procedure believed to be more closely related to lattice nuclear displacements is the energy deposition due to the nuclear interactions alone, described as a "non-ionizing energy loss", or NIEL [11]. The corresponding dosimetric quantity has been termed the "nirad" (non-ionizing radiation absorbed dose), calculated as

$$N = \int_0^\infty \phi(E) S_n(E) dE$$

where S_n is the energy loss due to nuclear interactions. The S_n functions for protons and neutrons in silicon are shown Fig. 9.
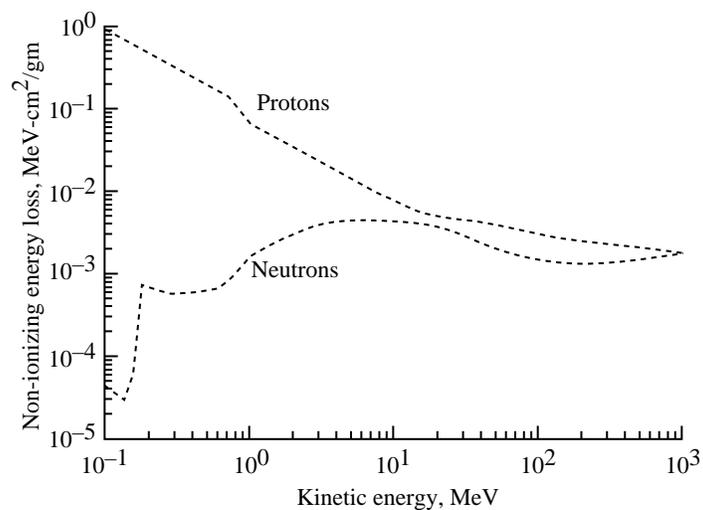
Figure 9.   Non-ionizing energy loss (NIEL) for neutrons and protons in silicon.

An important specification of CCD performance is the charge transfer efficiency (CTE), which is a measure of the capability of moving photoelectrons collected from one pixel to another in the detector array. A methodology has been developed [10] to evaluate the CTE, and the corresponding charge transfer inefficiency (CTI = 1 − CTE) for specific devices. Measured values for CTI [10] for a series of proton beam exposures are shown in Fig. 10. Such measurements have been shown [10] to bear a correspondence to calculated numbers of displacements in typical CCD structures, indicating that the non-ionizing component of the incident radiation is of most importance. However, even though actual numbers of displacements within the crystal lattice may be computed with some confidence, not all displacements result in permanent charge traps. Consequently, experimental measurements of CTI for individual detector types remain the most reliable way of assessing actual detector response to nucleon irradiation. The overall transfer inefficiency for the CCD measurements of Fig. 10 may be computed as

$$CTI = \int_0^\infty \phi(E)\left[\frac{CTI}{proton\,/\,pixel}\right]A_p\,dE$$

where A_p is the area of one pixel and the other symbols remain as previously defined.

CCD MISSION EXPOSURE AND SURVIVAL ESTIMATES

For the given external environment (Fig. 2), a rigorous calculation of the exposure at the CCD location within the instrument includes transport calculations along each directional ray, taking into account the material types and thicknesses. A great simplification results if the spacecraft is assumed to be composed of a single material. Then a
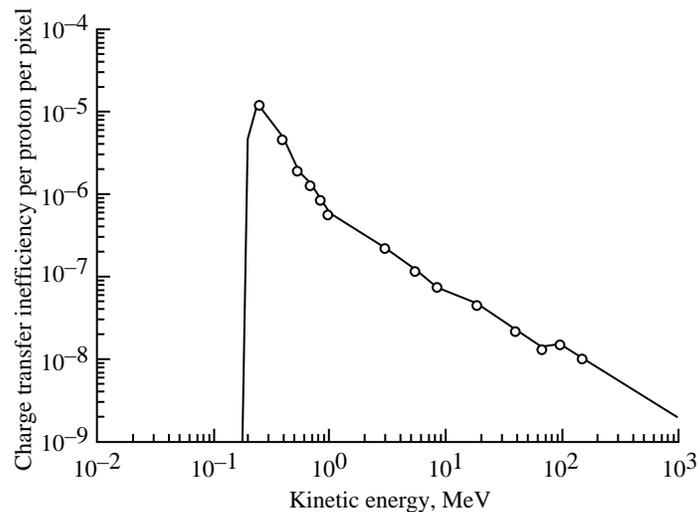
Figure 10. Measured values of charge transfer inefficiency for CCD exposed to accelerator proton beams (from Ref. 9).

precalculated dose-vs-depth function, $D(t)$, may be used in conjunction with the thickness (t) distribution, $p(t)$, of Fig. 7 to compute the dose at the target location, D_T, as

$$D_T = \int_0^\infty D(t)p(t)dt$$

Since the CCD shield and much of the spacecraft structure is aluminum, this material has been chosen for these approximate evaluations, referred to here as the "Aluminum Spacecraft" results. The dose-vs-depth functions used in this approach as calculated for the assumed environment are shown in Fig. 11. The difference between the proton and total curves for the nirad dose represents the neutron contribution; the proton and total dose for rad units are indistinguishable. The Aluminum Spacecraft results for the 5-year mission are: 687 rad and 0.424 nirad.

The detailed CAD model calculations include an evaluation of the directional dose for individual rays and a subsequent solid angle integration to arrive at the total dose. These results for the complete CAD model are: 782 rad and 0.373 nirad. The directional calculations can further be used to indicate along which directions the detector is most vulnerable, and as might be expected, this occurs in the region of the opening in the shield which admits the optical radiance to be measured.

In evaluating the ultimate degradation of the detector, the charge transfer inefficiency (CTI) has been determined according to the measured values of Janesick et al. [10]. The CTI can also be estimated according to a damage coefficient of .00075ΔCTE/nirad(Si) as deduced by Dale et al. [11]. For the Janesick function the computed CTI is .000136, and for Dale's coefficient the CTI is .000280, corresponding to CTE values of .999864 and .99972, respectively. Since the SAGE CCD is an 800×10 pixel array, 800 to 810 pixel transfers are involved in a CCD readout operation. From the two CTE values given above, the charge transfer efficiency for the entire device is predicted to be reduced by 10.4% and 20.3%, respectively. Since the lower CTI (Janesick transfer function)
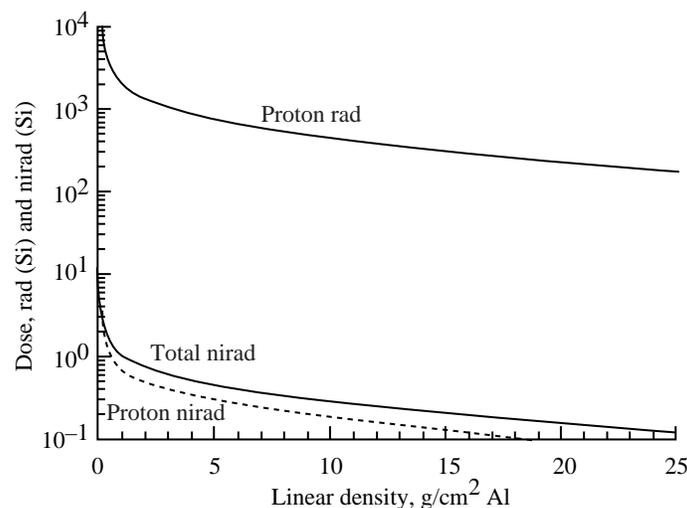

Figure 11. Dose-vs-depth functions for aluminum calculated for the SAGE-III space environment.
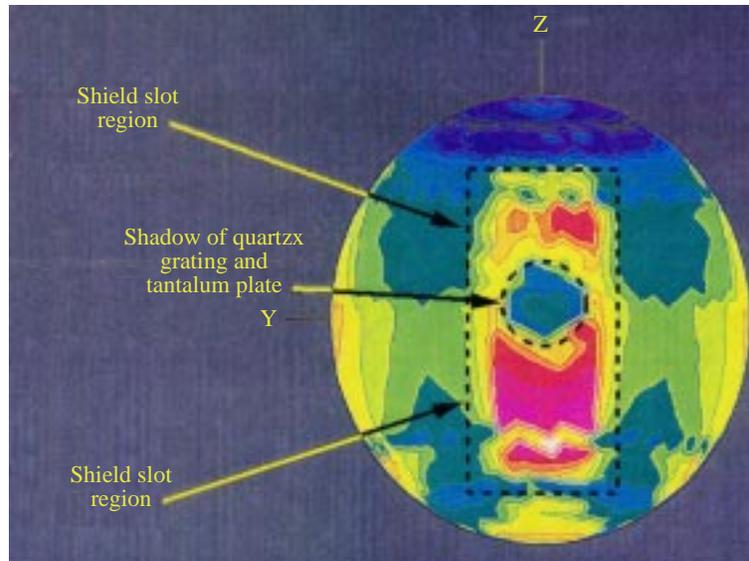
Figure 12. Directional Dose Pattern in the Region of the CCD Shield Opening (Darker Areas Represent Larger
           Radiation Intensities).

has been evaluated only for the proton dose and the nirad evaluation includes the dose due to secondary neutrons, the 20.3% degradation is felt to be a more representative prediction.

CONCLUDING REMARKS

A detailed analysis of the radiation exposure and subsequent effects on the SAGE III CCD photodetector has been performed for a five-year mission in Sun-synchronous orbit at 705-km altitude. A primary general conclusion is that the instrument should survive and produce acceptable data for the entire mission duration. Estimates of energetic particle damage to the detector are based on well-established environment data, detailed nucleon transport calculations through spacecraft materials, an elaborate CAD model of the spacecraft configuration, and currently accepted dosimetric evaluations for CCD detectors. The predicted degradation due to environment exposure for the subject mission is approximately 20%.

Methods for accurately and reliably predicting radiation effects on CCDs (and other radiation-sensitive electronic components) are still evolving. The modeled environment and associated transport calculations are felt to provide realistic particle fluxes and delivered dose amounts for this mission; however, the final step of predicting signal degradation for the device has relied heavily on experimental results obtained from exposures on relatively few specific devices. It is likely that future SEI missions (both manned and unmanned) will employ increasingly sophisticated electronic imagers such as CCDs which will require dedicated analyses of their behavior in the space radiation environment. The analysis described herein is felt to represent some logical steps in this direction.

REFERENCES

1. M. P. McCormick, W. P. Chu, J. M. Zawodny, L. E. Mauldin, and L. R. McMaster: Stratospheric Aerosol and Gas Experiment III (SAGE III) Aerosol and Trace Gas Measurments for Earth Observing System (EOS), SPIE Symposium on Aerospace Sensing, Orlando, FL, Paper No. 1491-16, 1991.

2. J. E. Nealy and B. E. Tipton: Galactic Cosmic Ray Exposure Estimates for SAGE-III Mission in Polar Orbit, NASA TM-107678, 1992.

3. D. M. Sawyer and J. I. Vette: AP8 Trapped Proton Model for Solar Maximum and Solar Minimum, National Space Science Data Center, Greenbelt, MD, Rept. NSSDC-76-06, 1976.

4. M. M. Gates and M. J. Lewis: A Rapid Method of Calculating the Orbital Radiation Environment, AIAA 27th Aerospace Sciences Conference, Reno, NV, Paper No. 91-0140, 1991.

5. J. E. Nealy, S. A. Striepe, and L. C. Simonsen: MIRACAL: A Mission Radiation Calculation Program for Analysis of Lunar and Interplanetary Missions, NASA TP-3211, 1992.

6. H. H. Sauer, R. D. Zwickl, and M. J. Ness: Summary Data for the Solar Energetic Particle Events of August Through December 1989, Space Environment Laboratory, National Oceanic and Atmospheric Admin., Boulder, CO, 1990.

7. J. N. Goswami, R. E. McGuire, R. C. Reedy, D. Lal, and R. Jha: Solar Flare Protons and Alpha Particles During the Last Three Solar Cycles, J. Geophys. Res., 93, A7, 7195, 1988.

8. J. W. Wilson, J. E. Nealy, W. Atwell, F. A. Cucinotta, J. L. Shinn, and L. W. Townsend: Improved Model for Solar Cosmic Ray Exposure in Manned Earth Orbital Flights, NASA TP-2887, 1990.

9. J. W. Wilson, L. W. Townsend, J. E. Nealy, S. Y. Chun, B. S. Hong, W. W. Buck, S. L. Lamkin, B. D. Ganapol, F. Khan, and F. A. Cucinotta: BRYNTRN: A Baryon Transport Model, NASA TP-2887, 1989.

10. J. Janesick, G. Soli, T. Elliot, and S. Collins: The Effects of Proton Damage on Charge-Coupled Devices, SPIE Proceedings, vol. 1447, 87-108, 1991.

11. C. J. Dale, P. W. Marshall, B. C. Cummings, L. J. Shamey, R. Howard, and A. Delamere: Spacecraft Displacement Dose Calculations for Shielded CCDs, Proc. SPIE Conf. on High Resolution Sensors and Hybrid Systems, Palo Alto, CA, 1992.

CHAPTER 19

SHIELDING MATERIALS DEVELOPMENT AND TESTING ISSUES

by

Sheila A. Thibeault[1]

Myung-Hee Y. Kim[2]

John W. Wilson[1]

Edward R. Long, Jr.[1]

Richard L. Kiefer[3]

Michael B. Glasgow[3]

Robert A. Orwoll[3]

[1] NASA Langley Research Center, Hampton, Virginia 23681-0001
[2] National Research Council-NASA LaRC Research Associate
[3] College of William and Mary, Williamsburg, Virginia 23185

Chapter 19

SHIELDING MATERIALS DEVELOPMENT AND TESTING ISSUES

SUMMARY

The alteration of space radiation by shield materials of specified elemental composition, density, and thickness is investigated theoretically by using the NASA LaRC's high-charge, high-energy nuclei transport (HZETRN) codes. The fluence of the projectile-fragment particles from energetic ion beams shows that the number of particles behind most shield materials increases with increasing shield thickness. The material's performance as shielding from galactic cosmic ray (GCR) is examined by comparing the shield effectiveness of risk reduction from the conventional quality factors and also from the probability of the neoplastic transformation ratio of shielded C3H10T1/2 mouse cells. The results show that the attenuation of biological effects within the shield and body tissues depends on the shielding nuclear properties and that hydrogenous materials are good candidates for high-performance shields.

Experimental studies have been conducted to validate the prediction of the fragmentation from the energetic heavy ion beams and to develop appropriate shielding technology for human protection from space radiation. Film castings of advanced polymeric materials are processed and characterized experimentally to evaluate the effect of the energy absorption from the neutron exposure. The preliminary results show that the addition of elemental boron powder to a polymer material allows the material to absorb low-energy neutrons. In addition, the boron does not cause a degradation in mechanical and thermomechanical properties. Relatively thick boron-loaded epoxy castings are processed and the detailed data analysis of the castings indicates that thermomechanical properties are not significantly changed from those of the neat epoxy resin and that boron-loaded epoxy castings show significantly higher mechanical properties, such as compressive strength and modulus, than those for the neat epoxy resin. Thus, hydrogen-containing advanced polymeric materials with boron provide both good structural stability toward radiation and high shielding capability for human protection.

INTRODUCTION

The NASA Space Exploration Initiative (SEI) Program recognized that heavy ion particle radiation (Galactic Cosmic Radiation), high-energy proton radiation (solar flares), and neutron radiation would be hazards to the human occupants and electronic components of spacecraft and that appropriate shielding technology needed to be developed. Radiation from solar flares consists primarily of protons with energies less than 1 GeV. Galactic cosmic rays (GCR) consist mostly of protons and alpha particles, with a small, but significant component of heavier particles (HZE), with kinetic energies up to 10^{10} GeV [1]. Humans in a lunar habitat or on a manned mission to Mars will require more protection from GCR than has been used heretofore on shorter missions.

As HZE in the GCR interact with a shield, they fragment and deposit energy at rates that depend on the nature and energy of the incident particles, the nature of the shield material, and the depth into the shield. The relationships are complex, so that, in some instances, the "shield" can cause an increase in both the number of particles and the dose due to the production of secondary particle radiation. For example, the dose equivalent from HZE particles absorbed by a human behind a 1.3-cm aluminum shield, the traditional structural material for spacecraft, exceeds by 10% the dose equivalent in free space [2]. This is due to a greater rate of energy transfer at the back side of the shield (*a*) by the projectile or its fragments after they have been slowed by their passage through the shield, (*b*) by secondary energetic nuclei and fragments generated in the shield, and (*c*) to a lesser extent, by secondary particles knocked out of the target material.

Computer codes [3] have been developed to calculate the fluences of primary and a large buildup of secondary particles from energetic ion beams and also to assess the biological response from annual GCR exposure behind a shield. Fluences of projectile fragments have been predicted behind polymeric materials to provide data for code validation [4, 5, 6]. Pilot experiments to validate this fragmentation have been conducted for graphite/epoxy composites at the Lawrence Berkeley Laboratory. The estimation of biological response due to energy deposition from the transmitted radiation behind a shield material provides the relative shield effectiveness [5, 6]. By comparing the theoretical calculations, the candidate materials concepts are identified for human protection from space radiation.

Energetic charged particles will suffer nuclear reactions and Coulomb dissociation processes and stop inside a shield. Low-energy, secondary-charged particles are stopped near their point of production. Although the production spectra of high-energy neutrons (E > 10 MeV) from the nuclear fragmentations are still not known and are very controversial [7], they are an important contributing factor in the overall exposure. Even the low-energy neutrons (below 1 MeV) are able to migrate far from the beam axis. Therefore, the shielding of these secondary neutrons occurring within a shield and their impact on a shield have been investigated experimentally [4, 8, 9] not only for the fundamental human protection, but also for the potential applications in the nonaerospace sector (e.g., nuclear power plants, nuclear-powered submarines, and medical facilities providing neutron radiation therapy).

GCR TRANSPORT

Cosmic ray nuclei are the only direct and measurable sample of matter from outside the solar system. Although GCRs probably include every natural element, not all are important for space radiation protection purposes. The abundances for species heavier than nickel (atomic number Z > 28) are typically 2 to 4 orders of magnitude smaller than that for iron [10]. Figure 1 illustrates fits to the measured spectra at 1 astronomical unit (AU) for hydrogen, helium, and heavy ions up to nickel (atomic number 28) at the 1977 solar minimum modulation from the relatively quiet solar cycle 21 (1975–1986) [11].

The propagation and interactions of high-energy ions up to atomic number 28 (Ni) in various target materials were simulated [2] using the transport code HZETRN [3]. The code applies the straightahead approximation with velocity conserving fragmentation interactions for high-charge, high-energy (HZE) nuclei and nucleons colliding with shield materials. These interactions depend on the shield material, thickness, and the projectile-target interaction parameters, such as nuclear fragmentation cross sections. This code accounts for the fragmentation of the incident HZE ions and nucleons, but neglects the secondary heavy fragments derived from heavy atoms of the shield material. Materials in the target shield are characterized for the computation by their bulk density and elemental composition. Their properties as a shield depend on the atomic and nuclear cross sections.

The primary mechanism for loss of energy by HZE particles is by means of Coulombic interactions with electrons in the target. Thus, high linear-energy transfer (LET) for HZE particles is more easily achieved with materials having large numbers of loosely bound electrons per unit mass. Additional energy is lost through collisions with target nuclei. Although nuclear reactions are far less numerous, their effects are magnified because of the large momentum transferred to the nuclear particles and the impacted nucleus itself. Many of the secondary particles of nuclear reactions are sufficiently energetic to promote similar nuclear reactions and thus cause a buildup of secondary radiation, which may pose an increased hazard. Because primary nuclei undergo nuclear fragmentation, less ionizing secondaries produced by fragmentation of HZE may pose a reduced hazard.

With cosmic rays propagating through shield materials, it is customary, and more useful physically, to express distances by the total mass of all atoms encountered, and to do so in units of grams per square centimeter (g/cm^2). The thickness of an absorber (areal density) can be converted to a linear thickness by dividing by the density of the matter.

Modeling of Monoenergetic, Single-Ion Beams Transport for Fragmentation

The high-energy heavy-ion radiation components are usually attenuated to lower linear energy transfer (LET) as a result of nuclear interactions between projectile and target nuclei. These processes become more significant as the particles penetrate further into the medium. Although heavy nuclei are present in small amounts in GCR, their effects are important because LET is proportional to the square of the ion charge. Radiation within a spacecraft structure, which interacts with onboard personnel or equipment, depends on the shield composition because of differences in atomic cross sections, nuclear attenuation, and the distribution of fragmentation products. Since

hydrogen has the propensity to fragment ions into smaller fragments [12], hydrogen-containing materials, such as polymers, are good candidates for shielding materials. Additionally, hydrogen is particularly effective in undergoing elastic collisions with the secondary neutrons generated within the shield, thereby reducing the neutrons' energies and making them susceptible for absorption by other hydrogen atoms or other elements.

Energetic primary particles suffer nuclear reactions before stopping in a shield medium. The secondary radiation resulting from these reactions yields a broad distribution of energies among the lighter particles. The most energetic secondaries are confined to a narrow cone about the initial direction and are close to the initial beam axis over at least the first mean-free path [3]. This cone narrows with increasing primary energy. The flux of each secondary radiation with a broad energy distribution was integrated numerically to compute the total ion fluence. This was then compared for different materials.

Calculations were performed for an irradiation of 33.88 GeV ^{56}Fe ions on graphite/epoxy composites; the fluence of the projectile and its fragments from the back face of the shield is shown in figures 2(a) and 2(b) for two thicknesses, 10 and 18 g/cm^2. The projectile was chosen for analysis because relativistic ^{56}Fe nuclei are among the dominant HZE particles in GCR of radiobiological significance for manned spaceflight. The beam energy matched experimental data taken at the Lawrence Berkeley Laboratory. Pilot experiments to validate theoretical results for the production of the projectile fragments have been performed for ICI Fiberite T300/934 graphite/epoxy composites with 33.88 GeV ^{56}Fe and 8.5 GeV ^{20}Ne beams for thicknesses of 0.822, 10, and 18 g/cm^2, but data reduction is not yet complete.

Extended calculations were performed for an irradiation with 33.88 GeV ^{56}Fe ions of six shield concepts constructed with the polymeric materials listed in table I. Figures 3(a) and 3(b) show the fluence of ^{56}Fe and its fragments from the back face of the shield for two thicknesses, 5 and 18 g/cm^2. For projectile fragments below atomic number 12, there is negligible distinction among the polymers selected. For Mg and above (i.e., for $Z \geq 12$), polyethylene (PE), with its high hydrogen density, is the most effective absorber for the thick shield, but the least effective for the thin. Polytetrafluoroethylene (PTFE), which contains heavier fluorine atoms but no hydrogen, lies at the other extreme. PE is the most effective shield material among several polymers at a thickness greater than 18 g/cm^2 for a 33.88 GeV ^{56}Fe beam.

Table I. Empirical Formulas and Densities of Six Polymers Studied

Epoxy	$C_{37}H_{42}N_4O_6S$	1.32 g/cm^3
Polyetherimide	$C_{37}H_{42}N_4O_6S$	1.27 g/cm^3
Polyethylene	CH_2	0.92 g/cm^3
Polyimide	$C_{22}H_{10}N_2O_5$	1.42 g/cm^3
Polysulfone	$C_{27}H_{22}O_4S$	1.24 g/cm^3
Polytetrafluoroethylene	CF_2	2.17 g/cm^3

Because lunar soil is a potential construction material for a habitat for long-term lunar missions, its suitability as a shield from HZE particles was studied. A representative sampling of lunar regolith was reported [13] to have a density of 1.5 g/cm^3 and to contain almost exclusively only five elements: O (61.5 mol-%), Si (19.3), Al (7.5), Fe (6.1), and Mg (5.5). As shown in figures 4(a) and 4(b), the addition of an epoxy (as a possible binder for the regolith) enhances the regolith's shielding capabilities. The degree of shielding can be very sensitive to the thickness of the material. For example, calculations show that increasing the thickness from 16 g/cm^2 (figure 4a) to 18 g/ cm^2 (figure 4b) would yield significant improvements.

The effects of introducing boron into shielding materials were also studied as a way of capturing neutrons. The neutrons are produced inside a spacecraft owing to neutron formation in the nuclear fragmentation processes from the GCR impacting on exterior walls. (Generally, the density of neutrons in free space is negligible owing to their 11-min half-life.) These neutral species cannot dissipate their kinetic energy through Coulombic interactions, but must do so with elastic collisions with atomic nuclei. As noted above, hydrogen is the most effective nucleus for reducing the energy of neutrons to the thermal region. The boron isotope ^{10}B, which constitutes 19.6 percent of the naturally occurring element, has a large neutron-capture cross section for thermal neutrons. Some benefits achievable for neutron capture by boron-loaded polymers will be discussed in the experimental section below.

Calculations were carried out for several polymeric shields containing amorphous, submicron boron powder (having a density of 2.35 g/cm^3 for the naturally occurring distribution of boron isotopes) dispersed uniformly throughout the polymers. The inclusion of boron slightly enhances the material's capacity to produce secondary HZE particles, as shown in figure 5 for a polyetherimide. As the fraction of boron is increased from 5 to 20 wt %, both the density of the material and the initial range of incident particles increase because boron has a higher atomic number than hydrogen. It should be noted that most of the contribution to fragmentation comes from a broad range of charges above Z = 3 (for Li). The code LBLBEAM [3] for laboratory ion beams does not include light fragments of Z < 3 in any realistic way because a greater knowledge of nuclear fragmentation processes and a corresponding theory are required for these fragments.

Modeling of GCR Transport and Bioresponse for Shield Effectiveness

Interaction data for atomic ionization and nuclear reactions were combined in the Boltzmann equation with the 1977 solar minimum cosmic ray spectrum [11] to assess the transmitted environment through various shields for evaluation of biological effects. The shield effectiveness is intimately related to the nature of the nuclear cross sections through the change in the microscopic fluctuations in biological response. Shield effectiveness was examined in terms of two biological models. The first model is the conventional risk assessment method using the quality factor as a function of LET [14]. The second model is a track-structure repair kinetic model [15] for the mouse cell C3H10T1/2.

Conventional Risk Assessment Method

The dose equivalent H(x), which is obtained by multiplying the absorbed dose at each LET by a corresponding quality factor [14], is a measure of the response of living tissue. The quality factor was used to estimate the dose equivalent because all cells do not absorb energy equally from each LET component. Materials with atoms of low atomic number (e.g., PE) attenuate a very broad range of LET components [2], even though there is a gain in many low LET components. However, the effects from these low LET components are due primarily to indirect damage in cellular DNA brought about by OH radicals and are of lessor significance [16]. Materials with atoms of higher atomic number (e.g., PTFE) attenuate only the highest LET components [2] at the expense of producing a broad range of LET components for which biological response may be enhanced relative to free space exposures. These results occur for shielding depths of 2 to 10 g/cm^2 of aluminum which are typical for the space program [17]. The relative attenuation of the dose equivalent, H(x)/H(0), with depth is shown in figures 6(a) and 6(b). It was found that, among the materials studied, PE provides the most effective shielding at all thicknesses. PE is more effective than PTFE even for very thin films because of its greater efficiency in attenuating the heavier ions that are the most destructive to living tissue. The calculations show lunar regolith to be a less effective shield material for HZE particles than the hydrogen-containing polymers studied.

Track-Structure Repair Kinetic Model

The second model of the response of living cells to the effects of GCR is represented here in terms of occurrences of neoplastic cell transformations T(x) resulting from a one-year exposure behind a shield of thickness x relative to occurrences T(0) in free space. Unlike conventional dosimetric analysis wherein radiation quality is represented by LET-dependent quality factors, the repair kinetics model is driven by track-structure-dependent injury coefficients from experimental data with various ions in the mouse cell C3H10T1/2 [15]. The variation in the calculated cell transformation ratio T(x)/T(0), shown in figures 7(a) and 7(b), shows that the dependence on material is qualitatively similar to that found for H(x)/H(0), as shown in figures 6(a) and 6(b), although the cell transformation model predicts a noticeable increase in risk for thin shields (1–5 g/cm^2). However, there are important quantitative differences in the protective properties of shield materials dependent on the biological model used. Clearly, many shield materials provide only modest reductions in neoplastic transformation ratios (figures 7(a) and 7(b)), whereas they show a much greater reduction in dose equivalent (figures 6(a) and 6(b)) for the same shield thickness.

Recently, the effects of the nuclear reactions of light ions (proton, neutron, ^{2}H, ^{3}H, ^{3}He, and ^{4}He) and the track-structure of heavy ions were added into the calculation in order to reduce the combined effects of uncertainty in biological response and nuclear parameters for various shield materials [18]. Even though the absolute risk contribution of light ions is apparently increased from the modified calculation [19], the result in figure 8 shows that the upper range of maximum performance is increased substantially by using liquid hydrogen. Once again, the unique role of hydrogenous materials as high-performance shields is clearly shown.

EXPERIMENTAL STUDY

Humans are protected from GCR basically by the structural material of the spacecraft during a long-duration exposure. Improved protection will be provided by using appropriate shielding materials either as a structural component or as another component of the spacecraft. Radiation is known to initiate chain scission and crosslinking in polymeric materials, both of which affect their structural properties. Thus, a study of the effect of radiation on polymers is important in estimating the impact of the space environment on polymer-matrix composite structures.

Fast neutrons (1 to 10 MeV) are one of the important contributing factors to space radiation and to the hazardous radiation encountered by commercial high-speed aircraft which will fly at supersonic altitudes in the near future [20]. They travel greater distances through matter than do charged particles of the same energy because the primary mechanism of Coulomb interactions with the atomic electrons of the shielding material does not occur. Their interactions with matter are almost exclusively with atomic nuclei. These nuclear events release energies far in excess of chemical bond energies and can be accompanied by nuclear transformation. Another source of neutron exposure comes from neutron production by HZE ions. These high-energy secondary neutrons (E > 10 MeV) are possibly the dominant player in biological exposure, because a large amount of energy is deposited through nuclear reaction events with the more massive nuclei of the tissue system [20].

Shielding which combines hydrogen-containing polymeric materials with boron may be useful to shield humans from secondary neutron irradiation. For this reason, high performance polymers, which are known to have good stability toward radiation [21, 22, 23], were used. They are a polyimide, a polyetherimide, and a polysulfone. The repeat units of the polymers are shown in figure 9. An epoxy resin, ICI Fiberite 934, which is aerospace-qualified was selected. The repeat unit of the epoxy resin enclosed with the dashed line is shown in figure 10. Elemental boron in the form of an amorphous submicron powder was added to the polymers to make boron-containing polymer films 1–3 mils thick. This method could have utility to make films, coatings, or fibers. For the epoxy, the boron powder was mixed physically with uncured resin to mold relatively thick (1/4–1/2 inch) boron-epoxy castings. This could be suitable for molding pieces of various sizes and shapes. The properties of the boron-loaded advanced polymeric materials were characterized to study the effects from the neutron irradiation. Their performance, both as a neutron shielding material and as a load-bearing structural piece, is discussed below.

Material Processing and Preparation

All films were made in pure form and with up to 20% by weight of boron powder. Boron was mixed with each material prior to curing or solvent evaporation. Films of the polyimide (polypyromellitimide) were made by drawing the corresponding polyamic acid over a glass plate and heating to 300℃. The resulting material was extremely stable toward degradation from charged particle radiation [21]. The polyetherimide was dissolved in chloroform and the solution was drawn over a glass plate. The solvent was slowly evaporated producing a good film. The effects of energetic electrons on this material have been well studied [22]. Films of the polysulfone were

made in the same manner as those of the polyetherimide. The effects of ionizing radiation on this material have also been well documented [23].

A disk of 4-mil thick indium foil approximately 3 cm in diameter was wrapped with films of the polymeric materials, both pure and containing varying amounts of boron powder, and exposed to low-energy neutrons in a 5-Curie plutonium/beryllium source. A radioactive isotope of indium, [116]In, is formed in the neutron capture reaction on [115]In (95.7% of natural indium). The film-wrapped indium foil was irradiated for at least 18 hours, long enough to saturate the production of [116]In, which has a half-life of 54.1 minutes. After an irradiation, the indium foil was placed next to an end-window Geiger counter. The radioactive indium was counted for about two half-lives, and the initial activity (the activity when the foil was removed from the neutron source) was determined. The percent boron in each film was determined by inductively coupled plasma (ICP) measurements. The data were also corrected for variations in the thickness of the individual films, which were each about 1 mil thick. In order to have reasonable differences in the activity of the indium, about 4 mils of each film surrounded the foil in the irradiations.

The weight percents of atomic constituents of the fourth material selected, ICI Fiberite 934 epoxy, were 63.7% C, 6.28% H, 6.84% N, 16.93% O, and 6.25% S, as determined from elemental analysis. Four different boron-epoxy formulations were processed. An ICP detection method was used to analyze the boron-epoxy; the achieved weight percents of the boron concentrations were 3.95, 8.45, 12.89, and 17.43%. The added weight percents of the boron prior to curing were 5, 10, 15, and 20%, respectively, as used for the theoretical calculations.

The viscous-uncured 934 epoxy resin and the boron powder were combined and thoroughly mixed by hand at a temperature of 66–71℃. Then, a vacuum was applied to the mixture at a temperature of 71–77°C until the mixture was deaerated. The mixture was then carefully transferred to a tooled mold and cured according to the following cure profile. It was heated at the rate of 1–3°C/min to 121°C, held at 121°C for 1 hour, then heated at the same rate to 177°C, and finally held at 177°C for 2 hours. As shown in figure 11, the distribution of the boron was not uniform. The oval shape in the photograph is a cluster of boron powder.

The measured specific gravities (densities) of the boron/epoxy casts were 1.30, 1.33, 1.36, 1.39, and 1.42 g/cm^3, for the 0, 3.95, 8.45, 12.89, and 17.43% boron concentrations, respectively. This indicates that good consolidation had been achieved and that the materials were essentially void free.

CHARACTERIZATION

Preliminary Analysis for Neutron Shielding

Figure 12 shows the results for irradiations in which the indium foil was wrapped with a pure polysulfone film and one containing 14.8% boron powder. Figure 13 shows the initial activity of the indium foil as a function of the percent boron in the film surrounding it. From these results, it can be seen that the addition of boron powder to a material allows the material to absorb low-energy neutrons.

Measurements of the glass transition temperature (T_g) and Young's modulus were made on pure and boron-loaded films of each polymer to determine whether the addition of boron caused a degradation in the polymer properties. Preliminary results show no change in value within experimental uncertainty, indicating that no degradation occurs. Thus, the presence of boron up to 20% by mass does not change the high-performance properties of these polymers. Detailed tests were conducted on the boron/epoxy materials and their properties are summarized below.

Thermomechanical Analysis

Thermomechanical analysis was used to measure the coefficients of thermal expansion (CTE) of the materials. The CTE values are given in figure 14. The data indicate that the boron slightly lowered the CTE, as would be expected. The glass transition temperatures (T_g) determined from these curves are 183, 184, 183, 175, and 177°C for the five respective boron concentrations. These values are close to the 177°C final curing temperature. These data indicate that the boron-epoxy composites should retain good mechanical properties up to at least 175°C. This is in contrast to boron-polyethylene, which is one of the popular commercially available neutron shielding materials. Polyethylene, a thermoplastic, begins losing mechanical stability at temperatures at least 50°C lower than does the thermosetting epoxy resin.

Thermogravimetric Analysis

The TGA curves for the boron-epoxy materials are shown in figure 15. The resulting ash was not analyzed; however, it is postulated that it was probably mostly boron in nature.

Neutron Absorption

Indium foil, sandwiched between two 1/8-inch-thick boron-epoxy specimens, was exposed to the low-energy neutron source mentioned earlier. Neutrons that penetrated the shields reacted with the indium to form a beta-emitting isotope as described above. The fraction of neutrons absorbed by the boron-loaded epoxy relative to the neat epoxy is given in figure 16. It shows that for an epoxy containing 17.43% boron, almost 92% of the incident neutrons were absorbed, while the neat epoxy absorbed less than 1%.

Mechanical Properties

Compressive properties were measured in accordance with the American Society of Testing and Materials Standard (ASTM Standard D695) [24] for all the boron loadings. The compressive failure strength is shown in figure 17. The average strength increased from 25.7 ksi for the neat epoxy to 33.2 ksi for the 17.43% boron loading, which is an increase of almost 30%.

The compressive failure strain for the different boron loadings is shown in figure 18. The strain does not appear to have varied significantly. It is noted, however, from figures 17 and 18 that there is more scatter in the mechanical data at the higher boron concentrations.

The compressive modulus values are presented in figure 19. The average value of the modulus increased from 1.56 Msi for the neat epoxy to 2.63 Msi for the 17.43% boron loading, almost a 70% increase.

From these thermomechanical and mechanical results, it can be seen that the advanced neutron shielding materials under development may have structural, as well as shielding, applications. The popular neutron shielding materials (polyethylene with boron additives or water with boron additives) are effective only for controlling neutron flux; since they do not constitute part of the load-bearing structures, they add parasitic weight and volume.

CONCLUDING REMARKS

The interaction of the incident space radiation with structural materials is a recognized means of reducing the exposure risk from space radiation. A theoretical study was initiated to investigate the alteration of space radiations by shield materials in order to evaluate the risk reduction through materials selection. Experimental studies were conducted to validate the theoretical predictions and to test materials for the development of shielding materials against GCR and neutrons.

The effects of various hydrogen-bearing compounds as potential space structural components were examined by comparing the total ion fluences after passing through the shields. For energetic ion beams, a polyethylene target with its high hydrogen density is the most effective absorber of HZE particles for thick shields, while a polytetrafluoroethylene target with the heavier fluorine atoms appears to be more effective for thin shields, with respect to the production of secondary radiation.

Adding an epoxy to lunar regolith to bind it into a composite enhances its shielding properties from HZE particles. The inclusion of boron in a polymeric material only slightly diminishes the capacity of the material to absorb HZE particles. Lunar regolith is a less effective shield material for HZE particles than the hydrogen-containing polymers studied. Therefore, a material with a high percentage of lighter atoms, such as hydrogen, would be effective for thick shields. However, a material composed of heavier atoms might yet prove to be more effective in thin shields for energetic ion beams, with respect to the number of secondary particles (without considering their radiation quality). A pilot experiment to validate the prediction has begun and data reduction is underway.

Radiation biological risks depend on the microscopic fluctuations of energy absorption events in specific tissues [17]. The number of particles and the energy deposited behind most shield materials increase for thin shields due to a buildup of secondary radiation, which increases the hazard. Biological effects are reduced efficiently not only by selecting different materials, but also by adjusting the thickness of the material. Polyethylene is an efficient shield material at all thicknesses for GCR exposure, in spite of the large number of heavy projectile fragments produced. There are important quantitative differences in the predicted biological effects between the two different biological models. Uncertainties in the nuclear database exist for the calculation of the radiation field modified by different polymeric materials. The greatest uncertainty in biological response is expected from high LET components [25]. This uncertainty will be reduced by using lighter shielding materials, such as polymers. The unique role of

hydrogenous materials as high-performance shields is clear, even though an accurate evaluation of risk reduction is not possible because of the current uncertainty. The appropriate shield material optimization against GCR for human protection depends on the improved understanding of biological response, as well as the development of an adequate nuclear cross-section database.

Advanced polymeric materials with boron have been processed as a potential material for neutron shielding. Boron submicron powder loadings up to 17.43% were studied. The modification of the structural properties, which affects the basic protection to humans against GCR for long-duration exposure, was studied experimentally. The results show that the thermal expansion, glass transition temperature, and thermal stability of the boron-epoxy composites are not significantly affected by the addition of the boron; whereas, their compressive strength and modulus rise significantly. Furthermore, the highest boron loading (17.43%) absorbed approximately 92% of the incident neutrons in a laboratory experiment with naturally occurring boron. A much better result would be easily achieved if a high concentration of ^{10}B, which is available commercially at greater than 95% purity, were to be used.

Photomicrographs of a boron-loaded material showed clustering of the boron. The nonuniformity of the boron loading did not adversely affect the compressive properties. However, the same may not be true for other mechanical properties, such as tensile and flexure strengths. Thus, the development of methods for a more uniform distribution of the boron powder in the epoxy resin may be an important consideration for future work.

Future candidates for high-performance structural/shielding materials may be processed and cured in space via electrons (for composites) or UV (for films) for rapid curing at ambient temperature. The rapid curing, without extreme temperature, and the absence of oxidative degradation aid crosslinking in polymerizations in space. The crosslinked resins have enhanced structural properties. Multilayered materials systems, where the different layers vary in composition and thickness, may provide a solution for shielding against the multiplicity of particles present.

The NASA LaRC is a leading center for radiation physics and the development of fast computational radiation transport codes. The LaRC nuclear models are constantly being improved. With these improved codes and bioresponse models, the selected candidate high-performance structural/shielding materials and multilayered materials systems will be examined to develop, design, and demonstrate various radiation structural/shielding materials concepts. Theoretical calculations will also guide the use of local materials for Moon-based and Mars-based operations.

Laboratory research will be necessary to validate the theoretical predictions for high-performance structural/shielding materials, regolith/polymer blocks, and multilayered materials systems. Laboratory research is needed to determine the feasibility of processing regolith/polymer building blocks and developing new processing methods. The advantages of regolith/polymer blocks are that they would provide more durable structures with significantly less material, more versatility in design and utility of structures, and increased safety from radiation. They might also provide a cost-savings to the mission plan due to a reduced need for heavy regolith-moving equipment.

ACKNOWLEDGMENT

REFERENCES

1. G. R. Choppin, J. Rydberg; *Nuclear Chemistry - Theory and Application*; Pergamon Press Inc.: New York, 1990: p 78.

2. M. Y. Kim, J. W. Wilson, S. A. Thibeault, J. E. Nealy, F. F. Badavi, R. L. Kiefer; *Performance Study of Galactic Cosmic Ray Shield Materials*; NASA TP-3473; 1994.

3. J. W. Wilson, L. W. Townsend, W. Schimmerling, G. S. Khandelwal, F. Kahn, J. E. Nealy, F. A. Cucinotta, L. C. Simonsen, J. L. Shinn, J. W. Norbury; *Transport Methods and Interactions for Space Radiations*; NASA RP-1257; Washington, DC, 1994.

4. W. B. Kraus, M. B. Glasgow, M. Y. Kim, D. L. Olmeijer, R. L. Kiefer, R. A. Orwoll, S. A. Thibeault; *Polym. Prep.*, **34(1)**: 592–593; 1993.

5. M. Y. Kim, S. A. Thibeault, J. W. Wilson, R. L. Kiefer, R. A. Orwoll; *Polymer. Prep.*, **35(2)**: 961–962; 1994.

6. M. Y. Kim, S. A. Thibeault, J. W. Wilson, R. L. Kiefer, R. A. Orwoll; In Performance of Polymeric Materials as Shielding for Cosmic Radiation; R. L. Clough and S. W. Shalaby Ed.; *Irradiation of Polymers*, ACS Symposium Series 620: Washington DC, 1996; 350–362

7. I. R. McAulay; Round Table Discussion. *Radia. Prot. Dosim*., **48(1)**:: 135–136; 1993.

8. J. M. Stephens, M. B. Glasgow, R. L. Kiefer, R. A. Orwoll; *Polym. Prep.*, **33(1)**: 1152–1153; 1992.

9. S. A. Thibeault, E. R. Long, Jr., M. B. Glasgow, R. A. Orwoll, R. L. Kiefer; *Polym. Prep.*, **35(2)**: 954–955; 1994.

10. J. H. Adams Jr., R. Silberberg, C. H. Tsao; NRL Memo. Rep. 4506-Pt. I, U.S. Navy; 1981.

11. G. D. Badhwar, F. A. Cucinotta, P. M. O'Neill; *Radia. Res*., **134**: 9–15; 1993.

12. J. L. Shinn, J. E. Nealy, L. W. Townsend, J. W. Wilson, J. S. Wood; *Adv. Sp. Res.*, **14(10)**: 863–871; 1994.

13. *Conceptual Design of a Lunar Colony*; Dalton, C.; Hohmann, E., Eds.; NASA CR-129164; 1972.

14. International Commission on Radiological Protection, *1990 Recommendations of the International Commission on Radiological Protection*; ICRP Publ. 60; Pergamon Press Inc.: New York, 1991; p. 81.

15. J. W. Wilson, F. A. Cucinotta, J. L. Shinn; In Cell Kinetics and Track Structure; Swenberg, C. E.; Horneck, G.; Stassinopoulos, E. G. Ed.; *Biological Effects and Physics of Solar and Galactic Cosmic Radiation*, Part B; Plenum Press: New York, 1993; pp. 295–338.

16. D. Billen; *Radia. Res*., **124** : 242–245; 1990.

17. J. W. Wilson, M. Y. Kim, W. Schimmerling, F. F. Badavi, S. A. Thibeault, F. A. Cucinotta, J. L. Shinn, R. L. Kiefer; *Health Phys.*, **68(1)**: 50–58; 1995.

18. F. A. Cucinotta, L. W. Townsend, J. W. Wilson, J. L. Shinn, G. D. Badhwar, R. R. Dubey: Light Ion Components of the Galactic Cosmic Rays: Nuclear Interactions and Transport Theory. Adv. Sp. Res. **17(2)**: 77–86; 1996.

19. M. Y. Kim, F. A. Cucinotta, J. W. Wilson, S. A. Thibeault, R. L. Kiefer; The Effects of Track Structure and Light Ion Components of GCR on Biological Systems behind Spacecraft Shielding, RADSCON'96 Symposium pp. 66–73, 1996.

20. J. W. Wilson, J. E. Nealy, F. A. Cucinotta, J. L. Shinn, F. Hajnal, M. Reginatto, P. Goldhagen; *Radiation Safety Aspects of Commercial High-Speed Flight Transportation*; NASA TP-3524; Washington, DC, 1995

21. D. R. Coulter, A. Gupta, M. V. Smith, R. E. Fornes; *The Effects of Energetic Proton Bombardment on Polymeric Materials: Experimental Studies and Degradation Models*, NASA JPL Publication 85–101, 1986.

22. S. A. T. Long, E. R. Long, Jr.; Effects of Intermediate-Energy Electrons on Mechanical and Molecular Properties of a Polyetherimide, *IEEE Trans. Nucl. Sci.*, **NS-31**: 1293; 1984.

23. J. R. Brown, J. H. O'Donnell; Effects of Gamma Radiation on Two Aromatic Polysulfones, *J. Appl. Poly. Sci.*, **19**: 405; 1975.

24. American Society of Testing and Materials: *ASTM Standard D695* (1989).

25. W. Schimmerling, J. W. Wilson, J. E. Nealy, S. A. Thibeault, F. A. Cucinotta, J. L. Shinn, M. Kim, R. Kiefer; *Adv. Space Res.*, **17(2)**: (2)31–(2)36; 1996.
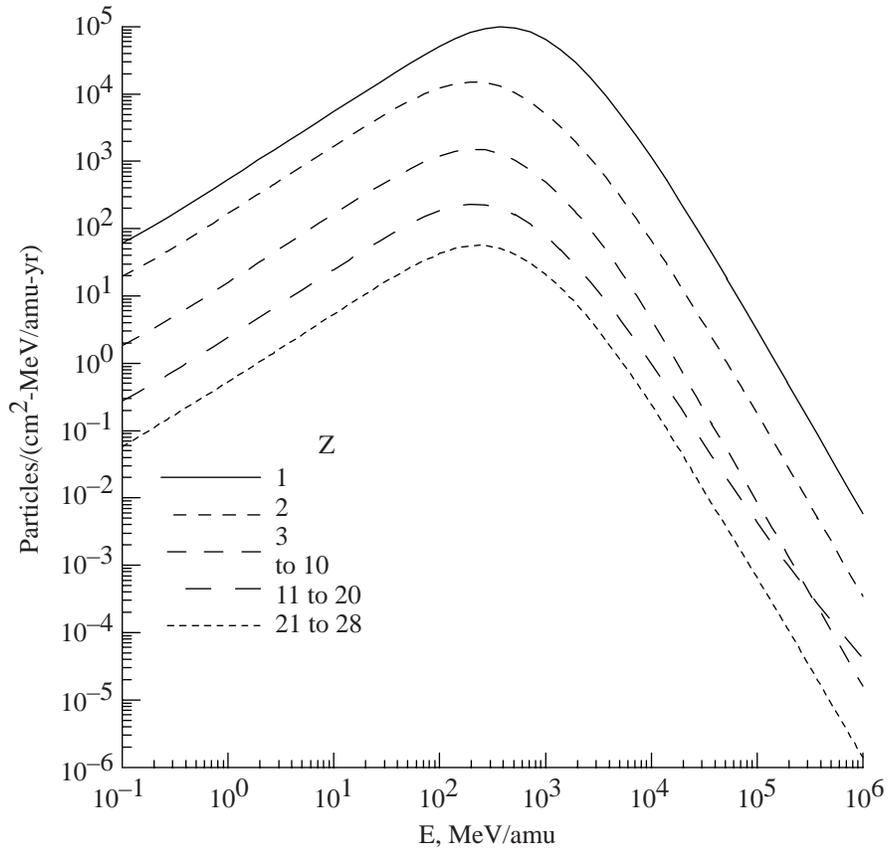
Figure 1.   Energy spectra of primary GCR ions at the 1977 solar minimum.
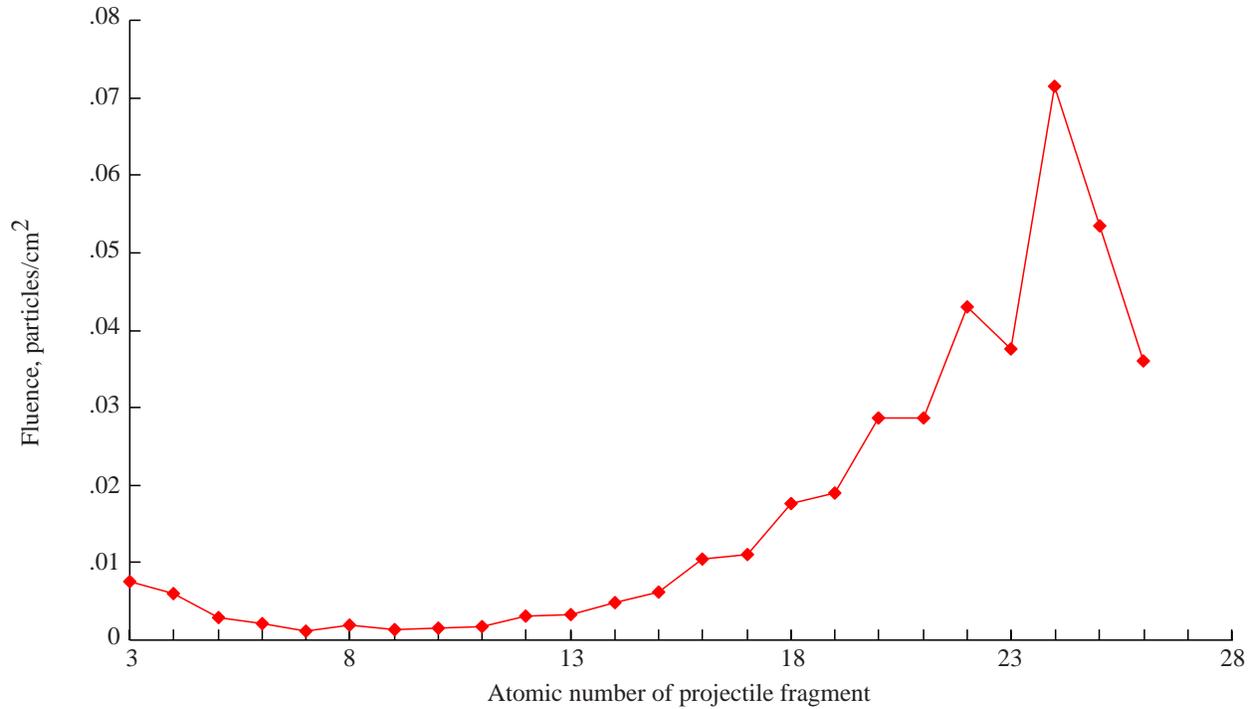
(a) 10 g/cm^2 thick.
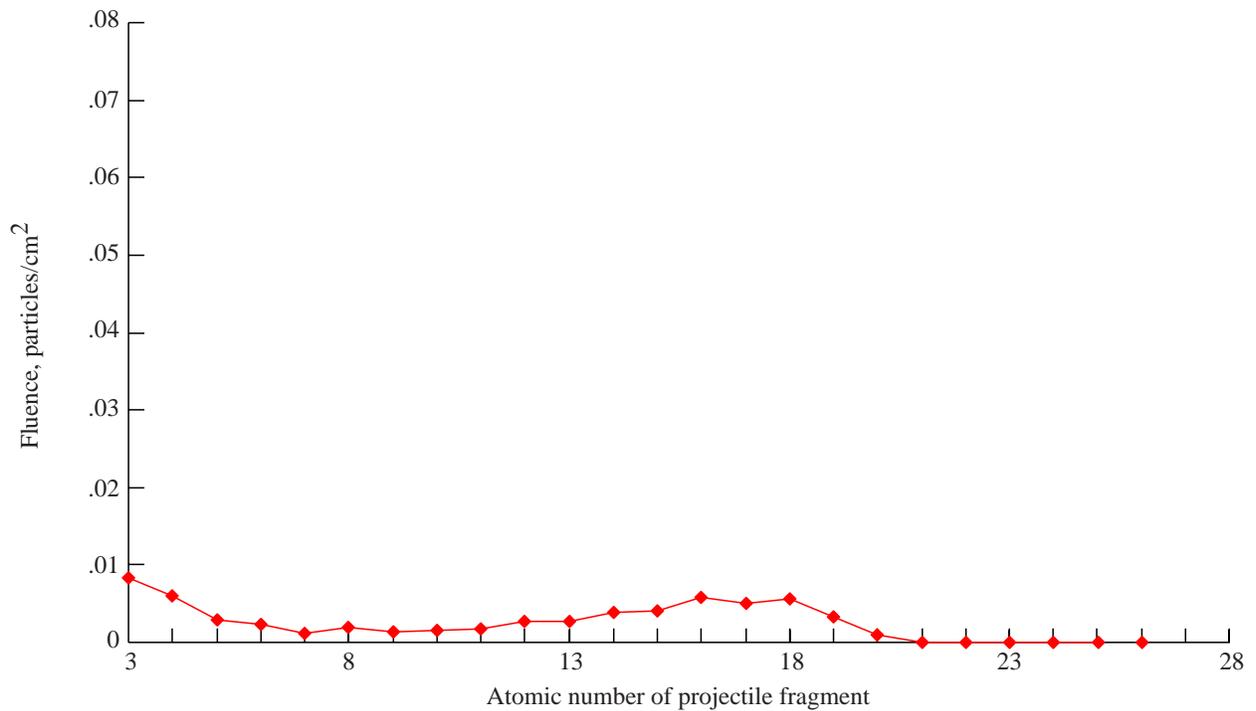
(b) 18 g/cm^2 thick.

Figure 2.   Predicted fluence of projectile fragments behind graphite/epoxy composite irradiated with 33.88 GeV ^{56}Fe beam.
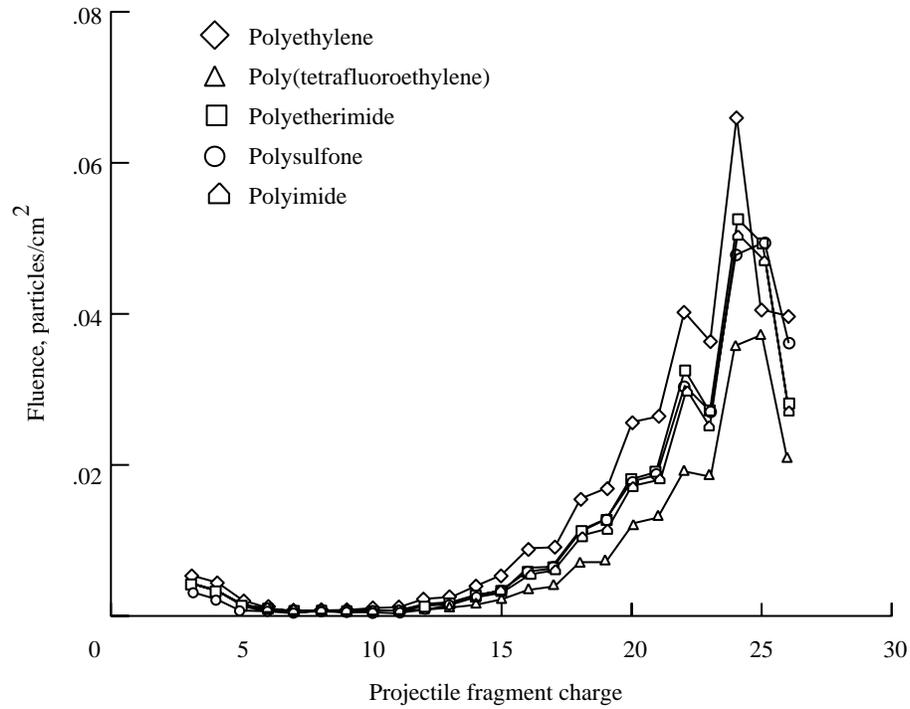
(a) 5 g/cm^2 thick.
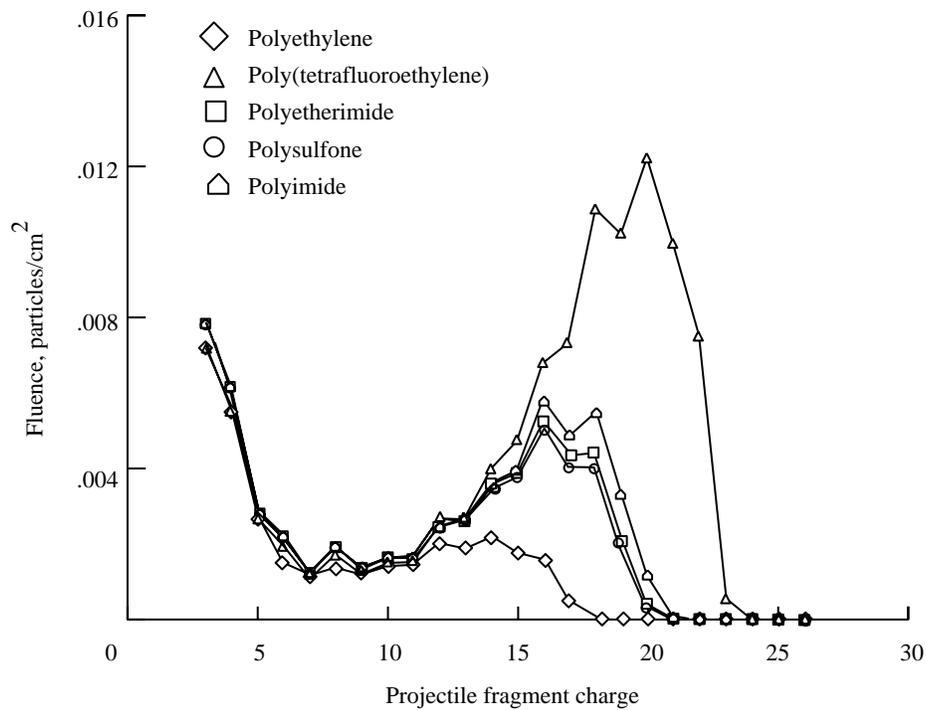
(b) 18 g/cm^2 thick

Figure 3.   Predicted fluence of projectile fragments behind polymeric shields irradiated with 33.88 GeV ^{56}Fe beam.
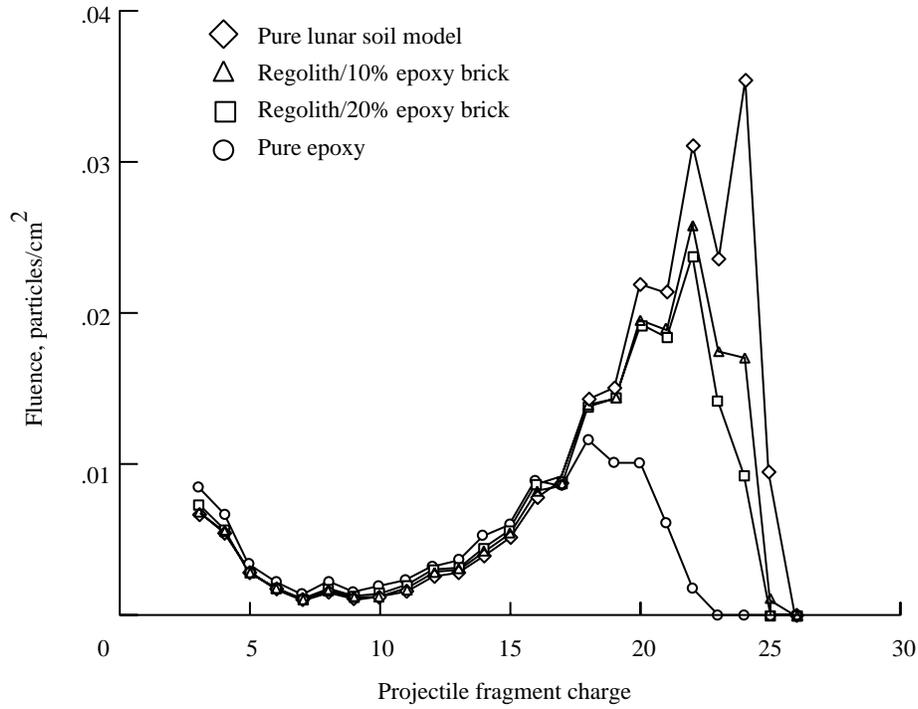
(a) 16 g/cm^2 thick.
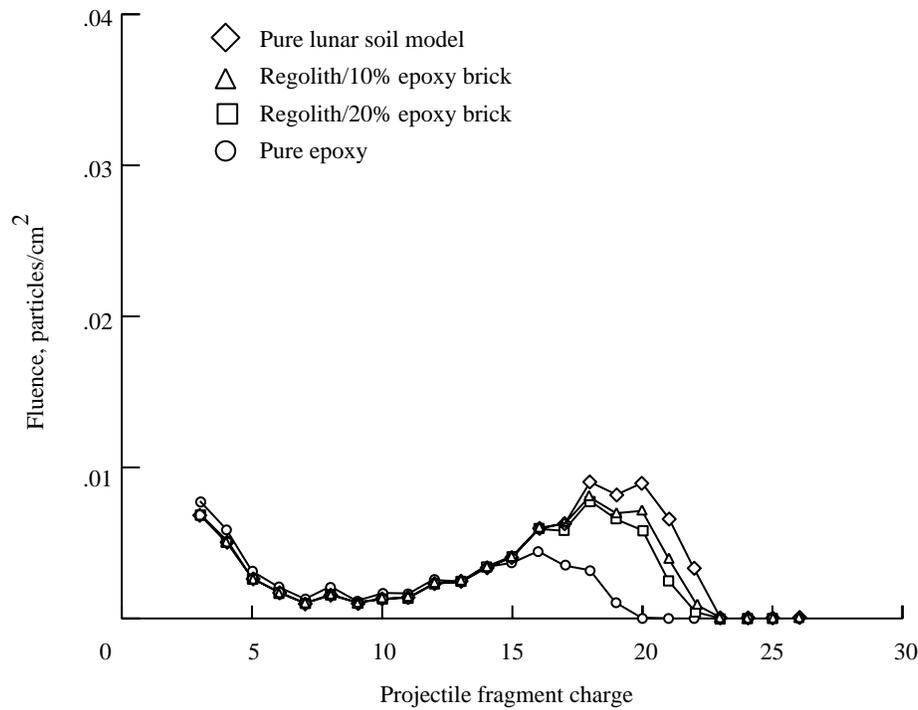
(b) 18 g/cm^2 thick

Figure 4.   Predicted fluence of projectile fragments behind lunar construction materials irradiated with 33.88 GeV ^{56}Fe beam.
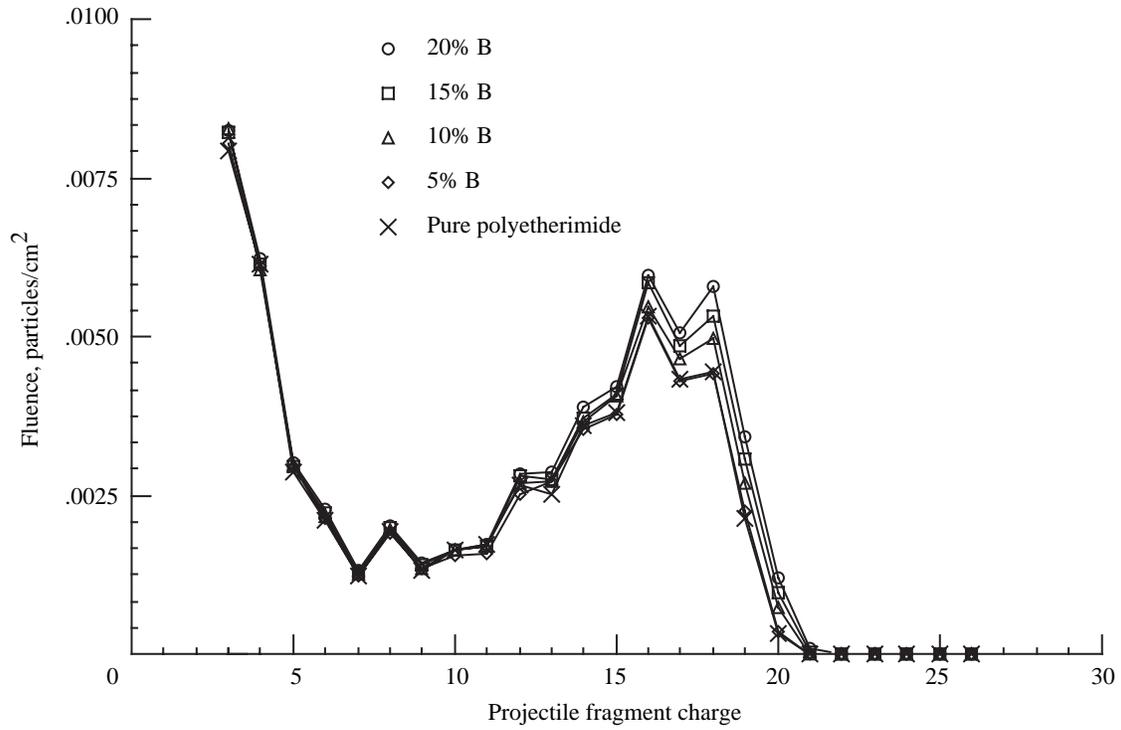
Figure 5.　Predicted fluence of projectile fragments behind 18-g/cm^2-thick polyetherimide shields containing differing weight fractions of elemental boron irradiated with 33.88 GeV ^{56}Fe beam.
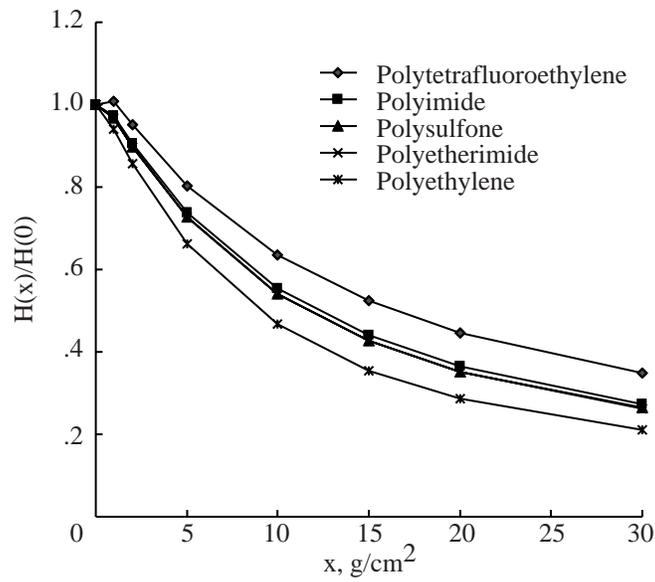
(a) Polymeric shields.
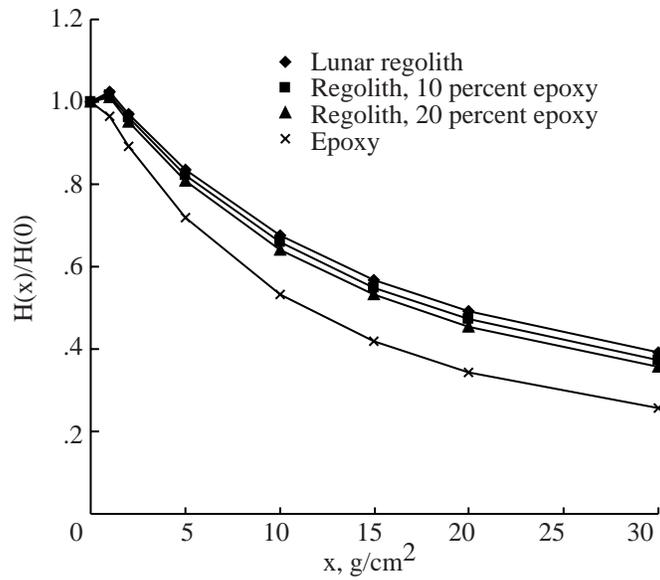
(b) Lunar construction materials

Figure 6.   Attenuation of dose equivalent behind several shield materials as a function of shield thickness.
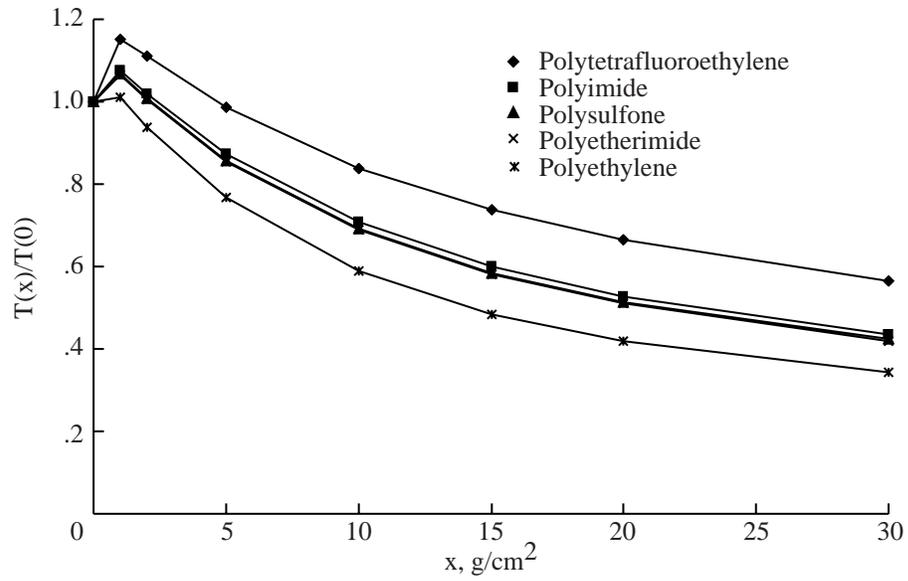
(a) Polymeric shields.
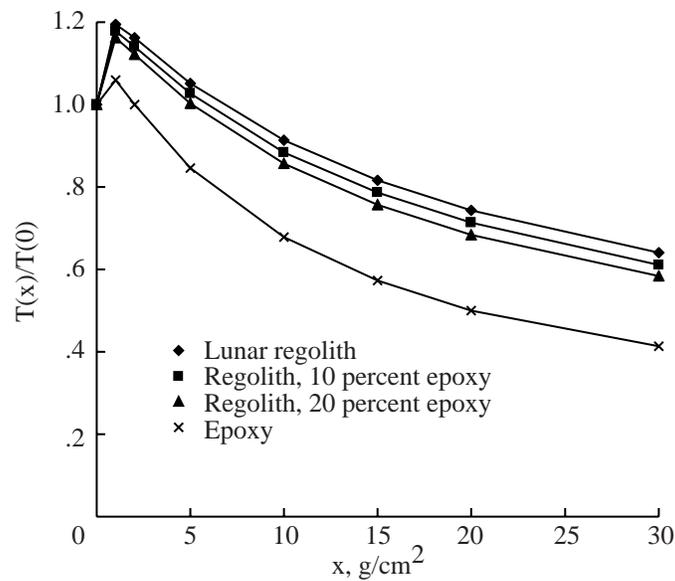
(b) Lunar construction materials.

Figure 7.   Attenuation of cell transformation behind several shield materials as a function of shield thickness.
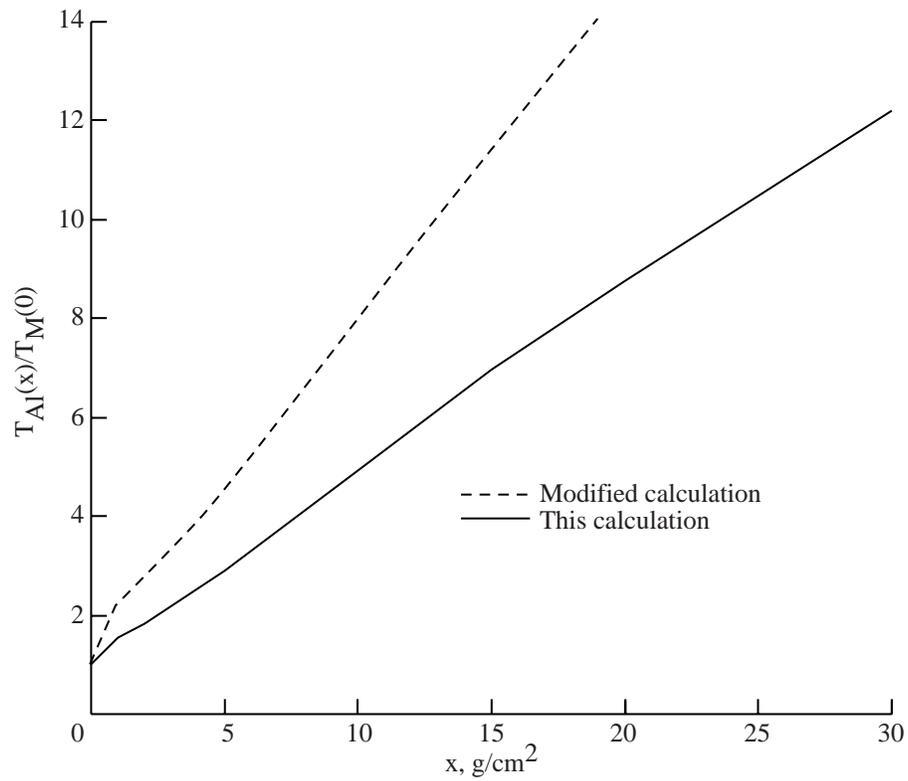
Figure 8.   Cell transformation ratio behind liquid hydrogen as a function of areal density relative to aluminum standard; solid line using HZETRN, dashed line including the effects of track-structure and light-ion knock-out.

(a) Polyetherimide

(b) Polysulfone   (c) Polyimide
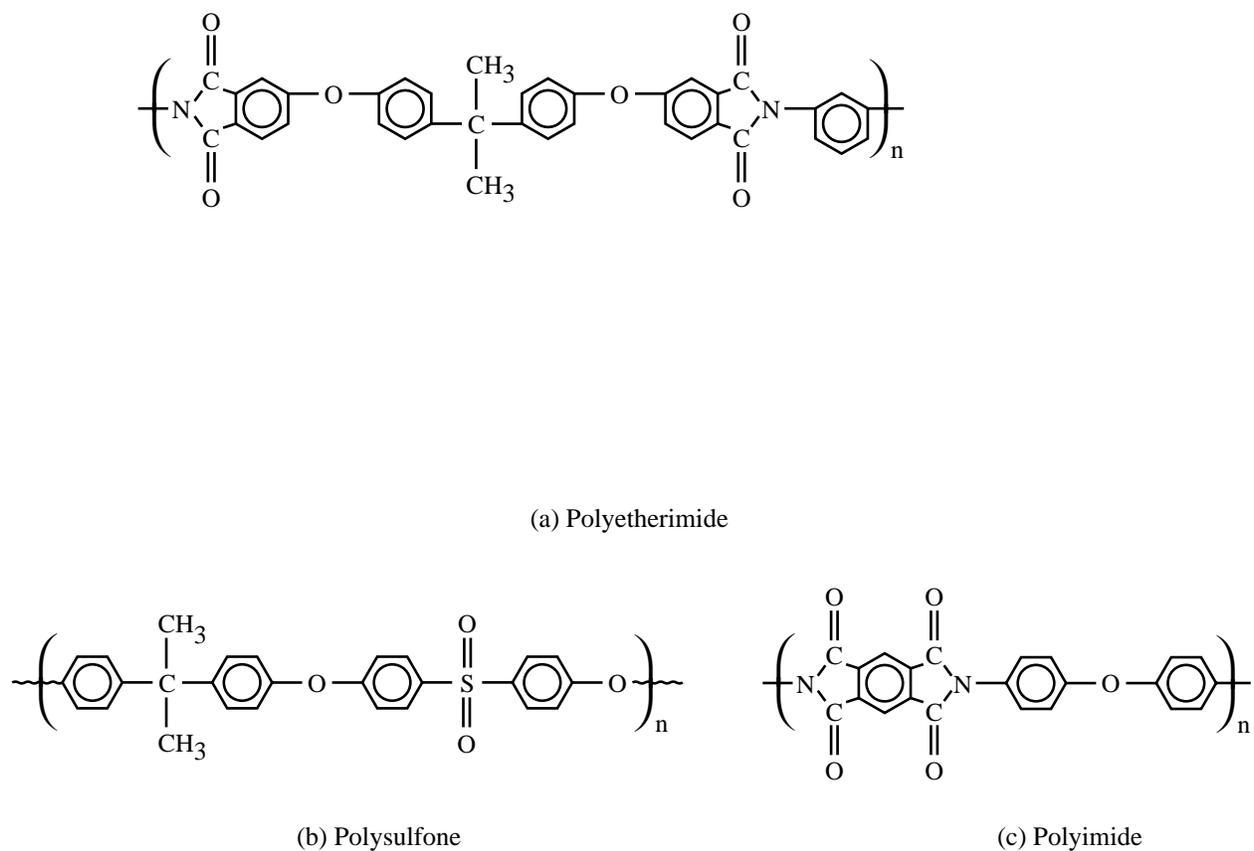
Figure 9.   Repeat units of three polymers studied.
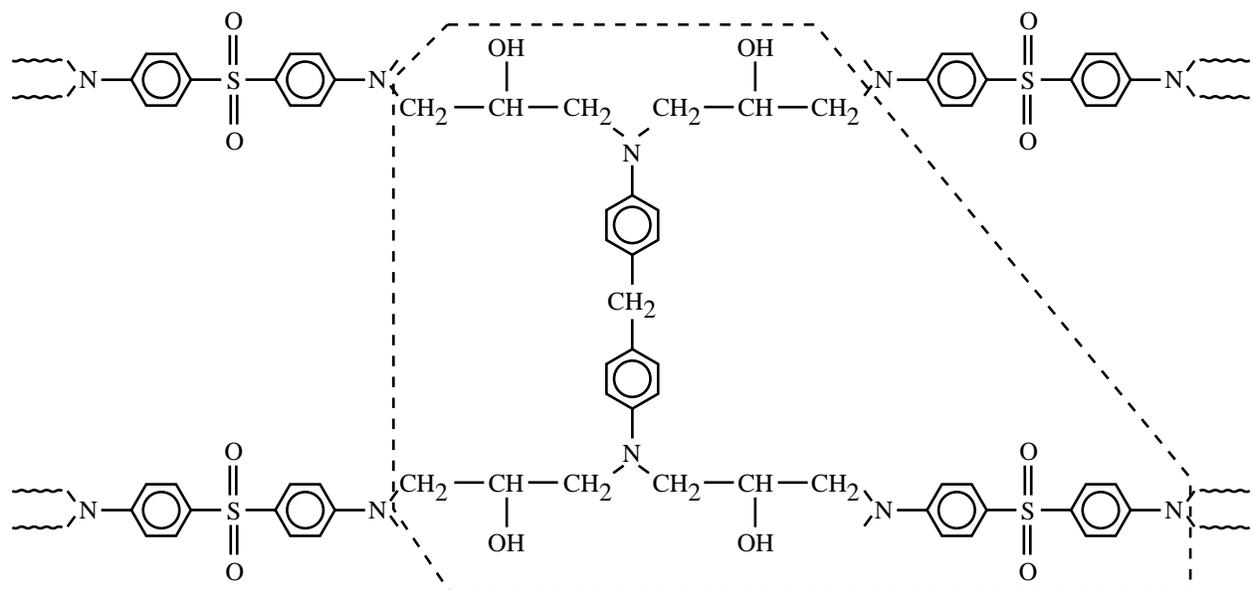
Figure 10.   Tetraglycidyl 4,4' diamino diphenyl methane epoxy cured with diamino diphenyl sulfone.
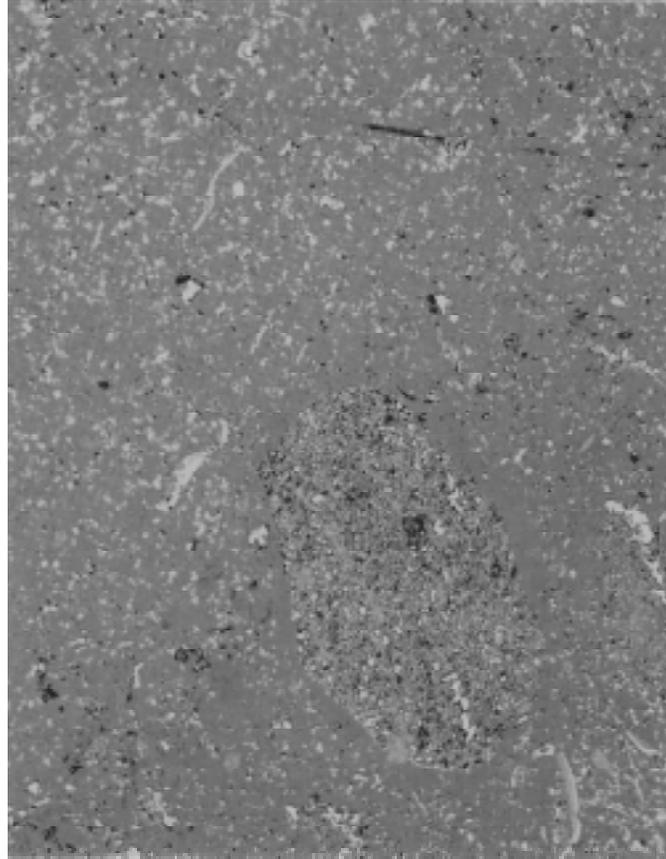
Figure 11. Photomicrograph of the epoxy with 17.43% by weight boron.
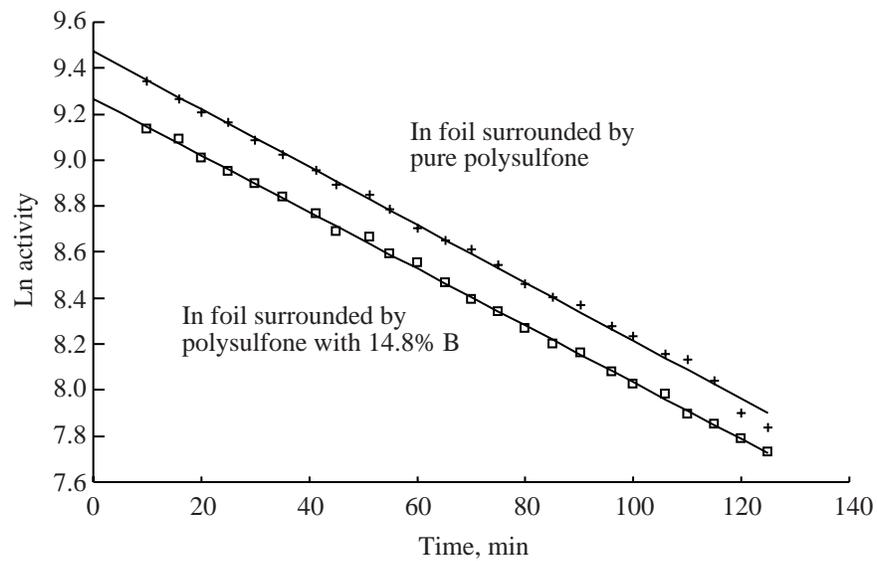
Figure 12. The activity of the indium foil after neutron irradiation.
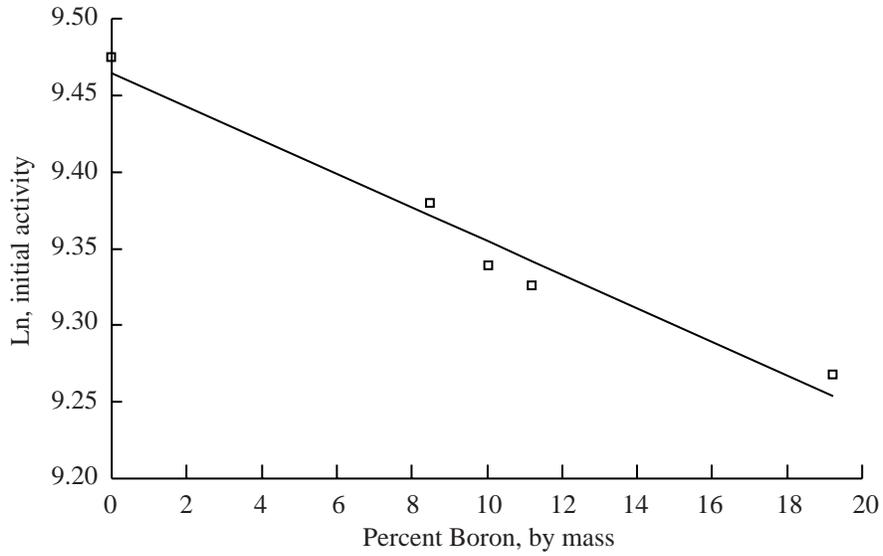
Figure 13.   The initial activity of the indium foil as a function of percent boron.
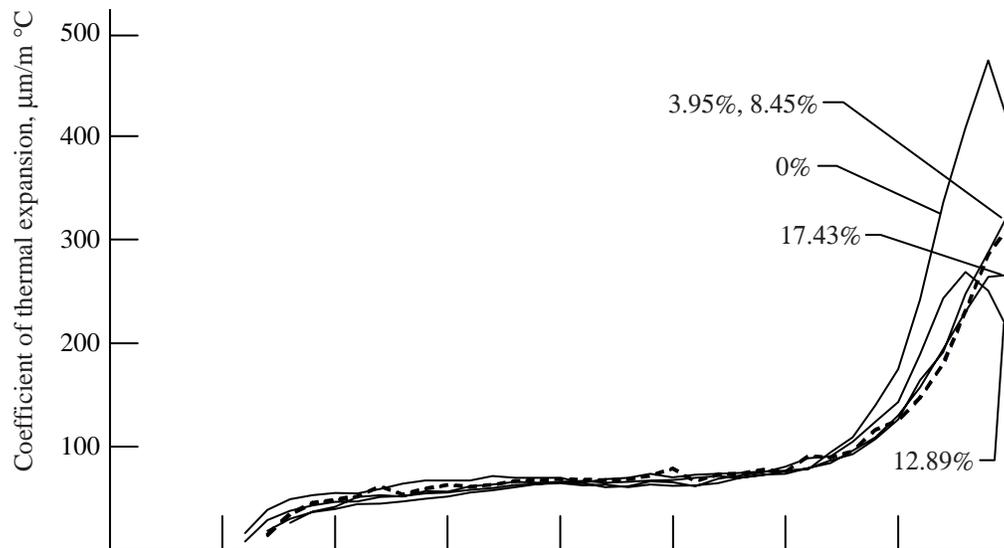
Figure 14.   Coefficient of thermal expansion versus temperature for the boron-epoxy.
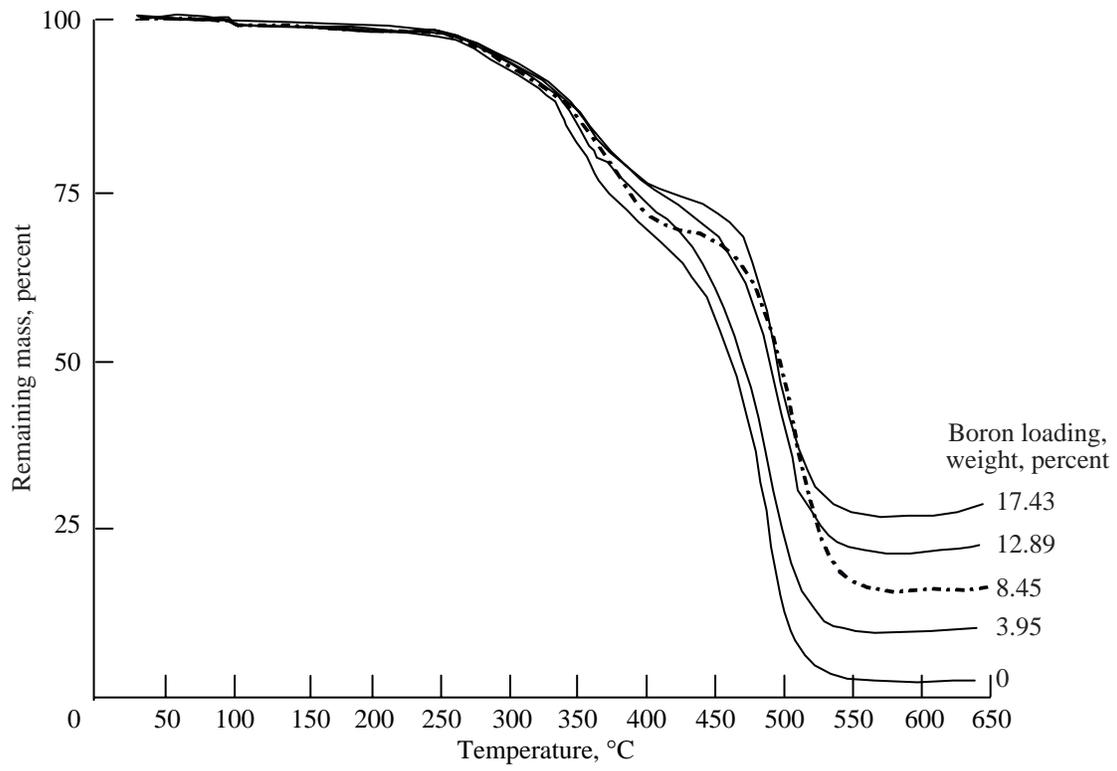
Figure 15. Thermogravimetric curves for the boron-epoxy.
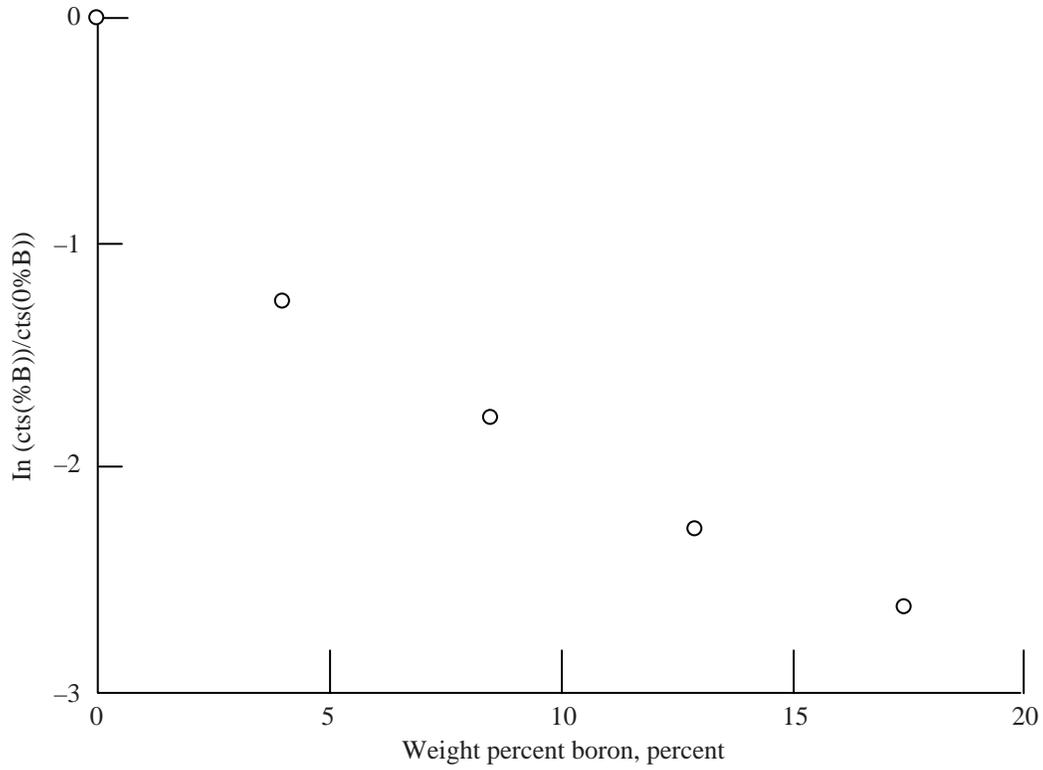
Figure 16.   Neutron absorption of the boron-epoxy.
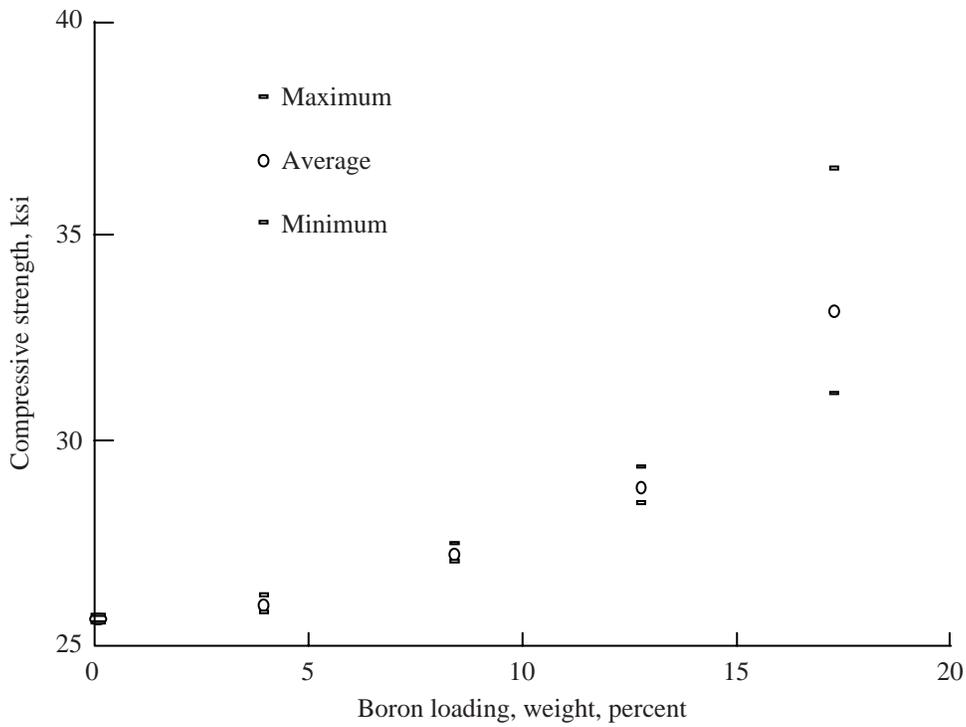
Figure 17. Compressive failure strength of the boron-epoxy.
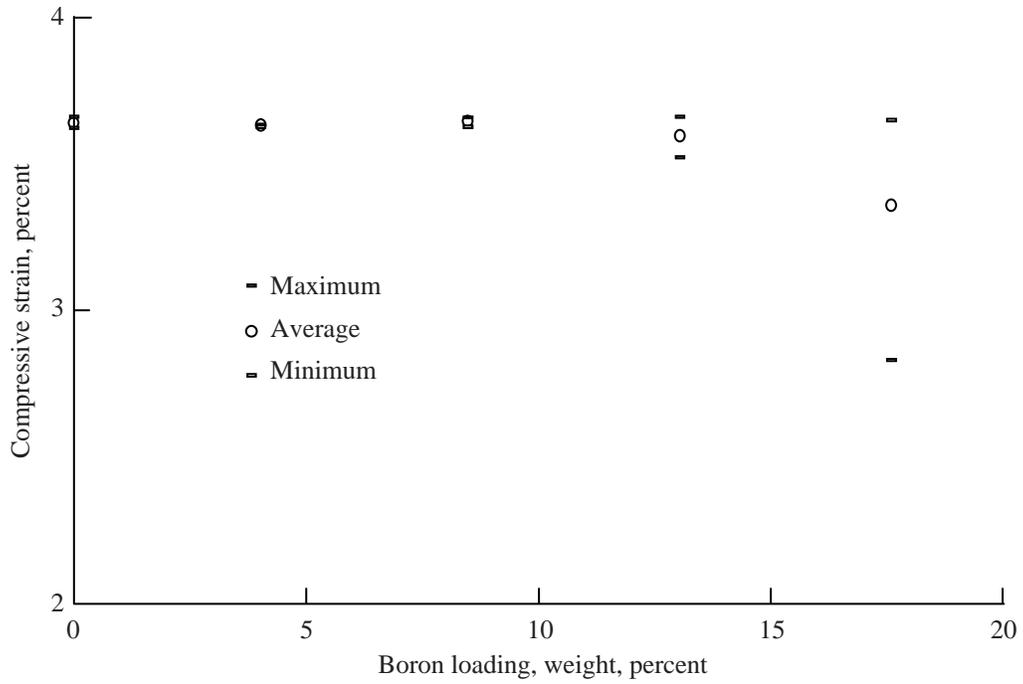
Figure 18. Compressive failure strain of the boron-epoxy.
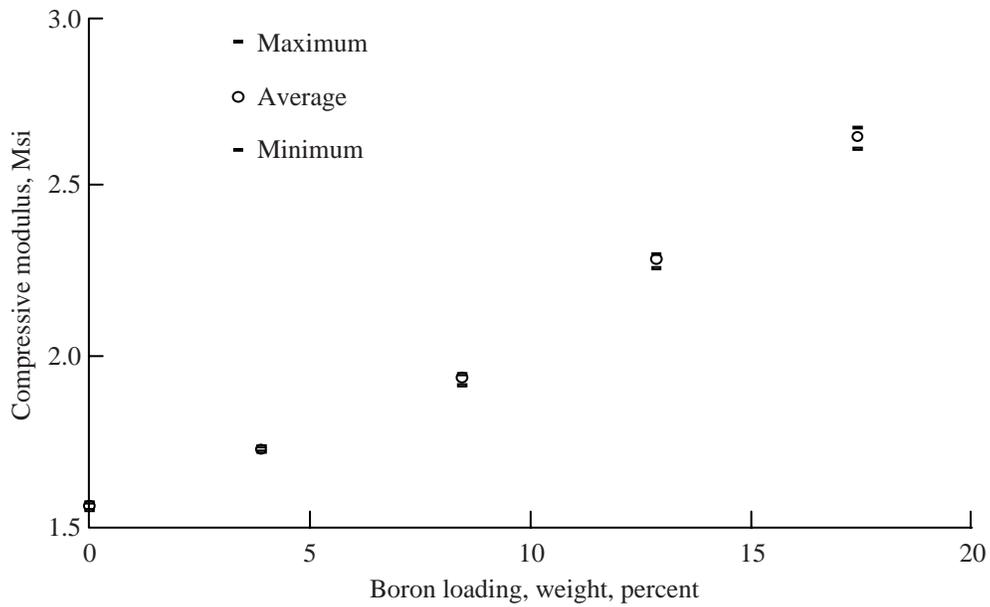
Figure 19. Compressive modulus of the boron-epoxy.

CHAPTER 20

LABORATORY VALIDATION OF MATERIAL SHIELDING PROPERTIES

by

J. Miller[1]

[1]Lawrence Berkeley Laboratory, Berkeley, CA 94720

Chapter 20

LABORATORY VALIDATION OF MATERIAL SHIELDING PROPERTIES

INTRODUCTION

It will obviously be impractical to verify the shielding properties of every candidate material and configuration in space. For this reason, shielding designers will rely heavily upon models of radiation transport. As discussed earlier [1], measurements at particle accelerators are an important part of the model design and validation process. Accelerator experiments generate high statistics data in a controlled setting with well-defined beams. While they cannot simulate the complex radiation fields found in space, they can be used to test model performance for selected critical parameter sets, for example, for particular incident particle charges, masses, and energies and target compositions and thicknesses. Similarly, they can be used at various stages of the shielding design process to test the response of particular candidate materials to a representative subset of space radiation components.

In ref. [1] I briefly surveyed some accelerator experimental methods and facilities relevant to space radiation research. Here I will discuss some examples in which accelerator experiments have been used to validate model predictions or to test shielding materials.

TISSUE EQUIVALENT MATERIALS

These are of interest for at least two reasons (not including the obvious implications for radiobiological experiments): as shielding materials in their own right, and for investigating the self-shielding properties of the human body. Water and polyethylene have been used as targets in a number of different measurements, of which I will discuss two: 636 MeV/nucleon ^{20}Ne+H_2O and 510 MeV/nucleon ^{56}Fe+CH_2.

Ne+H_2O

Data were taken at the Bevalac for fragments produced by a 636-MeV/nucleon ^{20}Ne beam in a variable thickness water target. Fragment charges between 4 and 10 (including ^{18}Ne and ^{19}Ne) were measured [2] and
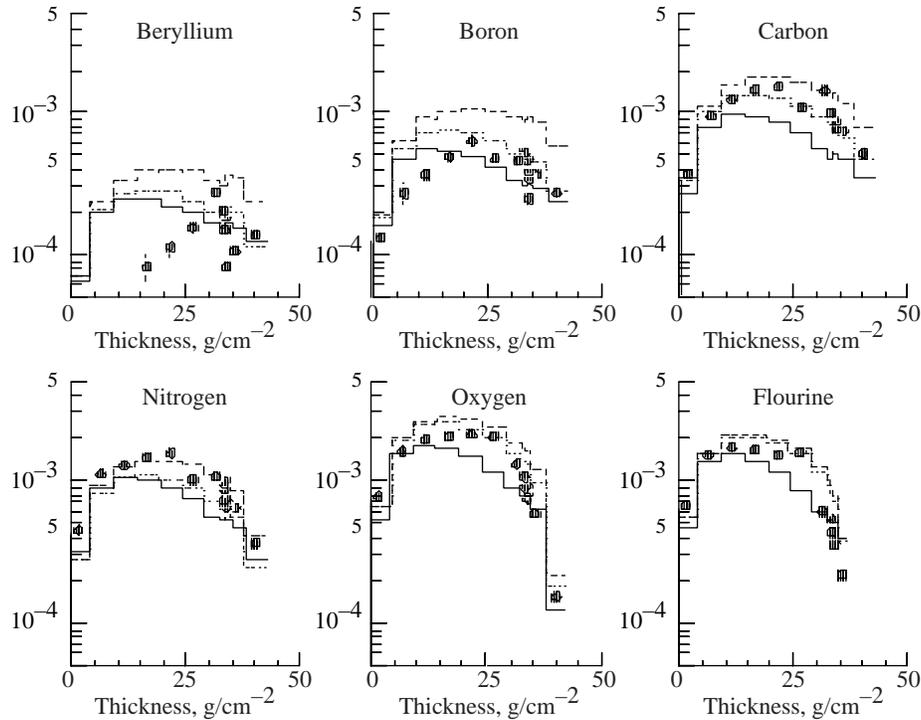
Figure 1.   Integral fluence for fragments produced by 636 MeV/nucleon neon incident on water of varying thicknesses (in g/cm^2).   The filled circles are data;   the dotted line is a model prediction of first generation fragments only;   the solid line is a model prediction including both first and second generation fragments. (From ref. [4].)

compared to single generation [3] and multi-generation [4] fragmentation models. Figure 1 shows the integral fluence spectra for $Z = 4 - 9$, compared to an analytic transport model calculation [5] with first and second generation fragments included. Data and model agree within about 30%, except for $Z = 4$ and 5, where the data were limited by detector threshold effects [2]. While this level of agreement was not good enough to distinguish the effect of higher order fragments, comparisons in this study between the data and the model were useful in a number of respects. For example, the model's overprediction of the integral fluence of heavy fragments ($Z = 8, 9$) and underprediction for $Z = 6$ is consistent with a prediction [6] of the consequences of using energy-dependent fragmentation cross sections. (See ref. [4] for additional details.)

Fe+CH$_2$

Also at the Bevalac, the fragmentation of iron in polyethylene was measured [7] and compared [8] to a Monte Carlo model which uses the NUCFRG2 nuclear fragmentation model [9]. Figure 2 is a comparison of the data to the Monte Carlo. The agreement between data and model is good, but the model's underprediction of the heavy fragment yield indicated that it could be improved, particularly in its treatment of nuclear structure effects. Also, in
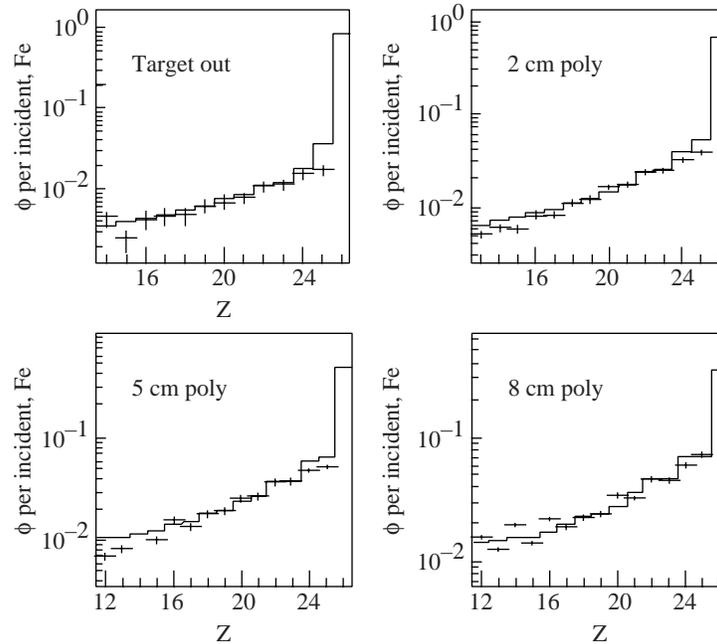
Figure 2.   Comparison of measured fragment production by 510 MeV/nucleon ^{56}Fe in CH$_2$ with a model calculation (solid line histogram), as described in the text and in ref. [8].

this case the uncertainties in both data and model were small enough that the effects of higher order fragmentation could be studied.   It was found that at least two generations of fragments must be included for the model to accurately reproduce the data [8].

FRAGMENTATION IN SHIELDING

Recently, 1.06 GeV/nucleon beams from the Brookhaven National Laboratory AGS accelerator were used to study fragmentation in several different types and thicknesses of prospective shielding materials. Figure 3 shows some preliminary results.

The primary iron beam produces the large peak at the right in each spectrum, and discrete energy loss peaks for charges from the primary ($Z = 26$) down to at least $Z = 4$ can be identified by eye. Analytical identification methods using the information from additional detectors have extended the range to $Z = 2$ and in some cases 1. The data can be readily converted into separate energy spectra for each fragment. This simple example shows the similarity in the fragmentation properties of 2.54 cm aluminum and 5 cm graphite-epoxy, and the effects of doubling the thickness of graphite-epoxy from 5 to 10 cm: note the slightly increased energy loss at 10 cm (due to the slowing of the beam) and the increased fragmentation–evidenced by the increased height of the fragment peaks relative to the primary iron.

As shown earlier [1], with the present system [10] the approximate time required to measure a single data point (projectile charge-projectile energy-target angle) is approximately 1 hour, although this does not include the time for setting up detectors and for changing beam ions and/or energies.
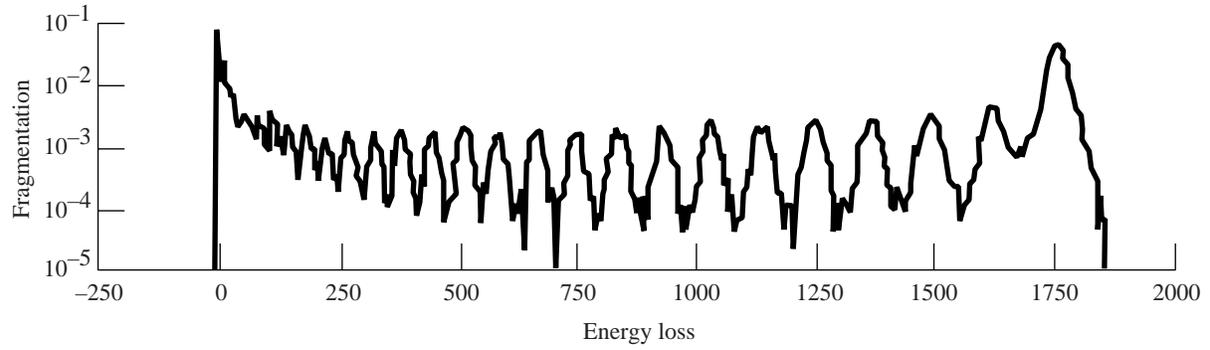
a) 10 cm graphite-epoxy
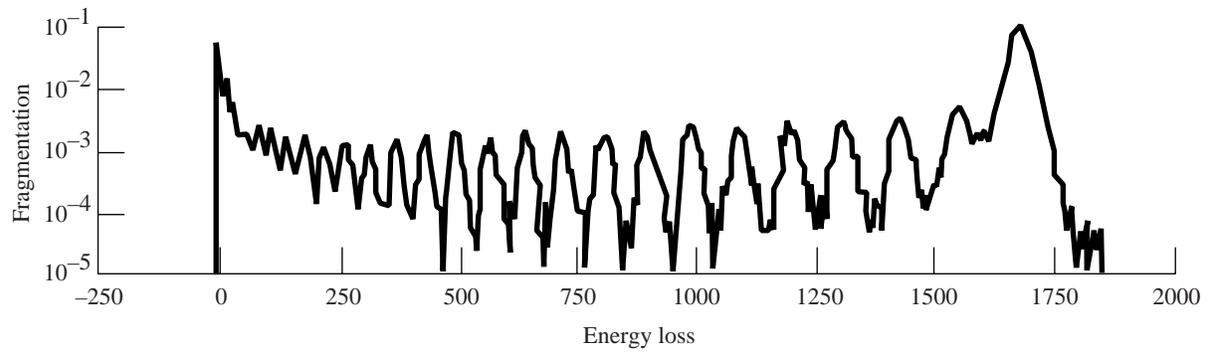
b) 5 cm graphite-epoxy
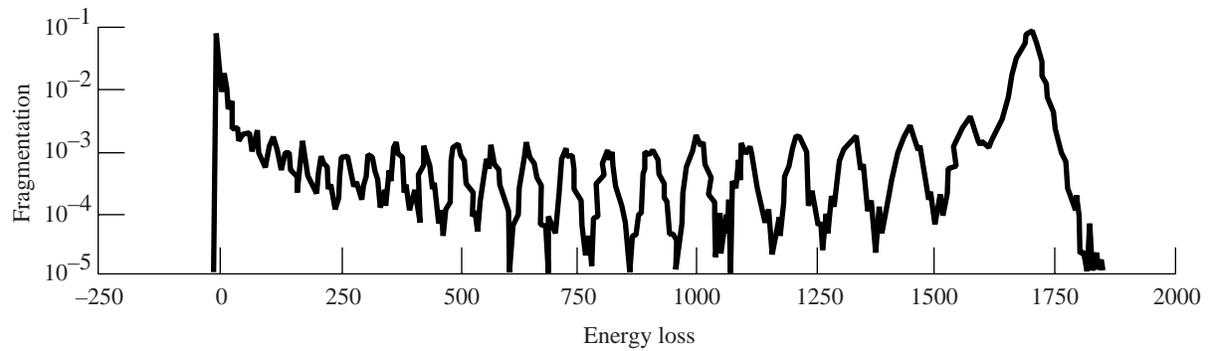
c) 2.54 cm aluminum

Figure 3.   Energy loss spectra from 1.08 GeV/nucleon ^{56}Fe fragmenting in three different shielding materials. The ordinate is number of counts (unnormalized). The abscissa is the summed energy loss (in MeV) in two 3 mm silicon detectors. (Preliminary).

CONCLUSIONS

Accelerator measurements provide accurate and precise data on the fragments produced by a particular heavy ion beam incident on shielding material of a specific composition and thickness. They are not an efficient means of replicating the complete space radiation environment, and it is therefore necessary to have accurate and precise (to the desired degree) heavy ion transport models. Accelerator measurements are used to validate the models and to directly evaluate the radiation transport properties of selected candidate shielding materials.

REFERENCES

1   J. Miller, "Database Development and Laboratory Validation", proceedings of this meeting.

2.   W. Schimmerling et al., Radiat. Res. **120**, 36 (1989).

3.   M. R. Shavers et al., Radiat. Res. **124**, 117 (1990).

4.   M. R. Shavers et al., Radiat. Res. **136**, 1 (1993).

5.   J. W. Wilson et al., Radiat. Res. **122**, 223 (1990).

6.   L. W. Townsend and J. W. Wilson, Health Phys. **54**, 409 (1988).

7.   C. Zeitlin et al., Radiat. Res. **145**, 655 (1996).

8.   C. Zeitlin et al., Radiat. Res. **145**, 666 (1996).

9.   J. W. Wilson et al., Nucl. Instr. Meth. B **94**, 95 (1994).

10. C. Zeitlin et al., Phys. Rev. C **56**, 388 (1997).

CHAPTER 21

SPACEFLIGHT VALIDATION OF MATERIAL SHIELDING PROPERTIES

by

Gautam D. Badhwar[1]

_____
[1]NASA Johnson Space Center, Houston, Texas 77058-3696

Chapter 21

SPACEFLIGHT VALIDATION OF MATERIAL SHIELDING PROPERTIES

Abstract

A comparison of measured absorbed dose, dose equivalent, and linear energy transfer spectra of galactic cosmic radiation (GCR) measured with a tissue equivalent proportional counter (TEPC) in the Space Shuttle and Mir orbital station has been made with model calculations using the 1995 version of the radiation transport code, HZETRN. The TEPC was flown under a variety of shielding geometries varying from the payload bay to a middeck locker in the Shuttle. Data from fifteen flights show that the combined root mean square errors from both the GCR environment model and HZETRN for absorbed dose and dose equivalent rates are 16.8% and 18.5%, respectively. There is a systematic under estimation of these rates by 6%. The model calculated integral fluxes, at a given linear energy transfer (LET), are lower by factors varying from 1.5–2.7. Comparison of the differential energy spectra of secondary protons, deuterons, triton, ^{3}He and ^{4}He generated by GCR with the Shuttle shielding materials obtained with a charge particle telescope with HZETRN model calculations showed that the secondary proton and deuteron fluxes can be calculated to an accuracy of 25%; however, considerable additional improvements in model calculations are required for the other three components. We suggest space based experiments and model improvements to reduce these errors. Improving and establishing the accuracy of these models is of fundamental importance to the design of exploration missions.

INTRODUCTION

Radiation risk from exposure to galactic cosmic radiation (GCR) is one of the main concerns for exploratory class space missions. For a fixed given biological response function, there are two sources of uncertainties: (1) estimating the GCR differential energy spectra of various ions, and (2) propagation errors in radiation transport model(s) due primarily to incomplete or inaccurate knowledge of nuclear fragmentation cross sections and their energy dependence. Model calculations using the 1965 solar minimum GCR spectrum from the CREME model [1] and HZETRN transport code show that to stay below an acceptable radiation exposure, small errors in calculating radiation exposure (dose equivalent) have a very large, nearly exponential effect, on the amount of shielding required.

This clearly increases the cost of an exploration class mission dramatically and as such there is a need to reduce these uncertainties. Widely varying uncertainties in predicting fluxes from the GCR environment model and the effects of errors in fragmentation cross sections have been cited [2]. It is therefore fairly important to first establish what the actual uncertainties really are. Uncertainties in the CREME model were quoted to be factors of 2–5, but were in fact closer to rms error of 30% [3]. Similarly the effect of errors in nuclear fragmentation parameters have been shown to lead, given the 1965 GCR solar minimum spectrum, to factors of 2–6 errors in dose equivalent depending of shielding depth. Significant improvements in modeling the GCR fluxes at 1 A.U. in the last three years [4–7] have led to lowering the rms error to 10% [4]. In this paper, we systematically examine the errors on ability of the combined GCR environment model of Badhwar and O'Neill [5] and the 1995 version of the Langley developed HZETRN (radiation through matter) transport code, to estimate the absorbed dose rate, dose equivalent rate, LET spectra, and secondary light ion spectra. The results of the model calculations are compared with measurements using TEPC and a charged particle spectrometer flown on the Space Shuttle.

EXPERIMENTAL DETAILS

The tissue equivalent proportional counter was flown under at least four distinct shielding configurations: near the crew sleeping area on the starboard side (Dloc 2) payload bay 2 (also on the starboard side), the tunnel connecting the middeck to the payload bay, and the middeck or Spacehab lockers. The charged particle spectrometer was flown in the middeck locker only. Both of these instruments and data processing procedures have been described [8,9]. The parameters of the Shuttle flights are given in [10].

RESULTS

The TEPC measures the differential lineal energy spectrum, dJ/dy. These are converted into dose rates (D), and given the definition of quality factor, Q, as a function of LET, l, to dose equivalent (H). These are given by:

$$\text{Rate} = k \int \psi(l) \, (dJ/dl) \, dl \qquad (1)$$

where k is conversion constant and $\psi(l)$ is a weighting function:

For Absorbed Dose rate (D) : $\qquad\qquad\qquad \psi(l) = 1$

For Dose Eq rate (ICRP-26) (H): $\qquad \psi(l) = 13.7 \ln(1 + l/47.7) \qquad\qquad 1 \leq \psi(l) \leq 20$

For cell transformation rate (T): $\qquad \psi(l) = \sigma_0 \, [1 - \exp(-\alpha \, f(l))]^m$

where f(l) is related to the effective charge Z^* and ion velocity β.

Figure 1 shows the observed GCR dose rates versus the model calculated dose rates. The solid line is the least square fit straight line and is given by: Observed Dose Rate = $(-0.47 \pm 9.3) + (1.06 \pm 0.11)$ Calculated Dose Rate.
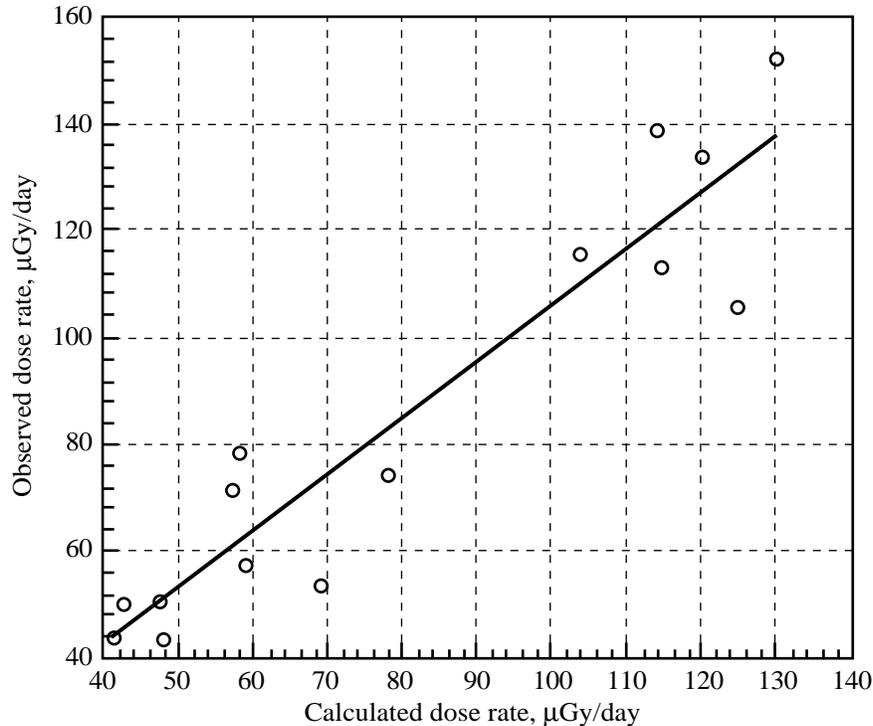
Figure 1.   Observed dose rate versus model calculated dose rate.

The root mean square error is 16.75% and within one standard deviation the bias is zero and the line has a slope of one. Similarly, we find that the least square fit line to dose equivalent rates is given by: Observed Dose Eq Rate = $(-32.8 \pm 58.0) + (1.06 \pm 0.18)$ Calculated Dose Eq Rate. The rms error is 18% and again within one standard deviation the bias is zero and slope of one. However, the fact that the mean slope of both the regression lines is > 1 can be easily understood. There are three additional sources of radiation that TEPC measures but are not included in GCR model calculations. These are: (1) albedo protons, (2) albedo neutrons, and (3) secondary neutrons generated by the nuclear interactions of GCR with spacecraft shielding.

The neutrons are detected by TEPC within an efficiency similar to that of body tissue and as their effective quality factor is higher than that of GCR, percentage wise they contribute more to dose equivalent rates than absorbed dose rates. Thus, one expects systematically higher rates. If we statistically subtract the rms error (10%) of the GCR environment model from dose rate rms errors, we get the estimates of HZETRN model errors to predict absorbed dose rates to be 13.4% and dose equivalent rates to 15%. In a comparison of the ability of HZETRN code and the GCR transport code of Dudkin and Potapov [11] that uses only the GCR charge group fragmentation parameters to predict absorbed dose, it was shown [12] that the two codes agree within ± 15%. This is also true of the NRL developed UPROP code [13] for modest shielding depths. Thus, current radiation transport models can predict GCR absorbed dose rate and dose equivalent rates to about 15% rms accuracy; the error in dose equivalent is always somewhat higher. Other important quantities for crew health and shielding studies are the cell killing and transformation rates. These can be obtained from a knowledge of the LET spectrum by using their weighting

functions. Note that these functions are also linear for small l values and saturates at large l values. This is a behavior similar to the ICRP-26 quality factor. We thus expect similar errors for these quantities to be somewhat higher than the dose equivalent.

Figure 2 is a cross plot of the observed and calculated integral fluxes from different Shuttle flights. The dashed line is the 1:1 line. A direct comparison of the differential fluxes is not possible with a TEPC type instrument because of the smearing of the LET values due to chord length variations. Thus, the model calculations have large flux spikes due to individual charges in GCR; these cannot be observed in TEPC data. These results show that the model sometimes overestimates and sometimes underestimates the observed fluxes. These factors vary from 1.5–2.7. Part of this discrepancy is certainly due to the neglect of albedo, proton, albedo, and secondary neutrons. Recent results from carbon, nitrogen, and oxygen heavy ion beams at GSI [14] show the need to improve the nuclear fragmentation part of the HZETRN code. This is precisely the LET region of the greatest difference between the calculated and observed fluxes.

In determining the errors of various quantities, it has been assumed that the orbit averaged geomagnetic transmission function as calculated by the CREME code is applicable to all flights and flight conditions. This code uses the vertical geomagnetic cutoffs calculated using the quiet time 1975 IGRF magnetic field. However, the magnetic field in 1995 has a lower field strength and has drifted westward by about 5°. Comparison of the 1975 cutoffs with HEAO-C data obtained in 1980 by Smart et al. [15] showed a systematic difference of about 2.5%. Nymmik et al. [16], using a combination of high inclination satellite data, and Boberg et al. [17], using the 28.5°
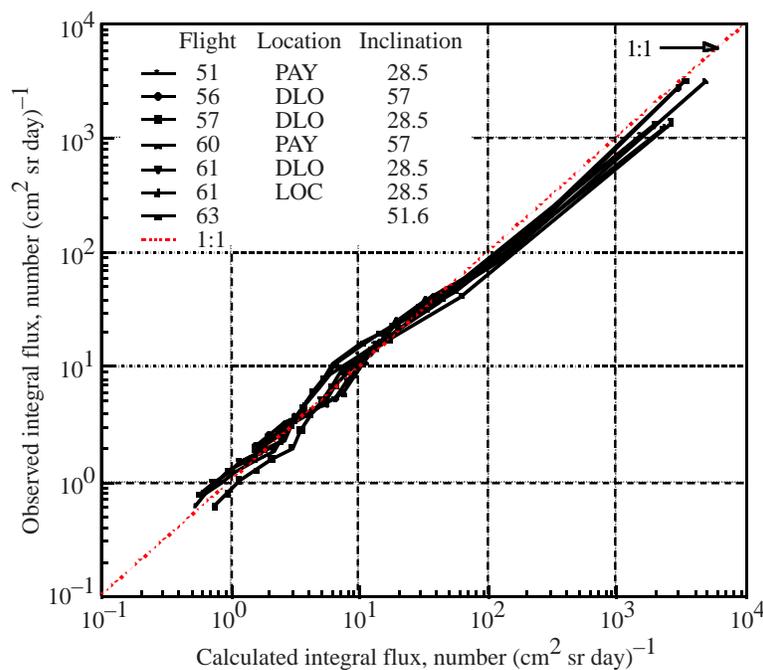

Figure 2. Plot of observed integral flux versus calculated integral flux.

LDEF data, have shown that the actual cutoff is lower compared to CREME code calculations. In addition, this code does not take into account that the change in cutoff due to variations in the K_p index, that reached up to 6 during some of the Shuttle flights. Thus, it is possible that part of the uncertainty can arise from the lack of complete knowledge of the transmission function.

PROPOSED SPACE VALIDATION OF HZETRN CODE

The approach of shielding code validation discussed above combines measurements for varying times in the solar cycle and significantly varying shielding distributions. As such, the lack of the knowledge of the shielding distribution, and changes in geomagnetic cutoff due, for example, to varying K_P index can introduce uncertainties.

These problems can be significantly reduced by carrying out an experiment to measure the dose-depth relation at one time in the solar cycle. Figure 3 shows the proposed flight configuration. There are four polyethylene spheres with diameters of 3", 5", 8", and 12". Each sphere has at its center one TEPC detector imbedded. In addition, one TEPC is deployed without a polyethylene sphere. The whole assembly is to be deployed at either the Dloc 2 location in the middeck or on the ceiling in the Spacelab module. Thus, we will have measurements of absorbed dose, dose equivalent, and LET spectra under five shielding thicknesses simultaneously. Currently, we are planning two flights, one with polyethylene and one with carbon spheres, with the first flight in August 1996 (STS-79) in a 51.6° orbit. The results would permit dose measurements from 0 to 15 g cm^{-2} of tissue thickness simultaneously. The results would be compared with the next generation HZETRN code. We hope to thus further reduce the errors.
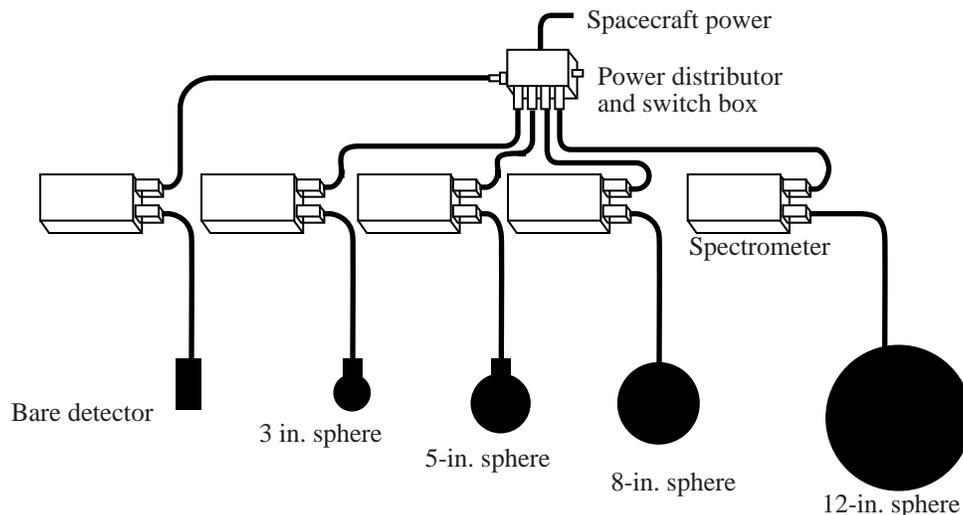

Figure 3.   Proposed deployment of a dose-depth experiment on the Shuttle.

COMPARISON OF LIGHT ION SECONDARY PARTICLE ENERGY SPECTRA

LET spectral measurements are the key variable of current crew health protection and risk assessment methodology and thus provide a good check of the accuracy of radiation transport model(s). However, from equation (1), it is clear that it is the weighted integral of the LET differential spectrum that is the key component and as such tends to smooth out differences between the model calculations and observations. It is clearly better to check the prediction of these models to calculate the energy spectra of secondary ions directly. Such experiments require the use of charge particle spectrometers with good charge, energy, and isotopic resolution. Two slightly different spectrometers of this type have been flown on two flights each: one on STS-37 (inclination 28.5°) and STS-48 (inclination 57°), and the other on STS-57 (28.5°) and STS-63 (57°), respectively.

Only the analysis of data from the two flights of the first spectrometer has been completed. Because of the time resolution, the GCR particles can be easily separated from trapped particles. In addition, particles below the geomagnetic cutoff can only arise from nuclear interactions of primary GCR with Shuttle shielding materials. This is also the energy region where isotopic resolution is possible with solid state detectors.

Figure 4 shows the ability of the spectrometer to provide light ion mass resolution. The flight duration (< 5 days) was too short to look at isotopes with charge > 3. Figure 5 shows a comparison of the observed secondary proton energy spectrum with the calculated spectrum. The two model curves correspond to the 1994 and 1995 version of the HZETRN model. Only particles entering through the forward direction are compared. The agreement is very good. Slight excess of observed particles could be due to albedo protons and (or) secondary pions and kaons that are not considered by the model. A similar comparison for STS-37 showed excellent agreement if the model was scaled down by a factor of 1.25. Thus the HZETRN predicts this spectrum to 25%. Figure 6 shows a similar comparison for secondary deuterons.

Again, the problems with the 1994 model were successfully resolved in the 1995 model and the agreement with observation is within 30%. Figure 7 shows the comparison with ^{4}He spectrum. Clearly, significant improvements in the model are needed. The advantage of this type of verification is, of course, that it really checks the ability of the model to describe the secondary particle production cross sections and their energy dependence. This is not the case when comparison is made with LET spectra because a significant part of the spectra is still due to primary particles. Thus, long flights of particle spectrometers in known shielding configurations can go a long way in establishing the model accuracies. Fluence based risk estimation methods, charge and velocity and not LET dependence of cell killing (transformation) and harderian gland tumor incidence rates, all point to the need for this type of code validation.
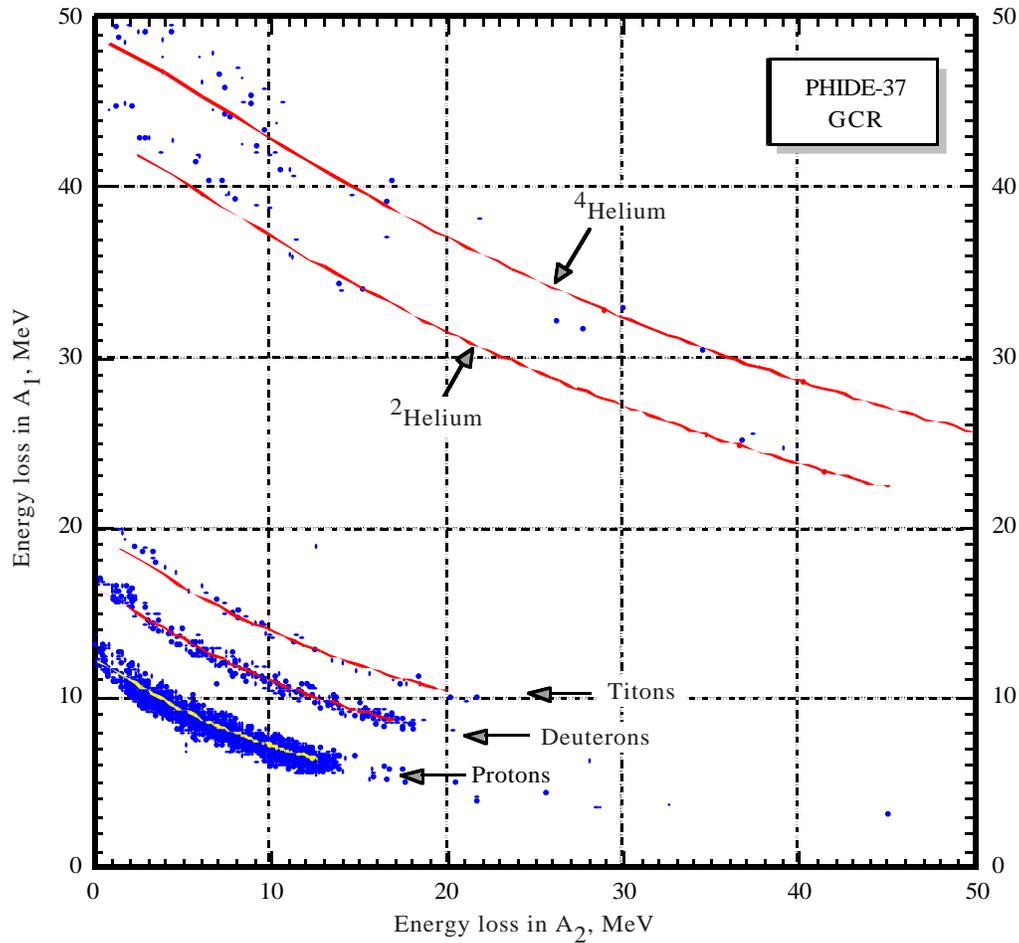
Figure 4.   Plot of energy loss in top two Si solid state detectors for secondary light ions.

CONCLUSIONS

A detailed evaluation of the 1995 version of the HZETRN radiation transport model and GCR environment model to predict the absorbed dose, dose equivalent, and LET spectra has been made. This was done using a systematic comparison of the model calculations with model predictions. The results show: (1) the model can predict the absorbed dose and dose equivalent to an rms accuracy of 15%, (2) there is clearly a need to update the nuclear cross-section database following recent results from carbon, nitrogen, and oxygen ions made at GSI, (3) the predictions of integral flux at a given LET can be off by factors of 1.5–2.7 with rms errors of 45%, and (4) the true errors may in fact be lower if other sources of radiation (albedo protons, albedo neutrons, and spacecraft secondary neutron) and errors in geomagnetic transmission function are taken into account.

A similar comparison of model calculated and measured secondary light ion spectra shows that the HZETRN model predicts the secondary proton spectra to an accuracy of 25%, deuterons to about 30%, and triton, ^{3}He and ^{4}He ion spectra to about a factor of two. This is a vast improvement over the 1994 HZETRN code. However, further
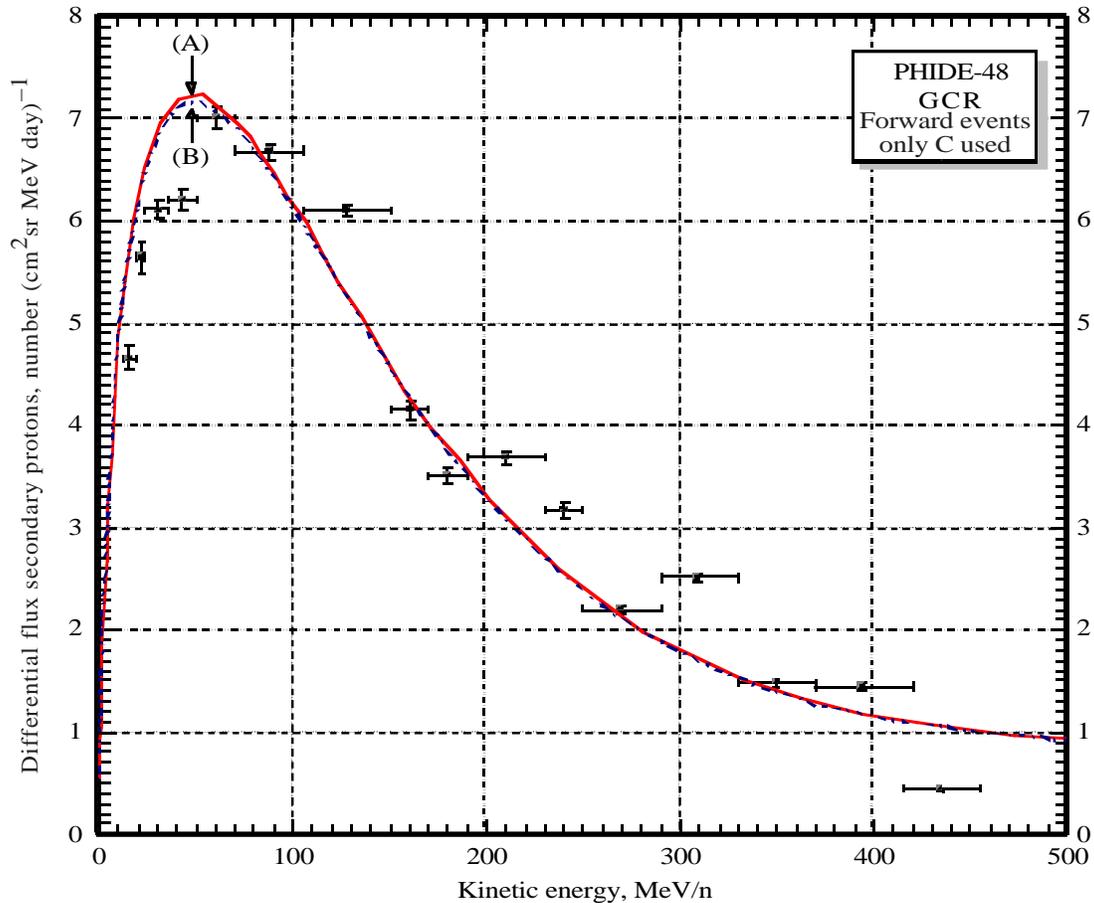
Figure 5.   Comparison of observed and calculated secondary proton energy spectra.

improvements are clearly needed. The GCR environment model needs to provide the spectra of important isotopes, such ^{3}He and ^{15}N. They form a considerable and energy dependent fraction of the ion fluxes. The geomagnetic transmission code needs to be updated to the IGRF 1990 field. Flight experiments to further verify the accuracy of these models, and reduce the level of uncertainty, would greatly benefit the exploration program by significantly lowering the cost of crew and component health protection.

REFERENCES

1.   J. H. Adams Jr., R. Siberberg, and C. H. Tsao, Cosmic ray effects on micro-electronics, Part IV, Naval Research Laboratory Memorandum Report 5901, 31 Decemeber, 1986.

2.   L. W. Townsend, F. A. Cucinotta, and J. W. Wilson, HZE reactions and data base development (Lecture 2). In *Proceedings, NATO Advnaced Study Institute on Biological Effects and Physics of Solar and Galactic Cosmic Radiation*

3.   G. Badhwar and P. M. O'Neill, An improved model of GCR for space exploration missions, *Nucl. Tracks. Meas.* **20**, 403–410 (1992).
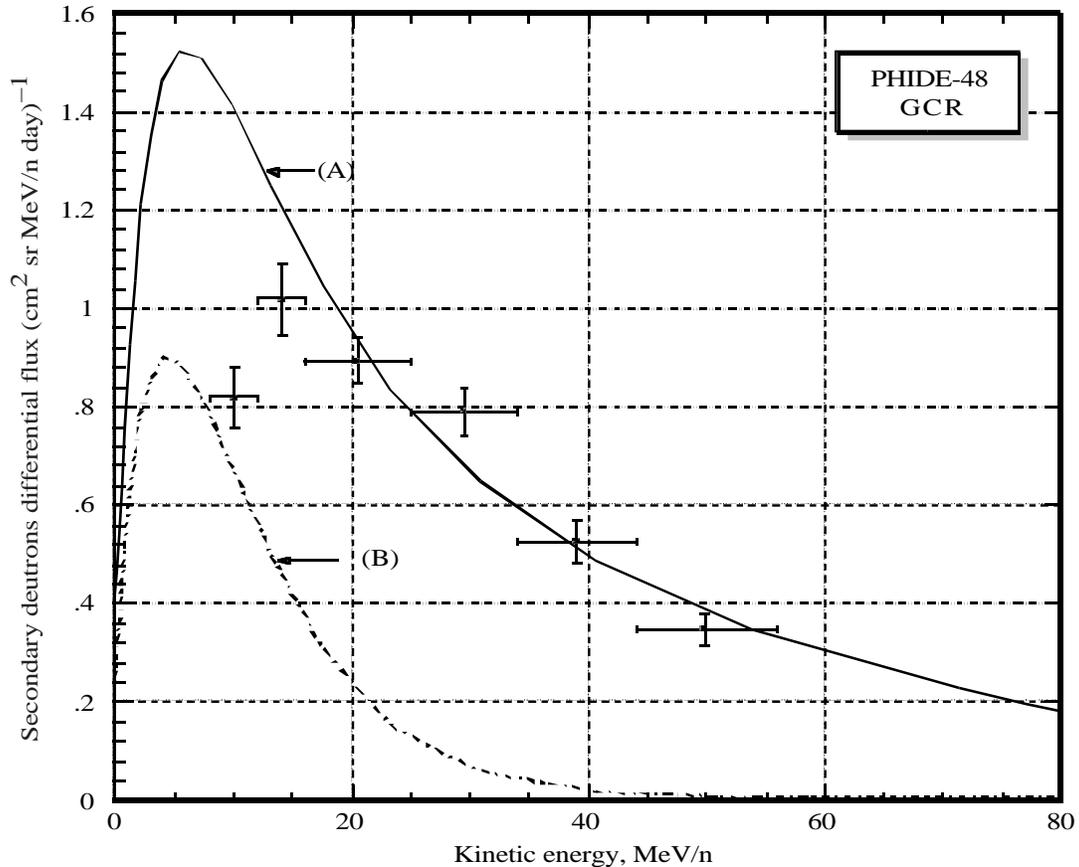
Figure 6.   Comparison of observed and calculated secondary deuteron energy spectra.

4.   G. D. Badhwar and P. M. O'Neill, Galactic cosmic radiation model and its applications, *Adv. Space Res.* **17**, 7–17 (1996).

5   R. A. Nymmik, M. I. Panasyuk and A. A. Suslov, Galactic cosmic ray flux simulation and prediction, *Adv. Space Res.* **17**, (1996).

6   J. Lee and J. H. Adams Jr., Long-Term modulation effects on the primary cosmic rays, In *Proceedings of 23th International Cosmic Ray Conference (Calgary),* **23**, 621–625 (1993).

7.   J. Chen, D. Chenette, R. Clark, M. Garcia-Monoz, T. G. Guzik, K. R. Pyle, Y. Sang, and J. P. Wefel, *Adv. Space Res.,* **14**, 765–769 (1994).

8.   G. D. Badhwar, A. Konradi, A. Hardy, and A. Konradi, L. A. Braby, Active dosimetric measurements on shuttle flights, *Nucl. Tracks and Radiat. Meas.,* **20**, 13–20 (1992).

9.   G. D. Badhwar, F. A. Cucinotta, L. A. Braby and A. Konradi, Measurements on the Shuttle of the LET spectra of galactic cosmic radiation and comparison with radiation transport model, *Radiat. Res.,* **139,** 344–351 (1994).

10. G. D. Badhwar, F. A. Cucinotta, and A. Konradi, Shuttle measurements of galactic cosmic radiation LET spectra, *Adv. Space Res.,* **17**, (1996).
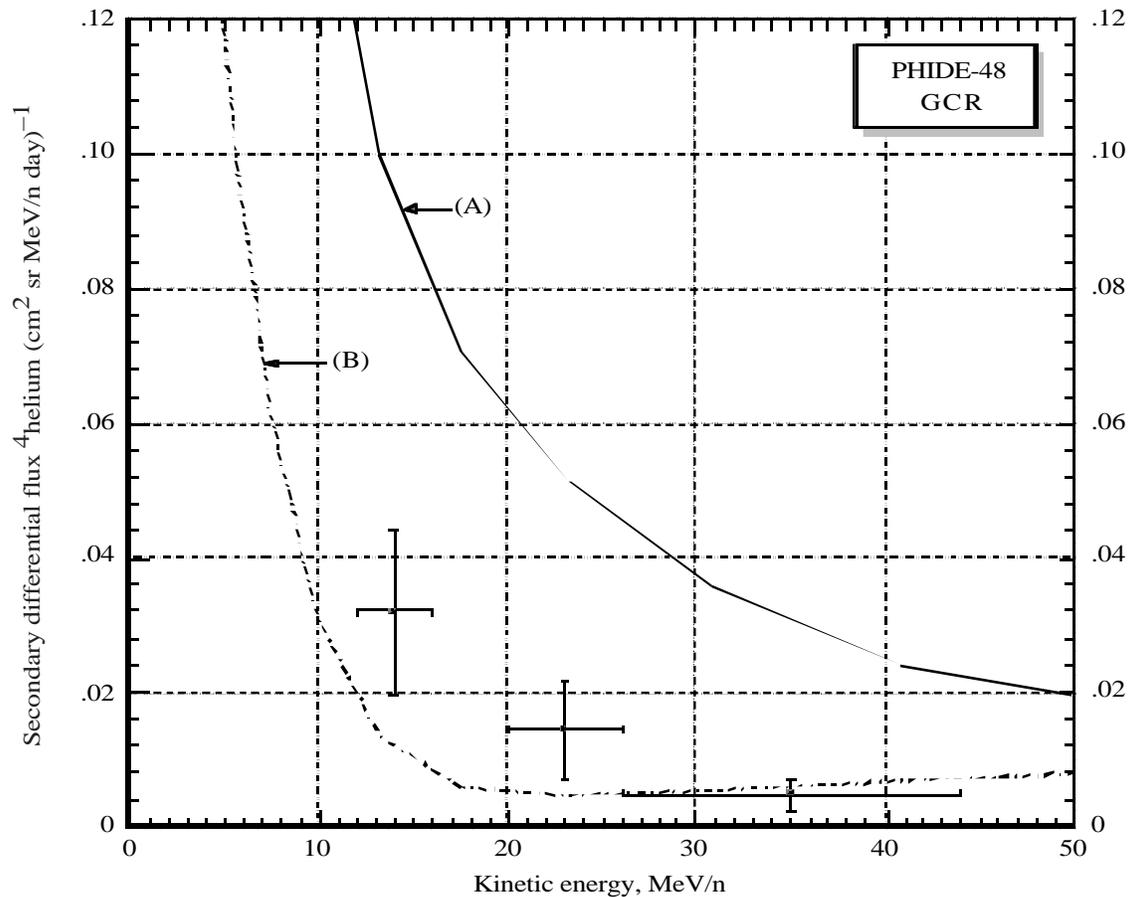
Figure 7.   Comparison of observed and calculated secondary ^{4}He energy spectra.

11. V. E. Dudkin and Yu. V. Potapov, Radiation shielding in manned Mars space flight, *Nucl. Tracks Radiat. Meas.* **20**, 33–40 (1992).

12. G. D. Badhwar, F. A. Cucinotta, and P. M. O'Neill, Depth-dose equivalent relationship for cosmic rays at various solar minima, *Radiat. Res.,* **134**, 9–15 (1993).

13. J. H. Adams Jr., G. D. Badhwar, R. A. Mewaldt, B. Mitra, P. M. O'Neill, J. F. Ormes, P. W. Stemwedel, and R. E. Streitmatter, The absolute spectra of galactic cosmic rays at solar minimum and their implications for manned space flight. In *Proceedings of the 22nd International Cosmic Ray Conference,* Dublin, (1991).

14. L. Sihver, C. H. Tsao, R. Silberberg, A. F. Barghouty, and T. Kanai, Calculations of depth-dose distributions, cross sections and momentum loss, GSI 95-23 Preprint, March 1995.

15. D. F. Smart and M. A. Shea, Geomagnetic cutoffs: A review for space dosimetry applications, *Adv. Space Res.,* **14**, 787–796 (1994).

16. R. A. Nymmik, An approach to determination of real cosmic-ray cut-off rigidities, In *Proceedings of the 22nd International Cosmic Ray Conference,* Dublin, **2**, 654 (1991).

17. P. R. Boberg, A. J. Tylka, J. H. Adams Jr., E. O. Fluckiger, and E. Kobel, *Geophys. Res. Lett*., (1995).

CHAPTER 22

ASSESSMENT OF CURRENT SHIELDING ISSUES

by

Francis A. Cucinotta and John W. Wilson[1]

---
[1]NASA, Langley Research Center, Hampton, VA 23681-0001

Chapter 22

ASSESSMENT OF CURRENT SHIELDING ISSUES

ABSTRACT

An overview of issues of radiation shielding effectiveness and the current limitations in making such assessments for space radiation exposures is presented. Current status and future emphasis of research in radiation physics are discussed. Most notably there is a limited number of existing measurements for nuclear interaction cross sections and spectra in thin targets and particle spectra in thick targets with high energy nuclei using advanced shielding materials. Several areas of improvement in theoretical and computational models for fragmentation parameters, light particle energy and angular distributions, and transport methods are suggested by existing numerical studies. The divergence in current assessments in shield effectiveness found using conventional determinations of radiation quality as compared to track structure models needs to be addressed. Flight measurements of individual particle energy distributions and the demonstration of risk assessment methods using advanced spacecraft material concepts will aid in validating models. In addition, due to lack of epidemiological data for radiation induced cancer in humans, computational approaches to study the effects of heavy ions in causing known genetic and epigenetic alterations involved in cancer formation should be developed for support of molecular biology studies focused on reducing the current uncertainties in assessing the cancer risk of astronauts.

INTRODUCTION

In this paper we consider risk assessment methods for radiation health effects, most importantly cancer and damage to the central nervous system (CNS), during interplanetary space travel where astronauts will experience prolonged exposures from the galactic cosmic rays (GCR) and possible exposures to solar particle events (SPE). The focus of this review is to consider current methods for evaluating the role of radiation shielding from the viewpoint of improving experimental and theoretical models and databases in radiation physics and biophysics. Radiation is an established carcinogen based on experimental studies with animals and epidemiological data. However, there is no human database for providing estimates of cancer induction for the high energy nuclei. Risk estimates are made by extrapolating knowledge of cancer incidence in the Japanese atomic bomb survivors and other exposed groups combined with estimates of the relative biological effectiveness (RBE) of individual radiation types using

experiments with animal and cell culture models [1,2]. The atomic bomb exposures consisted largely of energetic photons with a small contribution from neutrons. The radiation fields in space are distinct from energetic photons because of the unique track structure of ions [3,4]. Radiation protection boards have considered cancer induction in animals as a preferred system for recommending radiation quality factors [1,2]. Currently, only two animal systems have been studied with high energy nuclei: the Harderian gland in the mouse [5,6] and skin tumors in the rat [7]. These studies are limited to a small number of nuclear types and were performed at much higher dose-rates than will occur in space. Recent advancements in understanding the molecular pathways involved in the development of cancer in humans and animals suggest limitations of animal studies as a human model [8–12]. The evaluation of the cancer risk from space radiation and the effectiveness of shielding materials is thus severely limited at this time and points to a vital role for new studies in cancer biology using appropriate radiation fields.

In this paper we consider current issues in radiation physics and biophysics that will be important in determining spacecraft shield effectiveness. We focus on numerical studies and comparisons to ground-based and spaceflight dosimetry which highlight the uncertainties in current models. Traditionally, the assessment of risk from the galactic cosmic rays (GCR) and solar particle events (SPE) has separated into the areas of determining the radiation environment as a function of particle energy and type and temporal dependence, the physics and dosimetry of radiation transport and energy deposition, and applying methods for assessing acute and late health effects. The status of the current model of the radiation environment in space has been reviewed by Badhwar [13]. Shield design issues were considered by Wilson et al. [14]. Miller [15] has reviewed existing measurements of nuclear interaction cross sections and Cucinotta et al. [16] have reviewed models of radiation transport, nuclear interaction cross sections, and track structure models of energy deposition. Also, Yang et al. [17] and Curtis [18] have discussed radiobiology data and risk models, respectively, for high charge and energy (HZE) particles in this workshop.

RADIATION PHYSICS AND ESTIMATING SHIELD EFFECTIVENESS

Space radiation will undergo atomic and nuclear interactions within spacecraft structures and human tissues leading to large modifications in radiation types from the free space environment. Nuclear interactions alter the composition of the impinging radiation field and also lead to the production of new particles from the target materials atoms (spacecraft structures or tissues). Lower mass materials are advantageous due to their higher efficiency per unit mass for projectile fragmentation and because they reduce secondary ions produced from target atoms (target fragmentation). Secondary particles produced in high energy nuclear reactions will in almost all cases have lower charge than the primary particles and thus reduced rates of ionization and larger range. The reduction of secondary neutrons from lower mass materials is expected to be an important factor because of their excessive range and ability to produce low energy highly ionizing ions. Studies with the HZETRN radiation transport code [19, 20] for the GCR at solar minimum predicts that aluminum shielding will increase the total number of particles by a factor of 2 for shields of depth of 20 g/cm^2 while liquid hydrogen shielding leads to a decrease of a factor of about 2 at the same depth. The impact of such changes on shield evaluation depends critically on the method of quantifying biological effects. However, independent of a specific biological response model it can be stated that in

comparing the mass dependence of shielding materials that lower mass materials offer optimal reduction in total particle flux, secondary neutrons, and high charge and energy (HZE) particles.

Nuclear particles produce unique energy depositions due to the highly correlated ionization pattern from electron ejection about their path. The unique track structure of ions results from the lateral extension of their atomic or molecular excitation/ionization patterns which extends for many 10's of microns for relativistic ions with extremely high rates of ionization within the first few 10's of nm's from the track and decreasing approximately with inverse distance squared away from the ions path. The track structure of the ions results in highly correlated events when one considers the nucleosome and the higher order structure of DNA due to clustering of damage from individual electron tracks, contributions of electron track overlap, and the intersection of the track with several segments of DNA [5,21,22]. Individual electron tracks will produce several ionization events in volumes of sizes similar to a nucleosome or chromatin fiber [4]. The effects of electron overlap increase with the target volume and become substantial for higher charged ions leading to large RBE's for some endpoints. The importance of such effects for cancer induction are not known.

The use of the linear energy transfer (LET) to determine radiation quality in conventional risk assessment is at odds with many radiobiological experiments [23–25] and with most theoretical models of track structure [3,4,26,27]. Since radiation quality factors or weighting factors have primarily been assigned for assessing exposures to fission neutrons or radon, the impact of the simplistic nature of radiation quality assignment has been overlooked in the past. A major concern for understanding spacecraft shield effectiveness and ultimately radiation risk is then the understanding of the track structure of these ions in relationship to existing radiobiological experiments and the known genetic and epigenetic alterations seen in human cancers and damage to the CNS.

HEAVY ION FRAGMENTATION DATABASE ISSUES

GCR transport studies [16,19,28] indicate the importance of accurate determination of GCR fragmentation parameters. Current theoretical models of these parameters are described in this volume [16]. Validation of these models requires an adequate experimental database of cross sections. There is an inadequate number of measurements of nuclear fragmentation parameters and also systematic differences in existing measurements. In Figure 1, a X^2 comparison of the NUCFRG2 model [29] to experiments for Fe projectiles provides an indication of the systematic differences between this model and experiments. The quantum based model QMSFRG [16] will provide a better description of the reaction dynamics and nuclear structure effects; however, the systematic differences for similar projectile-target combinations points to the need for new measurements. Also, many of the existing data sets are incomplete in that a limited number of fragment charge or isotopic distributions were measured. There is a need for measurements that will give the complete set of parameters for all fragment charges and in some cases isotopic distributions or approaching this goal.

The QMSFRG theory of fragmentation will continue to be developed and is currently being used in the GCR transport code HZETRN in new systematic studies. Preliminary results suggest the importance of nuclear structure

effects in reducing differences in models and experiments. This is both true for the nuclear decay cascade [16] and the knockout process where clustering effects have been shown to be important [30,16]. Nuclear structure models based on clustering typically only treat the case of a single cluster configuration such as nucleon or alpha cluster coordinates. Predictions of spectroscopic factors from shell model representations of α-cluster nuclei usually differ with experiments by a factor of 2 or more [31]. Such models would be improved if several representations of the nucleus could be treated in a bound-state calculation; however, this would be an extremely complicated one. This points to the need for measurements to support theoretical efforts.

The target fragments produced in aluminum have been shown to provide 30–50% of the flux for linear energy transfer (LET) values above 50 keV/μm [32]. A significant portion of the target fragment flux is from Z>2 ions. The energy spectrum for the production of these ions may have an important impact and the adequacy of current models and experimental data should be tested.

LIGHT ION DATABASE ISSUES

In penetrating materials the heavy ion component of the GCR is attenuated rapidly because of the limited range of the lower energy components and nuclear absorption, most notably fragmentation. This is illustrated in figure 2 where the elemental distribution of ions at 0 and 20 g/cm^2 of Al as predicted by the HZETRN code is shown. Clearly, the Fe and other heavy ion components are greatly exhausted by significant shielding amounts. However, the reduction of heavy ions results in a buildup of lighter particle because of absorption including the production of neutrons which are the second most abundant nuclear species in the comparison of Fig. 2 at the larger depth. Not shown in Fig. 2 are the Z > 2 target fragments which have also buildup due to the spacecraft shielding. In Fig. 3 we show the fraction of the LET spectrum from target fragments as function of depth in aluminum [32]. At large depths most of the high LET particles (> 50 keV/μm) are low energy protons, alpha particles, and lighter charged ions with moderate energies (< 10 MeV/amu). These particles are produced along the paths of the high energy ions with dominate sources resulting from reactions by the more abundant hydrogen, neutron and helium ions. The effects of the uncertainties in the target fragment knockout components are seen in Fig. 4 where the dose and dose equivalent are shown with and without these components and for different model spectrum. These results point to the need for the development of nuclear reaction models which consider nuclear structure effects such as clustering, and also for new measurements of energy spectra for the light ions produced by high energy protons and neutrons.

A sensitivity study on the energy spectrum of light particles should be made. The physical bounds on the fragmentation parameters were evaluated by Townsend et al. [33] using a central and peripheral interaction model. For energy spectrum an analogous physical model should be devised to test the sensitivity of radiation transport codes to spectral shapes for light particle production. Currently, the effects of meson and anti-nucleon production have not been included in the HZETRN code. This limits our ability at this time to make a complete assessment of risk, especially on the Martian surface or in the upper atmosphere. The HZETRN code makes use of a straight-ahead approximation and the effects of this approximation should be most severe for low mass secondaries,

especially neutrons. The energy spectrum from light particles produced in heavy ion projectile fragmentation is assumed as a velocity conserving interaction in HZETRN which is in sharp disagreement with the physics of this process [34]. These and other aspects of light particle energy spectrum need to be gauged for accuracy of current databases that are used in radiation transport codes.

SPACEFLIGHT VALIDATION ISSUES

The paper by Badhwar in this workshop discusses spaceflight dosimetry [13]. There is a need for investigations of detector response for comparisons of transport code results with spaceflight measurements. In Fig. 5 we show comparisons of calculated LET spectra made with the HZETRN code to the measurements with a 2 micron diameter tissue equivalent proportional counter [35]. Although the comparisons are similar, issues related to detector response functions as discussed by Cucinotta et al. [36] need to be addressed. These include the effects of energetic delta-rays, the range of low energy ions, and the wall effects. Particle identification telescopes offer more direct comparison of models to spacelight measurements; however, particle telescopes will have insufficient counts on short spaceflight to measure HZE particles. In Figure 6 we show comparisons for light ion spectra measured on recent shuttle flights with calculations using the HZETRN code. These comparisons of light ion spectra have pointed out both agreements and suggested areas of improvements in radiation transport codes [35,29], and offer an excellent approach to identify other areas of improvements.

Validation of radiation transport models using space flight measurements is confounded by the large number of factors in comparisons such as radiation environment model, earth magnetic field models and spacecraft shielding models. However, as transport methods improve through theoretical efforts and laboratory validation, the use of space flight validation will become more advantageous. Ray tracing methods are used to represent complicated spacecraft shielding configurations. The use of minimally shielded locations on the space shuttle could allow advanced shielding concepts to be tested in space through the mapping and design of objects into the shuttle payload bay with similar ray tracing distributions as that of a realistic Lunar/Mars vehicle.

TRACK STRUCTURE MODELS

Conventional risk assessment uses linear energy transfer (LET) to represent radiation quality. This neglects the velocity dependent width of the ion track due to secondary electrons. The parameter Z^{*2}/β^2, where Z^* is the effective charge and β the ion's velocity, has been used by several models because the electron emission spectrum is known to scale approximately by this parameter. However, track width and thin-down effects are ignored in this approach as was noted in the 1960's by Katz [37] who suggested its use only for uniformly high energy radiation fields, not for complicated fields seen inside spacecraft. The model of Katz [3] uses the radial dose from electrons produced by an ion as the key physical parameter and the site size and radiation sensitivity of a biological target for determining radiation quality. Related approaches are used in the models of Scholtz and Kraft [26] and Chattergee and Holley [27]. In Figures 7 and 8 we show model calculations for SSB and DSB using the radial dose model [22] and the model of Chatterjee and Holley [27]. The Chatterjee and Holley model includes considerations of DNA

structure and early chemistry; however, both models point to the short comings of LET for describing biological endpoints such as SSB and DSB.

Monte-Carlo track structure simulations [38] use more realistic treatments including the transport of secondary electrons, including the stochastics of individual electron ionization events. These models are computationally less efficient than the radial dose base models which have prohibited their use for heavy ions studies in the past. These models have concentrated on defined initial lesions such as strand breaks and base damage. A recent comparison [22] has shown important differences between the radial dose and track simulation approaches at low energies (<1 MeV) for H and He. Shield effectiveness studies using quality factors, Z^{*2}/β^2 biological cross sections [39], and the radial dose approach [40] give diverging results for the effectiveness of spacecraft shielding. The effects of these differences on shield evaluation should be considered.

Current risk assessment procedures and several models of radiation risk incorrectly use a single parameter to specify radiation quality. Such approaches may seem justified due to the small number of radiation types studied in most radiobiological experiments. The incorrect application of a single parameter such as LET, lineal energy, or Z^{*2}/β^2 to specify radiation quality is a minor concern when the number of radiation types is minimal as, for example, with radon or neutron exposures, however is grossly in error for a dynamic field such as the GCR. Studies over the years for inactivation of biological samples have often concluded that the deviation from unique specification of radiation quality with LET is only important for LET's >100 keV/um. However, Katz has argued [3] that this conclusion is in error because of the fluence or dose levels used in such studies. For low LET ions, the probability of more than one ion passing through the cell nucleus is quite high at the doses investigated. This leads to an intertrack effect on the biological response which is appropriately described by LET [3]. A comparison of inactivation of V79 cells is shown in Figure 9a. Here the final slope cross sections in the model are compared to the experiments. In Figure 9b the initial slopes of the model are shown which display much larger branching with LET and charge especially below 100 keV/μm. The initial slopes are not accessible in experiments due to the doses used. More recent studies with the HPRT mutation assay [23,24] find significant branching with LET and charge with lower LET ions. For mutation the initial slopes of the response are more accessible at the doses used because of a smaller target size. Unique physical parameters that define radiation quality for mutation may be more difficult to define due to effects of inactivation which will reduce the mutation probability for the heavy ions. A comparison of the radial dose model for mutation [41] which includes inactivation effects is shown in Figure 10. A minimum in the mutation rate is predicted near the energy of maximum inactivation probability. The effects of inactivation on mutation rates at the HPRT locus may not be indicative of inactivation effects at other loci [42]. Factors such as the role of nearby loci in the genome [42,43] and recombination repair of DSB's [44] will be important to understand these effects.

CANCER BIOLOGY AND SHIELDING EFFECTIVENESS

Cancer is observed as a disease of accumulated genetic or epigenetic alterations in growth control, DNA repair, and cell adhesion genes [8–12]. Genetic models for cancers in several human tissues have been postulated from experimental evidence. In Figure 12 is the genetic model of colon cancer of Vogelstein and co-workers (9,10). The long postulated 4–7 mutations required for cancer formation has been provided a genetic basis in the last 15 years as discussed in this model. It is expected that a larger number of genetic alterations are required for humans than in rodents [10], possibly limiting the use of rodents for human risk assessment. Two common classes of genetic alterations have been observed in cancer cells. The first is observed to occur in genes denoted oncogenes and involves an activating event where a point mutation or insertion leads to gains in function within gene products involved in growth regulation such as trans-membrane proteins or transcription factors. Many oncogenes are serine/tyrosine kinases which undergo large changes in activity through covalent modification during signal transduction. Alteration in signal transduction pathways play important roles in most human cancers and the effects of radiation on such protein modifications have not been studied. A second class of genetic alteration found in most human cancers involves the tumor suppressor genes and occurs through loss of function in both copies of the gene through deletion, point mutation, or epigenetic alteration. Tumor suppressor genes code proteins which provide negative regulatory effects on the cell proliferation. The most widely categorized tumor suppressor gene is the p53 gene which undergoes altered function in about 50% of all human cancers. P53 functions as a transcription factor and negative regulator of cellular growth following DNA damage. Differences in the molecular interactions of human p53 and mouse p53 with proto-oncogenes have been observed which may limit the latter as representative of a human model. The importance of mutations in the formation of cancers suggests that ionizing radiation be studied for its mutagenic capability including studies of the types of mutations that are observed. Point mutations involving single base alterations may evolve directly from processing of DNA damage by radiation or indirectly through an induced instability caused by the radiation. RBE's for SSB and base-damage for heavy ions are generally less than one and may be indicative of point mutations that occur through direct damage to DNA. Studies of deletion formation in the HPRT gene [45] have found small differences in the types of deletions for heavy ions when compared to X-rays; however, large RBE's for heavy ions are observed for the total mutation frequency [23]. Experimental studies of mutations in mammalian cells have observed an increased effectiveness of lighter ions compared to heavy ions in comparison to inactivation experiments. This may be directly attributable to the effectiveness of heavy ions in causing inactivation and thus reducing their matagenic capability. Clearly, such factors are related to evaluating shield effectiveness.

Genomic instability refers to the increase rates of delayed chromosome aberrations, mutation, and inactivation seen in the daughters of irradiated cells [46]. Alpha particles and heavy ions have been observed to produce significantly higher rates of instability than X-rays [47,48]. The cause of this instability will play a key role in assessing the role of spacecraft shielding in reducing risk and estimating the carcinogenic potential of space radiation. Currently, genetic effects such as mutations in DNA synthesis or repair genes, in genes related to signal

transduction, and in genes that control apoptotic cell death are expected to play a causative role in producing instability. Also, damage to the extracellular matrix, epigenetic effects such as changes in DNA methylation or the persistence of oxidative stress following radiation exposure [49] are suspected of causing instability. As factors related to known mechanisms of cancer induction such as promotion, mutations in oncogenes, tumor suppressors, and DNA synthesis and repair genes, and the role of genomic instability begin to be studied experimentally with HZE particles, computational efforts in radiation physics and biochemistry will be needed for providing a theoretical framework for extrapolating experimental results to the low dose-rates and spectrum of radiation types seen in space.

CONCLUDING REMARKS

Shield evaluations using current methods indicate the advantage of using low mass materials for shielding because of their optimal ability to reduce HZE ions and to reduce target fragment buildup. The quantification of differences in proposed shielding materials such as carbon composites or aluminum is currently limited by the uncertainties in biological risk models such that error determinations cannot be made with sufficient accuracy. In fact, uncertainties in risk estimates are currently so large that selection of shielding materials is severly hindered. Areas of emphasis for improving existing theoretical and experimental databases were discussed. The ability to evaluate spacecraft shielding effectiveness will be improved by improved understanding of radiation cancer biology. Recent advances in the understanding of the molecular biology of cancer should be used as a guide in developing new experimental systems to quantify the role of radiation as a carcinogen. Biological issues are seen to both entail larger scientific questions than physics issues and also to be inseparable from the physics and engineering issues for the selection and evaluation of shielding materials and configurations.

REFERENCES

1. International Commission on Radiological Protection: 1990 Recommendations of the International Commission on Radiological Protection. Pergamon Press Inc., ICRP Report No. 60, 1991.

2. National Committee on Radiation Protection and Measurements: Guidance on radiation received in space activities, Bethesda, MD, NCRP Report No. 98, 1989.

3. R. Katz, B. Ackerson, M. Homayoonfar, and S. C. Scharma, Inactivation of Cells by Heavy Ion Bomabrdment, *Radiat. Res.* **47**, 404–425, 1971.

4. D.T. Goodhead, Initial Events in the Cellular Effects of Ionizing Radiations: Clustered Damage in DNA. *Int. J. Radiat. Biol*. **65**, 7–17, 1994.

5. R. J. M. Fry, P. Powers-Risius, E. L. Alpen, and E. J. Ainsworth, High LET Radiation Carcinogenesis, *Radiat. Res*. **104**, S188-195, 1985.

6. E. L. Alpen, P. Powers-Risius, S. B. Curtis, and R. DeGuzman, Tumorigenic Potential of High LET Charged Particle Radiations. *Radiat. Res*. **136**, 382–391, 1993.

7. F. J. Burns, Y. Jin, S. J. Garte, and S. Hosselet, Estimation of Risk Based on Multiple Events in Radiation Carcinogenesis of Rat Skin, *Adv. in Space Res*. **14**, 507–519 (1994).

8. I. B. Weinstein, The Origins of Human Cancer: molecular mechanisms of carcinogenesis in the genesis of human cancer. *J. Supramol. Struct. Cell. Biochem*. **17**, 133–146 (1981).

9. B. Vogelstein, E. R. Fearon, S. R. Hamilton, S. E. Kearn, A. C. Preisinger, M. Leppert, Y. Nakamura, R. White, A. M. M. Smitts, and J. L. Bos, Genetic Alterations During Colorectal Tumor Development. *N. Eng. J. of Med*. **319**, 525–532, 1988.

10. B. Vogelstein and K. M. Kinzler, The Multistep Nature of Cancer, Trends in Genetics 9, 138–141 (1993).

11. M. Strauss, L. Lukas, and J. Bartek, *Nat. Med*. 1, 1245, (1995).

12. C. J. Sherr and J. M. Roberts, Inhibitors of Mammalian Gl Cyclin–Dependent Kinanses. *Genes & Dev*. 9, 1145–1160 (1995).

13. G. D. Badhwar, Deep Space Radiation Sources, Models, and Environmental Uncertainty, this volume.

14. J. W. Wilson, F. A. Cucinotta, S. A. Thibeault, M. Kim, J. L. Shinn, and F. F. Badavi, Radiation Shielding Design Issues, this volume.

15. J. Miller, Database Development and Laboratory Validation, this volume.

16. F. A. Cucinotta, J. W. Wilson, J. L. Shinn, R. Tripathi, R. R. Dubey, F. F. Badavi, and R. Katz, Computational Procedures and Database Development, this volume.

17. T. Yang and L. M. Craise, Biological Response to Heavy Ion Exposures, this volume.

18. S. Curtis, Human Risk Models and Risk Uncertainty, this volume.

19. J. W. Wilson, L. W. Townsend, and F. F. Badavi, Galactic HZE Propagation Through the Earth's Atmosphere. *Radiat. Res*., **109**, 173–183, 1987.

20. J. W. Wilson, L. W. Townsend, W. S. Schimmerling, G. S. Khandelwal, F. Khan, J. Nealy, F. A. Cucinotta, J. L. Shinn, L. C. Simonsen, and J. W. Norbury, 1991, Transport methods and interactions for space radiations. NASA RP-1257, 1991.

21. B. Rydberg, Clusters of DNA Damage Induced by Ionizing Radiation: Formation of Short DNA Fragments II. Experimental Detection. *Radiat. Res*. **145**, 200, 1996.

22. F. A. Cucinotta, H. Nikjoo, J. W. Wilson, R. Katz, and D. T. Goodhead, Radial Dose Model for SSB, DSB, and Deletions and Comparison to Monte-Carlo Track Simulation Results. In: Microdosimetry: An Interdisciplinary Approach. Eds., D. T. Goodhead, P. O'Neill, and G. Menzel, pp. 35–38, (1997).

23. J. Kiefer, U. Stoll, E. Schenider, Mutation Induction by Heavy Ions. *Adv. in Space Res*. **14**, 257–265, 1994.

24. M. Belli, F. Cera, R. Cherubini, A. M. Haque, F. Ianzini, G. Moschini, O. Sapora, G. Simone, M. A. Tabocchini, and P. Tiverton, Inactivation and mutation induction in V79 cells by low energy protons and alpha particles: re-evaluation of the results at the LNL facility. *Int. J. Radiat. Biol*. **63**, 331–337, 1993.

25. E. H. Goodwin, E. A. Blakely, and C. A. Tobias, Chromosomal Damage and Repair in Gl Phase Chinese Hamster Ovary Cells Exposed to Charged-Particle Beams. *Radiat. Res*. **138**, 343–351, 1995.

26. M. Scholz, and G. Kraft, Track Structure and the Calculation of Biological Effects of Heavy Charged Particles. *Adv. in Space Res*. **18**, 5–14 (1994).

27. A. Chatterjee, and W. R. Holley, Computer Simulation of Initial Events in the Biochemical Mechanisms of DNA Damage. In Adv. in Radiat. Biol. Vol 17, ed. J. T. Lett, W. K. Sinclair, Academic Press, 1993.

28. F. A. Cucinotta, L. W. Townsend, J. W. Wilson, J. L. Shinn, R. D. Dubey, and G. D. Badhwar, Light ion component of the cosmic rays: nuclear interactions and transport theory. *Adv. In Space Res*. **17**, 77–86, 1995.

29. J. W. Wilson, J. L. Shinn, L. W. Townsend, R. K. Tripathi, F. F. Badavi, and S. Y. Chun, NUCFRG2: A Semi-empirical nuclear fragmentation model. *Nucl. Instrum. & Meth. Phys. Res*. **B94**, 95–102, 1995.

30. F. A. Cucinotta, and R. D. Dubey, Alpha cluster model of ^{12}C(^{12}C,3α)X at 2.1A GeV. *Phys. Rev*. **C50**, 974–984, 1994.

31. O. Bacheller et al., *Nucl. Phys*. **A268**, 488–512, 1976.

32. F.A. Cucinotta, J. W. Wilson, J. L. Shinn, F. F. Badavi, and G. D. Badhwar, Effects of Target Fragmentation on Evaluation of LET Spectra From Space Radiation: Implications for Space Radiation Protection Studies. Radiat. Meas. (in press) 1996.

33. L. W. Townsend, F. A. Cucinotta, J. L. Shinn, and J. W. Wilson, Effects of Fragmentation Parameter Uncertainty on Galactic Cosmic Ray Exposure Estimates: Dose Sensitivity Studies for Aluminum Shields. NASA TM 4386, 1992.

34. F. A. Cucinotta, Forward Production of Protons from ^{12}C in Heavy Ion Collisions. *J. Phys. G* **20**, 1803–1815, 1994.

35. F. A. Cucinotta, J. W. Wilson, R. Katz, W. Atwell, G. D. Badhwar, and M. R. Shavers, Track Structure and Radiation Transport Model for Space Radiobiology Studies. *Adv. in Space Res.* **18**, (12) 183-(12) 194, 1996.

36. G. D. Badhwar, J. U. Patel, F. A. Cucinotta, J. W. and Wilson, 1994, Measurements of the secondary particle energy spectra in the space shuttle. *Radiat. Meas*. **24**, 129–138.

37. R. Katz, LET, Z^{*2}/β^2, and RBE, Health Phys. 1970.

38. H. Nikjoo, P. O'Neill, M. Terrisol, and D. T. Goodhead, Modeling of Radiation Induced DNA Damage: The Early Physical and Chemical Events, *Int. J. Radiat. Biol*. **66**, 453, 1994.

39. J. W. Wilson, M. Kim, W. Schimmerling, F. F. Badavi, S. A. Thibeault, J. L. Shinn, and R. Kiefer, Issues in Space Radiation Protection: Galactic Cosmic Rays. Health Physics 68, 50–58, 1995.

40. F. A. Cucinotta and J. W. Wilson, Estimates of Cellular Mutagenesis From Cosmic Rays. NASA TP-3453, 1994.

41. F. A. Cucinotta, J. W. Wilson, M. R. Shavers, and R. Katz, The Effects of Track Structure and Cell Inactivation on the Calculation of Heavy Ion Mutation Rates in Mammalian Cells. *Int. J. of Radiat. Biol*. **69**, 593–600, 1996.

42. A. Kronenberg, and J. B. Little, Locus Specificity for Mutation Induction in Human Lymphoid Cells by Energetic Heavy Ions. *Int. J. of Radiat. Biol*. **55**, 913–924 (1989).

43. F. Hutchinson, Induction of Large DNA Deletions by Persistent Nicks. A New Hypothesis. *Mut. Res*. **299**, 211–219, (1993).

44. E. C. Friedberg, G. C. Walker, and W. Siede, DNA Repair and Mutagenesis, ASM Press, Washington D.C., 1995.

45. J. Thacker, A. Stretch, and M. A. Stevens, Mutation and Inactivation of Cultured Mammalian Cells Exposed to Beams of Accelerated Heavy Ions II. Chinese Hamster V79 Cells. *Int. J. Radiat. Biol*. **36**, 137–148, 1979.

46. W. F. Morgan, J. P. Day, M. I. Kaplan, E. M. McGhee, and C. L. Limoni, Genomic Instability Induced by Ionozing Radiation. Radiat. Res. 146, 247–258 (1996).

47. L. A. Loeb, Mutator Phenotype May be Required for Multistage Carinogenesis, Can. Res. 51, 3075–3079, 1991.

48. M. A. Khadim, D. A. Macdonald, D. T. Goodhead, S. A. Lorimore, S. T. Marsden, and E. G. Wright. Transmission of Chromosonal Instability After Plutonium α-particle Irradration. *Nature* **355**, 738–740, 1992.

49. S. M. Clutton, K. M. S. Townsend, C. Walker, J. D. Ansell, and E. G. Wright, Radiation Induced Genomic Instability and Persisting Oxidative Stress in Primary Bone Marrow Cultures. Carcinogenesis 17, 1633–1639, 1996.
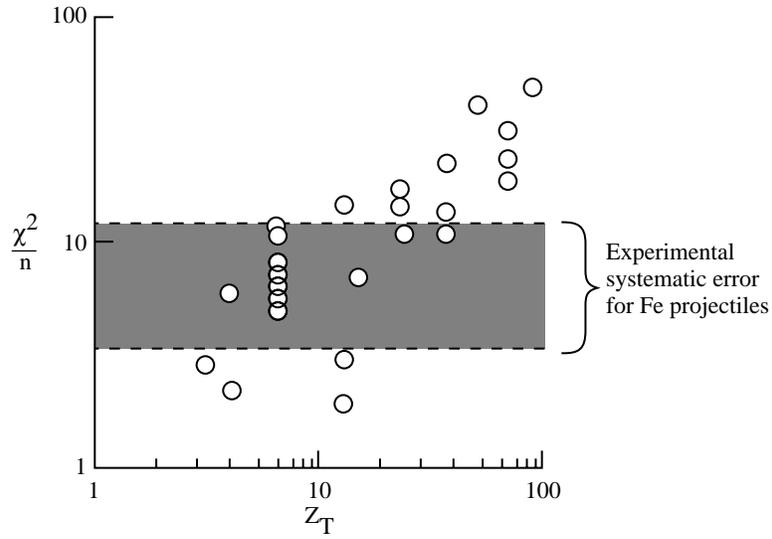
Figure 1. Comparison at systematic errors in experiments and NUCFRG2 model for Fe fragmentations.
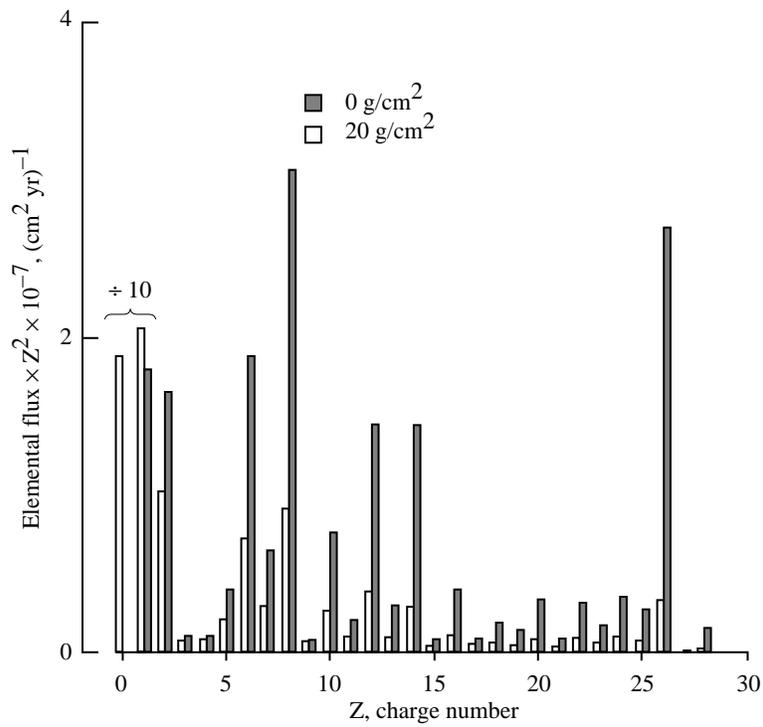
Figure 2. Calculations of elemental fluxes at 0 and 20 g/cm^2 of aluminum using HZETRN code.
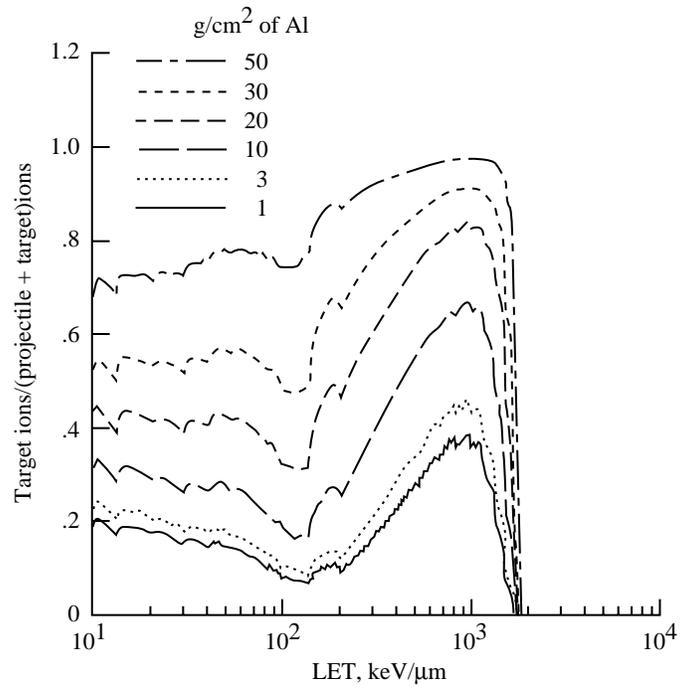
Figure 3.   Calculations of fractional contribution from target fragments to GCR particle flux at a given value of LET behind aluminum shielding.
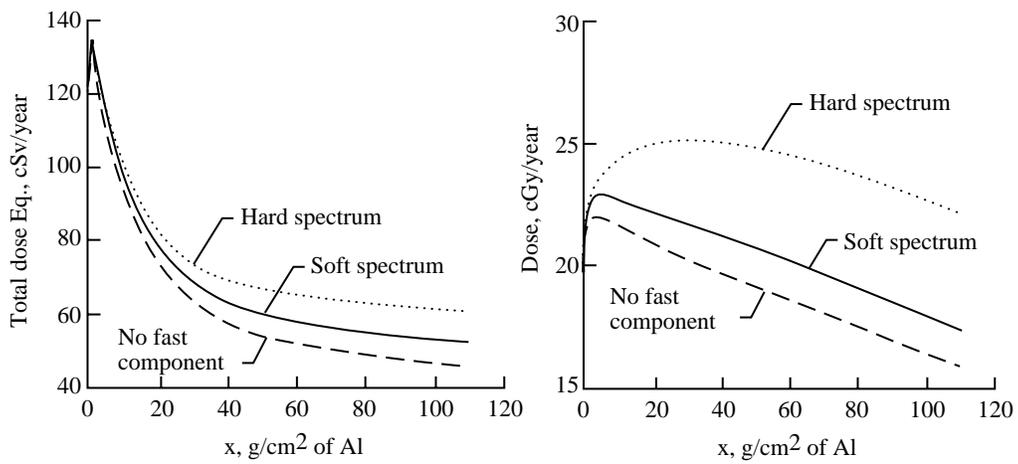

Figure 4. Calcualtions of GCR dose and dose equivalent showing importance of light ion production cross sections.
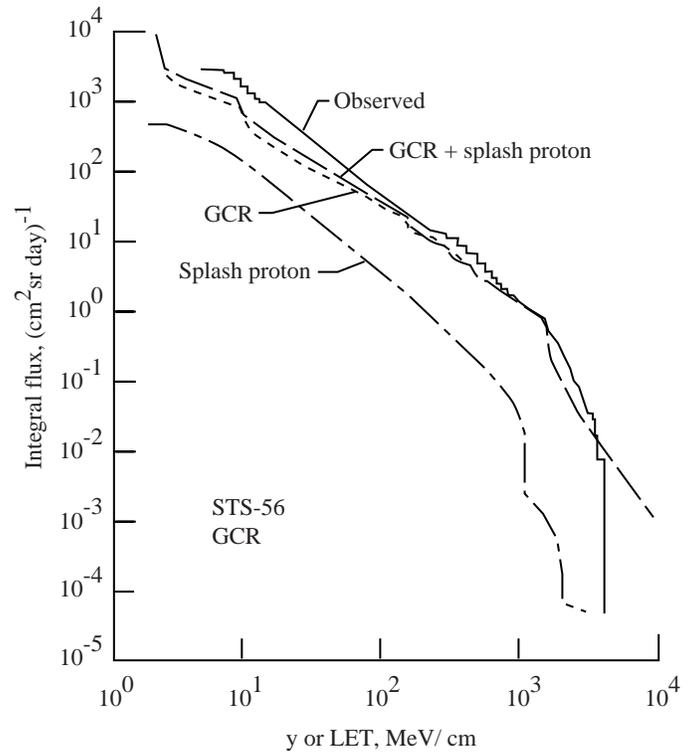
Figure 5. Comparison of LET spectrum from HZETRN model to measured y-spectrum on STS-56.
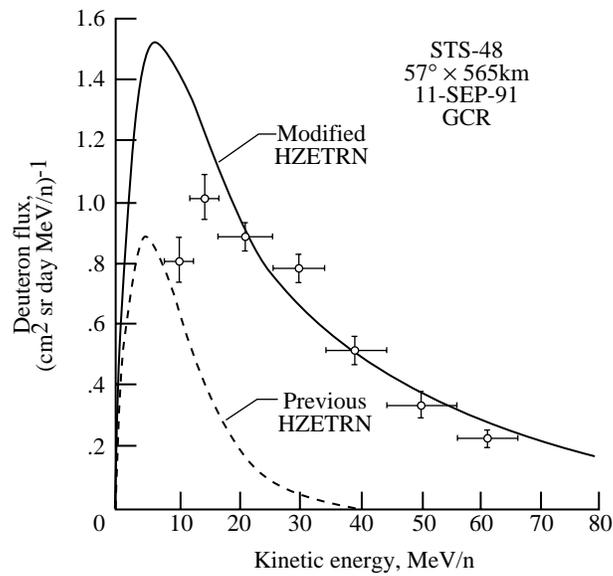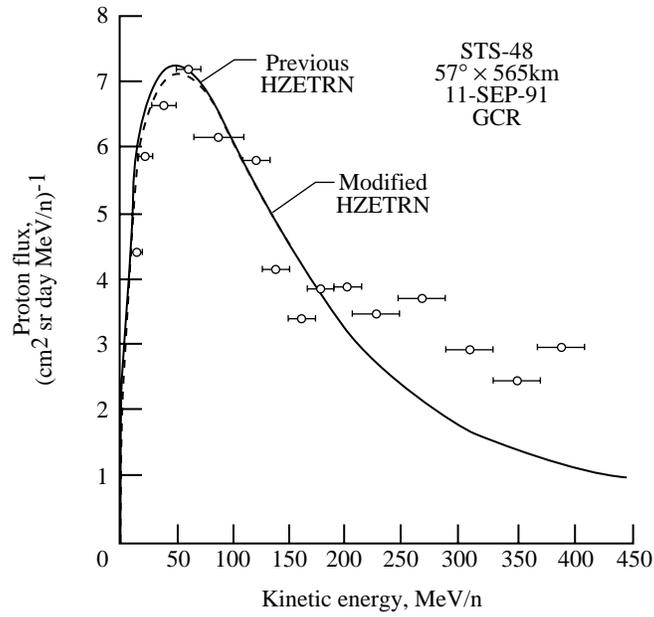
Figure 6. Comparisons of calculated and measured proton and deuteron flux versus energy on STS-48.
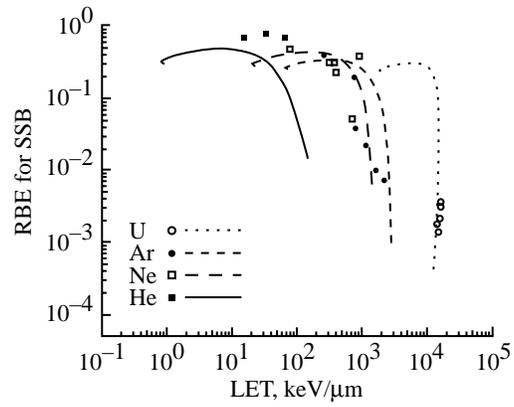
Figure 7a. Comparison of calculations (lines) in radial dose model and experiments (symbols) for RBE for SSB's in mammalian cells.
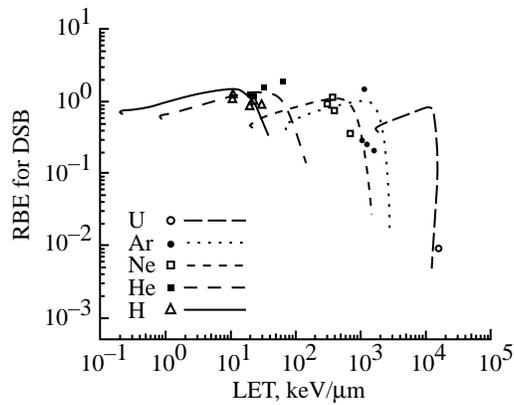

Figure 7b. Comparison of calculations (lines) in radial dose model and experiments (symbols) for RBE for DSB's in mammalian cells..
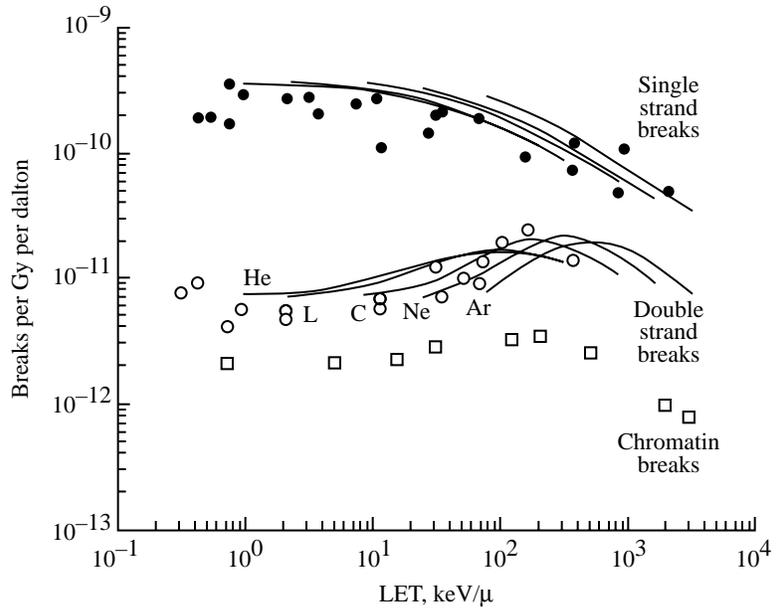
Figure 8. Comparisons of model of Holley and Chatterjee with experiments for number of SSB, DSB, and Chromatin breaks per Gy per Dalton.
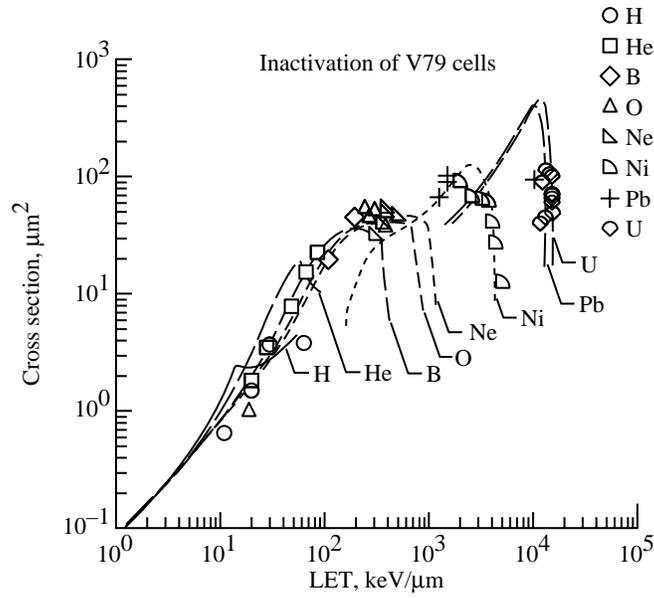
Figure 9a. Comparison of radial dose model to experiments for final slopes of inactivation cross sections in V79 cells.
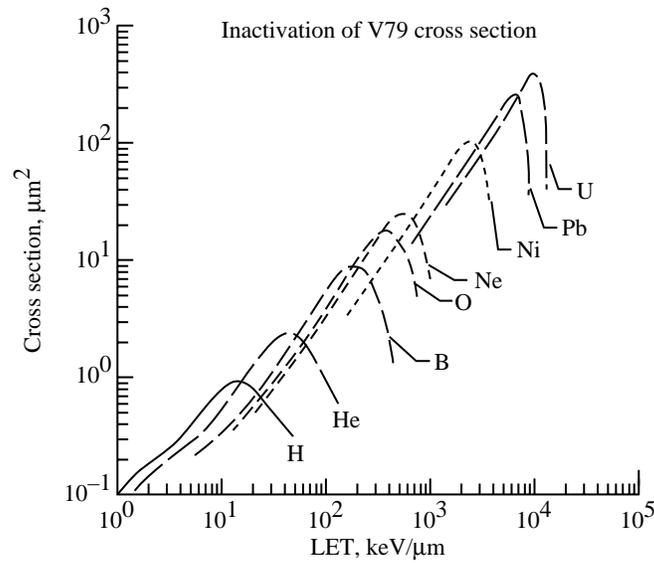
Figure 9b. Initial slope cross sections in radial dose model for inactivation of V79 cells.
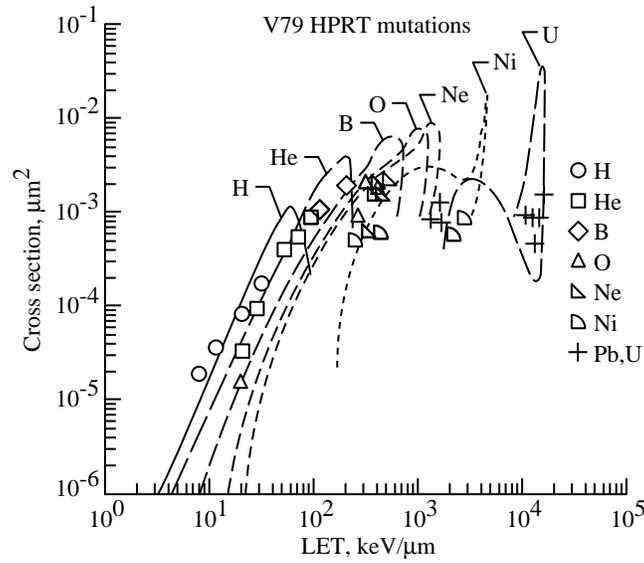
Figure 10.   Initial slope cross sections in radial dose model for HPRT mutation of V79 cells.
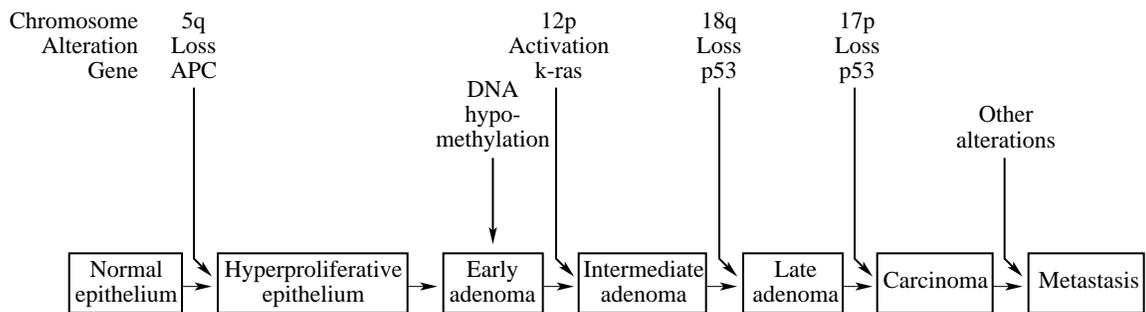
Figure 11.   Multi-stage model of Vogelstein and Kinzler for colon cancers.

CHAPTER 23

RECOMMENDED SHIELDING STRATEGIES FOR HUMAN EXPLORATION

by

Anonymous

Chapter 23

RECOMMENDED SHIELDING STRATEGIES FOR HUMAN EXPLORATION

# RECOMMENDATIONS OF WORKING GROUP A

The task of Working Group A was to recommend a strategy for the development and evaluation of materials for space use and space radiation protection. This included the materials currently used in space activities and material parameters for architecture, design methods, construction and human factors with the associated research requirements. A follow-on task will identify the parameters required for a design handbook to be used by mission planners/engineers to minimize the radiation risk to astronauts on Lunar and Mars missions.

MATERIALS/CONCEPTS

Five categories of shielding materials/concepts were identified and recommendations were generated for each category. The categories include: 1) New materials currently under development for space applications other than shielding 2) High performance shield materials 3) In-situ material utilization (e.g. regolith) 4) Combinations of materials for selective shielding of specific components and 5) Dynamic shielding concepts. Each material/concept should be evaluated using computational procedures and experimental testing (laboratory and flight as appropriate) as well as evaluating the impact of the shield material option on the entire mission. Recommendations for the validation of the shield material/concepts are also addressed.

Recommendations for 1) New materials currently under development for space applications other than shielding

A survey of existing material databases and literature should be performed to identify newly developed materials for space applications. The radiation properties for each material should be evaluated and catalogued along with other performance-related properties. Points of contact for material information exchange should be established. Both the high performing and poor performing shield materials should be noted. The newly created database should contain uniform, consistent, and traceable design data.

Recommendations for 2) High performance shield materials.

Both the high-performing and poor-performing characteristics of shielding should be identified and publicized to manufacturers of space materials in order to create a more synergistic approach to new material design. Favorable characteristics include: high electron density per unit mass, maximum nuclear cross section per unit mass, and high hydrogen content. A materials design study should be made to determine the design of practical maximum performance shields which are space stable and cost effective. Once the new materials are designed and fabricated as high performing shields, the radiation properties should be evaluated along with other performance-related characteristics and included in a database. An iterative process balancing shield performance with other performance-related characteristics will most likely take place.

Recommendations for 3) In-situ material utilization.

Many past lunar mission studies have identified the possible usage of in-situ resources, such as regolith or regolith-derived compounds, for space radiation shielding. These options have the possibility for the largest impact on mission surface operations. The requirements for in-situ material processing should be identified. Among those requirements are the design of ground operations equipment for the handling and processing of large volumes of regolith. The design of such equipment would depend on knowledge of the material sites. This would be gained in several steps in the following table.

Table 1. Lunar Materials Information Needs for In-Situ Material Characterization

• orbital reconnaissance (3m resolution)--density, surface and subsurface topography, regolith depth, mineralogy   • site selection for ground reconnaissance, angle of repose, bulking factor, flow traits, basic separation traits, abrasiveness, response to compaction, traction effects, force-displacement tests   • Earth-based tests on returned sample

Technology steps include surface reconnaissance by remote surface probes, automated remote recon, and finally a recon team for on-site data collection. A design study of surface operational equipment will then be required.

Recommendations for 4) Combinations of materials.

Possible hybrid shielding concepts require greater investigation. New combinations of materials, each possessing favorable performance-related characteristics (shielding, structural, etc.), may markedly improve synergistic possibilities for reduced launch mass. Some possible candidate material choices include the layering of various materials, regolith/epoxy mixtures, borated composites, and novel dual-use materials (e.g. Magnesium hydride as a hydrogen storage medium).

Recommendations for 5) Dynamic shielding concepts.

In addition to material selection, "dynamic" shielding concepts can also dramatically reduce parasitic shield requirements. Examples of such concepts warranting further investigation are mobile, personal, and reconfigurable shielding such as actively pumping water shielding to inhabited areas of the spacecraft or temporary use of structural elements to construct a temporary shelter from solar events such as movable flooring. More futuristic "dynamic" shielding concepts for further investigation may be the use of high-temperature superconductors for magnetic shielding or the use of plasmas.

RADIATION MATERIAL PROPERTY EVALUATION

Computational Evaluation

It is recommended that the radiation properties be evaluated relative to aluminum as illustrated in figure 1 with liquid hydrogen shown as the maximum performance limit. In this way, materials can be qualitatively evaluated while the debate ensues over the most appropriate risk model to use (dose equivalent, fluence-based, biologically based, etc.).
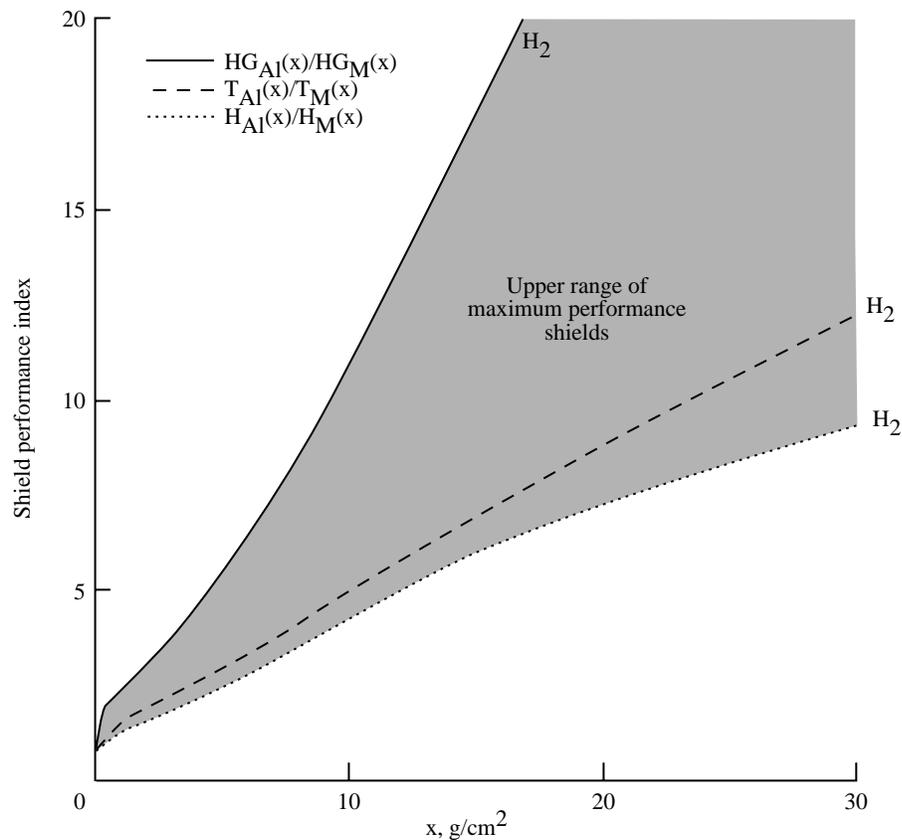

Figure 1. Maximum relative shield performance index relative to aluminum for various biological models.

It is recommended that both NASA and non-NASA codes be used for computational evaluation. A survey should be performed on the availability, applicability, and limitations of various industry tools. A written description of the survey results should be gathered in a single location.

Experimental Evaluation

Any specific mission will be designed on the basis of the current shielding codes and some testing will be required to assure that this developing technology in fact results in the anticipated protection factors. A design testing protocal must be developed with available accelerator facilities to ensure protection requirements are met. A shield materials design experiment for space exposure on International Space Station or a lunar return is highly recommended.

Mission Impact Evaluation

Ultimately, the impact of the shield materials/concept selection on the entire mission must be evaluated. The development of a 'top-level' parametric mission model is required for a meaningful trade study, including sample mission times, durations, surface stay-times, transit times, anticipated EVA's, and candidate habitat/spacecraft configurations. Shielding strategies will be required for each mission element including transit vehicles, habitats, storm shelters, EVA suits, and rovers. The development of a probabilistic solar particle event model would enhance mission impact evaluations. To accurately trade shielding strategies and options, design criteria must finally be established whether in the form of dose-equivalent limits, transformation rates, or acceptable risk, etc. Finally, guidelines addressing the impact of uncertainties on design goals and mission cost should be established.

RECOMMENDATIONS OF WORKING GROUP B

The task of Working Group B was to assess our knowledge of the physical processes and make recommendations on further requirements on database and transport code development and validation. Further emphasis on need for environment definition and risk evaluation methods are also given.

NUCLEAR FRAGMENTATION MEASUREMENTS

Ground-based measurements (i.e., at accelerators) are needed to validate the radiation transport model and associated database. Two types of experiments are required, thin-target experiments are used to evaluate cross section models used to generate the nuclear and atomic databases and thick-target are necessary to evaluate the representation of the material transmission factors by the transport models used in shield design:

1. Cross section measurements (thin-targets) (see Table 2 for summary)

   a. energy dependence of the iron fragmentation cross sections—^{56}Fe is the heaviest significantly abundant component of the GCR.

   b. light ion fragmentation cross sections to elucidate the role of nuclear structure effects in fragmentation.

   c. angle dependence of light fragments (including neutrons) produced by proton bombardment (double differential cross sections).

Table 2. Fragmentation Measurements (thin targets)

Projectile	Energy (GeV/nucleon	Target	Objective
^{1}H	0.25, 1.0	C, Al, Cu	$d^2\sigma / dEd\Omega$ (n, p, d, t, ^{3}He, α)
^{4}He	0.1–0.2, 0.6, 1.5	"" "" ""	nuclear structure
^{16}O	0.1–0.2, 0.6, 1.5	"" "" ""	nuclear structure
^{28}Si	0.1–0.2, 0.6, 1.5	"" "" ""	nuclear structure
^{40}Ca	1.5	C	nuclear structure
^{55}Mn	one energy	C, Al, Cu	nuclear structure
^{56}Fe	0.1–0.2, 0.6, 1.0, 1.5	"" "" ""	$d\sigma /dE$

The beam time required for these measurements are given in Table 3.

Table 3. Beam-time for thin-target experiments

Projectile	Approximate time needed	
^{1}H	21	days
^{4}He	3	days
^{16}O	3	days
^{28}Si	3	days
^{40}Ca	3	days
^{55}Mn	1	day
^{56}Fe	4	days

2. Thick target (fluence) measurements

Targets here are to include H_2O, composites and multiple-layered shielding materials. It is expected that many of the considerations noted by Group A will dictate targets for these measurements, and given the dynamic nature of materials science, and the short lead time required for selecting targets, we suggest deferring choices of targets until shortly before each accelerator run. The beam-time required for thick target experiments are estimated to be as follows:

8 hrs / ion / energy / target for charged particles

24 hrs / ion / energy / target for neutrons

(These times do not include beam tuning.)

LOW-DOSE RBE'S (ABOVE THRESHOLD) FOR DETERMINISTIC EFFECTS

Current radiation quality factors relate to the carcenagenic potential of the highly ionizing radiations. Quality factors required for other biological effects are expected to be quite different. Deterministic effects may pose limits in future space travel through deterioriation of the central nervous system or as early radiation syndrome. The associated RBE's for such effects as erythema, prodromal vomiting and cataracts (if considered a deterministic effect) should be included. The RBE's depend on the specific biological endpoint and should be tabulated and placed in the design handbook.

SPE (SOLAR PARTICLE EVENTS)

A probabilistic risk model for SPE protons and He ions from GOES data should be developed including particles above 100 MeV/amu and a methodology provided for applying it to given mission scenarios and shielding configurations. Ten times the October '89 event has been suggested for mission design.

ENVIRONMENTAL GCR MODEL

The present Badhwar-O'Neill GCR model is based on particle data of the more intense components as protons, helium ions, oxygen and iron flux spectra. The models need to be extended to include <u>all</u> components of the GCR in the Badhwar-O'Neill Model.

UNCERTAINTIES

Uncertainties in shield estimates arise from three sources: current inadequacies of the transport procedures and associated databases, uncertainty in environmental models, and the lack of knowledge of the biological response to space radiation exposures, especially the HZE particles. In this respect, there is a need to:

1. Document uncertainties for all Handbook quantities, in particular:

   a. low-LET risk coefficients

   b. high-LET response of risk (Q vs. L)

2. Document how uncertainties propagate--from source terms to risk. This is to be done in such a way that shielding designers will be able to use it as a design tool, plugging in the best available values for uncertainties in each quantity (i.e., environment, radiation transport, low-LET risk, high-LET dependence of Q) at the time of the design.

3. Evaluate various radiation risk models:

   a. the "modified" conventional (equiv. dose) methodology, which is presently accepted and is probably preferred at present.

   b. fluence-based (including multiple values for the radiation quality coefficient depending on charge and velocity of the ion).

   c. biologically-based LaRC model (based on cell mutation and other data in the literature).

TRACK STRUCTURE STUDIES

The density of ionization about the ion track is an important determinant of biological injury. Models have been developed based on mainly proton data and extended to heavy ions assuming effective charge for stopping. Experiments of delta-ray energy spectra, including angle dependence, for 0.1 GeV protons and 0.6 GeV/nucleon ^{56}Fe in a liquid H_2O target should be performed to test these models. The experiments will be necessary to provide data to validate a (Monte Carlo) track-structure code (that should include ionization clustering along the track). This code will be needed to ultimately understand mechanisms and to better determine risk from high-energy heavy ions. If disagreements are found then further research may be warranted.

SPACE VALIDATION OF TRANSPORT CODES (INCLUDING CAD)

The shield material concepts developed and validated in ground studies should be evaluated in the space environment as an integrated test of the design methods and models. The following experiments are recommended:

   a. fly one or two selected particle spectrometers (inside and outside payload bay) on long missions (16–90 days).

   b. spheres of different materials in payload bay with TEPC at the center of each.

   c. solid-state spectrometer for measuring LET spectra.

LIST OF PARTICIPANTS

WORKSHOP ON RADIATION SHIELDINGS

DECEMBER 6–8, 1995

Dr. Tony W. Armstrong
Science Applications Internal Corporation
Route 2
Prospect, TN 38477
Phone: 615-468-2603
Fax: 615-468-2676

Dr. Gautam D. Badhwar
NASA Johnson Space Center
Code SN
Houston, TX 77058
Phone: 713-483-5065
Fax: 713-483-5276

Mr. John F. Connolly
NASA Johnson Space Center
Mail Code SN2, Building 31
Houston, TX 77058
Phone: 713-483-5899
Fax: 713-483-5347
E-mail: connolly@snmail.jsc.nasa.gov

Dr. Michael B. Duke
NASA Johnson Space Center
Code SA
Houston, TX 77058
Phone: 713-483-4401
Fax: 713-483-9193

Mr. Bill Atwell
Rockwell Aerospace
555 Gemini
Houston, TX 77058
Mail Code SN32/31
Phone: 713-483-6194
Fax: 713-483-2696
E-mail: Atwell@Radlab.JSC.NASA.GOV

Dr. Eric Benton
University of San Francisco
Physics Department, Harney 113
2130 Fulton Street
San Francisco, CA 94117-1080
Phone: 415-422-6281
Fax: 415-422-2469
E-mail: Eric@Physics.USFCA.edu

Dr. Stanley B. Curtis
Fred Hutchinson Cancer Research Center
1124 Columbia St, MP-665
Seattle, WA 98104
Phone: 206-667-2685
Fax: 206-667-7004

Dr. Leslie Gertsch
Colorado School of Mines
Mining Eng. Dept.
1600 Illinois St.
Golden, CO 80401
Phone: 303-273-3306
Fax: 303-273-3719
E-mail: lgertsch@mines.edu

Mr. Michael J. Golightly
NASA Johnson Space Center
Code SN#
Houston, TX 77058
Phone: 713-483-6190
Fax: 713-483-2696

Dr. Andrei Konradi
NASA Johnson Space Center
Code SN3
Houston, TX 77058
Phone: 713-483-5059
Fax:
E-mail:

Dr. Jack Miller
Lawrence Berkely National Laboratory
Mail Code MS29-100
1 Cyclotron Road
Building 29
Berkeley, CA 94720
Phone: 510-486-7130
Fax: 510-486-6949
E-mail: Miller@lbl.gov.

Professor M. Eugene Rudd
Department of Physics & Astronomy
Behlen SB-58
University of Nebraska
Lincoln, NE 68588-0111
Phone: 402-472-2792
Fax: 402-472-2879
E-mail: erudd@unlinfo.unl.edu

Dr. Walter Schimmerling
NASA HQ
Code UL
Washington, DC 20546-0001
Phone: 202-358-2205
Fax: 202-358-4168
E-mail: wschimmerling@hq.nasa.gov

Dr. Lawrence Heilbronn
Lawrence Berkely Laboratory
MS 29-100
Berkeley, CA 94720
Phone: 510-486-4002
Fax: 510-486-6949
E-mail: Gunner@LBL.Gov

Dr. Jana H. MacGibbon
NASA Johnson Space Center
Code SN3
Houston, TX 77058
Phone: 713-483-5031
Fax: 713-483-5276
E-mail: Macgibbon@snmail.jsc.nasa.gov

Mr. Garry D. Qualls
AS&M Inc.
NASA Langley Reseach Center
MS 365
Hampton, VA 23681-0001
Phone: 757-864-4442
Fax: 757-864-8671
E-mail: g.d.qualls@larc.nasa.gov

Dr. Herbert Sauer
CIRES, University of Colorado
R/E/SE NOAA Space Environment Center
325 Broadway
Boulder, CO 80303
Phone: 303-497-3681
Fax: 303-497-3645
E-mail: HSauer@sel.noaa.gov

Ms. Lisa C. Simonsen
NASA Langley Research Center
MS 365
Hampton, VA 23681-0001
Phone: 757-864-4432
Fax: 757-864-8671

Mr. Mark Shavers
Texas A&M University
College Station, TX 77843-3133
Phone: 409-847-8838
Fax: 409-845-6443
E-mail: m-shavers@tamu.edu

Dr. Sheila Thibeault
NASA Langley Research Center
M/S 188B
Hampton, VA 23681-0001
Phone: 757-864-4250
Fax: 757-864-7730

Mr. Mark Weyland
Rockwell - NASA/JSC
Sn 32 - Building 31
Houston, TX 77058
Phone: 713-483-6193
Fax: 713-483-2696
E-mail: weyland@snmail.jsc.nasa.gov

Dr. Barbara Woolford
NASA Johnson Space Center
Code SP3
Houston, TX 77058
Phone: 713-483-3701
Fax: 713-483-1847

Mr. Robert R. Zimmerman
Symbiotek
265 Old Spanish Trail
Portola Valley, CA 94028
Phone: 415-851-2689
Fax: 415-851-3969
E-mail: rrzimmer@netcom.com

Dr. James Smathers
Department of Radiation Oncology
200 UCLA Medical Plaza, B 265
UCLA
Los Angeles, CA 90095
Phone: 310-825-5338
Fax: 310-794-9795
E-mail: Smathers@Radonc.UCLA.edu

Dr. Bruce Webbon
Code 239-15
NASA Ames Research Center
Moffett Field, CA 94035-1000
Phone: 415-604-6646
Fax: 415-604-1092

Dr. John Wilson
NASA Langley Research Center
MS 188B
Hampton, VA 23681-0001
Phone: 757-864-1414
Fax: 757-864-7730

Dr. Tracy C. Yang
Senior Scientist
NASA Johnson Space Center
Code SD4
Houston, TX 77058
Phone: 713-483-5583
Fax: 713-483-3058
E-mail: TYANG@PLATO.JSC.NASA.GOV

Dr. Frank Cucinotta
NASA Langley Research Center
MS 493/1200
18 Langley Blvd.
Hampton, VA 23681-0001
Phone: 757-864-1437
Fax: 757-864-7730

Mr. Paul D. Campbell
Lockheed Martin Engineering & Science
C44
2400 Nasa Road One
Houston, TX 77058
Phone: 713-483-9948
Fax: 713-483-1847
E-mail: paul.campbell@spmail.jsc.nasa.gov

REPORT DOCUMENTATION PAGE

Form Approved
OMB No. 0704-0188

Public reporting burden for this collection of information is estimated to average 1 hour per response, including the time for reviewing instructions, searching existing data sources, gathering and maintaining the data needed, and completing and reviewing the collection of information. Send comments regarding this burden estimate or any other aspect of this collection of information, including suggestions for reducing this burden, to Washington Headquarters Services, Directorate for Information Operations and Reports, 1215 Jefferson Davis Highway, Suite 1204, Arlington, VA 22202-4302, and to the Office of Management and Budget, Paperwork Reduction Project (0704-0188), Washington, DC 20503.

1. AGENCY USE ONLY *(Leave blank)*	2. REPORT DATE December 1997	3. REPORT TYPE AND DATES COVERED Conference Publication

4. TITLE AND SUBTITLE
Shielding Strategies for Human Space Exploration

5. FUNDING NUMBERS
WU 199-45-16-11

6. AUTHOR(S)
J. W. Wilson, J. Miller, A. Konradi, and F. A. Cucinotta, Editors

7. PERFORMING ORGANIZATION NAME(S) AND ADDRESS(ES)

NASA Langley Research Center
Hampton, VA 23681-2199

8. PERFORMING ORGANIZATION REPORT NUMBER
L-17661

9. SPONSORING/MONITORING AGENCY NAME(S) AND ADDRESS(ES)

National Aeronautics and Space Administration
Washington, DC 20546-0001

10. SPONSORING/MONITORING AGENCY REPORT NUMBER
NASA CP-3360

11. SUPPLEMENTARY NOTES
Wilson, Cucinotta: Langley Research Center, Hampton, VA; Miller: Lawrence Berkeley National Laboratory, Berkeley, CA; Konradi: Lyndon B. Johnson Space Center, Houston, TX

12a. DISTRIBUTION/AVAILABILITY STATEMENT

Unclassified–Unlimited
Subject Category 93   Distribution: Standard
Availability: NASA CASI (301) 621-0390

12b. DISTRIBUTION CODE

13. ABSTRACT *(Maximum 200 words)*

On December 6–8, 1995, a group of twenty-nine scientists and engineers convened a "Workshop on Shielding Strategies for Human Space Exploration" at the Lyndon B. Johnson Space Center in Houston, Texas. The provision of shielding for a Mars mission or a Lunar base from the hazards of space radiations is a critical technology since astronaut radiation safety depends on it and shielding safety factors to control risk uncertainty appear to be great. The purpose of the workshop was to define requirements for the development and evaluation of high performance shield materials and designs and to develop ideas regarding approaches to radiation shielding. The workshop was organized to review the recent experience on shielding strategies gained in studies of the "Space Exploration Initiative (SEI)," to review the current knowledge base for making shield assessment, to examine a basis for new shielding strategies, and to recommend a strategy for developing the required technologies for a return to the moon or for Mars exploration. The uniqueness of the current workshop arises from the expected long duration of the missions without the protective cover of the geomagnetic field in which the usually small and even neglected effects of the galactic cosmic rays (GCR) can no longer be ignored. It is the peculiarity of these radiations for which the interaction physics and biological action are yet to be fully understood.

14. SUBJECT TERMS
Space Radiation; Nuclear interactions; Atomic radiations; Radiation transport; Mars mission, Lunar base; Deep space travel; Biological hazards

15. NUMBER OF PAGES
456

16. PRICE CODE
A20

17. SECURITY CLASSIFICATION OF REPORT Unclassified	18. SECURITY CLASSIFICATION OF THIS PAGE Unclassified	19. SECURITY CLASSIFICATION OF ABSTRACT Unclassified	20. LIMITATION OF ABSTRACT

NSN 7540-01-280-5500

Standard Form 298 (Rev. 2-89)
Prescribed by ANSI Std. Z39-18
298-102